land

Special Issue Reprint

Land Use/Land Cover and Natural Hazards

Interactions, Changes, and Impacts, 2nd Edition

Edited by
Matej Vojtek, Andrea Petroselli and Raffaele Pelorosso

mdpi.com/journal/land

MDPI

Land Use/Land Cover and Natural Hazards: Interactions, Changes, and Impacts, 2nd Edition

Land Use/Land Cover and Natural Hazards: Interactions, Changes, and Impacts, 2nd Edition

Guest Editors

Matej Vojtek
Andrea Petroselli
Raffaele Pelorosso

MDPI

Basel • Beijing • Wuhan • Barcelona • Belgrade • Novi Sad • Cluj • Manchester

Guest Editors

Matej Vojtek
Department of Geography, Geoinformatics and Regional Development
Constantine the Philosopher University in Nitra
Nitra
Slovakia

Andrea Petroselli
Department of Agriculture and Forest Sciences (DAFNE)
Tuscia University
Viterbo
Italy

Raffaele Pelorosso
Department of Agriculture and Forest Sciences (DAFNE)
Tuscia University
Viterbo
Italy

Editorial Office
MDPI AG
Grosspeteranlage 5
4052 Basel, Switzerland

This is a reprint of the Special Issue, published open access by the journal *Land* (ISSN 2073-445X), freely accessible at: https://www.mdpi.com/journal/land/special_issues/S5B07718O5.

For citation purposes, cite each article independently as indicated on the article page online and as indicated below:

Lastname, A.A.; Lastname, B.B. Article Title. *Journal Name* **Year**, *Volume Number*, Page Range.

ISBN 978-3-7258-6378-5 (Hbk)
ISBN 978-3-7258-6379-2 (PDF)
https://doi.org/10.3390/books978-3-7258-6379-2

Contents

About the Editors

Matej Vojtek

Matej Vojtek is an Associate Professor at the Department of Geography, Geoinformatics and Regional Development, Faculty of Natural Sciences and Informatics, Constantine the Philosopher University in Nitra, Slovakia. He specializes in research on flood potential, flood hazard, and risk at various spatial scales (local, regional, and national) by applying hydrologic–hydraulic models, machine learning, and geoinformation technologies (geographic information systems—GIS, remote sensing—RS, and global navigation satellite systems—GNSS). Moreover, he focuses on the modeling and assessment of surface runoff, as well as the mapping of landslide hazard using GIS and RS applications. He currently leads two grant projects entitled "Flood Hazard Mapping with the Use of Detailed Geo-Spatial Data and Hybrid Approaches" and "Spatio-Temporal Changes and Prediction of Flood Risk in Municipalities of Slovakia".

Andrea Petroselli

Andrea Petroselli is an Associate Professor at Tuscia University (Italy), Department of Agriculture and Forest Sciences (DAFNE). He is an expert in modeling and monitoring hydrological processes. Recent research topics span from infiltration modeling to rainfall–runoff modeling. He is a member of GISTAR—GIS Terrain Analysis Research Group, a web portal for researchers and professionals involved in the investigation, development, and application of GIS-based terrain analysis tools for hydrologic and geomorphic models, and of MechHydroLab—Mechanical Engineering for Hydrology and Water Science, a multidisciplinary laboratory composed of mechanical engineers, hydrologists, and water scientists with the goal of combining mechanical engineering technologies and hydrological sciences toward the development of novel experimental systems for advanced environmental monitoring.

Raffaele Pelorosso

Raffaele Pelorosso is qualified as an Associate Professor by the Italian National Scientific Qualification in Urban and Landscape Planning and Design. His research aims to create more resilient, equitable, and sustainable cities and landscapes by adopting a systemic and spatial approach. Open-system thermodynamics forms the foundation upon which this research is developed. The low-entropy approach he has developed seeks to reduce dissipative systems by closing energy and material cycles, maximizing reciprocity, symbiosis, and cooperation among the various components of the socio-ecological systems that characterize landscape diversity and complexity. His research combines theories and case studies in urban and rural contexts, utilizing simulation models, geographic information systems, statistical analysis techniques, and stakeholder engagement. The main areas of focus include urban regeneration, performance-based planning, urban stormwater management, and climate adaptation through green and gray infrastructure, renewable energy, ecosystem services and nature-based solutions, landscape perception and participatory planning, land use and land cover changes, environmental impact assessment, and landscape connectivity. He is the author of more than 100 scientific publications and peer reviewerer for many international journals, including *Land Use Policy*, *Landscape and Urban Planning*, *Journal of Environmental Management*, *Science of Total Environment*, *European Planning Studies*, *Sustainable City and Society*, *Ecological Indicators*, and *Landscape Ecology*.

land

MDPI

Editorial

Editorial for the Special Issue "Land Use/Land Cover and Natural Hazards: Interactions, Changes, and Impacts, 2nd Edition"

Raffaele Pelorosso [1], Matej Vojtek [2,*] and Andrea Petroselli [1]

[1] Department of Agriculture and Forest Sciences (DAFNE), Tuscia University, 01100 Viterbo, Italy; pelorosso@unitus.it (R.P.); petro@unitus.it (A.P.)
[2] Department of Geography, Geoinformatics and Regional Development, Constantine the Philosopher University in Nitra, 949 01 Nitra, Slovakia
* Correspondence: mvojtek@ukf.sk

Land use and land cover (LULC) changes are among the most significant alterations of the Earth's surface, particularly following the acceleration of human-driven land transformations after the Second World War. Consequently, understanding and predicting the causes, interactions, and consequences of LULC have become major challenges for those involved in sustainable development and disaster mitigation [1]. The term 'natural hazards' has traditionally encompassed various physical phenomena, such as earthquakes, landslides, volcanic eruptions, floods, and more [2]. However, the concept of natural hazards has broadened in recent years, now including categories such as fires, meteorological/climatological, hydrological/geological, and environmental hazards [3]. This expanded definition also takes into account phenomena related to eutrophication, socio-economic impacts, and biodiversity disasters.

LULC changes significantly impact the frequency and intensity of natural hazards such as floods [4–6], landslides [7,8], heatwaves [9], wildfires [10], and erosion [11]. These changes also affect habitat composition and landscape connectivity, contributing to biodiversity loss and a reduction in ecosystem service provision [12,13]. LULC influences the quality of environmental matrices—such as water, air, and soil—either directly or indirectly (e.g., through induced climate change), impacting the natural capital essential for life and increasing associated risks for humans and other living beings [1]. To mitigate the anthropogenic pressures resulting from LULC, sustainable strategies such as restoring natural and semi-natural ecosystems, introducing nature-based solutions, and planning green infrastructure in both urban and rural landscapes are vital for enhancing the long-term resilience of socio-ecological systems [14–16].

The relationship between LULC changes and natural hazards is crucial for understanding how human activities influence the occurrence and severity of these hazards. Changes in LULC can drastically alter hydrological processes, increase vulnerability to disasters, and exacerbate the impacts of natural hazards. Therefore, beyond improving assessment and modeling tools, tailored approaches to land use planning are essential, as different land uses have varying effects on disaster risk.

The current Special Issue, 'Land Use/Land Cover and Natural Hazards: Interactions, Changes, and Impacts, 2nd Edition,' builds on the success of a previous Special Issue in the same journal, Land (https://www.mdpi.com/journal/land/special_issues/lulc_natural_hazards, accessed on 10 December 2025). The success of the previous edition, which featured 12 articles, motivated us to renew the call. This issue presents nine scientific papers—seven research articles and two reviews—that address various aspects of the LULC and natural hazard nexus at different spatial scales.

Nasrollahi et al. (List of Contributions, 1) evaluates flood adaptation strategies in Philadelphia's Eastwick, comparing levees, green stormwater infrastructure, and managed retreat under compound climate risks. Modeling shows nature-based and retreat approaches outperform levees, though no single solution suffices. Results highlight the need for integrated, multifunctional strategies considering cost, feasibility, and community preferences to effectively address future flood hazards.

Gaganis et al. (List of Contributions, 2) examines the link between reed bed burnings and wetland conversion in Greece, using Phragmites australis fires as indicators of historical wetland ecosystems. By analyzing fire patterns and land cover data, the research highlights a significant correlation between areas with frequent reed fires and former wetlands, particularly those converted to irrigated agricultural land. The findings emphasize how land use changes, such as wetland reclamation for agriculture, impact natural landscapes and contribute to ecosystem degradation. The study underscores the importance of wetland preservation and sustainable land use management to mitigate environmental hazards.

Elfadaly et al. (List of Contributions, 3) explores how urbanization and land use changes near the Giza Necropolis, including rapid expansion of urban areas, have led to groundwater level changes, threatening the Sphinx and Pyramids. Using satellite data, it analyzes the impact of land use dynamics on subsidence and water-related risks to these heritage sites, demonstrating how unregulated land changes can exacerbate natural hazards and cultural heritage vulnerability.

Benotmane et al. (List of Contributions, 4) assesses the impact of wild boar activity on soil properties in natural and post-fire environments. It highlights how land disturbance from fires and subsequent wildlife activity can alter soil chemical properties, affecting forest recovery. The study suggests that in post-fire areas, wild boars can significantly disrupt soil composition, exacerbating land degradation and influencing natural hazard risk.

Koutalakis et al. (List of Contributions, 5) examines stream bank erosion and deposition using satellite imagery and UAVs to identify erosion hotspots. It emphasizes how land use changes, particularly along watercourses, increase erosion risks. The study suggests that targeted interventions and nature-based solutions are needed to mitigate the erosion caused by human activities, highlighting the direct relationship between land use changes and increased vulnerability to natural hazards.

Ouallali et al. (List of Contributions, 6) analyzes erosion rates in Morocco's R'mel watershed, focusing on quarry activities as a major cause of sediment production. Through land use change simulations, it shows that reforestation can significantly reduce erosion compared to converting land for agriculture. This underscores the role of land management in mitigating erosion and protecting downstream areas from sedimentation hazards.

Thapa et al. (List of Contributions, 7) using geospatial analysis assesses landslide susceptibility in Nepal's Chure region, identifying land cover types, slope, and geology as key risk factors. The results show that land use, particularly deforestation and agricultural expansion, increases landslide vulnerability. The findings highlight the need for sustainable land use planning to reduce landslide risks in this fragile region.

Hanberry et al. (List of Contributions, 8) examines the interactions between land use changes and climate change in eastern U.S. forests. It highlights how human activities, such as fire suppression and increased tree density, have combined with increased precipitation to reduce wildfire frequency. However, these land use changes have also facilitated species invasions and outbreaks. The study suggests that future warming could reverse current land use and climate synergies, leading to more frequent wildfires and other forest disturbances, demonstrating the link between land use changes and heightened natural hazards.

Manandhar et al. (List of Contributions, 9) reviews the increasing frequency of urban flooding in South Asia, attributing it to rapid urbanization and unplanned land use changes, particularly the rise in impervious surfaces. The study explores flood assessment methods and highlights how land use changes, driven by urban growth, exacerbate flood risks. It calls for integrated urban planning that incorporates nature-based solutions to manage flood hazards and improve resilience to climate change-induced flooding.

Across these diverse studies, several common themes emerge, emphasizing the interplay between human activities, environmental change, and natural hazards. From the degradation of cultural heritage sites due to urban expansion to the vulnerability of landscapes to erosion and landslides, these articles underscore the urgent need for integrated approaches to environmental management and disaster risk reduction. Moreover, they highlight the importance of leveraging advanced technologies and interdisciplinary collaboration to address the complex challenges facing our planet and build more resilient communities for the future.

Nexus approaches aim at understanding connections, synergies, and trade-offs among sectors and research fields, considering impact on resources, landscape features and living beings [16]. While the articles in this Special Issue provide valuable insights into the interactions between LULC and natural hazards, there remain avenues for future research. Interdisciplinary research efforts combining remote sensing, GIS, ecology, and social sciences could enhance our understanding of the complex relationships between human activities and environmental dynamics, paving the way for more effective and sustainable approaches to land management and hazard mitigation. As we look to the future, let us continue to explore, innovate, and collaborate in addressing the pressing environmental challenges of our time.

In conclusion, urbanization, land use types, and vegetation cover all shape the risk landscape of natural disasters. Improved assessments of these phenomena at various spatial and temporal scales are essential. Effective solutions require integrated land use planning that considers multiple risk factors to reduce vulnerability and enhance resilience in the long term [17,18]. While this collection may not provide a definitive summary of the LULC/Natural Hazard nexus, we believe it will contribute to a better understanding of many processes and phenomena that occur in natural, rural, and urban environments as a result of human-induced changes. These contributions are intended to help risk managers and decision-makers adopt appropriate mitigation and adaptation actions, as well as suitable tools and frameworks for specific hazard assessments.

Funding: Funded by the EU NextGenerationEU through the Recovery and Resilience Plan for Slovakia under the project No. 09I03-03-V03-00085.

Data Availability Statement: Not applicable.

Conflicts of Interest: The authors declare no conflicts of interest.

List of Contributions:

1. Nasrollahi, F.; Orton, P.; Montalto, F. Modeling the Effectiveness of Alternative Flood Adaptation Strategies Subject to Future Compound Climate Risks. *Land* **2025**, *14*, 1832. https://doi.org/10.3390/land14091832.
2. Gaganis, C.; Troumbis, A.; Kontos, T. Leveraging Reed Bed Burnings as Indicators of Wetland Conversion in Modern Greece. *Land* **2024**, *13*, 538. https://doi.org/10.3390/land13040538.
3. Elfadaly, A.; Zanaty, N.; Mostafa, W.; Hendawy, E.; Lasaponara, R. Multi-Sensor Satellite Images for Detecting the Effects of Land-Use Changes on the Archaeological Area of Giza Necropolis, Egypt. *Land* **2024**, *13*, 471. https://doi.org/10.3390/land13040471.
4. Benotmane, K.; Boukheroufa, M.; Sakraoui, R.; Sakraoui, F.; Centeri, C.; Fehér, Á.; Katona, K. Comparative Effects of Wild Boar (*Sus scrofa*) Rooting on the Chemical Properties of Soils

in Natural and Post-Fire Environments of the Edough Forest Massif (Northeastern Algeria). *Land* **2024**, *13*, 382. https://doi.org/10.3390/land13030382.

5. Koutalakis, P.; Gkiatas, G.; Xinogalos, M.; Iakovoglou, V.; Kasapidis, I.; Pagonis, G.; Savvopoulou, A.; Krikopoulos, K.; Klepousniotis, T.; Zaimes, G. Estimating Stream Bank and Bed Erosion and Deposition with Innovative and Traditional Methods. *Land* **2024**, *13*, 232. https://doi.org/10.3390/land13020232.
6. Ouallali, A.; Kader, S.; Bammou, Y.; Aqnouy, M.; Courba, S.; Beroho, M.; Briak, H.; Spalevic, V.; Kuriqi, A.; Hysa, A. Assessment of the Erosion and Outflow Intensity in the Rif Region under Different Land Use and Land Cover Scenarios. *Land* **2024**, *13*, 141. https://doi.org/10.3390/land13020141.
7. Thapa, P.; Lamichhane, S.; Joshi, K.; Regmi, A.; Bhattarai, D.; Adhikari, H. Landslide Susceptibility Assessment in Nepal's Chure Region: A Geospatial Analysis. *Land* **2023**, *12*, 2186. https://doi.org/10.3390/land12122186.
8. Hanberry, B.; Abrams, M.; Nowacki, G. Potential Interactions between Climate Change and Land Use for Forest Issues in the Eastern United States. *Land* **2024**, *13*, 398. https://doi.org/10.3390/land13030398.
9. Manandhar, B.; Cui, S.; Wang, L.; Shrestha, S. Urban Flood Hazard Assessment and Management Practices in South Asia: A Review. *Land* **2023**, *12*, 627. https://doi.org/10.3390/land12030627.

References

1. Pelorosso, R.; Leone, A.; Boccia, L. Land Cover and Land Use Change in the Italian Central Apennines: A Comparison of Assessment Methods. *App. Geogr.* **2009**, *29*, 35–48. [CrossRef]
2. Gill, J.C.; Malamud, B.D. Reviewing and visualizing the interactions of natural hazards. *Rev. Geophys.* **2014**, *52*, 680–722. [CrossRef]
3. Debele, S.E.; Leo, L.S.; Kumar, P.; Sahani, J.; Ommer, J.; Bucchignani, E.; Vranić, S.; Kalas, M.; Amirzada, Z.; Pavlova, I.; et al. Nature-based solutions can help reduce the impact of natural hazards: A global analysis of NBS case studies. *Sci. Total Environ.* **2023**, *902*, 165824. [CrossRef] [PubMed]
4. Tasantab, J. Beyond the plan: How land use control practices influence flood risk in sekondi-takoradi. *Jàmbá J. Disaster Risk Stud.* **2019**, *11*, 1–9. [CrossRef] [PubMed]
5. Ighile, E.; Shirakawa, H. A study on the effects of land use change on flooding risks in Nigeria. *Geogr. Tech.* **2020**, *15*, 91–101. [CrossRef]
6. Hwang, S. The effect of land cover change on flooding in Texas. *J. Geosci. Environ. Prot.* **2017**, *5*, 123–137. [CrossRef]
7. Rimal, B.; Zhang, L.; Keshtkar, H.; Sun, X.; Rijal, S. Quantifying the spatiotemporal pattern of urban expansion and hazard and risk area identification in the kaski district of nepal. *Land* **2018**, *7*, 37. [CrossRef]
8. Chen, L.; Guo, Z.; Yin, K.; Shrestha, D.; Jin, S. The influence of land use and land cover change on landslide susceptibility: A case study in Zhushan town, Xuan'en county (Hubei, China). *Nat. Hazards Earth Syst. Sci.* **2019**, *19*, 2207–2228. [CrossRef]
9. Zou, Z.; Yan, C.; Yu, L.; Jiang, X.; Ding, J.; Qin, L.; Wang, B.; Qiu, G. Impacts of land use/ land cover types on interactions between urban heat island effects and heat waves. *Build. Environ.* **2021**, *204*, 108138. [CrossRef]
10. Vahedifard, F.; Abdollahi, M.; Leshchinsky, B.A.; Stark, T.D.; Sadegh, M.; AghaKouchak, A. Interdependencies Between Wildfire-Induced Alterations in Soil Properties, Near-Surface Processes, and Geohazards. *Earth Space Sci.* **2024**, *11*, e2023EA003498. [CrossRef]
11. Xiong, M.; Leng, G. Global soil water erosion responses to climate and land use changes. *Catena* **2024**, *241*, 108043. [CrossRef]
12. Pelorosso, R.; Apollonio, C.; Rocchini, D.; Petroselli, A. Effects of Land Use-Land Cover Thematic Resolution on Environmental Evaluations. *Remote Sens.* **2021**, *13*, 1232. [CrossRef]
13. Khan, M.; Bryceson, I.; Kolivras, K.; Faruque, F.; Rahman, M.; Haque, U. Natural disasters and land-use/land-cover change in the southwest coastal areas of Bangladesh. *Reg. Environ. Change* **2014**, *15*, 241–250. [CrossRef]
14. Nelson, D.R.; Bledsoe, B.P.; Ferreira, S.; Nibbelink, N.P. Challenges to realizing the potential of nature-based solutions. *Curr. Opin. Environ. Sustain.* **2020**, *45*, 49–55. [CrossRef]
15. Pelorosso, R.; Gobattoni, F.; Leone, A. The Low-Entropy City: A thermodynamic approach to reconnect urban systems with nature. *Landsc. Urban Plan.* **2017**, *168*, 22–30. [CrossRef]
16. Pelorosso, R.; Noce, S.; De Notaris, C.; Gobattoni, F.; Apollonio, C.; Petroselli, A.; Recanatesi, F.; Ripa, M.N. The nexus between connectivity, climate, and land use: A scenario assessment of bio-energy landscape connectivity in central Italy. *J. Environ. Manag.* **2025**, *376*, 124521. [CrossRef] [PubMed]

17. Su, Q.; Chen, K.; Liao, L. The impact of land use change on disaster risk from the perspective of efficiency. *Sustainability* **2021**, *13*, 3151. [CrossRef]
18. Vojteková, J.; Vojtek, M. GIS-Based Landscape Stability Analysis: A Comparison of Overlay Method and Fuzzy Model for the Case Study in Slovakia. *Prof. Geog.* **2019**, *71*, 631–644. [CrossRef]

land

MDPI

Article

Modeling the Effectiveness of Alternative Flood Adaptation Strategies Subject to Future Compound Climate Risks

Fatemeh Nasrollahi [1], Philip Orton [2] and Franco Montalto [2,*]

[1] Department of Civil, Architectural and Environmental Engineering, College of Engineering, Drexel University, Philadelphia, PA 19104, USA; fn72@drexel.edu
[2] Davidson Laboratory, Department of Civil, Environmental and Ocean Engineering, Charles V. Schaefer, Jr. School of Engineering and Science, Stevens Institute of Technology, Hoboken, NJ 07030, USA; porton@stevens.edu
* Correspondence: fam26@drexel.edu

Abstract: Climate change is elevating temperatures, shifting weather patterns, and increasing frequency and severity of extreme weather events. Despite the urgency with which solutions are needed, relatively few studies comprehensively investigate the effectiveness of alternative flood risk management options under different climate conditions. Specifically, we are interested in a comparison of the effectiveness of resistance, nature-based, and managed retreat strategies. Using an integrated 1D-2D PCSWMM model, this paper presents a comprehensive investigation into the effectiveness of alternative adaptation strategies in reducing flood risks in Eastwick, a community of Philadelphia, PA, subject to fluvial, pluvial, and coastal flood hazards. While addressing the urgent public need to develop local solutions to this community's flood problems, the research also presents transferable insights into the limitations and opportunities of different flood risk reduction strategies, manifested here by a levee, watershed-scale green stormwater infrastructure (GSI) program, and a land swap. The effectiveness of these options is compared, respectively, under compound climate change conditions, with the spatiotemporal patterns of precipitation and Delaware river tidal conditions based on Tropical Storm Isaias (2020). The hypothesis was that the GSI and managed retreat approaches would be superior to the levee, due to their intrinsic ability to address the compound climate hazards faced by this community. Indeed, the findings illustrate significant differences in the predicted flood extents, depths, and duration of flooding of the various options under both current and future climate scenarios. However, the ideal remedy to flooding in Eastwick is more likely to require an integrated approach, based on more work to evaluate cost-effectiveness, stakeholder preferences, and various logistical factors. The paper concludes with a call for integrating multiple strategies into multifunctional flood risk management.

Keywords: flood adaptation strategies; climate change; flood risk management

1. Introduction

In a world increasingly impacted by climate change, the risk of floods is escalating, particularly in urbanized landscapes. When natural permeable landscapes are transformed into impermeable surfaces, the infiltration capacity of the landscape is reduced, and the rates and volume of runoff generated by precipitation events are increased [1,2]. As climate change modifies precipitation patterns and elevates sea levels in complex and often uncertain ways, there is an urgent need for adaptive, resilient, and effective flood risk management (FRM) approaches [3].

A variety of FRM approaches are being piloted in urban areas. These can be broadly classified as resistance approaches, Nature-Based Solutions (NBSs), and community-scale transformations including managed retreat, each with a fundamentally different approach to risk reduction. Resistance approaches, such as dams and levees, provide immediate relief by physically attempting to keep water away from flood vulnerable communities. However, their static design may lead to obduracy and limit their long- term protective value, as climate change and urbanization processes continue [4]. Studies such as Jongman [4] have detailed the efficacy of resistance measures in providing protection against flood events. However, DiFrancesco [5] spotlights the inflexibility of resistance approaches in the face of climate change, also calling attention to their significant maintenance costs and potential for ecological disruption.

By contrast, NBSs and other non-structural measures, including land use planning, early warning systems, and the enhancement of natural flood management features like wetlands, present a more flexible approach. Although they may require more time to implement, NBSs offer long-term benefits that resistance approaches do not, including restoration of ecosystem features, biodiversity conservation, and other community co-benefits [6–8]. For example, Ahern [6] and Benedict [9] argue that NBSs are sustainable because they mitigate flood risks while also enhancing biodiversity, improving water quality, and providing recreational spaces. Mach et al. [10] emphasize the role of NBSs in accommodating water as part of a managed retreat strategy that also reduces the pressure on drainage systems. Eriksen [11] and Reid [12] provide examples from low-income countries where community-based NBS strategies have successfully built resilience to flooding, underscoring the importance of local knowledge and stakeholder engagement in the planning and implementation processes.

However, and despite the growing body of evidence supporting the benefits of NBSs, challenges remain in their wider adoption. These include funding limitations, the need for interdisciplinary and cross-jurisdictional planning, and the fact that it may take a relatively long time before many NBS benefits, already difficult to quantify, will accrue. NBS research needs include the development of robust methodologies for evaluating their cost-effectiveness, integrating their operation with technological advancements, and fostering policy frameworks that support the integration of green and gray infrastructure. For instance, a critical examination by Chiu [13] suggests that while NBSs can offer long-term resilience and ecological benefits, their effectiveness in extreme flood events can be limited without the support of structural measures. The study calls for an integrated approach, leveraging the strengths of both NBS and traditional methods to achieve optimal flood risk management.

The transformative, managed retreat approach to FRM gradually adjusts where and how people live in flood prone communities. Managed retreat refers to a sequence of actions, which ideally emerge from extensive community dialog, robust vulnerability assessments, and studies into potential changes in land use and repurposing of land that gradually move people and infrastructure away from flood hazard areas [14]. Advocates of managed retreat suggest that it is the only adaptation option for some communities. However, this approach needs to be undertaken carefully and with extensive input for those whose homes and lives could be impacted.

Recognizing the importance of exploring trade-offs between these three approaches, the Intergovernmental Panel on Climate Change (IPCC) and other entities have highlighted the need for studies that delve into the effectiveness of different adaptation strategies. Without such analyses, there is a risk that well-intentioned FRM strategies lead to unintended tradeoffs and consequences, typically referred to as maladaptation [3]. Cea et al. [15] provides a comprehensive overview of urban flood risk, highlighting the multifaceted challenges cities face due to complex flood sources—such as riverine, pluvial, and tidal floods—and the exacerbating effects of urbanization and climate change. The authors discuss a range of flood modeling techniques, from 1D and 2D hydrodynamic models to GIS-based and machine learning approaches, emphasizing the need for integrated models that capture both large-scale processes and fine urban details. Traditional flood defenses are reviewed alongside NBSs, with the authors advocating for hybrid approaches that blend engineered infrastructure with natural systems to boost urban resilience. The article stresses adaptive management in the face of climate uncertainty, recommending strategies such as flexible infrastructure, continuous monitoring, and community engagement to support dynamic and sustainable flood risk management [15].

This paper is a comparative analysis of three distinct flood risk reduction approaches in a Philadelphia community that is subject to compound flood risks. This community is ideal for this study because the leading FRM alternatives under consideration by local decision-makers and researchers include a resistance strategy (e.g., a levee that has been analyzed extensively by the US Army Corps of Engineers), an NBS strategy (e.g., watershed-scale green stormwater infrastructure that has emerged out of a watershed planning process), and a community-initiated proposal for managed retreat (e.g., a land swap proposed by members of a local community-based organization). Through computer simulations of flood exposure under historical and future climate scenarios, the study aims to compare the efficacy of each approach in mitigating flood risks. We are specifically interested in whether the newly conceptualized NBSs and managed retreat approaches offer benefits over the more extensively studied USACE levee.

2. Materials and Methods

2.1. Site Description

Eastwick, as depicted in Figure 1, is a mostly Black environmental justice community located at the downstream end of a 205 km^2 largely suburban watershed near the confluence of the Darby and Cobbs creeks, about 5 km from their confluence with the Delaware River. It is a low-lying community that presently experiences frequent fluvial flooding and in the future also coastal flooding [16] with most of the community within the FEMA 100- and 500-year floodplains. Eastwick meets the criteria outlined by the Environmental Protection Agency (EPA) for an Environmental Justice community, with a majority (76%) Black population, and pockets of low-income residents. Currently, there is insufficient information available on how to reduce Eastwick's long-standing flooding problem. Situated close to the 1.2 km^2 John Heinz National Wildlife Refuge, Eastwick is also adjacent to portions of the Lower Darby Creek Superfund Site. This proximity increases the health risks associated with any flooding events in the area. The combination of environmental challenges, frequent flooding, and demographic characteristics underscores the need for comprehensive assessment and planning to address the many resilience needs of the Eastwick community.

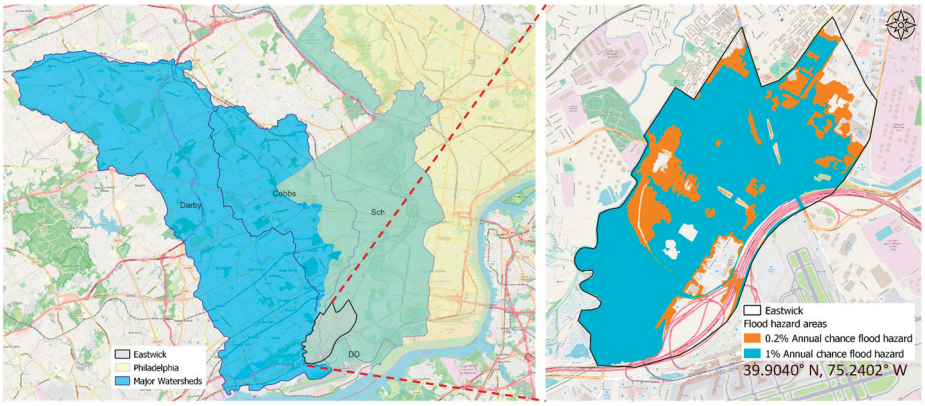

Figure 1. Study area, Eastwick. The map on the left shows that most of Eastwick lies within the 100-year floodplain, with only limited areas (in orange) falling within the 500-year floodplain.

2.2. Flooding in Eastwick Caused by Tropical Storm Isaias

Eastwick has flooded for decades. As of this writing, the most recent extreme flood occurred in August of 2020 when extreme precipitation in the upper reaches of the watershed (Figure 2) brought about by Tropical Storm Isaias, produced high riverine flows that persisted through two full tidal cycles. This storm inundated large parts of Eastwick under almost 1 m of water and required the evacuation of residents. When the flood waters receded, several blocks were rendered uninhabitable. Tropical Storm Isaias deposited nearly 203 mm of rain in the upper suburban portions of the watershed and only 63.5 mm in Eastwick where flooding was worst (Figure 2). In this region, climate change is expected to exacerbate these conditions in the years to come.

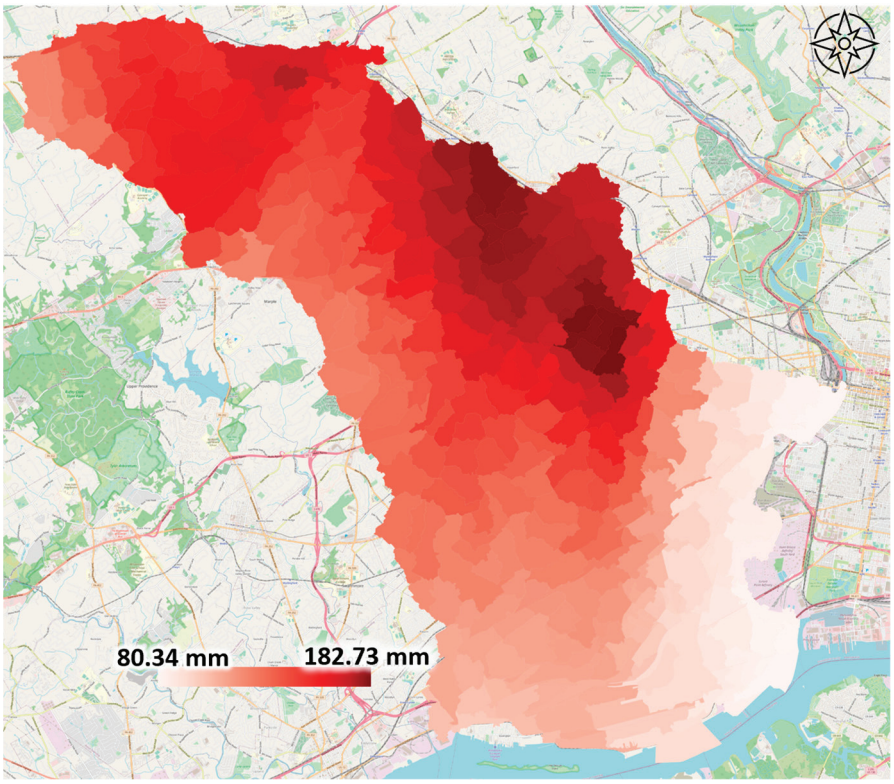

Figure 2. Gage-Adjusted Radar Rainfall (GARR) map of the Darby-Cobbs Watershed during Tropical Storm Isaias. The map indicates that most precipitation occurred in the upper watershed and not Eastwick. The most significant flooding took place downstream in the watershed and in Eastwick.

2.3. Model Development

An integrated 1D-2D H&H model was developed, calibrated, and validated to represent the flooding in Eastwick. A detailed description of the model is provided elsewhere [17,18], with only a summary provided here.

The model was developed in PCSWMM (Guelph, Canada), a proprietary version of EPA SWMM. The model domain includes the watersheds associated with Darby and Cobbs creeks, a composite area consisting of approximately 205 km^2 of largely suburban and urban land uses. The regions upstream of Eastwick were modeled in 1D, while Eastwick itself was modeled in 2D, as described below. The model is built on a 1 m resolution LIDAR-based raster DEM (2018) merged with boat-surveyed bathymetric data from the USACE, impervious surfaces, soil types, land use, and stream centerlines from the Pennsylvania Spatial Data Archive (PASDA), and field surveying of select bridges, culverts, and storm drains. PCSWMM's Watershed Delineation Tool was used to discretize the entire watershed into subcatchments that were between 0.936 and 342.364 ha in size. The % impervious, slope, area, and width of the subcatchments were established based on the geospatial datasets described above. Table 1 displays the Manning's n and depression storage values used for different surface types. Subarea routing was to the subcatchment outlet and the percent routed was 100%. Infiltration was modeled using the Green Ampt equation with capillary suction, saturated hydraulic conductivity derived from the watershed soil types (principally silty loam). Though only event-based simulations were performed, monthly average evaporation values were loaded into the model; groundwater was neglected after inspecting several recent geotechnical boring reports which suggested that water tables were significantly below existing grade. Baseflows were added to Darby and Cobbs creeks based on an analysis of several years of summer dry weather flows as reported by USGS on the two gage sites: Darby Creek, near Darby, PA (01475510), Cobbs Creek at Mt. Moriah Cemetery (01475548). Steady baseflow rates of 1.5 cms and 0.5 cms, respectively, were assumed for Darby and Cobbs creeks. Model boundary conditions include streamflow from USGS01474500 at the Schuylkill River dam, and Delaware River water levels measured by NOAA at the Ben Franklin Bridge (Gage ID: 8545249) and Marcus Hook (Gage ID: 8540433). Each 1D-2D simulation began 12 h before the target rainfall to let the various surface water bodies fill up, initializing the model.

Table 1. Subcatchments properties.

Subcatchment Parameters	Source
Area	Per PCSWMM watershed delineation tool, vary from 0.936 to 342.364 ha
Width	Per PCSWMM watershed delineation tool, vary from 96.72 to 6113.68 m
% slope	DEM
% impervious	PASDA
Mannings values (for overland flow over the impervious and pervious sub-area)	N Imperv: 0.012 N Perv: 0.13
Depression storage values	Imperv: 0.2 in, Perv: 0.3 in
%zero impervious	0
Subarea routing	Outlet
Percent routed	100
Infiltration	Green Ampt
Groundwater	Not included

In the larger watershed, the layout of the drainage network was based both on the PASDA stream centerline layers and flow pathways identified through the watershed delineation process. Details regarding the engineered drainage system in the larger watershed were not available to the project team. Thus, conduits used to represent upstream flow pathways were assumed to be open channels except for those representing 10 locations in the Cobbs watershed, and 9 locations in the Darby watershed where the respective creeks pass under overpasses. In these locations, the creek was represented as a rectangular culvert with dimensions based on field surveying conducted by the research team. All the inverts and slopes are based on bathymetric data made available to the project team, the DEM, and best professional judgment. Manning's roughness values for the center, left, and right overbanks were established based on [19,20] with an average of 0.05 across the channels and an average of 0.085 for the banks. Cross sections of the larger streams, as the boundaries of the watershed model, and Darby Bay are imported from a HEC-RAS model shared by AKRF [21].

Because the study involves the potential for water to back up at hydraulic constrictions, flow through the hydraulic system was modeled using a dynamic wave with 0.5 s computational time steps (per PC-SWMM recommendation for 2D modeling). Unlike the kinematic wave routing method, it allows simulation of hydraulic phenomena like backwater effects, flow reversals, pressurized flow, and energy losses at entrances and exits [22]. The timesteps were 15 min, 10 min and 5 sec for reporting, dry/wet weather and routing, respectively. All the nodes were assigned 9.3 sqm (100 sf) of ponded area. Precipitation from a quality-controlled, gage adjusted radar rainfall (GARR) product, produced at 1 km^2 resolution by Vieux Associates, was applied to the subcatchments.

2.3.1. One-Dimensional and Two-Dimensional Flow Pathways

In the upstream sections of the watershed, the outlet of each subcatchment was set to the closest 1D node, from which it flows through the 1D drainage network until if and when it encounters a 1D–2D connection node that allows it to enter the 2D surface used to represent Eastwick.

The 2D mesh was only included in the low-lying region encompassing and surrounding Eastwick (e.g., all portions of the watershed below 6 m in elevation). The 2D hexagonal mesh had a resolution of 7.6 m, 13.7 m and 30.5 m for the water pathways (such as streams and streets), main land surface, and the open water bodies, respectively (Figure 3).

Unlike in the upstream portions of the model, in Eastwick some information about the drainage network was available. In this version of the model, only the main trunk lines of Eastwick's drainage system were included (Figure 4). Other drainage flow paths were simplified, and flow could leave the mesh through the creek system, as well as through six pump stations in Mingo Creek. The pour points of subcatchments within the area covered by the mesh were set to the nearest 1D nodes. The pour points of several subcatchments that were >25 m from the nearest segment of the skeletonized drainage system were reassigned to the 2D node closest to their centroids. The 1D nodes were connected to 2D nodes through the use of the rectangular (3 m $\times$ 3 m) bottom orifices that allowed the water to move unobstructed between the 1D and 2D model elements (Figure 5). Water on the mesh flowed through 2D conduits connecting the 2D nodes in the direction of the topographic gradient. A total of 91,378 hexagonal mesh elements were included in the model, with no seepage. The 2D conduits have a roughness of 0.06, 0.035, 0.05, 0.1 and 0.15 for streams, streets, grassland, developed and forest lands, respectively, and slopes based on the DEM. The Manning's roughness values for the 2D mesh were established based on values suggested by Multi-Resolution Land Characteristics (MRLC) Consortium [23]. An initial depth of

0.6 m was assigned to all the 2D nodes within the streams and a large impoundment located inside the Heinz Wildlife Refuge.

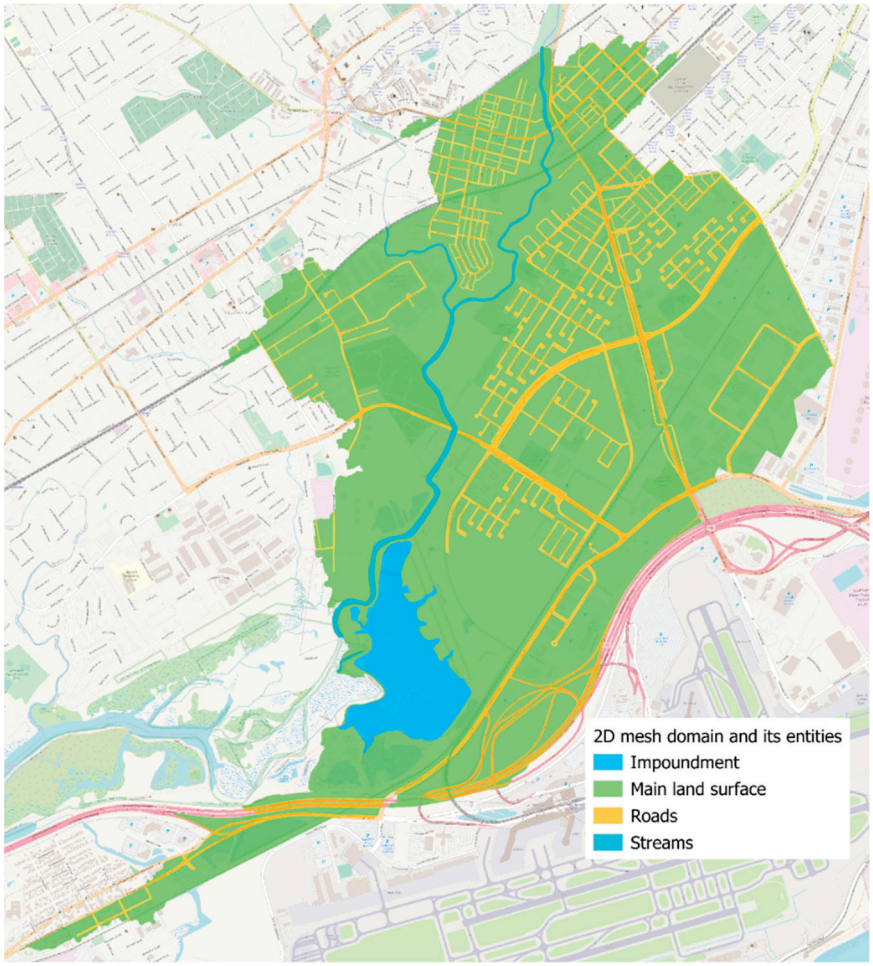

Figure 3. Map of the 2D PC-SWMM model domain.

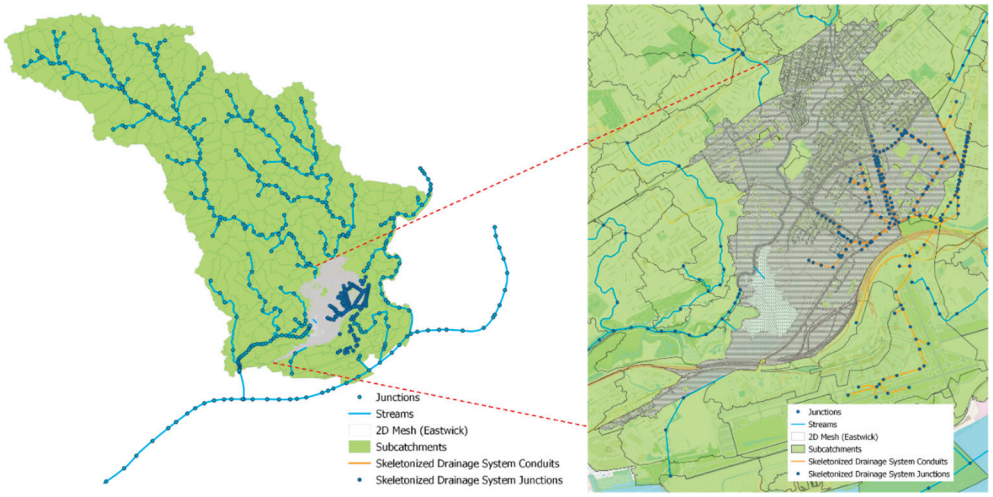

Figure 4. PC-SWMM integrated 1D–2D watershed model with skeletonized drainage representation in Eastwick.

It is worth noting that determining the appropriate degree of resolution to use to represent the subcatchments and drainage system within the 2D mesh area is an ongoing area

of our research, with a paper comparing low and high resolution with both skeletonized and all pipes representation of the drainage system in preparation.

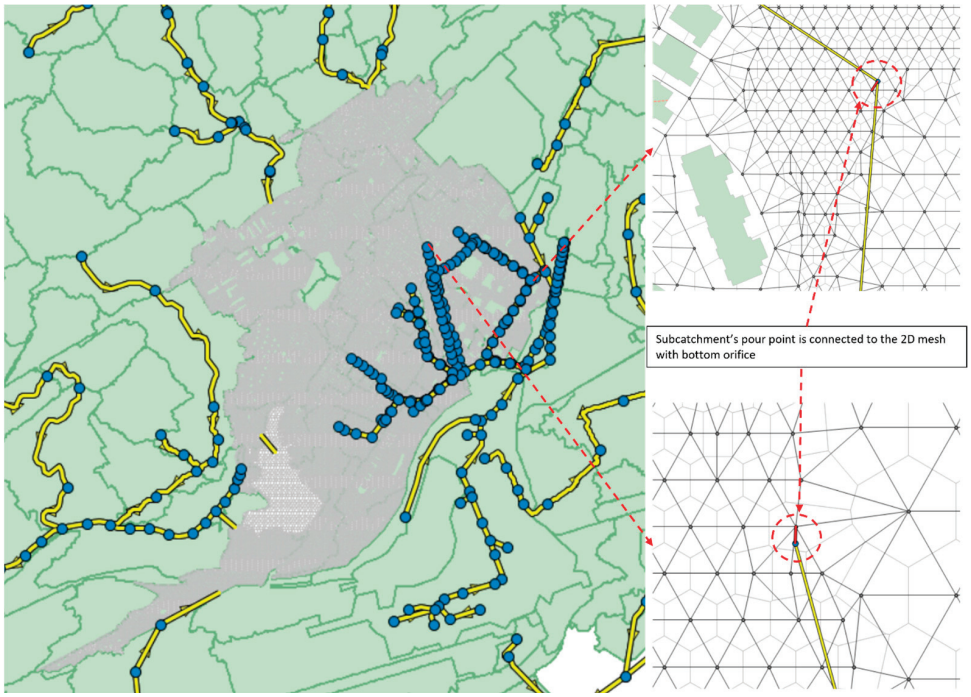

Figure 5. The 2D mesh domain (**left**) and connection of the mesh elements to the pipes (**right**) using bottom orifice in the skeletonized drainage model.

2.3.2. Model Calibration and Validation

In this version of model, calibration and validation processes were used to select the proper level of resolution to use in the model design, as well as to assess the goodness of fit of the model predictions. The 2D model was calibrated using various parameterizations of the drainage network, with the skeletonized approach selected to achieve a balance between computational efficiency and accuracy [18]. Table 2 summarizes the steps required to develop the skeletonized model from the original watershed model.

Table 2. Steps required to create skeletonized model.

Task Number	Task Description	Level of Effort (Hours, Days, or Weeks)
2.1	Insert and parameterize junctions and conduits representing a skeletonized version of the collection system into the model (provided by PWD in this case)	hours
2.2	Generate the 2D mesh from the DEM with buildings represented as obstacles	hours
2.3	Connect the 2D mesh to the broader natural drainage system and to the skeletonized drainage system using bottom orifice. Add the initial depth to 2D junctions within the streams and the impoundment	hours
2.4	Reassign the pourpoints of the existing subcatchments to junctions used to represent the collection system and/or to the nearest 2D mesh junction for subcatchments located that do not overlap spatially with the skeletonized collection system model	hours

For the validation, as described in Nasrollahi et al. [17], simulated runoff hydrographs were compared to stream stage observations at USGS gages 01475510 (Darby Creek, near Darby, PA), 01475548 (Cobbs Creek at Mt. Moriah Cemetery), and 0147553 (84th Street) for Tropical Storm Isaias (2020), as well as Hurricanes Irene and Lee (2011).

2.4. Adaptation Strategies

Three adaptation scenarios are quantified, assessed, and compared. These three approaches represent three of the leading approaches to FRM under consideration in urban areas: the NBS approach (#1), the resistance approach (#2), and managed retreat (#3). Each of these approaches is described in greater detail below.

2.4.1. Approach #1: Optimized Watershed-Scale NBS Approach Featuring Green Stormwater Infrastructure (GSI)

Approach #1 utilizes GSI to capture stormwater in the upstream watershed, theoretically to reduce downstream flooding in Eastwick. Since the precise level of GSI that would be required to reduce flooding was not known, the model was used to compare the effectiveness of different GSI schemes at reducing flooding associated with TS Isaias. These schemes differed from one another based on the percent of impervious area treated and the hydraulic loading ratio (HLR) (e.g., the ratio of a GSI practice's catchment area to its own area) associated with replicate GSI facilities, each assumed to be a 28 m^2 (e.g., 300 sf) bioretention practice (Figure 6).

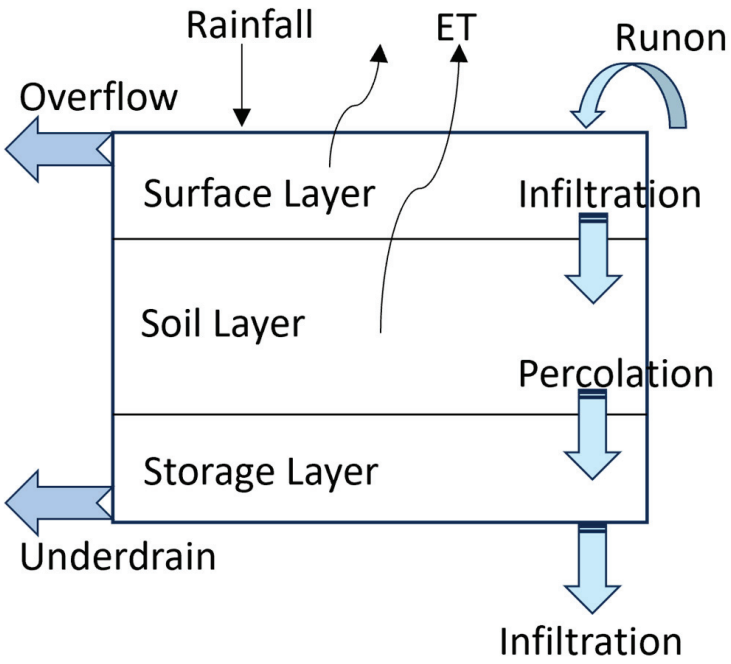

Figure 6. Conceptual diagram of a bio-retention cell LID (Source: Storm Water Management Model (SWMM) User's Manual Version 5.1. EPA [1].

This analysis, described in greater detail in Nasrollahi et al. [24], began by contacting the 31 upstream communities to quantify the level of GSI each intends to implement as part of its ongoing effort to comply with local and federal water quality regulations. The towns are required to manage stormwater to comply with federal (e.g., Clean Water Act), state (e.g., PA Stormwater Management Act of 1978-Act 167), and county clean water regulations. Because water quality impairment of the Darby and Cobbs creeks is primarily due to sediment inputs, stormwater management goals—articulated through Pollutant Reduction Plans (PRPs)—strive to reduce sediment loading. As of this writing, 26 of the

31 municipalities have publicly made these plans, making up roughly 4/5 of the land area within the watershed. Nine of the 26 municipalities (Upper Darby, East Lansdowne, Yeadon, Darby Township, Collingdale, Morton, Sharon Hill, Darby Borough, Glenoldon) collaborated to form the Eastern Delaware County Stormwater Collective (EDCSC) and submitted one PRP. The municipalities are required to update their PRPs every five years, A total of 18 PRPs were reviewed by the authors.

Based on the type and area of stormwater best management practices (BMPs) cited in the current round of PRPs, we estimate that NBS approaches to stormwater management, including GSI, could treat, at most, 12% of the impervious areas of the watershed (or 5% of the total watershed area as shown in Table 3. The project team conducted some preliminary model runs and concluded that this level of NBS application would be inadequate to reduce flooding in Eastwick under an event like TS Isaias.

Table 3. Final % treatment of the watershed and impervious surfaces based on the current round of the PRPs.

WS area	170 km^2
WS imp area	65 km^2
GSI area	8 km^2
% WS area treated	5%
% imp area treated	12%

To determine what level of NBS would provide a flood mitigation benefits, additional modeling was performed assuming that upstream GSI was in the form of replicate bioretention facilities, each 28 m^2 in area, that receive runoff from catchment areas that are between 5 and 10 times their size (e.g., their hydraulic loading ratios—or HLRs were varied to between 5 and 10. Multiple model runs were performed treating 0–40% of the total watershed (or 0–80% of the impervious areas)–see Table 4.

Table 4. GSI Modeling Assumptions.

Prototypical GSI Type	Prototypical GSI Area	HLR Range	% Watershed Treated	% Impervious Area Treated
Bioretention	300 sf	5–10	0–40%	0–80%

We selected bioretention due to its suitability for retrofit applications in urban and suburban land uses. Key operating parameters, such as hydraulic loading ratio, berm height, soil composition, porosity, and infiltration rates, were based on industry standards for urban stormwater management and adapted to match the specific hydrologic conditions of the Darby-Cobbs watershed. Bioretention was added to the model uniformly using PCSWMM's LID controls. This analysis revealed that if 65% of the watershed's impervious surfaces were directed to 28 m^2 bioretention practices, each of which treated runoff from an area 5× its size (e.g., HLR = 5), fluvial flooding of Eastwick during TS Isaias would have been significantly mitigated. This scenario, which would treat stormwater flows from 25% of the total watershed area, an area roughly equivalent to all of its parking lots, rooftops, and some roadway surfaces, is defined as Approach #1. Table 5 summarizes other parameters used to represent the GSI in the model.

Table 5. Bioretention area properties associated with Approach #2.

Bioretention Parameter	**Value**
Berm height (cm)	20.32
Vegetative Cover (fraction)	0
Surface roughness (Manning's n)	0.1
Surface slope (percent)	1
Soil Thickness (cm)	91.44
Porosity (volume fraction)	0.52
Field capacity (volume fraction)	0.15
Wilting point (volume fraction)	0.08
Soil Conductivity (cm/h)	11.94
Conductivity slope	39.3
Suction Head (cm)	4.83
Storage Height (cm)	91.44
Storage Void Ratio (voids/solids)	0.8
Seepage Rate (cm/h)	1.27
Storage Clogging Factor	0
Drain coefficient (cm/h)	0
Drain exponent	0.5
Drain offset height (cm)	15.24

2.4.2. Approach #2: Physical Protection Approach Proposing Constructing a Levee in Eastwick

Approach #2 was developed based on the Tentatively Selected Plan (TSP) of the US Army Corps of Engineers (USACE) for a FRM strategy for Eastwick [25]. In partnership with the Philadelphia Water Department (PWD), USACE has proposed a levee along the east bank of Cobbs Creek, situated within the city-owned Eastwick Regional Park and Clearview Landfill (Figure 7). The USACE levee design is based on extensive analysis and engineering studies by the Corps. The top of the levee is proposed at an elevation of 7.5 m (24.7 feet NAVD 88), with a section designed for managed overtopping at a slightly lower elevation of 7.2 m (23.7 feet NAVD 88, Figure 7). This TSP aims to mitigate fluvial flood risks associated with Darby and Cobbs Creek water levels up to the 1% Annual Exceedance Probability (AEP), with levee overtopping expected during more significant flood events, and additional optimization of the design expected in future project design phases.

The levee would primarily reduce fluvial flooding in Eastwick. However, as acknowledged by the USACE [26], by keeping Cobbs Creek flows out of Eastwick, the levee would induce flooding at points upstream and downstream and on the west side of Cobbs Creek. Compared to the fluvial condition, the levee is assumed less effective at managing pluvial, coastal, and compound flood events.

To simulate Approach #2, the elevations of the 2D mesh nodes located within the proposed levee alignment were raised to the USACE top of berm elevation (Figure 8).

Figure 7. Levee location and alignment along the east bank of Cobbs Creek, situated within the city-owned Eastwick Regional Park and Clearview Landfill.

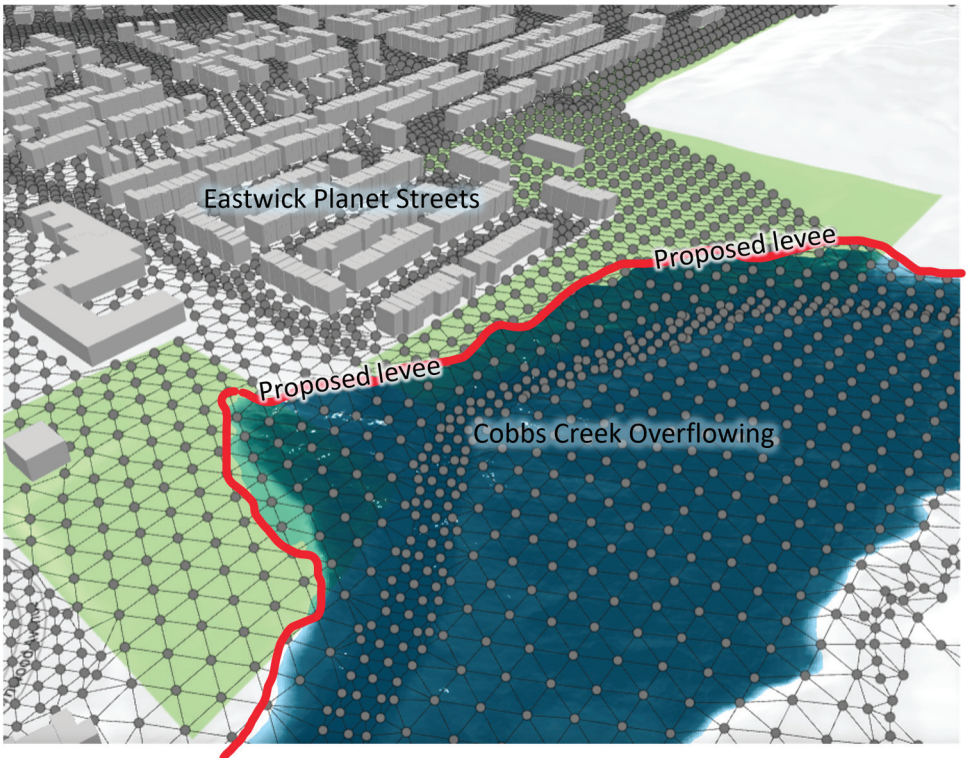

Figure 8. Levee protection along Cobbs Creek.

2.4.3. Approach #3: Managed Retreat Approach That Would Move Eastwick Residents to Higher Elevations Through a Land Swap Proposal

Approach #3 is a land swap concept that was conceived by Eastwick United Community Development Corporation, translated into a physical design by Drexel University design students, and eventually refined into a concept plan (Figures 9 and 10) by a Philadelphia-based urban design firm (Olin) working with the research team. The plan is only feasible because the City of Philadelphia owns a large tract of vacant land in Eastwick, a portion of which lies above the present day 500-year flood plain. Through the proposed land swap, flood-prone Eastwick homeowners would be allowed to swap title with the City and move to new flood-resilient housing constructed at higher elevation land. The design is attractive to some Eastwick residents because it does not require participation of upstream communities (as is required by Approach #1, the NBS approach), would not require Congressional approval and funding (like Approach #2, the levee), and would enable residents to reduce their flood risk without having to permanently leave the community.

Figure 11 shows the locations of flood prone households (in orange) that would be relocated to the new development (in yellow). The vacated area would be restored to a new fluvial floodplain and ecologically restored to freshwater tidal wetlands. An earthen berm would be constructed behind the wetlands using the regraded material. The design also calls for recontouring of a second parcel of vacant land located to the NE of 84th street (e.g., the decommissioned Pepper School) so that it can serve as a detention basin for coastal flood waters entering Eastwick from the south.

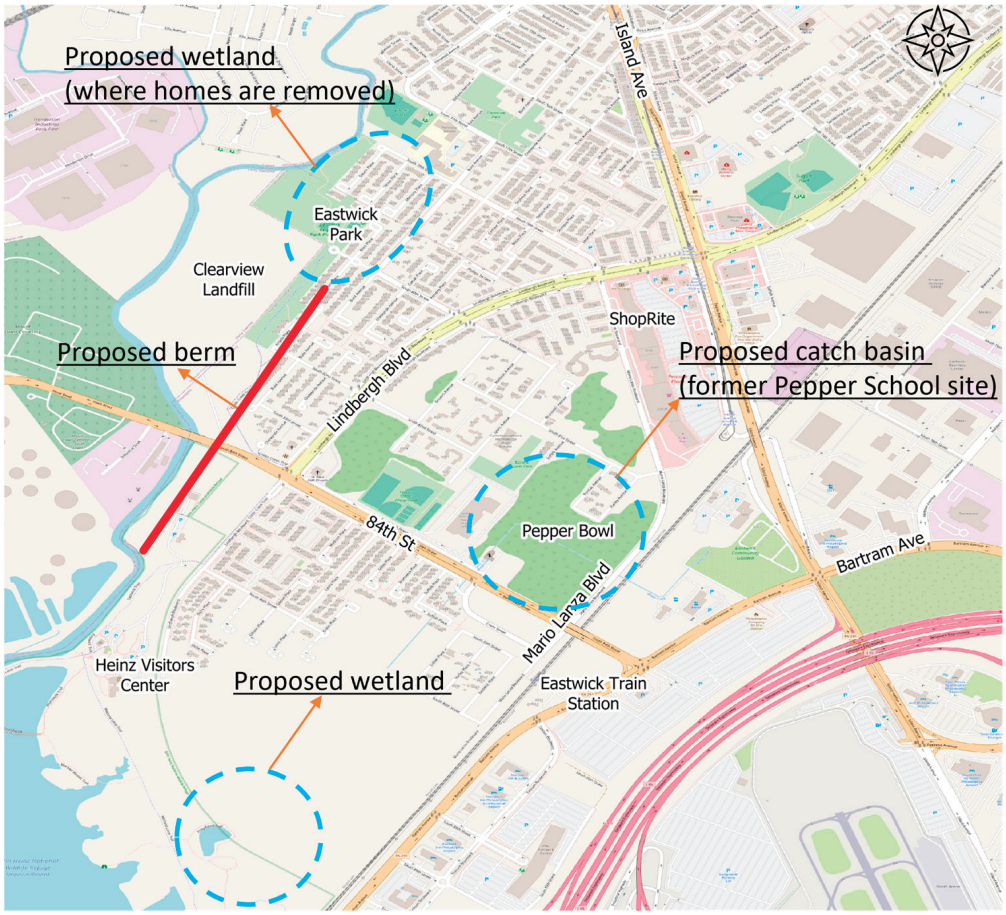

Figure 9. Proposed modifications to the existing condition in land swap design.

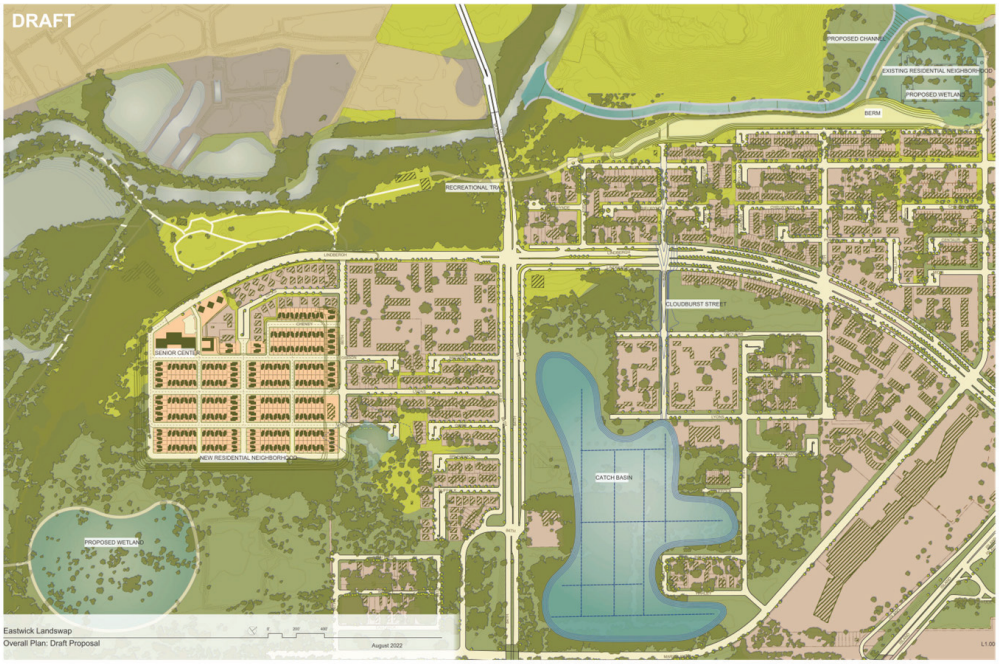

Figure 10. Draft of land swap design.

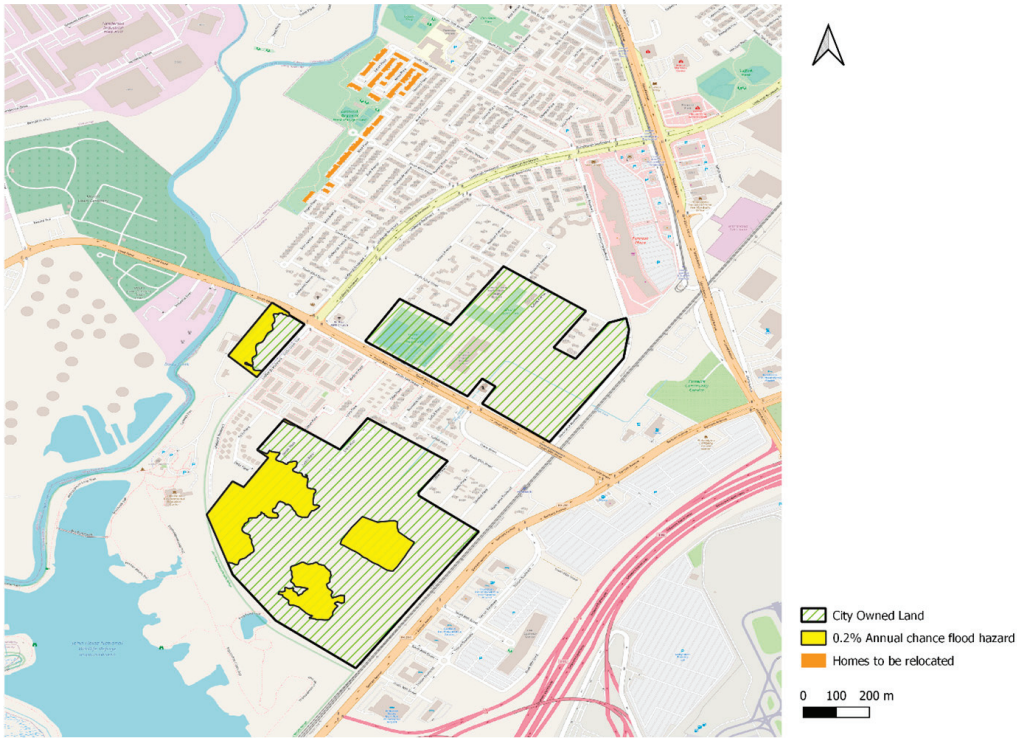

Figure 11. Land swap map of city owned lands and relocated homes.

To construct the land swap model a modified DEM that contained all the land swap features was utilized to regenerate the 2D mesh. The relocated houses near Cobbs Creek and the Pepper School were removed from the building layer that was used to indicate surface obstructions to flow. Once the new 2D mesh was created, the elevations of the 2D mesh junctions along the alignment of the proposed earthen berm were raised to elevations between 4.4 and 7.5 m per the proposed plan.

2.5. Climate Change Scenarios

To compare the effectiveness of the three different adaptation approaches, each model was subjected to two different climatic forcing scenarios. In Scenario #1, the models were forced with GARR precipitation and Delaware River and Schuylkill River water levels as recorded during TS Isaias. In Scenario #2, the time series representing precipitation and the tidal boundary conditions were made more severe to reflect high-end, late-century projections of compound climate change in the Philadelphia region (e.g., 50% increase in precipitation intensity and 1.2 m of sea level rise).

From a climate adaptation planning perspective, the conditions assumed in Scenario #2 are conservative, but also plausible given the latest climate projections for the Philadelphia region [16,27]. The use of conservative climate change projections to ensure preparedness and resilience against the increasing frequency and intensity of such events is recommended by the Philadelphia Water Department and its consultants [27], who also estimate that 100 year, 24 h rainfall amounts could increase by 50% by end of century [27].

The late century SLR scenario is based on the IPCC AR6 projections for Philadelphia (SSP5 8.5, 95th percentile) following [28]. This SLR value aligns with other estimates, illustrating the consistency in SLR projections across different research efforts, even considering emission reductions in the RCP 8.5 trajectory [29].

2.6. Metrics

Flooding associated with TS Isaias under both existing (Scenario #1) and future climate changed (Scenario #2) conditions were simulated for Adaptation Approaches #1, #2, and #3. Metrics used to compare the scenarios include:

I. Color coded maps of peak flood depths
II. Maps depicting avoided flooding associated with each approach, when compared to baseline conditions
III. Box plots depicting the max flood depths for 2D junctions in the streams
IV. Bar chart depicting the percentage of flood reduction area

3. Results

Figure 12 includes maps that compare peak flood extent and depths simulated for baseline conditions and Adaptation Approaches #1, #2, and #3 under Climate Scenario #1. The maps use a color gradient, where red-orange denotes deep flooding of greater than 4 m, and green-blue denotes shallow flooding of less than 3 m. Compared to existing conditions, peak flood extent is reduced the most with Approach #1, followed by Approach #2, and the least by Approach #3. Note that Approach #1 is the only approach to completely eliminate flooding.

Figure 13 includes maps comparing peak flood extent and depths simulated for baseline conditions when Approaches #1, #2, and #3 are subjected to Climate Scenario #2. Comparing Figure 12a to Figure 13a, it is evident that without adaptation, flooding associated with a storm like TS Isaias would increase due to climate change. Under Climate Scenario #2, Approach #1 is the most effective at reducing flooding, Approach #2 is the least effective, and Approach #3 of intermediate effectiveness. It is noteworthy that while all three approaches reduce flooding, none completely eliminate flood risk under Climate Scenario #2.

Figure 14 presents the effectiveness of different flood adaptation scenarios in eliminating flooding under Climate Scenario #1. Orange overlays depict areas that flooded under baseline conditions (e.g., no adaptation) but did not flood under each of the respective adaptation approaches. As was evident in Figures 12b and 13b, Approach #1 eliminated the greatest amount of flooding, including in areas outside of Eastwick. Both Approach #2 and Approach #3 eliminated a significant amount of flooding in Eastwick, with #2 slightly better than #3.

Figure 15 presents the effectiveness of different flood adaptation scenarios in eliminating flooding under Climate Scenario #2. The results are similar to those obtained with Climate Scenario #1. As was evident in Figures 12b and 13b, Approach #1 eliminated the greatest amount of flooding, including in areas outside of Eastwick. Both Approach #2 and Approach #3 eliminated a significant amount of flooding in Eastwick, with #2 slightly better than #3.

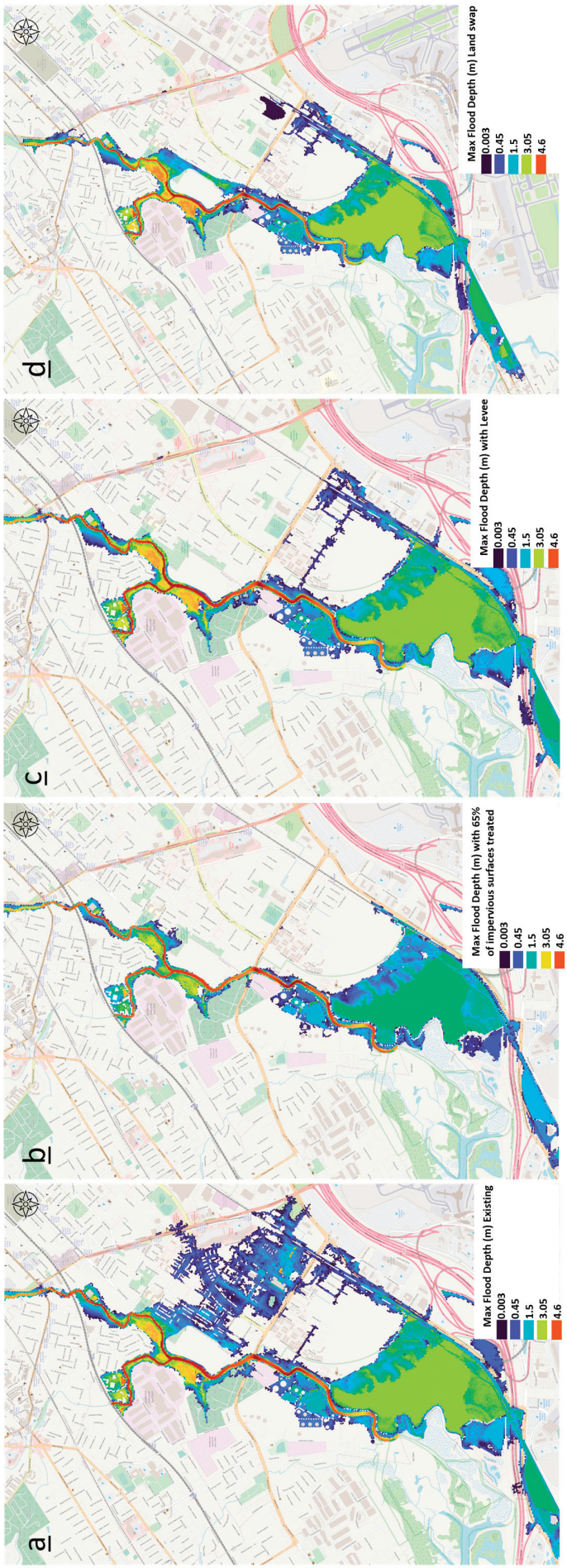

Figure 12. Flood inundation maps with and without adaptation approaches and with Climate Scenario #1 (TS Isaias) (**a**) Existing/no approach (**b**) Approach #1 (GSI) (**c**) Approach #2 (Levee) (**d**) Approach #3 (Land swap).

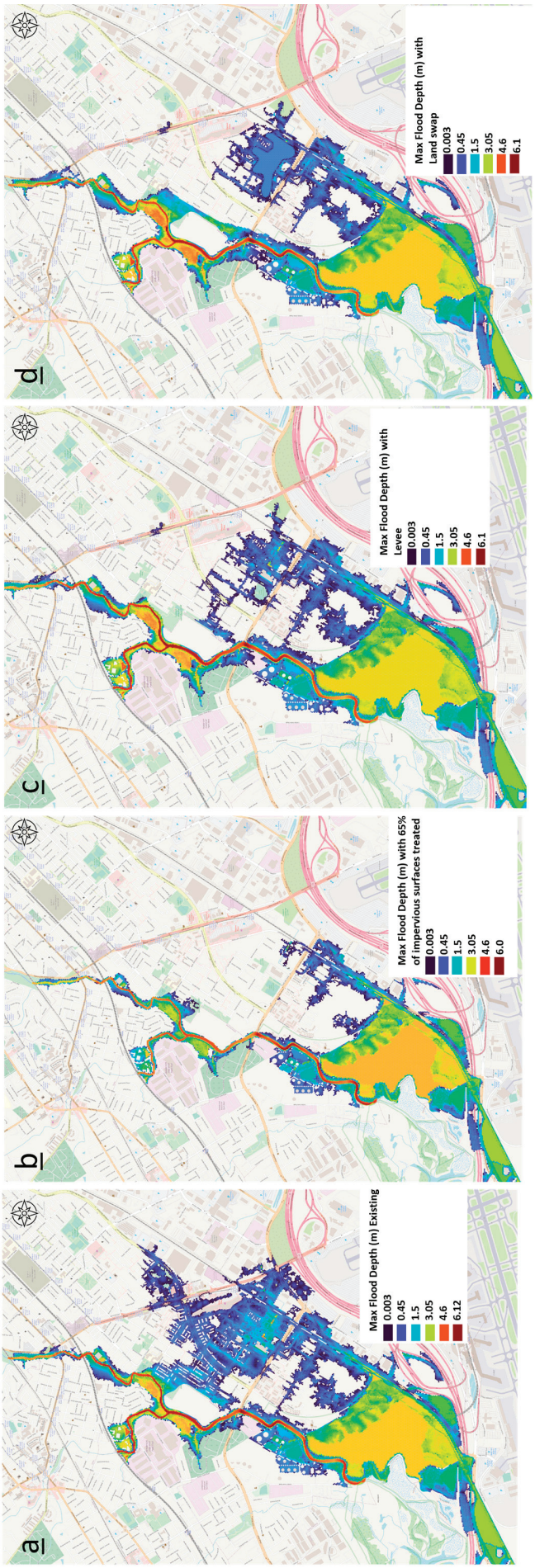

Figure 13. Flood inundation maps with and without adaptation approaches and with Climate Scenario #2 (TS Isaias) (**a**) Existing/no approach (**b**) Approach #1 (GSI) (**c**) Approach #2 (Levee) (**d**) Approach #3 (Land swap).

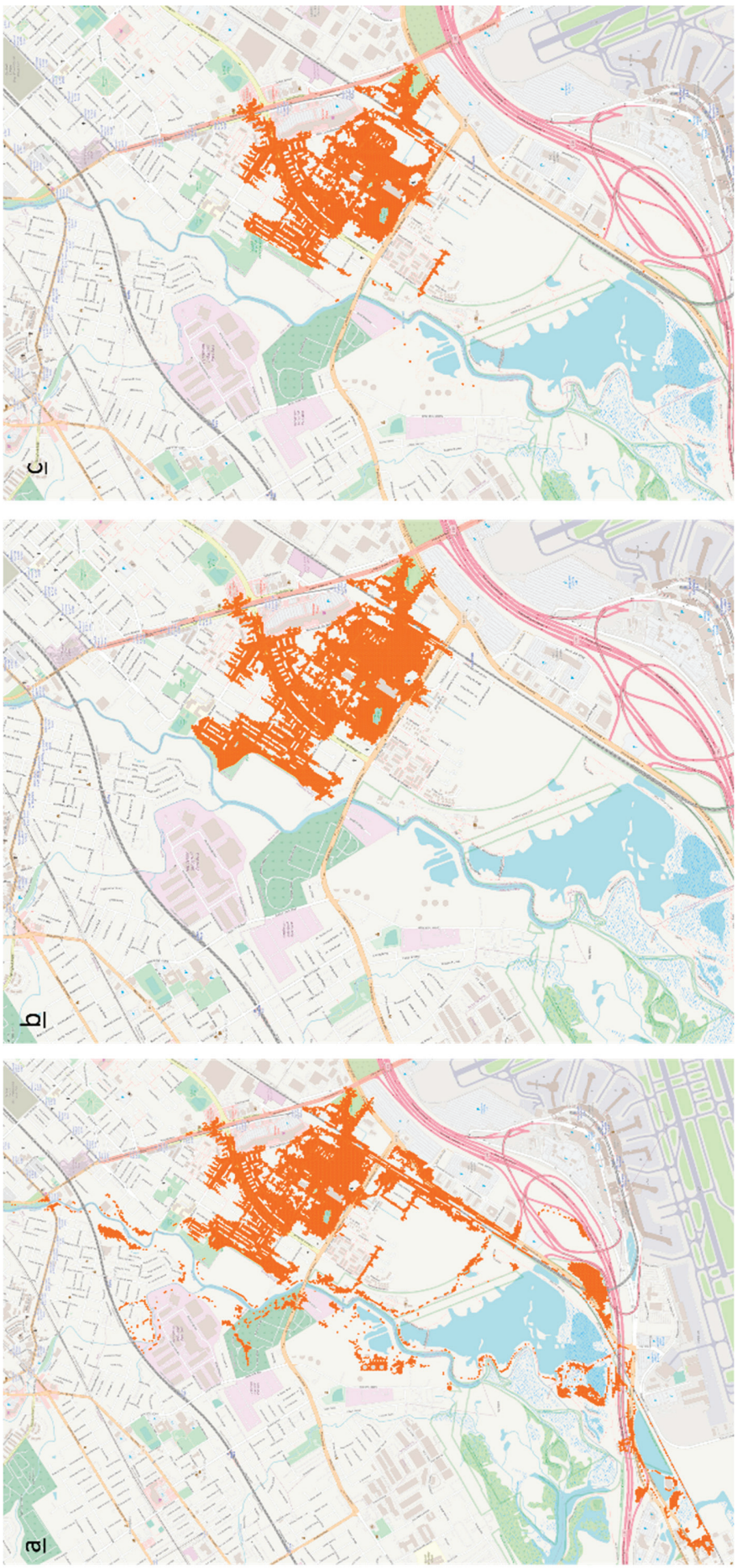

Figure 14. Flooding eliminated by each of the adaptation approaches under Climate Scenario #1: (**a**) flooding eliminated by Approach #1; (**b**) flooding eliminated by Approach #2; (**c**) flooding eliminated by Approach #3.

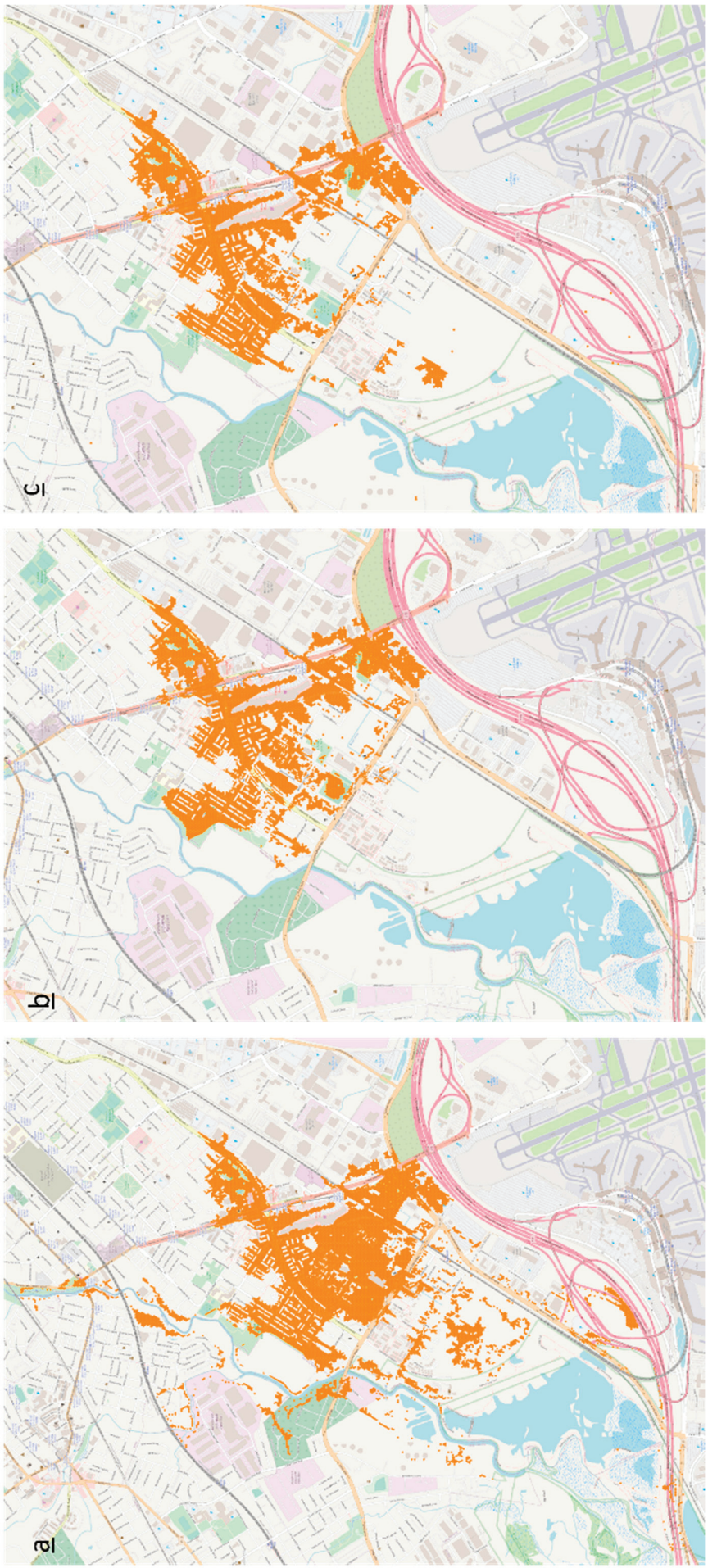

Figure 15. Flooding eliminated by each of the adaptation approaches under Climate Scenario #2: (**a**) Flooding eliminated by Approach #1 (**b**) Flooding eliminated by Approach #2 (**c**) Flooding eliminated by Approach #3.

Table 6 presents the number of flooded nodes (N) in each of the simulations under the two different climate scenarios. While the baseline (e.g., no adaptation) configuration consistently represents the highest number of flooded nodes, and all three approaches reduce the number of flooded nodes, Approach #1 has significantly lower *n* compared to the two other approaches.

Table 6. Summary of the number of flooded nodes.

Scenario/Adaptation Approach	Climate Scenario #1 Number of 2D Nodes with Depth > 10 cm	Climate Scenario #2 Number of 2D Nodes with Depth > 10 cm
Existing	22,261	35,298
Approach #1	13,577	20,475
Approach #2	18,936	28,351
Approach #3	20,655	27,164

In the chart above (Figure 16), the blue bars represent the percentage of flood reduction area achieved by each adaptation approach—GSI, levee, and land swap—under the existing condition (no climate change scenario). The yellow bars represent the percentage of flood reduction area with each adaptation approach under a climate change scenario.

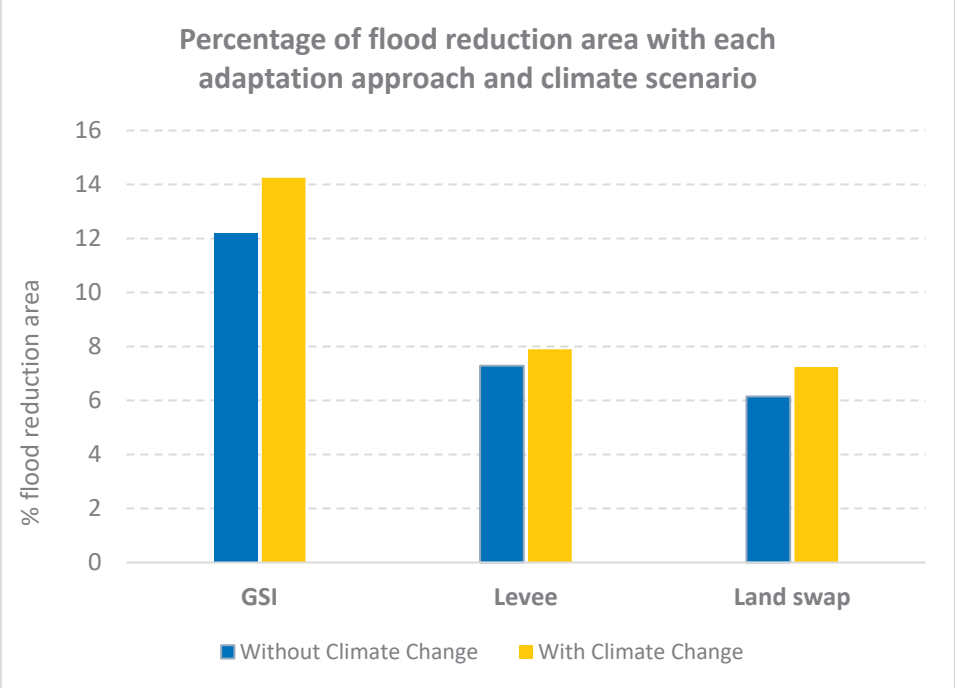

Figure 16. Flood reduction area (%) with each adaptation approach and climate scenario.

The results indicate that GSI is the most effective in reducing flood areas under both conditions, with a higher flood reduction percentage than the levee and land swap strategies. Additionally, we can observe that, with climate change (yellow bars), each approach shows a slight increase in flood reduction compared to the existing condition. This finding suggests that all three strategies maintain some level of effectiveness in reducing flood areas under projected climate changes, though GSI remains the most impactful of the three.

To investigate whether any of the approaches transfers the flood risk from Eastwick to another portion of the model domain, the box plots presented in Figure 17 compare the peak

flood depth of all 2D flooded nodes located within the streams for each adaptation approach and climate scenario. The first pair of boxes (leftmost) represent existing conditions, without any adaptation strategy in place. The other three pairs correspond to the three adaptation approaches, comparing climate scenario #1 (light blue) and #2 (dark blue).

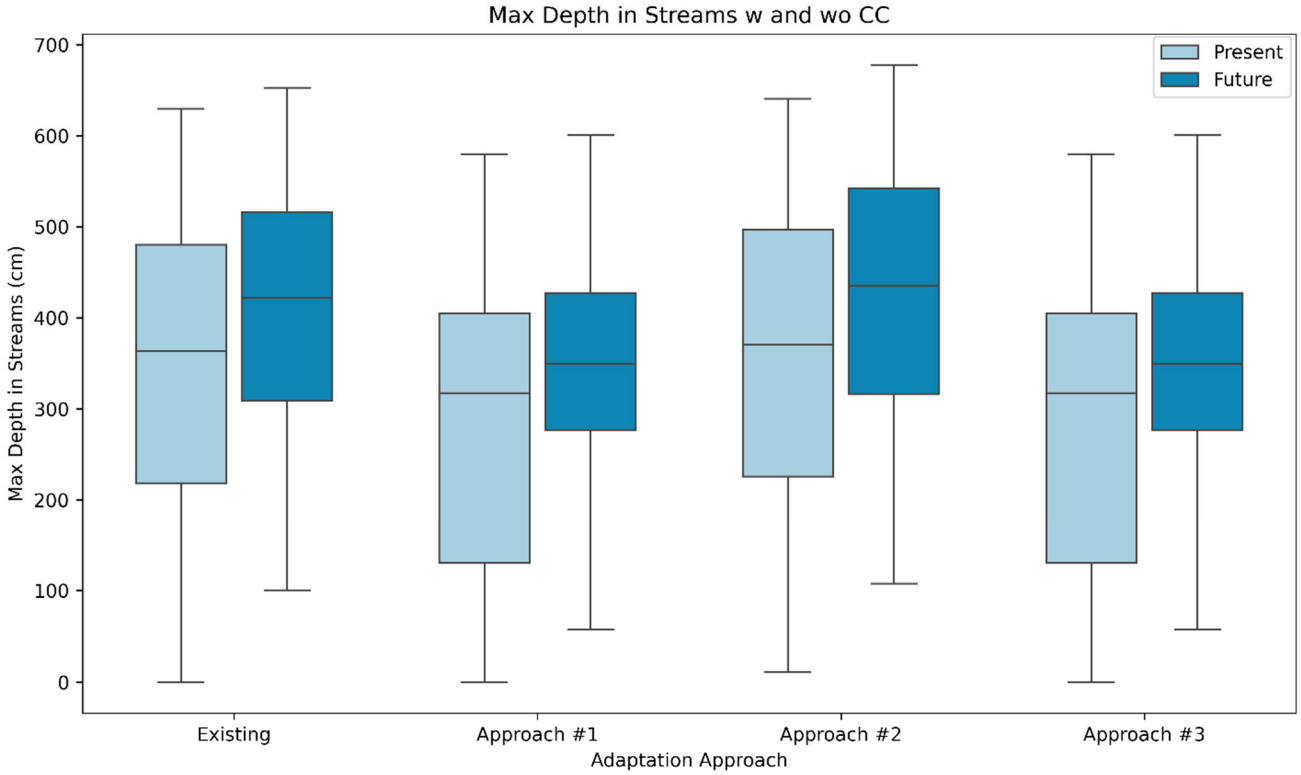

Figure 17. Box plots of max flood depth in streams with and without climate change, comparing the existing condition and the adaptation approaches.

The box plots in Figure 17 show a smaller increase in median flood depth from present to future with Approach #1 and the IQR remains relatively tight. This suggests better control over flood variability under future conditions with GSI. Approach #2 shows greater increase in median flood depth under future conditions. The upper whisker in the future scenario extends quite high, indicating potential vulnerability to extreme events. Approach #3 also exhibits an increase in median flood depth. The increase in the median and the presence of long upper whiskers in future scenarios across all groups highlights a vulnerability to extreme flood events. However, Approach #1 seems to cope better with the impacts of climate change on flood depths in streams, as they manage to keep the increase in median depths relatively moderate while controlling the range of outcomes.

4. Discussion

The results of this study underscore the complexities of selecting flood risk management (FRM) strategies for urban areas under shifting climate conditions. Effective FRM must address a variety of factors: effectiveness at reducing floods under both present and future climate conditions; logistical feasibility of construction; community acceptance; cost and cost-effectiveness; and ideally the ability to provide sustainability and resilience co-benefits. This study represents an initial exploration into only the first of these factors, setting the stage for more comprehensive evaluations of the options in the future.

The findings suggest that flood risk is most effectively reduced through the NBS approach, under both current and future climate scenarios. This approach, featuring the use of GSI, reduces flooding both in Eastwick and in nearby other communities. However,

this approach requires significant and extensive multi-jurisdictional collaboration. If this collaboration were feasible and if upscaling of GSI significantly managed runoff from 65% of all the impervious surfaces in the watershed were possible, the face of this watershed would fundamentally and radically change for the better. Unfortunately, it is not clear that such collaboration and upscaling is feasible, or that it can be accomplished within reasonable time frames.

The levee may be less institutionally complex to construct, and it is effective in reducing fluvial flooding under current climate. However, it too carries some challenges. By diverting pluvial flow out of Eastwick, the levee could induce flooding elsewhere in the lower Cobbs Creek watershed. It also does not effectively reduce coastal flooding originating from the Heinz refuge and would need to be accompanied by pumps to remove pluvial floodwaters that could accumulate on its landward side. Once built, it will also be difficult to modify, should current projections of future climate change be underestimated.

Like the NBS strategy, the land swap involves complex coordination and consent from multiple stakeholders. Unlike the NBS strategy, the required collaboration and coordination is only within Eastwick. Initial interactions of local residents suggest that there is currently no consensus around implementation of the land swap. Some residents do not wish to move (and prefer the protection perceived from the levee); while others seek buyouts. Though it is currently owned by the city, the potential relocation area is also of interest to different stakeholders, including the Heinz wildlife refuge.

These findings are broadly consistent with recent literature that has examined the trade-offs between structural and non-structural flood adaptation strategies in urban areas. For instance, studies by Frantzeskaki et al. [30] and Zhou et al. [31] have highlighted the growing importance of nature-based solutions in urban resilience planning, particularly in low-lying and socioeconomically vulnerable communities. Similarly, Pinter et al. [32] emphasize that structural protections like levees, while effective in the short term, can increase long-term vulnerability if not combined with flexible and adaptive measures such as GSI and land use planning.

Additionally, the modeling framework used here complements approaches taken in recent urban flood modeling efforts (e.g., Alves et al. [33]; Tang et al., [34]), which simulate compound flood risks and test adaptation strategies using 2D hydrodynamic models. Our skeletonized drainage representation balances model efficiency and accuracy, enabling tractable comparisons of large-scale interventions in complex systems—an approach aligned with current best practices in flood risk modeling.

By building on this body of work, our study contributes a localized, scenario-based evaluation of adaptation strategies under compound climate hazards, while also acknowledging the broader institutional and social challenges documented in the literature. The results reinforce the conclusion that no single solution is sufficient, and that integrated, adaptive strategies—ideally co-developed with affected communities—are more likely to provide sustainable and equitable outcomes.

Future decision-making around FRM in Eastwick requires deeper and more extensive engagement of both community and governmental stakeholders. Such efforts might also involve the development of hybrid approaches (for example, construction of a levee as Phase 1 of a long term FRM strategy that ultimately funds enough GSI to eliminate any induced flooding and/or to provide longer term, and more comprehensive flood resilience). Additional work also must involve benefit cost analyses that consider the construction and operation costs, as well as all the potential co-benefits and tradeoffs of any approach. Preliminary cost assessments by our team suggest that the levee is the least expensive project to construct, but when factoring in operation and maintenance costs and climate change, it is not clear that the long-term benefit cost ratio of the levee is superior to

the other options. A comprehensive analysis (in progress by our team) would require a detailed comparison of damages with and without the projects in place, under multiple probabilistic and compound flood conditions, and all their associated co-benefits (e.g., ecosystem services associated with the NBS approach) and potential disservices (e.g., false sense of security associated with the levee). Such analyses remain necessary to more thoroughly compare the implications of each strategy.

In conclusion, while our study provides foundational insights into the viability of various FRM strategies, extensive further research is necessary to comprehensively evaluate and compare these options across the outlined criteria. Future work should aim to develop a more detailed framework that incorporates these multiple dimensions, facilitating more informed decision-making in urban flood resilience planning. This ongoing research will also benefit from integrating findings from related studies, such as those outlined in our previous work [24], to refine and expand the strategies for managing urban flood risks under escalating climate pressures.

5. Conclusions

This study is a first step in comparing the effectiveness of three distinct flood adaptation strategies within the Eastwick community under both current and projected future climate conditions. The research uses a physically based H&H model to compare the effectiveness of GSI, a levee, and a land swap at reducing flooding in Eastwick. From a flood-risk-reduction perspective, the GSI approach is most effective. It is also the most adaptable and likely provides the greatest number of co-benefits of the three approaches considered here. However, selection of the best FRM strategy requires more work, particularly in light of the multifaceted threats posed by climate change. As urban areas like Eastwick continue to confront escalating climate-induced flood risks, the insights from this study advocate for a strategic pivot toward an integrated FRM framework. This framework, as supported by the Intergovernmental Panel on Climate Change (IPCC), should blend natural and engineered measures, thus embracing hybrid solutions that align with traditional categories yet are flexible enough to incorporate innovative adaptation strategies.

The Philadelphia Office of Sustainability (OOS) is currently undertaking a public engagement strategy to refine the selection of FRM strategies for Eastwick. It is likely that this process will ultimately lead to a hybrid strategy combining the individual strengths of the three approaches. Work in similar urban communities should focus on fostering collaborative, multi-disciplinary efforts that bring together stakeholders from across the spectrum of urban planning, environmental science, and community advocacy. By integrating the strengths of traditional and novel FRM approaches into a cohesive adaptation strategy, communities can enhance their resilience, safeguarding against present and future flood risks while advancing towards a more sustainable and equitable urban future.

Future studies could explore phased and combined strategies that integrate GSI, levee protection, and managed retreat options. A phased approach, starting with structural defenses like levees and evolving into comprehensive GSI implementation, could address both immediate and long-term flood risks while enhancing resilience. Additionally, as community perspectives are essential in determining viable flood solutions, future research should incorporate extensive community engagement to refine adaptation strategies. This could include studies that evaluate the social acceptability, economic feasibility, and long-term sustainability of different FRM options, informed directly by community input.

Further research is also needed to conduct detailed cost–benefit analyses that consider both short-term and long-term impacts. This analysis should account for not only construction and maintenance costs but also the economic, ecological, and social co-benefits of each strategy to provide a more holistic assessment of hybrid FRM approaches. Ad-

ditional studies could also involve detailed hydrologic and hydraulic modeling under a broader range of climate scenarios, including extreme rainfall events and sea-level rise. This would improve the understanding of each strategy's performance under varied conditions and help identify thresholds where hybrid approaches might be most beneficial. Establishing a long-term monitoring program to track the effectiveness of implemented strategies would provide critical data for adaptive management. By regularly assessing flood protection performance, future modifications could be made to enhance resilience as climate conditions evolve.

Author Contributions: Conceptualization, F.N. and F.M.; Methodology, F.N., P.O. and F.M.; Software, F.N.; Validation, F.M.; Data curation, F.N.; Writing—original draft, F.N.; Writing—review & editing, P.O. and F.M.; Visualization, F.N.; Supervision, F.M.; Funding acquisition, P.O. and F.M. All authors have read and agreed to the published version of the manuscript.

Funding: This research was funded by grants from the NOAA Climate Program Office Coastal and Ocean Climate Applications Program (NA19OAR4310307), the Climate Adaptation Partnerships, RISA/CAP, formerly the RISA, program (NA21OAR4310313), and the Societal Interactions Divisions Adaptation Sciences (AdSci) program (NA21OAR4310281-T1-01).

Data Availability Statement: The original contributions presented in the study are included in the article, further inquiries can be directed to the corresponding author.

Conflicts of Interest: The authors declare no conflict of interest.

References

1. Paul, M.J.; Meyer, J.L. Streams in the Urban Landscape. *Annu. Rev. Ecol. Syst.* **2001**, *32*, 333–365. [CrossRef]
2. McDonald, R.I.; Green, P.; Balk, D.; Fekete, B.M.; Revenga, C.; Todd, M.; Montgomery, M. Urban Growth, Climate Change, and Freshwater Availability. *Proc. Natl. Acad. Sci. USA* **2011**, *108*, 6312–6317. [CrossRef]
3. IPCC. Climate Change 2022: Impacts, Adaptation and Vulnerability. In *Contribution of Working Group Ii to the Sixth Assessment Report of the Intergovernmental Panel on Climate Change*; Roberts, D.C., Pörtner, H.-O., Tignor, M., Poloczanska, E.S., Mintenbeck, K., Alegría, A., Craig, M., Langsdorf, S., Möller, S.V., Löschke, A., et al., Eds.; Cambridge University Press: Cambridge, UK; New York, NY, USA, 2022.
4. Jongman, B. Effective Adaptation to Rising Flood Risk. *Nat. Commun.* **2018**, *9*, 1986. [CrossRef]
5. DiFrancesco, K.; Gitelman, A.; Purkey, D. Bottom-up Assessment of Climate Risk and the Robustness of Proposed Flood Management Strategies in the American River, Ca. *Water* **2020**, *12*, 907. [CrossRef]
6. Ahern, J. From Fail-Safe to Safe-to-Fail: Sustainability and Resilience in the New Urban World. *Landsc. Urban Plan.* **2011**, *100*, 341–343. [CrossRef]
7. Hino, M.; Christopher, B.F.; Katharine, J.M. Managed Retreat as a Response to Natural Hazard risk. *Nat. Clim. Change* **2017**, *7*, 364–370. [CrossRef]
8. Siders, A.R. Managed Retreat in the United States. *One Earth* **2019**, *1*, 216–225. [CrossRef]
9. Benedict, M.; Edward, M.; The Fund; Lydia, B. Green Infrastructure: Linking Landscapes and Communities. In *Bibliovault OAI Repository*; The University of Chicago Press: Chicago, IL, USA, 2006.
10. Mach, K.J.; Caroline, M.K.; Miyuki, H.; Siders, A.R.; Erica, M.J.; Christopher, B.F. Managed Retreat through Voluntary Buyouts of Flood-Prone Properties. *Sci. Adv.* **2019**, *5*, eaax8995. [CrossRef]
11. Eriksen, S.H.; Brown, K.; Kelly, P.M. The Dynamics of Vulnerability: Locating Coping Strategies in Kenya and Tanzania. *Geogr. J.* **2005**, *171*, 287–305. [CrossRef]
12. Reid, H.; Mozaharul, A.; Rachel, B.; Terry, C.; Saleemul, H.; Angela, M. Community-Based Adaptation to Climate Change: An Overview. *Particip. Learn. Action* **2009**, *60*, 11–60.
13. Chiu, Y.-Y.; Nidhi, R.; Chen, H.-E. Evolution of Flood Defense Strategies: Toward Nature-Based Solutions. *Environments* **2021**, *9*, 2. [CrossRef]
14. Haasnoot, M.; Judy, L.; Alexandre, K.M. Pathways to Coastal Retreat. *Science* **2021**, *372*, 1287–1290. [CrossRef] [PubMed]
15. Cea, L.; Costabile, P. Flood Risk in Urban Areas: Modelling, Management and Adaptation to Climate Change. A Review. *Hydrology* **2022**, *9*, 50. [CrossRef]
16. Drexel University. A Climate Resilience Research Agenda for the Greater Philadelphia Area. In *Findings from 2021 Working Group Discussions and Updated CMIP6 Projections for the Region*; Drexel University: Philadelphia, PA, USA, 2023.

17. Nasrollahi, F.; Alizadehtazi, B.; Montalto, F. *The Role of Spatial Rainfall Patterns in Determining Downstream Flood Risk*; Drexel University: Philadelphia, PA, USA, 2024; Chapter 1.
18. Nasrollahi, F.; Rockwell, J.; Montalto, F. *The Role That Engineered Drainage Systems Play in Determining Predicted Flood Risk*; Drexel University: Philadelphia, PA, USA, 2024; Chapter 2.
19. USACE. Hec-Ras River Analysis System User's Manual Version 6.0. In *U.S. Army Corps of Engineers*; USACE: Washington, DC, USA, 2021. Available online: https://www.hec.usace.army.mil/confluence/rasdocs/rasum/6.1 (accessed on 15 March 2024).
20. USGS. *U.S. Geological Survey*; USGS: Reston, VA, USA, 2024. Available online: https://pubs.usgs.gov/wsp/2339/report.pdf (accessed on 15 March 2024).
21. AKRF. *Lower Eastwick Infrastructure and Flood Evaluation Hydrology and Hydraulic Modeling*; AKRF: New York, NY, USA, 2021.
22. Rossman, L.A. *Storm Water Management Model, Quality Assurance Report: Dynamic Wave Flow Routing Water Supply and Water Resources Division*; Environmental Protection Agency: Washington, DC, USA, 2006. Available online: https://www.chiwater.com/Files/SWMM5_QA.pdf (accessed on 3 June 2024).
23. Multi-Resolution Land Characteristics (MRLC) Consortium. Available online: https://www.mrlc.gov/ (accessed on 15 March 2024).
24. Nasrollahi, F.; Montalto, A.F. Climate Resilient Coastal Protection—Guidelines for Development of Multifunctional Infrastructure. In *Towards a Nature-Positive Built Environment*; Victoria, E.E., Giuliana, I.C., Eds.; Springer Nature: Cham, Switzerland, 2025.
25. USACE. *Eastwick Flood Risk Management Study*; USACE: Washington, DC, USA, 2023. Available online: https://www.nap.usace.army.mil/Missions/Civil-Works/Eastwick-Flood-Risk-Management-Study/ (accessed on 15 March 2024).
26. Eastwick Flood Risk Management Feasibility Study. Available online: https://www.nap.usace.army.mil/Portals/39/docs/Civil/Reports/Eastwick/Eastwick-Draft-Report-Engineering-Appendices-August-2023.pdf?ver=VZrvy-TWBcN14fBq3U4BgA%3d%3d (accessed on 1 April 2024).
27. Maimone, M.; Malter, S.; Anbessie, T.; Rockwell, J. Three Methods of Characterizing Climate-Induced Changes in Extreme Rainfall: A Comparison Study. *J. Water Clim. Change* **2023**, *14*, 4245–4260. [CrossRef]
28. Mita, K.S.; Orton, P.; Montalto, F.; Saleh, F.; Rockwell, J. Sea Level Rise-Induced Transition from Rare Fluvial Extremes to Chronic and Compound Floods. *Water* **2023**, *15*, 2671. [CrossRef]
29. Strauss, B.H. Rapid Accumulation of Committed Sea-Level Rise from Global Warming. *Proc. Natl. Acad. Sci. USA* **2013**, *110*, 13699–13700. [CrossRef]
30. Frantzeskaki, N.; McPhearson, T.; Collier, M.J.; Kendal, D.; Bulkeley, H.; Dumitru, A.; Walsh, C.; Noble, K.; van Wyk, E.; Ordóñez, C.; et al. Nature-Based Solutions for Urban Climate Change Adaptation: Linking Science, Policy, and Practice Communities for Evidence-Based Decision-Making. *BioScience* **2019**, *69*, 455–466. [CrossRef]
31. Zhou, K.; Kong, F.; Yin, H.; Destouni, G.; Meadows, M.E.; Andersson, E.; Chen, L.; Chen, B.; Li, Z.; Su, J. Urban Flood Risk Management Needs Nature-Based Solutions: A Coupled Social-Ecological System Perspective. *npj Urban Sustain.* **2024**, *4*, 25. [CrossRef]
32. Pinter, N.; Huthoff, F.; Dierauer, J.; Remo, J.W.; Damptz, A. Modeling Residual Flood Risk Behind Levees, Upper Mississippi River, USA. *Environ. Sci. Policy* **2016**, *58*, 131–140. [CrossRef]
33. Alves, A.; Vojinovic, Z.; Kapelan, Z.; Sanchez, A.; Gersonius, B. Exploring Trade-Offs among the Multiple Benefits of Green-Blue-Grey Infrastructure for Urban Flood Mitigation. *Sci. Total Environ.* **2019**, *703*, 134980. [CrossRef]
34. Tang, B.; Nederhoff, K.; Gallien, T. Quantifying Compound Coastal Flooding Effects in Urban Regions Using a Tightly Coupled 1d–2d Model Explicitly Resolving Flood Defense Infrastructure. *Coast. Eng.* **2025**, *199*, 104728. [CrossRef]

land

MDPI

Article

Leveraging Reed Bed Burnings as Indicators of Wetland Conversion in Modern Greece

Cleo Maria Gaganis, Andreas Y. Troumbis * and Themistoklis Kontos

Department of the Environment, University of the Aegean, 81100 Mytilene, Lesvos, Greece; envm23043@env.aegean.gr (C.M.G.); kontos@aegean.gr (T.K.)
* Correspondence: atro@aegean.gr; Tel.: +30-6945877072

Abstract: This study explores the historical occurrence of wetland ecosystems in Greece by using recurring *Phragmites australis* (common reed) burnings as an indicator. *Phragmites australis*, a plant closely associated with wetlands, provides excellent insights into wetland distribution. We establish a substantial association between reed fires and historical wetland existence in Greece using geographical and statistical analysis, with these fires exhibiting remarkable constancy across time. Using Corine land-cover (CLC) data, we extend our analysis into land-use dynamics, demonstrating that places with the highest reed-bed-fire rates were originally wetlands, particularly those converted into permanent irrigated land and areas with complex agriculture patterns. We find spatial commonalities between reed fires and past wetland existence by analyzing fire occurrence across three main categories: reed fires, agricultural land fires, and grassland fires. Historical records of wetland conversion into agricultural land (or land reclamation works) in locations such as Yianitsa and Kopaida give context to our findings. Visualizations confirm the clustering of reed fires around these converted agricultural regions. In summary, our study offers a unique indicator based on *Phragmites australis* burnings that can be used to identify previous wetland-type ecosystems, with Mediterranean-wide implications. Despite data constraints, this study adds to the conversation about wetland preservation and sustainable land-use management.

Keywords: wetland; *Phragmites australis*; land reclamation; land use; fire statistics; burning; Corine data

1. Introduction

Land-use (LU) and land-use–cover change (LUCC) science has skyrocketed during the last half-century (exponential growth r = 6.57/year). From a few tens of publications/year in the 1970s and 1980s to several tens of thousands/year in the last decade (Web of Science records, ca 350,000 publications as of the end of 2023). From an epistemic point of view, almost 99% of the abundant LU/LUCC literature has traditionally used case-study approaches for in-depth investigations of land-use change processes and impacts rooted in a particular place and context but inherently limited to the historical and social-ecological contexts of the case [1]. Complementary meta-analysis and meta-studies [2–4] aim to synthesize case study findings to uncover statistical regularities and fit individual empirical cases in a certain common framework, methodologically and conceptually, regarding, e.g., deforestation, urbanization, desertification, or agricultural change [5–8]. From a thematic point of view, emphasis is mainly given to biogeochemical cycles and processes [9], eco-system service valuation [10], and their connection to human well-being [11].

Corresponding research on wetlands is at most 3.6% of the total LU/LUCC literature. This might appear at first sight paradoxical, given that (1) wetland losses, conversion, or degradation occur worldwide, sometimes at excessively high rates, although slight regional deviations might exist, peaking among ecosystem types, with up to 87% of global wetland resources having been lost since 1700 CE [12]; (2) the average annual rate of natural wetland loss is over three times faster than the average annual rate of loss of natural forests,

i.e., −0.78%/year vs. −0.24%/year, respectively [13,14]; (3) rates of natural wetland loss have accelerated to −1.60%/year since 2000 [15]; (4) wetlands (coastal wetlands, freshwater swamps and marshes, and peatlands) encompass about 8% of the earth's terrestrial surface and account for about 45% of the total economic value of all global ecosystems [16], initially estimated at ca 5000×10^9 USD (1994)/year [17]. Such an astronomical amount comes from the functions and processes wetlands contribute to human well-being, e.g., wildlife habitat support, water supply, carbon sequestration, the purification and filtration of agricultural pollutants, foods, medicine, and different recreational facilities [11,12]. One should notice that the cultural services of wetlands [18], among those of scientific interest, rank highly after utilitarian ones, e.g., for water regulation or waste management [17]. However, one should avoid misunderstandings or misinterpretations of the multifaceted study of wetlands despite its limited relative percentage within overall the LU/LUCC literature. It promotes or produces notable progress in fields supporting the specific interest of this article, e.g., remote sensing [19,20], ecology and biology of hydrophilous species, or focused conservation practices and guidelines [21,22].

Wetlands have been drained, converted, or filled in for centuries, with the anthropogenic drivers being agricultural and industrial production, urbanization, infrastructure development, water-use and -availability changes, disease control, and aquaculture, aggravated under climate change pressures [23–26]. Within that context, in a thorough analysis of the future of Mediterranean wetlands that could serve as a methodological guide worldwide, 50 key issues are cataloged and classified as conservation research priorities [27]. Among issues considered as "overlooked", i.e., likely to have a significant impact on Mediterranean wetlands but which are currently not well known in this regional context, increased fire risk within Mediterranean wetlands and their watershed figures are the highest-scoring issue within the physical environment and climate change issue cluster. The low-intensity prescribed fires in non-inundation periods are also reported as one conservation practice to control invasive species and increase wetland vegetation coverage and diversity [28].

Given the above, the present case study intends to explore the combination of four disparate sources of evidence of original wetland distribution in Greece. First, the pyrogeography [29] of reed bed fires in Greece; second, the use of *Phragmites australis* as a wetland habitat condition indicator species [30]; third, the Hellenic Firefighting Corp statistics—following the European harmonized classification scheme of fire causes protocol [31]; and fourth, the history of large-scale hydraulic works (called land reclamation works) undertaken during the last two centuries in Greece, i.e., the emergence and expansion of Greece as a modern nation state (1830).

The fundamental evolution of the modern Greek state is intricately connected to the extensive drainage of its wetlands [32]. Historical records indicate that the nascent government faced significant challenges in fostering the country's development. In response to the demand for real estate and agricultural land and securing food resources for its growing population, the state resorted to the systematical drainage of its wetlands until the 1960s. An estimated loss of 63% of the original wetland areas in Greece has occurred over the twentieth century [33]. This historical context is essential for comprehending that wetlands once characterized Greece's landscape despite its mountainous terrain or the dominant public perception as an insular setup. These former wetlands now constitute the existing plains and agricultural lands that play a crucial role in the country's current landscape and farming practices [34–36]. Today, about 400 large and small wetlands are inventoried in Greece. Despite the heavy losses during the last two centuries, their total area remains large (210,000 ha) [33]. Noteworthily, coastal and insular wetlands also suffer from multiple threats, mainly, relating to tourism development [37], although they are pivotal in ensuring functional connectivity for trans-Saharan migratory birds' flyways [38].

The detailed recordings of the recurring burnings of resilient reed beds, including the geographic coordinates, area, and duration of individual fire events, help approximate the original distribution of wetlands in Greece. We hypothesize that the geography of reed bed

fires or burnings, a "weed control" practice extensively applied wherever common reed stands recover, might allow the initial wetlands' distribution to be reconstructed before the most extensive land-use–cover change processes initiated in modern Greece. Regarding the scientific method we follow, it embodies empiricism, careful observation, and rigorous reasoning. One might risk qualifying this approach as an attempt to exploit solid bodies of knowledge and techniques, e.g., remote sensing, species biology, and conservation practices, to advance our understanding of wetland history and conservation. Therefore, the focus is synthesizing verisimilar storytelling of wetlands' fate in modern Greece rather than developing or improving technical aspects or data.

The spatial distribution of reed bed fires or burnings is contrasted with known land reclamation projects in Greece to control for the validity of the rationale that reed bed burnings might approximate historical wetland conversion into other land uses. For that purpose, Corine land-use data from two flag cases of drained lakes and marshes in Greece vs. two existing wetlands serve as a platform for the current situation in the corresponding geographical scale.

The paper develops around the following questions:

- What is the spatial distribution and magnitude of reed bed fires in Greece between 2000 and 2022?
- Is it feasible to construct pyrogeographic maps of high resolution for reed beds?
- Are there specific land-cover types, such as permanent irrigated land and areas with complex cultivation patterns, that exhibit a high frequency of recorded reed bed fires?
- How does the historical context of land conversion initiatives in land-reclaimed areas relate to the current distribution of reed bed fires?

Through these questions, we aim to quantify and establish the connection between these periodic burnings and degraded wetlands to contribute to the conversation surrounding land conversion and its potential long-term effects on different ecosystems. Acknowledging an area's past geomorphological and ecological characteristics is crucial for reclamation works since long-term effects must be assessed for feasible, sustainable development scenarios. Ultimately, the hypothesis was that the current interaction between humans and natural land expressed through fire allows for reconstructing a past image of Greek wetlands.

2. Materials and Methods

This section addresses the various clusters of biological and historical information and actual fire statistics integrated into a verisimilar narrative to establish the potential of recurrent reed bed burnings to reconstruct the original wetland distribution in Greece. Before delving into the core content of this research paper, it is imperative to provide some preliminary remarks that offer clarity and context for our study. These remarks serve as a foundational guide for readers to navigate the language, calculations, and terminologies utilized throughout the paper.

2.1. Terminology

Here, we provide definitions of terms central to our narrative. Specifically, they are as follows:

Original Wetlands: "original wetlands" denote the wetland areas that existed in their natural state before changing due to human activities, including drainage and conversion into other land-use types.

Reed Fires: Throughout this study, we refer to "reed fires" as incidents involving the burning of Phragmites australis, a common reed species. This terminology is used interchangeably with "reed bed fires" and encompasses fires occurring within wetland-type environments, affecting other helophytes.

Corine Land-Use (CLU) Data: The Corine land-use dataset classifies various land-cover categories, offering a comprehensive understanding of land-use dynamics. This

dataset encompasses diverse classes, from urban areas to natural vegetation, aiding in analyzing land-use changes.

Stremma: The term "stremma" is a unit of surface measurement used in Greece, equivalent to 1000 m^2 or 0.1 hectares or 0.001 sq. km. This paper uses this unit to quantify the area affected by fires and land-cover classifications according to the Hellenic Statistic Service (ELSTAT) accounting metric system.

NUTS: NUTS is a geographical nomenclature subdividing the economic territory of the European Union (EU) for statistical purposes into a hierarchical system divided into three levels since 2003. NUTS 1: major socio-economic regions, NUTS 2: essential regions for applying regional policies, NUTS 3: small regions for specific diagnoses. A NUTS 0 level, usually co-incident with national boundaries, is also available. A NUTS 3 level for Greece is equivalent to the former 51 prefectures. This number climbs to 74 when individual islands, administratively combined into a single prefecture, are listed separately.

Pyrogeography: "*An emerging discipline that provides the intellectual framework to understand the complexity of fire on Earth*" [29], whose scientific program's core mission is the understanding and interpretation of the spatial (local to global) and temporal scales and patterns of the combustion of biomass.

2.2. Phragmites australis (Common Reed): Traits and Reed Bed Burnings

In this paper, we refer to *Phragmites australis* (common reed) in the sense of morphospecies, adopting the Oxford Reference definition in the Dictionary of Plant Species: "*a group of biological organisms whose members differ from all other groups in some aspect of their form and structure (see morphology), but are so similar among themselves that they are lumped together for the purposes of analysis*". We consider that the morphospecies taxonomy best matches the level of knowledge of the average firefighter recording the fire event in the field. *P. australis* is a cosmopolitan wetland grass typically associated with standing water up to 1 m deep or even as a floating mat but also with damp ground or wet soil, a proxy indication of previously inundated land. The connection between the presence and abundance of *P. australis* and wetland soil types is well established, as a voluminous literature is available on the strong correlation between the two [39–46]. In suitable habitat conditions, e.g., hot summers and fertile growing conditions, *P. australis* effectively spreads (5 m or more per year) through a strong network of rhizomes, horizontal runners putting down roots at regular intervals, and a rich-soil seedbed. *P. australis* may be used as a species indicator of the specific type of ecosystem. Appearances of *P. australis* in reclaimed-land and drained-wetland locations may assimilate natural-wetland periodic-fluctuating conditions during the year when the soils are unsaturated and aerated [44].

Its competition-related functional phenotypic traits [47,48], e.g., fast growth rate, low wood density, high leaf area, and fast recovery after disturbance, besides its worldwide spread, may explain "reeds" sensu lato persistence, expansion, and invasiveness [46–53]. Then, one might easily identify the polysemic status of the species in the literature according to authors' research and conceptual priorities, e.g., conservation or biogeochemistry [54,55]. Similar divergences might be identified in the ecosystem services and socio-economic domains [47–49]. On the contrary, from the ecological engineering perspective, *P. australis* is often hailed in phytoremediation and greywater treatments [46]. Overall, the actual relationship, at least at the utilitarian or practical level, between *P. australis* and humans competing for wetland habitats can be described as "good" and "bad" news, depending on the circumstance [36,46]. Therefore, the adaptive feature of the plant allows it to regrow from its rich seedbed [46] routinely over one or three years, making its control follow the same pattern of reoccurrence. Appropriate indicators of wetland fire resilience should consider that fire-impacted wetland rapidly recovers plant cover, not carbon storage and plant biomass [52]. The common reed is a food source in grazing-marsh livestock or even for humans following certain diets and presents significant carbon dioxide uptake [54,55]. When considered as a non-native species or in land-reclaimed locations, it is perceived as a pest to be controlled [56].

Since no biological control methods for *Phragmites* are currently available, landowners have resorted to routine burns of reeds to prepare their land for its appropriate use [57]. The need to control *Phragmites* in some places has resulted in the need for proportionate legislation. Such a need is found in the US, where, as described in *A Landowner's Guide to Phragmites Control*, a burn permit must be issued from the local fire department for a routine extraction [58,59]. Burning is the lowest-cost method for landowners as other pesticides are highly damaging to the surrounding environment or ineffective on the reed population [60]. As previously mentioned, the recommended control method is to impose numerous stressors on the plants, but while burning is the most cost-effective and environmentally sound practice, we discover the current condition within Greece, where a significant quantity of data has been documented on the routine burning of reed beds [58].

2.3. Reed Bed Burnings as Mediators for Inference of Wetland Distribution

The methodological substratum of our exercise relates to the issue of inferring human–*P. australis* interactions (or wetlands in extenso), as actors historically competing for land, from spatial reed-bed-burning data [60]. As an axiom, we assume that the spatial distribution of any taxon, *P. australis* hereto results from all abiotic and biotic ecological interactions. Consequently, an (or some) underlying, potentially dynamic probability distribution that predicts and explains the taxon distribution should exist [59,61,62]. Then, identifying the principal factors and their relative impact that constrain the occurrence of *P. australis* might permit a better understanding and model of the current and future distribution of the species, as current research in ecology and biogeography steadily enforces [62–64], but also its past distribution, as we try to accomplish here. In this case, biotic interaction limitedly implies the *P. australis*—human interaction through burning, and abiotic interaction implies wetland-type soil and hydrological conditions and the presence of the indicator species.

Theoretically, the challenge is to calculate the joint probability distribution $P(W,R)$, where W represents a "wetland", and R is a reed fire event over a space, Greece *hereto*, using data from arbitrary spatial resolution [65]. We divided Greece into uniform square spatial cells, x_α, and counted the Boolean variables (presence/absence) of W and R over the grid. Using Bayes' theorem, this joint probability is formulated as

$$P(W,R) = P(R|W)\cdot P(R)$$

and the posterior conditional probability distribution $P(W \mid R)$ is as follows:

$$P(W|R) = \frac{P(R|W)\cdot P(W)}{P(R)}$$

In our case, the goal is to calculate the prior probability distribution $P(W)$ given the information R via the likelihood $P(W \mid R)$ and the evidence $P(R)$, according to the available data. Using the Naïve Bayes' approximation [66]:

$$P(W|R) = \frac{\prod_1^N P(R|W)\cdot P(W)}{P(R)}$$

where N is the number of grid cells considered.

It is almost self-evident that this formulation needs more depth since it is based on official fire statistics data collected by non-specialist firefighters. For instance, more than ten Corine Label 3 LU categories, e.g., estuaries, water bodies, inland marshes, etc., are cataloged as single "wetlands" in the Firefighting Corp database. Notice that in the Greek literature on wetlands (primarily coordinated by Gerakis PA since 1993), 27 types of natural and artificial wetlands are listed. The same applies to identifying other helophytes, e.g., *Scirpus* sp. or *Typha* sp., occurring (or co-occurring) in "wetlands". The orthodox formulation would include W_i and R_i as the various alternatives for wetland types and different taxa. Furthermore, the alternative features of W are considered independent.

The most exciting part of this approach is the calculation of the probabilities of co-occurrence $P(W,R)$ and $P(W|R)$. Both are approximated as relative frequencies over N cells, i.e.,

$$P(W,R) = \frac{N(W,R)}{N} \text{ and } P(W|R) = \frac{N(W,R)}{N_R}$$

However, regarding information, the probability $P(\overline{W})$, i.e., the complement probability of absence of a "wetland", is equally important. Then, as [62] proposed, the evidence function $P(R)$ is often not relevant for classification, with a score function as follows:

$$S(W|R) = \ln\left(\frac{P(W|R)}{P(\overline{W}|R}\right) + \ln\left(\frac{P(W)}{P(\overline{W})}\right)$$

Then, when $S(W|R) > 0$ per cell, one might interpret this condition of reed bed burning, i.e., the wetland indicator species, in areas that are currently converted wetlands as a strong indication of the existence of original wetland habitats.

One might plausibly hypothesize that $P(W|R)$ will have a high value in cells, including elements of the hydrographic network, the "wetlands" that are characterized as Ramsar wetlands, and the wetland-related LUs as recorded in the Corine Label 3 maps (Figure 1a–c).

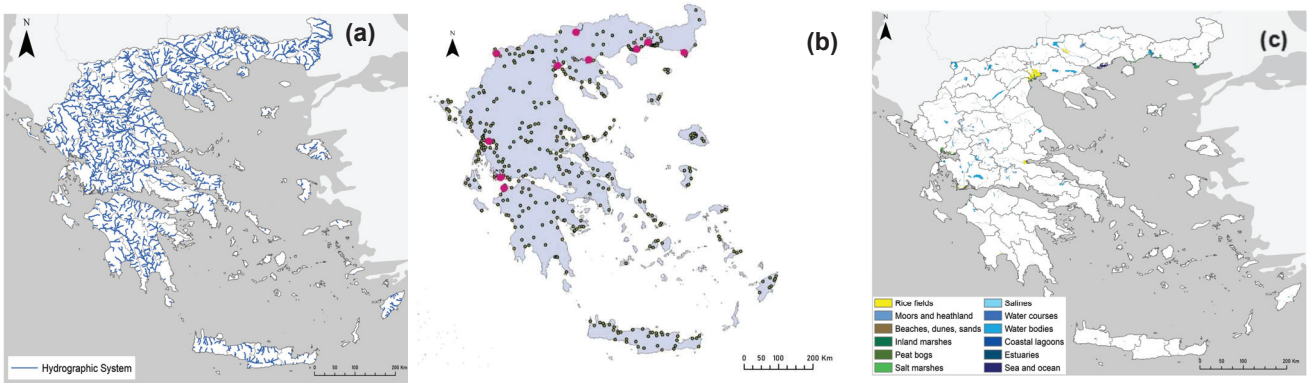

Figure 1. Abiotic and biotic conditions in Greece are suitable for reed beds and, indirectly, reed fire burning. (**a**) The hydrographic network of Greece (4th degree class) https://geodata.gov.gr/maps/?locale=el, accessed on 4 January 2024. (**b**) The location of the Ramsar wetlands in Greece (purple dots signify Ramsar wetlands of international importance, black dots signify the existence of general wetlands). Source: [67] using http://www.ekby.gr/ekby/en/EKBY_Publications_en.html, accessed on 4 January 2024, Reprinted/adapted with permission from Ref. [67]. (**c**) Corine Label 3 exclusively presenting LUs relating to current wetland conditions.

2.4. Fire Statistics in Greece

Fire data have been recorded in Greece since 1955 [68]. Since 2000, the wildfire database has been adapted to the European Fire Fighting Information System (EFFIS) and integrated into the Copernicus platform [69]. Table 1 presents the typical recording of any single fire event.

As pointed out earlier, wetland drainage and conversion were a core governmental strategy in Greece, addressing the need for agricultural land, primary sector productivity, and public health, especially in controlling malaria and other mosquito-borne diseases in rural populations [70]. Large-scale, costly works that transformed Greece's landscape are presented in Table 2. One should notice, however, that although mainly small-sized wetlands have continued to suffer losses in recent decades, primarily due to inadequate environmental governance and landowners' delinquency, hydraulic works are shifting towards dam construction, water reservoirs, and channels, or flood control mainly for irrigation and water supply purposes. Artificial lakes, i.e., Lake Kerkini in Northern Greece, are listed as Ramsar wetlands of international importance. Further, more than

800 wetlands on 75 islands in the Aegean and the Ionian archipelago have been discovered and detailed, and a Presidential Decree signed in June 2012 strictly protects 380 of these minor (<8 hectares) natural island wetlands [71].

Table 1. Template of individual fire event recordings (spreadsheet, .xls, .xlsx) since 2000. Data accessible in the Hellenic Firefighting Corp database (in Greek): https://www.fireservice.gr/el_GR/stoicheia-symbanton, accessed on 4 January 2024.

Category of Information	Class	Unit
Time	Year	20XX
	Date, time of fire ignition	dd/mm, xx:xx
	Date, time of fire suppression	dd/mm, xx:xx
Location	Prefecture (NUTS 3)	Name
	Community	Name
	Specific location name	Name
	Geographical coordinates	(from 2020 to)
Vegetation Type	Forest	Burned area in stremmas (1 stremma = 0.1 ha)
	Forested areas	
	Shrubland–grassland	
	Urban–periurban groves	
	Agricultural burnings	
	Reed bed burnings	
	Uncontrolled dumpsites	
General/Miscellaneous Information	Code number of the fire event	X
	Means and personnel engaged	# airborne/terrestrial means, # personnel (firefighters, volunteers, military)

#: Number of.

Table 2. The list, chronology, area, and wetland ecosystem type of significant land reclamation and drainage works in modern Greece (1830—to today). Notice that area is expressed in stremma units, each equal to 0.1 hectares.

		Major Land Reclamation—Wetland Drainage Works in Greece			
Drainage Work	**Code**	**Period**	**Area (Stremma)**	**Prefecture or Region**	**Ecosystem Type**
Kopaida	1	1880–1886	250,000	Viotia, Central Greece	Lake
Pamisos	2	1888–1970	15,000	Messynia, Peloponese	River
Karditsa	3	1931–1959	1,090,000	Thessalia	Marshes
Larisa (Karla)	4	1931–1960	660,000	Thessalia	Lake
Yiannitsa	5	1928–1932	1,054,000	Macedonia	Lake–marshes
Ahinos	6	1930–1933	100,000	Serres	Lake
Messologi	7	1959–1969	105,000	Aetolia-Acarnania	Lagoon

2.5. Large Wetland Reclamation Works in Greece (1830–1960)

For almost a century, converting extensive wetlands, mostly marshes and lakes, into agricultural land was a timeless central choice regardless of the governments in power. A total of ≈3,300,000 stremmas (or 330,000 ha) of wetlands have been actively converted into agricultural land through large-scale "land reclamation works". This has occurred regardless of the thousands of minor-scale interventions originating from local authorities, individuals or co-operatives of farmers, tourism developers, etc. The core assumption of our approach is that reed bed burnings are expected to cluster, primarily along locations

visualized in Figure 1a–c and the locations of drained wetlands in agricultural areas. For further details, see Table 2.

2.6. Indexes, Hypotheses, and Statistics

This sub-section presents the primary index used in fire suppression statistics, i.e., the fire severity index (SI). SI is calculated as the ratio between the total area burned during a certain period, usually a year or a month, per vegetation type and the corresponding number of fire events (frequency) in this type. Furthermore, SI may be calculated at various NUTS levels, e.g., administrative divisions (country, region, prefecture) or a certain geographical grid cell. SI and its component values help establish and test three null hypotheses related to the spatial and temporal patterns of reed bed burning. First, anthropogenic reed bed burnings present the lowest SI value among vegetation types, eventually of the same order as crop residue agricultural burnings. This mainly concerns sporadic appearances of post-burning recovering reed stands within agricultural lands. Second, the time series of SI, at any scale, is stationary, suggesting a constancy in basic statistical parameters, e.g., the mean and variance of the SI distribution.

The third hypothesis relates to the differing behavior of SI time series at various time scales. Metaphorically, burning reed beds signals an episode of human-nature interaction in the specific ecological setup of wetlands converted to agricultural land or suffering a plethora of pressures [24]. Suppose one imagines this setup as a single field driven by verisimilar human activities or processes at random locations. In that case, the genuine question is whether there is autocorrelation between burning events and the scale or time lag. In practice, this autocorrelation hypothesis could be controlled through autocorrelation and partial autocorrelation functions in ARIMA (p,d,q)—with or without seasonality decomposition—modeling and the Ljung–Box test, or white noise Fisher's kappa test. We run these tests at two data samples: (1) a yearly scale, i.e., 23 (2000–2022) SI/year data series; and (2) a monthly scale, i.e., 276 SI/month data series.

Concerning the spatial pattern, the complementary prediction is that the distribution of reed bed burnings matches the hydrographic network and, most importantly, clusters in current agricultural areas that correspond to the original wetlands. This pattern is examined at two scales. First is the national scale, where reed bed burnings are associated with the hydrographic network. Second, at the scale of two symbolic drained wetlands, i.e., Lake Kopaida (the first major land reclamation work) and the Yiannitsa marshes (one of the most significant land reclamation works attempted) in modern Greece (Table 2).

Integrating the Corine land-use (CLU) dataset (levels 1 and 3) provides a comprehensive classification of land-cover categories, enabling a systematic understanding of land-use dynamics. This dataset encompasses various classes that describe distinct land-cover types, ranging from urban areas to agricultural fields, natural vegetation, water bodies, and wetlands (Appendix A). Corine land-use data intersection with reed fires in Greece offers a unique avenue to ascertain the present status of once-wetland areas. By integrating Corine land-use classes with reed fire occurrences, it becomes possible to discern how these areas have evolved, transitioning from wetlands to their current land-use categories. This alignment provides an insightful lens to investigate the contemporary condition of former wetland areas, thereby contributing to a comprehensive understanding of the dynamic interplay between land-use changes, fire incidents, and ecological shifts, as well as the crossover of historical insight in the socioeconomic aspect of the phenomenon.

Hypotheses and predictions are controlled after data are processed using R Statistical Software (v4.1.2). ArcGIS (v. 10.8.2) is then employed for visualizations through coordinates per fire event available (2020–2022) that pinpoint fire distribution trends and clusters. Stationarity and time series statistics were controlled using R (series, v0.10–48), SPSS v.28 forecast functions, XLSTAT time series, and spectral density analyses, including Fast Fourier Transform smoothing. More specifically, the reed fire area dataset was treated to the Augmented Dickey–Fuller (ADF) test to determine its stationarity, critical for making accurate assumptions regarding temporal trends. Furthermore, ADF findings were con-

trolled with the ARIMA model's stationary R-squared values, previously used to predict the reed fire area time series. To attain stationarity, the ARIMA model, dubbed V2-Model_1, includes a comprehensive set of autoregressive (AR) and moving average (MA) terms and a differentiation step. Finally, the spatial distribution of reed fires and agricultural land utilization is examined through visual cluster land-use (CLU) analysis, where high-density reed fire clusters are identified, pinpointing areas of significant burning incidents. This integrated approach offers precise insights into wetland transformations, aiding informed policymaking for targeted conservation efforts and land management strategies in Greece.

3. Results

3.1. General Description of the Reed-Bed-Fire Phenomenon

During 23 years of observation, 248,537 fire events were recorded in the rural space of Greece; they burned a total of 13,526,844 stremma (or 1,352,685 ha or 13,526.8 sq. km) of various types of vegetation (excluding parklands or spinneys). Reed bed burning corresponds to 15.9% of events and 1.8% of burned areas. To better grasp the hidden significance of such pressures and economic and productive effects, notice that the average rural household farmland ownership is 53.8 stremma when the corresponding European average is 166. Figure 2 presents the relative frequencies of wildfires in various vegetation types and the reed fire size distribution. This information will differentiate the initial causes and effects of reed fires of multiple magnitudes. Notice here that our goal is not technical. In other words, to precisely calculate the value of the scaling factor γ of the classic frequency–size distribution, approximating the power law curve between the lower limit (smaller size) of burned area min and the upper limit, s_{max} (which is de facto truncated) [72–77]. Our goal is to propose categories of reed-bed-burning sizes and potential, but not definitive, explanations of the underlying mechanisms in each category.

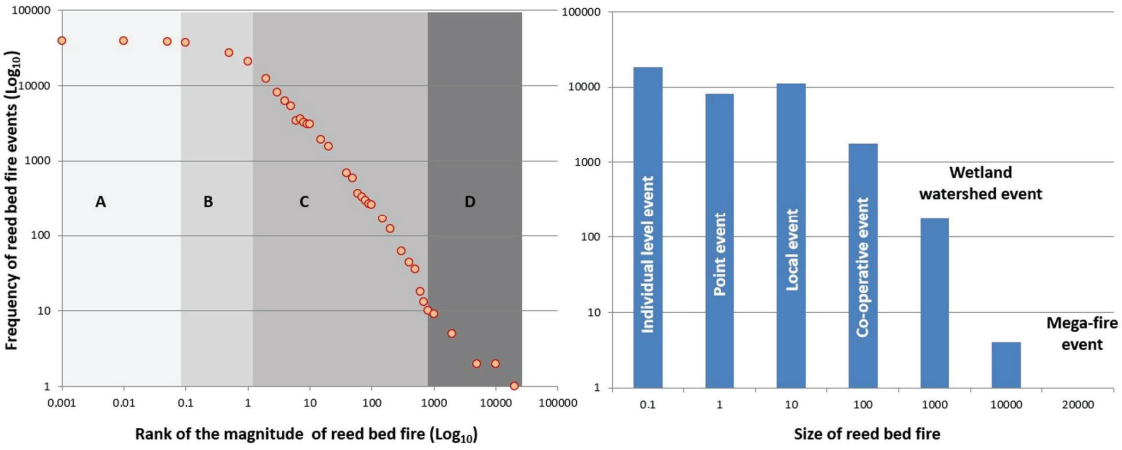

Figure 2. Two versions of the reed-bed-burning frequency vs. size or magnitude rank (in log-log space). **Left**: the classic power law representation of the frequency–size distribution. Tones of grey indicate hypothetical mechanisms generating different categories of reed bed burning sizes, explanations on the meanings of grey tones are provided in the text below. **Right**: the proposed categorizing of reed-bed-burning events according to their respective size. For further explanation and details, see the text below.

We call an "individual level event" (grey tone A, left panel, Figure 2) the case of the application of fire to eradicate sparse, rare individuals of *P. australis*. It corresponds to $\leq$0.1 stremma (or 0.01 ha) events. Such individual plants might be remnants of earlier burnings or new invading individuals, mainly in agricultural lands. The "point event" corresponds to burnings $\leq$1 stremma (or 0.1 ha). Most likely, they are a kind of "regrow", a strip of densely growing reed beds at the edges of agricultural lands near watercourses or artificial irrigation canals. The "local event" corresponds to burnings $\leq$10 stremma (1 ha). Most likely, they correspond to recovering reed beds, 3–5 years after a similar burning

event, most likely of a single farmland owner. The "co-operative event" corresponds to the same condition as the previous one, but most likely is organized and applied by a group of farmers over multiple farm properties. "Watershed events" and "mega-fire events" correspond to large-scale wildfires (order of sq. km.) ravaging various types of vegetation (forests, forested areas, groves, agricultural lands) and the wetland-related vegetation that is situated within the burned area, i.e., existing wetlands or reed beds occupying converted wetland soil types. For instance, the upper-limit-size truncation, smax, in reed burning, i.e., 20,000 stremma (or 2000 ha), occurred in Greece on 23–27 August, mainly in the Peloponnese (Appendix B, NASA Terra satellite image) [78]. There, this mega-fire event burned 1500 km² of forests, accounting for 4% of Greece's total forest area; more than 1500 houses; and caused 68 human casualties.

Similarly interesting is the spider chart (Figure 3), where frequencies, total area burned, and the severity index for various Corine Label 3 NUTS 0 wetland (existing or converted) Lus are compared. The most intriguing finding that differentiates reed bed burning from other vegetation type Lus is that although the frequency and total area "snowflakes" are somewhat similar in shape, the SI snowflake presents a different morphology, indicating higher severity in existing wetlands rather than in converted ones: the role of human control over reed bed burning in converted wetlands seems indirectly highlighted here.

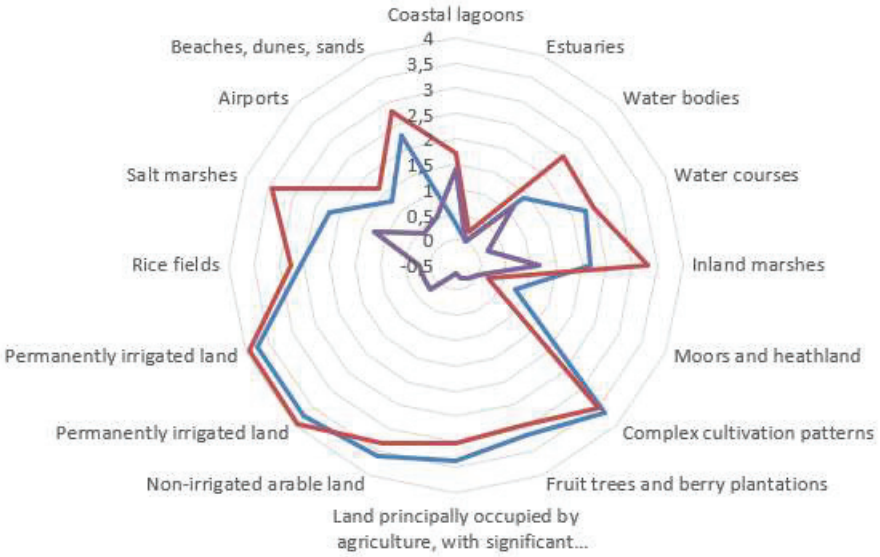

Figure 3. Spider chart comparing the frequencies, total area burned, and SI of reed bed burning in Greece (2000–2022). Data refer exclusively to land uses comprising existing or converted wetlands, primarily variations of agricultural land setups, but also infrastructure (airports), tourism activities (beaches, dunes, sands), and industrial activities (salines and salt marshes). Blue line: frequency; red line: total area burned; purple line: SI. Axes are log-transformed.

3.2. Comparison of Wildfire Severity Indexes vs. Agricultural Burnings

Statistical and geographical analysis results confirm the core hypotheses' validity, as announced in Section 2.4. Specifically, this is as follows:

The severity index of reed bed burnings presents the lowest value ($\mu \pm SD$) compared to that of other vegetation types, especially crop residue burnings. Figure 4 presents summary descriptives of the Sis of wildfires per vegetation type in Greece during 2000–2022, i.e., six series of 276 measurements each. No series is normal (Kolmogorov–Smirnov test: $p < 0.001$, a = 0.05), variances of Sis are not equal (Levene statistic $p < 0.001$), and parametric one-way ANOVA with contrasts is significant ($p < 0.001$). Tukey's test indicates a significant difference between distributions of reed bed burnings and forest wildfires.

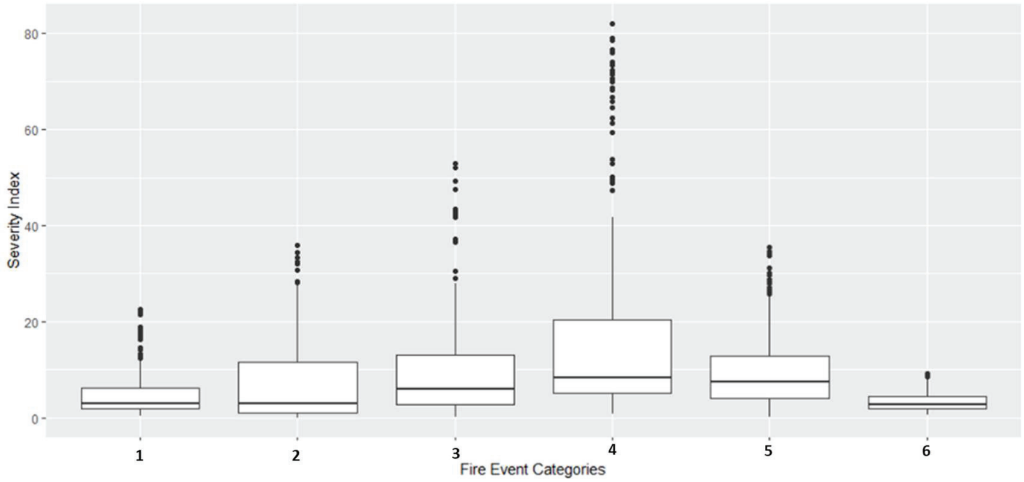

Figure 4. Summary descriptives of the severity index of wildfires per vegetation type in Greece, from 2000–2022. Boxplots represent the median (horizontal thick line), the first and third quartiles (box), and the 1.5 interquartile range (whiskers). Black dots are outliers. 1: Crop residue; 2: agricultural land; 3: forest; 4: forested area; 5: shrubland/grassland; 6: reed bed burning.

Non-parametric test (independent sample median test and independent sample Kruskal–Wallis test, i.e., same median and same distribution across vegetation types' Sis, respectively) results rejected the null hypothesis ($p < 0.001$, a = 0.05). Figure 5 presents the significance of pairwise comparisons of Sis after Kruskal–Wallis independent samples tests. The reed-bed-burning SI differs significantly from all other vegetation types' Sis, including crop residue burnings.

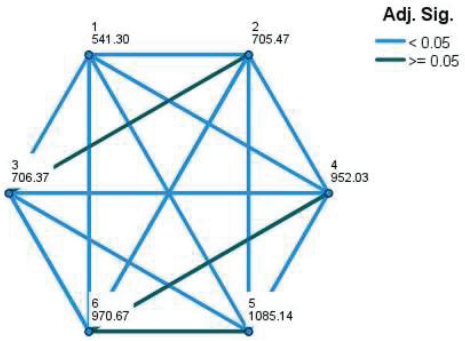

Figure 5. Pairwise comparison of severity indexes per vegetation type after Kruskal–Wallis independent sample test. Significance values have been adjusted after Bonferroni correction for multiple tests. Nodes show the average rank of SI per vegetation type. Code: 1: reed-bed-burning SI; 2. Crop residue burnings SI; 3. Agriculture land wildfire SI; 4. Forest wildfire SI; 5. Forested areas SI; 6. Shrubland/grassland wildfire SI. Each SI series consists of 276 monthly recordings, 2000–2022. Extract from the dashboard of IBM SPSS v. 28.

3.3. Stationarity of Reed-Bed-Burning Time Series

Time series analysis of reed-bed-burning data confirms the hypothesis of the stationarity of the SI of reed bed burnings and its components (area and frequencies/month at NUTS 0). Interestingly, the reed-bed-burning SI is stationary, i.e., its statistical properties, such as mean, variance, and covariance, are independent of the point in time at which they are observed without any data transformation. However, for comparison between the SI series of different vegetation types, data were natural-logarithm-transformed, linear trends were factored out (first-degree differencing), and outliers were removed. In most cases, SI outliers were related to extreme mega-fire events ravaging large areas indistinctively of vegetation types, e.g., the 2007 Peloponnese or the 2021 Attica and Evia events [70,79]. Figure 6 presents the reed-bed-burning series (SI, total area, and fre-

quency/month) during 1/2000–12/2022 at NUTS 0, with natural-logarithm-transformed data and first-degree differencing.

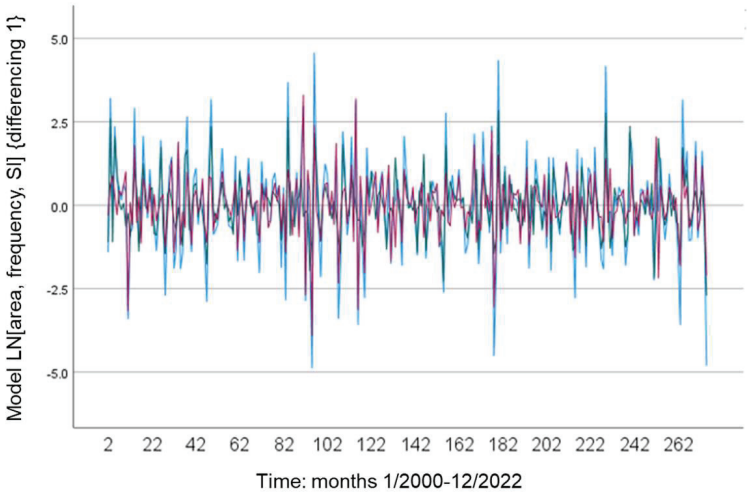

Figure 6. Sequence plot of the reed bed burnings/month time series at NUTS 0, i.e., Creece's level. Data are natural-logarithm-transformed, and first-degree differencing is applied. The blue line represents the area/month series, the green line the frequency/month series, and the red line the SI/month series. Two hundred seventy-six records (months) are reported (1/2000-12/2022). Extract from the dashboard of IBM SPSS v. 28.

The reed bed monthly burning dataset was subjected to the Augmented Dickey–Fuller (ADF) test to check for stationarity. The Dickey–Fuller statistic for the total area/month is −33.453 with a corresponding $p < 0.01$; for the frequency/month, the ADF statistic is −6.3751, $p < 0.01$; for the SI/month, the ADF statistic is −6.5328, $p < 0.01$. In all cases, the lag order = 6. Then, the null hypothesis of non-stationarity may be rejected, implying that the dataset does display stationary behavior. The significance of the *p*-value, which is less than the customary threshold of 0.05, emphasizes the resilience of the stationarity observed in the reed-burning dataset.

3.4. Time Series Analysis, Periodograms, and Spectral Analysis in Reed-Bed-Burning SI Series

Autocorrelation and partial autocorrelation in SI reed-bed-burning data series were extensively studied through several ARIMA (*p*,1,q) models, tested as the value of AR and MA values, and the lags that are taken into consideration (lag 1 to 24). This exercise aimed to examine the behavior of the Ljong–Box statistic, given the ecologically meaningful lags and plausible values of AR and MA. The main finding is that the time pattern of reed burnings differs remarkably when time scale enters into play. To attain stationarity, the ARIMA model, dubbed V2-Model_1, includes a comprehensive set of autoregressive (AR) and moving average (MA) terms and a differencing step. Such a model verifies the stationarity found in the ADF test findings.

Table 3 summarizes the time series analyses, spectral density, and FFT smoothing results at two time scales. The results in Table 3 resemble a verisimilar "umbrella" of slightly differing versions in the computational calculations of various parameters of statistical methods and techniques typically used in time series analysis. The core results can be summarized as follows: First, different-scale time series behave differently, i.e., monthly vs. yearly, as per serial correlations. Monthly-scale series with quarterly periodicity show autocorrelation according to the inclusion of seasonal periodicity or not; the yearly scales do not show serial correlations.

Second, as expected, Ljong–Box and white noise tests, at the yearly scale, concur that the series is significantly different from white noise at a significance level of 0.05. Figure 7 presents indicative graph examples of the above analyses. Overall, one might

detect two periodicities in reed bed burning. One relates to local small-scale events, most likely regarding human agricultural burning and management activities (scale of a few ha). The second refers to quasi-decade large-scale wildfires, ravaging complex landscapes, part of which are wetland systems (scale of square kilometers). In both time scales and burning areas, the effect of the 2007 mega-fire event is evident, as well as the return period of such events, that is, of $\leq$3 years for small-scale events and $\approx$8 years for large events.

Table 3. Summary of statistics for time series and white noise analyses of correlations between data samples of SI reed bed burnings at two time scales, i.e., monthly and yearly. The results presented are the best fitting versions to a series of models, ARIMA (seasonal and non-seasonal periodicity), and white noise after various smoothing techniques (e.g., exponential, Fourier, Holt–Winters, and moving average). FFT RMSE* refers to the normalized RMSE, i.e., RMSE/(max–min) values.

Time Scale/ Data Series	Sample Size/ Spatial Scale	ARIMA Model						White Noise	
		Non-Seasonal (p,1,q)			Seasonal (P,1, Q)			Fisher's K	FFT RMSE*
		Pseudo-R^2	RMSE	L-B Test	Pseudo-R^2	RMSE	L-B Test		
Monthly/SI reed bed burnings	276/NUTS 3	(1,1,1) 0.319	(1,1,1) 0.635	(1,1,1) 0.073	(1,1,1)(1,1,2) 0.192	(1,1,1) (1,1,2) 8.6	(1,1,1) (1,1,2) 0.705	p = 0.036	p = 0.102
Yearly/SI reed bed burnings	2/NUTS 0	(1,1,1) 0.793	(1,1,1) 2.12	(1,1,1) 0.364	-			p = 0.403	p = 0.052
		(3,1,3) 0.731	(3,1,3) 2.64	(3,1,3) 0.465					

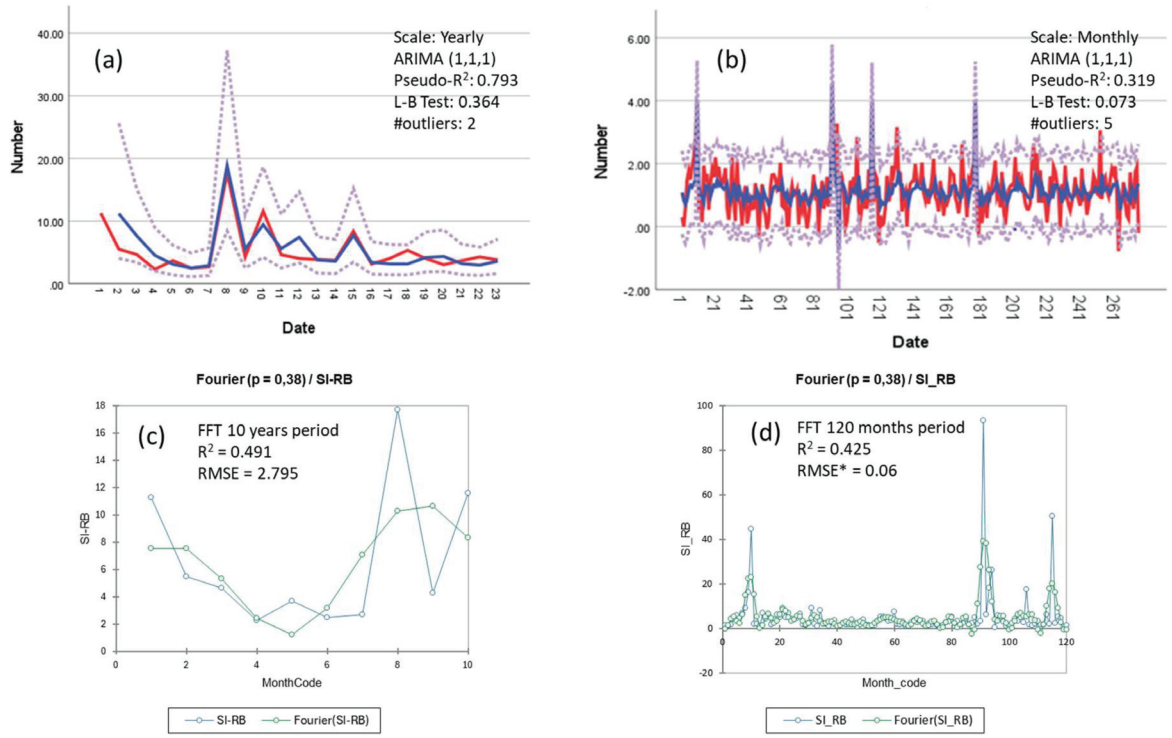

Figure 7. Indicative examples of ARIMA (1,1,1) models of time series analysis of severity indexes of reed bed burnings in two-time scales, yearly vs. monthly, (**a**) vs. (**b**). Red lines present the observed values, blue lines are the fit lines, and dots are the upper and lower confidence limits. Extracts from the dashboard of IBM SPSS v. 8. (**c**,**d**) present the Fast Fourier Transform smoothing of the SI series distribution models at a scale of 10 years (or 120 months)—extracts from the dashboard of the XLSTAT package. RMSE* represents the normalized value calculated as RMSE/(max–min values).

3.5. Spatial Patterns of Reed Bed Burnings

This section focuses on spatial patterns of reed bed burnings, i.e., the complementary aspect of the pyrogeographic analysis. To that end, we present two maps. Map 1 (or Figure 8) presents the totality of reed-bed-burning events (in x/y coordinates) during 2020–2022, for which such data are available in the EFFIS system. One might interpret this figure as the map of reed-bed-burning hotspots in Greece.

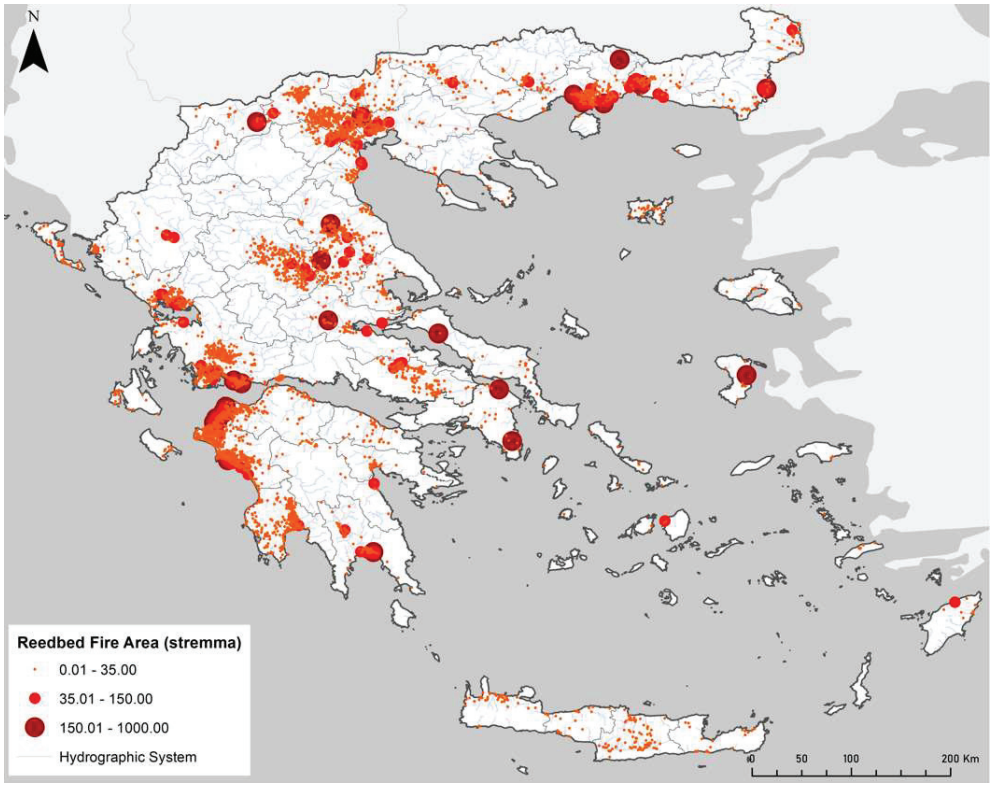

Figure 8. (**Map 1**) Pyrogeographic map of reed bed burning during 2020–2022. The size of the dots indicates the magnitude of burning events in the corresponding locations. Clusters of events suggest the reed-bed-burning hotspots in Greece (NUTS 0) and, indirectly, the presence of existing and converted wetlands where abiotic conditions, especially wetland-related hydric soil conditions, allow for the presence and post-burning recovery of *P. australis* beds. Light-black polygons are the boundaries of NUTS 1 (prefectures); light-grey lines are the hydrographic network of Greece.

Map 2 (or Figure 9) presents the fine-scale distribution of reed burnings in two converted wetlands and two existing wetlands over a Corine Label 3 LU background at a NUTS 0 level. Yiannitsa area is one of the most extensive "land reclamation works", and Copaida is Greece's first large-scale lake drainage work (see Table 2). Thrace and Ileia are existing Ramsar wetlands of international importance in the Ramsar Convention list. The reed-burning dots are georeferenced on extracts from the pyrographic data throughout 2020–2022, illustrating the precise locations and intensity of burning events in these wetlands.

"Hotspot" is used here in a casual and evocative manner. Hotspot encapsulates the meaning of an area of elevated burning incidence or prevalence or a geographic cluster of reed-bed-burning cases. It also indicates an area with a high frequency of occurrence or re-occurrence of burning events.

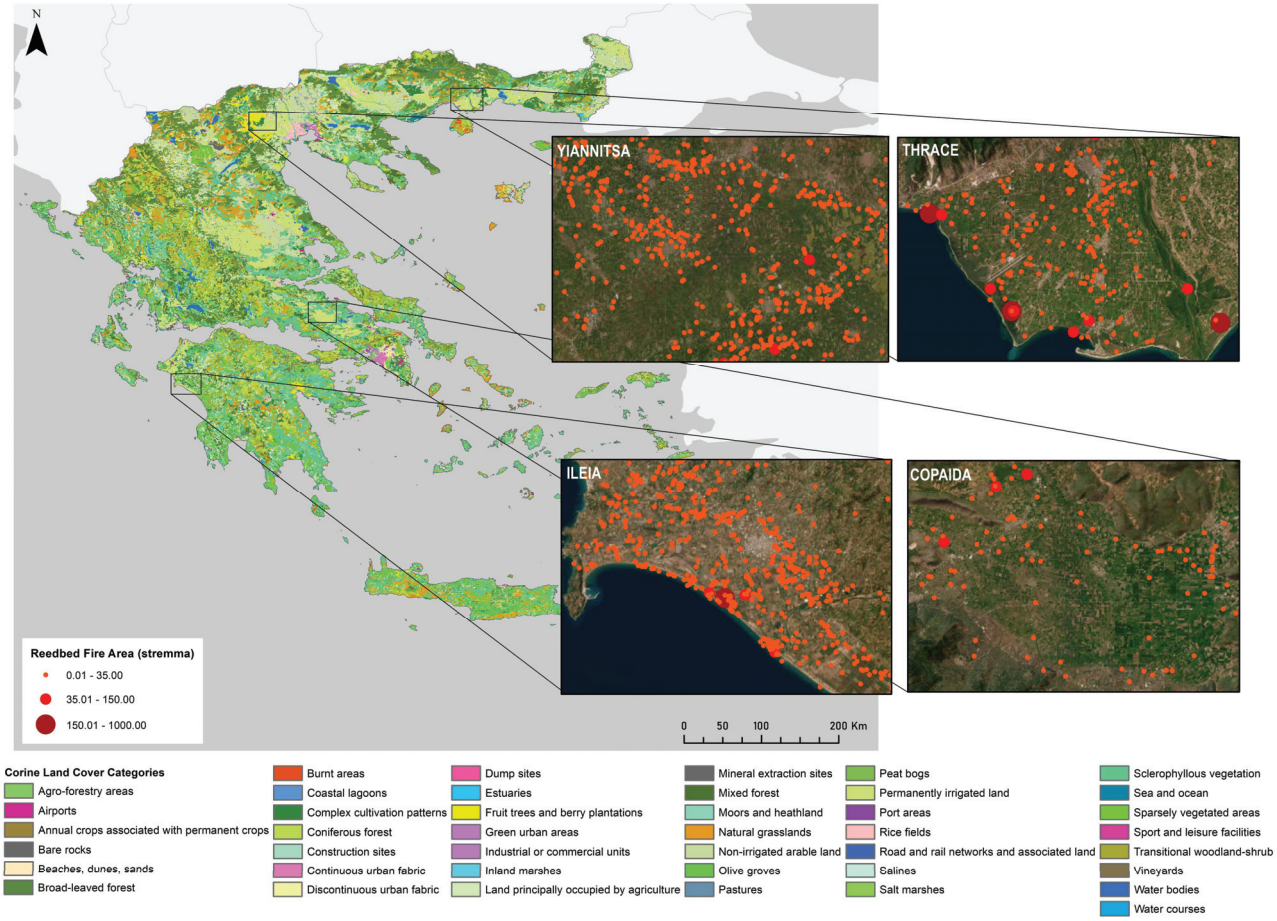

Figure 9. (**Map 2**) Indicative examples of reed-bed-burning distribution in two converted wetlands (Yiannitsa and Kopaida) and two existing Ramsar wetlands of international importance (Thrace: Lake Ismarida, Porto, and lagoons; and Ileia: Cothychi).

All wetlands suffer extensive reed bed burning, indicating the recovery potential of the indicator species *P. australis* and the need to apply fire in the converted wetlands as an agricultural management practice. Most importantly, the status of the protected area in the Ramsar wetlands is ineffective since in Thrace (Lake Ismarida, Porto, and lagoons) and Ileia (Cothychi), the density of the recurring reed burnings is practically higher than in the converted wetlands. Therefore, besides the value of reed burnings as an indicator of wetland conditions, these results are a "metric" of bad environmental governance in the country, even today.

Map 3 (or Figure 10) presents the results of applying the score function.

$$S(W|R) = \ln\left(\frac{P(W|R)}{P(\overline{W}|R}\right) + \ln\left(\frac{P(W)}{P(\overline{W})}\right) > 0$$

(See the analysis and rationale in Section 2.2 above.) Black-bordered polygons are neighboring grid cells delimiting those areas in Greece where the human–*P. australis* ('wetlands') interactions were continuous during the existence of modern Greece as a nation state.

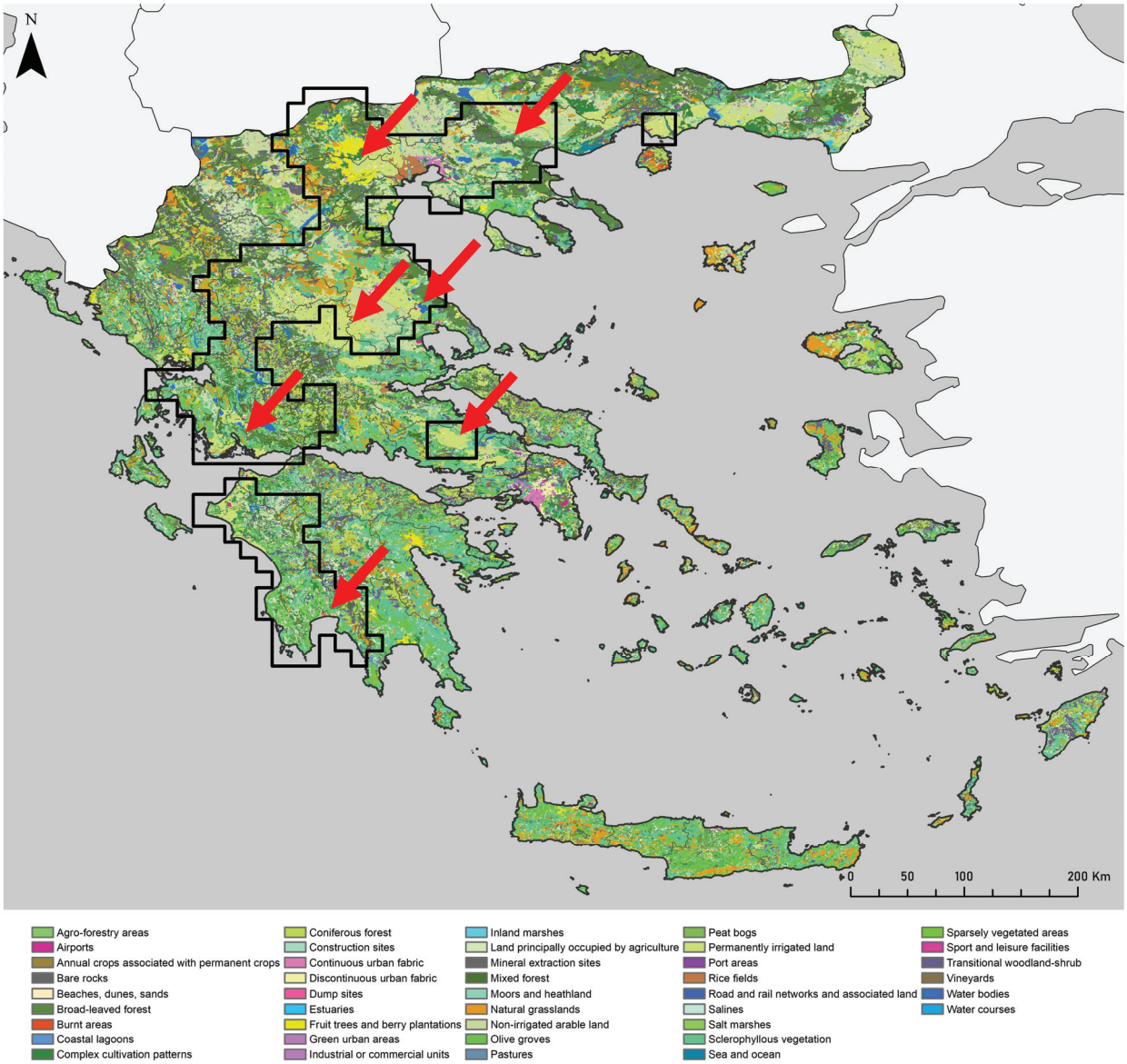

Figure 10. (**Map 3**) Blocks of adjacent grid cells present positive values of the score function. This applies to both converted and existing wetlands in Greece. Red arrows indicate the locations of the extensive land reclamation works in Greece for more than a century to develop agricultural land and secure food sufficiency for the growing population.

4. Discussion

The results allow for building storytelling to provide a verisimilar, credible, but not mispresented [80,81] interpretation of the complex evolving phenomenon of human–wetland interactions into simpler components [82]. Hopefully, this might help inspire future alternatives to socially relevant LU/LUCC scientific research in the polysemic perception of *P. australis* and, eventually, its companion species as an indicator of wetlands' spatial dynamics and uses.

At the nucleus of the present discussion puts forth the value of storytelling as a structured narrative [81] on wetlands' use—and abuse—trajectory in the case study of modern Greece. Storytelling might appear to deviate from the systematic and logical approach to discovering characteristics of the noble method of science, especially after the Popperian paradigm. The genuine scientific scrutiny of this contribution is the assertion that while storytelling and the scientific method may seem different at first glance, e.g., the lack of falsification, replication, or controlled experimentation, they are both essen-

tial tools for understanding and explaining the human–wetlands interactions in a country in the process of modernization and growth. They each have their strengths and can be used together to effectively communicate complex ideas and engage a broad audience. One would humbly underscore that our approach is somewhat inspired by the mixed scientific method that acquired its *lettres de noblesse* after J. Diamond's works, e.g., *Collapse*, although it is subject to ongoing debate and criticism in academic circles [83].

The core problem with storytelling constructions such as ours is the validation and limitations of data [84]. As clearly described in the Methods section, data on every fire event are published yearly and standardized under the EFFIS system (Table 1). Then, the categories and classes of fire events records present are uniform at the pan-European level. The same stands true for the causes of fires [31]. As to the limitations of data, possible sources of weak reliability are (1) the lack of standardized topographic data compatible with the modern georeferenced boundaries of converted wetlands in the 19th century and the first half of the 20th century. (2) Limited knowledge of firefighters on the ground as to the taxonomy of wetland keystone plant species. For example, the severity index (SI) mainly orbits around the reliability of data obtained from the Firefighting Corp database, as, at times, the separation of vegetation types is particularly difficult for non-specialists. Future research should include species-specific data to ensure the distinction between the types of fires and species and enhance the indicator's accuracy. This is why we adopted the morphospecies taxonomy of *P. australis* as the indicator of this category of helophytes. (3) Geographic coordinates of fire events have been kept on record since 2020. This is important for the systematic monitoring of reed bed fires or burnings, which are abundant in yearly frequency but of small size per event (Figures 2 and 4, Section 3). However, the pyrogeographic map of reed bed fires or burnings presents interannual consistency (Map 1, Figure 8).

The association of *P. australis* with wetland conditions, existing presently or converted in the past, appears well established in spatial, ecological, and time scales, as well as in land-use conditions. As strongly stated in earlier sections, the conversion of wetlands into agricultural land was inextricably intertwined with the establishment and development of modern Greece (especially the period 1830–1960). However, apprehending post-1960s reed bed burning as an exclusive agricultural practice like crop residue clearing in cereals' and industrial crops' cultures, e.g., cotton, tobacco, and biofuel-transformable plants, is a limited or narrow explanation of the dynamics of the phenomenon in the terrain. Although agriculture-related uses, as classified in the Corine NUTS 3 level, dominate the reed-bed-fire frequency, total area, and SI, it is remarkable that infrastructure, tourism-related, or semi-industrial activities present significant parts in the non-converted wetland reed-bed-fire phenomenon. For instance, in island setups, airfields are often situated in flat sea-shore areas that, in most cases, are or were coastal wetlands. Repeatedly burning the rapidly recovering reed beds is a safety measure for airplanes' movements in these airports (Map 2, Figure 9).

Our storytelling explanation articulates the hypotheses announced and explained in Methods Section 2.5. At first, anthropogenic reed bed burnings present the lowest severity index (SI) value among all vegetation types, more or less of the same order as crop residue agricultural burnings. This mainly concerns the sporadic appearance of post-burning recovering reed bed stands within agricultural lands. Second, the time series of SI, at any scale, is stationary (Figure 6), suggesting a constancy in the basic statistical parameters, e.g., the mean and variance of the SI distribution. However, it should be noted that two periodicities in the SI variation might be identified. The first relates to very small or small reed bed burnings; in such cases, the return time of the phenomenon is ~3 years. The second refers to large reed bed fires as parts of wetland watershed wildfires or mega-fires; in such cases, the return time has ~7–8 years in Greece since 2000 (Figure 7). Regarding the spatial pattern of reed bed burnings or fires, "hotspots", i.e., areas of elevated burning incidence or prevalence or a geographic cluster of reed-bed-burning cases, are discernable (Map 1, Figure 8).

Although indirectly suggested in the previous sections, one might attempt to complement the storytelling on reed bed burning as an indicator of the dynamics of the wetlands in modern Greece with a series of questions open for future research, either at the national or the international level. We focus on the following priorities:

1. Ecological Repercussions: while mainly affecting the keystone indicator species, reed bed burning impacts the broader wetland ecosystem. It influences the intricate web of biodiversity and ecosystem services, potentially impacting water quality, habitat availability, and overall resilience. Understanding these ecological implications is crucial for devising conservation strategies that address the multifaceted dynamics of wetland ecosystems.
2. Climate Change Resilience: Exploring the role of reed bed burning within climate change mitigation policies unveils its potential contributions to adaptive wetland management. Assessing its impact on carbon sequestration, water regulation, and ecosystem stability provides insights into whether this practice aligns with broader climate change mitigation goals. Acknowledging and evaluating the intricate relationship between reed bed burning and climate resilience is pivotal for sustainable land-use planning.
3. Policy and Management Recommendations: This research underscores the need for comprehensive policy frameworks and adaptive management strategies to balance agricultural, infrastructural, and conservation interests. By recommending nuanced approaches that integrate ecological sensitivity with socio-economic needs, this study underlines the need to develop effective wetland management plans. The presence of these historical, currently converted wetlands plays a significant role in recognizing the natural state of areas to avoid and prevent the destruction of human infrastructure, which in most cases would be flooding since wetlands are natural systems created in drainage basins.
4. Emphasizing the importance of collaborative governance ensures the sustainability of wetland ecosystems in the face of evolving land-use dynamics. An outstanding example certainly is the recent flooding of Lake Karla (September 2023), located in Thessaly (EM-DAT platform on natural hazards and disaster, record 2023-0582-GRC), i.e., one of the last large-scale drainage or land reclamation works (Table 2, Methods section). During the "Daniel storm", the original lake regained its initial place and area in less than two days (1,900,000 stremma flooded after precipitations >1000 tons/stremma). Efforts have been made during the last decades to correct the damage from such initial extensive drainage works, thus emphasizing the importance of collaborative governance between farmers, scientists, planners, and politicians to ensure the sustainability of wetland ecosystems in the face of evolving land-use dynamics and climate change pressures. This was going in the right direction but was also too late and too slow as a process.
5. Global Relevance: Extending the proposed indicator's applicability to a global context, the research suggests that insights gained from the study can inform wetland conservation efforts worldwide. By highlighting the index's transferability to diverse socio-ecological settings, this study emphasizes the potential for international collaboration in addressing the everyday challenges wetland ecosystems face. This global perspective underscores the importance of shared knowledge and cooperative efforts in safeguarding these critical habitats.
6. Community Engagement: Recognizing the pivotal role of local communities in wetland conservation, this study advocates for inclusive community engagement. By incorporating traditional ecological knowledge and fostering community-driven initiatives, this research promotes a sense of stewardship among residents. This collaborative approach ensures that wetland conservation aligns with the communities' values and agricultural land management practices intertwined with these ecosystems.

Expanding the proposed indicator species as a precise "locating device" for estimating converted wetland-type conditions requires a multifaceted approach. Additional parameters and pressures should be systematically incorporated to enhance the indicators' accuracy and applicability. Key considerations include introducing land-use history data to capture the temporal evolution of converted wetlands, offering a more nuanced understanding of their transformation over time. Hydrological dynamics, such as changes in water flow and soil moisture, should be integrated to provide insights into the ongoing ecological processes within converted wetlands.

Furthermore, socio-economic indicators, including land ownership patterns and agricultural practices, can contribute valuable context to the indicator. Understanding the human dimensions associated with converted wetlands enables a more comprehensive evaluation of the interplay between anthropogenic activities and ecological responses. Leveraging advanced geospatial technologies and machine learning algorithms may facilitate real-time monitoring and predictions of converted wetland conditions, enhancing the indicator's adaptive management capabilities. Collaborative initiatives involving researchers, land managers, and policymakers are essential to ensure that the index remains relevant, responsive, and effective in promoting sustainable land-use practices and the conservation of converted wetland ecosystems.

Author Contributions: Conceptualization, A.Y.T. and C.M.G.; methodology, A.Y.T.; software, C.M.G. and T.K.; validation, C.M.G., T.K. and A.Y.T.; formal analysis, C.M.G. and A.Y.T.; investigation, C.M.G. and A.Y.T.; resources, T.K.; data curation, C.M.G.; writing—original draft preparation, C.M.G. and A.Y.T.; writing—review and editing, A.Y.T.; visualization, C.M.G., T.K. and A.Y.T.; supervision, A.Y.T.; project administration, A.Y.T. All authors have read and agreed to the published version of the manuscript.

Funding: This research received no external funding.

Data Availability Statement: The data presented in this study are available on request from the corresponding author due to privacy restrictions.

Conflicts of Interest: The authors declare no conflicts of interest.

Appendix A

Appendix A presents a synopsis of spatial pyrogeographic data of a NUTS 3 level (prefectures of Greece), emphasizing the average severity index (2000–2022). Area/prefecture is presented in stremma (0.1 ha). AL: agricultural land; SG: shrubland/grasslands; WER: wetlands. This collection refers primarily to LUs that are prone to "arson" as management practices of farmers and shepherds.

Table A1. Severity index by prefecture 2000–2022 (stremma).

Prefecture	Area Stremma	% of AL	% of SG	% of WET	SI AL	SI SG	SI WET
Aetolia-Acarnania	5,461,000	32%	28%	3%	33.06	17.05	10.33
Larissa	5,381,000	52%	33%	2%	34.85	66.19	0.22
Ioannina	4,991,000	17%	38%	4%	13.91	32.85	2.09
Phthiotis	4,441,000	42%	34%	1%	14.81	44.93	7.94
Arcadia	4,419,000	27%	52%	1%	167.13	76.76	3.10
Evros	4,242,000	52%	16%	5%	54.92	65.57	2.73
Euboea	4,167,000	32%	40%	2%	6.64	12.07	15.92
Serres	3,968,000	51%	17%	3%	83.81	101.84	20.83
Attica	3,808,000	35%	28%	4%	91.74	43.45	13.10
Thessaloniki	3,683,000	55%	19%	2%	67.35	34.91	1.92
Laconia	3,636,000	39%	46%	3%	102.35	151.99	13.69

Table A1. *Cont.*

Prefecture	Area Stremma	% of AL	% of SG	% of WET	SI AL	SI SG	SI WET
Kozani	3,516,000	39%	29%	9%	310.03	479.58	22.52
Drama	3,468,000	20%	24%	1%	576.20	274.10	112.35
Trikala	3,384,000	28%	36%	3%	16.56	6.01	2.97
Achaea	3,271,000	38%	41%	3%	52.11	71.97	35.36
Messenia	2,991,000	54%	29%	1%	15.10	24.95	22.86
Boeotia	2,952,000	44%	40%	1%	71.57	62.40	6.36
Chalkidiki	2,918,000	43%	23%	0%	15.16	15.92	0.71
Dodecanese	2,714,000	26%	56%	5%	30.32	6.99	5.39
Heraklion (Crete)	2,641,000	59%	33%	3%	23.87	34.93	15.12
Karditsa	2,636,000	51%	22%	1%	52.03	73.87	3.35
Magnesia	2,636,000	37%	41%	1%	94.55	27.76	23.31
Ilia	2,618,000	69%	20%	1%	29.60	78.10	11.25
Cyclades	2,572,000	31%	61%	2%	6.21	15.15	0.00
Rhodope	2,543,000	46%	24%	3%	12.02	43.55	9.65
Kilkis	2,519,000	63%	13%	0%	42.47	213.63	1.38
Pella	2,506,000	47%	17%	1%	11.89	53.64	7.46
Chania (Crete)	2,376,000	32%	50%	4%	8.19	35.85	2.19
Corinthia	2,291,000	41%	35%	2%	696.00	190.26	35.54
Grevena	2,291,000	34%	26%	1%	14.74	63.16	5.66
Argolis	2,154,000	39%	52%	2%	28.54	17.09	17.30
Lesbos	2,154,000	47%	37%	1%	86.00	52.68	3.72
Phocis	2,121,000	14%	41%	3%	13.65	9.46	6.18
Kavala	2,111,000	33%	30%	3%	43.54	97.57	1.56
Florina	1,924,000	34%	26%	4%	22.72	39.13	17.04
Evrytania	1,869,000	8%	38%	3%	6.48	77.54	2.07
Lasithi (Crete)	1,823,000	34%	56%	5%	54.36	57.65	1.89
Xanthi	1,793,000	35%	18%	3%	52.78	45.93	1.85
Kastoria	1,721,000	29%	30%	1%	23.17	56.23	5.66
Imathia	1,701,000	50%	12%	2%	9.13	35.35	0.62
Arta	1,662,000	31%	42%	5%	250.58	221.33	23.32
Pieria	1,516,000	50%	8%	3%	123.63	110.30	0.29
Thesprotia	1,515,000	25%	51%	3%	20.29	172.49	6.67
Rethymno (Crete)	1,496,000	44%	46%	5%	120.60	11.46	2.05
Preveza	1,036,000	40%	40%	6%	11.00	25.53	10.92
Chios	904,000	28%	57%	10%	121.41	58.83	1.47
Kefalonia	904,000	33%	42%	2%	220.29	100.31	4.60
Samos	778,000	32%	42%	6%	11.99	30.47	2.81
Corfu	641,000	73%	13%	4%	43.86	77.31	5.78
Zakynthos	406,000	53%	35%	1%	155.93	185.08	1.22
Lefkada	356,000	47%	33%	1%	35.42	14.83	21.05

Appendix B

This is a NASA Terra satellite image of the mega-fire conditions in the Peloponnese on 26 August 2007. Coastal wetlands of the prefecture of Ilia burned for more than a week before suppression. It corresponds to the upper-limit truncation, smax, of the frequency–size distribution presented in Figure 2 (main text).

Figure A1. Satellite image (NASA Terra) of the mega-fire conditions in the Peloponnese on 26 August 2007. Coastal wetlands of the prefecture of Ilia burned for more than a week before suppression.

References

1. Flyvbjerg, B. Five misunderstandings about case-study research. *Qual. Inq.* **2006**, *12*, 219–245. [CrossRef]
2. Rudel, T.K. Meta-analyses of case studies: A method for studying regional and global environmental change. *Glob. Environ. Change* **2008**, *18*, 18–25. [CrossRef]
3. Magliocca, N.R.; Rudel, T.K.; Verburg, P.H.; McConnell, W.J.; Mertz, O.; Gerstner, K.; Heinimann, A.; Ellis, E.C. Synthesis in land change science: Methodological patterns, challenges, and guidelines. *Reg. Environ. Chang.* **2015**, *15*, 211–226. [CrossRef]
4. Van Vliet, J.; Magliocca, N.R.; Büchner, B.; Cook, E.; Benayas, J.M.R.; Ellis, E.C.; Heinimann, A.; Keys, E.; Lee, T.M.; Liu, G.; et al. Meta-studies in land use science: Current coverage and prospects. *Ambio* **2016**, *45*, 15–28. [CrossRef] [PubMed]
5. Rindfuss, R.R.; Entwisle, B.; Walsh, S.J.; An, L.; Badenoch, N.; Brown, D.G.; Deadman, P.; Evans, T.P.; Fox, J.; Geoghegan, J.; et al. Land use change: Complexity and comparisons. *J. Land Use Sci.* **2008**, *3*, 1–10. [CrossRef] [PubMed]
6. Scullion, J.J.; Vogt, K.A.; Drahota, B.; Winkler-Schor, S.; Lyons, M. Conserving the Last Great Forests: A Meta-Analysis Review of the Drivers of Intact Forest Loss and the Strategies and Policies to Save Them. *Front. For. Glob. Chang.* **2019**, *2*, 62. [CrossRef]
7. Fang, X.Z.; Ghazali, S.; Azadi, H.; Skominas, R.; Scheffran, J. Agricultural land conversion and ecosystem services loss: A meta-analysis. *Environ. Dev. Sustain.* **2023**.
8. Gao, J.; O'Neill, B. Different Spatiotemporal Patterns in Global Human Population and Built-Up Land. *Earth's Future* **2021**, *9*, e2020EF001920. [CrossRef]
9. Vereecken, H.; Amelung, W.; Bauke, S.L.; Bogena, H.; Brüggemann, N.; Montzka, C.; Vanderborght, J.; Bechtold, M.; Blöschl, G.; Carminati, A.; et al. Soil hydrology in the Earth system. *Nat. Rev. Earth Environ.* **2022**, *3*, 573–587. [CrossRef]
10. Ackerschott, A.; Kohlhase, E.; Vollmer, A.; Hörisch, J.; Von Wehrden, H. Steering of land use in the context of sustainable development: A systematic review of economic instruments. *Land Use Policy* **2023**, *129*, 106620. [CrossRef]
11. Let, M.; Pal, S. Socio-ecological well-being perspectives of wetland loss scenario: A review. *J. Environ. Manag.* **2023**, *326*, 116692. [CrossRef]
12. Kiviat, E. Ecosystem services of *Phragmites* in North America with emphasis on habitat functions. *AoB Plants* **2013**, *5*, plt008. [CrossRef]
13. IPBES. *Global Assessment Report on Biodiversity and Ecosystem Services of the Intergovernmental Science-Policy Platform on Biodiversity and Ecosystem Services*; Brondizio, E.S., Settele, J., Díaz, S., Ngo, H.T., Eds.; IPBES Secretariat: Bonn, Germany, 2019. [CrossRef]

14. FAO. *Global Forest Resource Assessment (GFRA) Summary 2015*; Food & Agriculture Organization: Rome, Italy, 2016.
15. Ramsar Convention on Wetlands. *Global Wetland Outlook: State of the World's Wetlands and Their Services to People*; Ramsar Convention Secretariat: Gland, Switzerland, 2018.
16. Mitsch, W.J.; Gosselink, J.G. *Wetlands*; John Wiley Sons: Hoboken, NJ, USA, 2015.
17. Costanza, R.; d'Arge, R.; De Groot, R.; Farber, S.; Grasso, M.; Hannon, B.; Limburg, K.; Naeem, S.; O'Neill, R.V.; Paruelo, J.; et al. The value of the world's ecosystem services and natural capital. *Nature* **1997**, *387*, 253–260. [CrossRef]
18. Romanazzi, G.R.; Koto, R.; De Boni, A.; Palmisano, G.O.; Cioffi, M.; Roma, R. Cultural ecosystem services: A review of methods and tools for economic evaluation. *Environ. Sustain. Indic.* **2023**, *20*, 100304. [CrossRef]
19. Demarquet, Q.; Rapinel, S.; Dufour, S.; Hubert-Moy, L. Long-Term Wetland Monitoring Using the Landsat Archive: A Review. *Remote Sens.* **2023**, *15*, 820. [CrossRef]
20. Abdelmajeed, A.Y.A.; Albert-Saiz, M.; Rastogi, A.; Juszczak, R. Cloud-based Remote Sensing for Wetland Monitoring—A Review. *Remote Sens.* **2023**, *15*, 1660. [CrossRef]
21. Lizotte, R.E.; Smiley, P.C.; Gillespie, R.B.; Knight, S.S. Agricultural Conservation Practices and Aquatic Ecological Responses. *Water* **2021**, *13*, 1687. [CrossRef]
22. Maltby, E. The Wetlands Paradigm Shift in Response to Changing Societal Priorities: A Reflective Review. *Land* **2022**, *11*, 1526. [CrossRef]
23. Reis, V.; Hermoso, V.; Hamilton, S.K.; Ward, D.; Fluet-Chouinard, E.; Lehner, B.; Linke, S. A global assessment of inland wetland conservation status. *Bioscience* **2017**, *67*, 523–533. [CrossRef]
24. Seifollahi-Aghmiuni, S.; Kalantari, Z.; Egidi, G.; Gaburova, L.; Salvati, L. Urbanization-driven land degradation and socioeconomic challenges in peri-urban areas: Insights from Southern Europe. *Ambio* **2022**, *51*, 1446–1458. [CrossRef]
25. White, E.E.; Ury, E.A.; Bernhardt, E.S.; Yang, X. Climate change driving widespread loss of coastal forested wetlands throughout the North American coastal plain. *Ecosystems* **2022**, *25*, 812–827.
26. Richards, D.R.; Friess, D.A. Rates and drivers of mangrove deforestation in Southeast Asia, 2000–2012. *Proc. Natl. Acad. Sci. USA* **2016**, *113*, 344–349. [CrossRef] [PubMed]
27. Taylor, N.G.; Grillas, P.; Al Hreisha, H.; Balkiz, Ö.; Borie, M.; Boutron, O.; Catita, A.; Champagnon, J.; Cherif, S.; Çiçek, K.; et al. The future for Mediterranean wetlands: 50 key issues and 50 important conservation research questions. *Reg. Environ. Chang.* **2021**, *21*, 33. [CrossRef]
28. Xiong, Y.; Mo, S.H.; Wu, H.P.; Qu, X.Y.; Liu, Y.Y.; Zhou, L. Influence of human activities and climate change on wetland landscape pattern—A review. *Sci. Total Environ.* **2023**, *879*, 163112. [CrossRef] [PubMed]
29. Bowman, D.M.J.S.; O'Brien, J.A.; Goldammer, J.G. Pyrogeography and the Global Quest for Sustainable Fire Management. *Annu. Rev. Environ. Resour.* **2013**, *38*, 57–80. [CrossRef]
30. Ludwig, D.E.; Iannuzzi, T.J.; Esposito, A.N. *Phragmites* and environmental management: A question of values. *Estuaries* **2003**, *26*, 624–630. [CrossRef]
31. Camia, A.; Durrant, T.; San-Miguel-Ayanz, J. *Harmonized Classification Scheme of Fire Causes in the EU Adopted for the European Fire Database of EFFIS*; Executive Report; European Commission, Joint Research Centre: Luxembourg, 2013. [CrossRef]
32. Gerakis, A.; Kalburtji, K. Agricultural activities affecting the functions and values of Ramsar wetland sites of Greece. *Agric. Ecosyst. Environ.* **1998**, *70*, 119–128. [CrossRef]
33. Mpeza, P.E. Management and Sustainability of Greek Wetlands. In *Protected Area Management—Recent Advances*; Suratman, M.N., Ed.; IntechOpen: London, UK, 2022; Volume 368. [CrossRef]
34. Christopoulou, O.G.; Tsachalidis, E. Conservation Policies for Protected Areas (Wetlands) in Greece: A Survey of Local Residents' Attitude. *Water Air Soil Pollut. Focus* **2004**, *4*, 445–457. [CrossRef]
35. Zalidis, G.C.; Mantzavelas, A.L.; Gourvelou, E. Environmental impact on Greek wetlands. *Wetlands* **1997**, *17*, 339–345. [CrossRef]
36. Zafeiriou, E.; Andrea, V.; Tampakis, S.; Karanikola, P. Wetlands Management in Northern Greece: An Empirical Survey. *Water* **2020**, *12*, 3181. [CrossRef]
37. Catsadorakis, G.; Paragamian, K. *Inventory of the Wetlands of the Aegean Islands: Identity, Ecological Status and Threats*; World Wide Fund for Nature—WWF Greece: Athens, Greece, 2007.
38. Merken, R.; Deboelpaep, E.; Teunen, J.; Saura, S.; Koedam, N. Wetland Suitability and Connectivity for Trans-Saharan Migratory Waterbirds. *PLoS ONE* **2015**, *10*, e0135445. [CrossRef]
39. Ailstock, M.S.; Cente, E. Adaptive strategies of common reed Phragmites australis. In Proceedings of the Role of Phragmites in the Mid-Atlantic Region, Princess Anne, MD, USA, 17 April 2000; Volume 17, pp. 1–7.
40. Gradstein, S.R.; Smittenberg, J.H. The hydrophilous vegetation of Western Crete. *Vegetation* **1977**, *34*, 65–86. [CrossRef]
41. Dinka, M.; Szeglet, P. Reed (*Phragmites australis* (Cav.) Trin ex Steudel) growth and production in different habitats of Neusiedlersee (Lake Fertö). *SIL Proc. 1922–2010* **1998**, *26*, 1830–1834. [CrossRef]
42. Goslee, S.C.; Brooks, R.P.; Cole, C.A. Plants as indicators of wetland water source. *Plant Ecol.* **1997**, *131*, 199–206.
43. Mal, T.K.; Narine, L. The biology of Canadian weeds. 129. *Phragmites australis (Cav.) Trin. Ex Steud. Can. J. Plant Sci.* **2004**, *84*, 365–396. [CrossRef]
44. Srivastava, J.; Kalra, S.J.S.; Naraian, R. Environmental perspectives of *Phragmites australis* (Cav.) Trin. Ex. Steudel. *Appl. Water Sci.* **2014**, *4*, 193–202. [CrossRef]

45. Krzton-Presson, A.; Davis, B.; Raper, K.; Hitz, K.; Mecklin, C.; Whiteman, H. Effects of *Phragmites* Management on the Ecology of a Wetland. *Northeast. Nat.* **2018**, *25*, 418–436. [CrossRef]
46. Trettin, C.C.; Kolka, R.K.; Marsh, A.S.; Bansal, S.; Lilleskov, E.A.; Megonigal, P.; Stelk, M.J.; Lockaby, G.; D'Amore, D.V.; MacKenzie, R.A.; et al. Wetland and Hydric Soils. In *Forest and Rangeland Soils of the United States Under Changing Conditions*; Pouyat, R.V., Page-Dumroese, D.S., Patel-Weynand, T., Geiser, L.H., Eds.; Springer Open: Berlin/Heidelberg, Germany, 2020; pp. 99–126. [CrossRef]
47. Navas, M.L.; Violle, C. Plant traits related to competition: How do they shape the functional diversity of communities? *Community Ecol.* **2009**, *10*, 131–137. [CrossRef]
48. Kunstler, G.; Falster, D.; Coomes, D.A.; Hui, F.; Kooyman, R.M.; Laughlin, D.C.; Poorter, L.; Vanderwel, M.; Vieilledent, G.; Wright, S.J.; et al. Plant functional traits have globally consistent effects on competition. *Nature* **2016**, *529*, 204–207. [CrossRef]
49. Milke, J.; Gałczyńska, M.; Wróbel, J. The Importance of Biological and Ecological Properties of *Phragmites australis* (Cav.) Trin. Ex Steud., in Phytoremediation of Aquatic Ecosystems—The Review. *Water* **2020**, *12*, 1770. [CrossRef]
50. Cronin, J.T.; Kiviat, E.; Meyerson, L.A.; Bhattarai, G.P.; Allen, W.J. Biological control of invasive *Phragmites australis* will be detrimental to native *P. australis*. *Biol. Invasions* **2016**, *18*, 2749–2752. [CrossRef]
51. Alvarez-Cobelas, M.; Sánchez-Carrillo, S.; Cirujano, S.; Angeler, D.G. Long-term changes in spatial patterns of emergent vegetation in a Mediterranean floodplain: Natural versus anthropogenic constraints. *Plant Ecol.* **2008**, *194*, 257–271. [CrossRef]
52. Coffman, G.C.; Ambrose, R.F.; Rundel, P.W. Wildfire promotes dominance of invasive giant reed (*Arundo donax*) in riparian ecosystems. *Biol. Invasions* **2010**, *12*, 2723–2734. [CrossRef]
53. Kimura, H.; Tsuyuzaki, S. Fire severity affects vegetation and seed bank in a wetland. *Appl. Veg. Sci.* **2011**, *14*, 350–357. [CrossRef]
54. Pérez, M.E.P.; Lindig-Cisneros, R.; Moreno-Casasola, P. Invasiveness of *Phragmites australis* in communities dominated by native species after fire disturbance under controlled conditions. *Hidrobiologica* **2018**, *28*, 201–207. [CrossRef]
55. Dámaso, W.; Ramirez, G.; Lértora, R.; Pujana, R.R. *Phragmites australis* effects on vegetation structure and functional diversity of the marsh area in NE Argentina. *J. Plant Ecol.* **2015**, *8*, 136–147. [CrossRef]
56. Link, N.T.; McLaughlin, D.L.; Bush, N.; Wurster, F.C. Phragmites-Fire Feedbacks: The Influence of Fire and Disturbance-Altered Hydrology on the Abundance of *Phragmites australis*. *Biol. Invasions* **2024**, *26*, 135–150. [CrossRef]
57. Martin, R.M.; Moseman-Valtierra, S. Greenhouse Gas Fluxes Vary Between *Phragmites australis* and Native Vegetation Zones in Coastal Wetlands Along a Salinity Gradient. *Wetlands* **2015**, *35*, 1021–1031. [CrossRef]
58. Avers, B.; Fahlsing, R.; Kafcas, E.; Schafer, J.; Collin, T.; Esman, L.; Finnell, E.; Lounds, A.; Terry, R.; Hazelman, J.; et al. *A Guide to the Control and Management of Invasive Phragmites*; Michigan Department of Natural Resources: Lake City, MI, USA, 2013.
59. Granholm, J.M.; Chester, S.E. *A Landowner's Guide to Phragmites Control*; Michigan Department of Environmental Quality (MDEQ): Ann Arbor, MI, USA, 1994. Available online: https://watershedcouncil.org/uploads/7/2/5/1/7251350/deq-ogl-guide-phragmites_204659_7.pdf (accessed on 16 December 2023).
60. Catling, P.M.; Mitrow, G.L. Major Invasive Alien Plants of Natural Habitats in Canada. 1. European Common Reed (Often Just Called Phragmites), *Phragmites australis* (Cav.) Trin. Ex Steud. Subsp. Australis. *Can. Field-Nat.* **2011**, *44*, 52–61.
61. Valkama, E.; Lyytinen, S.; Koricheva, J. The Impact of Reed Management on Wildlife, a Meta-Analytical Review of European Studies. *Biol. Conserv.* **2008**, *141*, 364–374. [CrossRef]
62. Stephens, C.R.; Sánchez-Cordero, V.; Salazar, C.G. Bayesian Inference of Ecological Interactions from Spatial Data. *Entropy* **2017**, *19*, 547. [CrossRef]
63. González-Salazar, C.; Stephens, C.R.; Marquet, P.A. Comparing the relative contributions of biotic and abiotic factors as mediators of species' distributions. *Ecol. Model.* **2013**, *248*, 57–70. [CrossRef]
64. Stephens, C.R.; González-Salazar, C.; Villalobos-Segura, M.D.; Marquet, P.A. Can ecological interaction be inferred from spatial data? *Biodivers. Inform.* **2020**, *15*, 11–54.
65. Araújo, M.B.; Guisan, A. Five (or so) challenges for species distribution modelling. *J. Biogeogr.* **2006**, *33*, 1677–1688. [CrossRef]
66. Fletcher, R.J.; Hefley, T.J.; Robertson, E.P.; Zuckerberg, B.; McCleery, R.A.; Dorazio, R.M. A practical guide for combining data to model species distributions. *Ecology* **2019**, *100*, e02710. [CrossRef]
67. Openshaw, S. *The Modifiable Areal Unit Problem Concepts and Techniques in Modern Geography*; Geo Books: Norfolk, UK, 1983.
68. Hand, D.; Mannila, H.; Smyth, P. *Principles of Data Mining*; MIT Press: Cambridge, MA, USA, 2001.
69. Spanos, K.; Gaitanis, D.; Skouteri, A.; Petrakis, P.; Meliadis, I. Implementation of Forest Policy in Greece in Relation to Biodiversity and Climate Change. *Open J. Ecol.* **2018**, *8*, 174–191. [CrossRef]
70. Troumbis, A.Y.; Kalabokidis, K.; Palaiologou, P. Diverging rationalities between forest fire management services and the general public after the 21st-century mega-fires in Greece. *J. For. Res.* **2022**, *33*, 553–565. [CrossRef]
71. Kousoulis, A.A.; Chatzigeorgiou, K.S.; Danis, K.; Tsoucalas, G.; Vakalis, N.; Bonovas, S.; Tsiodras, S. Malaria in Laconia, Greece, Then and Now: A 2500-Year-Old Pattern. *Int. J. Infect. Dis* **2013**, *17*, 8–11. [CrossRef]
72. Palaiologou, P.; Kalabokidis, K.; Troumbis, A.; Day, M.A.; Nielsen-Pincus, M.; Ager, A.A. Socio-Ecological Perceptions of Wildfire Management and Effects in Greece. *Fire* **2023**, *4*, 18. [CrossRef]
73. WWF Greece. Available online: https://www.wwf.gr/en/our_work/nature/terrestrial/protected_areas/island_wetlands/ (accessed on 16 December 2023).
74. Troumbis, A.Y.; Gaganis, C.M.; Sideropoulos, H. Probabilistic Wildfire Risk Assessment and Modernization Transitions: The Case of Greece. *Fire* **2023**, *6*, 158. [CrossRef]

75. Song, W.G.; Wang, J.; Satoh, K.; Fan, W.C. Three types of power-law distribution of forest fires in Japan. *Ecol. Model.* **2006**, *196*, 527–532. [CrossRef]
76. Bak, P.; Chen, K.; Tang, C. A Forest-Fire Model and Some Thoughts on Turbulence. *Phys. Lett. A* **1990**, *147*, 297–300. [CrossRef]
77. Newman, M. Power Laws, Pareto Distributions and Zipf's Law. *Contemp. Phys.* **2005**, *46*, 323–351. [CrossRef]
78. Serra-Peralta, M.; Serra, J.; Corral, A. Lognormals, power laws and double power laws in the distribution of frequencies of harmonic codewords from classical music. *Sci. Rep.* **2022**, *12*, 2615. [CrossRef] [PubMed]
79. Clauset, A.; Shalizi, C.R.; Newman, M.E.J. Power-Law Distributions in Empirical Data. *SIAM Rev.* **2009**, *51*, 661–703. [CrossRef]
80. Wikipedia. Available online: https://en.wikipedia.org/wiki/2007_Greek_forest_fires (accessed on 25 February 2024).
81. Ettinger, J.; Otto, F.E.L.; Schipper, E.L.F. Storytelling can be a powerful tool for science. *Nature* **2021**, *589*, 352. [CrossRef] [PubMed]
82. Maditinos, Z.; Vassiliadis, C. Mega Fires: Can They Be Managed Effectively? *Disaster Prev. Manag.* **2011**, *20*, 41–52. [CrossRef]
83. Gause, E. *A Critique: Jared Diamond's Collapse Put in Perspective*; Institute of Archaeology: London, UK, 2014; Volume 24, pp. 1–7. [CrossRef]
84. Blastland, M.; Freeman, A.L.J.; Van der Linden, S.; Marteau, T.M.; Spiegelhalter, D. Five rules for evidence communication. *Nature* **2020**, *587*, 362–364. [CrossRef]

land

MDPI

Article

Multi-Sensor Satellite Images for Detecting the Effects of Land-Use Changes on the Archaeological Area of Giza Necropolis, Egypt

Abdelaziz Elfadaly [1,*], Naglaa Zanaty [1], Wael Mostafa [2], Ehab Hendawy [1] and Rosa Lasaponara [3]

[1] National Authority for Remote Sensing and Space Sciences, Cairo 1564, Egypt; naglaa.zanaty@narss.sci.eg (N.Z.); ehab.hendawy20@gmail.com (E.H.)
[2] Department of Geography, Faculty of Arts, Kafrelsheikh University, Kafrelsheikh 1501, Egypt; wael_hassien@art.kfs.edu.eg
[3] Italian National Research Council, C.da Santa Loja, Tito Scalo, 85050 Potenza, Italy; rosa.lasponara@imaa.cnr.it
* Correspondence: abdelaziz.elfadaly@narss.sci.eg; Tel.: +20-1021390505

Abstract: The World Heritage Committee has been meeting to discuss the arrangements of existing World Heritage Sites, and, on 22–26 October, the area from Giza to the Dahshur was included in the list of World Heritage Sites. According to the Egyptian Antiquities Authority (EAA), the groundwater levels at the Pyramids Plateau are too shallow, which threatens the ancient Sphinx and Pyramids in Giza, Egypt. In addition, many geophysical studies have been carried out in the archaeological area of Giza, which prove that the area is facing the risk of a high level of groundwater, specifically threatening the Sphinx. Recent developments in Earth observation have helped in the field of land monitoring such as land use changes, risk observation, and the creation of models for protecting cultural heritage sites. This study aimed to examine the impact of land use changes on on the archaeological sites of the Giza Necropolis area by integrating various data sources including optical satellite imagery and SRTM data during the period of 1965–2019. A historical database of Corona 1965 and Landsat 2009 data was investigated along with the new acquisitions of Sentinel-2 2016 and Sentinel-1 2016 and 2019. In addition, the radar Sentinel-1 SLC data were collected and analyzed for calculating the land subsidence value in the area of interest through two periods between 6–30 July 2016 and 30 July–15 December 2016. Various methods were implemented, including cluster outliers, the Moran index, and spatial autocorrelation to examine the changes in urban masses. Additionally, the relationship between groundwater leakage and land subsidence in the region was investigated. The analysis was carried out using Envi5.3, ArcMap10.6.1, and SNAP6.0 software to extract spatial data from the raw data. The results from our investigation highlighted rapid changes in urban areas between 1965 and 2019. The data obtained and analyzed from optical and radar satellite imagery showed that changes in land use can cause changes in the topographic situation by decreasing the level of groundwater, which adversely affects Egyptian monumental pyramids and the Sphinx. Land use analysis showed that the urban area represented 7.63% of the total area of the study area in 1965, however it reached 32.72% in 2009, approximately half of the total area in 2016, and in 2019, the urban mass area increased to nearly two-thirds of the total area. The annual growth rate between 1965 and 2019 was estimated by nearly 0.642 km^2/year. These land-use changes possibly affected the land subsidence value (−0.0138 m), causing the rising groundwater level close to the Sphinx. Using the information obtained from our RS- and GIS-based analysis, mitigation strategies have also been identified to support archaeological area preservation.

Keywords: optical data; Sentinel-1 (SLC); land use; GIS tools; risk observation; cultural heritage site management

1. Introduction

Cultural heritage sites are considered a wealth of human civilization beyond their value and are rare and irreplaceable places that show the lifestyles of ancient people [1,2]. UNESCO defined cultural heritage sites as "the result of life and inspiration, which should be protected and preserved" [3]. Cultural heritage regions, encompassing the archaeological and historical built environment and movable heritage, are at risk and still suffer from a lack of specific and systematic risk [4–9]. In 2005, a study prepared by ICOMOS considered the threats to 641 cultural and mixed world heritage properties due to development projects in addition to the lack of quantitative data on trends between 1994 and 2004 [10]. Indeed, the risks that threaten heritage sites include natural (e.g., fires, earthquakes, flooding, tsunami, land and mudslides, winds, tropical storms, land subsidence, etc.) and human factors (e.g., urban development, land drainage, agricultural sprawling, etc.) [11,12]. Egypt has multiple cultural sites, objects, and artifacts, as well as historic rock art sites [13]. For instance, the pyramid fields from Giza to the Dahshur were accepted as one of the World Heritage Sites in October 1979 [14]. Unfortunately, thousands of known and unknown archaeological sites in Egypt are at risk of destruction from urban sprawl and expanding development [15]. Specifically, uncontrolled and unplanned urban growth threatens cultural and ecological heritage and are among the major causes of archaeological site loss and damage [16]. Urban sprawl is generally regarded as one of the major problems accompanying contemporary urbanization in less-developed countries [17]. Around the world, the impacts of urban sprawl include the loss of community and environmental assets, such as cultural heritage sites [18,19], as a result of difficult ground and geo-environmental conditions [20–22].

Recently, UNESCO became able to monitor the cultural heritage status via remote sensing data (e.g., satellite imagery) [23,24]. Indeed, satellite remote sensing is playing an increasingly important role in the risk detection, uncovering, and documentation of natural and human heritage sites [25]. Recently, in addition to archaeological site documentation, archaeological remote sensing and associated technologies (e.g., GIS tools) have enabled the monitoring of cultural heritage areas that are threatened by natural disasters (e.g., climate change, earthquakes) and unplanned human activities (e.g., land use changes) [26–28]. In the same context, the first launched satellite that was used in the field of archaeology, known as the Corona satellite, was produced for espionage and was launched in the 1960s. This satellite became a very important archive for archaeologists due to its high-resolution data and old landscape features [29].

Later, civilian satellites started with the launching of the family of Landsat (e.g., Land-sat-1 on 23 July 1972, Landsat-2 on 22 January 1975, Landsat-3 on 5 March 1978, and Landsat-4 on 16th July 1982), which continuously supported archaeologists with the required information with a spatial resolution data between 60 and 30 m [30]. Based on the need for clear data, multi-series satellite systems, including the French SPOT HRV, Orbview (GeoEye), Quickbird, and Sentinel-2, which are characterized by their high spatial resolution, were launched. In addition, more recent hyperspectral sensors and radar satellites (e.g., Cosmo-Skymed, Sentinel-1) were installed and enabled workers in the field of archaeology to discover several new archaeological sites [31,32].

Ten years ago, the Egyptian Antiquities Authority (EAA) declared that the Pyramids Plateau was threatened by shallow groundwater levels close to the Great Pyramids and the Sphinx in Giza, Egypt. Thus, Egypt and USAID worked together to lower the groundwater to safe levels to protect the archaeological site from further damage [33]. Unfortunately, recent studies revealed high groundwater levels close to the archaeological area [34], which has led to the need for additional extensive and serious work to provide solutions to reduce the groundwater level close to this heritage site.

Additionally, multiple geophysical measurements have been carried out in the region of the Great Pyramids in Giza and have proven that the area suffers from the near-subsurface groundwater level, which strongly affects some archaeological sites in the studied area [35] (Figure 1a). The Giza archive documents show not only a 4500-year-old urban history but also a rapid stream of environmental events [36]. Along with long and se-

quential environmental events, the phenomenon of urban growth had undesirable impacts on the entire Cairo region, particularly in the heritage area of the Great Giza pyramids close to Nazlet El-Samman city [37]. Indeed, geophysics measurements of the Giza Pyramids have indicated that the elevation of the groundwater table ranges mostly between 14.5 m and 17 m in the Khafre Causeway, Sphinx, and Sphinx Temple, central field of Mastaba, Valley Temple of Khafre, and Nazlet El-Samman areas [38]. In Nazlet El-Samman village, geophysical surveys revealed that the elevation of the groundwater was approximately 17 m. This elevation mostly has a link with the Nile alluvium aquifer, which might raise the water table level below the Sphinx area, causing a large risk to the heritage site. The groundwater values of the measured sites revealed that the elevation was between 15 m and 15.5 m. The base-level elevation of the Sphinx is 20 m lower than that of the suburban area of Nazlet El-Samman, which might indicate a recharge of the aquifer below the Sphinx and increased capillary water rise. In the Sphinx area, the groundwater table based on different techniques has an elevation of approximately 15.5 m to 15.8 m. In contrast, the Valley Temple of Khafre and the central field of Mastaba measured a groundwater elevation of approximately 15 m. On the other hand, the Queen Khentkawes tomb has a groundwater elevation of approximately 14.8–15.2 m. Similarly, the Menkaure Valley Temple had an average groundwater elevation of approximately 16 m (Figure 1b). According to the landscape, environment, and geo-environmental status of the study area, great attention should be given to the built-up spaces to the west of the Great Pyramids of Giza, which undoubtedly affected the groundwater table elevation of the area. Thus, a dewatering system should be implemented to lower the groundwater elevation to avoid aggressive hazards at archaeological sites [38].

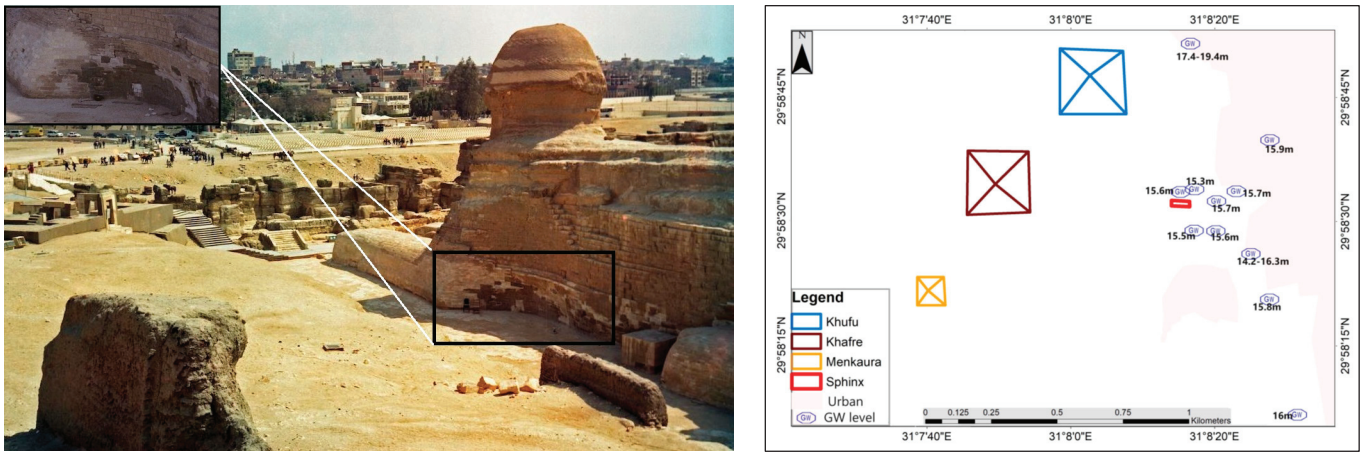

(**a**) (**b**)

Figure 1. Groundwater level close to study area: (**a**) partial deterioration in low part of Sphinx body due to near-subsurface groundwater [39]; (**b**) groundwater elevation values in area of Great Pyramids with particular focus on area of the Sphinx (based on [38]).

Remotely sensed land and groundwater indicators are more capable of providing useful data and information than traditional techniques. Thus, integrated remote sensing and GIS applications are widely utilized in groundwater mapping and have become the main focus of numerous geo-archaeological research, beginning with aerial pictures [40]. Therefore, this paper aims to assess the current status of the Giza heritage area based on the integration between remote sensing and GIS techniques. In addition, the study focuses on identifying and mapping the areas that are influenced by uncontrolled urban expansion and land use change, along with land subsidence. To achieve the study goals and quantify urban sprawl over the years, historical multi-temporal satellite data made up of Corona and Landsat have been investigated along with the new acquisitions provided by Orbview (GeoEye), Sentinel-1, and Sentinel-2 data. Results provided quantitative information on

changes in the uncontrolled urban expansion that occurred around Egyptian monumental sites. On the other hand, the changes in the topography of the study area (land subsidence) were calculated based on the radar Sentinel-1 and SRTM data to show the effects of land use change on the paleo-landscape setting. Finally, based on this remote sensing and GIS-based analysis of multi-temporal and multi-sensor data analysis, a mitigation strategy is proposed for supporting the preservation of the archaeological area.

2. Materials and Methods

2.1. The Study Area

This research focused on the Giza complex situated at 31°7′46.369″ E and 29°58′30.734″ N, which includes the Great Pyramids, funerary, and temples. This area is situated on a plateau approximately 66 m above sea level [41]. The study area includes the Great Pyramid (the pyramid of "Khufu"), which was built in the mid-20th century BC for the fourth-dynasty pharaoh; the pyramid of his son, "Khafre" (the middle one in size), is slightly smaller than that of Khufu; and the pyramid of "Menkaure" (his grandson), which is the third smallest in size and forms a complex beside the Sphinx [42]. This area is famed for the presence of various temples and tombs dated primarily to the Old Kingdom and later Egyptian Kingdoms, particularly the New until the Late Kingdoms (Pharaoh's age), in ancient Egyptian history [43,44] (Figure 2a,b).

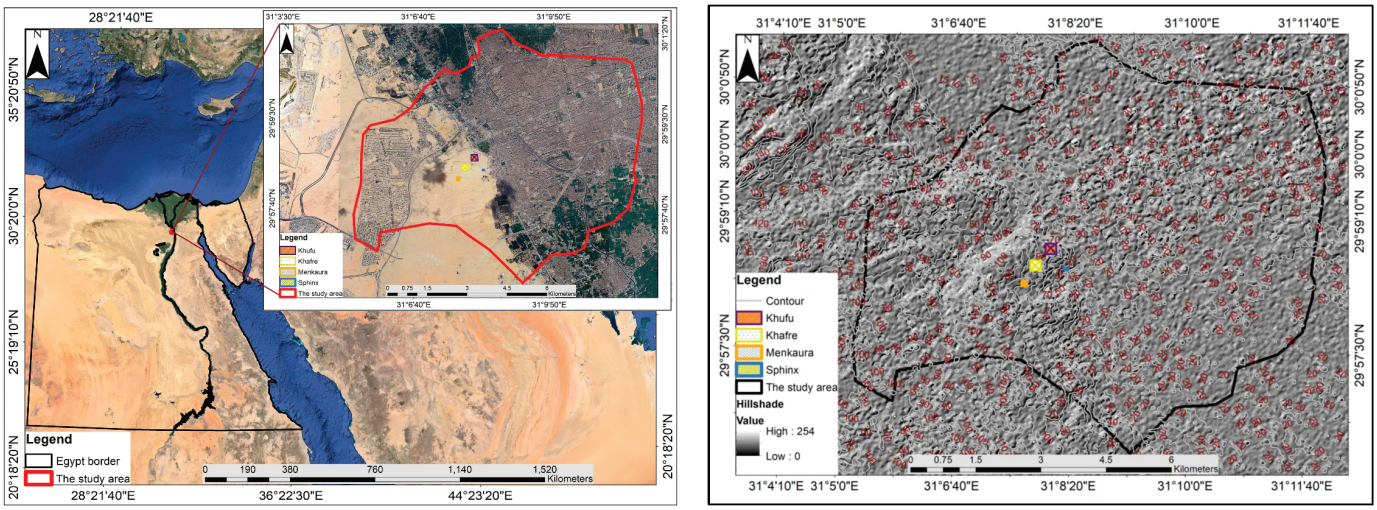

(**a**) (**b**)

Figure 2. It shows the study area: (**a**) location map of Egypt highlighting area of interest obtained from Google Earth and Sentinel-2 imagery with the Great Giza Pyramids and Sphinx; (**b**) hillshade of study area including contour lines and elevation points obtained from SRTM 1 Arc-Second Global.

2.2. Material

Multiple satellite sensors were utilized in this research, including the optical satellite imagery Corona (KH-4A) captured on 25 January 1965, Landsat5 (TM) captured on 7 May 2009, and the radar SRTM (1_arc-second) satellite image captured on 22 September 2014. These free-charge data were downloaded from the U.S. Geological Survey (USGS) website [45] and were used to detect and estimate the changes in the built-up areas close to the study area. In addition, it enables the creation of the SWAT model derived from SRTM data (ArcSWAT 2012.10.6.24) obtained from [46]. Additionally, the optical satellite Sentinel-2A image obtained from ESA [47] was captured on 25 December 2016, along with the radar Sentinel-1A (SLC) image acquired in 2016 and 2019 (Table 1). These data were used for calculating the changes in the built-up areas around the study area in addition to the effects of these changes on the study area topography. The data were analyzed, and the required information was obtained using SNAP 9.0, ArcMap 10.6.1, and Envi 5.3 software.

Table 1. Data utilized and satellite imagery specifications.

Number	Satellite	Sensor	Acquisition Date	Source
1	Corona	KH-4A	25 January 1965	USGS
2	Landsat5	TM	7 May 2009	USGS
3	Sentinel	2A	25 December 2016	USGS
4	SRTM	1 arc-second	22 September 2014	USGS
5	Sentinel	1A_IW_SLC	6 and 30 July, and 15 December 2016	ESA
6	Sentinel	1A_IW_SLC	3 July 2019	ESA

2.3. Methods

In this research, an integration between optical and radar data was implemented to detect the changes in the urban areas between 1965 and 2019, along with the geo-environmental status of the region. The optical Corona, Landsat, Sentinel-2, and radar Sentinel-1 data were preprocessed, processed, and post-processed to measure the changes in the built-up area. Based on the vector built-up data extracted from the raster satellite imagery, some spatial statistics were processed to calculate the changes in the space values between 1965 and 2019 using ArcMap software 10.6.1. Furthermore, the radar SRTM data were used to evaluate the topographic setting of the study area. Thus, the land subsidence rate was calculated based on the changes in elevation from 6–30 July 2016. The following sections will explain the applied techniques in this study in detail.

2.3.1. Optical Data Processing

The optical Corona, Landsat-5, and Sentinel-2 satellite data were downloaded, preprocessed, and processed to extract the urban areas. The Corona data were georeferenced and geometrically corrected based on the coordinates of the study area (WGS_1984_UTM_Zone_36N). The Sentinel-2 image was resampled, the Landsat image was preprocessed, and all the data were clipped based on the geographical boundary of the study area. In addition, unsupervised classification was performed to accurately detect the urban layer, and finally, the data were converted from raster to polygon. Based on the vector built-up data extracted from the raster satellite imagery, the changes in the urban areas between 1965 and 2019 were calculated.

2.3.2. Radar Data Processing

- Sentinel-1 (SLC) for extracting urban areas;

The Sentinel-1 radar image was analyzed to detect and calculate the area of built-up zones in 2019 based on a model arranged inside SNAP software (GraphBuilder tool) that includes eight principles steps as follows: Read, TOPSAR split, Apply Orbit File, Calibration, TOPSAR Deburst, Multilook, Terrain correction, and Write operators. The S-1 TOPS split is applied to create a new product with only a sub-swath covering the ROI. When the study area covers more than one sub-swath, the chosen sub-swaths must be merged by the S-1 TOPS Merge operator [48]. Thus, to apply orbit information, the precise orbit files are automatically downloaded for Sentinel-1 products by SNAP and added to its metadata, such as the accurate position of the satellite during the acquisition of the data. After that, the satellite image was radiometrically calibrated, and the sub-swaths were debuted to remove the seamlines between the single bursts [49]. The next step is to multilook the calibrated data. Multilooking is the process of determining which pixels are averaged in the range and/or azimuth direction in an SLC dataset. On the other hand, averaging also reduced some speckling effects and smoothed the image. In addition, because the study used a single image, a co-registration step was not required [50]. After performing the multilook step, the terrain correction method is applied to remove the misleading effect of topography on the backscatter values to remove the geolocation errors [51]. Finally, the processed data are written to save the output by the Write operator [52] in a tiff formatting to be readable in the ENVI and ArcMap software.

- Topographic setting of the study area based on the SRTM data;

The Soil and Water Assessment Tool (SWAT) is an open-source model installed in ArcMap software [53] that is used to classify and divide a watershed into subbasins according to the SRTM (digital elevation model), and the hydrologic parameters such as the area, slope, and length of the extracted subbasins are extracted. In SWAT, subbasins are subdivided into hydrologic response units (HRUs) consisting of homogeneous topographical, land use, and soil characteristics [54,55]. In this study, SWAT Version 2012, published by the Agricultural Research Service and the Texas Agricultural Experiment Station, was used. The ArcSWAT ArcGIS extension evolved from AVSWAT2000, an ArcView extension developed for an earlier version of SWAT [56]. In our case, the Nash-Sutcliffe coefficient (NSE) was used to validate the SWAT model (Equation (1)):

$$NSE = 1 - \frac{\sum_{i=1}^{n}(P_0 - P_x)^2}{\sum_{i=1}^{n}(P_0 - \overline{P}_0)^2} \quad (1)$$

where P_x represents the model outputs derived from other DEM data, $\overline{P}$ _0 represents the mean observed streamflow, P_0 is the observed streamflow, and n represents the number of measured streamflows [57].

- Sentinel-1 (SLC) for detecting land subsidence values;

The Sentinel-1 (SLC) imagery dated 6 July, 30 July, and 15 December 2016 were considered for calculating the land subsidence in the region over the short-term (between 6 and 30 July 2016) and long-term (between 30 July and 15 December 2016). The input data contained two single-look complex (SLC) data covering the study area in zip file format and were analyzed using SNAP software to perform the interferometric step. Thus, the split and apply orbit steps were applied by reading the two chosen data products (6 and 30 July–30 July and 15 December), specifically the VV polarization, selecting a sub-swath with TOPSAR-Split, and choosing the study area. After that, the two images were co-registered into a stack. The image on the first date (6 July–30 July 2016) was selected as the master image, and the other image (30 July–15 December 2016) was selected as the slave image, whereas each ground target contributed to both images having the same (range, azimuth) pixel. Thereafter, based on a series of steps automatically occurring based on a graph prepared on the SNAP software, the TOPS co-registered. Thus, the TOPS Deburst operator was used to seamlessly join all bursts in a swath into a single image. Subsequently, to emphasize phase signatures related to deformation, topographic phase contributions are typically removed using a known DEM. Then, to be able to properly analyze the phase signatures in the interferogram, the signal-to-noise ratio will be increased by applying multilooking and phase filtering techniques. In addition, for multilooking, a phase filtering step using a state-of-the-art filtering approach is performed. After the phase filtering step, the interferometric phase is significantly improved, and the value of the land deformation is clearly visible [58–60]. Finally, the output data were exported to GeoTIFF format to match the rate of land subsidence phenomena with other factors (e.g., urban sprawl and the SWAT model).

2.3.3. Spatial Statistical Analysis

The data obtained from the satellite was analyzed for spatial patterns using various techniques such as cluster outliers and standard distance, geographically weighted regression, K function multidistance spatial clustering, optimized hot spot analysis, and spatial autocorrelation by distance. These techniques were applied to the spaces occupied by built-up areas.

- Clusters outliers and standard distance;

The process mechanism of this spatial statistics method is that the cluster and outlier analysis classified the processed layer (feature) into various groups or anomalous values

based on the proximity criterion (attributes) to five degrees of geographical classes. The types of classification are (i) the spots that have either high or (ii) low values in concordance with their surroundings, (iii) anomalous areas where a spot has a value that is very different from the neighbors in higher or (iv) lower value, or (v) no relations can be made. This kind of process is mathematically implemented in ArcMap as follows (Equations (2) and (3)):

$$I_i = \frac{x_i - \overline{X}}{s_i^2} \sum_{j=1, j \neq i}^{n} w_{i,j}(x_j - \overline{X}) \quad (2)$$

where *x_i* represents an attribute for a feature *i*, $\overline{X}$ represents the mean of the corresponding attribute, $x\_(i, j)$ represents the spatial weight between features *i* and *j*, and n represents the total number of features as in Equation (3) [61]:

$$s_i^2 = \frac{\sum_{j=1, j \neq i}^{n} (x_j - \overline{X})^2}{n - 1} \quad (3)$$

- Spatial autocorrelation statistic using geographically weighted regression;

Geographically weighted regression (GWR) is a familiar tool that can easily produce detailed maps of spatial variations in relationships. In addition, geographically weighted regression is a tool that is used for exploring spatial heterogeneity [62]. This method also has the benefit of being able to produce local measures of conditional spatial dependency [63]. As in Equation (4), it seems intuitively appealing to base estimates *a_ik* on observations taken at sample points close to *i*. If some degree of smoothness of *a_iks* is assumed, then reasonable approximations may be made by considering the relationship between the observed variables in a region geographically close to *i* as follows:

$$y_i = a_{i0} + \sum_{k=1, m} a_{ik} x_{ik} + \varepsilon_i \quad (4)$$

where *a_ik* is the value of the *kth* parameter at location *i* [64]. GWR allows coefficients to vary continuously over the study area, and a set of coefficients can be estimated at any location—typically on a grid—so that a coefficient surface can be visualized and interrogated for relationship heterogeneity. In essence, GWR measures the inherent relationships around each regression point *i*, where each set of regression coefficients is estimated by weighted least squares. The mathematical expression for this case is explored in Equation (5):

$$\hat{\beta}_i = \left(X^T W_i X \right)^{-1} X^T W_{iy} \quad (5)$$

where *X* is the matrix of the independent variables with a column of 1 s for the intercept; *y* is the dependent variable vector; $\hat{\beta}_i = (\beta_{i0}, \ldots \beta_{im})^T$ is the vector of $m + 1$ local regression coefficients. W_i is the diagonal matrix denoting the geographical weighting of each observed data for regression point *i* [65].

- Space-time Ripley's K Function for Spatiotemporal Point Pattern Analysis

Space-time Ripley's *K* function is a statistical approach that computes space-time point events and estimates their second-order property based on point pair distance calculations [66]. It takes both the number of points and distances between points into account, which allows for quantitatively evaluating how much the observed point pattern deviates from randomness at multiple spatiotemporal scales. The theoretical space-time Ripley's *K* function is calculated by dividing *E*, the expected number of points within spatial distance *s* and temporal distance *t*, by the point intensity λst:

$$K(s, t) = \frac{E(s, t)}{\lambda_{st}} \quad (6)$$

Equation (6) characterizes the pattern of spatiotemporal points [67], where a cylinder of base $\pi s2$ and height $2t$ is centered on each point to count the number of neighboring points falling within. Then, the total number of points n is divided by the volume of the irregular cylinder formed by the study area and study duration, resulting in λst. It is expected that $(s,) = 2\pi s2t$, if the point distribution obeys complete spatiotemporal randomness (CSTR), $K(s,t) > 2\pi s2t$ if the points fit clustering within spatial distance s and temporal distance t, and $K(s,t) < 2\pi s2t$ for dispersed space-time patterns. Using Equation (7), the space-time K function is formulated as:

$$\hat{K}(s,t) = \frac{A \cdot D}{n^2} \sum_{i=1}^{n} \sum_{j \neq i} \frac{I_{s,t}(d_{ij}, u_{ij})}{\omega_{ij} v_{ij}} \tag{7}$$

where A denotes the area of the study region and D is the duration of the study period. The product of A and D results in the volume of the irregular cylinder that is formed by the study area (base) and study period (height). ωij and vij are spatial and temporal weighting functions that correct edge effects respectively. dij is the spatial distance between points i and j, and uij is the temporal distance between points i and j.

The statistics that allow the expression of the value of a variable taken in the neighborhood are defined by the product of a measurement allowing the establishment of the similarity, or dissimilarity, cij, between the values of y, and the indicator of the spatial connectivity between the variables, wij (Equation (8)):

$$\Gamma = \sum_{i=1}^{N} \sum_{j=1}^{N} \omega_{ij} \times c_{ij} \tag{8}$$

where ωij is the element located on line i and column j of the spatial weights matrix (W). The measurement of similarity or dissimilarity, cij, usually allows us to gauge the gap between the values taken in the neighborhood, yj and the value of the variable considered, yi. The statistics of the products are then normalized by various multiplicative constants. There are different measurements of similarity/dissimilarity between the values of variable y. The different measurements of detection are based on these differences in the specification of the measurements used [68].

- Optimized Hot Spot Analysis

The Getis-Ord $Gi*$ statistic [69–72] is a local statistical model that quantifies the degree of spatial dependence on the pronounced scale distance derived above. The *Gi** statistics were implemented to determine the clustering level of the PS/DS MP, specifying a single MP at location i and its neighbors j within a searching distance d. For each single MP at site i, the $Gi*$ index can be estimated as:

$$G_i^*(d) = \frac{\sum_{xj} + x_i - n_{ij} \times \overline{x}^*}{\sqrt{s^* \left\{ \left[(n \times n_{ij}) - n_{ij}^2 \right] / (n-1) \right\}}} \tag{9}$$

Here, n is the total number of PS/DS MPs, nij is the number of PS/DS MPs within the scale distance d, x is the surface displacement recorded by PS/DS, and x and s are the mean value and the standard deviation of all displacements, respectively, that are revealed by the whole PS/DS MP. Through these Getis-Ord Gi* statistics, clustered and random patterns can be separately identified. The outcomes of the Getis-Ord Gi* statistics for each PS/DS MP are the calculated values of the z score (standard deviation) and p value (independence probability), both of which are utilized to estimate the statistical significance of spatial autocorrelation. Positive and negative z scores indicate spatial clusters of PS/DS moving towards and away from the LOS, respectively. Figure 3 shows the data collected, processing steps, outputs, and the proposed solution of the study area problem.

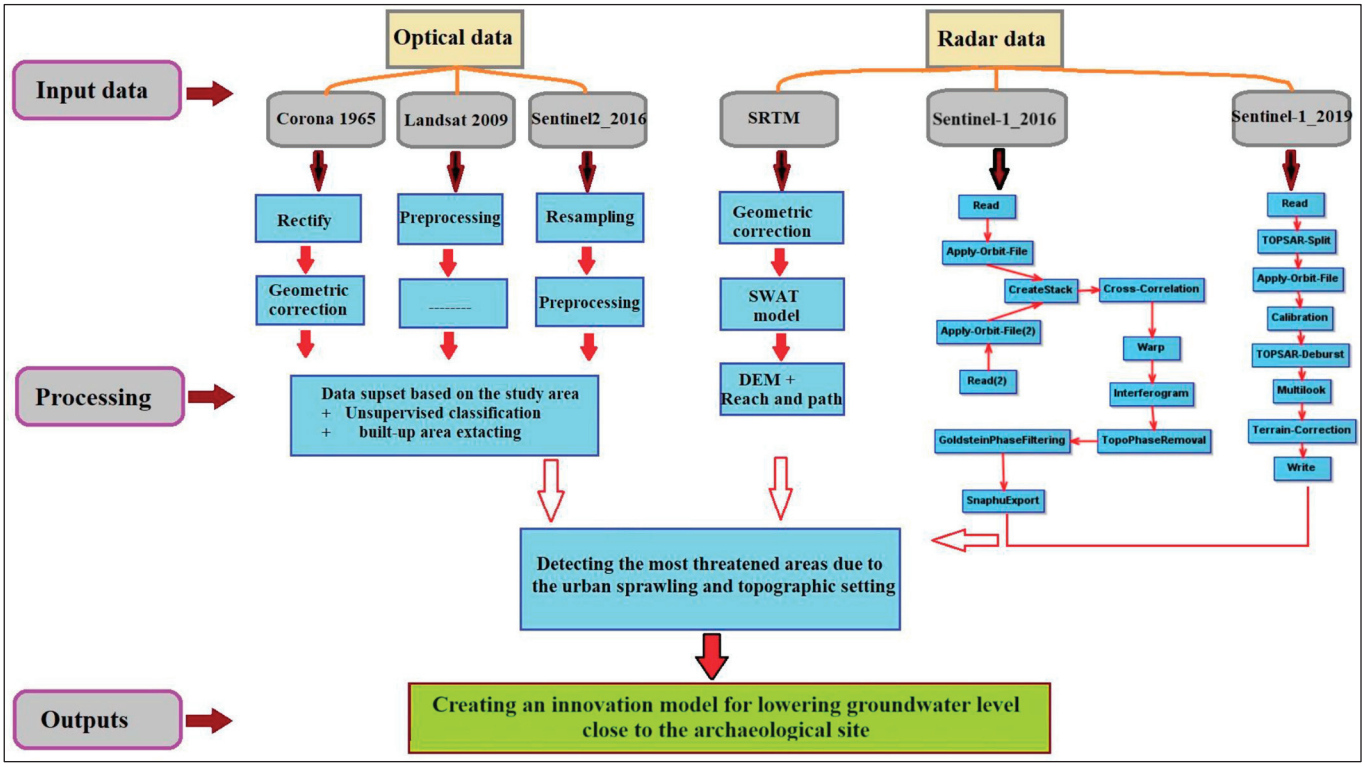

Figure 3. Schematic diagram of methodology adopted in this research.

3. Results and Discussion

3.1. Detect the Built-Up Area Time-Series Changes

The total area of the study area is estimated to be 66,614 km^2, and the urban area represents 5083 km^2 of this total area, which is equivalent to 7.63% of the total area of the study area in 1965. In 2009, the urban mass area reached 21,798 km^2, accounting for 32.72% of the total area of the study, with an annual increase of 0.379 km^2/year. The urban mass area in 2016 was 31,087 km^2, approximately half of the total area, with an annual increase of 1.327 km^2/year between 2009 and 2016. In 2019, the urban mass area reached 39,782 km^2, which is nearly two-thirds of the total area, with a high annual growth rate of approximately 2.898 km^2/year. The annual growth rate between 1965 and 2019 was approximately 0.642 km^2/year. The urban areas expanded approximately eight times in nearly 54 years and doubled twice in the last 10 years between 2009 and 2019. This can be attributed to significant population growth and security instability following the January 2011 revolution, which marked a turning point in continuous urban sprawl. This led to the establishment of new urban settlements that were not previously present in this area, as shown in Figure 4 and Table 2.

Table 2. Urban mass change between years of study (1965, 2009, and 2016) and 2019.

Year	Urban Mass (km^2)	Change Detection ± (km^2)
1965	5083	16,715
2009	21,798	9289
2016	31,087	8695
2019	39,782	-

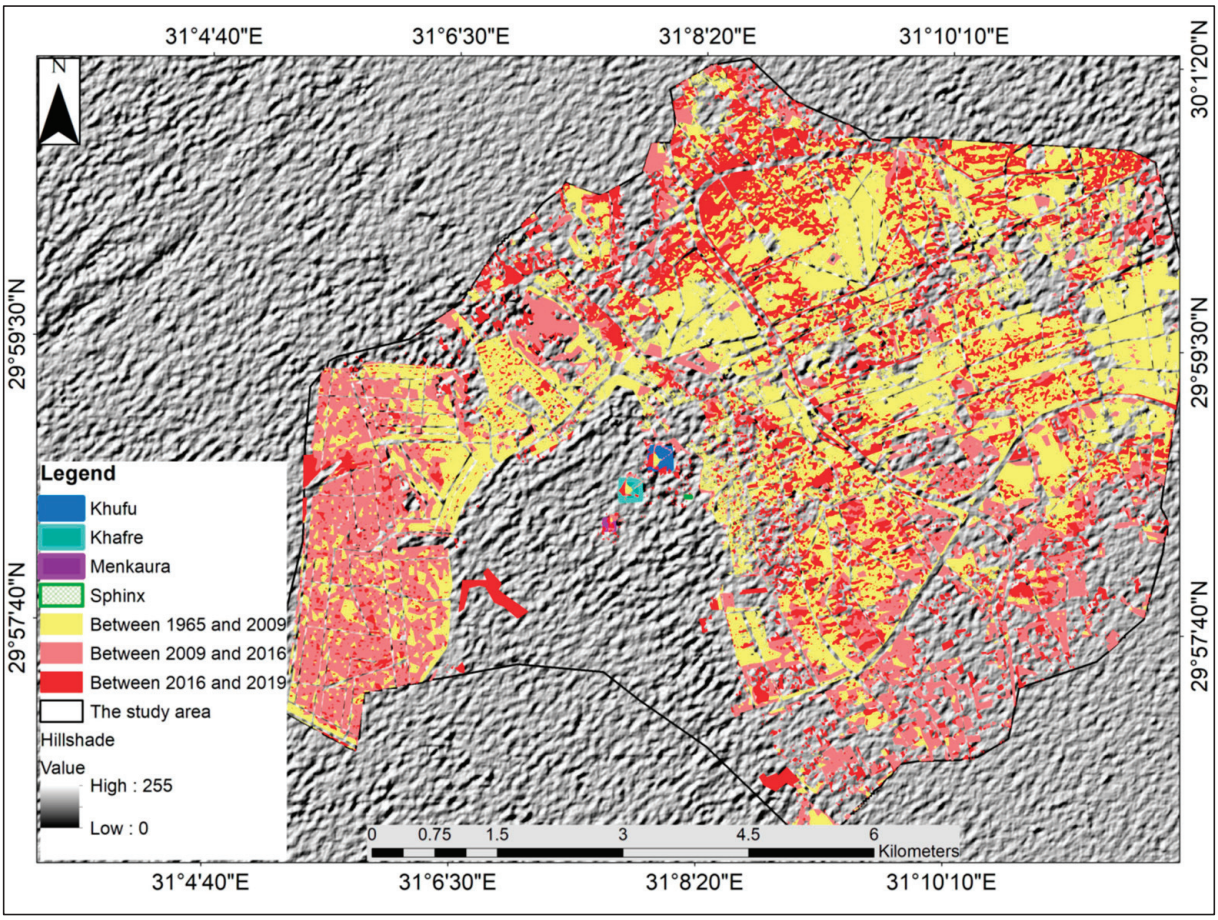

Figure 4. Variations in built-up area in study area for period of 1965–2019.

3.2. Detect the Changes by Clusters Outliers and Standard Distance

Based on Figure 5, it can be observed that the standard distances in shapes a, b, c, and d vary and are inconsistent. The center of the circle changes corresponding to the increase in urban mass area in the study area between 1965 and 2019. Shapes a and b are more concentrated and clustered as their circle radius decreases, while shapes c and d are more dispersed, indicating the spread of urban masses as their circle radius increases. This observation is further supported by the locations of the three pyramids. At the beginning of the period (Figure 5a), they were situated far from the circle representing the standard distance, while at the end of the period, they were closer to the central point of the figure representing the standard distance in 2019 (Figure 5d).

For the cluster outliers, it can be observed that the urban masses in the years 1965–2009 exhibit random distributions, as well as dispersion and divergence. The areas with a Z score less than 1, especially those ranging between (1: −1), whether in the western, northern, or southern regions, are shown in Figure 5a,b. The distances between urban masses converge and cluster in the center of the area in small spaces, while the remaining urban masses spread over a large area on the outskirts of the region. In contrast, in 2016 and 2019 (Figure 5c,d), an increase in the areas with a Z score greater than one, especially those with a Z score exceeding two, was observed. This indicates that the dominant urban pattern is clustering and convergence, especially in the eastern and western regions of the study area. This is due to the increase in the urban mass area in the study area.

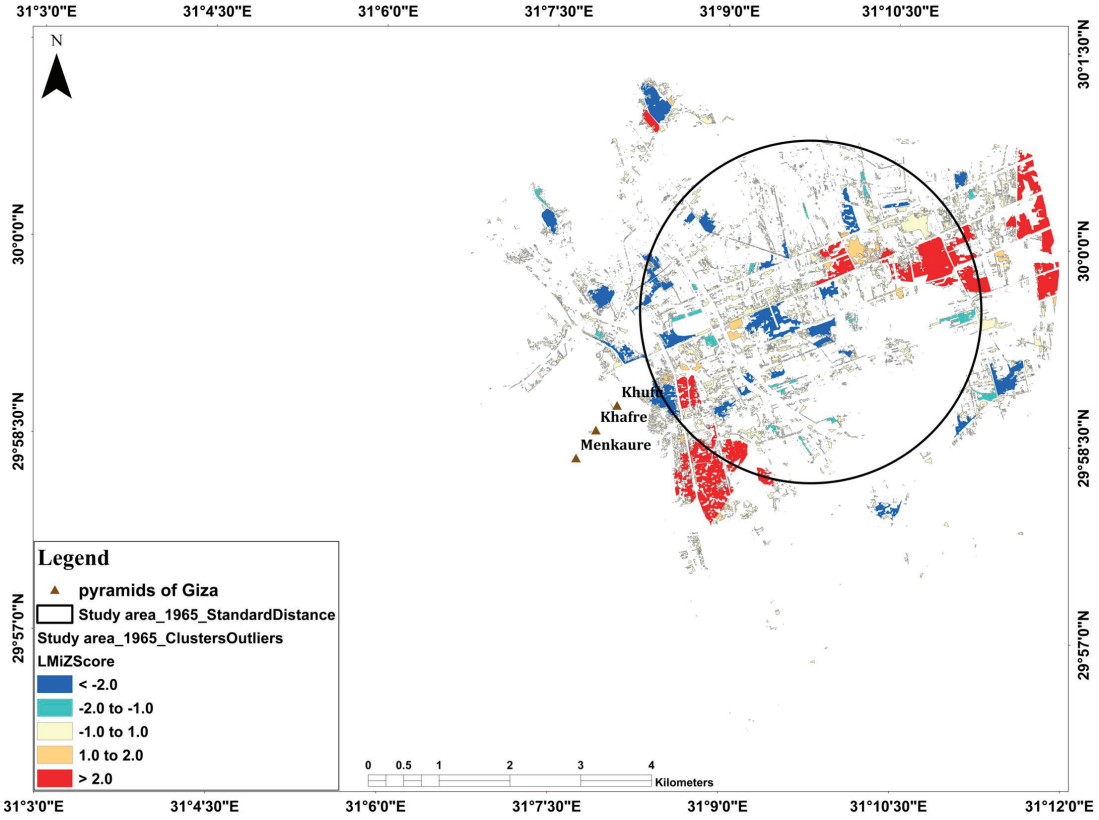

(**a**)

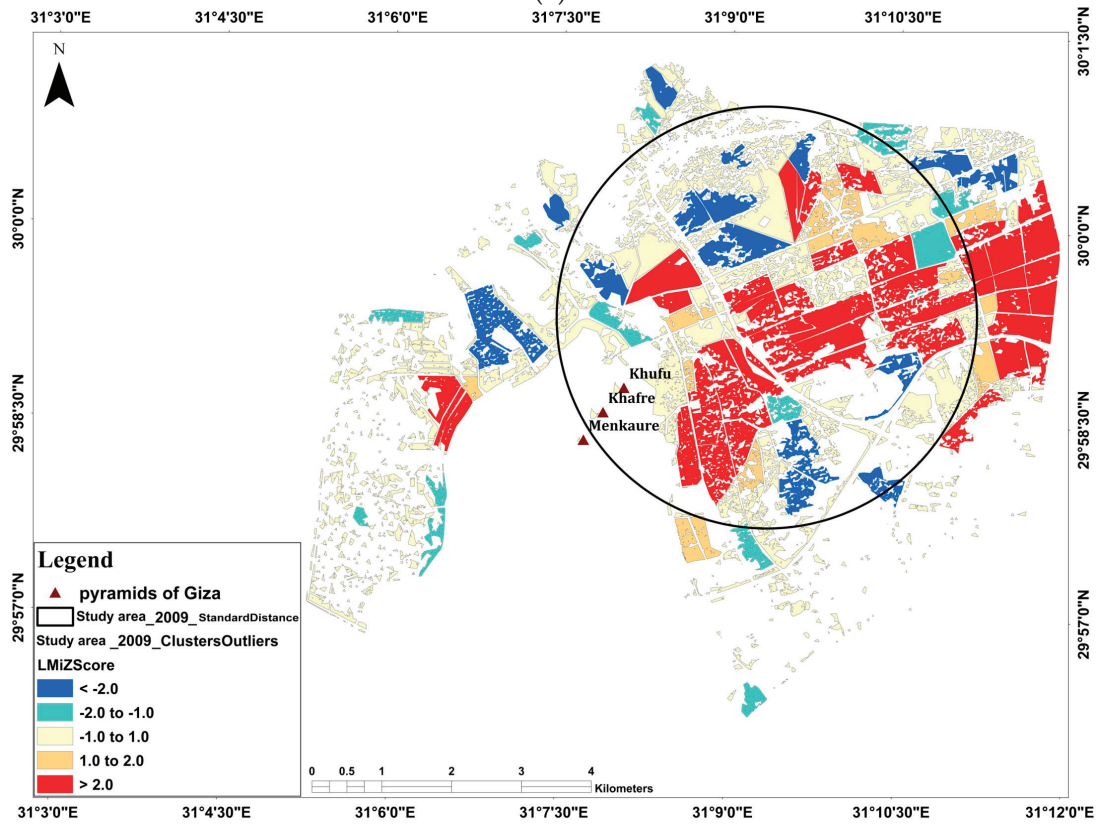

(**b**)

Figure 5. *Cont.*

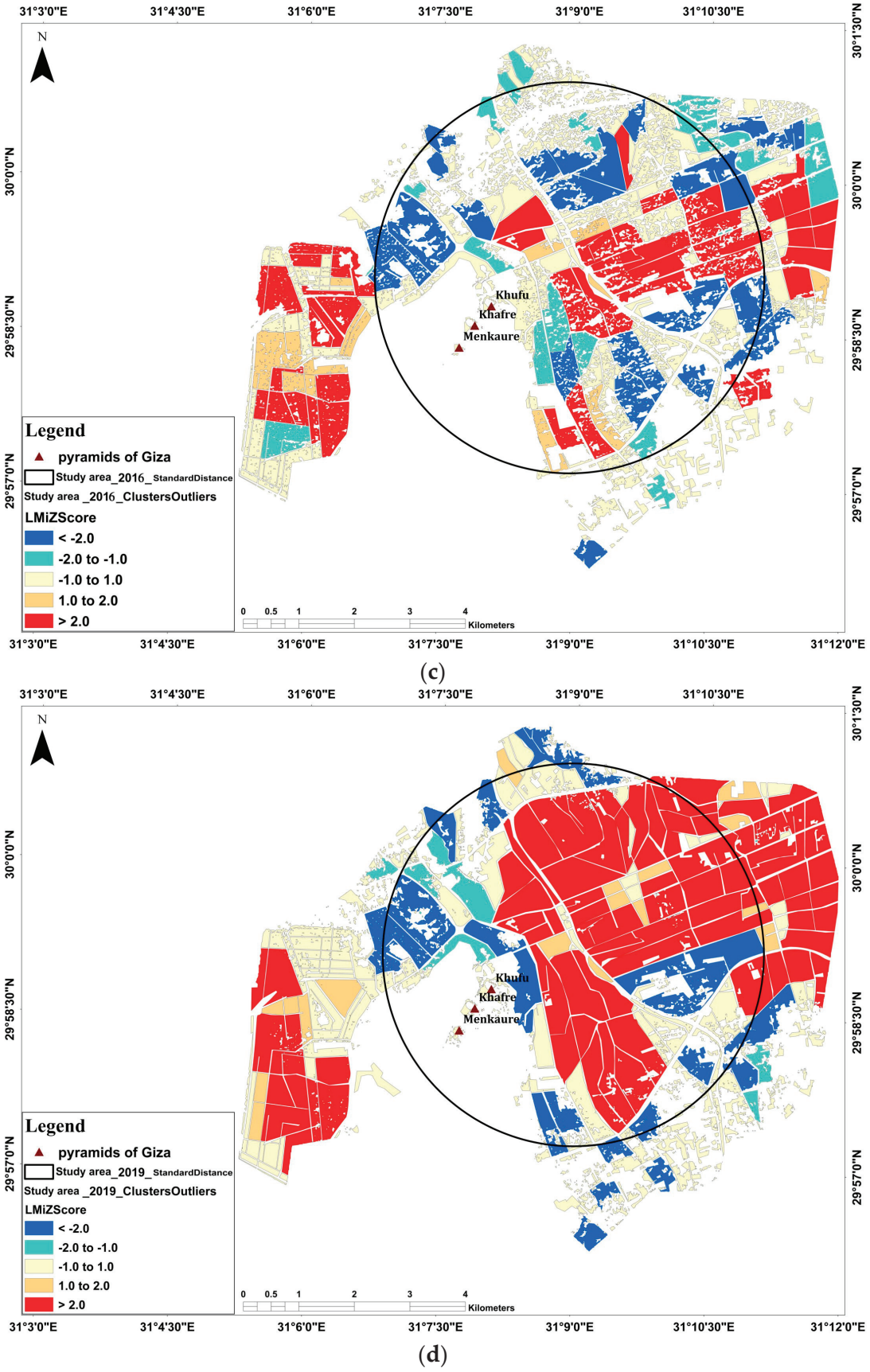

Figure 5. Standard distance of urban mass and pyramids for years from 1965 to 2019. (**a**) 1965; (**b**) 2009; (**c**) 2016; (**d**) 2019.

3.3. Detect the Changes by Geographically Weighted Regression

Based on Figure 6, the weighted geographic regression analysis indicated that the study area exhibited spatial heterogeneity during the period from 1965 to 2019. The red areas on the map indicate higher rates of urban expansion compared to the four forms (a, b, c, and d). These areas extended significantly in the inner parts of the study area during 1965, 2009, and 2016, and spread to the northern and southern parts in 2019. On the other hand, the blue areas on the map represent regions that experienced more urban growth than expected. Despite not being expected to occur, urban clusters spread significantly on the margins of the northern, eastern, southern, and western parts of the study area during the entire study period.

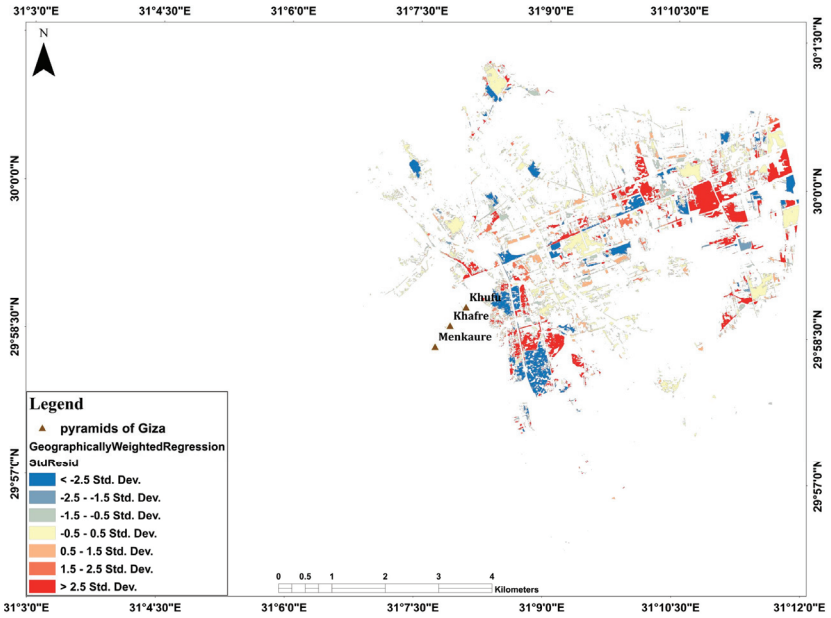

(**a**)

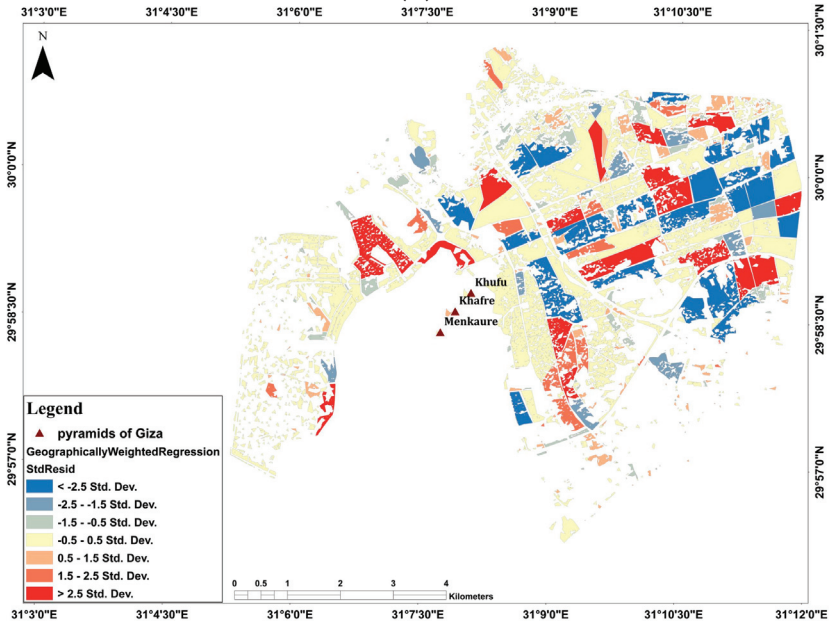

(**b**)

Figure 6. *Cont.*

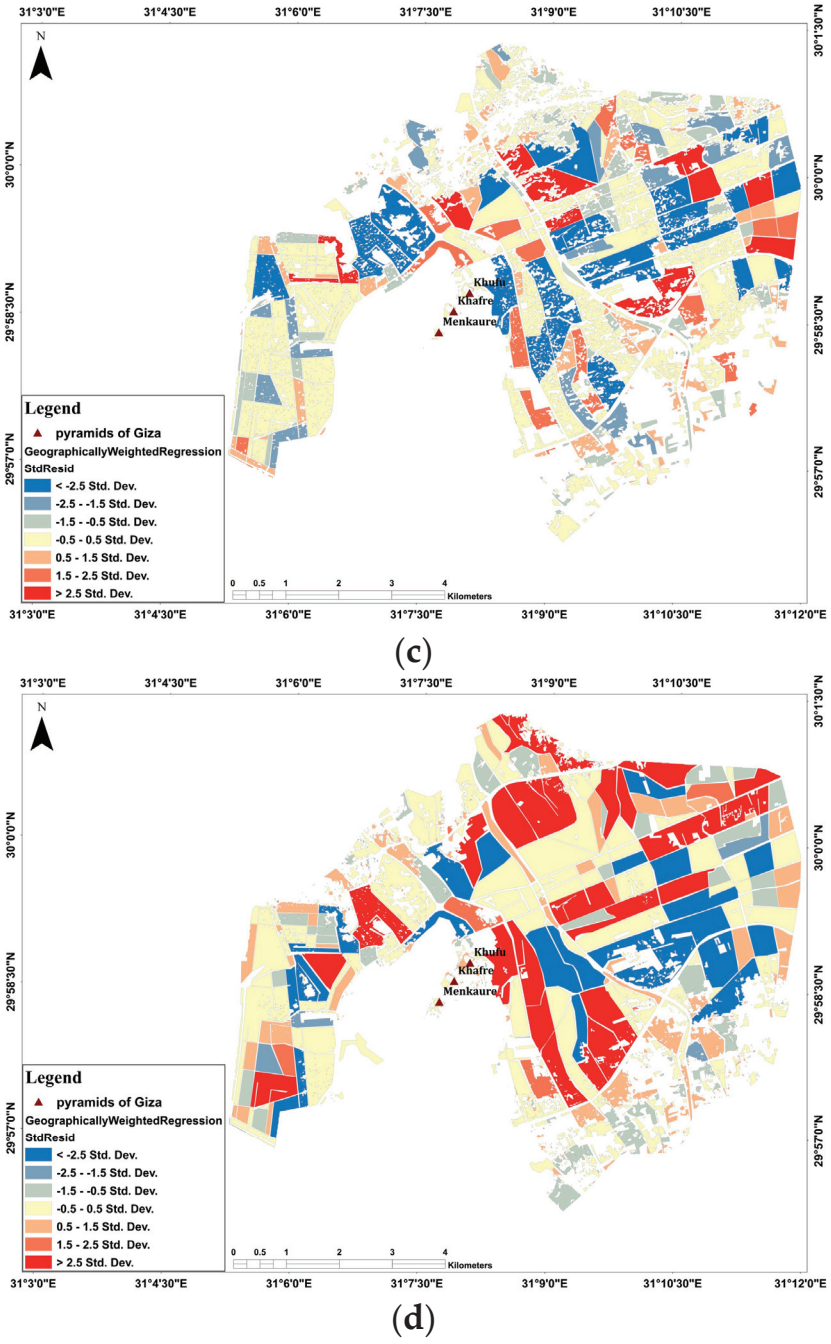

Figure 6. Weighted applied geographic regression for years from 1965 to 2019, respectively. (**a**) 1965; (**b**) 2009; (**c**) 2016; (**d**) 2019.

3.4. Multidistance Spatial Cluster (K Function) Time-Series Changes

The mathematical transformation of Ripley's K-function performed in ArcGIS is slightly different, and as a final result, the expected index of a random pattern is equal to the input distance [64]. To assess the pattern type, the observed L(d) value must be compared with the expected value. In each distance increment, the actual distribution is compared against a random distribution, and if the observed L(d) value is greater than expected, a clustered pattern is dominant at that scale of analysis. In turn, if this value is smaller than expected, the distribution is considered to be dispersed. Moreover, for the index of clustering or dispersion to be statistically significant, it must be greater or smaller, respectively, than the high or low level of the confidence interval [65]. In our study, Figure 7a indicates that there is a clustering and agglomeration of urban masses that are concentrated

near distances of approximately 800 to 2000 m in which the red line (observed) deviates above the blue line (expected). This deviation reached a maximum distance between the two lines at 1400 m, where it reached 600 concerning L(d). Additionally, Figure 7b indicates that there is dispersion and divergence in the urban masses when the distance is less than 400 m, where the blue line deviates above the red line. This dispersion and divergence gradually decrease until there is a concentration of urban masses, especially at distances ranging between 1200 and 2400 m.

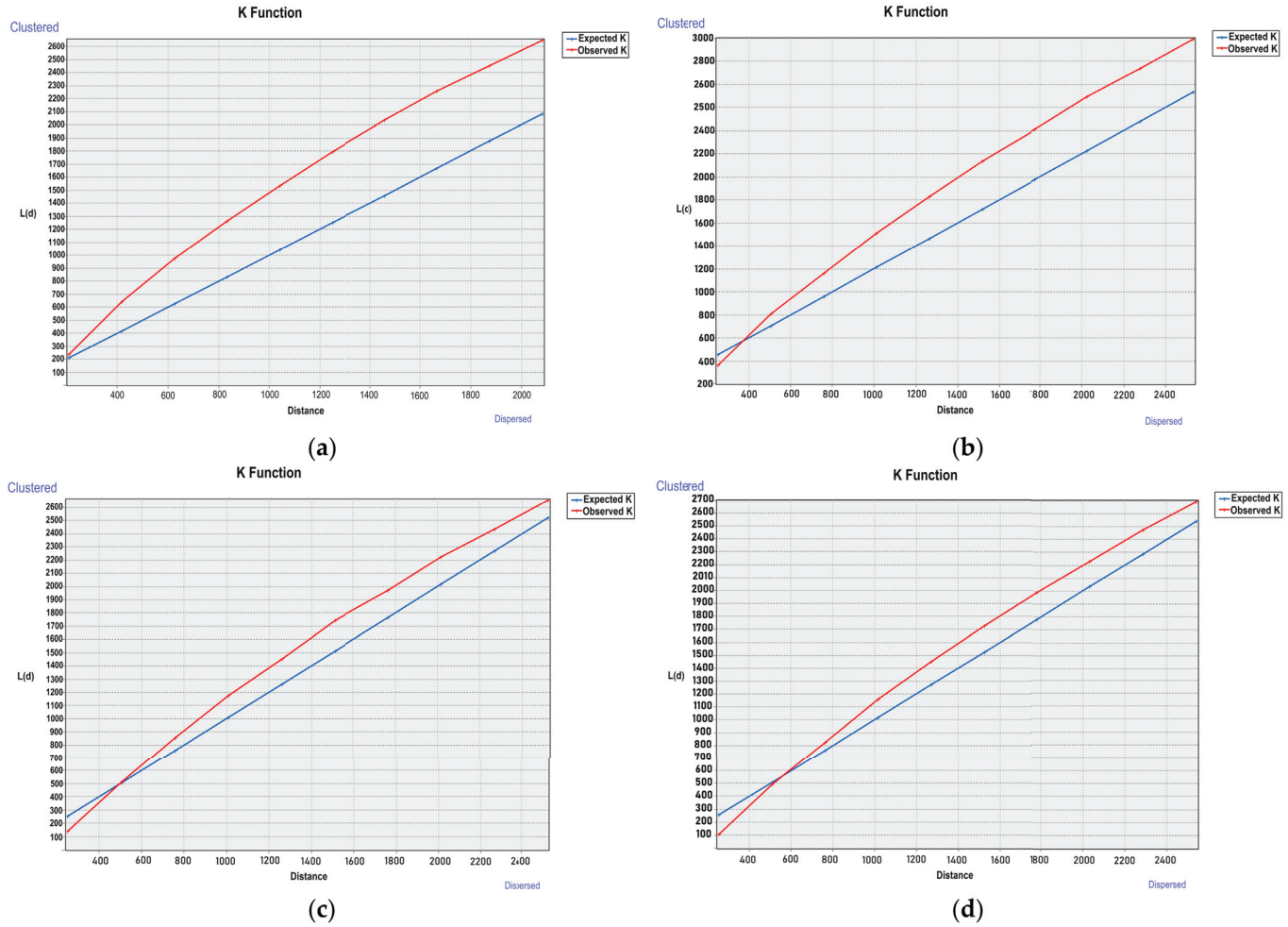

Figure 7. Changes in urban areas by clustering and dispersion, red line (observed) and blue line (expected) for years (**a**) 1965; (**b**) 2009; (**c**) 2016; (**d**) 2019.

Figure 7c indicates the dispersion and separation of urban masses when the distance is less than approximately 500 m, and there was an agglomeration of urban blocks, especially when the distance exceeded 1400 m. Figure 7d shows that dispersion and separation increased to reach distances less than 600 m, while there was urban clustering and agglomeration at distances exceeding 600 m. The deviation between the red and blue lines decreased, and they became closer to each other, as shown in Figure 7c,d, as a result of the increase in urban growth between 2016 and 2019. The urban masses moved closer together due to increasing urban growth.

3.5. Spatial Autocorrelation Statistic Time-Series Changes

In 1965, the Global Moran's Index Summary by Distance for the Spatial Autocorrelation statistic for the urban layer indicated that the beginning distance was 829, the distance increment was 13.95, the first peak (distance, value) was 842.95 and 2.53, respectively, and the maximum peak (distance, value) was 940.63 and 2.56, respectively. The results revealed

that Moran's index is greater than zero, which indicates that the distribution is regular and clustered but not to a large extent (Table 3 and Figure 8a). All the Z score values were limited to the range of 1.96–2.58, and the highest value was 2.56 at a distance of 940.63 m, while the lowest value was 2.23 when the distance was 884.81 m. Furthermore, the lowest distance between urban masses was nearly 829 m, while the largest distance was 954.58 m. This closeness between the distances indicates that this clustering is regular, which reflects the unfair distribution of urban masses in the region in 1965.

Table 3. Moran's Index summary by Distance for Spatial Autocorrelation statistic for urban layer in 1965.

Distance (m)	Moran's Index	z-Score
829.00	0.000859	2.468979
842.95	0.000868	2.526718
856.91	0.000820	2.430553
870.86	0.000767	2.312585
884.81	0.000723	2.229052
898.77	0.000796	2.516628
912.72	0.000729	2.349612
926.67	0.000697	2.280936
940.63	0.000780	2.562688
954.58	0.000734	2.450355

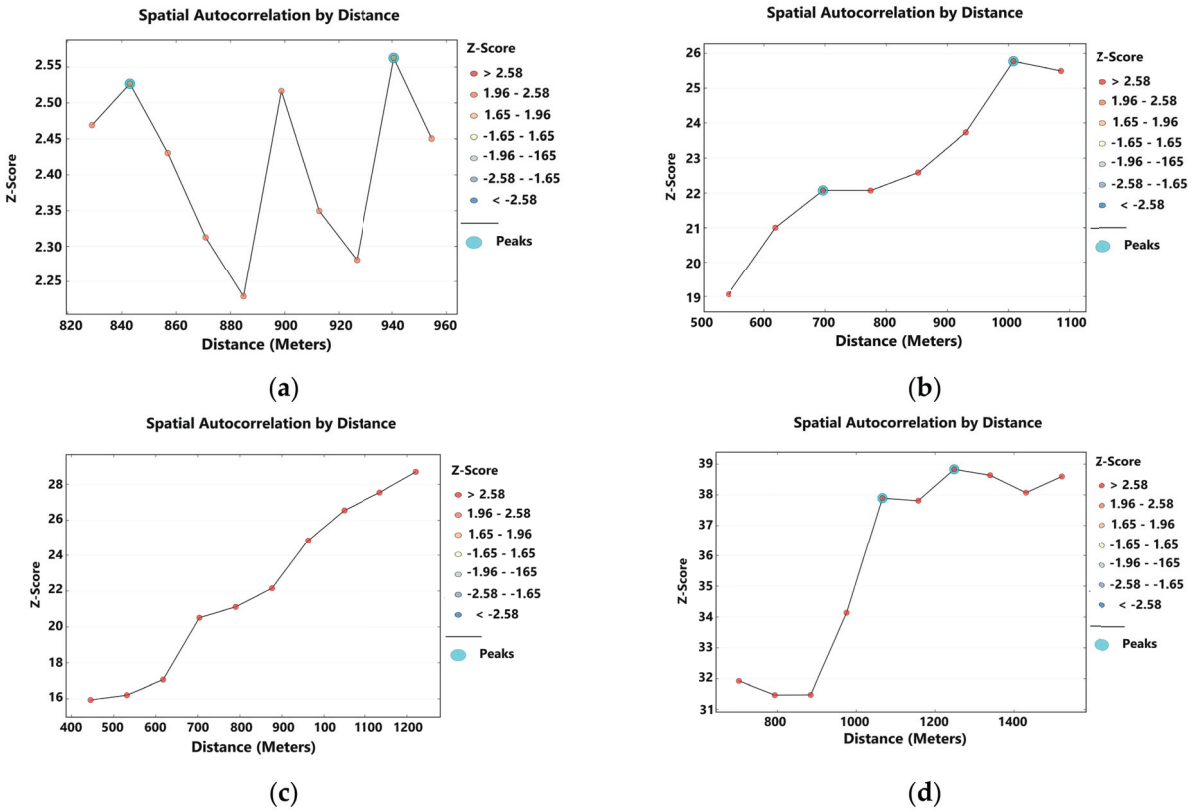

Figure 8. Spatial Autocorrelation by Distance (Global Moran's Index) for urban layer for years (**a**) 1965; (**b**) 2009; (**c**) 2016; (**d**) 2019.

Additionally, for 2009, the Global Moran's Index Summary by Distance for the Spatial Autocorrelation statistic for the urban layer showed that the initial distance was 541.0, the distance increment was 77.8, the first peaks (distance, value) were 696.6 and 22.1, respectively, and the maximum peaks (distance, value) were 1007.8 and 25.77, respectively. The results indicated that the Moran coefficient increased compared to that in the previous

period, and the z score also increased significantly, ranging between 19.06 when the distance was 541 m and 25.77 when the distance was 1007.82 m (Table 4 and Figure 8b). This demonstrates the agglomeration and clustering of urban masses due to the great urban expansion witnessed by the region between 1965 and 2009. This leads to all Z score values increasing to more than 2.58.

Table 4. Moran's Index summary by Distance for Spatial Autocorrelation statistic for urban layer in 2009.

Distance (m)	Moran's Index	z-Score
541.00	0.114091	19.059431
618.80	0.110322	21.001711
696.61	0.102889	22.071586
774.41	0.092411	22.068745
852.21	0.085496	22.583187
930.01	0.082103	23.730188
1007.82	0.082640	25.771371
1085.62	0.076208	25.492819

For 2016, the Global Moran's Index Summary by Distance for the Spatial Autocorrelation statistic for the urban layer proved that the beginning distance was 445, the distance increment was 86.22, and the first peak (distance, value) and max peak (distance, value) were recorded as none. The results revealed that the Moran coefficient increased compared to that in the previous period, as did the z score. The z score ranged between 15.94 when the distance was 445 m and 28.70 when the distance was 1220.98 m (Table 5 and Figure 8c). This indicated that urbanization became closer and more clustered during this period in 2016 than during the previous period in 2009.

Table 5. Moran's Index summary by Distance for Spatial Autocorrelation statistic for urban layer in 2016.

Distance (m)	Moran's Index	z-Score
445.00	0.150765	15.941361
531.22	0.125013	16.208135
617.44	0.112533	17.062234
703.66	0.118415	20.513646
789.88	0.109149	21.116408
876.10	0.103648	22.154363
962.32	0.106204	24.861730
1048.54	0.104824	26.548377
1134.76	0.100804	27.544697
1220.98	0.097990	28.696645

In 2019, the Global Moran's I Summary by Distance for the Spatial Autocorrelation statistic for the urban layer showed that the initial distance was 702, the distance increment was 91.07, the first peaks (distance, value) were 1066.28 and 37.89, respectively, and the maximum peaks (distance, value) were 1248.41 and 38.83, respectively. The results in Table 6 and Figure 8d show that the distance between urban masses increased due to the newly developed urban communities along the region's outskirts. Additionally, a noticeable increase in the z score was detected, ranging between 31.47 when the distance was 793.07 m and 38.83 when the distance was 1248.41 m. This stage is considered the urban explosion in the region, in which urbanization became more clustered, agglomerated, and closer in this period of 2019 compared to the previous periods of study.

Table 6. Moran's Index summary by Distance for Spatial Autocorrelation statistic for urban layer in 2019.

Distance (m)	Moran's Index	z-Score
702.00	0.216568	31.928737
793.07	0.188440	31.472736
884.14	0.167797	31.479186
975.21	0.166038	34.136998
1066.28	0.169543	37.894397
1157.34	0.156790	37.813164
1248.41	0.150946	38.830281
1339.48	0.140816	38.636843
1430.55	0.130735	38.070068
1521.62	0.125271	38.597769

3.6. Land Subsidence (Deformation)

The study area was analyzed using Sentinel-1 (SLC) data that were collected over the short and long terms for showing the effects of urban expansion on the rise in groundwater levels in the area around the archaeological area of Giza Necropolis. For instance, Bokhari et al. (2023) analyzed land subsidence based on long-term data spanning from July 2017 to July 2019 [73]. Similarly, Ghazifard et al. (2017) evaluated subsidence rates during two extended periods, from March to December 2005 and from July 2011 to January 2012. Their findings indicated that the primary causes of ground subsidence were declining groundwater levels and changes in sediment composition and thickness [74]. Additionally, Tiwari et al. (2017) estimated subsidence over an urban area using a time series of Sentinel-1 data from 2014 to 2017, with an image acquired on 29 May 2016, serving as the master image, resulting in a maximum perpendicular baseline of 150 m [75]. Bhattarai et al. (2017) detected land subsidence in the Kathmandu Valley over an extended period from 2007 to 2010 [76]. Furthermore, Nalakurthi and Behera (2022) examined the rate of land subsidence in Mumbai and investigated the impact of groundwater exploitation using Sentinel-1 SAR imagery collected from October 2014 to May 2019. Mumbai, being one of the most densely populated cities in the world with significant urban sprawl and water scarcity issues, experiences groundwater exploitation for domestic and industrial purposes, resulting in land subsidence and affecting coastal communities due to the influence of sea levels [77].

In this study, the two chosen dates were between 6 and 30 July 2016 and in the period between 30 July and 15 December 2016. The data showed that land subsidence occurred in this area, as illustrated in Figure 9a,b. The changes were mostly observed in the southern region near Nazlet El-Samman, which is close to the pyramids. On the other hand, the northern region experienced little change. The subsidence in the southern region reached about −0.0138 m over the period between 30 July and 15 December 2016. It is believed that groundwater may have caused the land subsidence, leading to the gradual sinking or settling of the land surface. When water seeps into the ground and saturates the soil layers, the soil can lose its structural integrity and contract. Consequently, structures such as the Great Pyramids and the Sphinx may have started sinking, which could eventually lead to structural damage.

The historical geophysical characteristics showed that there was a waterway in this region, with a groundwater level ranging between 14.2–16.3 m, and higher values were observed close to the Pyramid of Khufu, which is approximately 17.4–19.4 m [38]. Moreover, urban expansion increased in recent years, particularly in 2019, which put pressure on the area and increased land subsidence. The threat facing the Great Pyramids and Sphinx region arose from the impact of groundwater leakage from nearby irrigation canals and condensed urban masses [35].

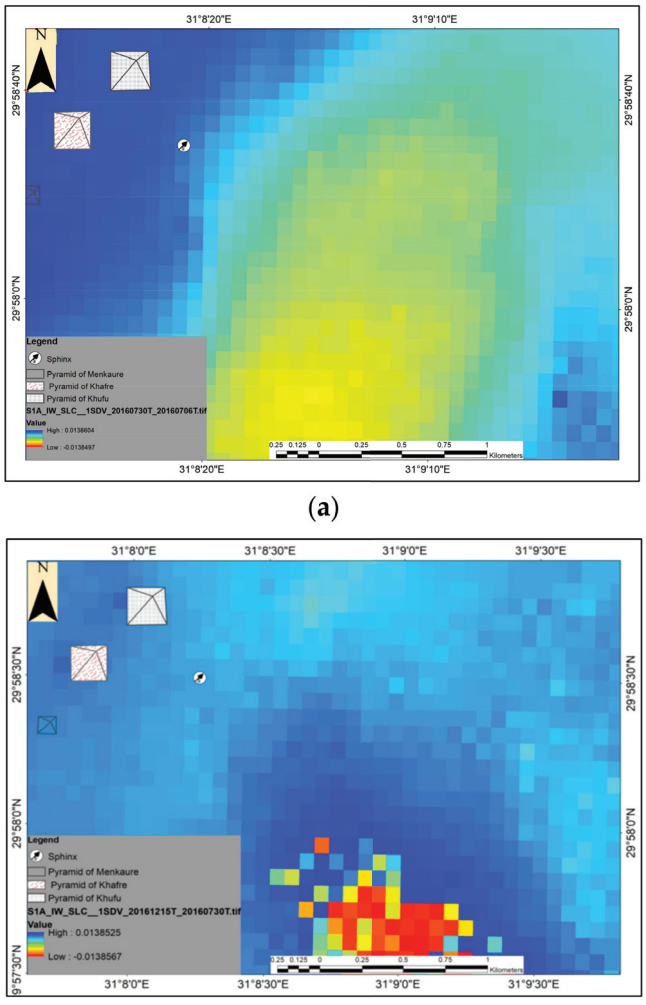

Figure 9. Changes in land subsidence values of study area over short and long terms: (**a**) between 6 and 30 July 2016; (**b**) between 30 July and 15 December 2016.

Overall, the results show that urban expansion greatly influenced the study area, particularly in 2019. Urban masses increased and clustered in the region, which was proven by different indices, such as geographically weighted regression, the Multidistance spatial cluster (K function), and Moran's index. The study revealed that newly developed urban communities led to an increase in the spaces between urban masses along the region's outskirts in 2019. This new development in the region resulted in urban explosions becoming more clustered and condensed in 2019 compared to previous years. This unmanaged urban expansion resulted in increased water leakage to groundwater in neighboring areas. The great pyramids of Giza have been threatened by this rise in groundwater level resulting from water infiltration from nearby urban masses. Two main aquifers are located near the Sphinx, with water levels of 1.5–4 m and 4–7 m below the surface [34]. These aquifers are recharged by water leakage from urban areas, leading to severe hazards in the area. Pyramid construction materials and structures might be damaged as a result of this water infiltration.

4. Recommendation

Monitoring and regulating groundwater levels, implementing efficient drainage systems, and managing leaks from urban growth and irrigation canals are essential to reduce their impact on the Great Pyramids and Sphinx area. To reduce the impact of groundwater on the Great Pyramids and the Sphinx area, the stabilization of structures and moisture

management should also be given top priority in preservation and restoration activities. Protecting cultural heritage, such as archaeological and cultural sites, is undoubtedly considered a critical issue and an urgent need [78–81]. In addition, the preservation of cultural heritage should be planned as a means of promoting conservation, documentation, and even restoration based on a specific strategy [82–85]. Therefore, many efforts have been made to address the issues of urban expansion and groundwater leakage and their massive impacts on the Great Pyramids and the Sphinx region, in addition to mitigating their impact on the region. Based on the topography, built-up areas, and subsidence value properties, this research suggested a scenario for minimizing the groundwater level close to the Giza Pyramids area. Figure 10a–d illustrates the factors that influence groundwater leakage in the study area, which includes the topography, urban mass distribution, and land subsidence level. Figure 10e shows the suitable locations of the proposed trenches that could help reduce the impact of the groundwater level on the Great Pyramids and the Sphinx.

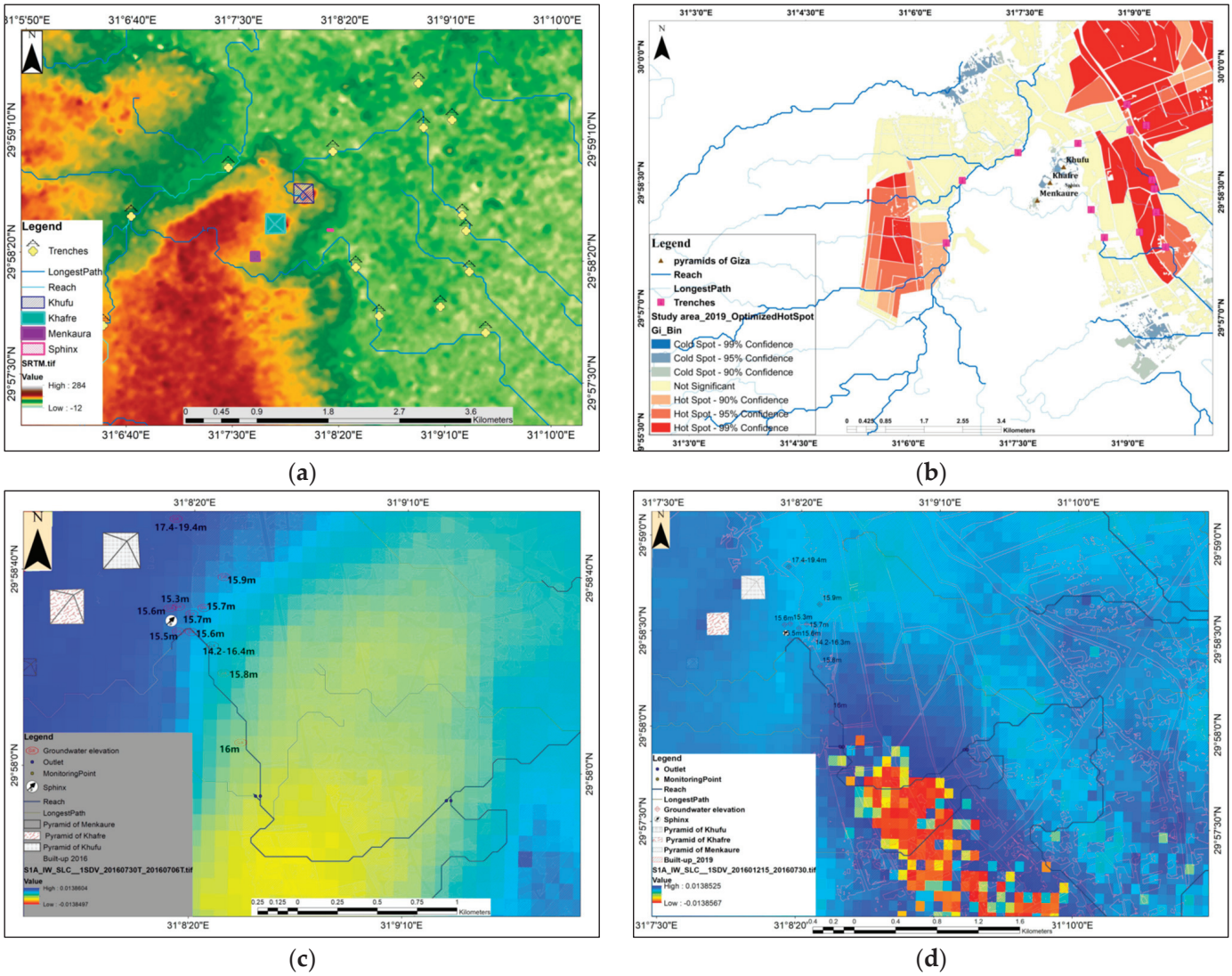

Figure 10. *Cont.*

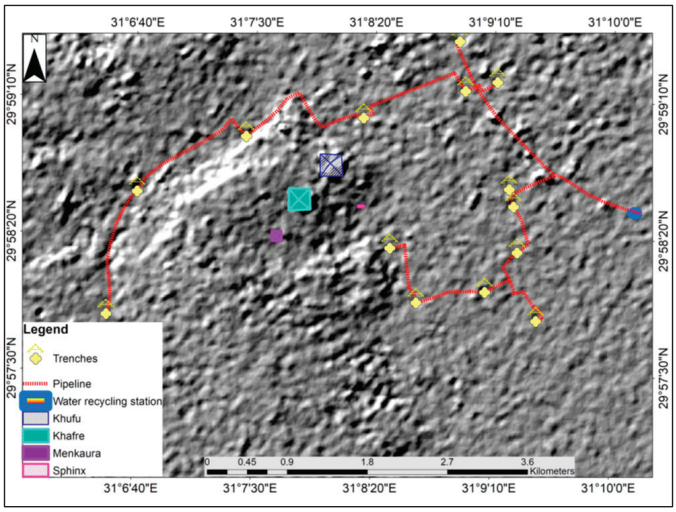

(**e**)

Figure 10. Recommended model for lowering groundwater level close to the Giza Pyramids area based on: (**a**) topographic setting; (**b**) built-up areas; (**c**,**d**) subsidence values properties; (**e**) including recommended locations for trenches, pipeline, and water recycling station.

5. Conclusions

Changes in land use and land cover can have significant impacts on archaeological areas such as the Giza Necropolis in Egypt. Detecting the impacts of land-use change on this archaeological area is essential for its preservation and management. Therefore, this study aimed to track the extent of land-use changes over time for 1965, 2009, 2016, and 2019 based on remote sensing and GIS integration. In addition, the relationships between groundwater leakage and land subsidence in the region were studied. Multiple satellite sensors were utilized in the current study such as Landsat, Corona, as well Sentinel 1 and 2. These satellite data were analyzed based on different techniques, including cluster outliers, the Moran index, and spatial autocorrelation, to examine the changes in urban masses between the 1965 and 2019 period. This study revealed that urban expansion and infrastructure development can, directly and indirectly, impact the Giza Necropolis. The land use changed in the study area due to human interactions, in which the urban masses increased from 5.083 km^2 in 1965 to 39.782 in 2019 with an annual growth rate of 0.642 Km^2/year. Urbanization led to encroachment, increased population density, construction, and the establishment of modern settlements near the archaeological site. These changes resulted in physical damage, disturbance of underground structures, increased pollution, and alteration of the surrounding landscape. Understanding the linkage between land-use changes and archaeological areas enables the identification of areas at greater risk from urban sprawl and the identification of areas that require immediate attention for preservation efforts. This study proposed new locations for trenches that can minimize the effect of groundwater discharge and reduce the impact on the Giza Pyramids and Sphinx.

Author Contributions: The authors declare that the conceptualization of this scientific research has been performed by A.E. and R.L.; the methodology has been performed by A.E.; the software has been performed by A.E.; the validation has been performed by A.E. and R.L.; the formal analysis has been performed by A.E.; the investigation has been performed by A.E., N.Z., W.M. and E.H.; the resources have been performed by A.E., N.Z., W.M. and E.H.; the data curation has been performed by N.Z., W.M. and E.H.; the writing—original draft preparation has been performed by A.E., N.Z., W.M. and E.H.; and the writing—review and editing have been performed by A.E. and R.L. All authors have read and agreed to the published version of the manuscript.

Funding: This research received no external funding.

Data Availability Statement: The data used in this research will be available once requested from the authors.

Acknowledgments: The authors would like to thank the National Authority for Remote Sensing and Space Sciences, Egypt; Kafrelsheikh University, Egypt; and the Italian National Research Council, Italy, for supporting the study.

Conflicts of Interest: The authors declare no conflicts of interest in the collection, analysis, or interpretation of the data or in the decision to publish the results.

References

1. Grimwade, G.; Carter, B. Managing small heritage sites with interpretation and community involvement. *Int. J. Herit. Stud.* **2000**, *6*, 33–48. [CrossRef]
2. Kammeier, H.D. Managing cultural and natural heritage resources: Part I–from concepts to practice. *City Time* **2008**, *4*, 1–13.
3. Bamert, M.; Ströbele, M.; Buchecker, M. Ramshackle farmhouses, useless old stables, or irreplaceable cultural heritage? Local inhabitants' perspectives on future uses of the Walser built heritage. *Land Use Policy* **2016**, *55*, 121–129. [CrossRef]
4. Ravankhah, M.; Schmidt, M. Paper 1: Developing Methodology of Disaster Risk Assessment for Cultural Heritage Sites. *ANDROID Dr. Sch. Disaster Resil.* **2014**, *2014*, 13.
5. Abate, N.; Elfadaly, A.; Masini, N.; Lasaponara, R. Multitemporal 2016–2018 Sentinel-2 data enhancement for landscape archaeology: The case study of the Foggia province, Southern Italy. *Remote Sens.* **2020**, *12*, 1309. [CrossRef]
6. Elfadaly, A.; Abutaleb, K.; Naguib, D.M.; Lasaponara, R. Detecting the environmental risk on the archaeological sites using satellite imagery in Basilicata Region, Italy. *Egypt. J. Remote Sens. Space Sci.* **2022**, *25*, 181–193. [CrossRef]
7. Attia, W.; Ragab, D.; Abdel-Hamid, A.M.; Marghani, A.M.; Elfadaly, A.; Lasaponara, R. On the use of radar and optical satellite imagery for the monitoring of flood hazards on heritage sites in Southern Sinai, Egypt. *Sustainability.* **2022**, *14*, 5500. [CrossRef]
8. Elfadaly, A.; Shams eldein, A.; Lasaponara, R. Cultural heritage management using remote sensing data and GIS techniques around the archaeological area of ancient Jeddah in Jeddah City, Saudi Arabia. *Sustainability.* **2019**, *12*, 240. [CrossRef]
9. Lasaponara, R.; Elfadaly, A.; Attia, W. Low cost space technologies for operational change detection monitoring around the archaeological area of Esna-Egypt. In *Computational Science and Its Applications–ICCSA 2016, Proceedings of the 16th International Conference (Proceedings, Part II 16), Beijing, China, 4–7 July 2016*; Springer International Publishing: Berlin/Heidelberg, Germany, 2016; pp. 611–621.
10. Badman, T.; Bomhard, B.; Fincke, A.; Langley, J.; Rosabal, P.; Sheppard, D. World Heritage in Danger. *IUCN World Herit. Stud.* **2009**, *7*.
11. Mazurczyk, T.; Piekielek, N.; Tansey, E.; Goldman, B. American archives and climate change: Risks and adaptation. *Clim. Risk Manag.* **2018**, *20*, 111–125. [CrossRef]
12. Holden, J.; West, L.J.; Howard, A.J.; Maxfield, E.; Panter, I.; Oxley, J. Hydrological controls of in situ preservation of waterlogged archaeological deposits. *Earth-Sci. Rev.* **2006**, *78*, 59–83. [CrossRef]
13. Tassie, G.; Hassan, F. Sites and Monuments Records (SMRs) and Cultural Heritage Management. In *Managing Egypt's Cultural Heritage, Proceedings of the First Egyptian Cultural Heritage Organisation Conference on Egyptian Cultural Heritage Management*; Golden House and ECHO Publications: London, UK, 2009; pp. 191–205.
14. Memphis and its Necropolis—The Pyramid Fields from Giza to Dahshur. Available online: https://whc.unesco.org/en/list/86 (accessed on 8 February 2024).
15. El-Bayomi, G.; Ali, R.R. Assessment of Urban Sprawl on El Minya Archeological Sites, Egypt. *J. Appl. Sci.* **2015**, *15*, 264–270. [CrossRef]
16. de Noronha Vaz, E.; Cabral, P.; Caetano, M.; Nijkamp, P.; Painho, M. Urban heritage endangerment at the interface of future cities and past heritage: A spatial vulnerability assessment. *Habitat Int.* **2012**, *36*, 287–294. [CrossRef]
17. Smith, M.E. Sprawl, squatters and sustainable cities: Can archaeological data shed light on modern urban issues? *Camb. Archaeol. J.* **2010**, *20*, 229–253. [CrossRef]
18. Choy, D.L.; Clarke, P.; Serrao-Neumann, S.; Hales, R.; Koschade, O.; Jones, D. Coastal urban and peri-urban indigenous people's adaptive capacity to climate change. *Balanc. Urban Dev. Options Strateg. Liveable Cities* **2016**, *72*, 441–461.
19. Isendahl, C.; Smith, M.E. Sustainable agrarian urbanism: The low-density cities of the Mayas and Aztecs. *Cities* **2013**, *31*, 132–143. [CrossRef]
20. Price, S.J.; Burke, H.F.; Terrington, R.L.; Reeves, H.; Boon, D.; Scheib, A.J. The 3D characterisation of the zone of human interaction and the sustainable use of underground space in urban and peri-urban environments: Case studies from the UK. *Z. Der Dtsch. Ges. Geowiss.* **2010**, *161*, 219–235. [CrossRef]
21. Elfadaly, A.; Wafa, O.; Abouarab, M.A.; Guida, A.; Spanu, P.G.; Lasaponara, R. Geo-environmental estimation of land use changes and its effects on Egyptian Temples at Luxor City. *ISPRS Int. J. Geo-Inf.* **2017**, *6*, 378. [CrossRef]
22. Elfadaly, A.; Lasaponara, R.; Murgante, B.; Qelichi, M.M. Cultural heritage management using analysis of satellite images and advanced GIS techniques at East Luxor, Egypt and Kangavar, Iran (a comparison case study). In *Computational Science and Its Applications–ICCSA 2017, Proceedings of the 17th International Conference (Proceedings, Part IV 17), Trieste, Italy, 3–6 July 2017*; Springer International Publishing: Berlin/Heidelberg, Germany, 2017; pp. 152–168.

23. Satellite-Based Damage Assessment of Cultural Heritage Sites 2015. Available online: https://whc.unesco.org/en/activities/890/ (accessed on 8 February 2024).
24. Santos, C.; Rapp, L. Satellite imagery, very high-resolution and processing-intensive image analysis: Potential risks under the gdpr. *Air Space Law* **2019**, *44*.
25. Corrie, R.K. October. Detection of ancient Egyptian archaeological sites using satellite remote sensing and digital image processing. In *Earth Resources and Environmental Remote Sensing/GIS Applications II*; SPIE: Ile-de-France, France, 2011; Volume 8181, pp. 270–288.
26. Maheshwari, B.; Singh, V.P.; Thoradeniya, B. *Balanced Urban Development: Options and Strategies for Liveable Cities*; Springer Nature: Berlin/Heidelberg, Germany, 2016; p. 601.
27. Bonazza, A.; Bonora, N.; Duke, B.; Spizzichino, D.; Recchia, A.P.; Taramelli, A. Copernicus in support of monitoring, protection, and management of cultural and natural heritage. *Sustainability* **2022**, *14*, 2501. [CrossRef]
28. Elfadaly, A.; Attia, W.; Qelichi, M.M.; Murgante, B.; Lasaponara, R. Management of cultural heritage sites using remote sensing indices and spatial analysis techniques. *Surv. Geophys.* **2018**, *39*, 1347–1377. [CrossRef]
29. Orlando, P.; Villa, B.D. Remote sensing applications in archaeology. *Archeol. E Calc.* **2011**, *22*, 147–168.
30. Lauer, D.T.; Morain, S.A.; Salomonson, V.V. The Landsat program: Its origins, evolution, and impacts. *Photogramm. Eng. Remote Sens.* **1997**, *63*, 831–838.
31. Campana, S. Archaeology, remote sensing. In *Encyclopedia of Geoarchaeology*; Springer: Dordrecht/Berlin/Heidelberg, Germany; New York, NY, USA; London, UK, 2016; pp. 703–724.
32. Cian, F.; Blasco, J.M.D.; Carrera, L. Sentinel-1 for monitoring land subsidence of coastal cities in Africa using PSInSAR: A methodology based on the integration of SNAP and staMPS. *Geosciences* **2019**, *9*, 124. [CrossRef]
33. U.S. Helps Preserve base of Sphinx by Lowering Groundwater. Available online: https://eg.usembassy.gov/u-s-helps-preserve-base-sphinx-lowering-groundwater/ (accessed on 8 February 2024).
34. Hemeda, S.; Sonbol, A. Sustainability problems of the Giza pyramids. *Herit. Sci.* **2020**, *8*, 1–28. [CrossRef]
35. Sharafeldin, S.M.; Essa, K.S.; Youssef, M.A.; Karsli, H.; Diab, Z.E.; Sayil, N. Shallow geophysical techniques to investigate the groundwater table at the Great Pyramids of Giza, Egypt. *Geosci. Instrum. Methods Data Syst.* **2019**, *8*, 29–43. [CrossRef]
36. Butzer, K.W.; Butzer, E.; Love, S. Urban geoarchaeology and environmental history at the Lost City of the Pyramids, Giza: Synthesis and review. *J. Archaeol. Sci.* **2013**, *40*, 3340–3366. [CrossRef]
37. de Noronha Vaz, E.; Caetano, M.; Nijkamp, P. A multi-level spatial urban pressure analysis of the Giza pyramid plateau in Egypt. *J. Herit. Tour.* **2011**, *6*, 99–108. [CrossRef]
38. Sharafeldin, M.; Essa, K.S.; Sayıl, N.; Youssef, M.A.S.; Diab, Z.E.; Karslı, H. Geophysical investigation of ground water hazards in Giza Pyramids and Sphinx using electrical resistivity tomography and ground penetrating radar: A case study. In Proceedings of the 9th Congress of the Balkan Geophysical Society, Antalya, Turkey, 5–9 November 2017; European Association of Geoscientists & Engineers: Utrecht, The Netherlands, 2017; Volume 2017, No. 1. pp. 1–5.
39. A Report Published by National Geographic about the Urban Sprawling Effects on the Giza Plateau Area. Available online: https://www.nationalgeographic.com/science/article/140418-egypt-population-heritage-conservation-threats-world (accessed on 8 February 2024).
40. Ancient Thebes with Its Necropolis. Available online: http://whc.unesco.org/en/soc/3597 (accessed on 8 February 2024).
41. Morsy, S.W.; Halim, M.A. Reasons why the great pyramids of Giza remain the only surviving wonder of the ancient world: Drawing ideas from the structure of the Giza pyramids to nuclear power plants. *J. Civ. Eng. Archit.* **2015**, *9*, 1191–1201.
42. Nell, E.; Ruggles, C. The orientations of the Giza pyramids and associated structures. *J. Hist. Astron.* **2014**, *45*, 304–360. [CrossRef]
43. Der Manuelian, P. Giza 3D: Digital archaeology and scholarly access to the Giza pyramids: The Giza project at Harvard university. In *2013 Digital Heritage International Congress (DigitalHeritage)*; IEEE: New York, NY, USA, 2013; Volume 2, pp. 727–734.
44. Magli, G. The Giza 'written' landscape and the double project of King Khufu. *Time Mind* **2016**, *9*, 57–74. [CrossRef]
45. USGS. Available online: https://earthexplorer.usgs.gov/ (accessed on 8 February 2024).
46. ArcSWAT. Available online: https://swat.tamu.edu/software/arcswat/ (accessed on 8 February 2024).
47. The Copernicus Data Space Ecosystem. Available online: https://dataspace.copernicus.eu/ (accessed on 8 February 2024).
48. Duan, W.; Zhang, H.; Wang, C.; Tang, Y. Multi-temporal InSAR parallel processing for Sentinel-1 large-scale surface deformation mapping. *Remote Sens.* **2020**, *12*, 3749. [CrossRef]
49. Richards, M.A. A Beginner's Guide to interferometric SAR concepts and signal processing [AESS tutorial IV]. *IEEE Aerosp. Electron. Syst. Mag.* **2007**, *22*, 5–29. [CrossRef]
50. Vrînceanu, C.A.; Grebby, S.; Marsh, S. The performance of speckle filters on Copernicus Sentinel-1 SAR images containing natural oil slicks. *Q. J. Eng. Geol. Hydrogeol.* **2023**, *56*, qjegh2022-046. [CrossRef]
51. How to Radiometrically Terrain-Correct (RTC) Sentinel-1 Data Using GAMMA Software. Available online: https://asf.alaska.edu/how-to/data-recipes/how-to-radiometrically-terrain-correct-rtc-sentinel-1-data-using-gamma-software/ (accessed on 8 February 2024).
52. Semenzato, A.; Pappalardo, S.E.; Codato, D.; Trivelloni, U.; De Zorzi, S.; Ferrari, S.; De Marchi, M.; Massironi, M. Mapping and monitoring urban environment through sentinel-1 SAR data: A case study in the Veneto region (Italy). *ISPRS Int. J. Geo-Inf.* **2020**, *9*, 375. [CrossRef]

53. Koltsida, E.; Kallioras, A. Multi-Variable SWAT Model Calibration Using Satellite-Based Evapotranspiration Data and Streamflow. *Hydrology* **2022**, *9*, 112. [CrossRef]
54. Al-Khafaji, M.S.; Al-Sweiti, F.H. Integrated impact of digital elevation model and land cover resolutions on simulated runoff by SWAT Model. *Hydrol. Earth Syst. Sci. Discuss.* **2017**, 1–26. [CrossRef]
55. Lin, S.; Jing, C.; Chaplot, V.; Yu, X.; Zhang, Z.; Moore, N.; Wu, J. Effect of DEM resolution on SWAT outputs of runoff, sediment and nutrients. *Hydrol. Earth Syst. Sci. Discuss.* **2010**, *7*, 4411–4435.
56. Winchell, M.; Srinivasan, R.; Di Luzio, M.; Arnold, J. *ArcSWAT Interface for SWAT2012: User's Guide*; Blackland Research Center, Texas AgriLife Research, College Station: Temple, TX, USA, 2013; pp. 1–464.
57. Tan, M.L.; Ficklin, D.L.; Dixon, B.; Yusop, Z.; Chaplot, V. Impacts of DEM resolution, source, and resampling technique on SWAT-simulated streamflow. *Appl. Geogr.* **2015**, *63*, 357–368. [CrossRef]
58. Zhang, Y.; Wu, H.; Li, M.; Kang, Y.; Lu, Z. Investigating ground subsidence and the causes over the whole Jiangsu Province, China using sentinel-1 SAR data. *Remote Sens.* **2021**, *13*, 179. [CrossRef]
59. Rateb, A.; Abotalib, A.Z. Inferencing the land subsidence in the Nile Delta using Sentinel-1 satellites and GPS between 2015 and 2019. *Sci. Total Environ.* **2020**, *729*, 138868. [CrossRef] [PubMed]
60. Hu, L.; Dai, K.; Xing, C.; Li, Z.; Tomás, R.; Clark, B.; Shi, X.; Chen, M.; Zhang, R.; Qiu, Q.; et al. Land subsidence in Beijing and its relationship with geological faults revealed by Sentinel-1 InSAR observations. *Int. J. Appl. Earth Obs. Geoinf.* **2019**, *82*, 101886. [CrossRef]
61. Sánchez-Martín, J.M.; Rengifo-Gallego, J.I.; Blas-Morato, R. Hot spot analysis versus cluster and outlier analysis: An enquiry into the grouping of rural accommodation in Extremadura (Spain). *ISPRS Int. J. Geo-Inf.* **2019**, *8*, 176. [CrossRef]
62. Martin, C.; Stewart, F. *Geographically Weighted Regression: A Tutorial on Using GWR in ArcGIS 9.3*; National Centre for Geocomputation, National University of Ireland: Maynooth, Ireland, 2009; pp. 1–27.
63. Fotheringham, A.S.; Brunsdon, C.; Charlton, M. *Geographically Weighted Regression: The Analysis of Spatially Varying Relationships*; John Wiley & Sons: Hoboken, NJ, USA, 2003.
64. Brunsdon, C.; Fotheringham, A.S.; Charlton, M.E. Geographically weighted regression: A method for exploring spatial nonstationarity. *Geogr. Anal.* **1996**, *28*, 281–298. [CrossRef]
65. Lu, B.; Charlton, M.; Harris, P.; Fotheringham, A.S. Geographically weighted regression with a non-Euclidean distance metric: A case study using hedonic house price data. *Int. J. Geogr. Inf. Sci.* **2014**, *28*, 660–681. [CrossRef]
66. Dubé, J.; Legros, D. Spatial autocorrelation. In *Spatial Econometrics Using Microdata*; Springer: Berlin/Heidelberg, Germany, 2014; pp. 59–91. [CrossRef]
67. Wang, Y.; Gui, Z.; Wu, H.; Peng, D.; Wu, J.; Cui, Z. Optimizing and accelerating space–time Ripley's K function based on Apache Spark for distributed spatiotemporal point pattern analysis. *Future Gener. Comput. Syst.* **2020**, *105*, 96–118. [CrossRef]
68. Getis, A.; Ord, J.K. The analysis of spatial association by use of distance statistics. *Geogr. Anal.* **1992**, *24*, 189–206. [CrossRef]
69. Getis, A. Local spatial statistics: An overview. In *Spatial Analysis: Modelling in a GIS Environment*; John Wiley & Sons: Hoboken, NJ, USA, 1996; pp. 261–277.
70. Ord, J.K.; Getis, A. Local spatial autocorrelation statistics: Distributional issues and an application. *Geogr. Anal.* **1995**, *27*, 286–306. [CrossRef]
71. Casarotto, A.; Pelgrom, J.; Stek, T.D. Testing settlement models in the early Roman colonial landscapes of Venusia (291 BC), Cosa (273 BC) and Aesernia (263 BC). *J. Field Archaeol.* **2016**, *41*, 568–586. [CrossRef]
72. Casarotto, A. *Spatial Patterns in Landscape Archaeology: A GIS Procedure to Study Settlement Organization in Early Roman Colonial Territories*; Leiden University Press: Leiden, The Netherlands, 2018.
73. Bokhari, R.; Shu, H.; Tariq, A.; Al-Ansari, N.; Guluzade, R.; Chen, T.; Jamil, A.; Aslam, M. Land subsidence analysis using synthetic aperture radar data. *Heliyon* **2023**, *9*, e14690. [CrossRef]
74. Ghazifard, A.; Akbari, E.; Shirani, K.; Safaei, H. Evaluating land subsidence by field survey and D-InSAR technique in Damaneh City, Iran. *J. Arid. Land* **2017**, *9*, 778–789. [CrossRef]
75. Tiwari, R.K.; Malik, K.; Arora, M.K. Urban subsidence detection using the sentinel-1 multi-temporal INSAR data. In Proceedings of the 38th Asian Conference on Remote Sensing-Space Applications: Touching Human Lives, New Delhi, India, 23–27 October 2017; ACRS: Seattle, WA, USA, 2017; Volume 27, pp. 2410–2414.
76. Bhattarai, R.; Alifu, H.; Maitiniyazi, A.; Kondoh, A. Detection of land subsidence in Kathmandu Valley, Nepal, using DInSAR technique. *Land* **2017**, *6*, 39. [CrossRef]
77. Nalakurthi, N.S.R.N.; Behera, M.R. Detection of Land Subsidence using Sentinel-1 Interferometer andIts Relationship withSea-Level-Rise, Groundwater, andInundation: A Case Study along Mumbai Coastal City. 2022. Available online: https://www.researchsquare.com/article/rs-1392714/v1 (accessed on 8 February 2024).
78. Holtorf, C.; Ortman, O. Endangerment and conservation ethos in natural and cultural heritage: The case of zoos and archaeological sites. *Int. J. Herit. Stud.* **2008**, *14*, 74–90. [CrossRef]
79. Elfadaly, A.; Attia, W.; Lasaponara, R. Monitoring the environmental risks around Medinet Habu and Ramesseum Temple at West Luxor, Egypt, using remote sensing and GIS techniques. *J. Archaeol. Method Theory* **2018**, *25*, 587–610. [CrossRef]
80. Elfadaly, A.; Murgante, B.; Qelichi, M.M.; Lasaponara, R.; Hosseini, A. A comparative analysis of temporal changes in urban land use resorting to advanced remote sensing and GIS in Karaj, Iran and Luxor, Egypt. In *Computational Science and Its Applications–*

ICCSA 2019, Proceedings of the 19th International Conference (Proceedings, Part V 19), Saint Petersburg, Russia, 1–4 July 2019; Springer International Publishing: Berlin/Heidelberg, Germany, 2019; pp. 689–703.
81. Engeman, R.M.; Couturier, K.J.; Felix, R.K.; Avery, M.L. Feral swine disturbance at important archaeological sites. *Environ. Sci. Pollut. Res.* **2013**, *20*, 4093–4098. [CrossRef] [PubMed]
82. Louiset, T.; Pamart, A.; Gattet, E.; Raharijaona, T.; De Luca, L.; Ruffier, F. A shape-adjusted tridimensional reconstruction of cultural heritage artifacts using a miniature quadrotor. *Remote Sens.* **2016**, *8*, 858. [CrossRef]
83. Balla, A.; Pavlogeorgatos, G.; Tsiafakis, D.; Pavlidis, G. Recent advances in archaeological predictive modeling for archeological research and cultural heritage management. *Mediterr. Archaeol. Archaeom.* **2014**, *14*, 143–144.
84. Elfadaly, A.; Lasaponara, R. On the use of satellite imagery and GIS tools to detect and characterize the urbanization around heritage sites: The case studies of the Catacombs of Mustafa Kamel in Alexandria, Egypt and the Aragonese Castle in Baia, Italy. *Sustainability* **2019**, *11*, 2110. [CrossRef]
85. Lasaponara, R.; Murgante, B.; Elfadaly, A.; Qelichi, M.M.; Shahraki, S.Z.; Wafa, O.; Attia, W. Spatial open data for monitoring risks and preserving archaeological areas and landscape: Case studies at Kom el Shoqafa, Egypt and Shush, Iran. *Sustainability* **2017**, *9*, 572. [CrossRef]

land

Article

Comparative Effects of Wild Boar (*Sus scrofa*) Rooting on the Chemical Properties of Soils in Natural and Post-Fire Environments of the Edough Forest Massif (Northeastern Algeria)

Kamelia Hesni Benotmane [1,*], Mehdi Boukheroufa [2], Rym Sakraoui [2], Feriel Sakraoui [2], Csaba Centeri [3,*], Ádám Fehér [4] and Krisztián Katona [4]

[1] Soil and Sustainable Development Laboratory, Department of Biology, Faculty of Science, Badji Mokhtar Annaba University BP 12, Annaba 23 200, Algeria
[2] Ecobiology for Marine Environments and Coastal Areas Laboratory, Faculty of Sciences, Badji Mokhtar Annaba University BP 12, Annaba 23 200, Algeria; mehdiboukheroufa@yahoo.fr (M.B.); r.sakraoui@gmail.com (R.S.); f.sakraoui@gmail.com (F.S.)
[3] Department of Nature Conservation and Landscape Management, Institute for Wildlife Management and Nature Conservation, Hungarian University of Agriculture and Life Sciences, H-2100 Gödöllő, Hungary
[4] Department of Wildlife Biology and Management, Institute for Wildlife Management and Nature Conservation, Hungarian University of Agriculture and Life Sciences, H-2100 Gödöllő, Hungary; katona.krisztian@uni-mate.hu (K.K.)
* Correspondence: kameliabenotmane@gmail.com (K.H.B.); centeri.csaba@uni-mate.hu (C.C.)

Abstract: Wild boars use a wide range of habitats. Their invasive nature is gaining attention due to the complexity of its impact. The goal of this research is to analyze the impact of the wild boar on the chemical properties of soils in a natural and a post-fire forest in the Edough Forest Massif in Algeria. This study compares the impact of wild boar rooting on soil parameters to determine the functional role of the wild boar. The research was conducted during the winter of 2022. The study sites included a natural forest and a post-fire area. Rooting tracks were geolocated and soil samples were collected. The results show significant differences between rooted and control patches in the chemical parameters measured in the two environments. However, in the natural environment, significant differences were only noted for the calcium content and electrical conductivity. But in the post-fire environment, strong significant differences were observed for all measured parameters, suggesting that wild boars do not exert a noticeable soil homogenization effect on the soil properties. This research highlights the importance of understanding and managing the impact of wild boars in natural and post-fire forests on soil formation processes, the diversity of soil properties, and their magnitude.

Keywords: wildlife impact; soil disturbance; soil properties; comparative analyses

1. Introduction

The wild boar (*Sus scrofa*) is one of the most controversial wild species due to its invasive and prolific nature, ranking among the top 100 worst invasive species responsible for agricultural crop damage and conflicts with humans [1–3]. However, this ecosystem engineer plays a crucial role in its native habitats, including forests: it regulates the density of plant species and disperses fruit seeds through its feces, facilitating the spread of various (including invasive) plant species [4–8]. It contributes to the balance of populations in the trophic chain, particularly for insects and micromammals. It also aids soil aeration and soil organic matter formation [9] while causing physical modifications to the habitat, affecting soil structure and composition [10]. These findings emphasize the importance of developing management and monitoring strategies for wild boar populations to maintain

the carrying capacity of forest ecosystems and, consequently, mitigate potential damage in agricultural areas [11], wetlands [12], and urban environments where the species has penetrated.

There is a never-ending debate about the role of the wild boar. Is it a natural effect or is it a damage that we see when we encounter wild boar rooting? Since wild boars have been in the investigated area during the formation of recent soils, one must consider that—in addition to other factors—wild boars played a crucial role in the formation of the soils that we can see today. The question of where the population size should end is a complicated one and is perceived by many interested parties from many points of view: foresters, hunters, wildlife biologists, wildlife managers, rangers or nature conservationists in general, tourists, joggers, walkers, technical sports enthusiasts, parents, etc., all have their own specific view or perception of the same situation [8–12].

Mediterranean forests have faced numerous environmental and anthropogenic pressures, including deforestation, fragmentation, and especially wildfires in recent years, which have had devastating effects on vegetation cover and associated fauna [13–15].

In this study, we investigate the role of the wild boar and its effects on the quality of forest soils. This study was conducted in the Edough Mountain Massif, a region in northeastern Algeria that is part of a regional biodiversity hotspot and is considered an endemism center for many plant species [16]. Like all Mediterranean forests, this area has been exposed to numerous wildfires, the recurrence of which could threaten the integrity of this biodiversity hotspot [17]. Due to climate change, it is predictable that precipitation and temperature will change dramatically in the near future, possibly causing more wildfires. This is why the investigation of the effects of fires with the combination of wild boar rooting on soil parameters can help to find the appropriate number of wild boars (or, more generally speaking, the optimal population size) in these forests.

We hypothesize that soil bioturbation by wild boars has different effects when other factors such as wildfires are prevalent.

The objective of this study is to analyze the impact of wild boar activity on soil chemical parameters in natural forest and post-fire forest environments and to deduce the functional role played by the wild boar in each environment.

2. Materials and Methods

2.1. Short Description of the Studied Areas

This study was carried out on the Edough Peninsula during the winter period of 2022 (from the end of December until the end of February). The Edough Mountain Range is located in the extreme north-east of Algeria, with 35,423 hectares of forest area and 4880 hectares of maritime area, and is limited to the south-east by the Guerbès Senhadja wetland complex, to the south by the Fetzara Lake Basin, to the west by the lower course of Oued El Kébir, and by the Kharraza Plain to the east; to the north, the peninsula is bordered by the Mediterranean Sea [18]. A Mediterranean-type climate and northeast winds prevail in the region. The Edough Massif is populated on its northern slope by forest species. The Edough Massif corresponds to crystalline, eruptive, sedimentary, and metamorphic formations. Lithological analysis reveals a large area occupied by Numidian sandstones and another by gneisses. These siliceous rocks provide an acidic substrate, and the soils resemble brown forest soils (Cambisols and Luvisols) and shallow soils (Leptosols) on steep slopes where water erosion is a natural phenomenon. The combination of humidity and acidity sometimes results in soils with podzolic tendencies, especially those forming on Numidian sandstones [19]. We chose two sites for sampling, mainly based on the significant and regular presence of traces of rooting by the boars: the natural site of Bouzizi and the post-fire site of Aïn Barbar (Figure 1).

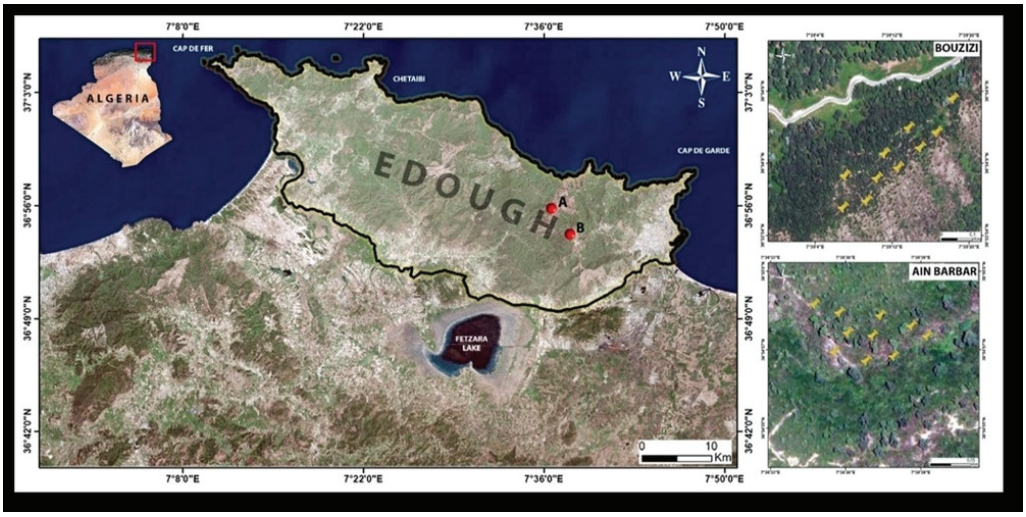

Figure 1. The study area with sampling sites of wild boar rooting in the north-east corner of Algeria (A: Aïn Barbar; B: Bouzizi. Source: Google Earth).

The Bouzizi forest (36°53′59.7″ N–7°39′10.2″ E) is located in Algeria, southeast of the Edough Massif, between 800 and 850 m above sea level. This locality is characterized by cork oak (*Quercus suber* L.) forests and its rich associated floristic procession. The post-fire forest of Aïn Barbar is located near the road (36°55′03.8″ N–7°36′43.0″ E). The area burnt down totally in August 2021. The locality was characterized by the dominance of the cork oak and by the presence of some specimens of the zean oak (*Quercus canariensis*) and maritime pine (*Pinus pinaster*), located at an altitude of 579 m above the Mediterranean Sea (Figure 2).

Figure 2. Photos of the two study sites. (**A**): natural site of Bouzizi, (**B**): post-fire site of Aïn Barbar (on the right) (Photo: Kamelia Benotmane, 5 January 2022).

Figure 2 shows the characteristic differences between the two study sites. The burnt site after 4–5 months shows some regeneration effects, and there are some flowering plants already on the soil surface.

Both sites are characterized by shallow soils. The A horizon is 28–38 cm thick, its color is black, the texture is loamy sand, the lime content is zero, roots are present in the whole depth of the horizon, it is slightly compacted, and the soil moisture was low at the time of the evaluation. Below the A horizon there is the C horizon; its color is yellow, the texture is loamy, the lime content is zero, roots are visible as deep as 72 cm, and it is

medium compacted and also dry. Wild boars did not reach the C horizon during their rooting activities.

2.2. Soil Sampling on the Field

Sampling was carried out from the end of December 2021 until the end of February 2022, with two prospecting trips per month, to identify new rooting. The selection and sampling protocol was carried out according to the method of Pitta-Osses et al. (2020) [8]. Only so-called deep rooting was considered during the measurements, meaning that there is a visible/considerable depth (e.g., approximately a minimum of 20 cm) of the inner part of the rooting, and the deep rooting is surrounded by a visible and distinguishable ring formed from the excavated soil material (Figure 3). This deep rooting differs from shallow rooting by its spatial extent; while one deep rooting is approximately typically 1–5 m^2, shallow rooting is typically 5–50 m^2. Each rooting was geolocated by the Map mobile application (Figure 3).

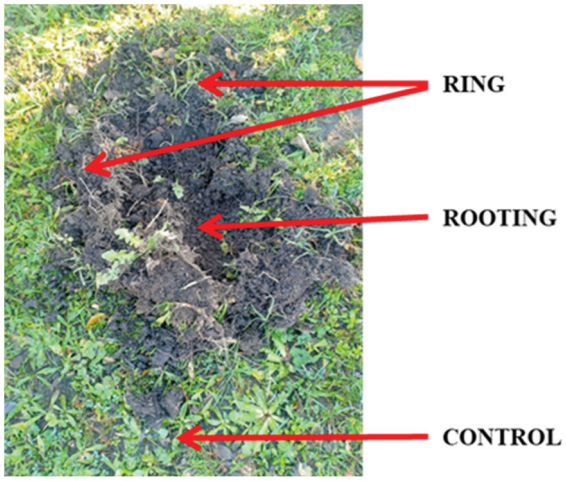

Figure 3. The photo of the rooting where standard measurements were taken in each rooting, ring, and nearby control area (Photo: Benotmane, K., January 2021, Edough).

During the winter period, 10 rooting areas in the natural and 10 rooting areas in the burnt area were sampled from 0 to 20 cm depths. Three samples of 250 g of soil were taken from each rooting: one in the middle of the dug-out depression (rooting), the second from the ring that surrounds the rooting (ring), and the third as a control or outside the rooting (control), which was taken next to the rooting at the intact surface. A total of 60 samples (30 in a natural area and 30 in a burnt area) were collected for analysis.

2.3. Laboratory Analysis of the Soil Samples

Soil samples were dried at ambient temperatures for about 5 days, crushed and sieved with 2 mm sieves, and then analyzed for different chemical properties: total calcium (Ca mg/L), total magnesium (Mg mg/L), total potassium (K mg/L), and total sodium (Na mg/L) were determined by extraction with buffered ammonium acetate at pH 7.0 before reading with an atomic absorption spectrometer for Ca, Mg, and K and Na with a flame spectrometer [20]. Total nitrogen (N %) was determined by the Kjeldahl method [21] and phosphorus (P mol/L) was measured by colorimetry using the Murphy and Riley methods [22]. Electrical conductivity (EC mS/cm) was measured by a conductivity meter [23]. The equivalent calcium carbonate was determined by the gasometrical method (Bernard's Calcimeter). The pH was determined by using a pH meter (HANNA HI 8520) after mixing soil with distilled water (1:2.5 w/v) [24]. Samples were digested in a mixture (3:1) of Nitric Acid (HNO_3) and Perchloric Acid ($HClO_4$), and the contents of Ca (mg/L), Mg (mg/L), and K (mg/L) were determined using an atomic absorption spectrophotometer (AAS) (Model Analyst 700, Perkin Elmer).

2.4. Applied Statistical Analyses for Evaluation of Soil Data

Statistical analysis of the data was conducted in R (R Development Core Team, 2021) using separate factorial MANOVA tests for the two study sites to depict local differences in soil parameters affected by wild boar rooting. Furthermore, we implemented an additional MANOVA test to verify the effect of fire disturbance, wild boar rooting, and their interaction on soil parameters in general. Pillai's trace was used as a test statistic in all cases. Variables were checked for multicollinearity; neither of them showed high correlation ($r_{max} < 0.65$). Visualizations were created with the *ggplot2* package [25]. We also performed a principal component analysis with the Minitab (version 14) software. The first component included the chemical elements, and the second component represented the different sampled groups (rooting, ring, and control).

3. Results

3.1. Analysis of the Wild Boar's Impact on the Natural Environment (Bouzizi, Algeria)

The results of the MANOVA test performed on soil data collected from the natural environment revealed differences between the characteristic parts of the rootings ($F(16, 42) = 6.08$, $p < 0.001$; Pillai's trace = 1.39). However, the related univariate test revealed that only the calcium content and electrical conductivity (EC) differed between groups (Table 1). This suggests that the rooting activity of wild boars did not cause major changes in the general composition of the soil, except for a few specific elements (calcium: control = 247.8 ± 26.9, ring = 257.9 ± 40.9, rooting = 202.9 ± 41.1 mg/L; EC: control = 0.15 ± 0.02, ring = 0.19 ± 0.03, rooting = 0.18 ± 0.02 mS/cm).

Table 1. Univariate test statistics of separate MANOVA tests performed on soil attribute data. The rooting effect (rooted area, ring, control) was used as an explanatory variable.

	Bouzizi (Rooting)	**Aïn Barbar (Rooting and Fire)**
df	*2*	*2*
K	3.08	22.3 ***
Na	0.92	7.27 **
Mg	1.32	11.9 ***
Ca	6.3 **	103.3 ***
P	3.32	45.36 ***
N	0.97	26.5 ***
pH	0.53	24.5 ***
EC	10.9 ***	26.3 ***
Residuals:	*27*	*27*

*** $p < 0.001$; ** $p < 0.01$.

The calcium content was the lowest in the core part of the rooting, while it was nearly similar in samples collected from the redistributed soil (ring) and the control (Figure 4). Additionally, the electrical conductivity was the lowest in samples free from wild boar disturbance (control) and higher in the rooting and the ring, with extremes at both ends of their ranges (Figure 4).

These results indicate that, although the overall impact of wild boars on soil composition in a natural environment is limited, they can nevertheless have significant local effects on certain chemical elements in the soil.

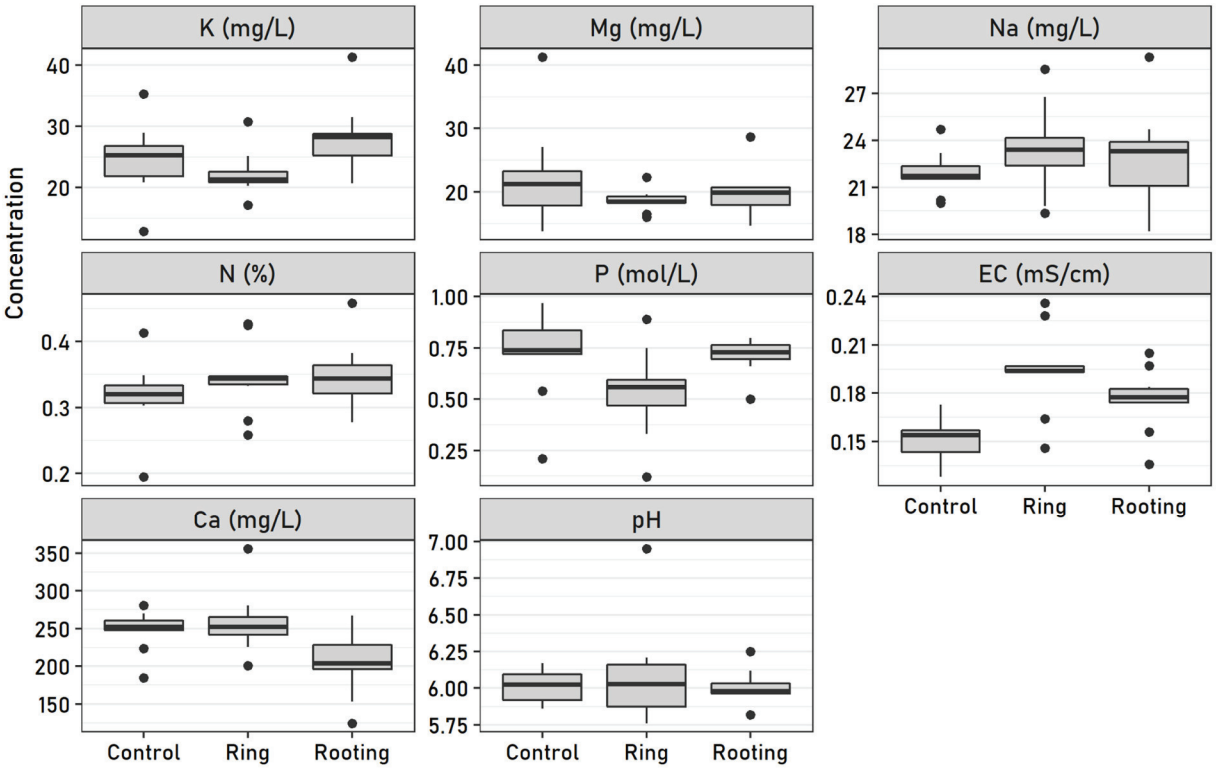

Figure 4. Boxplots showing the distribution of the measured soil parameters originating from Bouzizi, where wild boar rooting but no wildfire occurred. (Boxes show the interquartile range, the black line in the box shows the median value, whiskers show the maximum and minimum values except for outliers, and dots show outlier values.)

3.2. Analysis of the Wild Boar's Impact on the Post-Fire Environment (Aïn Barbar)

The results obtained in the post-fire environment indicate statistically significant differences regarding wild boar rooting ($F(16, 42) = 19.23$, $p < 0.001$; Pillai's trace = 1.76). This was confirmed for all measured soil parameters (Table 1). Contrasts were more pronounced in relation to the control samples. Potassium, sodium, nitrogen, phosphorus, electrical conductivity, calcium, and pH levels were equally the lowest in samples collected from plots free from wild boar disturbance, while in the case of magnesium, we observed quite the opposite (Figure 5).

The variability in parameters among groups was much larger in this post-fire environment than in the first study site where only wild boar disturbance occurred (Table 2).

Table 2. The mean and standard deviation of the measured soil parameters in Aïn Barbar, where wild boar rooting occurred after a wildfire.

	Control	Ring	Rooting
K (mg/L)	13.6 ± 2.2	25.6 ± 4.2	24.3 ± 6
Mg (mg/L)	30.8 ± 5.3	27.5 ± 3.3	22.2 ± 2.9
Na (mg/L)	19.8 ± 1.4	19.2 ± 2	22.7 ± 3
N (%)	0.21 ± 0.04	0.34 ± 0.03	0.32 ± 0.05
P (mol/L)	0.16 ± 0.07	0.62 ± 0.15	0.41 ± 0.1
EC (mS/cm)	0.13 ± 0.02	0.21 ± 0.03	0.19 ± 0.03
Ca (mg/L)	188.7 ± 31	395.8 ± 25	331.7 ± 41
pH	5.9 ± 0.2	6.5 ± 0.1	6.2 ± 0.2

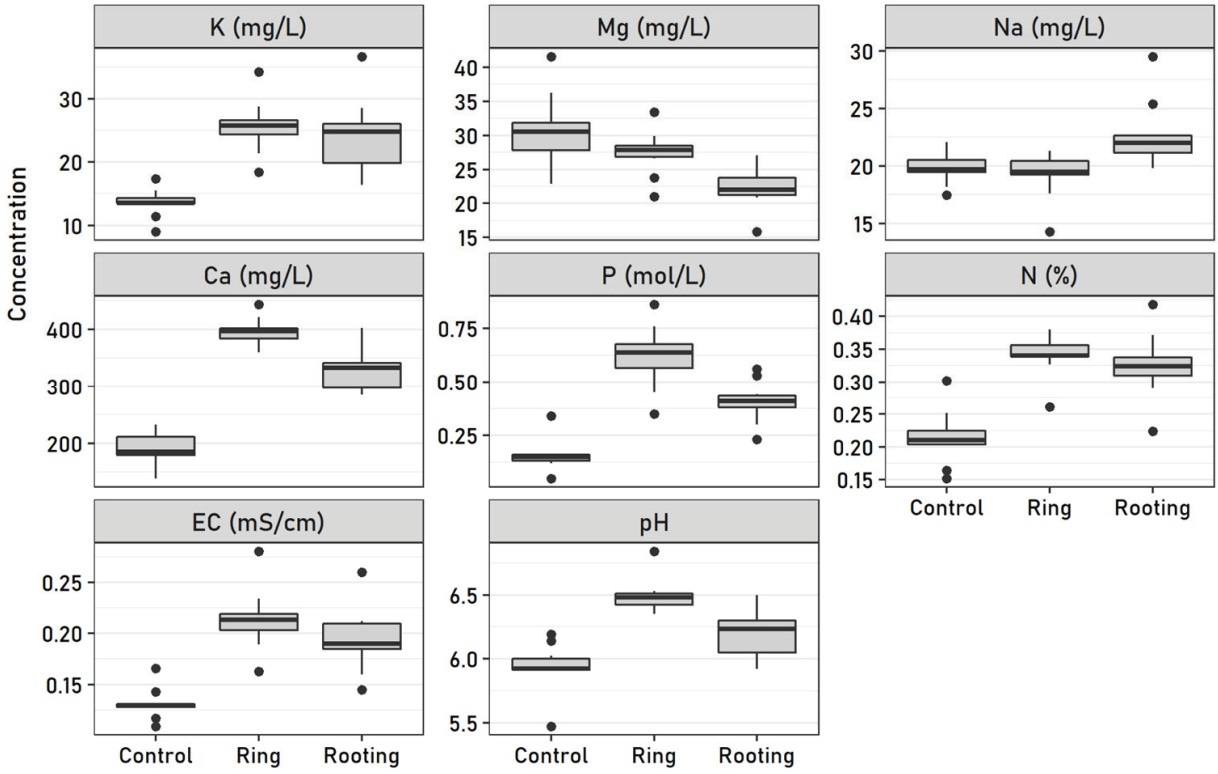

Figure 5. Boxplots showing the distribution of the measured soil parameters originating from Aïn Barbar, where wild boar rooting occurred after a wildfire. (Boxes show the interquartile range, the black line in the box shows the median value, whiskers show the maximum and minimum values except for outliers, and dots show outlier values.)

3.3. Comparative Analysis of the Wild Boar's Impact between the Natural Environment (Bouzizi) and the Post-Fire Environment (Aïn Barbar)

The final MANOVA test on the joint dataset of the two study sites verified our hypothesis that soil bioturbation by wild boar has different effects when other factors such as wildfires are prevalent. The soil parameters were statistically different between the study sites, rooting effect groups, and with the combined impact of wild boar and fire disturbance (Table 3).

Table 3. Multivariate test statistics of MANOVA performed on soil attributes data. The study sites (Aïn Barbar and Bouzizi), the groups of the rooting effect (rooted area, ring, control) and their interaction were used as explanatory variables.

	df	**Pillai's Trace**	**F**
Study site	1	0.85	29.37 ***
Rooting	2	1.38	11.65 ***
Study site × Rooting	2	1.17	7.35 ***

*** $p < 0.001$.

Almost every parameter was significantly different among groups of the studied factors (Table 4), but we need to note that the confirmed significant effects for rooting alone come from the effect of merging the datasets of the two areas and were largely affected by the significant differences observed in the Aïn Barbar area (see Table 1).

Table 4. Univariate test statistics performed on soil attribute data. The study sites (Aïn Barbar and Bouzizi), the groups of the rooting effect (rooted area, ring, control), and their interaction were used as explanatory variables.

	Study Site	Rooting	Study Site × Rooting
df	*1*	*2*	*2*
K	9.3 **	11.2 ***	11.1 ***
Na	12.7 ***	3.5 *	3.8 *
Mg	30.9 ***	7.4 **	3.3
Ca	58.5 ***	48.3 ***	50.5 ***
P	45.3 ***	5.5 **	23.9 ***
N	12.7 ***	15.9 ***	6.2 **
pH	12.8 ***	11.8 **	7.4 **
EC	0.9	36.6 ***	4.4 *
Residuals: 54			

*** $p < 0.001$; ** $p < 0.01$; * $p < 0.05$.

On the other hand, significant interactions of the site and rooting indicate that wild boar rootings could have various effects on soil properties depending on the presence/absence of fire disturbance. In the case of potassium, its concentration was different between sites without rooting (control: Bouzizi = 24.6 ± 5.8 vs. Aïn Barbar = 13.6 ± 2.2 mg/L), but wild boar rooting induced the convergence of these tendencies (Figure 6). In contrast, sodium levels were the most different in the redistributed soil (ring) between the natural environment and the post-fire site (ring: Bouzizi = 23.5 ± 2.8 vs. Aïn Barbar = 19.2 ± 2 mg/L), and its levels were more similar even in the rooting or in the control samples.

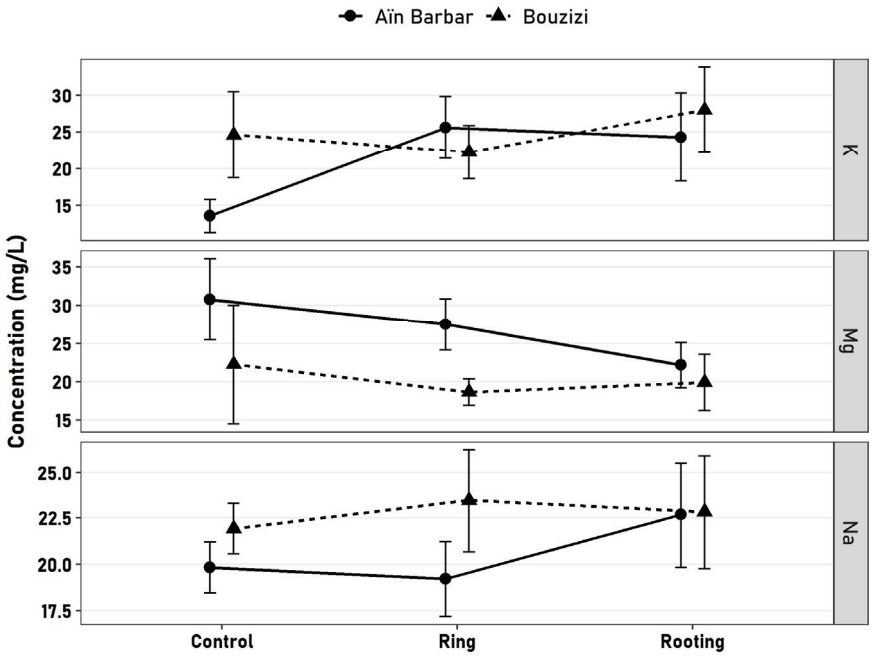

Figure 6. Interaction plots of rooting and site effects on potassium, magnesium, and sodium content of the soil. The solid line with black points indicates data collected from Aïn Barbar, the dotted line with black triangles indicates data collected from Bouzizi.

The same converging tendencies can be observed in total nitrogen and phosphorus (Figure 7), where the redistributed soil (ring) showed very similar levels (nitrogen: Bouzizi = 0.34 ± 0.05 vs. Aïn Barbar = 0.34 ± 0.03%; phosphorus: Bouzizi = 0.53 ± 0.21 vs. Aïn Barbar = 0.62 ± 0.15 mol/L), while calcium levels tend to separate in rooted patches between the two sites, as noted in the case of phosphorus.

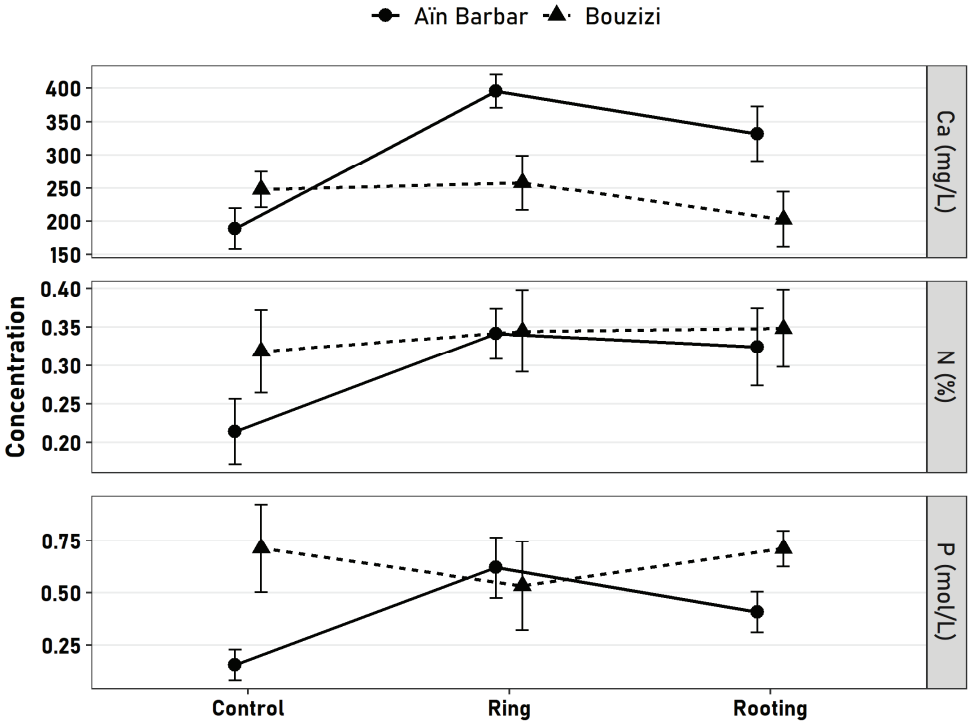

Figure 7. Interaction plots of rooting and site effects on calcium, total nitrogen, and phosphorus content of the soil. The solid line with black points indicates data collected from Aïn Barbar, the dotted line with black triangles indicates data collected from Bouzizi.

Electrical conductivity values were similar between sites; only rooting affected them significantly (Table 4). The variability was not impressive considering the pH of the samples, but still reached a significant difference between sites and among rootings, where the differences were the highest in the redistributed soil (ring: Bouzizi = 6.1 $\pm$ 0.3 vs. Aïn Barbar = 6.5 $\pm$ 0.1) (Figure 8).

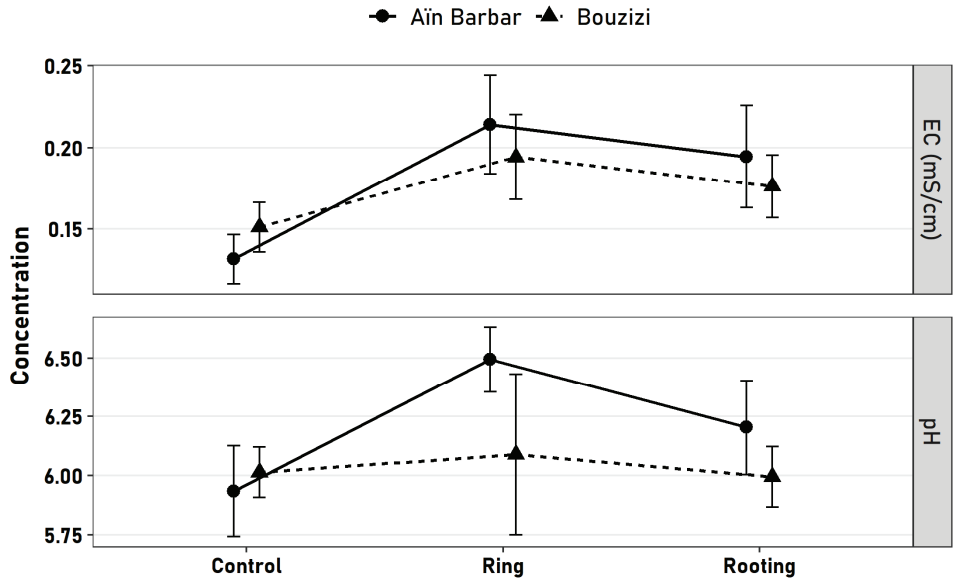

Figure 8. Interaction plots of rooting and site effects on electric conductivity and pH of the soil. The solid line with black points indicates data collected from Aïn Barbar, the dotted line with black triangles indicates data collected from Bouzizi.

3.4. Principal Component Analysis on Soil Parameters of the Two Study Sites

We conducted a principal component analysis (PCA) by correlating all the chemical parameters of the soil in two types of environments (Figures 9 and 10).

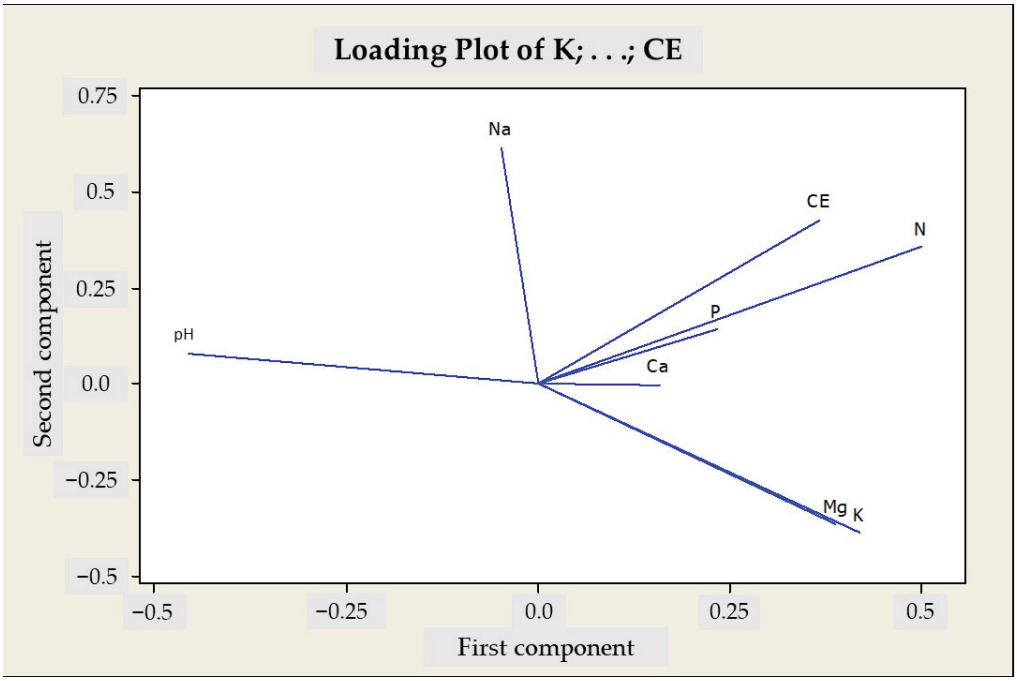

Figure 9. Principal component analysis of the measured parameters of the soil in the natural forest of Bouzizi, Algeria. First component: the chemical elements; second component: rooting, ring, and control.

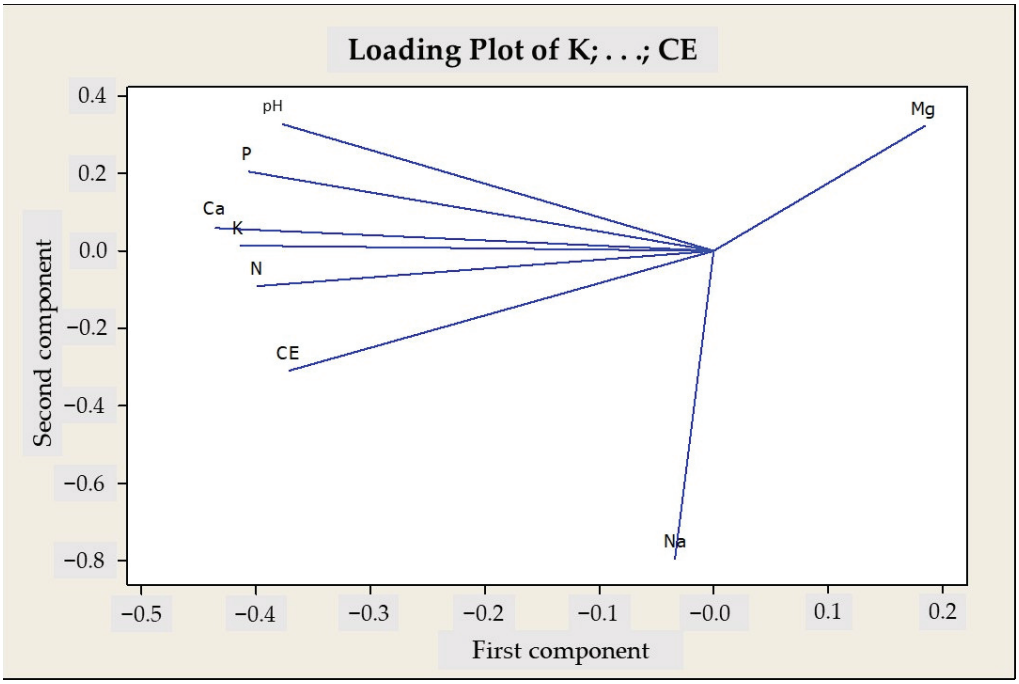

Figure 10. Principal component analysis of the measured parameters of the soil in the post-fire forest of Aïn Barbar, Algeria. First component: the chemical elements; second component: rooting, ring, and control.

This analysis revealed the following findings:

- In the natural environment, pH, Na, and Mg and K appear to behave separately from the other parameters.
- In the post-fire environment, pH has a positive correlation with P, Ca, and K.
- Magnesium (Mg) is negatively correlated with the other parameters in the post-fire environment.
- Magnesium (Mg) and potassium (K) are strongly positively correlated in the natural environment, whereas Mg tends to be negatively correlated with other components in the post-fire environment (just as well as sodium).
- In both environments, sodium (Na) exhibits a negative correlation with the other parameters.

4. Discussion

Rooting is a trophic behavior of wild boars in the forest environment that results in soil renewal, leading to its aeration, as well as improved oxygen penetration and the mixing of nutrients and organic matter [26,27]. Several studies have highlighted numerous positive effects of this species, which exerts a natural plowing effect on the soil [6,8,28]. These studies have rehabilitated the functional role of the wild boar, which appears to be ecologically beneficial for both fauna and flora, and especially for the soils of the environments they colonize [29]. The rooting effect is particularly crucial for improving physical characteristics, as it even contributes to slowing down the erosion process by creating depressions to halt water runoff [8]. These benefits can be advantageous for other ecologically important animal groups, such as amphibians, earthworms, and insects, many of which rely on consistently moist soils for feeding and breeding, and for which the use of these rootings and depressions in the soil caused by ungulates has been reported [8,30]. This soil humidification action also allows for better growth of organisms that colonize the soil (soil microfauna and macrofauna) [30]. Our results are consistent in some cases with existing studies, as we observed a modification of the analyzed chemical parameters between the rooting, ring, and control zones. In the same study area, Benotmane et al. [31] found no statistically significant differences in soil chemical parameters in the natural forest environment, except for organic matter. Other studies, such as Singer et al. [32], have observed that disturbed soils had lower concentrations of certain elements, such as Ca, P, Mg, Mn, Zn, Cu, H, and N, as well as reduced cation exchange capacity. Siemann et al. [33] noted an increase in the nitrogen mineralization rates in rooted plots in deciduous pine forests in the United States. The work by Bruinderink and Hazebroek [34] and Mohr et al. [35] found no effect of rooting on characteristics such as soil horizon depth, soil pH, organic matter, and nitrogen content. A more recent study showed that some values do not illustrate significant differences but suggest that wild boars engage in a natural plowing action by mixing litter with the upper mineral horizons of the soil, resulting in a more homogeneous distribution of nutrients [36–39].

The results obtained in the post-fire environment, a few months after the fire, highlight significant differences between the values of the chemical parameters in the three analyzed zones (rooting, control, and ring). In the literature, it is well established that wildfires have an impact on the chemical properties of soils, especially in Mediterranean ecosystems [40–42]. Many studies indicate a substantial increase in nutrients immediately after a fire event [41,43–46], caused by the combustion of vegetation and debris, which significantly affects their availability. Our study supports these findings, as we observed very high concentrations of K, Na, Mg, Ca, P, N, pH, and EC in the examined soils. The PCA analysis reveals two distinct configurations that suggest that, unlike in the natural environment, wild boars do not exert a noticeable soil homogenization effect in the post-fire forest. Few studies have assessed the effects of fires on herbivore diversity profiles, establishing a connection between fire occurrence gradients, climate, soil fertility, and the alpha and beta diversity profiles of ungulates [47–49]. The recent works of Lewis et al. [50] showed that fire

severity and wild and domestic ungulate herbivory can strongly influence the long-term (10 years post fire) regeneration and recruitment of plant species over varying durations.

Similar disturbances occur in soils when other natural phenomena happen. In the Tatra Mountain, windfall caused losses of all measured nutrients (Ca, Mg, K, Fe, Al, ammonium-N, nitrate-N, S) except P [51]. These nutrient leaching were due to the strongly acid soils (pH 3.0–4.5). The examined area of Algeria did not have this very low pH so the results are not comparable.

Regardless of the lack of data, mainly concerning the joint impact of forest fires and wild boar rooting, we tried to build some foundation on the findings of the recent research, and taking into account the complexity of the soil, some statistical data could establish some of our further discussion in this manner. For example, not strictly speaking but searching for solutions, our results might help to evaluate the magnitude of wild boar impacts by taking the following findings into account:

(a) The statistical tests confirmed differences in soil parameters between sites, rooting effects, and the interaction of the two. This suggests that each site has its own specific soil system that can react differently to biotic and abiotic disturbances like wild boar rooting or wildfires. Since we lack soil data of the pre-fire status from Aïn Barbar, we cannot depict the extent of how significant the impact of wildfire could be on the alteration of soil attributes. If we can consider the two sites rather similar in their pedological attributes, then forest fires did exert a notable impact on soil life and its parameters (Table 4). For example, phosphorus levels were statistically different between sites as well: this can be the result of receiving extra phosphorus from the ashes after the forest fire.

(b) While forest fires can highly affect topsoil layers, bioturbations by wild boars could reach deeper in the soil, homogenizing layers and nutrients or creating much larger disparities in nutrient levels. We found examples for both cases (Table 1), but it seems that bioturbation's effects were more prevalent in the post-fire environment.

(c) This twofold effect of wild boar rooting was also confirmed when the interacting terms of fire and rooting were tested (Figures 6–8). The redistributed soil showed especially high variability in this context: some soil parameter levels converged (N, P, K), while others tended to separate here (Na, Ca, pH).

As soils are very complex and very diverse, these considerations might help in the further evaluation of the effect of wild boar rooting, especially on areas after forest fires, as there is very little information available from the literature. The size of the deep rooting is obviously an important influencing factor on water retention, missing the less permeable ash layer and thus helping the infiltration of rainwater into the soil, which can also prevent soil, nutrient, and water runoff, reducing the effect of soil water erosion as described by Pitta-Osses et al. [8].

5. Conclusions

The comparison of the rooting, ring, and control areas of wild boar rooting at two Algerian sites proved that wild boar have more significant effects on the soil parameters (K, Na, Mg, Ca, P, N, pH, EC) in natural environments than after a recent forest fire.

Based on the literature review, we can also conclude that the Algerian natural (non-disturbed = non burnt) site is similar to those natural forest areas described in numerous studies from the wild boar rooting point of view (with lots of non-significant effects).

The last conclusion is that more research is needed on the analysis of the effects of wild boar rooting in areas after forest fires, by regular and progressive monitoring of edaphic parameter characterization, over long periods (up to 10 years post fire). This can help us to assess when the wild boar's action becomes beneficial for forest regeneration, and to deduce the processes influenced by the rootings after forest fires.

Author Contributions: Conceptualization, all authors; methodology, all authors; software, M.B. and Á.F.; validation, C.C., Á.F. and F.S.; formal analysis, M.B., R.S. and M.B.; investigation, K.H.B., M.B., R.S. and F.S.; resources, K.H.B.; data curation, K.H.B., Á.F. and C.C.; writing—original draft preparation, K.H.B.; writing—review and editing, K.H.B., C.C., Á.F., K.K. and F.S.; visualization, M.B., R.S. and Á.F.; supervision, M.B., R.S. and F.S.; project administration, K.H.B.; funding acquisition, M.B. All authors have read and agreed to the published version of the manuscript.

Funding: The Algerian Fund for Scientific Research and the Ministry of Higher Education and Scientific Research funded this study (PRFU project/code: D00L02UN230120230005, to Dr. M. Boukheroufa).

Data Availability Statement: The data presented in this study are available upon request from the authors.

Conflicts of Interest: The authors declare no conflicts of interest.

References

1. Olivier de Sardan, J.P.; Bierschenk, T. Les courtiers locaux du développement. *Bull. l'APAD* **1993**, *5*, 1–7. [CrossRef]
2. Tack, J. Wild Boar (*Sus scrofa*) populations in Europe: A scientific review of population trends and implications for management. *Eur. Landowners' Org. Bruss.* **2018**, *56*, 29–30.
3. Risch, D.R.; Ringma, J.; Price, M.R. The global impact of wild pigs (*Sus scrofa*) on terrestrial biodiversity. *Sci. Rep.* **2021**, *11*, 13256. [CrossRef]
4. Dovrat, G.; Perevolotsky, A.; Ne'eman, G. The response of Mediterranean herbaceous community to soil disturbance by native wild boars. *Plant Ecol.* **2014**, *215*, 531–541. [CrossRef]
5. Picard, M.; Papaïx, J.; Gosselin, F.; Picot, D.; Bideau, E.; Baltzinger, C. Temporal dynamics of seed excretion by wild ungulates: Implications for plant dispersal. *Ecol. Evol.* **2015**, *5*, 2621–2632. [CrossRef]
6. Vallée, M.; Lebourgeois, F.; Baudet, É.; Said, S.; Klein, F. Le sanglier en Europe: Une menace pour la biodiversité? *Biol. Ecol.* **2016**, *68*, 505–518. [CrossRef]
7. Slawski, M.; Slawska, M. Collembolan assemblages' response to wild boars (*Sus scrofa* L.) rooting in pine forest soil. *Forests* **2020**, *11*, 1123. [CrossRef]
8. Pitta-Osses, N.; Centeri, C.; Fehér, Á.; Katona, K. Effect of wild boar (*Sus scrofa*) rooting on soil characteristics in a deciduous Forest affected by sedimentation. *Forests* **2022**, *13*, 1234. [CrossRef]
9. Labadessa, R.; Ancillotto, L. Beauty and the beast: Multiple effects of wild boar rooting on butterfly microhabitat. *Biodiv. Cons.* **2023**, *32*, 1189–1204. [CrossRef]
10. Katona, K.; Fehér, Á.; Pitta-Osses, N.; Centeri, C. The impact of wild boar rooting on soil chemical attributes along a slope combined effects of bioturbation and water erosion. In *Hydrological Processes in the Soil–Plant–Atmosphere System, Electronic Book Contemporary Challenges in Environmental Research*; Botyanszká, L., Vitková, J., Eds.; Ústav hydrológie SAV: Bratislava, Slovakia, 2023; pp. 169–174.
11. Ropars-Collet, C.; Le Goffe, P. *La Gestion du Sanglier: Modèle Bioéconomique, Dégâts Agricoles et Prix des Chasses en Forêt*; UMR INRA-Agrocampus Ouest SMART: Rennes France, 2009; pp. 1–40. Available online: https://institut-agro-rennes-angers.hal.science/hal-00729245 (accessed on 5 February 2024).
12. Benotmane, K.H.; Boukheroufa, M.; Guediri, M.; Hadiby, R.; Frih, A.; Sakraoui, F. Impact of the wild boar *Sus scrofa* Linnaeus, 1758 (Mammalia *Suidae*) on wetlands soil quality: Case of Black and Blue Lakes (National Parc of El Kala, northeastern Algeria). *Biodiv. J.* **2022**, *13*, 799–804. [CrossRef]
13. Adamjy, T.; Dobigny, G.; Aholou, S.; Mourlon, M. La gouvernance des risques liés aux invasions biologiques. L'exemple du Bénin. *Sci. Eaux Terr.* **2020**, *5*, 11–12. Available online: https://www.cairn.info/revue-sciences-eaux-et-territoires.htm (accessed on 5 February 2024). [CrossRef]
14. Meddour-Sahar, O.; Derridj, A. Bilan des feux de forêts en Algérie: Analyse spatio-temporelle et cartographie du risque (période 1985–2010). *Sci. Chang. Planétaires/Sécheresse* **2012**, *23*, 133–141. [CrossRef]
15. Guérin-Turcq, A. Les Forêts dans le Monde, des Milieux Anthropisés: Un état Des Lieux. *Géoconfluences* **2023**, 1–15. Available online: https://geoconfluences.ens-lyon.fr/informations-scientifiques/dossiersthematiques/changement-global/articles-scientifiques/forets-dans-le-monde (accessed on 18 December 2021).
16. Véla, E.; Benhouhou, S. Evaluation d'un nouveau point chaud de biodiversité végétale dans le bassin méditerranéen (Afrique du Nord). *C. R. Biol.* **2007**, *330*, 589–605. [CrossRef] [PubMed]
17. Hadiby, R.; Boukheroufa, M.; Adjami, Y.; Djedda, H.; Boussaha, A.; Frih, A.; Benotmane, K.; Sakraoui, F. Part comparée des saproxyliques dans le peuplement de Coléoptères entre milieu naturel et milieu post-incendié du massif forestier de l'Édough (Nord-Est, Algérie). *Bull. Soc. Zool. Fr.* **2022**, *147*, 167–175.
18. Oularbi, A.; Zeghiche, A. La sensibilité à l'érosion du massif cristallophyllien de l'Edough (Nord-est Algérien). *Rev. Synt. Sci. Technol.* **2009**, *20*, 61–75.

19. Toubal, O. Les Ressources Phytogénétiques du Massif de l'Edough (Algérie Nord-Orientale). Ph.D. Thesis, Ecologie Appliquée, Université Scientifique Technologique et Medicate de Grenoble France, Grenoble, France, 1986; 111p.
20. Clément, A.; Vigouroux, B. Unsupervised segmentation of scenes containing vegetation (*Forsythia*) and soil by hierarchical analysis of bi-dimensional histograms. *Pattern Recognit. Lett.* **2003**, *24*, 1951–1957. [CrossRef]
21. Bremner, J.M.; Mulvaney, C.S. Nitrogen-Total. In *Methods of Soil Analysis. Part 2. Chemical and Microbiological Properties*; Page, A.L., Ed.; American Society of Agronomy, Soil Science Society of America: Madison, WI, USA, 1982; pp. 595–624.
22. Olsen, S.R.; Sommers, L.E. Phosphorus. In *Methods of Soil Analysis Part 2 Chemical and Microbiological Properties*; Page, A.L., Ed.; American Society of Agronomy, Soil Science Society of America: Madison, WI, USA, 1982; pp. 403–430.
23. Bonneau, M.; Souchier, B. Constituants et propriétés du sol. Pédologie. *Paris Masson* **1979**, *XVIII*, 32–35.
24. Baise, D.; Girard, M. Pedological reference. In *AFES*; INRA: Paris, France, 1995; p. 336.
25. Wickham, H. *ggplot2: Elegant Graphics for Data Analysis*; Springer-Verlag New York: New York, NY, USA, 2016; ISBN 978-3-319-24277-4.
26. Massei, G.; Genov, P.V.; Staines, B.W. Diet, food availability and reproduction of wild boar in a Mediterranean coastal area. *Acta Ther.* **1996**, *41*, 307–320. [CrossRef]
27. Wirthner, S.; Schütz, M.; Page-Dumroese, D.S.; Busse, M.D.; Kirchner, J.W.; Risch, A.C. Do changes in soil properties after rooting by wild boars (*Sus scrofa*) affect understory vegetation in Swiss hardwood forests? *Canad. J. For. Res.* **2012**, *42*, 585–592. [CrossRef]
28. Imbert, C.; Caniglia, R.; Fabbri, E.; Milanesi, P.; Randi, E.; Serafini, M.; Torretta, E.; Meriggi, A. Why do wolves eat livestock? Factors influencing wolf diet in northern Italy. *Biol. Conserv.* **2016**, *195*, 156–168. [CrossRef]
29. Baruzzi, C.; Krofel, M. Friends or foes? Importance of wild ungulates as ecosystem engineers for amphibian communities. *North-West. J. Zool.* **2017**, *13*, 320–325.
30. Macci, C.; Doni, S.; Bondi, G.; Davini, D.; Masciandaro, G.; Pistoia, A. Effects of wild boar (*Sus scrofa*) grazing on soil properties in Mediterranean environment. *Catena* **2012**, *98*, 79–86. [CrossRef]
31. Benotmane, H.K.; Boukheroufa, M.; Kahli, I.; Hadiby, R.; Sakraoui, F. Impact of wild boar (Sus scrofa) rooting on the physico-chemical properties of soil in the Edough forest (Northeast, Algeria). In Proceedings of the 13th ICEEE-2022 International Annual Conference "Global Environmental Development & Sustainability: Research, Engineering & Management", Budapest, Hungary, 17–18 November 2022; pp. 322–326.
32. Singer, F.J.; Swank, W.T.; Clebsch, E.E. Effects of wild pig rooting in a deciduous forest. *J. Wildl. Man.* **1984**, *48*, 464–473. [CrossRef]
33. Siemann, E.; Carrillo, J.A.; Gabler, C.A.; Zipp, R.; Rogers, W.E. Experimental test of the impacts of feral hogs on forest dynamics and processes in the southeastern US. *For. Ecol. Man.* **2009**, *258*, 546–553. [CrossRef]
34. Bruinderink, G.G.; Hazebroek, E. Wild boar (*Sus scrofa scrofa* L.) rooting and forest regeneration on podzolic soils in the Netherlands. *For. Ecol. Man.* **1996**, *88*, 71–80. [CrossRef]
35. Mohr, D.; Cohnstaedt, L.W.; Topp, W. Wild boar and red deer affect soil nutrients and soil biota in steep oak stands of the Eifel. *Soil Biol. Biochem.* **2005**, *37*, 693–700. [CrossRef]
36. Don, A.; Hagen, C.; Grüneberg, E.; Vos, C. Simulated wild boar bioturbation increases the stability of forest soil carbon. *Biogeosciences* **2019**, *16*, 4145–4155. [CrossRef]
37. Barrios-Garcia, M.N.; Gonzalez-Polo, M.; Simberloff, D.; Classen, A.T. Wild boar rooting impacts soil function differently in different plant community types. *Biol. Invasions* **2023**, *25*, 583–592. [CrossRef]
38. Alkhasova, P.; Katona, K. Comparison of some soil properties of wild boar (Sus scrofa) rootings. In *Hydrological Processes in the Soil–Plant–Atmosphere System*; Electronic Proceeding Book of the 28th Poster Day; Botyanszká, L., Vitková, J., Eds.; Ústav hydrológie SAV: Bratislava, Slovakia, 2021; pp. 25–30.
39. Sütő, D.; Siffer, S.; Farkas, J.; Katona, K. Predictability of the Spatiotemporal Pattern of Wild Boar (*Sus scrofa*) Rooting Influenced by Acorn Availability. *Forests* **2023**, *14*, 2319. [CrossRef]
40. Valkanou, K.; Karymbalis, E.; Bathrellos, G.; Skilodimou, H.; Tsanakas, K.; Papanastassiou, D.; Gaki-Papanastassiou, K. Soil Loss Potential Assessment for Natural and Post-Fire Conditions in Evia Island, Greece. *Geosciences* **2022**, *12*, 367. [CrossRef]
41. Xofis, P.; Buckley, P.G.; Kefalas, G.; Chalaris, M.; Mitchley, J. Mid-Term Effects of Fire on Soil Properties of North-East. Mediterranean Ecosystems. *Fire* **2023**, *6*, 337. [CrossRef]
42. García-Carmona, M.; García-Orenes, F.; Arcenegui, V.; Mataix-Solera, J. The recovery of Mediterranean soils after post-fire management: The role of Biocrusts and soil microbial communities. *Span. J. Soil Sci.* **2023**, *13*, 11388. [CrossRef]
43. Certini, G. Effects of fire on properties of forest soils: A Review. *Oecologia* **2005**, *143*, 1–10. [CrossRef] [PubMed]
44. Cerdan, O.; Desprats, J.-F.; Fouché, J.; Le Bissonnais, Y.; Cheviron, B.; Simonneaux, V.; Raclot, D.; Mouillot, F. Impact of global changes on soil vulnerability in the Mediterranean Basin. In Proceeding of the International Symposium on Erosion and Landscape Evolution (ISELE), Anchorage, Alaska, 18–21 September 2011; pp. 495–503.
45. McLauchlan, K.K.; Higuera, P.E.; Miesel, J.; Rogers, B.M.; Schweitzer, J.; Shuman, J.K.; Tepley, A.J.; Varner, J.M.; Veblen, T.T.; Adalsteinsson, S.A.; et al. Fire as a Fundamental Ecological Process: Research Advances and Frontiers. *J. Ecol.* **2020**, *108*, 2047–2069. [CrossRef]
46. Moussaoui, M.; Sidi, H.; Derbak, H.; Bekdouche, F. Post-fire dynamics of the main biogenic nutrients of the *Pinus pinaster* forest soil of Jijel, Northeastern Algeria. *Ekológia* **2022**, *41*, 212–218. [CrossRef]
47. Kramer, M.G.; Sollins, P.; Sletten, R.S.; Swart, P. N Isotope fractionation and measures of organic matter alteration during decomposition. *Ecology* **2003**, *84*, 2021–2025. [CrossRef]

48. Klop, E.; Prins, H.H.T. Diversity and species composition of West African ungulate assemblages: Effects of fire, climate and soil. *Glob. Ecol. Biogeogr.* **2008**, *17*, 778–787. [CrossRef]
49. Stritar, M.L.; Schweitzer, J.A.; Hart, S.C.; Bailey, J.K. Introduced ungulate herbivore alters soil processes after fire. *Biol. Invasions* **2010**, *12*, 313–324. [CrossRef]
50. Lewis, J.S.; Clair, S.B.S.; Fairweather, M.L.; Rubin, E.S. Fire severity and ungulate herbivory shape forest regeneration and recruitment after a large mixed-severity wildfire. *For. Ecol. Manag.* **2024**, *555*, 121692. [CrossRef]
51. Bischoff, W.-A.; Mayer, M.; Schrumpf, M.; Freibauer, A. Nutrient Leaching from Soils affected by Windfall in the High Tatra. Available online: https://www.researchgate.net/publication/266491857_Nutrient_Leaching_from_Soils_affected_by_Windfall_in_the_High_Tatra (accessed on 12 March 2024).

land

Article

Estimating Stream Bank and Bed Erosion and Deposition with Innovative and Traditional Methods

Paschalis Koutalakis [1], Georgios Gkiatas [1], Michael Xinogalos [2], Valasia Iakovoglou [1], Iordanis Kasapidis [1], Georgios Pagonis [1], Anastasia Savvopoulou [1], Konstantinos Krikopoulos [1], Theodoros Klepousniotis [1] and George N. Zaimes [1,*]

[1] Geomorphology, Edaphology and Riparian Areas Lab (GERi Lab), Department of Forestry and Natural Environment Science, International Hellenic University, University Campus, 1st km Dramas-Mikrohoriou, 66100 Drama, Greece; ptkouta@for.ihu.gr (P.K.); ggiatas@emt.ihu.gr (G.G.); valaiako@for.ihu.gr (V.I.); io_kasapidis@yahoo.gr (I.K.); gqpagon1995@hotmail.com (G.P.); anastasiaasavvopoulou@gmail.com (A.S.); blockerxd12@gmail.com (K.K.); kleptheodoros@gmail.com (T.K.)
[2] Astrolabe Engineering, Miaouli 26, 14671 Néa Erithraía, Attiki, Greece; mix@astrolabe.gr
* Correspondence: zaimesg@for.ihu.gr

Abstract: Understanding the contributions of stream bank and bed erosion will allow us to implement the most effective management practices. The objective of this study was to assess different methods to measure bank and bed erosion at different scales, specifically the watershed, reach and plot. Innovative and traditional methods were utilized. At the watershed scale, indices based on free satellite images were used. For the reach scale, indices were used, but the images with higher accuracy were purchased and captured by unmanned aerial vehicles (UAVs). At the plot scale, erosion pins, cross-sections and laser scanning were applied. The watershed scale analysis showcased "hot spots". These "hot spots" were reaches vulnerable to erosion and deposition. The indices of the purchased images were applied to these "hot spots" and allowed us to narrow the length of the reaches where UAV flights took place. These flight images located where erosion and deposition occurred. Finally, at the plot scale, laser scanning provided more detailed and accurate data at a greater scale compared to the traditional methods. The implementation of these methods allows us to find the areas vulnerable to erosion and deposition. These are the areas where nature-based solutions should be implemented to effectively mitigate erosion problems.

Keywords: watershed scale; reach scale; plot scale; satellite images; unmanned aerial vehicles; laser scanning

1. Introduction

Stream bank and bed erosion and deposition (Figure 1) are complex phenomena that can negatively affect societies and communities worldwide [1]. Fluvial erosion is the detachment of material from the stream/riverbed and its banks. Both erosion and deposition are natural processes, but anthropogenic activities and climate change have substantially accelerated their rates. Thus, stream bank and bed erosion and deposition monitoring and assessment are a priority worldwide because of the many negative impacts that they cause, but they can be difficult to achieve because of the episodic nature and the many factors that influence them [2]. These factors can be spatial, such as bank aspect, height and slope, or temporal, such as seasonal and yearly precipitation and streamflow events. Riparian land use also has a major influence. Typically, banks with natural vegetation have significantly less erosion than banks with agricultural activities [3].

Riparian areas are semi-aquatic ecosystems located in the transition area where the two adjacent ecosystems, the terrestrial and the aquatic, meet and integrate [4]. The aquatic system can be a river and stream and, along with the adjacent riparian area, can influence and impact of the fluvio-geomorphic processes including erosion and deposition.

Accelerated and extensive stream bank erosion and deposition can have detrimental effects on aquatic, terrestrial and semi-aquatic ecosystems [3]. Human alterations in land use and the developed infrastructure have increased the water concentration time of rainfall reaching streams. This is the result of the decreased water storage capacity of the landscape and increased surface runoff. Overall, the total amount of rainfall water reaching the channels has substantially increased, leading to higher annual and peak discharges. This leads to accelerated stream scouring potential and sediment transport capacity, leading to extensive channel incision [5,6]. A good understanding of stream bank erosion processes is necessary to manage streams, rivers and their riparian areas sustainably. Although many studies on stream bank and bed erosion have been conducted during recent decades, many facets of its processes are still not well explained because of their high temporal and spatial complexity [7–10].

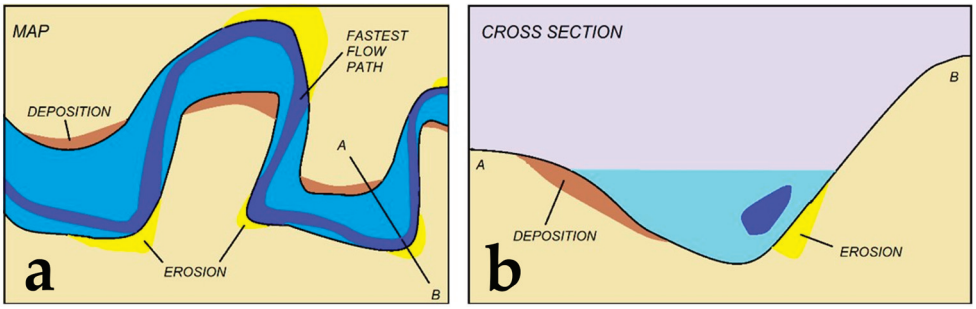

Figure 1. (**a**) Typical erosion (in yellow) and deposition (in brown) areas along a stream reach. (**b**) The cross-section A to B, from image (**a**), showing the erosion (in yellow) and deposition (in brown) areas. The dark blue indicates the area with the fastest stream flow.

Various methods and tools have been used to study and monitor stream bank erosion [11]. Traditional examples are the placement of erosion pins or Gerlach traps to monitor the geomorphologic changes by taking periodical field measurements [12]. Field monitoring stations, such as sensors of ultrasonic technology, can be used to estimate the distance changes between soil surface and the sensor [13]. In addition, photo-electronic erosion pins and the thermal consonance timing principle have been employed to increase the frequency and accuracy of erosion or deposition measurements [14]. Cross-section surveys and terrestrial laser scanners are other field methodologies that study soil erosion and deposition [15]. Field application erosion methods typically demand hard-working laborious tasks, are spatially limited and are time-consuming in contrast to remote sensing applications [16].

Remote sensing has been lately widely utilized for mapping, monitoring and predicting soil erosion [17]. An example of remote sensing monitoring is the utilization of satellite images [18] in combination with spatial datasets in geographical information systems (GIS) to implement the Universal Soil Loss Equation (USLE) model [19]. Other characteristic examples of models utilized for erosion include the following: (a) the Water Erosion Prediction Project (WEPP) model, which is a process-based continuous simulation model, (b) the Gavrilovic Equation [11], (c) the Soil and Water Assessment Tool (SWAT), which is based on the empirical Modified Universal Soil Loss Equation (MUSLE) [20], etc. Satellite images provide a wide range of possibilities for soil erosion monitoring in a fast way, especially in areas where a field survey is difficult or impossible due to the topography, dense vegetation or other local factors [21]. Vegetation and water indices based on satellite-derived images are very helpful for studies focused on soil erosion monitoring, since both the land cover and the soil moisture affect the soil erosion rate [22]. Lately, the combination of aerial photographs and images from unmanned aerial vehicles (UAVs) have been widely utilized in geomorphologic studies to monitor soil erosion or deposition areas [23]. UAV-based photogrammetry is considered the most advanced measurement approach in photogrammetry, resulting in high-accuracy and -resolution products captured by the remote-control

aircraft [24]. In addition, UAVs, apart from the usually attached camera, can carry other sensors for mapping, such as a light detection and ranging system (LiDAR) [25]. The flight can be manual, semi-automated or assisted and fully automated [26]. Higher spatial accuracy can be achieved either by using ground control points (GCPs) or by (global navigation satellite system) GNSS-tagged imagery [27]. GCPs are collected by using a rover and base station with a real-time kinematic (RTK) surveying system or by using a UAV with on-board an RTK positioning system [28]. Future monitoring belongs to UAVs since their increasing capabilities are enabling many new applications in photogrammetry. UAVs' performance has enhanced accuracy at larger scales and they are quicker compared to other methods [29].

Laser scanner instruments are based on the triangulation principle and are able to achieve high measuring accuracy (less than 1 mm) [30]. The laser scanner fits on a regular surveying tripod, while the survey data can be stored on its disk or a laptop. The scanned (X, Y and Z) data are stored on a local or global reference grid, while an expert software is used to process and develop the georeferenced point clouds or even orthomosaics [31]. There are several companies offering various 3D laser scanners to the market but their cost remains higher in contrast to other measuring techniques [32,33]. Terrestrial laser scanning (TLS) has proven to be an efficient and reliable method for collecting point clouds for a wide range of applications in architecture, engineering and construction [34]. Furthermore, TLS has been applied in earth sciences for many disciplines such as forest management, geology, seismology, natural hazards, geomorphology and glaciology, among others [35]. The use of TLS for measuring stream morphology is still in its early stages of research due to the complex environmental factor affecting the results (vegetation and other artifacts that are a considerable "noise") [36]. Heritage and Milan [37] successfully used TLS to measure the grain roughness heights of exposed bars and riverbed surfaces. Picco et al. [38] utilized TLS to study the short-term morphological dynamics and the processes of erosion and sediment deposition along a small gravel-bed braided river by comparing point clouds before and after a stream flow episode. Mayer et al. [39] compared three techniques for measuring stream bank erosion: erosion pins, total station and terrestrial laser scanning at nine site locations of the Indian Mill Creek watershed of Michigan, USA. They did not detect significant differences between measurement techniques but found a strong correlation between the last two techniques. Finally, TLS has been previously applied to collect high-resolution stream bank topography data and to estimate the volume of stream bank retreat [40].

This specific research presents the application of different methodologies to assess and estimate stream bank erosion and deposition at different spatial levels, from the watershed to the reach scale and finally to the plot scale. The many methods utilized and the technological advances require the assessment and comparison of the utility and ability to implement different methods for erosion and deposition. The study area was a typical Mediterranean watershed, the Aggitis watershed, in northern Greece. At the watershed scale, vegetation and water indices were developed based on freely available satellite imagery. At the reach scale, again, vegetation and water indices were utilized, but in this case, they were developed based on purchased satellite imagery of substantial higher resolution of targeted areas of the watershed. In addition, UAV-captured imagery was utilized to detect fluvio-geomorphologic changes in different cross-sections of selected reaches. The plot-scaled assessment included (a) the placement of erosion pins in selected stream banks with different land uses and soils, (b) taking cross-sections at the same locations and c) 3D laser scanning at specific vulnerable selected cross-sections. The ultimate goal of this research was to develop a framework of erosion and deposition measuring methods at different scales. The proposed framework will allow us to identify areas with the most geomorphologic activity (vulnerable areas of erosion and deposition). These areas should be targeted for erosion and deposition mitigation where nature-based solution implementation can help achieve the sustainable environmental management of the entire watershed.

2. Materials and Methods

2.1. The Study Area

The Aggitis River watershed is located in the Regional Unit of Eastern Macedonia in northern Greece (Figure 2). It belongs to the GR11 water division of Eastern Macedonia and the greater water basin GR11 of the Strymonas River. It covers an area of 2700 km^2 and it belongs to three regional units: (a) the Regional Unit of Serres (621 km^2 or 23%), (b) the Regional Unit of Drama (1647 km^2 or 61%) and (c) the Regional Unit of Kavala (432 km^2 or 16%) [41]. The watershed is surrounded by the mountain ranges of Menoikio to the west, Falakro to the north, the Lekani mountains to the east, Simvolo to the south and Paggaio to the southwest [42].

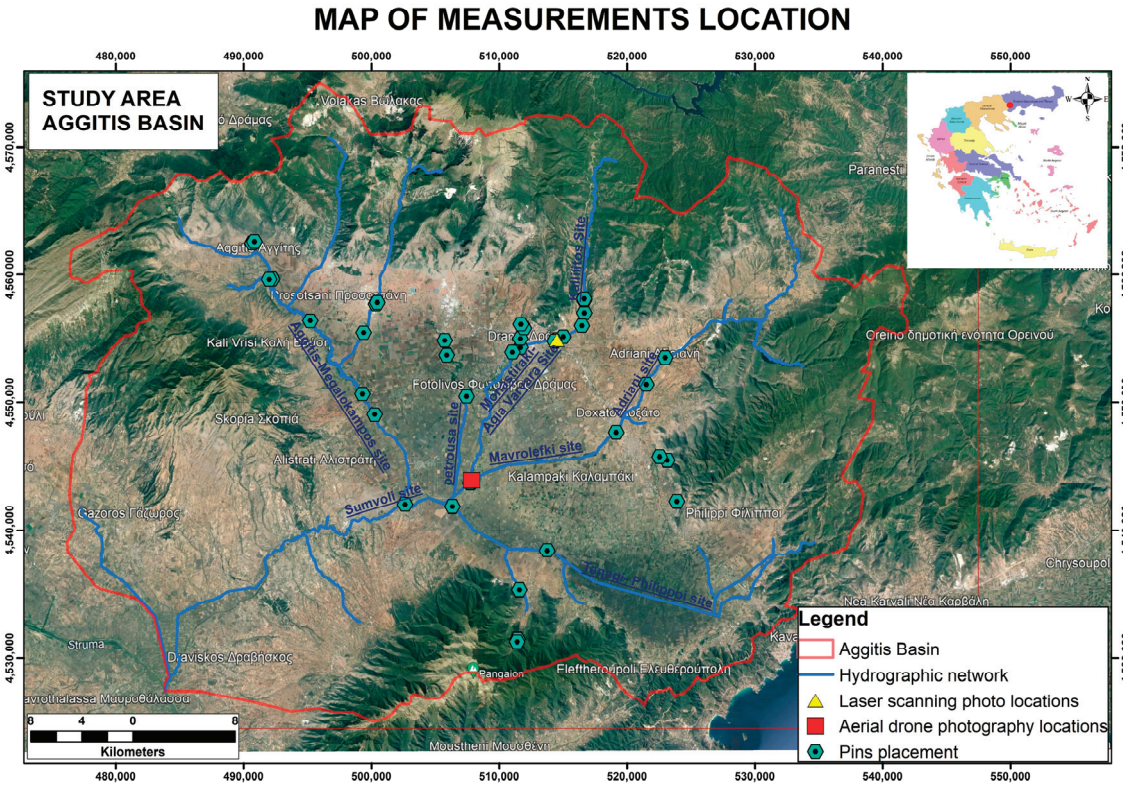

Figure 2. The Aggitis basin (red divide line) with the main stream network (blue lines) and the many monitoring locations with erosion plots and cross-sections of areas of different land use and soil types.

There are 21 different land uses that occupy the entire area. The four main land uses were selected to install erosion plots (forests/riparian zones, sclerophyllous vegetation, natural grassland/pastures and agricultural land) [43]. The watershed is characterized by the typical Mediterranean climatic conditions, land uses, soils, stream flows (ephemeral, intermittent and perennial), anthropogenic pressures and a channelized irrigation network for agricultural purposes [44]. In addition, several fluvio-geomorphological events have been recorded in the past. With limited studies on stream bank erosion and deposition in Greece and the Mediterranean, this study can be used as a benchmark for similar watersheds of the region. The Aggitis River length is 14.66 km and the water discharge volume is estimated as 495 m^3. The average annual precipitation varies from about 500 to 600 mm in lowlands, 600 to 1000 mm in the interior and exceeds 1000 mm in the highlands. The average annual relative humidity ranges from 65% to 70%. The average annual cloud cover is about 4.5 degrees, with the number of clear days ranging from 100 to 120.

The Aggitis basin is a tectonic depression created by faults in the wider area during the Alpine Orogeny. Based on the geologic map, of particular importance are the large

extent and thickness of the marbles located in the mountainous zone which have been affected by karst phenomena and tectonism (faults recorded in many places). Gneisses, schists and amphibolites are included within the marbles. The hilly and semi-mountainous areas are composed exclusively of tertiary sediments which, in their surface parts, consist of cohesive cobblestones and sandstones while at depths up to 250 m consist of marl. The lowland part consists of quaternary sediments, characterized by alternating layers of clay, gravel, sand and silt. In the deeper layers, clay materials and limestone silt prevail and are interrupted by lignite layers (depth reaches 370 m).

The marbles of the mountainous zone and the quaternary deposits of the plains are of great interest from a hydrogeological point of view. The marbles host huge amounts of groundwater. The underground water of these aquifers is discharged through a significant number of karst springs in the quaternary deposits. The aquifer of the Ochiro Basin is located in the mountainous zone north of the basin named as the Ochiro (Kato Nevrokopi) plateau and it is the source of the Aggitis River (Maara Cave or Aggitis Cave).

The peat area of Tenagi Filippon (55 km^2) with interspersed inorganic materials (mainly clay) of Holocene age is unique. This is a vulnerable hot spot as this area (formerly marsh and lake) is drained by a central agricultural ditch. Other hot spots are along the Aggitis River course and the mountainous torrents. Concerning the city of Drama, flooding was very frequent in the past, especially in the former torrent of the "19th of May". The area was urbanized and the specific torrent was covered by the street. The Kallifytos torrent is also an underground stream, but on the east side, entering the city, it has natural vegetation. It is considered dangerous, with many flooding phenomena along its course and with a large sediment transport capacity. Projects have recently been approved for its management with construction works. The below-mentioned are examples of flood events:

- Floods of 13–14 October 2002. Damage to 15.2 km^2 of crops in the plain of Drama.
- Floods of 18 November 2007. Great material damage in the local communities (Antifilippi, Eleftheroupolis, etc.)
- Floods of 10–11 February 2010. The fire service was called on dozens of occasions to clear water from flooded houses and warehouses.
- Floods of 10 March 2015. Major flooding phenomena in the Tenagi–Philippoi marsh plain, 80 square km of arable land under water.
- Floods of 13 December 2021. Flooding, landslides, infrastructure failures, road closures and transported materials (trees, rubble and other materials) in the Kallifytos torrent.

This study focused on the Aggitis watershed for the watershed-scaled assessment and afterwards examined specific reaches (e.g., Kallifytos torrents and Mavrolefki stream) and plots on selected stream banks and beds that had different land uses and soil types. Since stream bank erosion and deposition have high temporal variation [2], all monitoring methods were applied for at least one year to capture seasonal variability.

2.2. The Watershed-Scaled Assessment

2.2.1. The Free Satellite Images

Initially, free satellite images (Sentinel-2) were downloaded from the USGS EROS Archive (https://earthexplorer.usgs.gov last accessed on 12 February 2022). The Sentinel-2 satellite system has been developed and is being operated by the European Space Agency [45]. Sentinel-2 is an Earth observation mission from the Copernicus Programme that systematically acquires optical imagery at high spatial resolution (10 m to 60 m) over land and coastal areas [46]. The mission currently has a constellation of two satellites, Sentinel-2A and Sentinel-2B [47]. The images are multi-spectral with 13 bands in the visible, near-infrared, and short-wave infrared part of the spectrum [48]. Free satellite images covering different time periods (from winter to late autumn images) were downloaded to detect erosion-vulnerable areas. The images were acquired for dates when the vegetation cover was less developed, at the same enabling us to capture floods events (e.g., 18 February 2019). Another important parameter for the selection of the specific images was to have

less than 5% of cloud cover. Overall, a total of nine images were selected, three for each year of interest, 2019, 2020 and 2021. The specific dates of the images are as follows:

- 18 February 2019;
- 14 August 2019;
- 16 October 2019;
- 10 May 2020;
- 5 September 2020;
- 22 October 2020;
- 10 May 2021;
- 3 August 2021;
- 25 October 2021.

The selected images were processed in the ArcGIS software. The boundaries of the study area were delineated and used as a mask to crop the needed section of the satellite images. The next step was to produce the two indices: (a) the Normalized Difference Vegetation Index (NDVI) and (b) the Normalized Difference Water Index (NDWI). This was performed in the "Spatial Analysis Toolbox–Map Algebra–Raster Calculator" utilizing the corresponding spectral bands. The indices were classified into six groups/classes based on previous researchers' works (see Table 1) [49–51]:

Table 1. The classification of NDVI and NDWI values into the 6 classes.

No #	NDVI	Description	NDWI	Description
1	−1.0 to 0.0	No vegetation	−1.0 to −0.5	Very high drought or terrestrial vegetation
2	0.0 to 0.2	Unhealthy vegetation	−0.5 to −0.2	High drought or terrestrial vegetation
3	0.2 to 0.4	Poorly healthy vegetation	−0.2 to 0.0	Moderate drought
4	0.4 to 0.6	Moderately healthy vegetation	0.0 to 0.2	Poor water content/ low drought
5	0.6 to 0.8	Healthy vegetation	0.2 to 0.5	Moderate water content
6	0.8 to 1.0	Very healthy vegetation	0.5 to 1.0	High water content

2.2.2. The Vegetation Index

The Normalized Difference Vegetation Index (NDVI) is a frequently utilized proxy for vegetation cover in environmental and climatic change studies [52]. Equation (1) is used to calculate the NDVI as follows [53]:

$$\text{NDVI} = (\text{NIR} - \text{Red})/(\text{NIR} + \text{Red}), \quad (1)$$

The NDVI is a dimensionless index that describes the difference between visible and near-infrared reflectance of vegetation cover [54]. The index receives values from −1 to +1. The higher the value (close to +1), the more it reflects high near-infrared (NIR) light, which means dense, greener and healthier vegetation cover, while clouds and snow are characterized by negative values. Typical vegetation values range from 0.2 to 1. Healthy plants, which are in very good condition, are reflected by values greater than 0.6 [55]. The values close to zero correspond to the absence of vegetation. The vegetation cover but also the road network and vehicles are clearly identified in the developed image, while the implementation of more enhanced calibration techniques could also separate the water surface. This index can be also used for soil erosion and drought monitoring [56,57].

2.2.3. The Water Index

The Normalized Difference Water Index (NDWI) is related to the water concentration levels on and in the soil or the existence of water bodies including flooded areas. Equation (2) is used to calculate it as follows:

$$\text{NDWI} = (\text{Green} - \text{NIR})/(\text{Green} + \text{NIR}), \quad (2)$$

The NDWI was developed in 1996 [58] and is frequently utilized in remote sensing analysis of satellite images to map and detect surface water bodies. One of the key utilities of NDWI is the analysis before and post flood–storm events [59]. In addition, it can be used to predict erosion rates since it estimates the soil moisture [60]. Areas with higher values of the index indicate areas that may significantly influence the process of soil erosion and thus impact sediment concentration and deposition [61,62]. Similar to the NDVI, the values of the NDWI index vary from −1 to +1. Positive values (greater than 0.2) usually represent areas with high soil water concentrations, flooded areas or water bodies [63].

2.3. The Reach-Scaled Assessment

2.3.1. The Purchased Satellite Images

High-resolution satellite images were acquired in order to further assess the areas that were found to be vulnerable to soil erosion or deposition based on the results of the watershed-scale study (targeted areas). This enabled us to develop the vegetation indices at a different scale (reach scale) and study the areas in greater detail with substantially higher accuracy. The selected area of 25 km^2 in the Aggitis watershed was the confluence of the three main channels (Aggitis River, Tenagi Filippon Ditch and Agia Varvara Stream) in the Aggitis Dam in Symvoli Village, based on the watershed-scale analysis. A thorough study of the available satellite images, emphasizing the area after major events (dry/wet periods), was conducted in order to select those providing full coverage with no cloud cover. The final selection included 2 images captured by the Gaofen Satellite and 2 images captured by the WorldView-2 (WV2). The satellite images captured different extreme weather events (specifically after flood events). Gaofen is a series of Chinese high-resolution Earth imaging satellites launched as part of the China High-Resolution Earth Observation System (CHEOS) program [64]. The specific images have 80 cm resolution and were captured on 29 October 2016 and 21 March 2017. WorldView-2 is an imaging and environment-monitoring satellite from Maxar of the United States which was launched on 8 October 2009 that continues to remain operational [65]. The WV2 collects images that have a 50 cm resolution and the dates of the purchased images were 30 April 2019 and 11 June 2019. These images were used to develop the NDVI and NDWI for the selected areas based on the watershed analysis for the specific dates. The water boundaries of the natural channelized stream were delineated and any geomorphological changes (erosion/deposition along riverbanks and riverbed) were recorded in the ArcGIS 10.4 software.

2.3.2. The UAV-Based Orthomosaics from the UAV Flights

The UAV Flights

The flights were performed by using a powerful tetra-copter: the DJI Phantom 4 RTK. Using the DJI Phantom 4 RTK can be advantageous as it is user-friendly, low-cost (free and/or low-cost tools/software) and quick, as images can be captured in 10 min or less (depending on the area) and the results can be produced in a few hours (depending on the hardware capabilities). Their use also provides safety, since the user can hover the UAV remotely from a distance from the riverbanks and channel. The UAV is capable of capturing the stream bed and banks of a reach as its battery life is 30 min [66]. The UAV hovered at 50 m or 100 m height from the ground. The height was based on the conditions and dimensions of each stream reach that would allow us to capture the widths of its channel and its riparian zone in greater detail. The UAV can be coupled with the D-RTK 2 mobile high-precision GNSS receiver that supports all major global satellite navigation systems,

providing real-time differential corrections. This allows us to generate centimeter-level positioning data for improved relative accuracy. In addition, the GCPs included natural points (e.g., trees and rocks), human constructions and artificial marks (e.g., black/white targets in A4 size) that were used to calibrate the produced orthomosaics. The coordinates were taken by the GPS-GNSS Ruide Pulsar R6p device and the GPS-GNSS receiver of the UAV. The georeferencing was performed in the World Geodetic Reference System coordinate reference system (WGS84). The literature offers a wide range of choices for the number and spatial distribution of the GCPs used for photogrammetric applications [67].

The Photogrammetric Software

The Pix4Denterprize 4.5.6. is a powerful software capable of combining and merging the images based on common points; this methodology is commonly used for photogrammetric applications. Pix4D includes a set of tools, such as Pix4Dcapture, which is a mobile application that defines and executes the flight plan, and Pix4Dmapper that can be utilized to edit the captured data and create photogrammetric products [68]. The Pix4Dcapture tool is a mobile application that enables autonomous flight missions (grid, double-grid, polygon, circular, and free flight) and provides the estimated flight time, which is calculated based on the predefined mission parameters [69]. The Pix4Dmapper tool generates the point cloud, the mesh model, the texture, the orthomosaics, the 3D model (if images are captured from different ankles) and the digital surface model (DSM). One of the Pix4D's advantages is that it produces a feature report and a processing log which provides the detailed results [70]. Pix4D Mapper is a commercial software with the advantages that it is very easy to apply, even for beginners [71]. The developed orthomosaics and DSMs enable us to locate hot spots along the stream banks, even under water, either showcasing erosion or deposition areas.

2.4. The Plot-Scaled Assessment

2.4.1. The Stream Bank Erosion Pins

One of the best methods to capture the temporal (seasonally and yearly) and spatial (top and bottom bank) variability in stream bank erosion/deposition is erosion pins [72]. The main reason is because of the ability to frequently measure them and the high accuracy of the measurements. Erosion pins are narrow metal rods installed horizontally that are commonly used to measure the retreat or advancement of the streambanks over time [73]. They are suitable for a wide range of fluvial environments, inexpensive, and simple to maintain and measure. However, erosion pins can have difficulty accounting for larger scale (stream or reach scale) and very detailed spatial variability in streambanks. Totally, 400 erosion pins were placed in 40 selected positions throughout the stream network of Aggitis watershed (10 erosion pins per plot). The positions of the erosion plots were distributed equally among the four (4) main riparian land uses along the three main channels. The exact locations of the erosion pins were established by using the GPS-GNSS. Each plot had two spatially distinct erosion pin zones (five erosion pins in each one). The bottom zone was placed at 1/3 of the bank height (bottom bank) and the top zone at 2/3 of the bank height (top bank) (Figure 3). Vertical distances between the pins in the plots were 1 m. The erosion pins were 730 mm long, 7 mm in diameter, made of steel and inserted perpendicularly into the bank face.

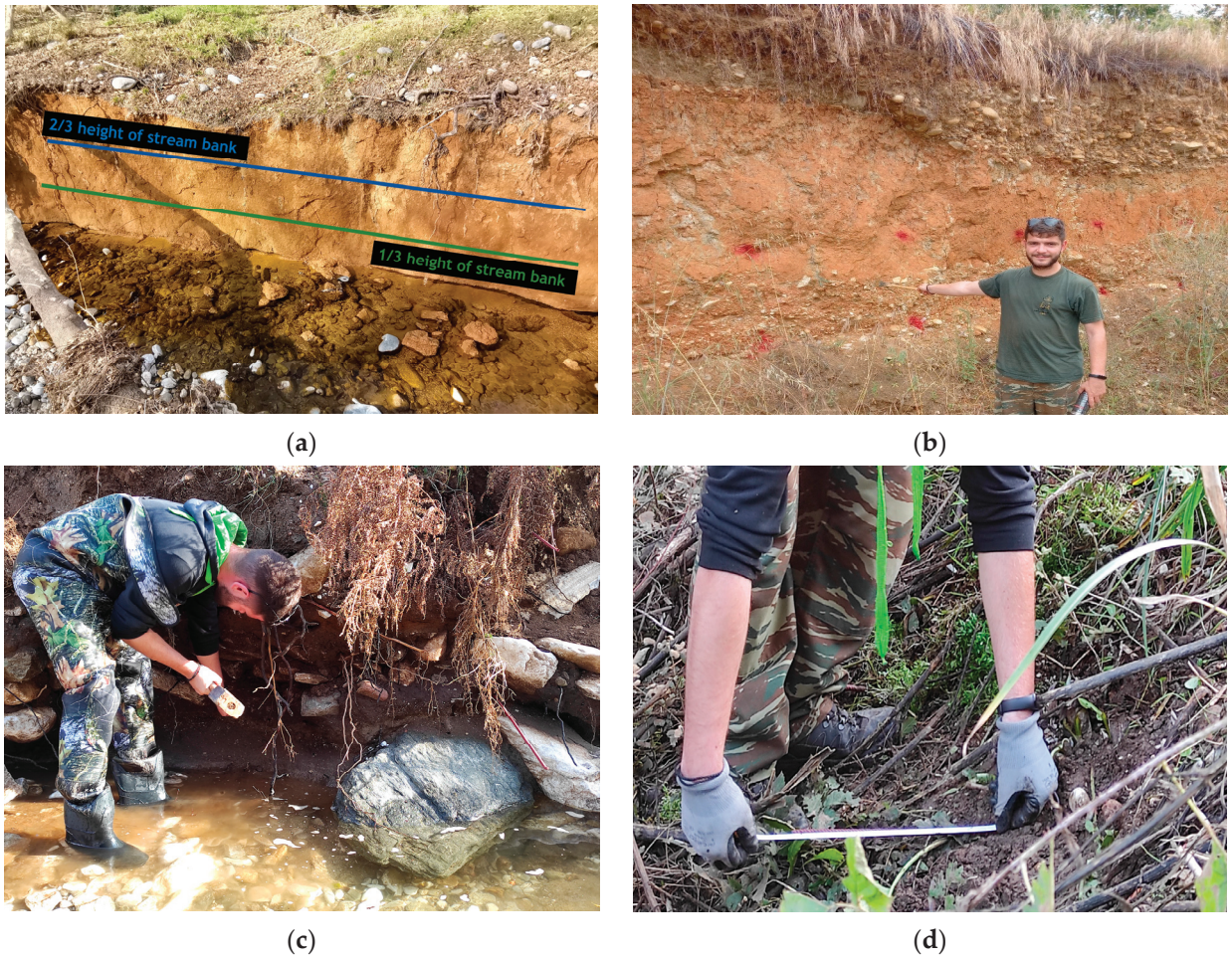

Figure 3. Examples of stream bank erosion pins in Kallifytos torrent: (**a**) the two different height zones of erosion pin placements; (**b**) erosion pins marked with red paint for better identification; (**c**) placement of the erosion pins; (**d**) measuring erosion/deposition of the erosion pins.

Hooke [74] recommends that at least one-third of the pin remains buried in the stream bank face to reduce the risk of loss during a major erosion event. Pins also should not exceed 800 mm in length because when greater than that length, they can increase bank stability by reinforcing the soil, particularly increasing cantilever stability. The 7 mm diameter is small enough to cause minimum disturbance to the stream bank but large enough not to bend in high discharge events. The placement of erosion pins started on 13 November 2021 and finished on 5 December 2021. After the placement of the pins, five repeated measurements were made over a period of 2 years systematically and/or after major weather events (dry or wet days). The specific dates were as follows:

1. 25 April 2022;
2. 18 June 2022;
3. 8 October 2022;
4. 28 February 2023;
5. 15 June 2023.

2.4.2. The Stream Cross-Sections

Bench-marked cross-sections (Figure 4) were used to monitor the contemporary changes in the same plots where the erosion pins were placed [75]. The positions of the cross-sections were as follows: (a) one meter before the first pins, (b) in the middle of the erosion pin plot and (c) one meter after the last pins. The measurement days were

identical to the erosion pin measurement days mentioned above. The variables measured in each cross-section were as follows:

1. Length of each stream bank.
2. Length of the stream bed.
3. Slopes along each stream bank (left and right). More than one measurement was taken when slopes differed substantially along the bank.
4. Slopes along the stream bed. More than one measurement was taken when slopes differed substantially along the bank.
5. Cross-sections were compared among dates to detect changes in the morphological characteristics of the stream over time.

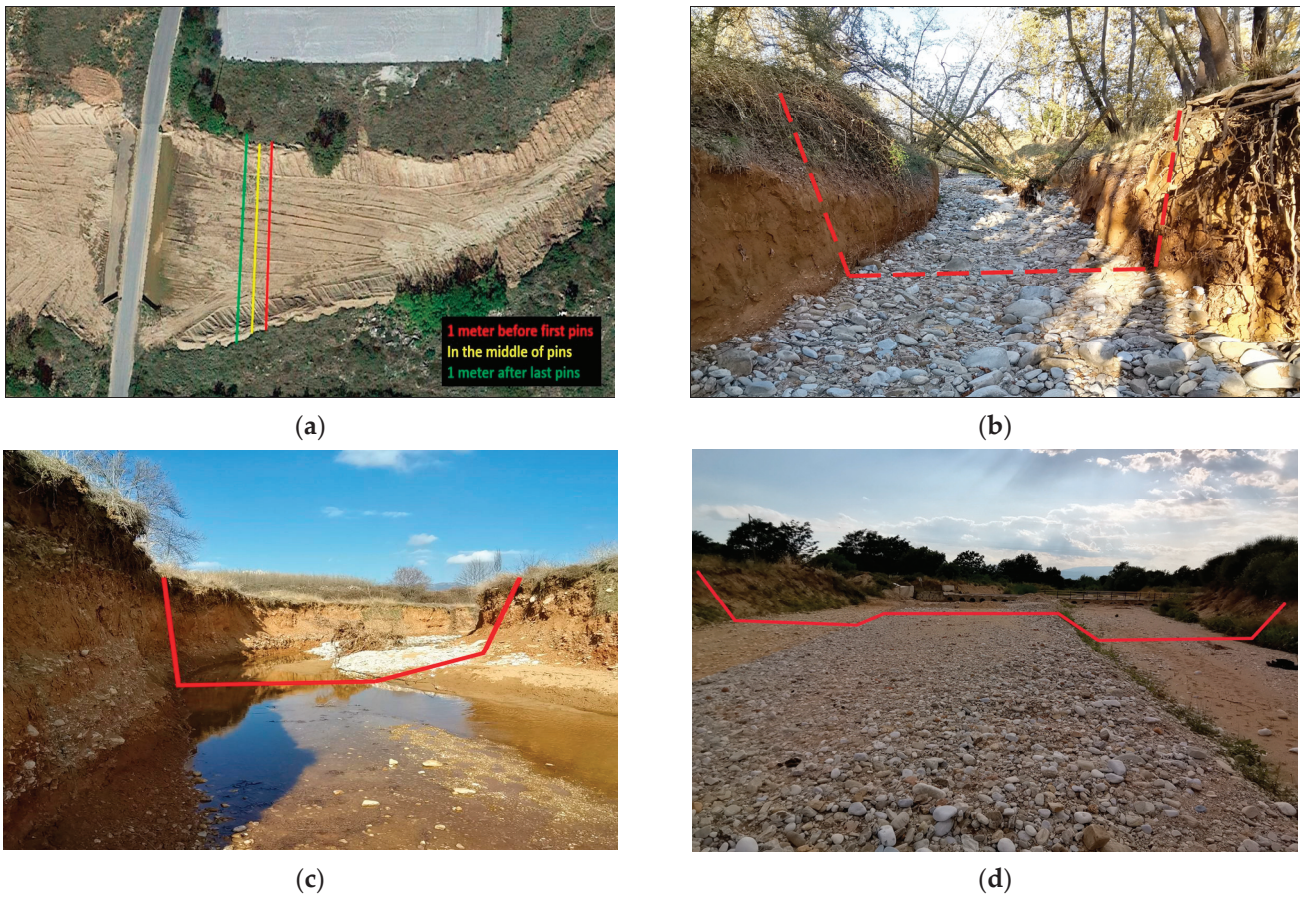

Figure 4. Examples of cross-sections in Kallifytos torrent: (**a**) UAV image captured an erosion cross-section; the different colors indicate the location of the three cross-sections; (**b**) field image of a narrow cross-section; (**c**) field image of a wide cross-section; (**d**) field image of a wide cross-section after torrential phenomena.

For the measurements of the above variables, the following equipment was used:

- A GPS-GNSS receiver to find the locations of the plots;
- A measuring tape for the channel's length (bank and bed);
- An inclinometer for the slope of streambanks and streambed;
- Height poles for the bank height/depth.

2.4.3. 3D Laser Scanning of Stream Cross-Sections

3D laser scanning is a method of collecting spatial measurement data from a distance. It is based on LIDAR (light detection and ranging) or laser radar technology: determining the position of an object by sending and receiving a laser beam [76]. The 3D laser scanners use a mirror mechanism that deflects the laser beam to scan the entire space or object with the desired density (resolution) and at a very high collection speed (recording up to

millions of points per second) [77]. With this method, a dense cloud of measuring points (3D point cloud) is quickly produced that documents with great completeness, precision and reliability the geometry of the space or the object captured [78]. 3D mapping was carried out on 18 February 2022 (1st date) and 24 April 2023 (2nd date) using the Faro Focus3D X 130 laser scanner in order to assess any geomorphological changes on the stream banks and bed of three different sites of interest. Only the Kallifytos site (X: 41.146953, Y: 24.171873) data are presented as the most representative channel type of the study area (see Figure 5).

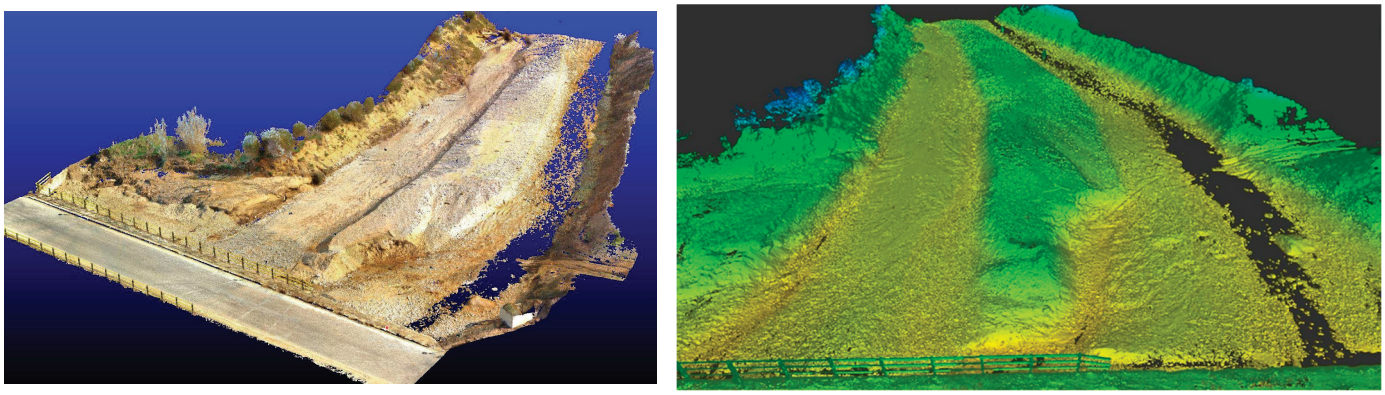

(**a**) (**b**)

Figure 5. An example of 3D scanning capturing (**a**) the RGB image and (**b**) the 3D point cloud from the Kallifytos torrent.

3D scanning was conducted from an appropriate number of scanning positions to completely cover the area of the channel to be mapped, with an average resolution of 1 cm. Alongside the scan, high-resolution panoramic images were taken from each location via the scanner's built-in camera. Eighteen (18) scan sites were used on the 1st date, while 17 sites were used on the 2nd one.

To process and analyze the captured data, the Faro Scene, Autodesk ReCap 2023.1.1 and Gexcel Reconstructor 4.4.1 software were utilized for the following:

- Processing of the georeferenced measurements (control points).
- Generating the point cloud for each scan position.
- Preprocessing of the point clouds (cleaning, filtering, quality control, target identification, etc.).
- Aligning the clouds from successive scan positions. This was performed with the cloud-to-cloud methodology using the least squares and iterative closest point (ICP) algorithms.
- Georeferencing based on georeferencing measurements.
- RGB color rendering from panoramic images.
- Creating a single-colored 3D georeferenced point cloud.

The produced deliverables were color 3D point clouds for the Kallifyto site per date and various visual 2D and 3D visualizations (in the form of digital images) of the 3D point clouds. This enabled us to visualize the stream bank and bed of the captured areas and to understand and interpret the geometric changes in their slopes between the two measurement dates.

3. Results

3.1. The Watershed-Scaled Assessment

3.1.1. The NDVI

The distribution of the NDVI classes differed for each satellite image (Figure 6). The NDVI for class #6 was present only during spring and summer, specifically on 14 August 2019, 10 May 2020, 5 September 2020, 10 May 2021 and 3 August 2021, with a maximum

coverage of 8%. The NDVI for class #1 was only visible on the 08.02.2019 satellite image (4%), with classes #2 and #3 dominating with a coverage of 38% and 42%, respectively. In the autumn months, specifically, 16 October 2019, 22 October 2020 and 25 October 2021, the NDVI classes #3 and #4 (both approximately 33%) had the highest percentage followed also by classes #2 and #5. On all of the other satellite images, the NDVI class #5 had the highest coverage percentage and was dominant.

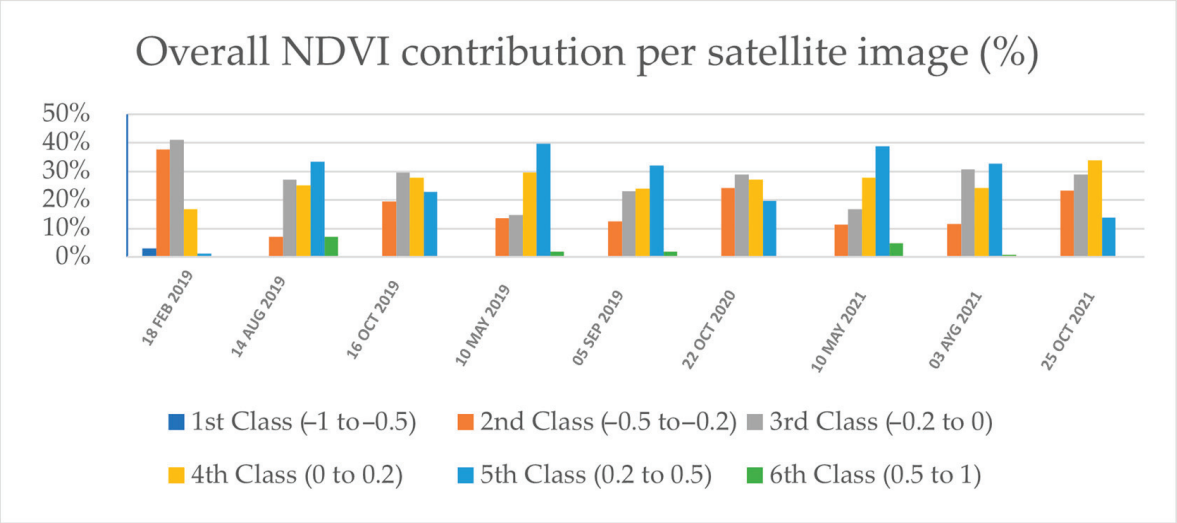

Figure 6. The percentages of the NDVI six classes for each satellite image.

3.1.2. The NDWI

The NDWI class #2 was dominant in all satellite images, with percentages ranging from 50% to 72%, followed by the NDWI class #1 (19–45%) (Figure 7). The specific classes correspond either to terrestrial vegetation (mostly sparse sclerophyllous vegetation and pastures) but also to bare soil, which indicates a high degree of soil erosion mostly on higher altitude and intense slopes of the surrounded mountainous areas. The classes #5 and #6 were very limited and adjacent to existing water resources that enabled us to narrow this study focus to the "hot spots" of soil erosion: areas near floodplains of torrents/streams/rivers.

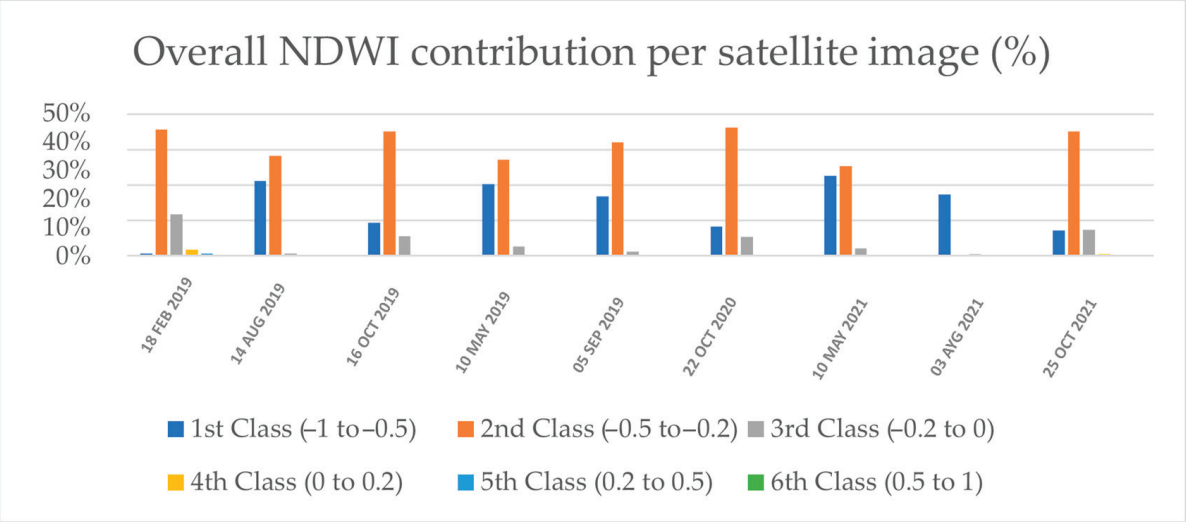

Figure 7. The percentages of the NDWI six classes for each satellite image.

3.1.3. Soil, Land Uses and Slope Characteristics

Three characteristics, soil types, land uses and slopes percentages, were calculated based on the developed NDVI and NDWI maps (for each satellite image). Specifically, the percentage of the indices' classes for these characteristics could highlight which reaches would be more vulnerable to erosion or deposition (higher percentages of a certain class).

The NDWI class #6 was dominated by "Calcaric Fluvisols", "Calcaric Leptosols" and "Dystric Leptosols". This class represents flat areas with vulnerable soils to erosion and deposition affected by the stream network in the pilot area of the Aggitis River watershed. Furthermore, if we include the NDWI class #5, the areas were dominated by "Calcaric Fluvisols", "Eutric Histosols" and "Vertic Cambisols". On the other hand, the "Dystric Cambisol" was the soil that dominated the areas of the NDWI class #1. Concerning the NDVI, classes #1 and #2 (which may indicate soil erosion) had the highest percentages for "Vertic Cambisols", "Calcaric Fluvisols", "Chromic Luvisols", "Calcaric Leptosols" and "Eutric Histosols" soils, although this was highly different in each satellite image. There were occasions when class #6 of the NDVI was not recorded at all.

The urban areas (specifically industrial or commercial units), non-irrigated arable land and complex cultivation patterns have the highest share in land cover for the NDVI class #1. Furthermore, the land uses, permanently irrigated land, natural grasslands, sparsely vegetated areas and water courses, also had a significant contribution. It must be highlighted that similar land uses were recorded for potential erosion and deposition in the NDWI. Specifically, complex cultivation patterns and industrial or commercial units had high NDWI #6 percentages, followed by water courses, permanently irrigated land and non-irrigated arable land but also broad-leaved forests that had high NDWI #5 percentages.

The slope (%) had five discrete categories based on the natural breaks of its values: (i) areas with slope angles less than 12% (gentle slopes), (ii) areas with slope angles between 12% and 29%, (iii) areas with slope angles between 29% and 48%, (iv) areas with slope angles between 48% and 72%, and (v) areas with slope angles greater than 72% (steep slopes). Gentle slopes stood out for their extent and moderate exposure to erosion, especially based on the NDWI (classes #1 and #2). In contrast, steep slopes dominated areas characterized by no or sparse vegetation which form stream network valleys.

3.2. The Reach-Scaled Assessment Results

3.2.1. The Purchased Satellite Images

An automatic classification of the indices' values in ArcGIS enabled us to delineate the boundaries of the water surface. The area captured by the purchased satellite images was the main water course near the confluence of the Aggitis River in the plain of the Regional Unit of Drama. According to the watershed-scale analysis, this area along these perennial streams is one of the most vulnerable to soil erosion and deposition. Many changes have been recorded throughout time on the stream banks and the main channel geomorphology (especially in the confluences where the tributaries meet). Figure 8 includes the boundaries as polylines in four different locations for different dates.

3.2.2. The UAV Images

Based on the previously purchased satellite image analysis, the Mavrolefki reach of the hydrologic network of the study area is one of the most vulnerable. This reach collects the water from Drama city but also from Kalabaki and Doxato towns. This reach is located along the southeast side of the village Mavrolefki (Y: 41.053137, X: 24.104371 in WGS84) where there was a temporary earth-filled dam (or embankment dam) established during the summer to store water from agricultural purposes (Figure 9). During the UAV flight (23 October 2021), this dam was destroyed, and the flowing water even covered the nearby gravel road for agricultural vehicles. The Mavrolefki reach (part of Tenaghi stream) has intense meanders that are covered with water during high rainfall events. The entire stream has many "hot spots" of erosion and deposition, including islands in the main channel bed (Figure 9). In addition, there were other locations along the same reach with litter present

(plastic bottles, tree trunks or tires) as well as locations where the color of the water was cloudy, probably due to agricultural practices (see Figure 10).

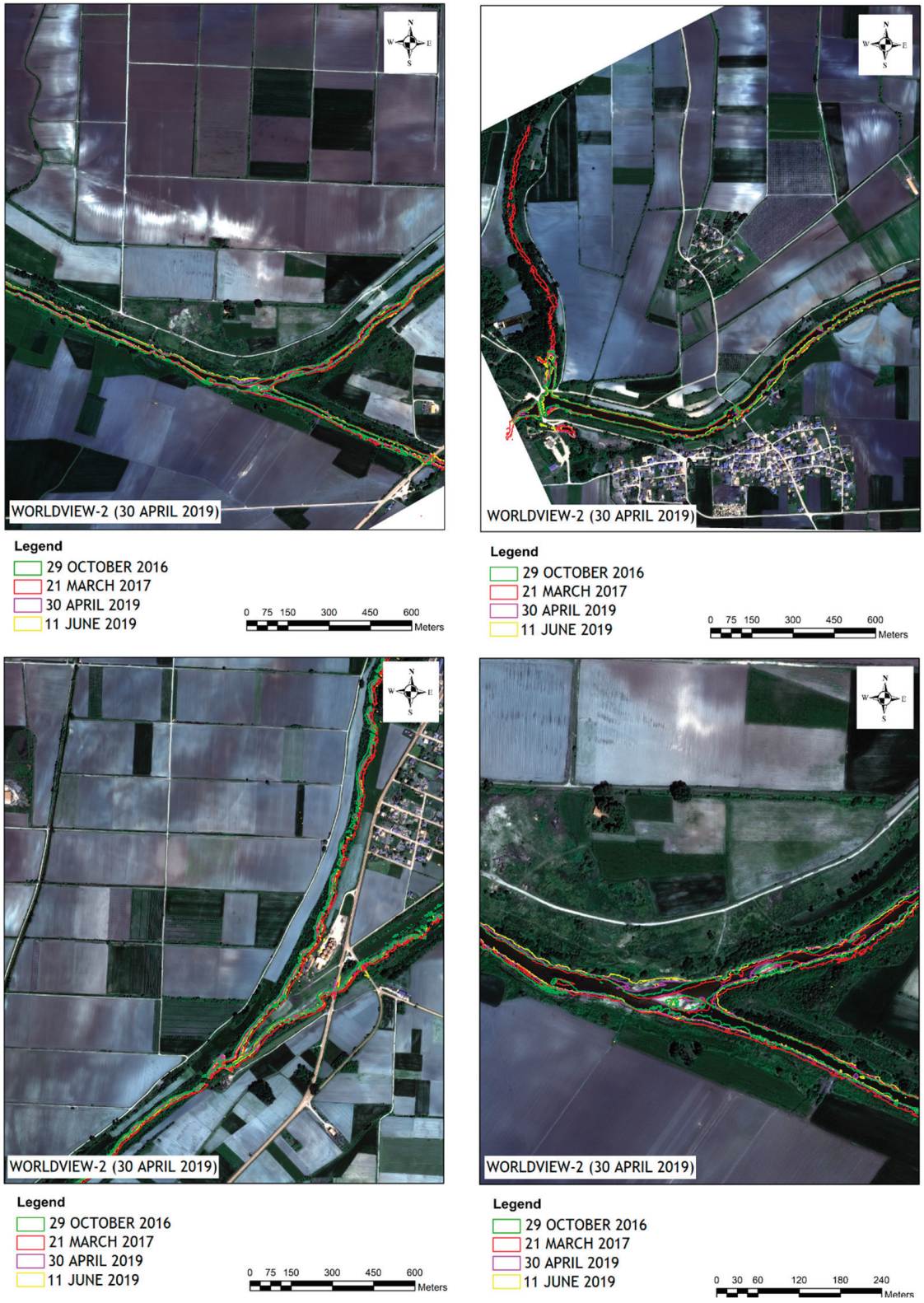

Figure 8. The stream water boundaries are seen as polylines in four different locations on four different satellite dates. The background satellite image is the same for all dates.

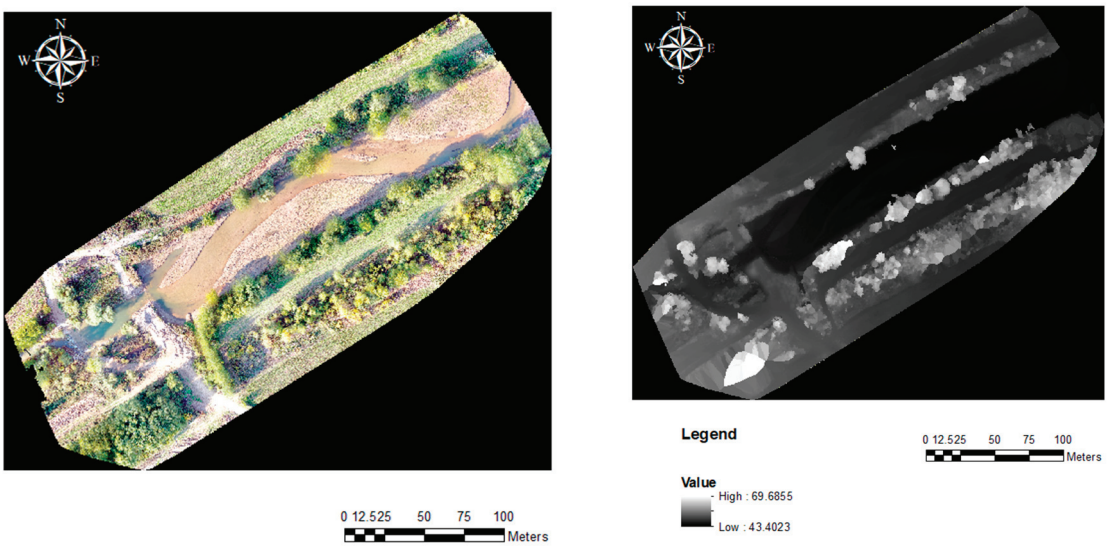

(**a**) (**b**)

Figure 9. (**a**) The orthomosaic and (**b**) the DSM for the Mavrolefki reach near the Mavrolefki village.

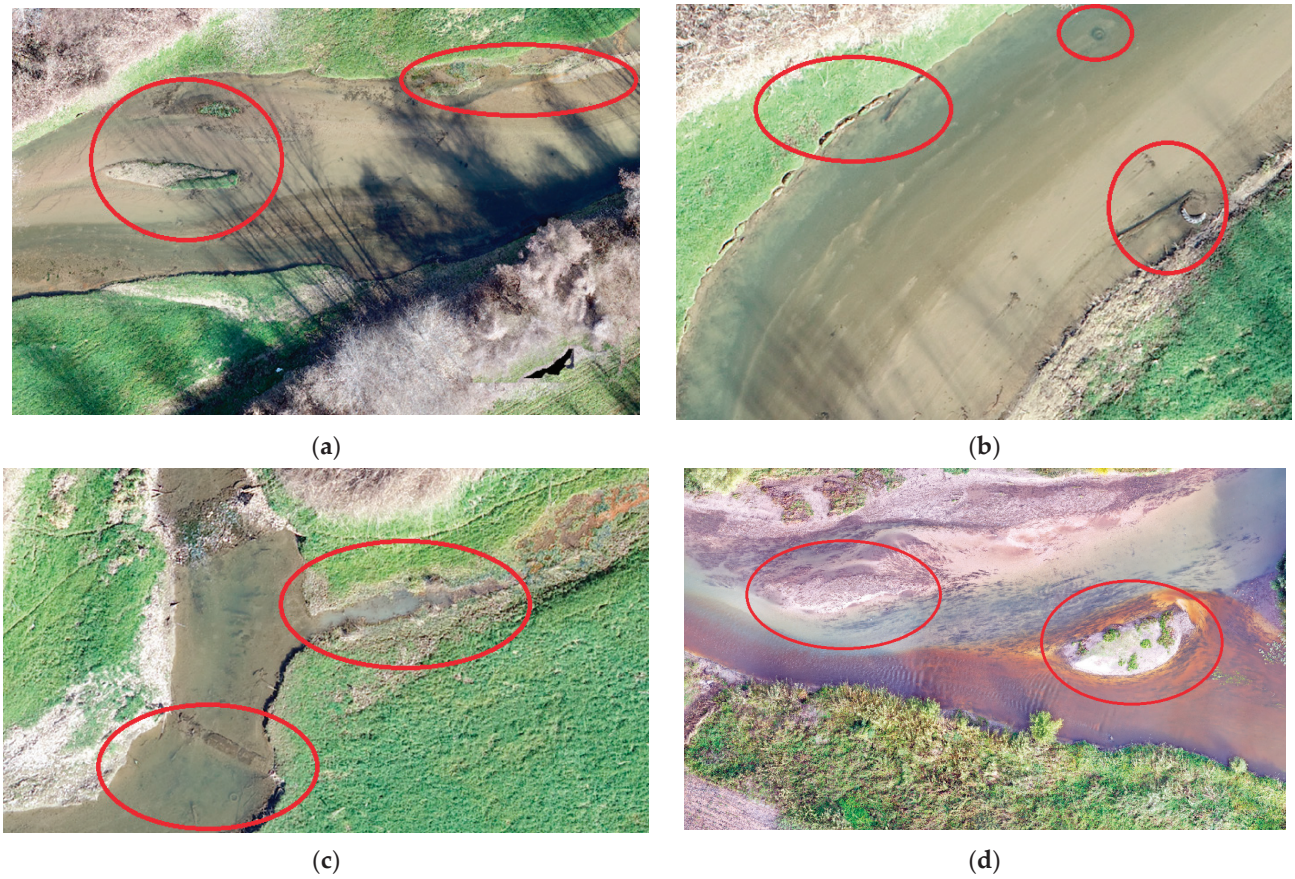

(**a**) (**b**)

(**c**) (**d**)

Figure 10. Examples (in red circles) of soil erosion, deposition and littering in different sections of the Mavrolefki reach detected by using UAV images: (**a**) sediment deposits as small islands and stream bank erosion, (**b**) stream bank erosion and plastic tires in the stream, (**c**) littering accumulation and cloudy water and (**d**) sediment deposits as small islands in the confluence of two streams. Different color due to a rainfall event that occurred mainly in one of these two watersheds. Water color is much clearer in the top than in the bottom.

The second targeted location of the same reach (Figure 10a,b) is at the main road network (Y: 41.047003, X: 24.094152 in WGS84), specifically at a bridge. The specific stream reach has also intense meanders that are covered with water during high rainfall events. The DSM was very helpful to distinguish the main channel curves of current water flow. There are parts of the stream banks that were vulnerable to soil erosion and others that are characterized by soil deposition. Another important point that needs to be mentioned is that the land use of the adjusted area is grazed pastures which enhances soil erosion.

Another location of the same stream is at its confluence with other streams (Y: 41.045076, X: 24.090637 in WGS84) that is mainly characterized by frequent sediment deposition (Figure 10c,d). The specific reach reveals both soil erosion (on the north side) but also sediment deposition (on the south side) and small island formation at the junction of the two stream networks. The UAV flight was performed during a rainfall event that covered the east side of the watershed of Aggitis and supplied with water the area of Tenagi Philippon (Kavala region) in contrast to the Drama region which was not affected by the rainfall event and its stream was not supplied with water. This fact led to a color difference due to the high sediment concentration in the streams from Kavala.

3.3. The Plot-Scaled Assessment Results

3.3.1. The Stream Bank Erosion Pins

The monitored banks (Figure 11) show differences according to the land-use types. The positive values indicate erosion, while negative values refer to deposition. In natural grazed grasslands, there are fluctuations in the erosion of the banks after intense rainfall events. These differences in erosion and deposition appear more on the pins at 2/3 of the bank height (Figure 11a,b). In the riparian forested areas (Figure 11c,d), the erosion of the bank is very low and in most of the measured pins does not exceed 10 cm. Overall, we can state that the observed changes were not substantial. In the agricultural areas, there was extreme erosion measured, in some cases exceeding 40 cm on the monitored banks (Figure 11e,f). It is important to mention that in several cases, erosion pins were completely lost. This happened on the first (25 April 2022), second (18 June 2022) and fifth measurement (15 June 2023). Also, for this land use, we observed that at 1/3 of the bank height, there was more erosion than at 2/3 of the bank height. At locations characterized by sclerophyllous vegetation, there were also strong geomorphologic changes, with both erosion and deposition recorded (Figure 11g,h). Specifically, the erosion rate was lower at 1/3 of the height, approximately 5 cm, than at 2/3 of the bank height, ranging from 10 to 15 cm.

3.3.2. The Stream Cross-Sections (Plot Scale)

Erosion and deposition events were recorded on the sampled surfaces with the changes in the dimensions of the cross-sections (Figure 12). In general, the changes were small, but several large differences were observed between the measurements that reached 1–2 m. Such differences were recorded more in agricultural areas, while for the other land uses such as grazed natural grassland and sclerophyllous vegetation, the changes in the cross-sections were smaller, with a difference ranging from 0.30 to 0.80 m. Finally, it is important to mention that in riparian forested areas, the changes in the cross-sections were minimal, with values ranging from 0.10 to 0.20 m. An example is the Kallifytos torrent, where the material which was transported and deposited was mainly located in the area upstream of the Irish Bridge (before the east entrance to the city of Drama). The material deposited is frequently removed by the local authorities using heavy bulldozers that can compact the stream bed material (Figure 12a).

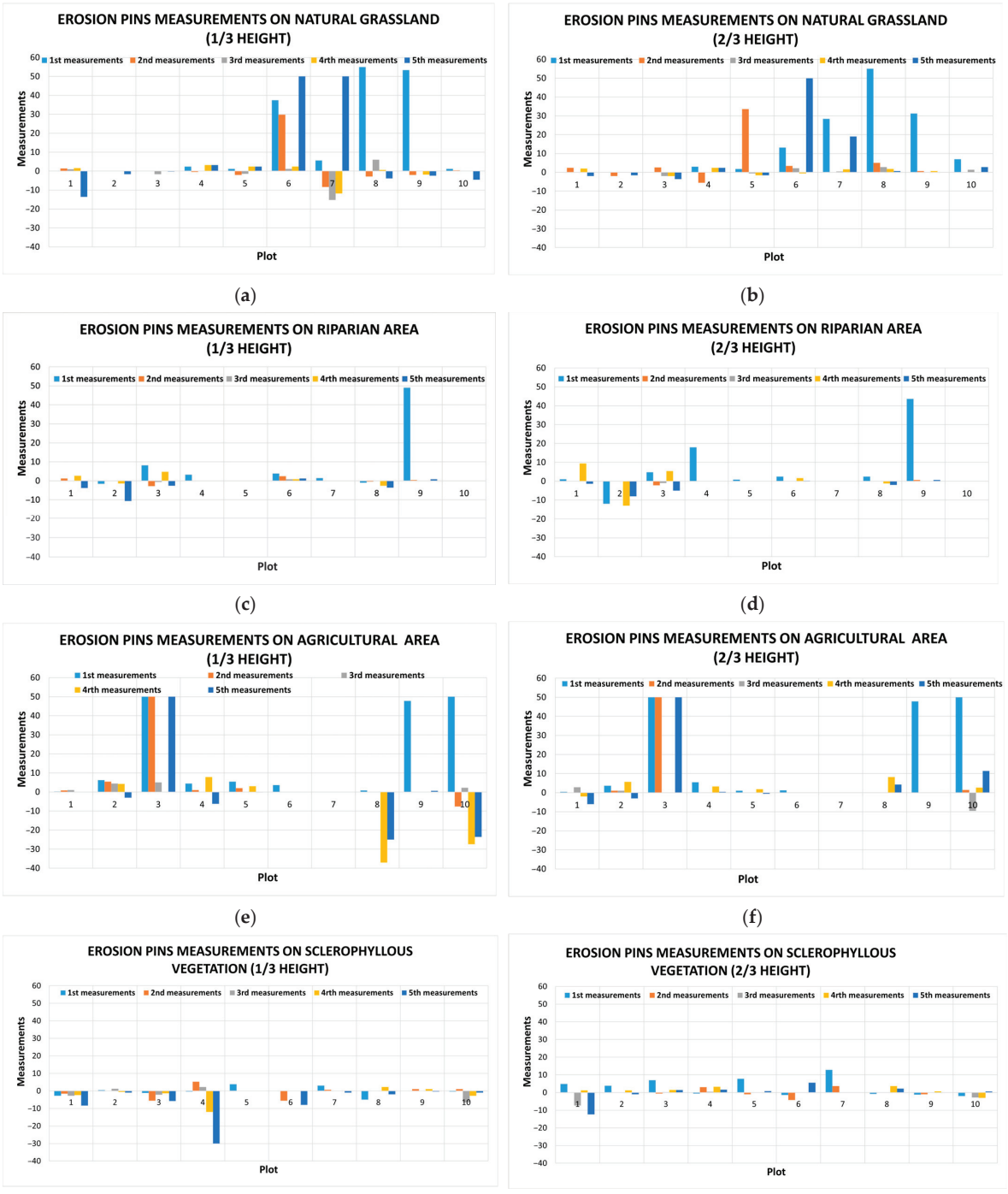

Figure 11. Bar diagrams of erosion and deposition for the four land uses (positive values = erosion and negative values = deposition). (**a**) Erosion and deposition rates at 1/3 of stream bank height in natural grazed grasslands, (**b**) erosion and deposition rates at 2/3 of stream bank height in natural grazed grasslands, (**c**) erosion and deposition rates at 1/3 of stream bank height in riparian forested areas, (**d**) erosion and deposition rates at 2/3 of stream bank height in riparian forested areas, (**e**) erosion and deposition rates at 1/3 of stream bank height in agricultural areas, (**f**) erosion and deposition rates at 2/3 of stream bank height in agricultural areas, (**g**) erosion and deposition rates at 1/3 of stream bank height with sclerophyllous vegetation and (**h**) erosion and deposition rates at 2/3 of stream bank height with sclerophyllous vegetation.

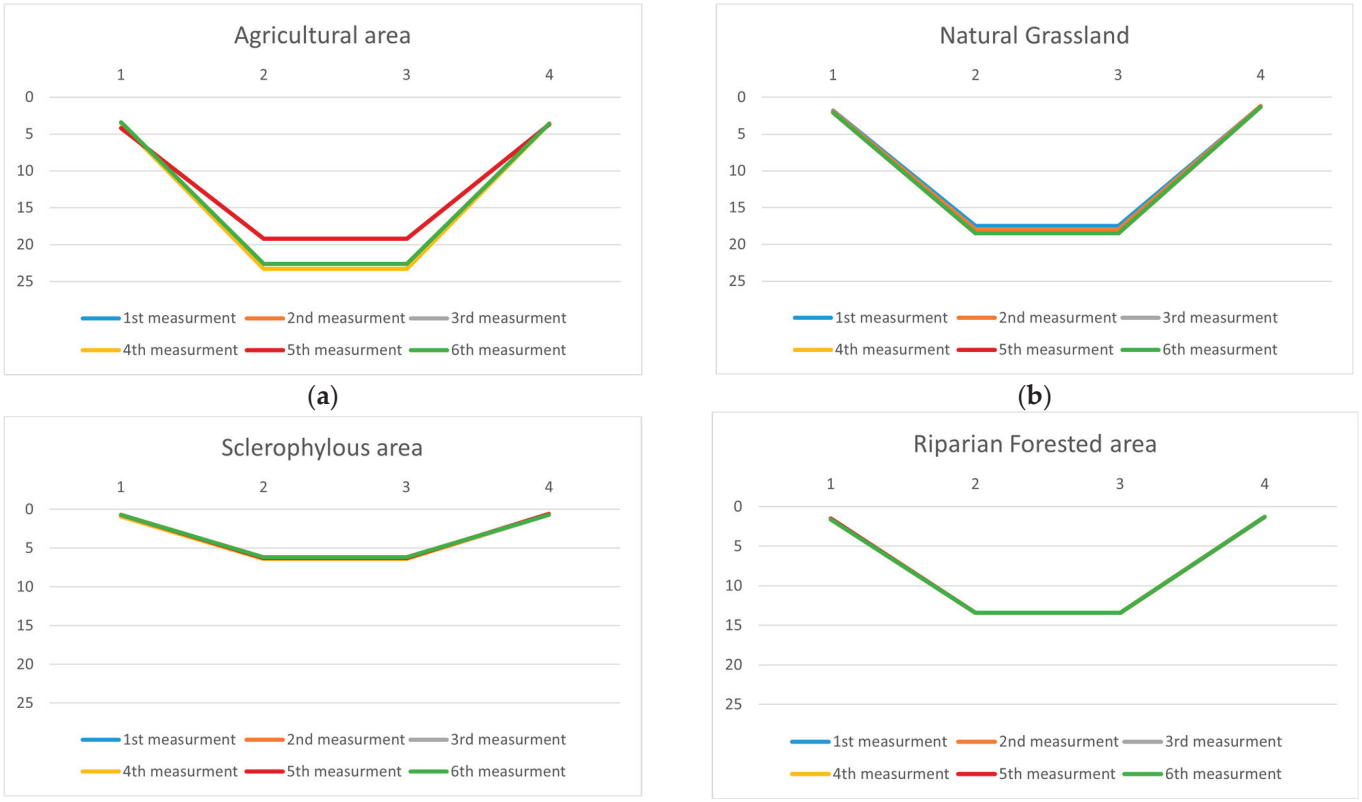

Figure 12. A typical cross-section of each land use in six different areas: (**a**) agricultural area; (**b**) natural grasslands; (**c**) sclerophyllous vegetation; (**d**) riparian forests.

3.3.3. The 3D Laser Scanning Streams' Cross-Sections (Plot Scale)

The Kallifytos torrent is a typical intermittent Greek torrent that has flash flood risk potential particularly after heavy rainfalls [75]. The torrent was selected (erosion pins, cross-sections and laser scanning) because it has a diverse fluvio-geomorphologic profile, with rapid changes in the channel and bed shape due to the large amounts of water, sediments and debris transported [79]. The Kallifytos torrent passes through chutes under the city of Drama before discharging into the Agia Barbara stream, which is a tributary of the Aggitis River.

The comparative 3D sections from the Kallifytos reach based on the 3D field scanning allowed us to estimate the fluvio-geomorphological changes between the two surveying dates (Figure 13). The point clouds (Figure 13a: first survey and Figure 13c: second survey) along with the mesh models (Figure 13b: first survey and Figure 13d: second survey) were developed. Furthermore, five selected cross-sections were drawn to estimate the material loss or gained between the two survey dates.

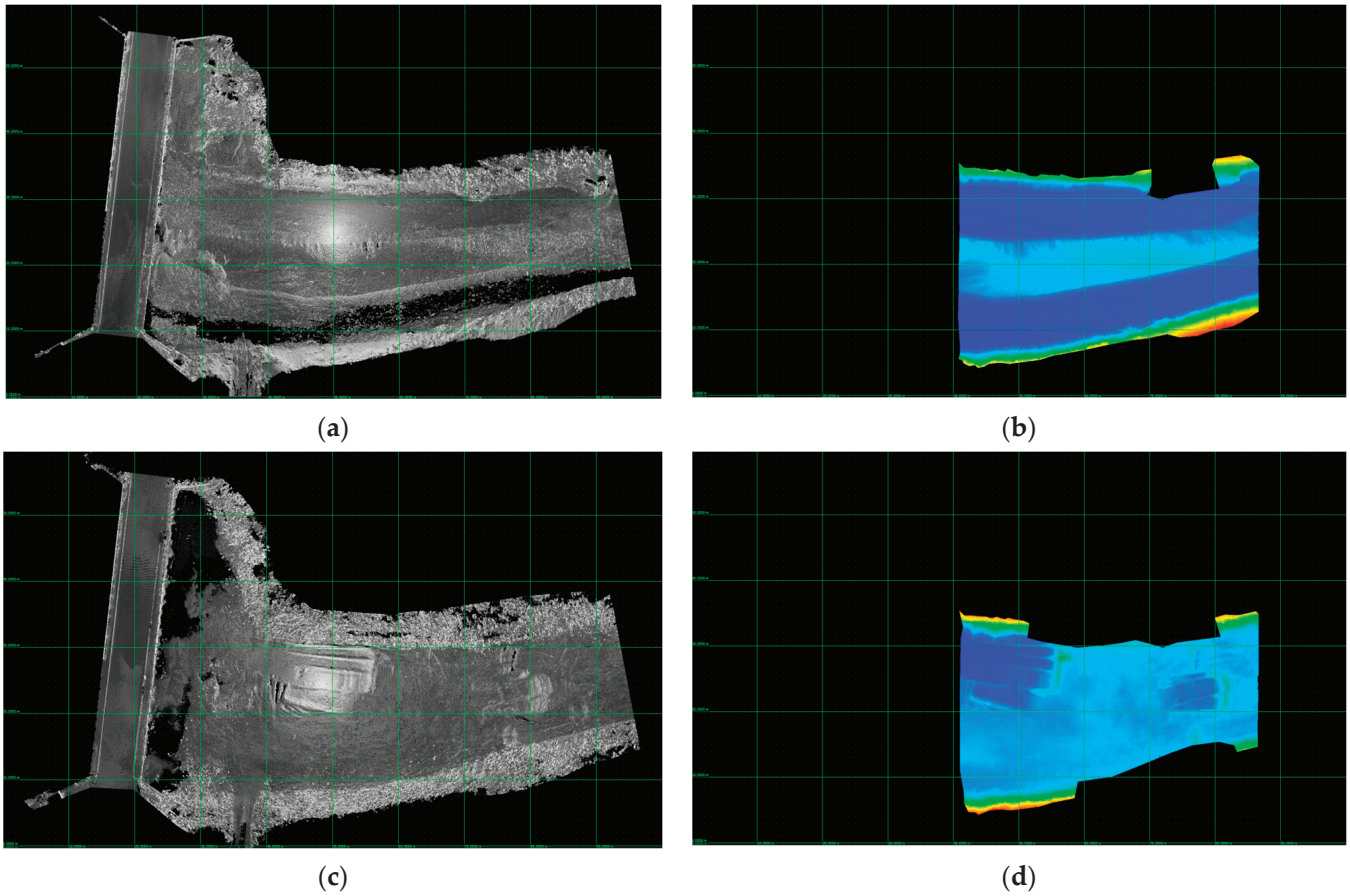

Figure 13. The 3D outputs based on the 3D laser scanning application in Kallifytos torrent reach: (**a**) the point cloud (1st survey); (**b**) the mesh model (1st survey); (**c**) the point cloud (2nd survey); (**d**) the mesh model (2nd survey).

There are clearly visible geomorphological changes in the stream bed. During the first survey, there was deposited material in the center of the stream bed which was distinguished by the lighter blue color. The second survey captured the manmade sand excavations and the removal of deposited material carried out by municipality bulldozers (rectangular formations depicted in darker blue color). There were also differences in the stream banks which are depicted more clearly in the selected 2D cross-sections of the same captured location (Figure 14). In the cross-sections, the first survey is shown in red and the second in green, while both the X and Y axis scales are in meters. Specifically, height differences ranging from 0.00 to 1.26 m of removed material (section B) were detected. The removed material was estimated to be equal to 412.01 m^3 for the stream bed, 2.55 m^3 for the north stream bank and 2.21 m^3 for the south stream bank (Figure 14). Similarly, the gained material was estimated to be equal to 2.82 m^3 for the stream bed, 0.58 m^3 for the north stream bank and 0.70 m^3 for the south stream bank (Figure 13).

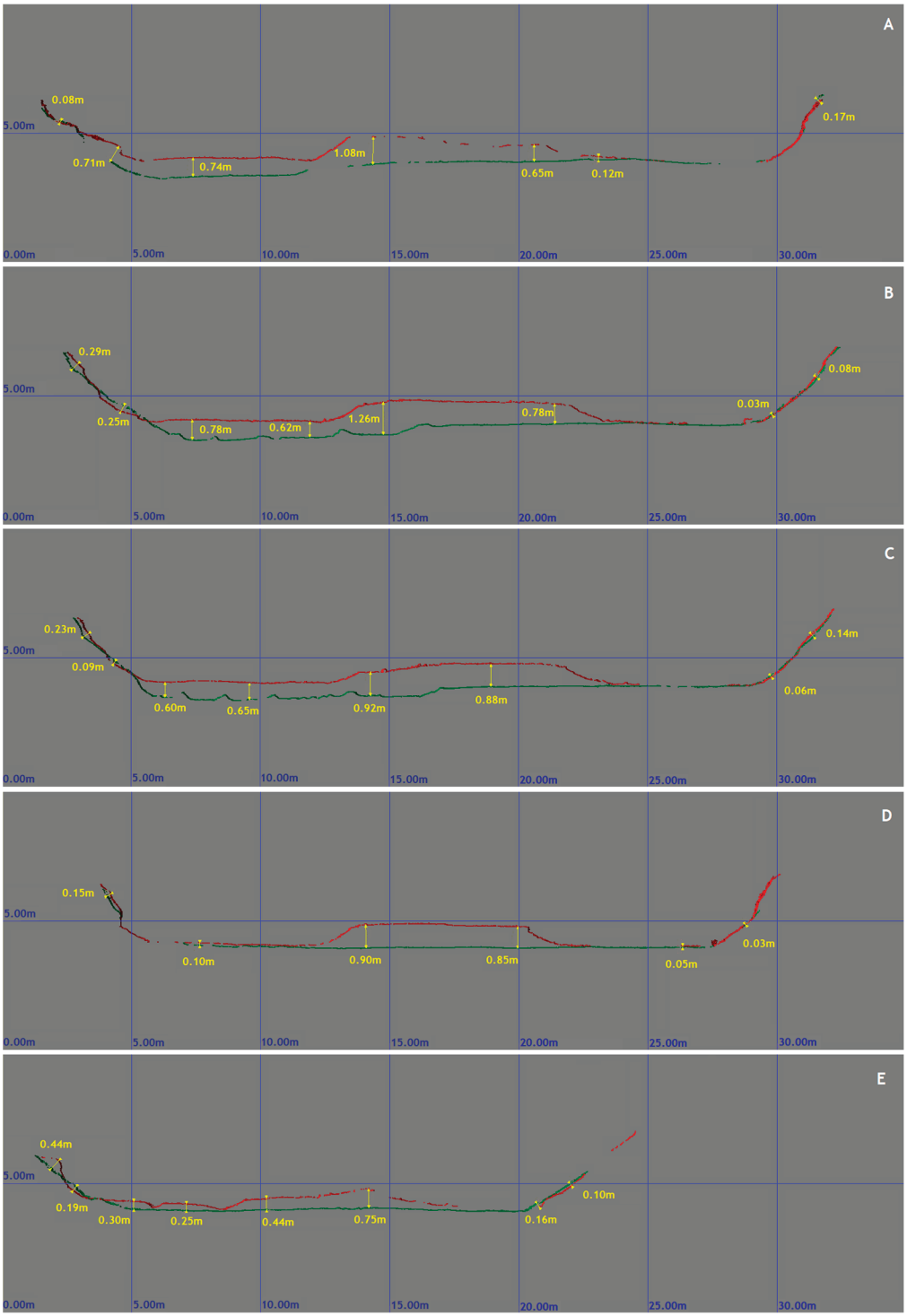

Figure 14. The selected five 2D cross-sections based on 3D laser scanning application in Kallifytos torrent reach. The red lines indicate the 1st survey and the green lines indicate the 2nd survey.

4. Discussion

Erosion and deposition are two of the main fluvio-geomorphologic processes that at both the watershed and/or stream channel scale need to be measured and understood in order to achieve sustainable watershed management, especially under the auspices of the Water Framework Directive and the EU Green Deal. In this study, different measuring methods were utilized at the watershed, reach and plot scale to assess erosion and deposi-

tion (Figure 15). These methods included remote sensing, UAV monitoring, terrestrial 3D scanning and traditional commonly used field monitoring tools (pins and cross-sections).

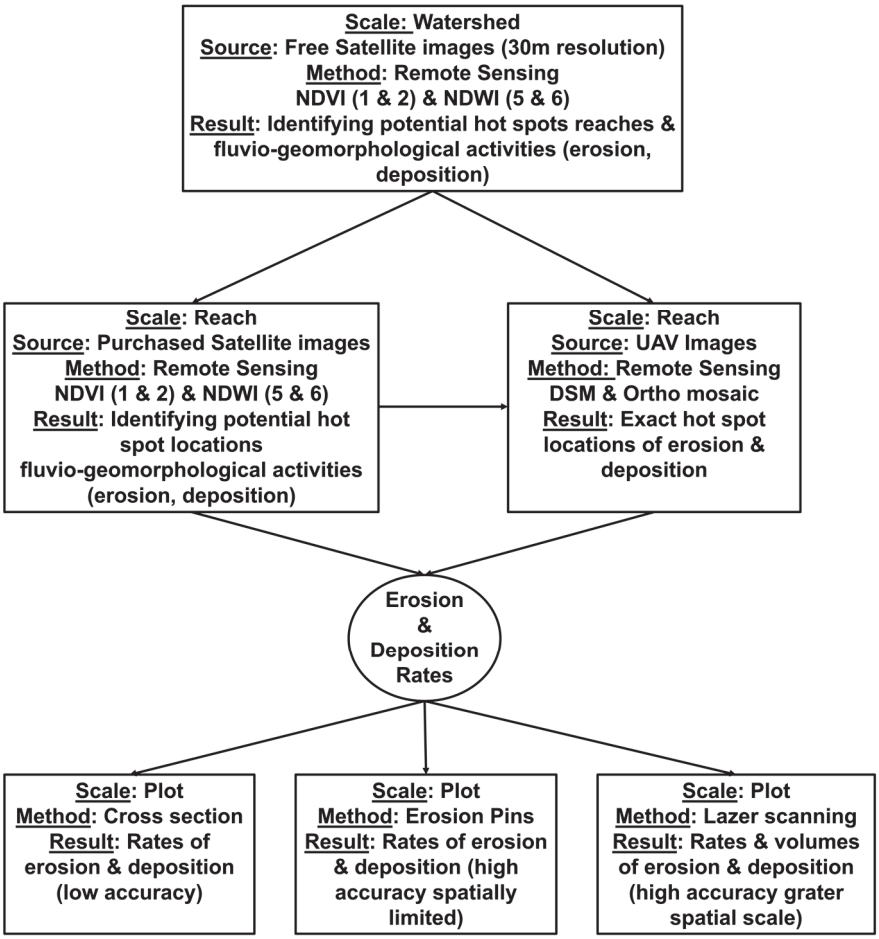

Figure 15. The flowchart of different stream bank and bed erosion and deposition methods. The methods are for different scales: some are for identifying erosion and deposition hot spots and others are for measuring exact rates.

The technological and methodological advancements in the field of Earth observation has contributed to the widespread increase in the use of satellite remote sensing approaches that have enhanced the monitoring of the Earth's surface and its changes [80,81]. Today, there is a readily available large collection of imagery in Google Earth, including satellite, aerial, and even 3D and street view images. Furthermore, free available satellite imagery (e.g., Landsat and Copernicus) is of high importance for remote sensing in geomorphology [82,83]. Free SENTINEL-2 satellite images have been used in various studies to develop indices, as they are competent at highlighting differences in vegetation and water content. The NDVI enables the monitoring of ecosystem and fluvio-geomorphological changes based on the large-scale land monitoring/mapping of floodplains [84]. In addition, as a globally used index of vegetation's health and moisture presence, it is used for the assessment of watershed soil erosion and sediment yield in the floodplains [85]. The NDWI, the other index utilized, can characterize soil and vegetation moisture content before and after flooding events. In addition, it is used to monitor the channel migration [86]. Channel bank and bed erosion occurs mainly in the floodplains; thus, the NDWI was used to detect the water presence lines that can lead to short-term stream bank erosion [87,88]. Its effectiveness decreases with intermittent or ephemeral streams typical in Mediterranean ecosystems [89]. Both indices enabled us to map the most vulnerable areas to erosion and deposition along the stream network and their floodplains. The results of the NDVI and

NDWI showcased the most critical areas prone to erosion. Those which belong to NDVI #1 and NDVI 2 classes represented 7–40%. On the other hand, the affected areas by water (areas adjusted to the water courses and floodplains, NDWI classes #5 and #6) represented only up to 1% of the total studied area. It must be noted that these areas are highly important for the dynamic procedures of stream bank erosion and sediment transportation and should be focal points for stream conservation [12]. In general, erosion occurs when the force of the river's flow removes sediment from the stream bed and banks, widening and deepening the river channels. It is typically caused by the high velocity and turbulent flow of water [90]. The confluence of rivers are such dynamic locations of a hydrologic network where soil erosion or deposition have high rates [91]. The convergence of flow often leads to erosion (downcutting) of the stream bed. Tributaries also alter the hydraulic geometry of the receiving streams (due to stream water turbulence) including width, depth, and bar size and occurrence. Typically, they can alter the particle size distribution, either coarsening or fining the channel bed material. The morphological effects of confluences tend to be most pronounced in lower-gradient portions of rivers. These areas are "hot spots" and allow us to determine potential targeted areas so we can move management from the watershed to the reach scale. Additionally, we used ancillary information (soils, land cover and slope) to determine whether we can find any connection between these characteristics and vulnerability to erosion and deposition (watershed-scale approach).

These vulnerable reaches were further investigated by the comparisons of purchased satellite images that had substantially better resolution. These images were taken before and after flood events in order to capture deposition and erosion phenomena. Low spatial resolutions images are appropriate to be applied at perennial and large dimension temporary streams and for the identification of individual large and medium-sized gullies but do not allow for gully growth analysis with sequential imagery that requires higher resolution [92,93]. Medium and low-resolution images are effective for erosion risk mapping if they present data shortly before and after the first erosion event [94]. High-resolution satellites have enhanced the ability to detect and monitor individual small-scale geomorphologic features [95]. Studies have applied high-resolution products for monitoring erosion by mapping ephemeral streams, as well as smaller (even temporary) gullies and rills that are not covered by dense vegetation (dry and semi-dry environments) [96–99]. There is a place to utilize both free and commercial satellite products, as nowadays there are more options for economical topographical mapping [100]. The selection of higher to low spatial resolution satellite products depends on the ground sampling distance needed based on the research objective [101]. In addition, the size of the study area and the available funds must be considered. High-resolution imagery should be used for study areas of 20–100 km^2 study, while low resolution for areas > 100 km^2 [102]. This is the reason we proposed to firstly use the free low-resolution satellite imagery in the watershed-scale phase (in our case study Aggitis basin is 2700 km^2) and secondly, to use higher-resolution products (if available) on the selected "hot spots". The results of this study show the utility of both and how they can be complimentary to each other. The free satellite images can indicate where there is a need (hot spots) to purchase the high-resolution satellite images. This allows for the cost-effective use of funds, and the more targeted approaches for the placements of conservation practices (e.g., nature-based solutions) can be implemented with higher-resolution purchased images.

Furthermore, UAV-based orthomosaics were developed in some of these vulnerable selected reaches. UAVs have been applied worldwide as a monitoring methodology to improve the monitoring of fluvio-geomorphologic changes [103,104]. The advantages of UAV-based photogrammetry are the ability to reconstruct the stream bank topography in very high detail and very quickly [105]. The results produced by the UAV's flights enabled us to monitor the fluvio-geomorphologic changes again at the reach scale but also at a smaller scale and with enhanced resolution. Orthomosaics developed by UAV images taken at different times provide detailed stream channel features to detect changes between periods [75].

Site assessments and in-situ measurements (erosion pins, stream cross-sections and 3D laser scanning) have been used to evaluate and monitor the stream bank erosion or deposition at the plot scale. The analysis of the results from the field measurements of this study showcased high erosion on some stream banks, especially after extreme rainfall phenomena. In several plots, bank erosion exceeded the 50 cm, while in a few, deposition was also recorded. Deposition was recorded mainly in sclerophyllous vegetation (both bank heights) but also in agricultural areas (1/3 of bank height). Stream bank erosion was high in most of the natural grasslands/pastures and agricultural areas. Agricultural and livestock activities are highly associated with erosion phenomena since they weaken bank stability though different activities [106]. Finally, it should be noted that on stream banks covered with riparian vegetation, the erosion was limited or non-existent. Many studies have shown that maintaining or re-establishing the riparian vegetation is optimal to reduce erosion and a highly recommended nature-based solution [107]. Land cover types, and their changes, have different hydrological and geomorphological effects on controlling bank stability or enhancing soil erosion [108]. Forests are considered to stabilize slopes and banks, while human intervention on stream banks and riparian zones may reduce stability [109,110]. For agricultural lands, the implementation of conservation practices can have a significant impact on soil erosion reduction, especially in the Mediterranean dry region which suffers from tillage agriculture erosion impacts [111]. The produced point clouds of the plot-scaled laser scanning approach were of high resolution and estimated soil volume changes (erosion or deposition) before and after events. Specifically, soil deposition was recorded after an extreme flood event, while soil removal (erosion) was detected after excavations were performed by bulldozers. The amount of stream bed and bank material was also easily estimated in these specific cross-sections through the point-cloud comparison when riparian or stream bed vegetation was limited or absent [112]. Overall, the results of laser scanning and traditional field plot measurements were similar. The advantage of laser scanning was the higher accuracy and also the larger scale it can implemented on in comparison with traditional methods.

The studied targeted reaches of Mavrolefki stream showed that erosion can lead to the formation of sandbars and islands within the stream channels. Deposition occurs when sediment carried by the stream flow decreases, and thus settles and accumulates in the bed. This is also evident in the main course of theAggitis River and its tributary streams with intermittent flow. On the other hand, Kallifytos showed more episodic flow characteristics, typical of Euro-Mediterranean torrents (ephemeral and intermittent flows) [113]. For most of the year, these torrents have no flow, but a few times during the year, they can have very high flows and transport large amounts of sediment.

The results of this study are similar to others that utilized such methodologies, although our study was the first detailed research incorporating all of these methods [23]. UAV-based surveys have been also conducted by the authors before, in selected reaches of the region, for the first time with successful results [75]. Flooding is a common phenomenon in the Aggitis basin after extreme rainfall events or snowmelt causing serious damage in the area [114]. There is high connectivity between extreme flood events and stream bank and bed erosion and deposition in the channels and floodplains [115]. Anthropogenic activities and climate change are accelerating soil erosion, fluvial activity and extreme flood events [116]. Along the Aggitis River and its tributaries, alluvial aggradation was accelerated by 6000 BP due to climate change between 6500 and 5000 BP [117]. Such events were also recorded during the Ottoman period, linked to the intensification of farming in the Aggitis river plain along with the increase in grazing and logging in the surrounding mountainous areas [118]. This study also revealed that extensive erosion occurs by anthropogenic activities in channels when the major land cover in the riparian areas and the watershed is agricultural or grazed grasslands.

The different studied stream bank and bed monitoring techniques presented advantages and disadvantages that have been presented previously. Their selection and application is highly dependent on the scale and accuracy required, the site-specific conditions and

the experience of the researcher. Traditional field monitoring approaches can be laborious, time-consuming and resource-demanding, especially when examining lengthy reaches of rivers or streams [119]. Erosion pins can be used in vegetated banks but with coarse spatial and temporal resolution. UAV mapping or laser scanning have higher resolution for larger reaches but can have problems when the stream banks have dense vegetation. A UAV survey requires low vegetation, as tree canopy may cover the ground, while terrestrial laser scanning can be applied in a forested environment when employing the vegetation filter to extract the tree trunks, but it is difficult, or even impossible, when riparian vegetation is low or mixed. As a consequence, the final choice of the appropriate technique depends on the goals of the project and the desired resolution, the stream bank or bed conditions, and the available resources, tools and finances [39].

5. Conclusions

Stream bank and bed erosion and deposition are natural process, but anthropogenic pressures and climate have and will continue to accelerate stream bank and bed deposition but also other types of erosion. A framework with a cadre of different methodologies to monitor and understand erosion is a necessity, especially in climate change-vulnerable regions such as the Mediterranean. This is what this study tried to achieve by showcasing different methods that can be used at different scales and with different accuracy. In addition, all of these methods could be used together since they are complimentary to one another. Remote sensing products such as free satellite imagery and Google images can be the first step in order to identify stream bank changes over short periods of time (e.g., after a flood event) or over many years. UAVs can be utilized as a second step to provide higher accuracy and analysis at a larger scale (reach scale) of specific locations. Field measurements at the plot scale, such as erosion pins and cross-sections, can be used at a very narrow scale (specific bank), focusing on intense rainfall events or anthropogenic alterations (excavations) that change stream bed and bank morphology and provide validation data for the satellite and UAV images. Finally, through 3D terrestrial scanning, the determination of accelerated bank erosion or deposition is more accurate and enables the land managers to identify vulnerable areas to erosion and deposition. Once these areas are identified, nature-based solution should be implemented by land managers in order to stabilize stream banks, reduce erosion or deposition rates and consequently mitigate non-point source pollutants. Nature-based solutions are preferred because they try to emulate nature, thus reducing the acceleration of erosion and deposition. This proposed framework has high utility since it will allow managers to target the areas that produce the greatest erosion and deposition, and thus utilize funds more cost-effectively and promote sustainable management. In addition, because of the better erosion mitigating results, this framework is more likely to achieve the approval of the policy makers and general public, thus helping obtain the needed funding.

Author Contributions: Conceptualization, G.N.Z.; methodology, G.N.Z., P.K. and M.X.; software, P.K., G.G. and G.P.; validation, G.N.Z., V.I. and I.K.; analysis P.K., G.N.Z., G.G., M.X. and G.P.; data curation, P.K., G.G., G.P., I.K., M.X., A.S., K.K. and T.K.; writing—original draft preparation, P.K., G.G. and I.K.; writing—review and editing, P.K., G.N.Z. and V.I.; visualization, P.K., G.G. and G.P.; supervision, G.N.Z.; project administration, G.N.Z. All authors have read and agreed to the published version of the manuscript.

Funding: This research was funded by the Joint Operational Black Sea Programme 2014–2020 and the Project BSB 963 "Protect-Streams-4-Sea", with the financial assistance of the European Union. The content of this publication is the sole responsibility of the authors and in no case should it be considered to reflect the views of the European Union.

Data Availability Statement: Data and reports are available at http://websites3.teiemt.gr/p4sea. (accessed on 30 December 2023).

Conflicts of Interest: The authors declare no conflict of interest. The funders had no role in the design of the study; in the collection, analyses or interpretation of data; in the writing of the manuscript; or in the decision to publish the results.

References

1. Pimentel, D. Soil erosion: A food and environmental threat. *Environ. Dev. Sustain.* **2006**, *8*, 119–137. [CrossRef]
2. Zaimes, G.N.; Schultz, R.C. Riparian land-use impacts on bank erosion and deposition of an incised stream in north-central Iowa, USA. *Catena* **2015**, *125*, 61–73. [CrossRef]
3. Zaimes, G.N.; Tamparopoulos, A.E.; Tufekcioglu, M.; Schultz, R.C. Understanding stream bank erosion and deposition in Iowa, USA: A seven-year study along streams in different regions with different riparian land-uses. *J. Environ. Manag.* **2021**, *287*, 112352. [CrossRef]
4. Zaimes, G.N. Mediterranean riparian areas–climate change implications and recommendations. *J. Environ. Biol.* **2020**, *41*, 957–965. [CrossRef]
5. Simon, A.; Rinaldi, M. Disturbance, stream incision, and channel evolution: The roles of excess transport capacity and boundary materials in controlling channel response. *Geomorphology* **2006**, *79*, 361–383. [CrossRef]
6. Schumm, S.A.; Holdbrook, J. Geomorphic and sedimentary response of rivers to tectonic deformation: A brief review and critique of a tool for recognizing subtle epeirogenic deformation in modern and ancient settings. *Tectonophysics* **1999**, *305*, 287–306.
7. Bull, W.B. Discontinuous ephemeral streams. *Geomorphology* **1997**, *19*, 227–276. [CrossRef]
8. Pollen-Bankhead, N.; Simon, A. Hydrologic and hydraulic effects of riparian root networks on streambank stability: Is mechanical root-reinforcement the whole story? *Geomorphology* **2010**, *116*, 353–362. [CrossRef]
9. Wynn, T.M.; Henderson, M.B.; Vaughan, D.H. Changes in streambank erodibility and critical shear stress due to subaerial processes along a headwater stream, southwestern Virginia, USA. *Geomorphology* **2008**, *97*, 260–273. [CrossRef]
10. Langendoen, E.J.; Richard Lowrance, R.; Simon, A. Assessing the impact of riparian processes on streambank stability. *Ecohydrol. Ecosyst. Land Water Process Interact. Ecohydrol.* **2009**, *2*, 360–369. [CrossRef]
11. Koutalakis, P.; Zaimes, G.N.; Iakovoglou, V.; Ioannou, K. Reviewing soil erosion in Greece. *Int. J. Geol. Geotech. Eng.* **2015**, *9*, 936–941.
12. Zaimes, G.N.; Tufekcioglu, M.; Schultz, R.C. Riparian land-use impacts on stream bank and gully erosion in agricultural watersheds: What we have learned. *Water* **2019**, *11*, 1343. [CrossRef]
13. Zaimes, G.N. Utilizing new and innovative tools to mitigate surficial erosion in Mediterranean environments. *Kastamonu Univ. Orman Fak. Derg.* **2017**, *17*, 373–382. [CrossRef]
14. Lawler, D.M. The importance of high-resolution monitoring in erosion and deposition dynamics studies: Examples from estuarine and fluvial systems. *Geomorphology* **2005**, *64*, 1–23. [CrossRef]
15. Resop, J.P.; Hession, W.C. Terrestrial Laser Scanning for Monitoring Streambank Retreat: Comparison with Traditional Surveying Techniques. *J. Hydraul. Eng.* **2010**, *136*, 794–798. [CrossRef]
16. McBride, M. Riparian Reforestation and Channel Morphology. Ph.D. Dissertation, University of Vermont, Burlington, VT, USA, 2007.
17. King, C.; Baghdadi, N.; Lecomte, V.; Cerdan, O. The application of remote-sensing data to monitoring and modelling of soil erosion. *Catena* **2005**, *62*, 79–93. [CrossRef]
18. Benzer, N. Using the geographical information system and remote sensing techniques for soil erosion assessment. *Pol. J. Environ. Stud.* **2010**, *19*, 881–886.
19. Ganasri, B.P.; Ramesh, H. Assessment of soil erosion by RUSLE model using remote sensing and GIS-A case study of Nethravathi Basin. *Geosci. Front.* **2016**, *7*, 953–961. [CrossRef]
20. Shen, Z.Y.; Gong, Y.W.; Li, Y.H.; Hong, Q.; Xu, L.; Liu, R.M. A comparison of WEPP and SWAT for modeling soil erosion of the Zhangjiachong Watershed in the Three Gorges Reservoir Area. *Agric. Water Manag.* **2009**, *96*, 1435–1442. [CrossRef]
21. Szabó, S.; Gácsi, Z.; Balázs, B. Specific features of NDVI, NDWI and MNDWI as reflected in land cover categories. *Acta Geogr. Debr. Landsc. Environ. Ser.* **2016**, *10*, 194–202. [CrossRef]
22. Kosmas, C.; Danalatos, N.; Cammeraat, L.H.; Chabart, M.; Diamantopoulos, J.; Farand, R.; Gutierrez, L.; Jacob, A.; Marques, H.; Martinez-Fernandez, J.; et al. The effect of land use on runoff and soil erosion rates under Mediterranean conditions. *Catena* **1997**, *29*, 45–59. [CrossRef]
23. Koutalakis, P.; Tzoraki, O.; Gkiatas, G.; Zaimes, G.N. Using UAV to capture and record torrent bed and banks, flood debris, and riparian areas. *Drones* **2020**, *4*, 77. [CrossRef]
24. Eisenbeiss, H. UAV photogrammetry in plant science and geology, In Proceedings of the 6th ARIDA Workshop on "Innovations in 3D Measurement, Modelling and Visualization", Trento, Italy, 25–26 February 2008.
25. Wallace, L.; Lucieer, A.; Watson, C.; Turner, D. Development of a UAV-LiDAR system with application to forest inventory. *Remote Sens.* **2012**, *4*, 1519–1543. [CrossRef]
26. Eisenbeiss, H.; Sauerbier, M. Investigation of UAV systems and flight modes for photogrammetric applications. *Photogramm. Rec.* **2011**, *26*, 400–421. [CrossRef]
27. Eker, R.; Alkan, E.; Aydin, A. A Comparative Analysis of UAV-RTK and UAV-PPK Methods in Mapping Different Surface Types. *Eur. J. For. Eng.* **2020**, *7*, 12–25. [CrossRef]

28. Taddia, Y.; Stecchi, F.; Pellegrinelli, A. Coastal mapping using DJI Phantom 4 RTK in post-processing kinematic mode. *Drones* **2020**, *4*, 9. [CrossRef]
29. Gabara, G.; Sawicki, P. Multi-variant accuracy evaluation of uav imaging surveys: A case study on investment area. *Sensors* **2019**, *19*, 5229. [CrossRef] [PubMed]
30. Ebrahim, M.A.B. 3D laser scanners' techniques overview. *Int. J. Sci. Res.* **2015**, *4*, 323–331.
31. Tong, X.; Liu, X.; Chen, P.; Liu, S.; Luan, K.; Li, L.; Liu, S.; Liu, X.; Xie, H.; Jin, Y.; et al. Integration of UAV-based photogrammetry and terrestrial laser scanning for the three-dimensional mapping and monitoring of open-pit mine areas. *Remote Sens.* **2015**, *7*, 6635–6662. [CrossRef]
32. Fröhlich, C.; Mettenleiter, M. Terrestrial laser scanning–new perspectives in 3D surveying. *Int. Arch. Photogramm. Remote Sens.* **2004**, *36*, W2.
33. Baltsavias, E.P. A comparison between photogrammetry and laser scanning. *ISPRS J. Photogramm. Remote Sens.* **1999**, *54*, 83–94. [CrossRef]
34. Wu, C.; Yuan, Y.; Tang, Y.; Tian, B. Application of terrestrial laser scanning (TLS) in the architecture, engineering and construction (AEC) industry. *Sensors* **2021**, *22*, 265. [CrossRef] [PubMed]
35. Telling, J.; Lyda, A.; Hartzell, P.; Glennie, C. Review of Earth science research using terrestrial laser scanning. *Earth Sci. Res.* **2017**, *169*, 35–68. [CrossRef]
36. Brasington, J.; Vericat, D.; Rychkov, I. Modeling river bed morphology, roughness, and surface sedimentology using high resolution terrestrial laser scanning. *Water Resour. Res.* **2012**, *48*, 11519. [CrossRef]
37. Heritage, G.L.; Milan, D.J. Terrestrial laser scanning of grain roughness in a gravel-bed river. *Geomorphology* **2009**, *113*, 4–11. [CrossRef]
38. Picco, L.; Mao, L.; Cavalli, M.; Buzzi, E.; Rainato, R.; Lenzi, M.A. Evaluating short-term morphological changes in a gravel-bed braided river using terrestrial laser scanner. *Geomorphology* **2013**, *201*, 323–334. [CrossRef]
39. Myers, D.T.; Rediske, R.R.; McNair, J.N. Measuring streambank erosion: A comparison of erosion pins, total station, and terrestrial laser scanner. *Water* **2019**, *11*, 1846. [CrossRef]
40. Longoni, L.; Papini, M.; Brambilla, D.; Barazzetti, L.; Roncoroni, F.; Scaioni, M.; Ivanov, V.I. Monitoring riverbank erosion in mountain catchments using terrestrial laser scanning. *Remote Sens.* **2016**, *8*, 241. [CrossRef]
41. Riegels, N.; Jensen, R.; Bensasson, L.; Banou, S.; Møller, F.; Bauer-Gottwein, P. Estimating resource costs of compliance with EU WFD ecological status requirements at the river basin scale. *J. Hydrol.* **2011**, *396*, 197–214. [CrossRef]
42. Pennos, C.; Lauritzen, S.E.; Pechlivanidou, S.; Sotiriadis, Y. Geomorphic constrains on the evolution of the Aggitis River Basin Northern Greece (a preliminary report). *Bull. Geol. Soc. Greece* **2016**, *50*, 365–373. [CrossRef]
43. Savopoulou, A.; Giatas, G.; Pagonis, G.; Iakovoglou, V.; Zaimes, G.N. Visual protocols and GIS as preliminary investigative tools to locate potential ecoengineering in streams and riparian areas. *Procedia Environ. Sci. Eng.* **2017**, *4*, 227–234.
44. Koutalakis, P.; Zaimes, G.; Ioannou, K.; Iakovoglou, V. Application of the SWAT model on torrents of the Menoikio, Greece. *Fresen. Environ. Bull.* **2017**, *26*, 1210–1215.
45. Segarra, J.; Buchaillot, M.L.; Araus, J.L.; Kefauver, S.C. Remote Sensing for Precision Agriculture: Sentinel-2 Improved Features and Applications. *J. Agron.* **2020**, *10*, 641. [CrossRef]
46. Szantoi, Z.; Strobl, P. Copernicus Sentinel-2 calibration and validation. *Eur. J. Remote Sens.* **2019**, *52*, 253–255. [CrossRef]
47. Li, J.; Roy, D.P. A global analysis of Sentinel-2A, Sentinel-2B and Landsat-8 data revisit intervals and implications for terrestrial monitoring. *Remote Sens.* **2017**, *9*, 902. [CrossRef]
48. Drusch, M.; Del Bello, U.; Carlier, S.; Colin, O.; Fernandez, V.; Gascon, F.; Bargellini, P. Sentinel-2: ESA's optical high-resolution mission for GMES operational services. *Remote Sens. Environ.* **2012**, *120*, 25–36. [CrossRef]
49. Chatziantoniou, A.; Petropoulos, G.P.; Psomiadis, E. Co-Orbital Sentinel 1 and 2 for LULC mapping with emphasis on wetlands in a mediterranean setting based on machine learning. *Remote Sens.* **2017**, *9*, 1259. [CrossRef]
50. Eid, A.N.M.; Olatubara, C.O.; Ewemoje, T.A.; Farouk, H.; El-Hennawy, M.T. Coastal wetland vegetation features and digital Change Detection Mapping based on remotely sensed imagery: El-Burullus Lake, Egypt. *Int. Soil Water Conserv. Res.* **2020**, *8*, 66–79.
51. Kashyap, M.; Bhatt, C.M.; Rawat, J.S. Application of Sentinel-2 Data for Extraction of Flood Inundation along Ganga River, Bihar. *Int. J. Mech. Eng. Res.* **2021**, *6*, 47–52. [CrossRef]
52. Bhandari, A.K.; Kumar, A.; Singh, G.K. Feature extraction using Normalized Difference Vegetation Index (NDVI): A case study of Jabalpur city. *Proc. Technol.* **2012**, *6*, 612–621. [CrossRef]
53. Johansen, B.; Tømmervik, H. The relationship between phytomass, NDVI and vegetation communities on Svalbard. *Int. J. Appl. Earth Obs. Geoinf.* **2014**, *27*, 20–30. [CrossRef]
54. Price, J.C.; Bausch, W.C. Leaf area index estimation from visible and near-infrared reflectance data. *Remote Sens. Environ.* **1995**, *52*, 55–65. [CrossRef]
55. Wang, J.; Rich, P.M.; Price, K.P.; Kettle, W.D. Relations between NDVI and tree productivity in the central Great Plains. *Int. J. Remote Sens.* **2004**, *25*, 3127–3138. [CrossRef]
56. Nanzad, L.; Zhang, J.; Tuvdendorj, B.; Nabil, M.; Zhang, S.; Bai, Y. NDVI anomaly for drought monitoring and its correlation with climate factors over Mongolia from 2000 to 2016. *J. Arid Environ.* **2019**, *164*, 69–77. [CrossRef]

57. Peters, A.J.; Walter-Shea, E.A.; Ji, L.; Vina, A.; Hayes, M.; Svoboda, M.D. Drought monitoring with NDVI-based standardized vegetation index. *Photogramm. Eng. Remote Sens.* **2002**, *68*, 71–75.
58. Gao, B.C. NDWI—A normalized difference water index for remote sensing of vegetation liquid water from space. *Remote Sens. Environ.* **1996**, *58*, 257–266. [CrossRef]
59. Bannari, A.; Guedon, A.M.; El-Ghmari, A. Mapping Slight and Moderate Saline Soils in Irrigated Agricultural Land Using Advanced Land Imager Sensor (EO-1) Data and Semi-Empirical Models. *Commun. Soil Sci. Plant Anal.* **2016**, *47*, 1883–1906. [CrossRef]
60. Aslam, B.; Maqsoom, A.; Salah Alaloul, W.; Musarat, M.A.; Jabbar, T.; Zafar, A. Soil erosion susceptibility mapping using a GIS-based multi-criteria decision approach: Case of district Chitral, Pakistan. *Ain Shams Eng. J.* **2021**, *12*, 1637–1649. [CrossRef]
61. Rose, C.W.; Williams, J.R.; Sander, G.C.; Barry, D.A. A mathematical model of soil erosion and deposition processes: I. Theory for a plane land element. *Soil Sci. Soc. Am. J.* **1983**, *47*, 991–995. [CrossRef]
62. Gómez-Gutiérrez, Á.; Conoscenti, C.; Angileri, S.E.; Rotigliano, E.; Schnabel, S. Using topographical attributes to evaluate gully erosion proneness (susceptibility) in two mediterranean basins: Advantages and limitations. *Nat. Hazards* **2015**, *79*, 291–314. [CrossRef]
63. McFeeters, S.K. The use of the Normalized Difference Water Index (NDWI) in the delineation of open water features. *Int. J. Remote Sens.* **1996**, *17*, 1425–1432. [CrossRef]
64. Chen, L.; Lety, H.; Fan, M.; Shang, H.; Tao, J.; Wu, L.; Zhang, Y.; Yu, C.; Gu, J.; Zhang, N.; et al. An Introduction to the Chinese High-Resolution Earth Observation System: Gaofen-1~7 Civilian Satellites. *J. Remote Sens.* **2022**, *2022*, 9769536. [CrossRef]
65. Coffer, M.M.; Schaeffer, B.A.; Darling, J.A.; Urquhart, E.A.; Salls, W.B. Quantifying national and regional cyanobacterial occurrence in US lakes using satellite remote sensing. *Ecol. Indic.* **2020**, *111*, 105976. [CrossRef]
66. Michez, A.; Philippe, L.; David, K.; Sébastien, C.; Christian, D.; Bindelle, J. Can low-cost unmanned aerial systems describe the forage quality heterogeneity? Insight from a Timothy Pasture case study in Southern Belgium. *Remote Sens.* **2020**, *12*, 1650. [CrossRef]
67. Manfreda, S.; Dal Sasso, S.F.; Pizarro, A.; Tauro, F. New insights offered by UAS for river monitoring. In *Applications of Small Unmanned Aircraft Systems: Best Practices and Case Studies*; Sharma, J.B., Ed.; CRC Press, Taylor and Francis Group: New York, NY, USA, 2019; pp. 211–234.
68. Hung, I.; Unger, D.; Kulhavy, D.; Zhang, Y. Positional precision analysis of orthomosaics derived from drone captured aerial imagery. *Drones* **2019**, *3*, 46. [CrossRef]
69. Psirofonia, P.; Samaritakis, V.; Eliopoulos, P.; Potamitis, I. Use of unmanned aerial vehicles for agricultural applications with emphasis on crop protection: Three novel case-studies. *J. Agric. Sci. Technol.* **2017**, *5*, 30–39. [CrossRef]
70. Ihsan, M.; Somantri, L.; Sugito, N.T.; Himayah, S.; Affriani, A.R. The Comparison of Stage and Result Processing of Photogrammetric Data Based on Online Cloud Processing. In Proceedings of the IGEOS International Geography Seminar, IOP Conference Series: Earth and Environmental Science, Tanjong Malim, Malaysia, 3–4 December 2018.
71. Firdaus, M.I.; Rau, J.Y. Comparisons of the three-dimensional model reconstructed using MicMac, PIX4D mapper and Photoscan Pro. In Proceedings of the 38th Asian Conference on Remote Sensing-Space Applications: Touching Human Lives 2017, New Delhi, India, 23–27 October 2017.
72. Jugie, M.; Gob, F.; Virmoux, C.; Brunstein, D.; Tamisier, V.; Le Coeur, C.; Grancher, D. Characterizing and quantifying the discontinuous bank erosion of a small low energy river using Structure-from-Motion Photogrammetry and erosion pins. *J. Hydrol.* **2018**, *563*, 418–434. [CrossRef]
73. Simon, A.; Curini, A.; Darby, S.; Langendoen, E. Streambank mechanics and the role of bank and near-bank processes in incised channels. In *Incised River Channels*; Darby, S., Simon, A., Eds.; John Wiley: London, UK, 1999; pp. 123–152.
74. Hooke, J.M. Magnitude and distribution of rates of riverbank erosion. *Earth Surf. Process Landf.* **1979**, *5*, 143–157. [CrossRef]
75. Gkiatas, G.T.; Koutalakis, P.D.; Kasapidis, I.K.; Iakovoglou, V.; Zaimes, G.N. Monitoring and Quantifying the Fluvio-Geomorphological Changes in a Torrent Channel Using Images from Unmanned Aerial Vehicles. *Hydrology* **2022**, *9*, 184. [CrossRef]
76. Lopac, N.; Jurdana, E.; Brnelic, A.; Krljan, T. Application of Laser Systems for Detection and Ranging in the Modern Road Transportation and Maritime Sector. *Sensors* **2022**, *22*, 5946. [CrossRef]
77. Liang, X.; Kankare, V.; Hyyppä, J.; Wang, Y.; Kukko, A.; Haggrén, H.; Yu, X.; Kaartinen, H.; Jaakkola, A.; Guan, F.; et al. Terrestrial laser scanning in forest inventories. *ISPRS J. Photogramm. Remote Sens.* **2016**, *115*, 63–77. [CrossRef]
78. Wenzel, K.; Rothermel, M.; Fritsch, D.; Haala, N. Image acquisition and model selection for multi-view stereo. *Int. Arch. Photogramm. Remote Sens. Spat. Inf. Sci.* **2013**, *40*, 251–258. [CrossRef]
79. Diaconu, D.C.; Koutalakis, P.D.; Gkiatas, G.T.; Dascalu, G.V.; Zaimes, G.N. River Sand and Gravel Mining Monitoring Using Remote Sensing and UAVs. *Sustainability* **2023**, *15*, 1944. [CrossRef]
80. Zhao, Q.; Yu, L.; Du, Z.; Peng, D.; Hao, P.; Zhang, Y.; Gong, P. An overview of the applications of earth observation satellite data: Impacts and future trends. *Remote Sens.* **2022**, *14*, 1863. [CrossRef]
81. Ouma, Y.O. Advancements in medium and high resolution Earth observation for land-surface imaging: Evolutions, future trends and contributions to sustainable development. *Adv. Space Res.* **2016**, *57*, 110–126. [CrossRef]
82. Smith, M.J.; Pain, C.F. Applications of remote sensing in geomorphology. *Prog. Phys. Geogr.* **2009**, *33*, 568–582. [CrossRef]

83. Boothroyd, R.J.; Williams, R.D.; Hoey, T.B.; Barrett, B.; Prasojo, O.A. Applications of Google Earth Engine in fluvial geomorphology for detecting river channel change. *Wiley Interdiscip. Rev. Water* **2021**, *8*, e21496. [CrossRef]
84. Ablat, X.; Liu, G.; Liu, Q.; Huang, C. Using MODIS-NDVI time series to quantify the vegetation responses to river hydro-geomorphology in the wandering river floodplain in an arid region. *Water* **2021**, *13*, 2269. [CrossRef]
85. Ouyang, W.; Hao, F.; Skidmore, A.K.; Toxopeus, A.G. Soil erosion and sediment yield and their relationships with vegetation cover in upper stream of the Yellow River. *Sci. Total Environ.* **2010**, *409*, 396–403. [CrossRef] [PubMed]
86. Williams, F.; Moore, P.; Isenhart, T.; Tomer, M. Automated measurement of eroding streambank volume from high-resolution aerial imagery and terrain analysis. *Geomorphology* **2020**, *367*, 107313. [CrossRef]
87. Bannari, A.; Kadhem, G.; El-Battay, A.; Hameid, N.A.; Rouai, M. Assessment of land erosion and sediment accumulation caused by runoff after a flash-flooding storm using topographic profiles and spectral indices. *Adv. Remote Sens.* **2016**, *5*, 315–354. [CrossRef]
88. Tha, T.; Piman, T.; Bhatpuria, D.; Ruangrassamee, P. Assessment of riverbank erosion hotspots along the mekong river in cambodia using remote sensing and hazard exposure mapping. *Water* **2022**, *14*, 1981. [CrossRef]
89. Xu, H. Modification of normalised difference water index (NDWI) to enhance open water features in remotely sensed imagery. *Int. J. Remote Sens.* **2006**, *27*, 3025–3033. [CrossRef]
90. Laonamsai, J.; Julphunthong, P.; Saprathet, T.; Kimmany, B.; Ganchanasuragit, T.; Chomcheawchan, P.; Tomun, N. Utilizing NDWI, MNDWI, SAVI, WRI, and AWEI for Estimating Erosion and Deposition in Ping River in Thailand. *Hydrology* **2023**, *10*, 70. [CrossRef]
91. Benda, L.E.E.; Poff, N.L.; Miller, D.; Dunne, T.; Reeves, G.; Pess, G.; Pollock, M. The network dynamics hypothesis: How channel networks structure riverine habitats. *BioScience* **2004**, *54*, 413–427. [CrossRef]
92. Vrieling, A. *Mapping Erosion from Space*; Wageningen University and Research: Wageningen, The Netherlands, 2007.
93. Desprats, J.F.; Raclot, D.; Rousseau, M.; Cerdan, O.; Garcin, M.L.; Le Bissonnais, Y.; Ben Slimane, A.; Fouché, J.; Monfort-Climent, D. Mapping linear erosion features using high and very high resolution satellite imagery. *Land Degrad. Dev.* **2013**, *24*, 22–32. [CrossRef]
94. Vrieling, A.; de Jong, S.M.; Sterk, G.; Rodrigues, S.C. Timing of erosion and satellite data: A multi-resolution approach to soil erosion risk mapping. *Int. J. Appl. Earth Obs. Geoinf.* **2008**, *10*, 267–281. [CrossRef]
95. Saadat, H.; Adamowski, J.; Tayefi, V.; Namdar, M.; Sharifi, F.; Ale-Ebrahim, S. A new approach for regional scale interrill and rill erosion intensity mapping using brightness index assessments from medium resolution satellite images. *Catena* **2014**, *113*, 306–313. [CrossRef]
96. Phinzi, K.; Holb, I.; Szabó, S. Mapping permanent gullies in an agricultural area using satellite images: Efficacy of machine learning algorithms. *Agronomy* **2021**, *11*, 333. [CrossRef]
97. Hamada, Y.; O'Connor, B.L.; Orr, A.B.; Wuthrich, K.K. Mapping ephemeral stream networks in desert environments using very-high-spatial-resolution multispectral remote sensing. *J. Arid. Environ.* **2016**, *130*, 40–48. [CrossRef]
98. Liu, G.; Zheng, F.; Wilson, G.V.; Xu, X.; Liu, C. Three decades of ephemeral gully erosion studies. *Soil Tillage Res.* **2021**, *212*, 105046. [CrossRef]
99. Fiorucci, F.; Ardizzone, F.; Rossi, M.; Torri, D. The use of stereoscopic satellite images to map rills and ephemeral gullies. *Remote Sens.* **2015**, *7*, 14151–14178. [CrossRef]
100. Jacobsen, K. Which Satellite Image should be used for Mapping. *ISPRS Ann. Photogramm. Remote Sens. Spat. Inf. Sci.* **2023**, *10*, 827–834. [CrossRef]
101. Petitjean, F.; Inglada, J.; Gancarski, P. Assessing the quality of temporal high-resolution classifications with low-resolution satellite image time series. *Int. J. Remote Sens.* **2014**, *35*, 2693–2712. [CrossRef]
102. Stroosnijder, L. Measurement of erosion: Is it possible? *Catena* **2005**, *64*, 162–173. [CrossRef]
103. Tmušić, G.; Manfreda, S.; Aasen, H.; James, M.R.; Gonçalves, G.; Ben-Dor, E.; Brook, A.; Polinova, M.; Arranz, J.J.; János Mészáros, K.; et al. Current practices in UAS-based environmental monitoring. *Remote Sens.* **2020**, *12*, 1001. [CrossRef]
104. McCabe, M.F.; Rodell, M.; Alsdorf, D.E.; Miralles, D.G.; Uijlenhoet, R.; Wagner, W.; Lucieer, A.; Houborg, R.; Verhoest, N.E.C.; Franz, T.E.; et al. The future of Earth observation in hydrology. *Hydrol. Earth Syst. Sci.* **2017**, *21*, 3879–3914. [CrossRef]
105. Meinen, B.U.; Robinson, D.T. Streambank topography: An accuracy assessment of UAV-based and traditional 3D reconstructions. *Int. J. Remote Sens.* **2020**, *41*, 1–18. [CrossRef]
106. García-Ruiz, J.M.; Nadal-Romero, E.; Lana-Renault, N.; Beguería, S. Erosion in Mediterranean landscapes: Changes and future challenges. *Geomorphology* **2013**, *198*, 20–36. [CrossRef]
107. Zaimes, G.N.; Schultz, R.C.; Isenhart, T.M. Stream bank erosion adjacent to riparian forest buffers, row-crop fields, and continuously-grazed pastures along Bear Creek in central Iowa. *J. Soil Water Conserv.* **2004**, *59*, 19–27.
108. Reichenbach, P.; Busca, C.; Mondini, A.C.; Rossi, M. The Influence of Land Use Change on Landslide Susceptibility Zonation: The Briga Catchment Test Site (Messina, Italy). *Environ. Manag.* **2014**, *54*, 1372–1384. [CrossRef]
109. Heede, B.H. Deteriorated watersheds can be restored: A case study. *J. Environ. Manag.* **1979**, *3*, 271–281. [CrossRef]
110. Knevels, R.; Brenning, A.; Gingrich, S.; Heiss, G.; Lechner, T.; Leopold, P.; Plutzar, C.; Proske, H.; Petschko, H. Towards the use of land use legacies in landslide modeling: Current challenges and future perspectives in an austrian case study. *Land* **2021**, *10*, 954. [CrossRef]

111. Tsanis, I.K.; Seiradakis, K.D.; Sarchani, S.; Panagea, I.S.; Alexakis, D.D.; Koutroulis, A.G. The Impact of Soil-Improving Cropping Practices on Erosion Rates: A Stakeholder-Oriented Field Experiment Assessment. *Land* **2021**, *10*, 964. [CrossRef]
112. Fan, L.; Powrie, W.; Smethurst, J.; Atkinson, P.M.; Einstein, H. The effect of short ground vegetation on terrestrial laser scans at a local scale. *ISPRS J. Photogramm. Remote Sens.* **2014**, *95*, 42–52. [CrossRef]
113. Vázquez-Tarrío, D.; Ruiz-Villanueva, V.; Garrote, L.; Benito, G.; Calle, M.; Lucía, A.; Díez-Herrero, A. Effects of sediment transport on flood hazards: Lessons learned and remaining challenges. *Geomorphology* **2024**, *446*, 108976. [CrossRef]
114. Petalas, C.P.; Moutsopoulos, K.N. Hydrogeologic behavior of a complex and mature karst aquifer system under drought condition. *Environ. Process* **2019**, *6*, 643–671. [CrossRef]
115. Guan, M.; Wright, N.G.; Sleigh, P.A. Multiple effects of sediment transport and geomorphic processes within flood events: Modelling and understanding. *Int. J. Sediment Res.* **2015**, *30*, 371–381. [CrossRef]
116. Owens, P.N. Soil erosion and sediment dynamics in the Anthropocene: A review of human impacts during a period of rapid global environmental change. *J. Soils Sediments* **2020**, *20*, 4115–4143. [CrossRef]
117. Lespez, L. Geomorphic responses to long-term land use changes in Eastern Macedonia (Greece). *Catena* **2003**, *51*, 181–208. [CrossRef]
118. Walsh, K.; Berger, J.F.; Roberts, C.N.; Vanniere, B.; Ghilardi, M.; Brown, A.G.; Woodbridge, J.; Lespez, L.; Estrany, J.; Glais, A.; et al. Holocene demographic fluctuations, climate and erosion in the Mediterranean: A meta data-analysis. *Holocene* **2019**, *29*, 864–885. [CrossRef]
119. Woodget, A.S.; Austrums, R.; Maddock, I.P.; Habit, E. Drones and digital photogrammetry: From classifications to continuums for monitoring river habitat and hydromorphology. *Wiley Interdiscip. Rev. Water* **2017**, *4*, e1222. [CrossRef]

land

MDPI

Article

Assessment of the Erosion and Outflow Intensity in the Rif Region under Different Land Use and Land Cover Scenarios

Abdessalam Ouallali [1,2], Shuraik Kader [3,4,*], Youssef Bammou [5], Mourad Aqnouy [6], Said Courba [1], Mohamed Beroho [7], Hamza Briak [8], Velibor Spalevic [9], Alban Kuriqi [10,11,*] and Artan Hysa [12]

1 Process Engineering and Environment Laboratory, Faculty of Sciences and Techniques of Mohammedia, Hassan II University of Casablanca, BP 146, Mohammedia 28806, Morocco; abdessalam.ouallali@univh2c.ma (A.O.); said_courba@um5.ac.ma (S.C.)
2 Laboratory of Geosciences, Water and Environment, Faculty of Sciences, Mohammed V University in Rabat, BP. 1014 R.P., Rabat 10000, Morocco
3 School of Engineering and Built Environment, Griffith University, Nathan, QLD 4111, Australia
4 Green Infrastructure Research Labs (GIRLS), Cities Research Institute, Griffith University, Gold Coast, QLD 4215, Australia
5 Geo-Resources, Geo-Environment and Civil Engineering Laboratory, Faculty of Science and Techniques of Marrakech, Cadi Ayyad University, Marrakech 40000, Morocco; youssef.bammou@ced.uca.ma
6 Applied Geology Research Laboratory, Faculty of Sciences and Techniques of Errachidia, Moulay Ismail University of Meknes, Errachidia 52000, Morocco; m.aqnouy@umi.ac.ma
7 Georisk & Georesources (G2R) Research Team, Faculty of Sciences and Techniques of Tangier (FST), Abdelmalek Essaadi University (UAE), Tangier 90000, Morocco; mohamed.beroho@etu.uae.ac.ma
8 Center of Excellence for Soil and Fertilizer Research in Africa (CESFRA), Mohammed VI Polytechnic University (UM6P), 660 Lot, Ben Guerir 43150, Morocco; hamza.briak@um6p.ma
9 Biotechnical Faculty, University of Montenegro, 81000 Podgorica, Montenegro; velibor.spalevic@gmail.com or velibors@ucg.ac.me
10 CERIS, Instituto Superior Técnico, University of Lisbon, 1649-004 Lisbon, Portugal
11 Civil Engineering Department, University for Business and Technology, 10000 Pristina, Kosovo
12 Faculty of Architecture and Engineering, Epoka University, 1032 Tirana, Albania; ahysa@epoka.edu.al or artan.hysa@tum.de
* Correspondence: shuraik10@gmail.com or shuraik.mohamedabdulkader@griffithuni.edu.au (S.K.); alban.kuriqi@tecnico.ulisboa.pt (A.K.); Tel.: +61-4937-508-65 (S.K.); +351-918-014-510 (A.K.)

Abstract: The port of Tangier Med is essential due to its strategic location, as it is an important trading center linking Europe, North America, and Africa. However, the increased rates of downstream sediment transportation put pressure on the sustainable future of the port. Thus, assessing the existing erosion rates and future improvement scenarios is imperative for planning sustainable management at the catchment level. We utilize the Erosion Potential Model (EPM) combined with the Intensity of Erosion and Outflow (IntErO) algorithm to assess the erosion and outflow intensity and to distinguish the sediment-producing areas in the R'mel watershed. The port's proximity at the bottom of the slope opposite the R'mel Dam is relevant in this context. Initial results show an average erosion rate of 13 t/ha/year. Quarry operations were identified as the primary sediment source, as indicated by the factors contributing to erosion. The qualitative PAP/RAC (Priority Actions Program/Regional Activity Center) model was used to assess the development trends in the watershed, confirming a clear tendency toward irreversible degradation in the quarry areas. Considering that the mined carbonate lithology represents 23.77% of the total area of the catchment, the situation in the region could deteriorate if quarry operations continue. The simulation of quarry rehabilitation scenarios through land use and land cover change (LULC) with IntErO shows that reforestation of quarries can significantly reduce erosion rates (4.78 t/ha/year) compared to their conversion to agricultural land. This study underlines the effectiveness of IntErO, based on the EPM model, in quickly and effectively mapping and quantifying water erosion.

Keywords: Intensity of Erosion and Outflow (IntErO) algorithm; Erosion Potential Model (EPM); quarry operations; reforestation; R'mel watershed

1. Introduction

The northern region of Morocco, geographically known as the Rif, is highly vulnerable to water erosion risk. Numerous recent and long-term studies have highlighted the high erosion rates in the Rif watersheds [1,2]. This increased susceptibility to erosion is mainly due to the relatively young age of the lithological formations, which consist primarily of friable material dominated by marl and clay [3]. The rugged topography and steep slopes that characterize the Rif area further facilitate the detachment and mobilization of sediments [4]. The adverse effects of erosion are particularly noticeable regarding water and soil resources, as the storage capacity of the hydraulic infrastructure has decreased significantly in recent years. Soil resources are exposed to the leaching of organic and mineral matter due to erosion [5,6], which leads to progressive soil degradation and threatens the food security of all living beings, including humans [7,8].

The scientific community and public and private institutions have been intensively involved in studying water erosion and erosion control for many years. The aim is to improve the understanding of this phenomenon and to develop appropriate erosion control measures that would ensure the sustainability of water and soil resources for as long as possible. As a result, numerous quantitative and qualitative models have been developed over the years. For example, some models are based on radioactive tracers such as Caesium-137 (137Cs) [9,10], Pb Lead-210 (210Pbex) [11], and Beryllium-7 (7B) [12,13]. These techniques have been widely criticized, mainly because of the high costs associated with laboratory analysis, the short half-life of these isotopes [14,15], and their inability to account for specific parameters that control the erosion process [16].

In addition, methods based on hydrological modeling have been developed, with the Soil and Water Assessment Tool (SWAT) model being one of the most widely used worldwide [17,18]. This model facilitates the assessment of sediment and water supply with optimal sensitivity parameters, and its main strength lies in ensuring the connectivity of hydrological systems within catchments. However, its application in Morocco is limited by the need for data measured by hydrometric stations over relatively long periods [19,20]. Other methods are based on a geographic information system (GIS) and remote sensing, such as the Revised Universal Soil Loss Equation (RUSLE) [21], Modified Universal Soil Loss Equation (MUSLE) [22], RUSLE-3D [23], and the Erosion Potential Method that is known as EPM [24] and which is a frequently used empirical model across the Balkan area, North Africa, and Europe along with the Middle East [25]. These models differ in terms of the type of data used.

EPM is one of the most used models by researchers as it considers various factors of water erosion [26–28]. It also assesses the effects of erosion forms and lithological substrates when evaluating the erosion process [29]. It has been integrated into an intensity of Error and outflow algorithm called IntErO (Intensity of Error and outflow) [30]. The integration of EPM into IntErO has facilitated the execution and application of EPM and has led to the international dissemination of the EPM method. However, in Morocco, the application of EPM still needs to be further improved [29,31]. This limitation can be overcome with IntErO, as it allows a fast and practical simulation of the physical catchment parameters. Previous studies have been conducted in the Arbaa Ayacha watershed using IntErO to assess erosion potential and show the influence of geomorphologic factors on soil erosion [29,30]. The successful implementation of previous studies has shown great potential for applying IntErO for advanced lithological applications in the Rif region.

IntErO is also a practical tool for qualitative erosion assessment. Previous studies have shown the importance of qualitative and holistic assessment methods for erosion prediction in risk mitigation measures in North African landscapes [32,33]. The qualitative method differs from the quantitative method in that it assigns weights to geographical units corresponding to soil erosion intensity [34]. The qualitative and quantitative models consider the same erosion factors, such as land use and land cover, soil type, slope gradient, and precipitation [35]. However, in the qualitative approach, each erosion control factor is given a specific weight depending on the researchers' assessment or understanding of the local erosion

processes and the importance of each parameter in controlling the phenomenon [35–37]. The PAP/RAC method [38] is one of the most used qualitative approaches in Morocco. The main objective of this method is the management of the Mediterranean coastal areas and the evaluation of the condition of the soil surfaces concerning their susceptibility to erosion. The PAP/RAC enables the visualization of erosion conditions, the analysis of water erosion relationships, and the assessment of risk trends in different catchment sizes [32].

An essential objective of this study is to adapt the IntErO model to the environmental conditions of the Moroccan Rif region to study erosion and runoff. The choice of the study area is not arbitrary but essential for several reasons. First, a reservoir in the downstream watershed of the R'mel serves as the primary source of drinking water for the city of Kser Essghir. Directly opposite the reservoir is the most critical national coastal structure, the international port of Tangier Med [39]. This vital infrastructure must be protected from flooding and the damaging effects of water erosion. In addition, the basin's soils must be safeguarded through land management, especially as agriculture is the most important source of economic activity for the local population. In addition, the assessment of the current state of the R'mel catchment shows that land use has changed significantly and rapidly over time. The anthropogenic influence in this catchment is particularly pronounced and can be seen above all in the extensive quarrying activities concentrated in the central region of the catchment. The economies of many Mediterranean countries have benefited from the extraction of raw materials. Unfortunately, many quarries in Mediterranean countries caused severe damage to the environment and landscape [31,40,41]. Numerous studies have demonstrated the direct impact of operating or abandoned quarries on soil, water quality, and siltation of dams [42,43]. Therefore, soil conservation practices must be implemented to ensure soil protection and reduce the direct impact of the quarry on the ecosystem. Among these practices, the transformation of quarries to forests or vegetated areas, commonly known as afforestation, is of great scientific importance in the efforts to combat climate change, preserve biodiversity, stabilize soils, prevent erosion, and protect reservoirs as natural filters that retain sediments and pollutants before they enter the reservoirs [44]. In addition, reforestation helps to stabilize soils by strengthening their structure and water retention capacity, thus reducing the risk of erosion. Soil conservation is essential to maintain the fertility of adjacent agricultural land and prevent soil degradation.

The goal of this study is to determine the rate of erosion and the amount of sediment moving downstream of the basin using an efficient but not widely used model across the country. Sediment sources were identified and analyzed with respect to land use change scenarios in the region. Two scenarios regarding quarry surfaces were simulated utilizing the IntErO tool to assess the reliability of quarry rehabilitation and its impact on reducing erosion rates and sediment yield to the reservoir. Finally, the influence of erosion control factors on the erosion process was evaluated by incorporating qualitative aspects to determine the development trends of erosion in the region.

This study demonstrates the importance of quarry rehabilitation for environmental protection and ecosystem sustainability, highlighting the priority areas where erosion control measures are needed. Proactively managing these issues is essential to protect water and soil resources while maintaining the integrity of ecosystems in the region.

2. Materials and Methods

2.1. Study Area

The water catchment area of the R'mel lies in the northern Rif region of Morocco. It belongs to the province of Ksar Essghir, located in the Tangier-Tetouan Elhoceima region. The watershed covers an area of 34 km^2. Its altitude ranges from 12 to 572 m (Figure 1a).

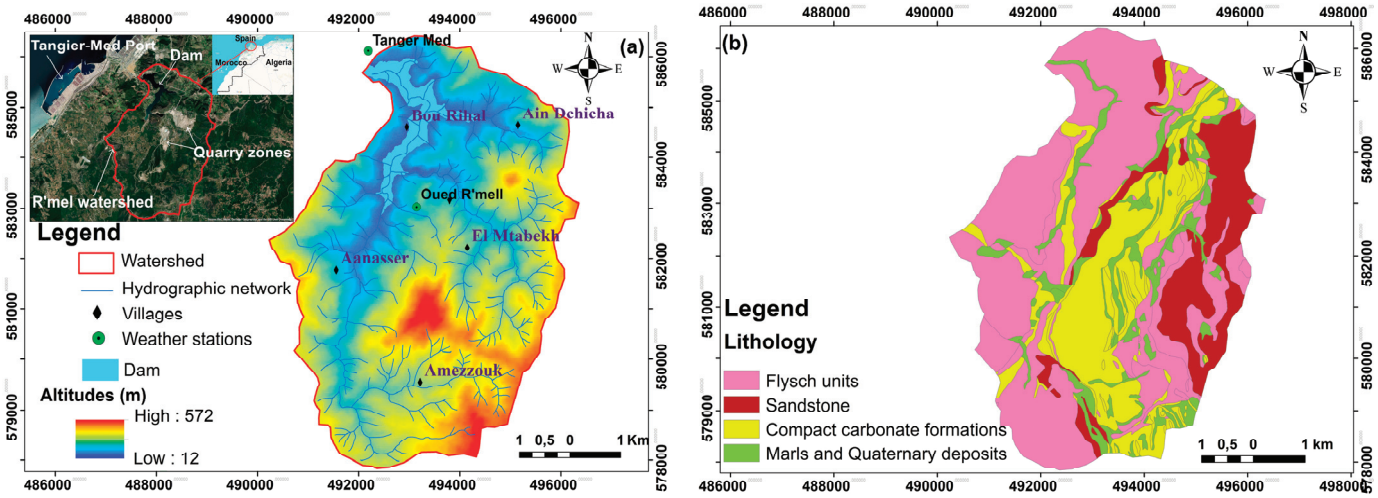

Figure 1. Geographical location of the (**a**) R'mel watershed and the Tanger Med port in Northern Morocco, (**b**) lithological map of the study area.

The topographic data for this watershed were extracted from the ASTER digital terrain model (DTM) downloaded from the Earth Explorer website (https://earthexplorer.usgs.gov (accessed on 27 August 2023)). In the central and upstream parts of the watershed, the two highest points are located at the villages of Aanasser and Amezzouk. However, the lowest elevations are downstream of the watershed where the R'mel Dam was built. This dam collects water from the surrounding slopes and surface runoff through the hydrographic network.

The study area has a Mediterranean sub-humid climate with an average annual precipitation of about 820.3 mm, calculated based on a 12-year precipitation data series measured at the meteorological station of the catchment area. Land use and land cover (LULC) data were obtained using geospatial remote sensing by processing a Landsat OLI8 image downloaded from the United States Geological Survey (USGS) website (https://www.usgs.gov/ (accessed on 27 August 2023)) and processed with ENVI software version 5.5.2 [45]. This software facilitated the supervised classification of the different LULC classes within the watershed, with in-depth field checks performed for specific classes. The resulting map illustrates that most of the watershed is covered by dense scrubland, followed by open scrubland, which is detailed in the Results and Discussion section. On the other hand, dense natural forests are limited to the southern and northeastern parts of the watershed. Arable land is generally located in the central part of the watershed and near the villages and accounts for 22.7% of the total watershed area. The watershed's unvegetated areas include rocks, bare land, and quarry areas (Table 1).

Table 1. Percentage of land use land cover (LULC) classes in the study area.

LULC	Area (km^2)	%	LULC	Area (km^2)	%
Dam	1.1	3.1	Dense forest	0.3	0.9
Quarrying areas	1.4	4.2	Moderately dense forest	1.1	3.1
Bare lands	0.5	1.5	Clear forest on dense scrublands	1.5	4.5
Rock outcrop	1.5	4.4	Dense reforestation	1.1	3.3
Agricultural land	4.8	13.9	Clear reforestation	0.04	0.1
Association: agricultural and built land	3.0	8.8	Dense scrubland	8.9	25.8
			Clear scrubland	91	26.4

The lithological data of the basin were taken from the geological map at a scale of 1:50,000, inspired by successful previous studies with aligning research objectives [46,47]. The basin has a variety of lithological formations (Figure 1b). The flysch formations, mainly located in the western part of the basin, cover about 49.77% of the basin's total area. In the

eastern part of the basin, sandstone formations dominate, covering approximately 15.25% of the site. Marl and quaternary deposits are mainly found on the banks of the gorge and make up 11.21% of the basin's area. Finally, compact carbonate rock outcrops in the central part of the basin make up about 23.77% of the total area. This carbonate formation was mined on a large scale, mainly for the construction industry.

We engaged a specialist pedologist from our authors' team, who conducted a comprehensive field visit in collaboration with our team. Drawing on the insights gained from this fieldwork and in conjunction with the data obtained from the prior geological survey, our team, comprising specialist pedologists and geologists, derived numerical values needed for the IntErO calculations in relation to the soils of the river basin. These values were then instrumental in the evaluation of the soils within the basin.

2.2. Intensity of Erosion and Outflow Assessment

2.2.1. IntErO Model Description and Implementation

EPM models [24] use multiple components to obtain a global estimate of soil loss. Each factor quantifies one or more processes and their relationships [30,39]. EPM quantitatively estimates erosion intensity, sediment production, and sediment transport [48]. Most models are used to predict long-term annual rates of soil loss to crops due to sheet erosion, gully processes, sediment transport, rill erosion, and deposition on the soil surface. The EPM model predicts the extent of erosion due to sheet or gully erosion and accounts for additional soil losses due to gully erosion, wind erosion, or soil erosion [49,50]. The IntErO model of Spalevic [24,51,52] integrates Erosion Potential Model (EPM) of Gavrilovic [24] into its algorithm. It is an improvement over the previously used river basin and area/distance measurement programs [29,53]. The method is useful and can handle large amounts of data. It requires only 25 input parameters to generate 22 output parameters (Table 2).

The IntErO model program package of Spalevic [54] takes six elements into account: soil type and lithology are represented by the coefficient Y, land use data represents Xa, temperature is linked to the parameter t, and erosion patterns are represented by the coefficient Q [51]. These coefficients must be thoroughly evaluated in various processes, including data collection, fitting, analysis, and integration into the model equations. The annual volume of sediments 'Wyear' eroded because of soil erosion was calculated using the following equations, Equations (1) and (2).

$$\mathrm{Wyear} = \mathrm{T} \times \mathrm{Hyear} \times \pi \times \sqrt{\mathrm{Z}^3} \times \mathrm{F} \quad (1)$$

where F is the watershed area (km^2), and T is the temperature coefficient derived as follows:

$$\mathrm{T} = \sqrt{(\frac{t}{10} + 0.1)} \quad (2)$$

Hyear is the yearly average rainfall between 2007 and 2022 in mm. The Z coefficient, which can be categorized according to the degree of erosion (Table 3), represents the strength of the erosion process, and is calculated as follows in Equation (3):

$$\mathrm{Z} = \mathrm{Xa} \times \mathrm{Y} \times \left(\varnothing + \sqrt{\mathrm{Isr}}\right) \quad (3)$$

The variable (Xa) represents the degree of soil protection. Xa considers land use and the extent of vegetation cover. With values close to 0, indicating low soil protection, and values around 1, indicating strong soil protection, this coefficient typically varies between 0.05 and 1 [20,55,56]. The Xa values were obtained by assigning the classes suggested by the EPM technique and comparing the LULC map of the watershed with previous studies [51,57].

Table 2. Input data used for the IntErO model in the R'mel watershed.

Parameters	Symbols	Values	Units
The watershed's length	F	34.4	km^2
The length of the main watercourse	O	25.7	km
The quickest path from the mouth to the fountainhead	Lv	12.3	km
The entire length of the primary watercourse, including tributaries of classes I and II	Lm	7.3	km
A set of parallel lines indicates the length of the river basin.	ΣL	110.1	km
The more significant portion of the river basin	Lb	9.3	km
The region of the shorter river basin	Fv	23	km^2
The watershed's length	Fm	11.4	km^2
Length of contour lines	Liz	50-100-150-200-250-300-350-400-450-500-550	km
The area between two adjacent contour lines	fiz	0.3-2.23-3.9-4.32-5.8-6.44-5.06-3.13-1.84-0.91-0.38-0.09	km
The first contour line's altitude	h0	50	m
Equidistance	Δh	50	m
The lowest elevation in the river basin	Hmin	12	m
The highest elevation in the river basin	Hmax	572	m
The portion of the river basin comprises a highly porous rock product (limestone, sand, and gravel).	fp	0.14	
The portion of the river basin comprises moderately permeable rocks (slates, marls, and brownstone).	fpp	0.18	
The portion of the river basin comprises low-permeability rocks (thick clay, compact eruptive).	fo	0.68	
The area of the river basin is covered with forests	fš	0.64	
The portion of the river basin covered in grasslands, meadows, and orchards	ft	0	
The section of the river basin is bare land, plowland, or ground devoid of grass vegetation.	fg	0.36	
The torrential rain's volume	hb	61.13	mm
Incidence	Up	100	years
Annual average air temperature	t0	17.5	°C
Annual precipitation average	Hgod	677.02	mm
Soil product categories and associated types	Y	1.1	
River basin planning, river basin planning coefficient	Xa	0.53	
Numeral equivalents of visible and exposed erosion processes	φ	0.32	

Table 3. Ranges of the Z coefficient in the Erosion Potential Method (EPM) [24,54].

Erosion Intensity	Erosion Type	Z	Mean Value Z
Excessive	Deep	1.51	1.25
	Mixed	1.21–1.50	
	Surface	1.01–1.20	
Strong	Deep	0.91–1	0.85
	Mixed	0.81–0.90	
	Surface	0.71–0.80	
Medium	Deep	0.61–0.70	0.55
	Mixed	0.51–0.60	
	Surface	0.41–0.50	
Low	Deep	0.31–0.40	0.3
	Mixed	0.25–0.30	
	Surface	0.20–0.24	
Very low	Deep	0.01–0.19	0.1
	Mixed		
	Surface		

The soil erodibility coefficient Y is a dimensionless factor that reflects the erosion resistance of the soil and depends on the pedological lithological characteristics of the basin [20]. The Y factor was evaluated in this study using lithological data from the study area. Values for each soil type were then assigned based on EPM recommendations and previous studies [20,55,56]. Values below 0.25 indicate moderate erodibility, while values above 2 indicate extremely erodible formations [56,58].

The coefficient φ is a one-dimensional component with values between 0.1 and 1. This parameter is related to active erosion and was calculated using the erosion pattern map of the R'mel basin. Values were then assigned to each erosion type using the recommendations of the previous studies [20,56,58]. Finally, the average percentage of basin slope Isr in the study area was calculated using DEM (DTM-ASTER-GDEM). Calculating the specific sediment production (*Gsp*) was undertaken in $m^3\ km^{-2}\ year^{-1}$ as some sediments are re-deposited in rivers or other catchments. This can be achieved using the following equation, Equation (4):

$$Gsp = Wyear \times Ru \tag{4}$$

This can be accomplished by multiplying the average yearly sediment production (Wyear) by an R coefficient (delivery ratio), Equation (5):

$$R = \frac{\sqrt{O \times D}}{0.25 \times (Lv + 10)} \tag{5}$$

The parameters O and D are given in kilometers, where O is the extent of the catchment area, D is the average height of the basin in the final section, and Lv is the length of the main river.

2.2.2. Land Cover Change Scenarios and Effect of Geomorphological Conditions

The investment directed toward implementing anti-erosion practices, along with their subsequent production, has the potential to yield satisfactory economic efficiency. This indicates that the allocation of resources to these measures can result in favorable returns, balancing both the financial aspect and the effectiveness of mitigating erosion-related challenges [59,60]. In this study, two scenarios were simulated in quarry areas using the IntErO algorithm to assess the reliability of quarry rehabilitation and its impact on erosion rates and sediment yield in the reservoir. This simulation involves utilizing the methodology outlined in Table 2 and Equations (1)–(5), incorporating alterations to the Xa coefficient within Equation (3). In the initial scenario, the land use and land cover (LULC)

category associated with quarries has been substituted with a vegetation zone. In contrast, quarries have been reclassified as cultivated land in the second scenario.

To analyze the effect of geomorphological conditions on the erosive process, we created an intersection between the individual erosion factors and the erosion rate map to illustrate the influence of crucial erosion variables on sediment formation. This link was created through a GIS process between the files in vector format. This method requires two vector layers for the slope factor: one for erosion classes and one for slope classes [29]. To create the low, medium, high, and excessive classes in the resulting EPM model map, we first divided the slope map into four categories: 0–15%, 15–30%, 30–45%, and above 45%. The two files were then overlaid using the ArcGIS 10.8 intersect command to determine the erosion rate for each slope class. To determine the proportion of low, moderate, high, and excessive erosion classes, we used a map showing the erosion rates for each slope class generated by this process. The contribution of each factor to sediment production was indicated using the same methods for other factors and maps illustrating lithological, land use, and erosion features [29,52]. The slope map and sediment production map classes are sliced from each map using the same ArcGIS 10.8 commands and tools.

2.3. Evolutionary Trends of Erosion in the Basin and Its Qualitative Assessment

Several organizations (UNEP, FAO, and DGCONA) have mapped and measured the erosion processes caused by rainfall in the Mediterranean regions [32]. The PAP/RAC approach was developed to analyze the sensitivity of water erosion [33,61]. It is based on the interrelationships and interdependence of water erosion risk variables. Specific procedures are required to map each element of the approach, primarily the processing, intersection, and analysis of the data sets.

Generally, the technique can be divided into three main steps. The first step is the predictive approach to assign values to water-eroding variables such as lithology and soil type, LULC, slope, and vegetation density. In this phase, a map of the erosive state is created (Figure 2), and the catchment is prioritized according to the degree of erosion. The second step is the descriptive stage based on a map of the erosion forms and patterns of the site and its erosion risk.

The third step is the integration phase, which is the culmination of the previous two processes. It overlays the map of erosion forms with the map of erosion conditions (Matrix 4 in Figure 2). An interactive map of water erosion is displayed. It helps to identify development trends in the catchment areas concerning erosion risk. Using a systematic approach, the PAP/RAC method examines the potential risk of soil erosion by emphasizing conservation measures and implementing effective erosion control methods. The PAP/RAC method for measuring soil erosion risk in Mediterranean regions includes the following steps:

- Data collection: The first step is to collect data on the many factors that influence the risk of soil erosion, including rainfall, soil type, lithology, LULC, and vegetation cover. This data can be collected through surveys, remote sensing, or existing databases.
- Data preparation involves digitizing and arranging the data obtained in a geographic information system (GIS) to process and prepare them for analysis.
- Erosion risk assessment: The next step is to assess the erosion risk by summarizing the information on the different aspects using a matrix technique. Under the matrix approach, each element is given a score based on how much it contributes to erosion risk. These scores are then added together to provide an overall erosion risk score for each area (Tables 4 and 5).

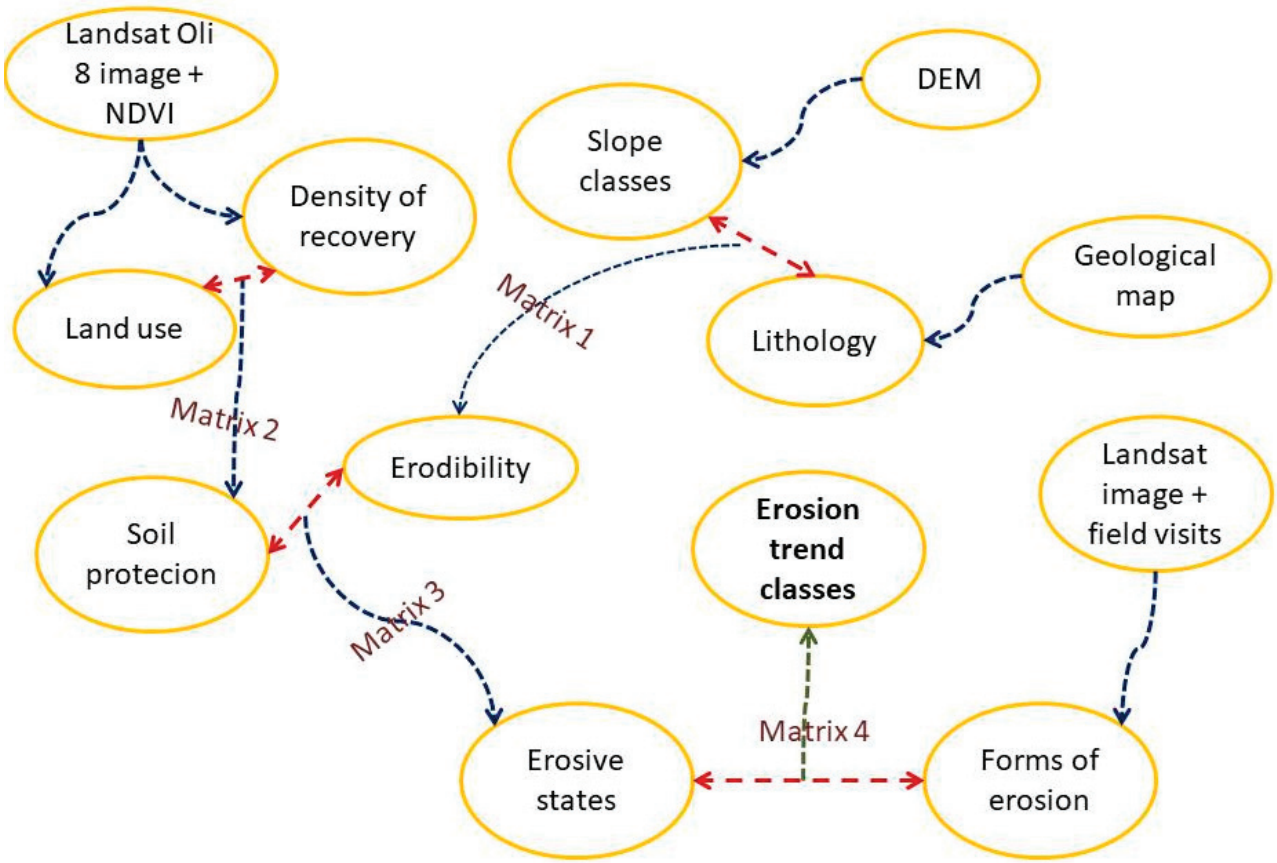

Figure 2. Methodology for assessing erosional trends in the basin using the PAP/RAC method [62].

Table 4. Matrices for assessing soil erodibility and soil protection degree.

	Lithofacies Classes					Density of Recovery				
Classes of Slope	**a-1**	**b-2**	**c-3**	**d-4**	**Land Use**	**1 (<25%)**	**2 (25–50%)**	**3 (50–75%)**	**4 (>75%)**	**5 (dam)**
1	1: EN	1: EN	1: EN	2: EB	1	2: M	1: A	1: A	1: A	0
2	1: EN	1: EN	2: EB	3: EM	2	3: B	2: M	1: A	1: A	0
3	2: EB	2: EB	3: EM	4: EA	3	4: MB	4: MB	3: B	2: M	0
4	3: EM	3: EM	4: EA	4: EA	4	4: MB	4: MB	3: B	2: M	0
5	4: EA	4: EA	5: EX	5: EX	5 (dam)	0	0	0	0	0
Matrix 1: Degrees of erodibility EX: Extreme, EA: High, EM: Medium, EB: Moderate, EN: Low						Matrix 2: Degree of protection of the soil MB: Very low, B: Low, M: Medium, A: High				

Table 5. Matrices for assessing erosive states and erosion trends.

	Erodibility Classes						Erosion Forms	
Soil Protection Classes	**1-EN**	**2-EB**	**3-EM**	**4-EA**	**5-EX**	**Erosive States**	**Minor Forms of Erosion (SP, L, D)**	**Major Forms of Erosion (M, C, Cx, Lx)**
1 (A)	1	1	1	2	2	1	1	3
2 (M)	1	1	2	3	4	2	1	3
3 (B)	1	2	3	4	4	3	2	4
4 (MB)	4	4	5	5	5	4	2	4
5 (Dam)	0	0	0	0	0	5	2	4
Matrix 3: Erosive states 5: Very High, 4: High, 3: Notable, 2: Low, 1: Very low							Matrix 4: Erosion trends (*): (1), (2), (3), (4)	

(*) 1. Erosion processes tend to stabilize, retreat, or limit their spatial expansion. 2: Erosion processes tend to extend or intensify locally. 3: Erosion processes have a typical tendency to expand or increase. 4: A general trend toward irreversible degradation.

- Erosion risk mapping uses erosion risk scores to show where there is a high risk of erosion. This allows you to prioritize protection measures and visualize the areas at risk of erosion.
- Selection of conservation measures: Appropriate soil conservation measures can be selected for each erosion-prone area based on the erosion risk mapping. These measures may include terracing, contour plowing, improved plant cover, soil management techniques, and engineering structures.
- Finally, the selected protective measures are implemented, monitored, and tested for their effectiveness in minimizing erosion risk.

3. Results and Discussion

3.1. Erosion Potential Assessment

The IntErO model calculates the sediment supply and the maximum discharge in the R'mel catchment area. Table 6 shows the results obtained after applying this model. According to the symmetry coefficient A (0.67), the catchment can experience large flood waves. The coefficient G of 3.20 indicates that the drainage network is very dense. The Isrvalue of 479.65% suggests the catchment has almost vertical slopes. The Z-value of the catchment area of 1.424 indicates that it is damage category I. The erosion process is excessive due to the type of erosion; in this case, it is mixed erosion. According to Gavrilovic, a watershed with a value of 1101.36 m^3/km^2 is classified as category III, which indicates moderate to severe surface erosion.

Table 6. Analysis of the current situation using IntErO.

Parameters	Symbols	Values	Units
The river basin shape coefficient.	A	0.41	
Watershed development coefficient.	m	0.59	
The average breadth of a river basin.	B	3.7	km
The river basin A's symmetry.	a	0.67	
The density of the basin's river network.	G	3.2	km/km^2
The tortuousness of the river basin.	K	1.68	
Average river basin elevation.	Hsr	255.19	m
The river basin's average elevation difference.	D	243.19	m
Decrease in the typical river basin.	Isr	479.65	%
The elevation of the river basin's local erosion base.	Hleb	560	m
Coefficient of the river basin relief's erosion energy.	Er	73.6	
Coefficient of permeability in the area.	S1	0.86	
Coefficient of the cover of vegetation.	S2	0.74	
Water retention in influx is presented analytically.	W	0.7704	m
Water flow's potential for energy during torrential downpours.	$2gDF^{½}$	405.14	m km s
Maximum outflow in the river basin.	Qmax	81.51	$m^3\ s^{-1}$
Coefficient of temperature.	T	1.36	
Coefficient of erosion in the river basins.	Z	1.424	
Erosion material produced in the river basin.	Wgod	169,137.6047	m^3/god
Coefficient for the retention of deposits.	Ru	0.224	
Actual losses in soil.	Ggod	37,886.82	m^3/god
Actual losses of soil per km^2.	$Ggod/km^2$	1101.36	m^3/km^2 god

The degree of soil protection is assessed using the parameter Xa. The values for the soil protection coefficient Xa range from 0.05 to 0.9. A significant part of the catchment area had to be adequately protected, as 35.69% of the area had values for Xa on bare soils and plowed fields above 0.8. Lower Xa values correspond to some units of old dense afforestation, dense scrubland, and dense deciduous forest, which account for 34.5% of the basin. This value shows that one-third of this catchment is developed, slightly reducing erosion. Degraded forests and scrubland represent mean values of Xa in the remaining catchment (29.61%). Using the erodibility coefficient Y, the IntErO model evaluates the erodibility of the soil. The soil type and the lithology influence the soil erodibility (Y).

The study region's lithological and pedological maps were classified according to the terminology of the IntErO program. The soils of this catchment have an average erodibility in 50% of the catchment, a high erodibility in 43.26%, and a very high erodibility in 6.74% of the catchment. The parameter φ in this model expresses how far the erosion forms extend. It is a numerical representation of an evident and exposed erosion process. The values assigned to this component by Gavrilovic [63] have been applied. At the same time, forests and permanent vegetation cover 56.84% of the surface, 32.6% of the basin is subject to surface erosion, 2.34% to erosion by creeks and gullies, and 8.22% to deep erosion.

The erosion rates determined with the EPM model integrated into the IntErO program are shown in Figure 3. The average sediment production is 1101.36 m^3/km^2/year (Figure 3a) or 13.22 t/ha/year (Figure 3b), with minimum and maximum values between 5 and 300 t/ha/year. This uniform conversion is intended to compare the results with erosion studies in the Moroccan Rif region. Most of these studies give the results in t/ha/year, while the EPM-IntErO models are not widely used in Morocco [20,64].

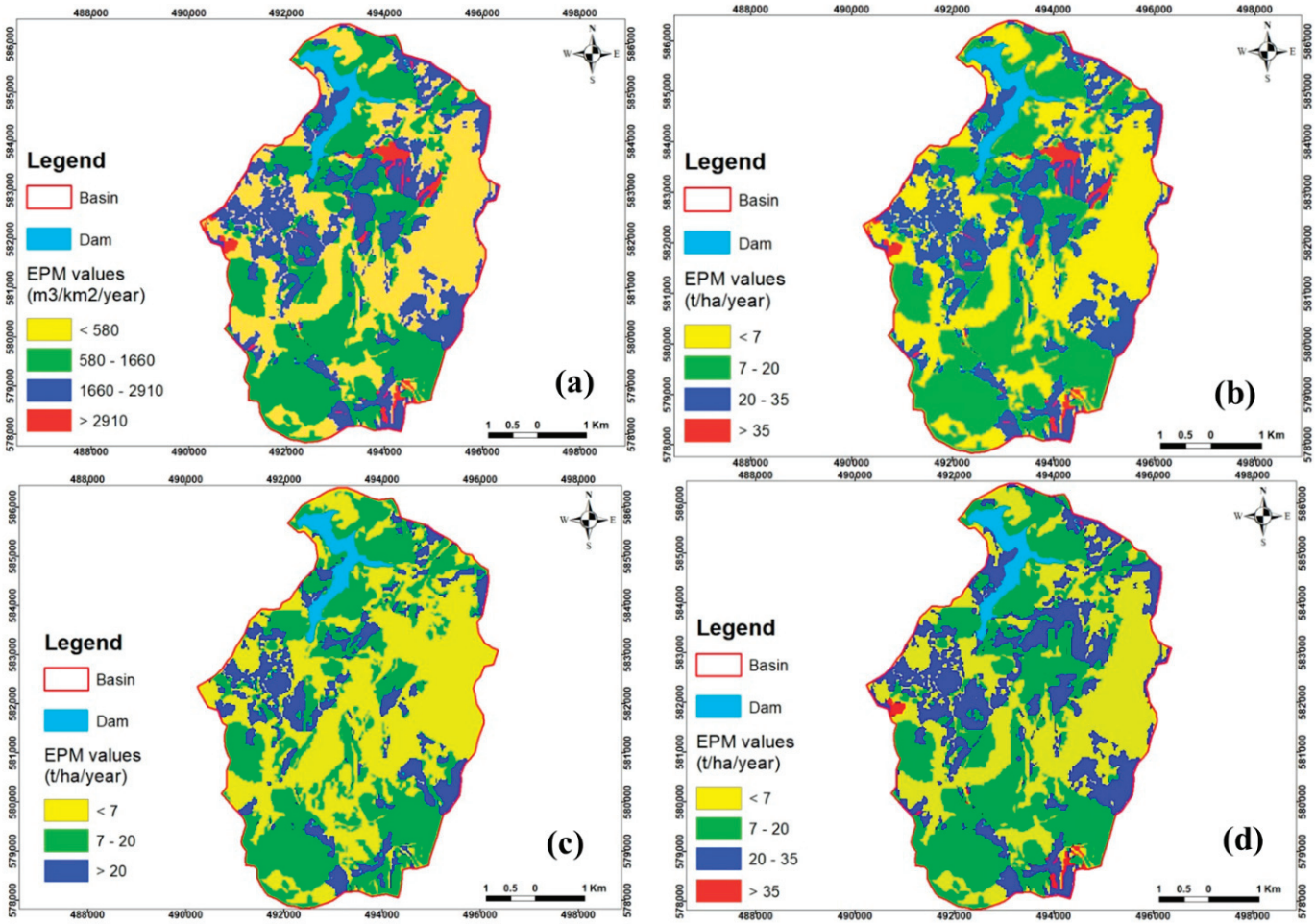

Figure 3. Erosion rates were obtained for the current situation in (**a**) m^3/km^2/year, (**b**) t/ha/year, (**c**) for reforestation in Scenario 1, (**d**) cropping and plowing in Scenario 2 Compared to other sections of the Moroccan Rif, the average erosion rate in the R'mel basin is low. For example, the average rate in the Nakhla catchment is 38.7 t/ha/year [65], while the RUSLE and SWAT models in the Arbaa Ayacha catchment showed 25.77 $tha^{-1}y^{-1}$ and 28.09 $tha^{-1}y^{-1}$, respectively [29]. Erosion in the Raouz catchment area is estimated at 26.6 $tha^{-1}y^{-1}$ using remote sensing [66] and 16.53 $tha^{-1}y^{-1}$ using the RUSLE model [67]. These differences are mainly explained by the characteristics of the catchment area and the numerous interventions and developments carried out in the R'mel catchment area to maintain the dam and the downstream port.

The LULC parameter plays an important role. Over 60% of the R'mel catchment is covered by land uses that limit erosion, including dense and moderately dense forests, scrubland, and afforested areas. Moreover, the lithological substrate of the basin is mainly composed of fractured and compact erosion-resistant rocks such as tight carbonate rocks, sandstones, and flysch. In contrast, only a tiny part of the basin contains friable lithologies like marls and fluvial deposits. Consequently, anthropogenic activities, such as quarrying, are assumed to be the leading cause of erosion rates and the source of sediments moving downstream from the basin. These results highlight the need to analyze the basin's physico-chemical characteristics and assess each parameter's impact and contribution to erosion rates.

3.2. Effect of Basin Geomorphological Conditions

Bare areas and quarries, mainly located in the central zone of the basin, are the leading cause of excessive erosion (Figure 4a). The dense vegetation largely contributes to the low sediment input (34%). Open scrublands and agricultural land are essential in developing moderate erosion processes [68,69]. These observations also become apparent when analyzing the impact of erosion forms on sediment production (Figure 4c). Indeed, the areas exploited by quarries have the highest percentage in the excessive erosion class. Conversely, the regions stabilized by dense vegetation and afforestation mitigate the spread of erosion processes and ensure the stability of a considerable part of the basin (30%).

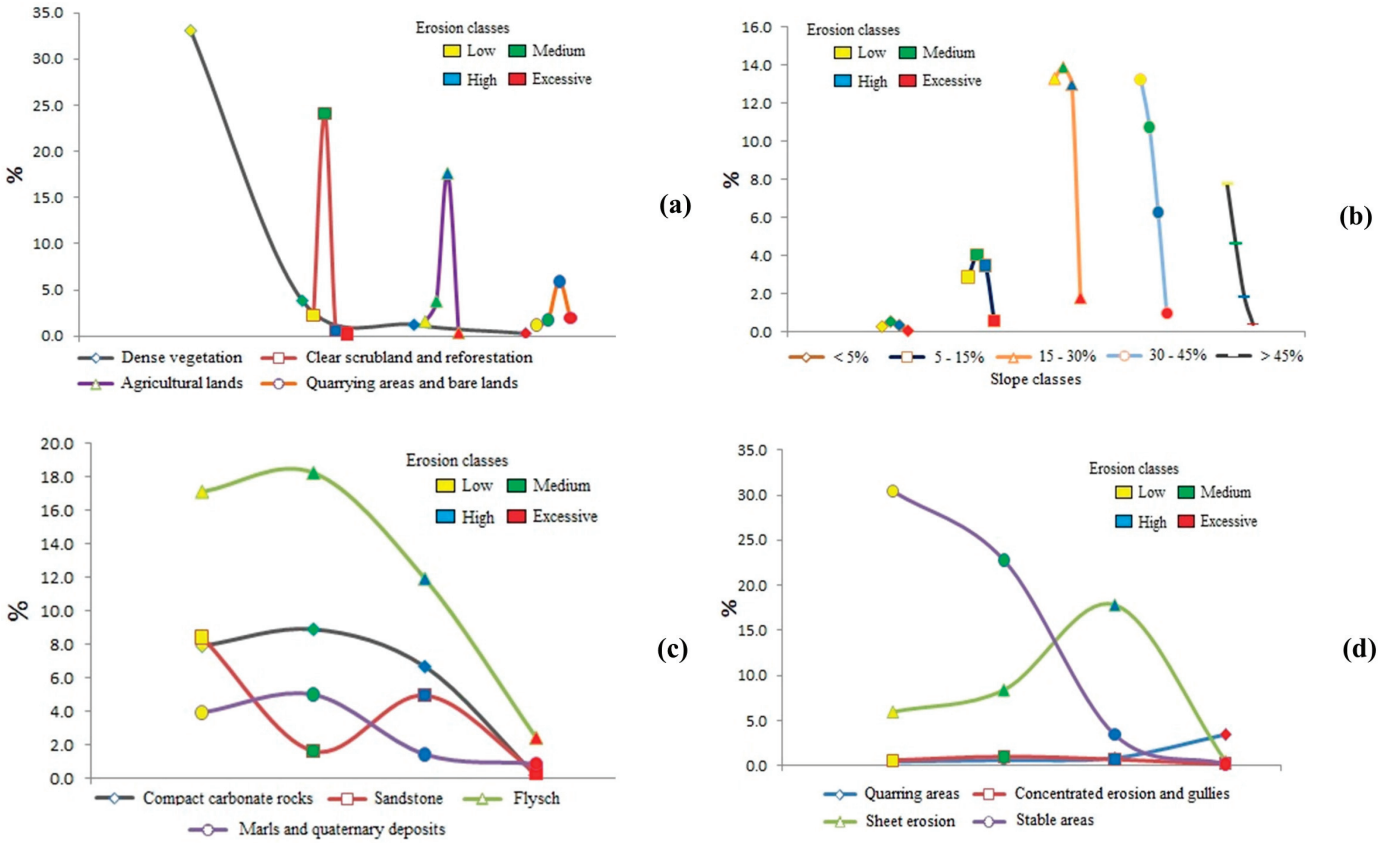

Figure 4. Analysis of erosion-contributing factors to the erosion rate, (**a**) LULC, (**b**) slope classes, (**c**) lithology, (**d**) forms of erosion.

The other erosion classes generate more particles in the study area than the slope class (0 to 15%). Due to the combination of this component and other variables that determine the amount of sediment production, areas with a slope of 15 to 30% are most likely to be affected by erosion (Figure 4b). This slope class is associated with poorly developed, highly erodible soils in the basin's center and downstream. The lithology in this part of the

basin is essentially marble and clay, and all formerly vegetated areas have been replaced by agriculture.

All these features favor large amounts of sediment and accelerate the erosion process. However, slopes with more than 45% inclination, especially upstream in the basin, favor small amounts of sedimentation. In this area, erosion is limited by the extensive regeneration of matorral shrubs, deciduous vegetation, lithosols, and sandstones. The erosion-limiting effect is known for these lithologies and land use patterns [29,70]. The steep slope, dense vegetation, and hard rock limit sediment production in this case.

3.3. Soil Erosion Scenarios

Analyzing factors controlling erosion in the catchment has shown that quarries are the primary activity responsible for erosion and the main sediment source. Two simulation scenarios were investigated to mitigate the impact of the quarry on the erosion process in the study area. The first scenario (Table 7), which involved replacing the quarries with dense vegetation through afforestation, resulted in a significant reduction in erosion rates, which decreased from 13.22 to 8.44 t/ha/year, a decrease of 4.78 t/ha/year (Figure 3c).

Table 7. Analysis of Scenario 1 (reforestation) using IntErO.

Parameters	Symbols	Values	Units
The river basin shape coefficient.	A	0.41	
Watershed development coefficient.	m	0.59	
The average breadth of a river basin.	B	3.7	km
The river basin A's symmetry.	a	0.67	
The density of the basin's river network.	G	3.2	
The tortuousness of the river basin.	K	1.68	
Average river basin elevation.	Hsr	255.19	m
The river basin's average elevation difference.	D	243.19	m
Decrease in the typical river basin.	Isr	479.65	%
The elevation of the river basin's local erosion base.	Hleb	560	m
Coefficient of the river basin relief's erosion energy.	Er	73.6	
Coefficient of permeability in the area.	S1	0.86	
Coefficient of the cover of vegetation.	S2	0.69	
Water retention in influx is presented analytically.	W	0.7704	m
Water flow's potential for energy during torrential downpours.	$2gDF^{½}$	405.14	m km s
Maximum outflow in the river basin.	Qmax	75.72	m^3/s
Coefficient of temperature.	T	1.36	
Coefficient of erosion in the river basins.	Z	1.056	
Erosion material produced in the river basin.	Wgod	10,7971.3	m^3/god
Coefficient for the retention of deposits.	Ru	0.224	
Actual losses in soil.	Ggod	24,185.57	m^3/god
Actual losses of soil per km^2.	Ggod/km^2	703.06	m^3/km^2 god

According to the asymmetry coefficient A, severe floods are possible in the watershed. The drainage network is highly dense according to the G value of 3.20. The watershed's slopes are steep and nearly vertical, according to the Isr value of 479.65%. Based on a Z-value of 1.056 (Scenario 1) and 1.366 (Scenario 2), the watershed is classified as Destruction Category I. The erosion strength is considerable, and the type of erosion is surface erosion (Scenario 1) and mixed erosion (Scenario 2). Gavrilovic classifies the basin as category IV, i.e., an area of low erosion, with a value of 703.74 m^3/km^2god (Scenario 1), and as category III, a region of medium erosion, with a value of 1035.62 m^3/km^2god (Scenario 2).

It should be noted that reforestation requires a lot of time until the trees reach full maturity and can develop their protective effect. The second scenario (Table 8), which involves the conversion of quarries to cropland, also reduced erosion rates slightly by almost 1 t/ha/year, from 13.22 to 12.42 t/ha/year (Figure 3d). Although this approach is less practicable than reforestation, it has the advantage that it takes less time to convert

quarries into agricultural land. The conversion of quarries into arable land is less effective than afforestation in erosion control. However, it has the advantage that the conversion and restoration of quarry areas take less time.

Table 8. Analysis of Scenario 2 (cropping and plowing) using IntErO.

Parameters	Symbols	Values	Units
The river basin shape coefficient.	A	0.41	
Watershed development coefficient.	m	0.59	
The average breadth of a river basin.	B	3.7	km
The river basin A's symmetry.	a	0.67	
The density of the basin's river network.	G	3.2	
The tortuousness of the river basin.	K	1.68	
Average river basin elevation.	Hsr	255.19	m
The river basin's average elevation difference.	D	243.19	m
Decrease in typical river basin decrease.	I.sr	479.65	%
The elevation of the river basin's local erosion base.	Hleb	560	m
Coefficient of the river basin relief's erosion energy.	Er	73.6	
Coefficient of permeability in the area.	S1	0.86	
Coefficient of the cover of vegetation.	S2	0.74	
Water retention in influx is presented analytically.	W	0.7704	m
Water flow's potential for energy during torrential downpours.	$2gDF^{½}$	405.14	mkms
Maximum outflow in the river basin.	Qmax	81.51	m^3/s
Coefficient of temperature.	T	1.36	
Coefficient of erosion in the river basins.	Z	1.366	
Erosion material produced in the river basin.	Wgod	158,888.9	m^3/god
Coefficient for the retention of deposits.	Ru	0.224	
Actual losses in soil.	Ggod	35,591.11	m^3/god
Actual losses of soil per km^2.	Ggod/km^2	1034.62	m^3/km^2god

Both scenarios are critical to reducing erosion, protecting the downstream dam and harbor from the adverse effects of erosion, and promoting the restoration of regional ecosystem balance through reintroducing native fauna and flora. The combination of these approaches would enable more sustainable management of the quarry while maintaining water quality and biodiversity and helping to protect vital infrastructure.

3.4. Quantitative Analysis of Erosion Trends in the Basin

To assess these trends and anticipate potential impacts, the applied PAP/RAC method allowed us to simulate future regional developments regarding degradation or stabilization [32,33,61]. The findings of this study show that the areas occupied by quarries (Figure 5a,b) exhibit a pronounced trend toward irreversible degradation, mainly concentrated in the central and upstream sections of the watershed where unprotected rocks predominate (Figure 6).

A widespread trend of widening or intensification of erosion was observed in areas with deep gullies, especially downstream of the basin. The zones around the dam are also moderately threatened (Figure 5c), indicating a localized trend of widening or intensifying erosion processes and highlighting the need for erosion control measures in this location. In contrast, the rest of the watershed appears to be relatively well preserved, with low erosion conditions and a trend toward stabilizing and regressing the spatial distribution of erosion processes (Figure 6).

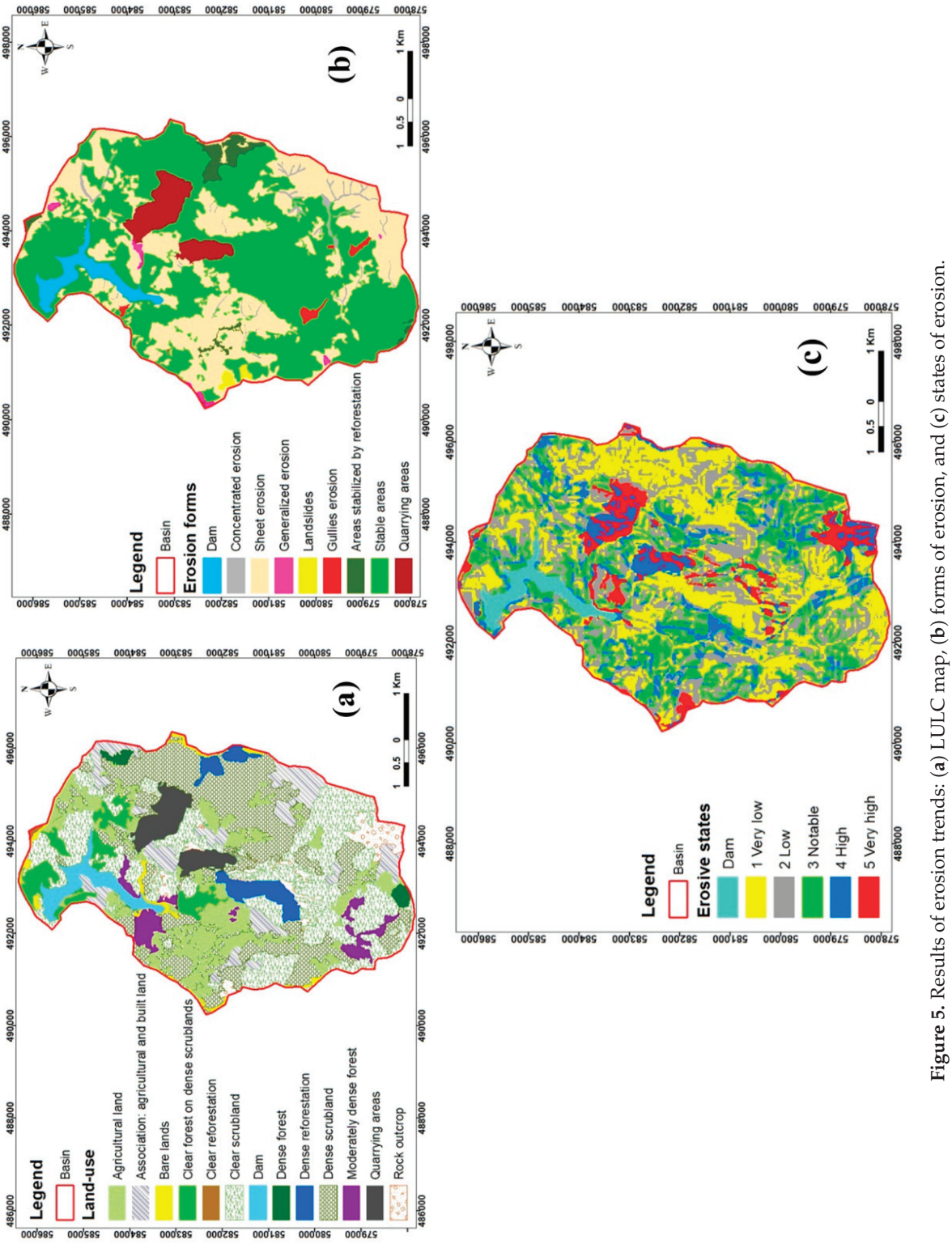

Figure 5. Results of erosion trends: (**a**) LULC map, (**b**) forms of erosion, and (**c**) states of erosion.

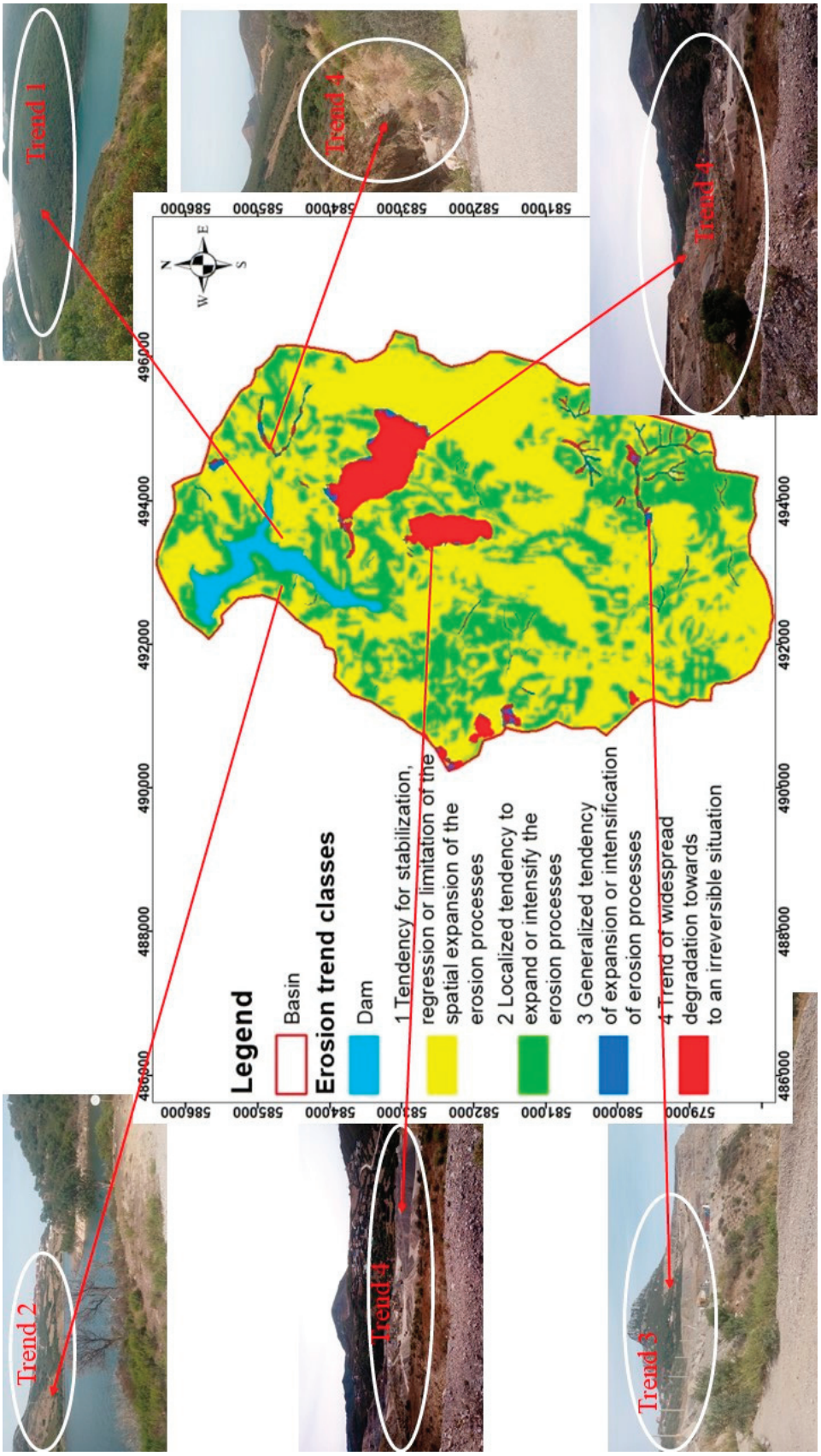

Figure 6. Erosion trend classes map in R'mel watershed.

4. Conclusions

Applying the IntErO algorithm based on the EPM model has proven to be a valuable tool for assessing sediment production under Moroccan environmental conditions. The study showed an average sediment production rate of 13.22 t/ha/an. Quarry areas were identified as the main contributors to sediment production, significantly influencing erosion and deposition downstream. These results are consistent with the qualitative model used by PAP/RAC, which shows a worrying trend of irreversible degradation in the quarry areas. In addition, the analysis has demonstrated that IntErO's ability to simulate quarry rehabilitation scenarios supports reforestation as an effective strategy to mitigate erosion. This approach helps control erosion, promotes ecosystem restoration, and contributes to the recovery of local flora and fauna in the catchment. The study found that several factors influence sediment mobilization within the catchment, including land use, lithology, erosion forms, slopes, and rainfall. The results highlight the robustness and effectiveness of the IntErO algorithm in erosion studies and sediment assessment under Morocco's unique environmental conditions. This research provides valuable insights for informed decision-making and promoting sustainable regional land management practices. By facilitating the conservation and restoration of critical ecosystems, the study contributes to the global scientific community and has broader implications for land management and erosion control research.

Author Contributions: Conceptualization, A.O., S.K., S.C., M.B. and V.S.; methodology, A.O., S.K., Y.B., M.A., S.C., M.B. and V.S.; software, A.O., S.K., Y.B., H.B., V.S., A.K. and A.H.; validation, A.O., S.K., Y.B., H.B., V.S., A.K., M.B. and A.H.; formal analysis, A.O., S.K., Y.B., S.C., H.B., V.S., A.K. and A.H.; investigation, A.O., S.K., Y.B., S.C., H.B., V.S., A.K. and A.H.; resources, A.O., S.K., Y.B., M.A., S.C. and V.S.; data curation, A.O., S.K., Y.B., M.A., S.C. and V.S.; writing—original draft preparation, A.O., S.K., Y.B., S.C., M.B., H.B., V.S., A.K. and A.H.; writing—review and editing, A.O., S.K., V.S., A.K. and A.H.; visualization, A.O., S.K., Y.B., S.C., H.B., V.S., A.K. and A.H.; supervision, V.S., A.K. and A.H.; project administration, V.S. All authors have read and agreed to the published version of the manuscript.

Funding: This research received no funding.

Institutional Review Board Statement: Not applicable.

Informed Consent Statement: Not applicable.

Data Availability Statement: Data is contained within the article. The IntErO model, developed by Professor Velibor Spalevic (2011), is available for free download and installation. It can be accessed at www.geasci.org/IntErO. Detailed instructions for downloading and installing the model can be found on the provided website.

Conflicts of Interest: The authors declare no conflicts of interest.

References

1. Sadiki, A.; Faleh, A.; Navas, A.; Bouhlassa, S. Using magnetic susceptibility to assess soil degradation in the Eastern Rif, Morocco. *Earth Surf. Process. Landf.* **2009**, *34*, 2057–2069. [CrossRef]
2. Okacha, A.; Salhi, A.; Arari, K.; El Badaoui, K.; Lahrichi, K. Soil erosion assessment using the RUSLE model for better planning: A case study from Morocco. *Model. Earth Syst. Environ.* **2023**, *9*, 3721–3729. [CrossRef]
3. Sadiki, A.; Faleh, A.; Navas, A.; Bouhlassa, S. Assessing soil erosion and control factors by the radiometric technique in the Boussouab catchment, Eastern Rif, Morocco. *CATENA* **2007**, *71*, 13–20. [CrossRef]
4. Ouallali, A.; Bouhsane, N.; Bouhlassa, S.; Moukhchane, M.; Ayoubi, S.; Aassoumi, H. Rapid magnetic susceptibility measurement as a tracer to assess the erosion–deposition process using tillage homogenization and simple proportional models: A case study in northern of Morocco. *Int. J. Sediment Res.* **2023**, *38*, 739–753. [CrossRef]
5. Khodabin, G.; Lightburn, K.; Hashemi, S.M.; Moghada, M.S.K.; Jalilian, A. Evaluation of nitrate leaching, fatty acids, physiological traits and yield of rapeseed (Brassica napus) in response to tillage, irrigation and fertilizer management. *Plant Soil* **2022**, *473*, 423–440. [CrossRef]
6. Qasim, W.; Wan, L.; Lv, H.; Zhao, Y.; Hu, J.; Meng, F.; Lin, S.; Butterbach-Bahl, K. Impact of anaerobic soil disinfestation on seasonal N2O emissions and N leaching in greenhouse vegetable production system depends on amount and quality of organic matter additions. *Sci. Total. Environ.* **2022**, *830*, 154673. [CrossRef]

7. Liu, T.; Xu, X.; Yang, J. Experimental study on the effect of freezing-thawing cycles on wind erosion of black soil in Northeast China. *Cold Reg. Sci. Technol.* **2017**, *136*, 1–8. [CrossRef]
8. Kader, S.; Raimi, M.O.; Spalevic, V.; Iyingiala, A.-A.; Bukola, R.W.; Jaufer, L.; Butt, T.E. A concise study on essential parameters for the sustainability of Lagoon waters in terms of scientific literature. *Turk. J. Agric. For.* **2023**, *47*, 288–307. [CrossRef]
9. Xinbao, Z.; Higgitt, D.; Walling, D. A preliminary assessment of the potential for using caesium-137 to estimate rates of soil erosion in the Loess Plateau of China. *Hydrol. Sci. J.* **1990**, *35*, 243–252. [CrossRef]
10. Ritchie, J.C.; Ritchie, C.A. *Bibliography of Publications of 137 Cesium Studies Related to Erosion and Sediment Deposition*; 1011-4289; International Atomic Energy Agency (IAEA): Vienna, Austria, 1995; pp. 125–201.
11. Preiss, N.; Mélières, M.A.; Pourchet, M. A compilation of data on lead 210 concentration in surface air and fluxes at the air-surface and water-sediment interfaces. *J. Geophys. Res. Atmos.* **1996**, *101*, 28847–28862. [CrossRef]
12. Walling, D.E.; He, Q.; Blake, W. Use of 7Be and 137Cs measurements to document short-and medium-term rates of water-induced soil erosion on agricultural land. *Water Resour. Res.* **1999**, *35*, 3865–3874. [CrossRef]
13. Sepulveda, A.; Schuller, P.; Walling, D.E.; Castillo, A. Use of 7Be to document soil erosion associated with a short period of extreme rainfall. *J. Environ. Radioact.* **2008**, *99*, 35–49. [CrossRef]
14. Fesenko, S.; Prudnikov, P.; Isamov, N.; Emlyutina, E.; Titov, I. Dynamics of 137Cs concentration in fodder in the long-term after the Chernobyl accident. *Biol. Bull.* **2022**, *49*, 2359–2368. [CrossRef]
15. Cabrera, M.; Sanabria, R.; González, J.; Cabral, P.; Tejeda, S.; Zarazua, G.; Melgar-Paniagua, E.; Tassano, M. Using 137Cs and 210Pbex to assess soil redistribution at different temporal scales along with lithogenic radionuclides to evaluate contrasted watersheds in the Uruguayan Pampa grassland. *Geoderma* **2023**, *435*, 116502. [CrossRef]
16. Lizaga Villuendas, I.; Latorre, B.; Gaspar, L.; Navas, A. Effect of historical land-use change on soil erosion in a Mediterranean catchment by integrating 137Cs measurements and WaTEM/SEDEM model. *Hydrol. Process.* **2022**, *36*, e14577. [CrossRef]
17. Tan, M.L.; Gassman, P.W.; Yang, X.; Haywood, J. A review of SWAT applications, performance and future needs for simulation of hydro-climatic extremes. *Adv. Water Resour.* **2020**, *143*, 103662. [CrossRef]
18. Hao, Z.; Wu, D. Data Preprocessing of Soil Attributes for Ecohydrological Applications Using SWAT Model at Xin'anjiang Upstream Watershed, China. *Ecohydrol. Hydrobiol.* **2023**, *23*, 198–210. [CrossRef]
19. Briak, H.; Moussadek, R.; Aboumaria, K.; Mrabet, R. Assessing sediment yield in Kalaya gauged watershed (Northern Morocco) using GIS and SWAT model. *Int. Soil Water Conserv. Res.* **2016**, *4*, 177–185. [CrossRef]
20. Ouallali, A.; Briak, H.; Aassoumi, H.; Beroho, M.; Bouhsane, N.; Moukhchane, M. Hydrological foretelling uncertainty evaluation of water balance components and sediments yield using a multi-variable optimization approach in an external Rif's catchment. Morocco. *Alex. Eng. J.* **2020**, *59*, 775–789. [CrossRef]
21. Renard, K.G. *Predicting Soil Erosion by Water: A guide to Conservation Planning with the Revised Universal Soil Loss Equation (RUSLE)*; US Department of Agriculture, Agricultural Research Service: Beltsville, MD, USA, 1997.
22. Williams, J.; Berndt, H. Sediment yield prediction based on watershed hydrology. *Trans. ASAE* **1977**, *20*, 1100–1104. [CrossRef]
23. Mitasova, H.; Mitas, L. *Modeling Soil Detachment with RUSLE 3D Using GIS*; University of Illinois at Urbana-Champaign: Champaign, IL, USA, 1999.
24. Gavrilović, S. *Inženjering o Bujičnim Tokovima i Eroziji*; Izgradnja: Belgrade, Serbia, 1972.
25. Bezak, N.; Borrelli, P.; Mikoš, M.; Jemec Auflič, M.; Panagos, P. Towards multi-model soil erosion modelling: An evaluation of the erosion potential method (EPM) for global soil erosion assessments. *CATENA* **2024**, *234*, 107596. [CrossRef]
26. Tangestani, M.H. Comparison of EPM and PSIAC models in GIS for erosion and sediment yield assessment in a semi-arid environment: Afzar Catchment, Fars Province, Iran. *J. Asian Earth Sci.* **2006**, *27*, 585–597. [CrossRef]
27. Ahmadi, M.; Minaei, M.; Ebrahimi, O.; Nikseresht, M. Evaluation of WEPP and EPM for improved predictions of soil erosion in mountainous watersheds: A case study of Kangir River basin, Iran. *Model. Earth Syst. Environ.* **2020**, *6*, 2303–2315. [CrossRef]
28. Sestras, P.; Mircea, S.; Roșca, S.; Bilașco, Ș.; Sălăgean, T.; Dragomir, L.O.; Herbei, M.V.; Bruma, S.; Sabou, C.; Marković, R.; et al. GIS based soil erosion assessment using the USLE model for efficient land management: A case study in an area with diverse pedo-geomorphological and bioclimatic characteristics. *Not. Bot. Horti Agrobot. Cluj-Napoca* **2023**, *51*, 13263. [CrossRef]
29. Ouallali, A.; Aassoumi, H.; Moukhchane, M.; Moumou, A.; Houssni, M.; Spalevic, V.; Keesstra, S. Sediment mobilization study on Cretaceous, Tertiary and Quaternary lithological formations of an external Rif catchment, Morocco. *Hydrol. Sci. J.* **2020**, *65*, 1568–1582. [CrossRef]
30. Spalevic, V.; Barovic, G.; Vujacic, D.; Curovic, M.; Behzadfar, M.; Djurovic, N.; Dudic, B.; Billi, P. The impact of land use changes on soil erosion in the river basin of Miocki Potok, Montenegro. *Water* **2020**, *12*, 2973. [CrossRef]
31. Youssef, B.; Bouskri, I.; Brahim, B.; Kader, S.; Brahim, I.; Abdelkrim, B.; Spalević, V. The contribution of the frequency ratio model and the prediction rate for the analysis of landslide risk in the Tizi N'tichka area on the national road (RN9) linking Marrakech and Ouarzazate. *CATENA* **2023**, *232*, 107464. [CrossRef]
32. Tahouri, J.; Sadiki, A.; Karrat, L.h.; Johnson, V.C.; Chan, N.w.; Fei, Z.; Kung, H.T. Using a modified PAP/RAC model and GIS-for mapping water erosion and causal risk factors: Case study of the Asfalou watershed, Morocco. *Int. Soil Water Conserv. Res.* **2022**, *10*, 254–272. [CrossRef]
33. Elbadaoui, K.; Mansour, S.; Ikirri, M.; Abdelrahman, K.; Abu-Alam, T.; Abioui, M. Integrating Erosion Potential Model (EPM) and PAP/RAC Guidelines for Water Erosion Mapping and Detection of Vulnerable Areas in the Toudgha River Watershed of the Central High Atlas, Morocco. *Land* **2023**, *12*, 837. [CrossRef]

34. Diani, K.; Ettazarini, S.; Hahou, Y.; El Belrhiti, H.; Allaoui, W.; Mounir, K.; Gourfi, A. Chapter 11—Identification of soil erosion sites in semiarid zones: Using GIS, remote sensing, and PAP/RAC model. In *Handbook of Hydroinformatics*; Eslamian, S., Eslamian, F., Eds.; Elsevier: Amsterdam, The Netherlands, 2023; pp. 169–183. [CrossRef]
35. Huang, W.; Ho, H.C.; Peng, Y.; Li, L. Qualitative risk assessment of soil erosion for karst landforms in Chahe town, Southwest China: A hazard index approach. *CATENA* **2016**, *144*, 184–193. [CrossRef]
36. Drzewiecki, W.; Wężyk, P.; Pierzchalski, M.; Szafrańska, B. Quantitative and qualitative assessment of soil erosion risk in Małopolska (Poland), supported by an object-based analysis of high-resolution satellite images. *Pure Appl. Geophys.* **2014**, *171*, 867–895. [CrossRef]
37. Kader, S.; Jaufer, L.; Bashir, O.; Raimi, M.O. A Comparative Study on the Stormwater Retention of Organic Waste Substrates Biochar, Sawdust, and Wood Bark Recovered from Psidium Guajava L. Species. *Comp. Study Stormwater Retent. Org. Waste Substrates* **2023**, *69*, 105–112. [CrossRef]
38. Chikh, H.A.; Habi, M.; Morsli, B. Influence of vegetation cover on the assessment of erosion and erosive potential in the Isser marly watershed in northwestern Algeria—Comparative study of RUSLE and PAP/RAC methods. *Arab. J. Geosci.* **2019**, *12*, 154. [CrossRef]
39. Mohamed-Chérif, F.; Ducruet, C. Regional integration and maritime connectivity across the Maghreb seaport system. *J. Transp. Geogr.* **2016**, *51*, 280–293. [CrossRef]
40. Sort, X.; Alcaniz, J. Contribution of sewage sludge to erosion control in the rehabilitation of limestone quarries. *Land Degrad. Dev.* **1996**, *7*, 69–76. [CrossRef]
41. Ozcelik, M. Comparison of the environmental impact and production cost rates of aggregates produced from stream deposits and crushed rock quarries (Boğaçay Basin/Antalya/Turkey). *Geoheritage* **2022**, *14*, 18. [CrossRef]
42. Taoufik, M.; Loukili, I.; Hadi, H.E.; Baghdad, B. Soil erosion risk assessment in an extraction area: Case of abandoned quarries in the Akreuch region (Morocco). In Proceedings of the 2020 IEEE International conference of Moroccan Geomatics (Morgeo), Casablanca, Morocco, 11–13 May 2020; pp. 1–5. [CrossRef]
43. Costa, J.P.R.; Gomes, G.J.; Fernandes, G.; Magarinos, D.M.; Fonseca, A.; Pires, P.J. Ferronickel slag as free-draining rockfill dike material: A novel waste solution for mining regions. *J. Mater. Cycles Waste Manag.* **2023**, *25*, 128–143. [CrossRef]
44. Elaloui, A.; Khalki, E.M.E.; Namous, M.; Ziadi, K.; Eloudi, H.; Faouzi, E.; Bou-Imajjane, L.; Karroum, M.; Tramblay, Y.; Boudhar, A. Soil erosion under future climate change scenarios in a semi-arid region. *Water* **2022**, *15*, 146. [CrossRef]
45. López, S.; Wright, C.; Costanza, P. Environmental change in the equatorial Andes: Linking climate, land use, and land cover transformations. *Remote Sens. Appl. Soc. Environ.* **2017**, *8*, 291–303. [CrossRef]
46. Henriques, C.; Zêzere, J.L.; Marques, F. The role of the lithological setting on the landslide pattern and distribution. *Eng. Geol.* **2015**, *189*, 17–31. [CrossRef]
47. Abdolmaleki, M.; Mokhtari, A.R.; Akbar, S.; Alipour-Asll, M.; Carranza, E.J.M. Catchment basin analysis of stream sediment geochemical data: Incorporation of slope effect. *J. Geochem. Explor.* **2014**, *140*, 96–103. [CrossRef]
48. Efthimiou, N.; Lykoudi, E.; Karavitis, C. Comparative analysis of sediment yield estimations using different empirical soil erosion models. *Hydrol. Sci. J.* **2017**, *62*, 2674–2694. [CrossRef]
49. Raissis, F.; Theochari, A.-P.; Baltas, E. Soil transportation assessment of an eastern Mediterranean basin in Greece using GIS techniques. *Euro-Mediterr. J. Environ. Integr.* **2022**, *7*, 361–376. [CrossRef]
50. Roy, P.; Pal, S.C.; Chakrabortty, R.; Saha, A.; Chowdhuri, I. A systematic review on climate change and geo-environmental factors induced land degradation: Processes, policy-practice gap and its management strategies. *Geol. J.* **2023**, *58*, 3487–3514. [CrossRef]
51. Chalise, D.; Kumar, L.; Spalevic, V.; Skataric, G. Estimation of sediment yield and maximum outflow using the IntErO model in the Sarada river basin of Nepal. *Water* **2019**, *11*, 952. [CrossRef]
52. Pavlova-Traykova, E.; Grigorova-Pesheva, B.; Petrova, K. Soil loss assessment by applying intero model. *For. Sci.* **2023**, *59*, 41–46.
53. Sestras, P.; Mircea, S.; Cîmpeanu, S.M.; Teodorescu, R.; Roșca, S.; Bilașco, Ș.; Rusu, T.; Salagean, T.; Dragomir, L.O.; Marković, R. Soil erosion assessment using the intensity of erosion and outflow model by estimating sediment yield: Case study in river basins with different characteristics from Cluj County, Romania. *Appl. Sci.* **2023**, *13*, 9481. [CrossRef]
54. Spalevic, V. Impact of Land Use on Runoff and Soil Erosion in Polimlje. Ph.D. Thesis, Faculty of Agriculture of the University of Belgrade, Belgrage, Serbia, 2011.
55. Spalevic, V. Assessment of soil erosion processes by using the 'IntErO'model: Case study of the Duboki Potok, Montenegro. *J. Environ. Prot. Ecol.* **2019**, *20*, 657–665.
56. Mohammadi, M.; Khaledi Darvishan, A.; Spalevic, V.; Dudic, B.; Billi, P. Analysis of the impact of land use changes on soil erosion intensity and sediment yield using the intero model in the talar watershed of Iran. *Water* **2021**, *13*, 881. [CrossRef]
57. Rajabi, A.M.; Yavari, A.; Cheshomi, A. Sediment yield and soil erosion assessment by using empirical models for Shazand watershed, a semi-arid area in center of Iran. *Nat. Hazards* **2022**, *112*, 1685–1704. [CrossRef]
58. Berteni, F.; Barontini, S.; Grossi, G. Evaluating soil erosion by water in a small alpine catchment in Northern Italy: Comparison of empirical models. *Acta Geochim.* **2021**, *40*, 507–524. [CrossRef]
59. Tričković, N.; Rončević, V.; Živanović, N.; Grujić, T.; Stefanović, L.; Jovanović, N.; Zlatić, M. Ecological and Economic Effects of Applying the Future Agricultural Production Structure Model (FAPSMS): The Case Study of the Barička River Basin. *Sustainability* **2023**, *15*, 8434. [CrossRef]

60. Rončević, V.; Zlatić, M.; Todosijević, M. Environmental and economic effects of investments in sustainable land management in the basin of Šutilovac stream. *Glas. Sumar. Fak.* **2019**, *19*, 213–232. [CrossRef]
61. Lamane, H.; Moussadek, R.; Baghdad, B.; Mouhir, L.; Briak, H.; Laghlimi, M.; Zouahri, A. Soil water erosion assessment in Morocco through modeling and fingerprinting applications: A review. *Heliyon* **2022**, *8*, e10209. [CrossRef]
62. Griesbach, J.; Ruiz Sinoga, J.; Giordano, A.; Berney, O.; Gallart, F. Directives pour la Cartographie et la Mesure des Processus d'Erosion Hydrique dans les Zones Cotieres Mediterraneennes. 1998. Available online: https://www.academia.edu/76126325/Directives_pour_la_cartograophie_et_la_mesure_des_processus_d_erosion_hydrique_dans_les_zones_cotieres_mediterraneennes (accessed on 17 June 2023).
63. Gavrilovic, Z. Use of an Empirical Method(Erosion Potential Method) for Calculating Sediment Production and Transportation in Unstudied or Torrential Streams. In Proceedings of the International Conference on River Regime, Wallingford, UK, 18–20 May 1988; Hydraulics Research Limited: Wallingford, UK, 1988; pp. 411–422.
64. Sabri, E.; Spalevic, V.; Boukdir, A.; Karaoui, I.; Ouallali, A.; Mincato, R.L.; Sestras, P. Estimation of soil losses and reservoir sedimentation: A case study in Tillouguite sub-basin (High Atlas-Morocco). *Agric. For./Poljopr. Sumar.* **2022**, *68*, 207–220. [CrossRef]
65. Aït Brahim, L.; Sossey Alaoui, F.; Siteri, H.; Tahri, M. Quantification of soil loss in the Nakhla watershed (northern Rif). *Sécheresse-Sci. Chang. Planétaires* **2003**, *14*, 101–106.
66. Damnati, B.; Ibrahimi, S.; Benhardouze, O.; Benhardouze, H.; Reddad, H.; Radakovitch, O. Quantification de l'érosion par le 137Cs et le 210Pb: Cas de deux bassins versants au Nord-Ouest du Maroc (Région de Tanger-Tétouan). *Notes Mémoires Serv. Géologique Maroc* **2012**, *575*, 74–80.
67. Ed-daoudy, L.; Lahmam, N.; Benmansour, M.; Afilal, H.; Ben harra, A.; Damnati, B. Hydric erosion rates in Raouz watershed, Morocco: RUSLE, GIS, and remote sensing. *Remote Sens. Appl. Soc. Environ.* **2023**, *32*, 101056. [CrossRef]
68. Kader, S.; Novicevic, R.; Jaufer, L. Soil Management in Sustainable Agriculture: Analytical Approach for the Ammonia Removal from the Diary Manure. *J. Agric. For.* **2022**, *68*, 69–78. [CrossRef]
69. Kostadinov, S.; Braunović, S.; Dragićević, S.; Zlatić, M.; Dragović, N.; Rakonjac, N. Effects of erosion control works: Case study—Grdelica Gorge, the South Morava River (Serbia). *Water* **2018**, *10*, 1094. [CrossRef]
70. Manojlović, S.; Antić, M.; Šantić, D.; Sibinović, M.; Carević, I.; Srejić, T. Anthropogenic impact on erosion intensity: Case study of rural areas of pirot and dimitrovgrad municipalities, Serbia. *Sustainability* **2018**, *10*, 826. [CrossRef]

land

MDPI

Article

Landslide Susceptibility Assessment in Nepal's Chure Region: A Geospatial Analysis

Purna Bahadur Thapa [1], Saurav Lamichhane [2,*], Khagendra Prasad Joshi [3], Aayoush Raj Regmi [4], Divya Bhattarai [5] and Hari Adhikari [6,*]

[1] Institute of Forestry, Hetauda Campus, Tribhuvan University, Hetauda 44100, Nepal
[2] Faculty of Forestry, Agriculture and Forestry University, Hetauda 44100, Nepal
[3] Kathmandu Forestry College, Tribhuvan University, Kathmandu 44600, Nepal
[4] School of Forestry & NRM, Institute of Forestry, Tribhuvan University, Kathmandu 44600, Nepal
[5] Institute of Botany and Landscape Ecology, University of Greifswald, Soldmannstraße 15, 17489 Greifswald, Germany
[6] Department of Geosciences and Geography, University of Helsinki, P.O. Box 64, FI-00014 Helsinki, Finland
* Correspondence: sauravlc8@gmail.com (S.L.); hari.adhikari@helsinki.fi (H.A.)

Abstract: The Chure Hills, already vulnerable due to their fragile nature, face increased landslide risk, prompting the need for reliable susceptibility assessment. This study uses Poisson regression modeling to assess landslide susceptibility in two highly susceptible districts of the Chure region. Variance inflation factor (VIF) tests were conducted to ensure robustness, indicating no multicollinearity among the variables. Subsequently, Poisson regression analysis identified eight significant variables, among which geology, lineament density, elevation, relief, slope, rainfall, solar radiance, and land cover types emerged as important factors associated with landslide count. The analysis revealed that higher lineament density and slope were associated with lower landslide counts, indicating potential stabilizing geological and topographical influences. The categorical variable, namely geology, revealed that middle Siwalik, upper Siwalik, and quaternary geological formations were associated with lower landslide counts than lower Siwalik. Land cover types, including areas under forest, shrubland, grassland, agricultural land, water bodies, and bare ground, had a substantial significant positive association with landslide count. The generated susceptibility map that exhibited a substantial portion (23.32% in Dang and 5.22% in Surkhet) of the study area fell within the very-high-susceptibility categories, indicating pronounced landslide susceptibility in the Dang and Surkhet districts of the Chure hills. This study offers valuable insights into landslide vulnerability in the Chure region, serving as a foundation for informed decision-making, disaster risk reduction strategies, and sustainable land-use and developmental policy planning.

Keywords: landslide susceptibility; Chure region; poisson regression; susceptibility map

1. Introduction

Landslides, a significant geo-hazard, have profound implications worldwide, causing substantial loss of life, damage to infrastructure, and environmental degradation [1,2]. Nepal, nestled in the Himalayas, faces significant landslide challenges due to its rugged terrain and complex geology, causing substantial economic and human loss [3]. One region particularly susceptible to landslides is the Chure region of Nepal, located in the southern foothills of the Himalayas. The Chure region's unique topography, geological composition, and anthropogenic activities contribute to its heightened vulnerability to slope failure and landslides [4]. Understanding the causes and impacts of landslides in this region is crucial for effective susceptibility assessment, mitigation, and sustainable development.

The Chure region of Nepal has key ecological and socioeconomic significance. It is one of the country's major carbon reservoirs, is rich in biodiversity, possesses high-value

timber species, and is the efficient water supply source for the Terai region of the country [5]. Nearly four million populations from the Chure and Bhabhar regions depend on the site's local natural resources to generate livelihoods and income [6]. Despite its broad ecological and socioeconomic significance, it faces substantial outside challenges. The environment of the Chure region is undergoing unprecedented changes through illegal logging, uncontrolled mining, and increased anthropogenic activities [7]. The other activities contributing to the loss of its environmental assets are over-exploitation of natural resources, free livestock grazing, and the illegal trade in forest products [8]. The region is delicate and environmentally sensitive due to the composition of loose materials that are derived from soft rocks [6]. Foreseeing its threat and considering its significance, the Government of Nepal created the President Chure Terai Madesh Conservation Development Board in 2010 to conserve and manage the region's land, water, and forest for ecological stability in the region [9].

Technological advancements and data analysis tools have recently revolutionized our understanding of landslides. Google Earth data, geographic information systems (GIS), remote sensing, and modeling techniques have become indispensable for studying landslide dynamics and assessing their potential risks [10–12]. Google Earth's high-resolution satellite imagery provides valuable visual information, enabling researchers to identify landslide-prone areas and study their geomorphological characteristics [13]. GIS facilitates the integration and analysis of diverse spatial datasets, aiding in identifying the factors contributing to landslide occurrences [14]. Furthermore, freely available high-resolution data, such as the digital elevation models, have aided in precisely mapping terrain features and monitoring landslide activity [15,16].

There are two major approaches in the landslide susceptibility assessment: qualitative and quantitative methods. Qualitative methods are inventory-based and knowledge-driven, whereas quantitative methods are data-driven and physically based models [17]. According to its occurrence data, the qualitative methods classify areas with similar geomorphological and lithological properties, ultimately indicating the region that is highly susceptible to landslides [18]. On the other hand, the quantitative methods include statistical, probabilistic, artificial intelligence-based, and deterministic approaches [19,20]. The quantitative approach is more reliable as this technique's prediction of landslide susceptibility is based on actual data and interpretations [21,22]. Many techniques, such as statistical tools [23,24], frequency ratios [25,26], the weight of evidence [27], and the analytical hierarchical process [21,28], are used by many researchers to produce precise results with reasonable accuracy for landslide assessment. Among the various approaches, the generalized linear model (GLM) is one of the most common statistical methods for landslide prediction modeling [29]. GLMs offer greater flexibility in analyzing relationships among variables because they can handle a wide range of continuous and categorical data [30].

Landslides occur at unexpected sites and uncertain times; thus, they are called stochastic processes. These stochastic processes are often modeled using a probability-based approach. The Poisson model, a mathematical framework that operates in a continuous time and consists of random point-events (landslide) in ordinary time, which is treated as a continuous and uninterrupted flow, is used for the calculation of the occurrence of random point-events in time and is used commonly to model the occurrence of landslides [31,32]. Geographic information systems (GIS) have been found to play beneficial roles in the study of landslides since they combine the functions of data collection, storage, manipulation, display, and analysis with a spatial framework. Integrating GIS and multivariate statistics is a fruitful approach in landslide mapping [14,33]. Previously, many studies have used GIS and other evaluation techniques (frequency ratio, logistic regression method) for landslide hazard assessments [34,35]. However, limited research has been conducted focusing specifically on the Chure Hills for landslide susceptibility and factors influencing it. Thus, this study attempts to explore the application of the Poisson model and GLM, as it is mainly based on actual data, requires less theoretical data, and enables the researchers and

policymakers to gain crucial insights into landslide dynamics and preparedness measures and develop sustainable land management strategies in similar geographical regions of Nepal. Such comprehensive approaches will be instrumental to mitigating landslide risks and fostering resilient communities in this vulnerable region.

2. Study Area

The Chure range of Nepal is a long strip spanning from its western to its eastern boundary (Figure 1). It constitutes almost 26% of the total population of Nepal across 37 districts [36]. The Chure range accounts for 12.78% of the country's land area, containing 14 forest ecosystems [37]. Climate-wise, the Chure range mainly falls under temperate regions with an elevation of 120–2000 m, a temperature of 15.8–31.8 °C, and precipitation between 1400 and 2000 mm per year [6,9]. The region is very young and geologically composed of loose and soft rocks, which are very vulnerable to sedimentation during peak monsoon due to a high number of gullies [4,6]. The physiography of the Chure range can be divided into the main Chure hillslopes, the Bhawar Dun valleys, and the inner river valley [38]. Among these different physiographical divisions of the Chure region, the hills of Chure are in the greatest danger of landslides due to their weak geomorphic structure, very dry summers, and high risk of erosion in monsoon due to the larger number of rivers running throughout the hills [4]. In contrast, the Bhawar region is densely covered with forests [39], reducing landslide risk.

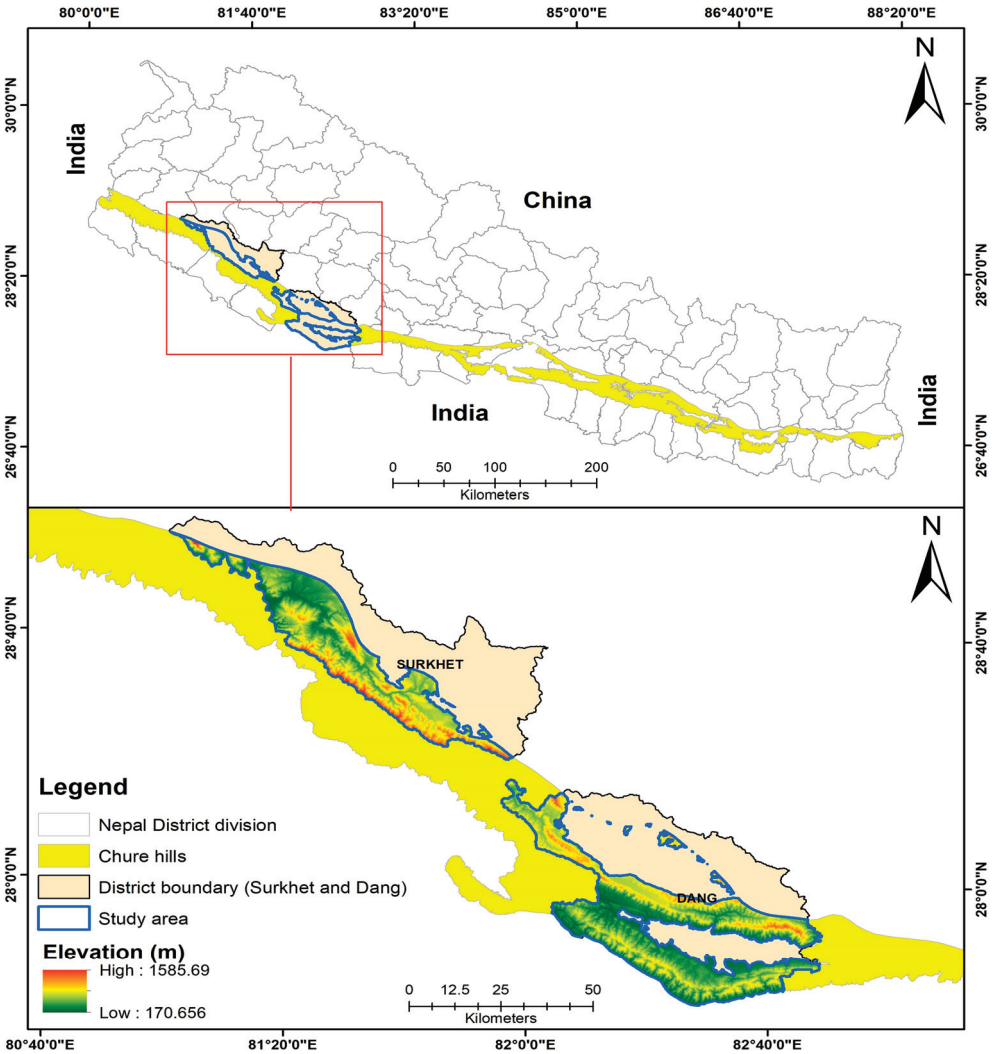

Figure 1. The geographical location of Nepal, along with study area.

Meanwhile, the Dun and the inner river valley are mostly urbanized and agricultural plain areas, which, when building landslide inventory, created a high number of non-occurrence data. This can lead to a misbalance in occurrence and non-occurrence data, leading to biases in predictive modeling [40]. Therefore, we only assessed the Chure Hills area, neglecting the Bhawar and the valleys. The shapefile of the Chure hills in Figure 1 was downloaded from https://www.chureboard.gov.np/ (accessed on 15 July 2023).

As a case study approach, our analysis focused on two districts, namely Dang and Surkhet. According to Petley et al. [3], population growth, land-use changes, urbanization, and linear infrastructure development are the driving factors of landslides. Therefore, the selection of these districts was made purposively with the following criteria: (1) a high proportion of fragile Chure hills, (2) a high population growth rate, (3) biologically significant areas, (4) land-use changes, and (5) the excavation of sand, gravel, and boulders.

Dang district comprises the largest portion of the Chure Hills, covering around 11% of the total area, making it the largest district in the Chure Hills. Similarly, Surkhet district ranks fifth, encompassing approximately 7% of the Chure Hills region. The total area of Dang along with Surkhet is 5548.44 km^2 (https://sthaniya.gov.np/gis, accessed on 20 July 2023), with the Chure hills in the region covering 2577.06 $km^{2,}$ which is nearly half of the total area of these two districts in the Chure region. These two districts also have very high population growth rates, with Dang and Surkhet having rates of 1.92% and 1.62%, respectively [36]. These two districts contain rich species diversity and are home to various biologically significant areas. For instance, the Kakrebihar protected forest, ten wetlands in Surkhet, and the Dang–Deukhuri foothills forest, which is a part of the Terai Arc Landscape conservation, are key providers of the livelihoods of local people and harbor various endangered species [37].

Despite their profound importance, the Chure hills in Surkhet and Dang are at high risk of soil erosion, landslides, and river-bank cutting. This risk is mainly due to existing excavation sites—nine in Dang and one in Surkhet—with the potential for a further increase to eight in Dang and four in Surkhet [9]. Furthermore, the increased number of settlements, intense land-use change, encroachment, geology, and many other anthropogenic factors make this region prone to natural hazards, such as landslides and erosion [39].

3. Materials and Methods

3.1. Data Collection and Processing

Our methodology integrates advanced remote sensing technology, ArcGIS 10.3 software, manual interpretation, field verification, and statistical modeling to investigate landslides. This study utilized Remote Sensing data from Google Earth™ and applied ArcGIS 10.3 software for interpretation and analysis. Firstly, the landslide inventory was manually created by visually interpreting landslides in Google Earth in 2022. Each landslide-impacted area was clipped into landslide polygons and converted into shape files to enable further processing and analysis within the ArcGIS 10.3 software. Secondly, a comprehensive analysis is needed to determine the distribution and frequency of landslide occurrences using the compiled landslide inventory data. By employing this data-processing approach, we aimed to enhance the effectiveness and accuracy of our study, providing valuable insights into landslides in the specified timeframe. A subset of 10% of the total landslide incidents was verified through direct field observations to validate the occurrence of landslides in the study region (Figure 2). This verification process was conducted to ensure the accuracy of our results. Finally, the analysis for the predictive assessment of the landslide-susceptible area was conducted through a grid-based generalized linear model (GLM). The study area was divided into grids with sizes of 5×5 km^2 (i.e., (25 km^2) grids (n = 620) using "Fish net" tools in Arc GIS 10.3. We examined 1279 locations where landslides had occurred, allowing us to derive comprehensive insights for our study.

3.2. Factors Influencing Landslides

Landslides, like many natural hazards, result from a combination of various factors rather than a single, specific cause. There is no consensus about which variables give the best outcome for landslide prediction and modeling; rather, various studies have utilized various factors for landslide analysis [18,21,41,42]. In this study of landslide hazard assessments, various factors influencing landslide occurrences were thoroughly examined, analyzing the previous landslide research. Curvature, a key aspect impacting surface runoff and ground infiltration, was found to play a significant role in surface erosion and groundwater conditions [43]. As curvature values become increasingly negative, the likelihood of landslides occurring escalates [43,44]. Elevation, a vital component in landslide susceptibility mapping, also influences environmental conditions on slopes, including human activity, vegetation, soil moisture, and climate [43,45,46]. Past studies have suggested that higher elevations are more prone to landslides than lower elevations [41,47]. The topographical wetness index (TWI) was identified as another significant factor contributing to landslides, as it quantitatively displays terrain control on soil moisture's spatial distribution [43].

Slope angles are directly related to landslide occurrence, where steeper slopes increase the likelihood of landslides [43,48,49]. Drainage density was also positively correlated with erosion, making it a factor responsible for landslide occurrence [50]. Lineament distance, as determined by Lee and Talib [44], was found to influence landslide conditions. Land cover types were shown to have varying impacts on landslides [51–53], and, hence, land cover was incorporated as a significant landslide conditioning factor in this research.

Geology emerged as a factor in accelerating landslides [54,55]. Previous studies highlighted rainfall as another important factor involved in causing landslides [43,56]. Additionally, annual solar radiation, expressed as the mean solar radiation at a specific pixel over a year, significantly influences landslides [47]. Higher solar radiation in certain areas intensifies sunlight, causing increased moisture evaporation from the exposed soil [57]. Consequently, this heightened evaporation can render these areas more susceptible to landslides [58]. Hence, the solar radiation map was created by utilizing the digital elevation model (DEM) using the "Area solar radiation" toolkit in ArcGIS and then converted to KWH/m^2 using a raster calculator. The relative relief of the study area, as demonstrated by Singh and Kumar [59], profoundly impacted natural conditions, shaping the susceptibility to landslides. Furthermore, the distance from roads emerged as a crucial parameter affecting landslide occurrence, with road construction activities disrupting natural slopes and rendering areas near the toe more vulnerable and weakened along highways [60]. Incorporating these factors into the study provides valuable insights into the complex interplay between elements influencing landslide hazard assessment. Figure 3 illustrates the comprehensive methodological framework employed in this study.

3.3. Data Analysis

The statistical data analysis process involved a series of sequential steps used to comprehensively examine the features of landslide occurrences. Initially, the R Statistical package v4.0.4 [61] was utilized for data analysis. They were systematically divided into groups to enhance the understanding of the assigned predictors, as illustrated in Table 1. Descriptive summaries of landslides were then computed using the Pivot table function in Microsoft Excel 2013. Subsequently, a generalized linear model (GLM) was employed, incorporating 15 independent variables (Figure 4) as predictors with a Poisson error distribution. The GLM, known for its versatile utilization of variables through a link function that accommodates categorical, continuous, and both types of data, was chosen rather than traditional linear regression modeling [30]. Specifically, the Poisson family GLM was utilized in this study, considering the presence and absence of the grid and the frequency of data in each grid.

Table 1. Description of the significant variables used in this study.

S.N.	Variables	Type	Unit	Source
1.	Elevation	Continuous	Meter	(LPDAAC, 2019, [62])
2.	Curvature	Continuous	Degrees/m	Delineated from DEM
3.	Drainage density	Continuous	km/km^2	Delineated from DEM
4.	Lineament	Continuous	km/km^2	Delineated from DEM
5.	Rainfall	Continuous	Millimeter	(Fick and Hijmans, 2017, [63])
6.	Relief	Continuous	Meter	Delineated from DEM
7.	Slope	Continuous	(°)	Delineated from DEM
8.	Topographical wetness index	Continuous	Unit less	Delineated from DEM
9.	Geology (Lower Siwalik = 0)	Categorical	Unit less	(ICIMOD, 2020, [64])
10.	Area of water bodies	Continuous	m^2	(ESRI, 2020, [65])
11.	Area under forest	Continuous	m^2	(ESRI, 2020, [65])
12.	Area of grassland	Continuous	m^2	(ESRI, 2020, [65])
13.	Area of agricultural land	Continuous	m^2	(ESRI, 2020, [65])
14.	Area of shrubland	Continuous	m^2	(ESRI, 2020, [65])
15.	Distance from road	Continuous	Meter	(OCHA Nepal, 2021, [66])
16.	Solar radiance	Continuous	KWh m^{-2}	Delineated from DEM

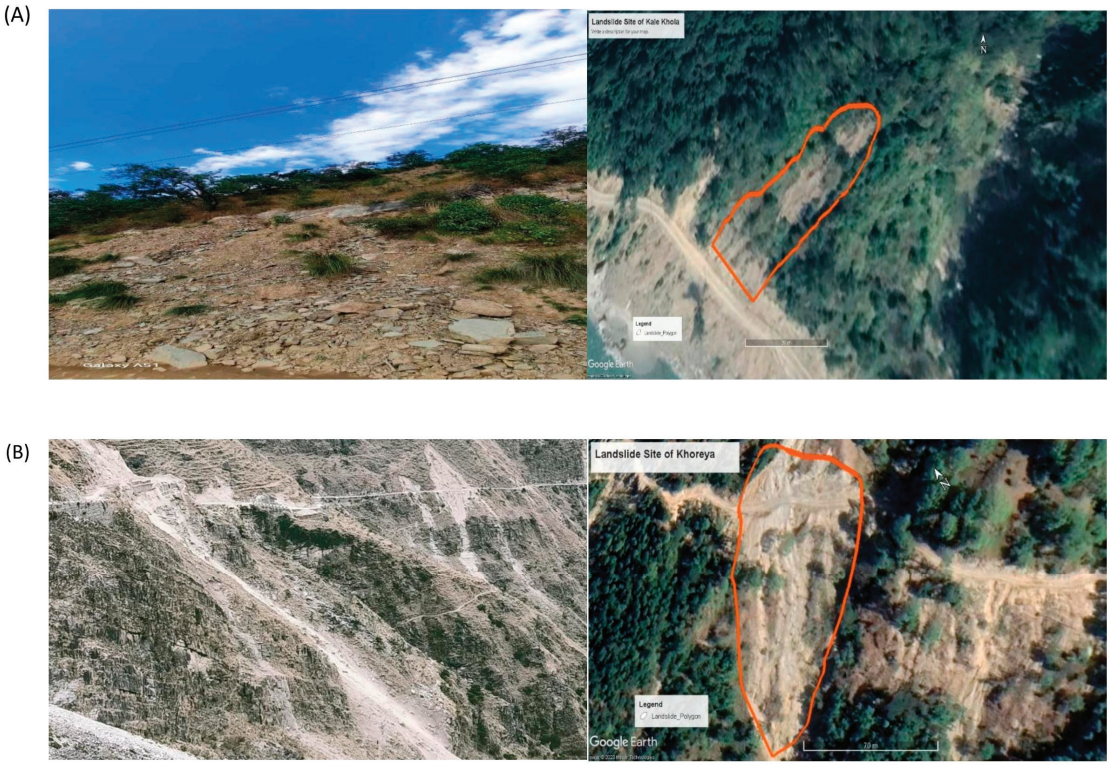

Figure 2. Ground verification and Google Earth points: (**A**) western Side of Chure region of Surkhet district (Location: Kale Khola); (**B**) eastern side of Chure region of Dang district (Location: Khoreya).

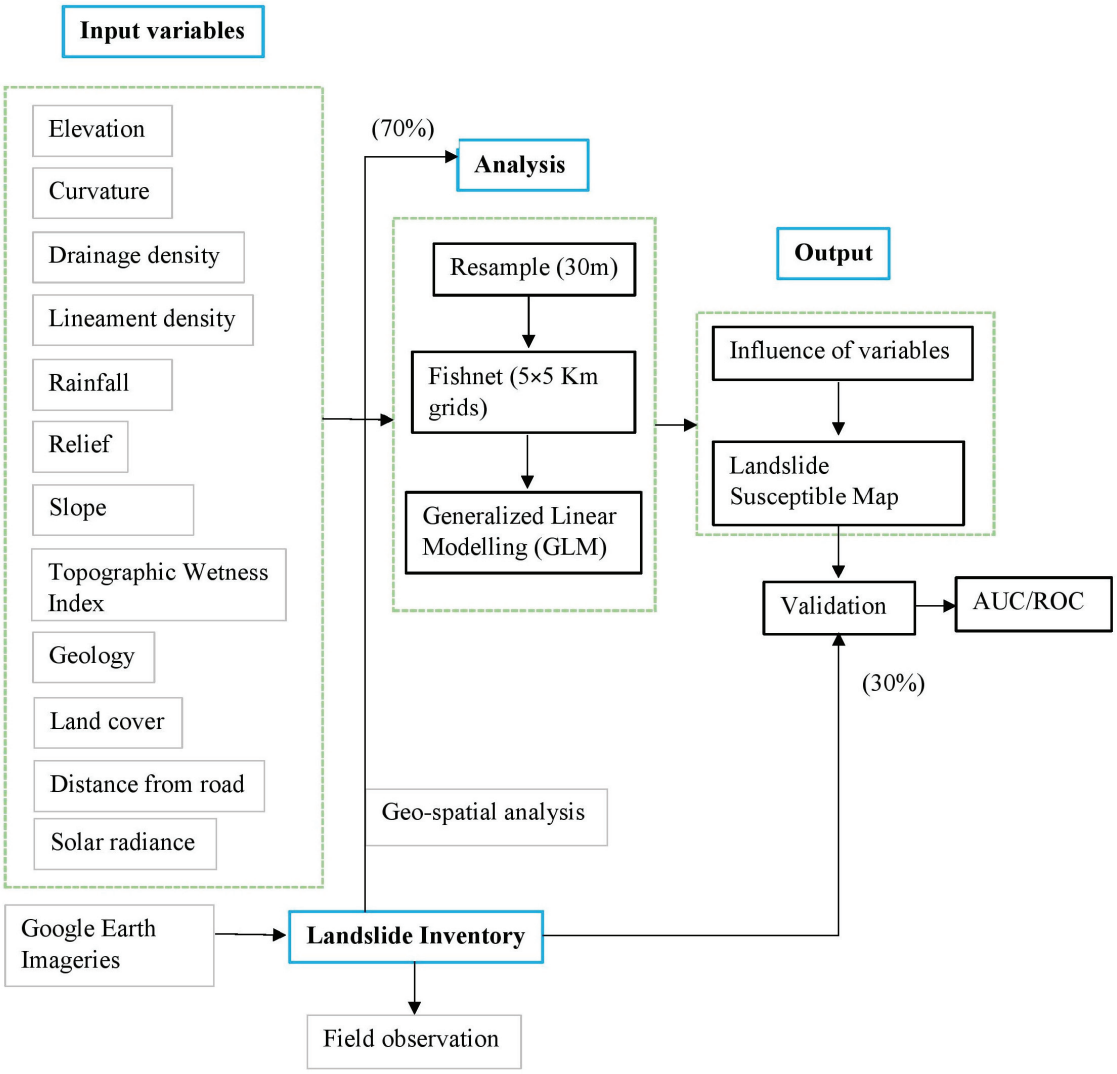

Figure 3. Methodological framework of this study.

Once all the variables were finalized and compiled, they were resampled to the same extent and resolution of 30 m for further analysis. This involved clipping the variables to form 30 km^2 cells. Model fitting was performed using the 'DescTools' package [67] and the 'manipulate' package [68]. Prior to constructing the model, a multicollinearity test was conducted using the VIF (variance inflation factor) function from the 'faraway' package [69] for all variables. Importantly, none of the variables exhibited significant multicollinearity (VIF value > 5), thereby allowing the inclusion of all variables in the model construction [70]. Weightage was assigned to each variable based on the coefficient values obtained from the model to predict the potential landslide susceptibility map. ArcGIS 10.8 was then employed to prepare the final landslide susceptibility map. The model's effectiveness was assessed through the AUC curve, ranging between 0 and 1, where a value of 1 is considered the maximum. Models or classifications with an AUC value above 0.9 were regarded as outstanding, those in the range of 0.8–0.9 were regarded as excellent, and those in the range of 0.7–0.8 were regarded as acceptable. Values below 0.5 were considered false and inaccurate [71].

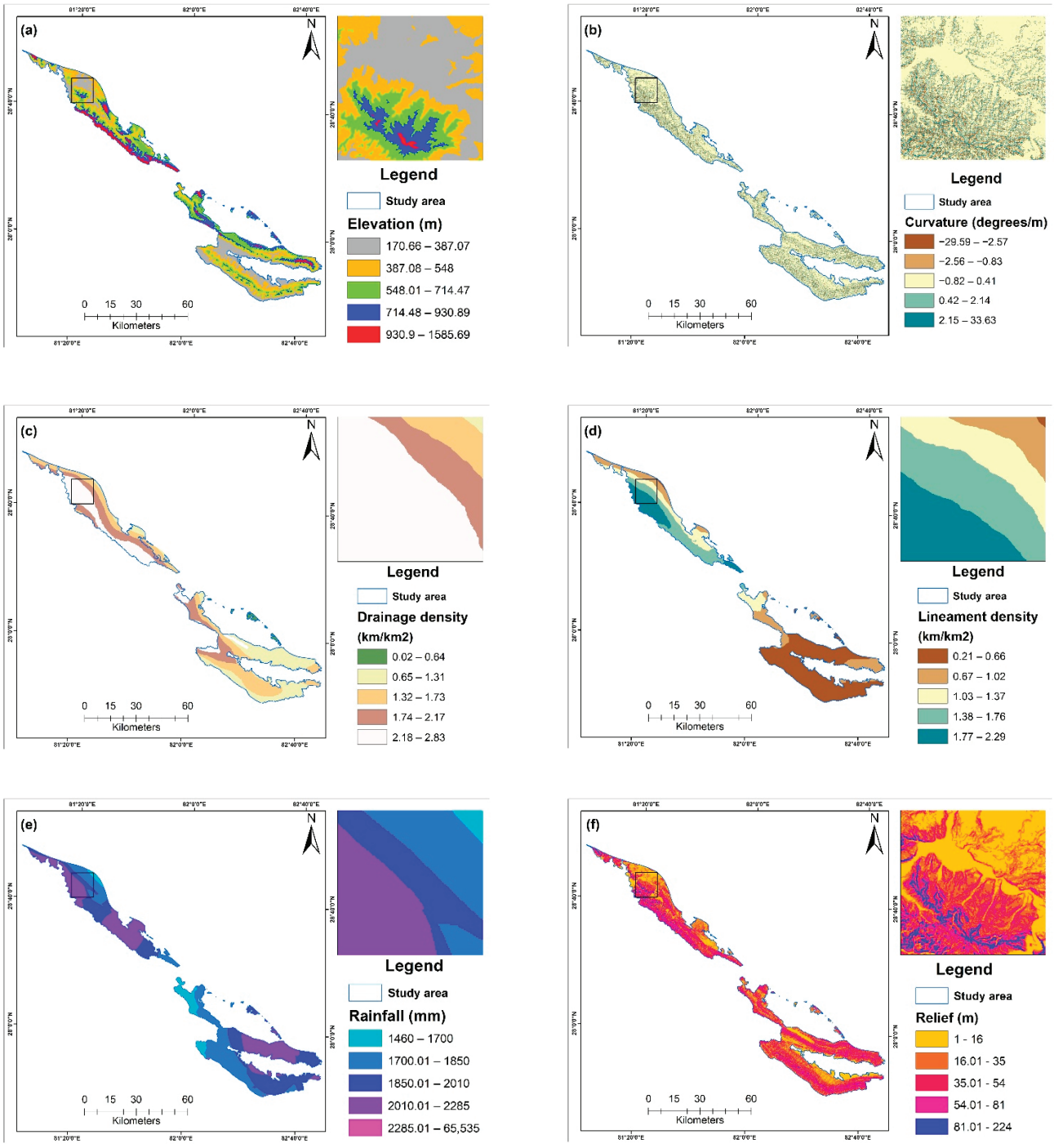

Figure 4. *Cont.*

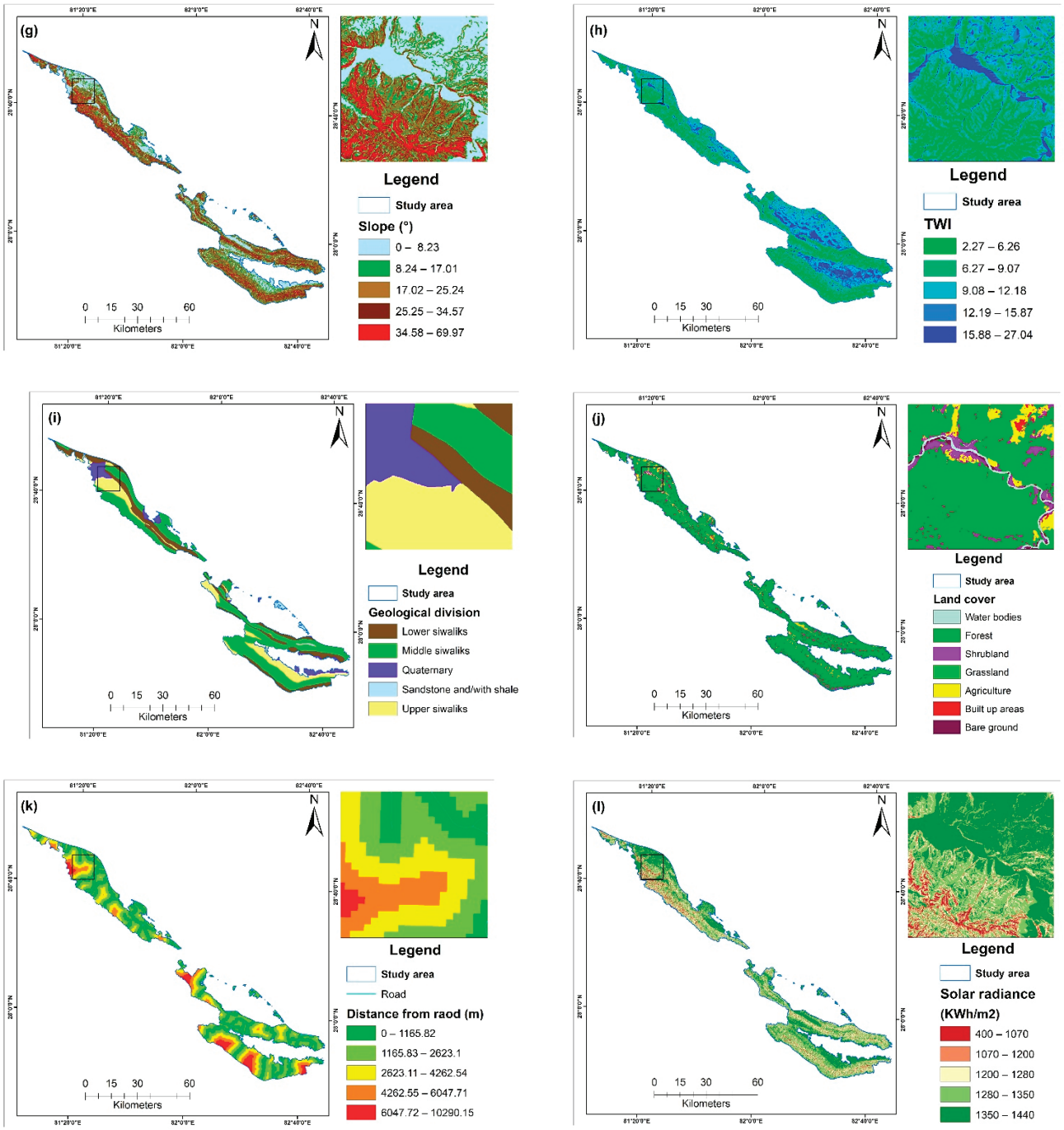

Figure 4. Predictor variables considered for spatial analysis: (**a**) elevation, (**b**) curvature, (**c**) drainage density, (**d**) lineament density, (**e**) rainfall, (**f**) relief, (**g**) slope, (**h**) topographical wetness index (TWI), (**i**) geology, (**j**) land cover, (**k**) distance from road, and (**l**) solar radiance.

4. Results

4.1. Geospatial Analysis of Landslide

The spatial analysis of the landslide points was conducted to determine the spatial pattern of landslides across variables. In examining the land cover within the study area, disparities in the distribution of different land cover classes were identified. The forest area emerged as the dominant cover class, constituting approximately 83% (n = 1041) of the total landslide count. Shrubland and grassland followed with 15.2% (n = 189) and 3%

(n = 49), respectively. Other land cover types, including water bodies, agricultural areas, and bare ground, collectively accounted for less than 1% of the total landslides.

Concerning the geological divisions, the middle Siwalik region exhibited the highest concentration of landslides, representing approximately 51% of the cases, while the lower Siwalik, upper Siwalik, and quaternary divisions contributed 35% (n = 441), 11% (n = 142), and 1% (n = 22) of the landslides, respectively. Proximity to roads played a crucial role in landslide occurrence, with a notable increase in incidence within 2000 m. Furthermore, areas at altitudes between 300 and 600 m above mean sea level demonstrated the highest incidence of landslides, comprising a significant portion of the total landslides (n = 642). The examination of relief, representing elevation variations between points, identified the 50–60 m range as having the highest landslide frequency. Regarding drainage and lineament density, the distribution of landslide data exhibited an uneven pattern. However, the 1–1.5 km/km^2 drainage density range and the above 1.2 km/km^2 lineament density range were associated with the greatest number of landslides, accounting for 54% (n = 671) of the cases. Landslides with slopes between 20 and 50 degrees, particularly those with slopes above 35 degrees that are concave in nature, contributed to nearly 64% of landslides (n = 539). Furthermore, concerning the climatic variables, it was observed that regions characterized by rainfall exceeding 1800 mm/month exhibited the highest landslide frequency, accounting for a substantial 81% (n = 1017) of the recorded cases. Similarly, areas displaying a topographical wetness index (TWI) within the range of 5–10 constituted 53% (n = 659), and solar radiance between 1300 and 1350 KWh m^{-2} demonstrated elevated landslide occurrence (Figure 5).

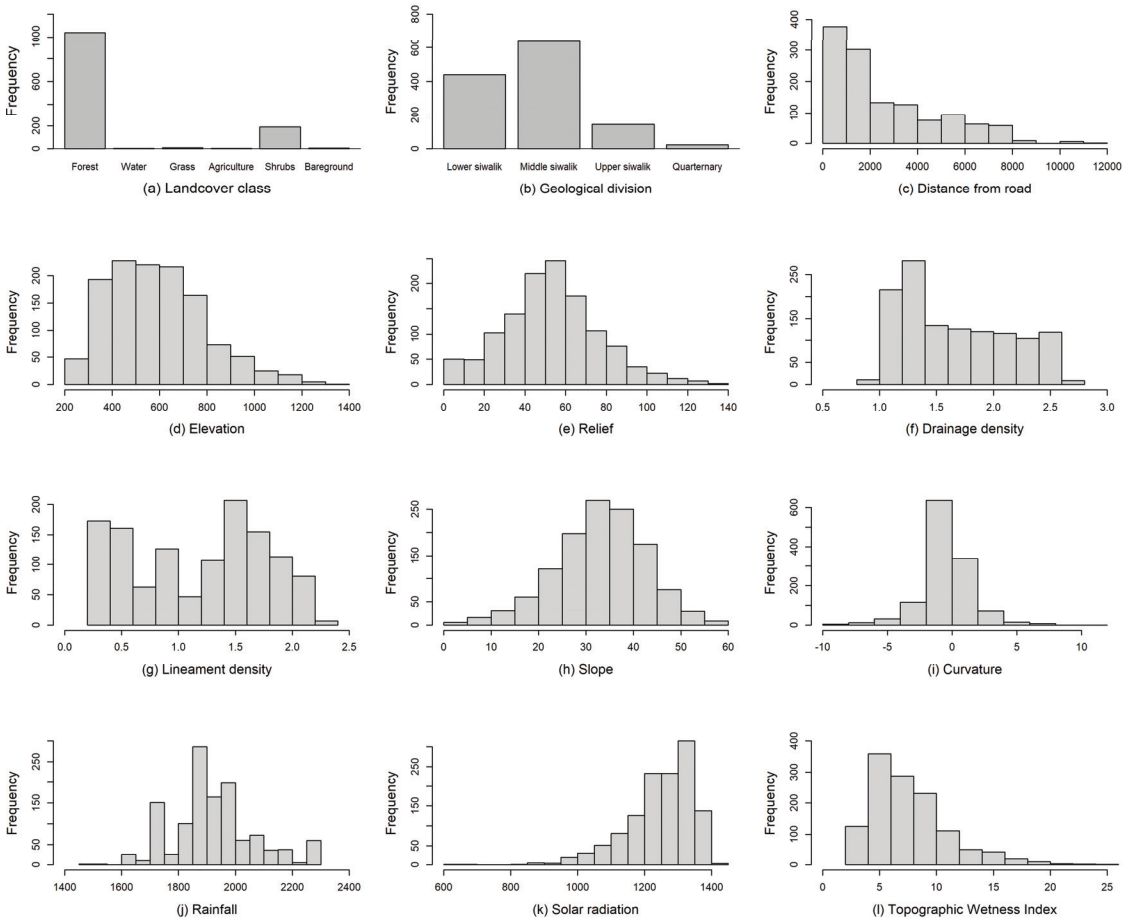

Figure 5. Landslide frequency across various variables: (**a**) land cover, (**b**) geology, (**c**) distance from road, (**d**) elevation, (**e**) relief, (**f**) drainage density, (**g**) lineament density, (**h**) slope, (**i**) curvature, (**j**) rainfall, (**k**) solar radiation, and (**l**) topographical wetness index.

4.2. Influence of Variables on Landslides

We conducted a comprehensive analysis to understand the factors influencing the occurrence of landslides in the study area. The Poisson regression model that we employed yielded valuable insights into the relationship between landslide count and several environmental variables (Table 2).

Table 2. Generalized linear model with the Poisson structure for the probability of landslide occurrence.

	Estimate	Std. Error	z Value	Pr (>|z|)
(Intercept)	-5.25	3.62×10^{-1}	-14.503	$<2.00 \times 10^{-16}$ ***
Curvature	-2.07×10^{-2}	1.80×10^{-2}	-1.155	0.248151
Digital elevation model	1.32×10^{-3}	1.91×10^{-4}	6.903	5.08×10^{-12} ***
Drainage density	-1.37×10^{-5}	4.68×10^{-5}	-0.292	0.770134
Lineament	-5.83×10^{-1}	8.50×10^{-2}	-6.86	6.91×10^{-12} ***
Rainfall	1.46×10^{-3}	2.04×10^{-4}	7.168	7.63×10^{-13} ***
Relief	6.42×10^{-3}	1.93×10^{-3}	3.324	0.000889 ***
slope	-1.09×10^{-4}	1.90×10^{-5}	-5.719	1.07×10^{-8} ***
Solar	2.01×10^{-2}	2.80×10^{-3}	7.171	7.44×10^{-13} ***
Topographical wetness index	4.31×10^{-4}	1.05×10^{-2}	0.041	0.96737
Middle Siwalik	-5.94×10^{-1}	6.84×10^{-2}	-8.673	$<2.00 \times 10^{-16}$ ***
Upper Siwalik	-1.20	1.25×10^{-1}	-9.636	$<2.00 \times 10^{-16}$ ***
Quaternary	-1.32	2.66×10^{-1}	-4.965	6.87×10^{-7} ***
Area of water bodies	1.24×10^{-6}	4.79×10^{-7}	-2.587	0.009679 **
Area of forest	2.73×10^{-7}	2.72×10^{-8}	10.03	$<2.00 \times 10^{-16}$ ***
Area of grassland	2.21×10^{-5}	5.07×10^{-6}	4.35	1.36×10^{-5} ***
Area of agricultural land	6.63×10^{-7}	2.39×10^{-7}	2.779	0.005454 **
Area of bare ground	2.08×10^{-6}	8.61×10^{-7}	2.414	0.015764 *
Area of shrubland	3.84×10^{-7}	8.51×10^{-8}	4.51	6.49×10^{-6} ***
Distance from road	-3.06×10^{-6}	1.73×10^{-5}	-0.177	0.859502

Null deviance: 3965.54 on 620 degrees of freedom. Residual deviance: 926.22 on 601 degrees of freedom. AIC: 1612.8. Number of Fisher scoring iterations: 6. Significance codes: 0, '***' 0.001, '**' 0.01, '*' 0.05, 0.1, 1.

Starting with the intercept, which represents the expected log of the mean landslide count when all other variables are zero, we found it to be highly significant (-5.249, $p < 2 \times 10^{-16}$). Among the continuous variables, we observed significant associations between landslide count and several factors. Curvature did not significantly affect landslide count ($p = 0.248151$). Elevation, as represented via the DEM (digital elevation model), had a positive coefficient (0.00132, $p < 5.08 \times 10^{-12}$), suggesting that higher elevations are associated with increased landslide counts. This is understandable since steep slopes at higher elevations are more prone to slope instability and, thus, landslides.

Similarly, rainfall (0.001463, $p < 7.63 \times 10^{-13}$) was positively correlated with landslide count, implying that regions with higher rainfall tend to experience more landslides. Lineament was an important variable in our analysis, and it exhibited a significant negative coefficient (-0.5829, $p < 6.91 \times 10^{-12}$). This suggests that areas with a higher density of lineaments are associated with a lower incidence of landslides. Furthermore, relief (0.006422, $p < 0.000889$) positively affected the landslide count. Conversely, slope (-0.0001088, $p < 1.07 \times 10^{-8}$) had a negative coefficient, indicating that steeper slopes tend to have fewer landslides. This finding suggests that beyond a certain threshold, highly steep slopes may not provide the conditions necessary for landslides to occur.

For the categorical variable, namely geology, we included four categories: lower Siwalik, middle Siwalik, upper Siwalik, and quaternary. Middle Siwalik (-0.5935, $p < 2 \times 10^{-16}$) and upper Siwalik (-1.201, $p < 2 \times 10^{-16}$) both had negative coefficients, indicating that these geological formations were associated with lower landslide counts compared to lower Siwalik ones. Quaternary (-1.322, $p < 6.87 \times 10^{-7}$) also had a negative coefficient, implying a similar trend.

Additionally, several other variables were significant predictors of landslide count. Solar radiation (2.007×10^{-2}, $p < 7.44 \times 10^{-13}$) had a positive effect, implying that areas

with higher solar radiation levels experience more landslides. This could be attributed to the influence of solar radiation on soil moisture, vegetation growth, and erosion processes, which, in turn, affect landslide activity. The area under water (1.239×10^{-6}, $p = 0.009679$) showed a negative coefficient, suggesting that the presence of water bodies might decrease landslide counts. Several land cover types were also found to be significant predictors of landslide count. The areas under forest (2.73×10^{-7}, $p < 2 \times 10^{-16}$), grassland (2.207×10^{-5}, $p < 1.36 \times 10^{-5}$), agricultural land (6.629×10^{-7}, $p = 0.005454$), bare ground (2.079×10^{-6}, $p = 0.015764$), and shrubland (3.836×10^{-7}, $p < 6.49 \times 10^{-6}$) all had positive coefficients, suggesting that larger areas covered by forests, grasslands, agricultural land, bare ground, and shrubland positively influence landslide counts. Lastly, the distance to roads did not significantly affect the landslide count ($p = 0.859502$). This indicates that the distance to roads may not significantly influence landslide activity in the study area.

The model fit was assessed using the deviance statistic. The substantial reduction in the residual deviance (from 3965.54 to 926.22) indicates that the included variables explain a considerable portion of the variation in landslide counts. This suggests that the model effectively captures the relationship between the predictors and landslide occurrence. The low AIC value (1612.8) further supports the adequacy of the model fit, indicating its ability to balance goodness-of-fit and model complexity.

4.3. Landslide Susceptible Map

Utilizing the modeling above result, we delineated the landslide susceptibility map of the region in ArcGIS using the raster calculator toolkit, and this tool was further categorized into five categories using the built-in Jenks natural breaks classification (Figure 6). It showed that around 16%, or 414 km^2, area of the Chure region of Dang and Surkhet district falls in the very-high-susceptibility zone; about 69%, or 1793 km^2, area lies in the high-susceptibility zone; 12%, or 313 km^2, area lies in the moderate-susceptibility zone; 2%, or 58 km^2, area lies in the low-susceptibility zone, and 0.03%, or 1 km^2, area lies in the very-low-susceptibility zone (Table 3). Overall, the Chure region of Dang is more vulnerable, with about 23% of the area having very high susceptibility compared to around 5% in the Surkhet district.

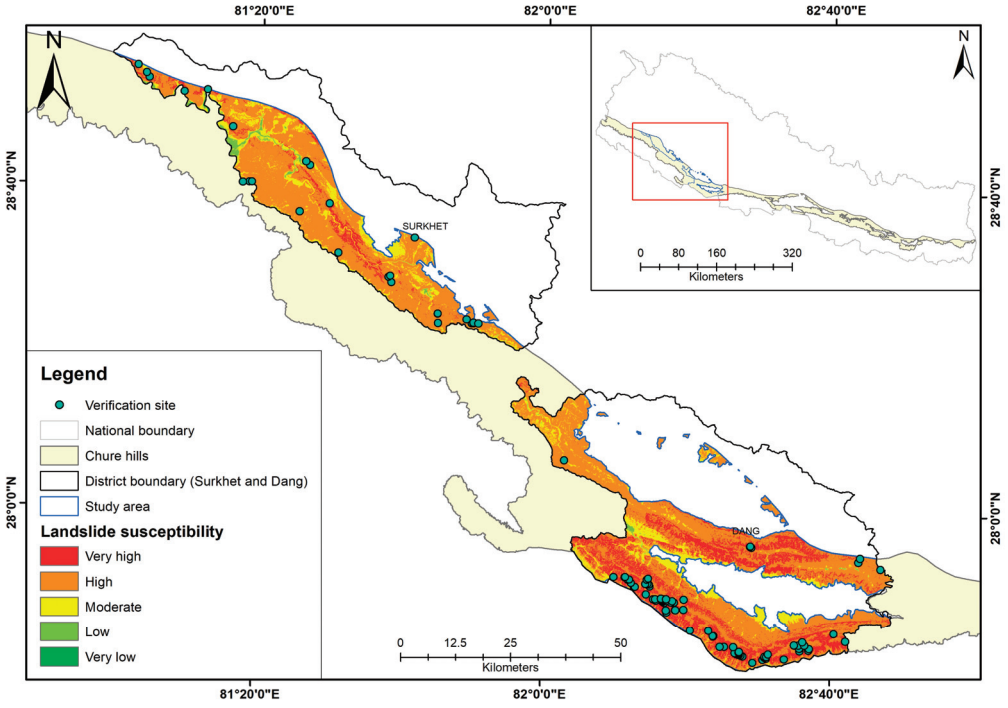

Figure 6. Landslide susceptibility map.

Table 3. The areas of Dang and Surkhet are located in different categories of the susceptibility map.

Risk Zone	Dang (km^2)	Surkhet (km^2)	Total
Very high	360 (23.32%)	54 (5.22%)	414 (16.05%)
High	994 (64.38%)	799 (77.20%)	1793 (69.52%)
Moderate	159 (10.30%)	154 (14.88%)	313 (12.14%)
Low	31 (2.01%)	27 (2.61%)	58 (2.25%)
Very low	0	1 (0.1%)	1 (0.04%)
Total (km^2)	**1544**	**1035**	**2579**

4.4. Validation

The validation was carried out for both the landslide points and the produced map. Due to resource constraints, only around 10% (n = 124) of the randomly selected landslide points were verified in the field. From the field verification, we found that around 72% (n = 89) of the landslides represented accurate landslide occurrences, and 28% might have been falsely identified as landslides. Furthermore, the produced landslide hazard map was validated through the ROC/AUC curve. The validation was conducted using the ArcSDM tool kit in ArcGIS, utilizing about 30% of the landslide points. The produced AUC value for the map was 0.779, which shows that the results are accurate (Figure 7).

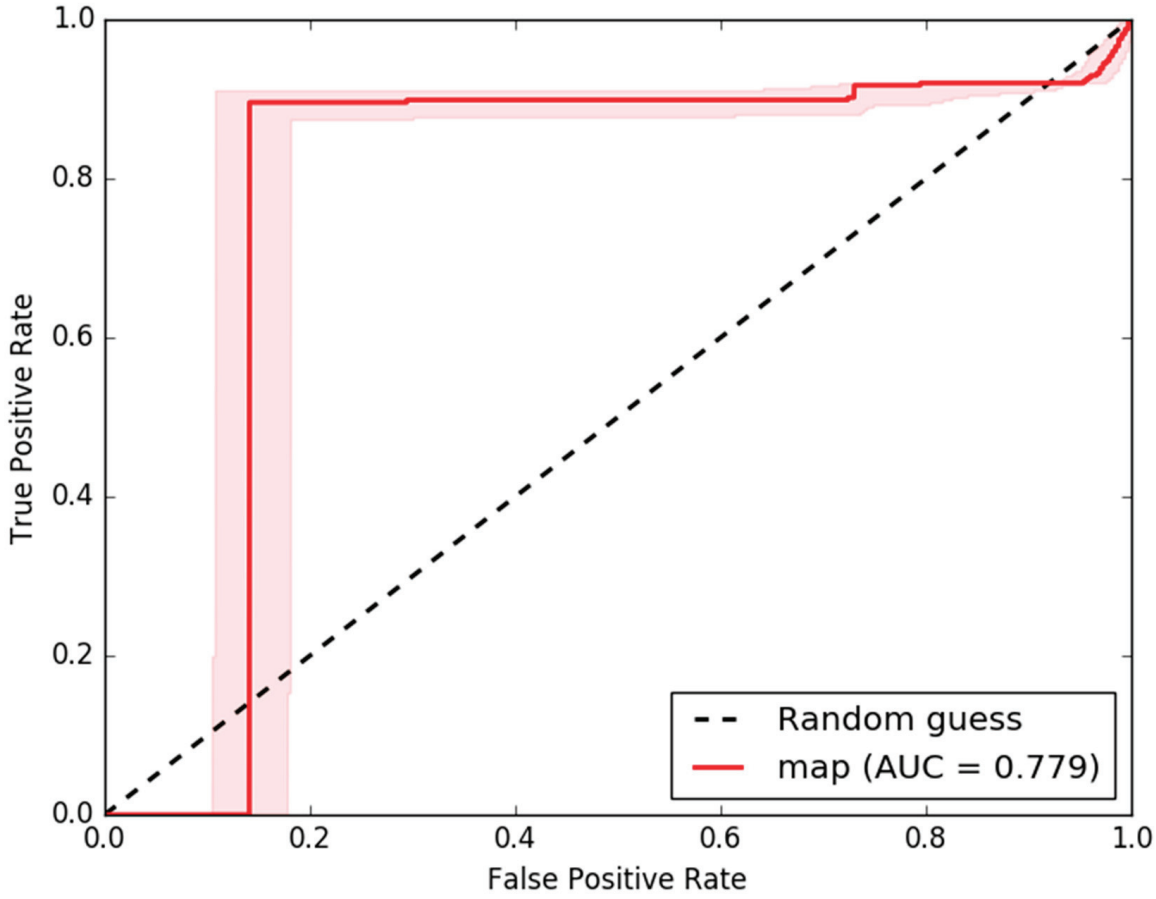

Figure 7. ROC-AUC curve for the landslide susceptibility map.

5. Discussion

The main objective of this study was to assess landslide susceptibility in the highly vulnerable districts of the fragile Chure region using Poisson regression modeling. Previous studies have highlighted the geological fragility of the Chure region for landslides, and our findings are consistent with this trend. We observed a higher frequency of landslides

in the middle Siwalik, which aligns with the study by Bhandari and Dhakal [72] in the Babai Khola watershed. However, our modeling results suggest that lower Siwaliks are more susceptible to landslides. This could be due to the presence of a thicker weathered mudstone layer in the lower Siwalik, making it highly vulnerable to erosion-induced landslides [73]).

Moreover, improper drainage management and the likelihood of floods in the lower Siwaliks [74,75] could exacerbate landslides and mass movement in this region. Another significant variable in our analysis was lineament density. The negative relationship indicates that higher lineament density reduces landslide susceptibility in this region. This finding contradicts the results of Lee and Talib [44], who conducted a factor analysis of landslides in Malaysia. Generally, higher lineament density is associated with more faults and fractures, weakening geology through weathering and erosion, especially during rainfall, when fractures induce soil movement [76,77]. However, in the case of our study area, the negative relationship means that a lower density of lineament is associated with a higher risk of landslides. According to Saha & Saha [78], areas with lineament density above 1.5 km/km^2 are highly susceptible to landslides, but in our study area, almost 81% of the total areas were below the 1.5 km/km^2 range.

The topographical variables found to be significant were elevation, relief, and slope. In our study, elevation was found to positively affect landslides. This can be attributed to various anthropogenic activities, such as development and agriculture, along the fragile and sloping regions at higher elevations, as Gurung et al. [79] reported in the Indrawati watershed of Nepal. Similarly, relief and slope were also found to be significant factors causing landslides, which is in line with the results of Ghimire [80], who reported slope and relief as proxy indicators for landslide susceptibility mapping in the Siwalik region. Furthermore, our study suggests that the probability of landslide occurrence in the Chure region decreases as the slope increases. Similar findings have been reported by Devkota et al. [41] in the Mugling–Narayanghat road section of Nepal and Regmi and Poudel [42] in the Patlu Khola watershed in Dang. This characteristic nature of landslides might have been observed due to fewer anthropogenic activities occurring on higher slopes, which can cause slope failure [79].

Among the three climatic variables, rainfall and solar radiation were significant in our modeling results. We observed a positive relationship between rainfall and landslide occurrence, suggesting that higher amounts of precipitation increase the risk of landslides. This finding is in congruence with the study by Petley et al. [3], which reported a strong correlation between the monsoon season and landslides in Nepal. Furthermore, solar radiation was found to have a positive relationship with and be an important predictor of regional landslides. Similar positive relationships between solar radiation and landslide occurrences have been reported by Cheng et al. [81] in their landslide prediction study conducted in Taiwan. The impact of solar radiation on landslides is similar to that of aspect, as described by Du et al. [82], where southern aspects receiving higher sunlight are more vulnerable to landslides [83]. The relationship between landslides and solar radiation can also be explained by the fact that areas with higher solar exposure tend to have less moisture and sparse vegetation, making them more susceptible to landslides [82,84].

Despite very low estimates, we found that areas under forest, shrubland, grassland, agricultural land, and bare ground were significant and positively related to landslides. Various studies have also reported the outburst of and debris flow from water bodies like rivers, streams, and waterfalls, which are severe problems for landslides [85,86]. Similarly, increasing unsustainable agricultural activities and unmanaged development activities have also been reported by Alimohammadlou et al. [87] as major triggering agents for landslides. Contrastingly, vegetation areas like forests have been reported as insignificant variables in various studies worldwide [88,89]. The significant result in our case may be due to the less productive land of the Chure region, resulting in a struggle for vegetation growth and low stem volume per ha, along with the middle mountains [7]. Hence, restrictions have been implemented in green felling to reduce the vulnerability of the Chure region.

Furthermore, indicative growing stock increments for the Chure region have been limited to 1% in forest management plans, out of which only 40% is allowed to be harvested in the community forests of the Chure region of Nepal to minimize ecological degradation [90]. Similar actions and policies enforced in the region further support our results, as even forests and other vegetative areas are prone to landslides in the Chure region.

We created a susceptibility map from the modeling results with five categories: very high, high, moderate, low, and very low. Our findings indicate that most of the study area falls into the very-high- (16%) and high (69%)-susceptibility categories, highlighting the high vulnerability of the Chure region in the Dang and Surkhet districts. These results align with the findings of Gyawali and Tamrakar [86], whose landslide susceptibility assessment of the Chure Khola catchment area reported around 72.46% of their study area to be in the very-high- and high-susceptibility categories.

To assess the accuracy of our susceptibility map, we employed the area under curve (AUC) technique and obtained a value of 0.779 (77.9%). This indicates that our final susceptibility map has accurate results and is consistent with other studies that used different techniques in Nepal. For example, Dahal et al. [91] utilized a weight of evidence modeling approach in the Lesser Himalaya range of the Kathmandu Valley and achieved a prediction rate of 79%. Similarly, Gyawali and Tamrakar [92] reported a 78% accuracy using their statistical index method. We recommend incorporating land cover changes into the modeling process to further improve the model and its accuracy. Dynamic land cover data can provide valuable insights regarding the changes in vegetation, urbanization, and other land-use practices that may influence landslide occurrences over time. By considering these temporal changes, the model can be better calibrated and adapted to the evolving landscape of the Chure region.

Our analysis observed an insignificant relationship between the distance to roads and landslide counts. This finding is consistent with the study conducted by Thapa and Bhandari [35], which also reported a weak relationship between road networks and landslide susceptibility in the Siwalik region. In contrast, we found that geology, climatic, and topographical variables had higher influences on landslide susceptibility in our study. The region's high percentage of landslide-susceptible areas underscores the need to carefully consider developmental activities and anthropogenic projects, such as sand mining, in the Chure region. It is essential for such projects to undergo a comprehensive environmental impact assessment (EIA) before their commencement.

6. Conclusions

Our comprehensive Poisson regression analysis of landslide occurrences in the sandy Chure region revealed significant insights regarding the relationships between various environmental variables and landslide counts. The results highlighted the significance of geology, lineament density, elevation, relief, slope, solar radiation, and land cover types as crucial predictors of landslide counts. Higher elevations and increased rainfall were positively correlated with landslide counts, while lineament density and slope exhibited negative relationships. Relief and solar radiation had positive effects, indicating that areas with higher relief and solar exposure experienced more landslides. The categorical variable, namely geology, highlighted lower landslide counts in middle Siwalik, upper Siwalik, and Quaternary geological formations compared to lower Siwalik. The distance to the road did not significantly affect landslide counts. The developed landslide susceptibility map identified high-susceptibility areas in the Chure hills of the Dang and Surkhet districts, emphasizing the urgent need for disaster mitigation measures and responsible land-use planning. Dang, in particular, was identified as more vulnerable, with about 23% of the area falling into the very-high-susceptibility zone, compared to around 5% in Surkhet. The robustness of our model, which is supported by a 77.9% accuracy rate in the AUC analysis, solidifies the reliability of our findings. Overall, this study provides valuable insights into the factors influencing landslide occurrences in the Chure region, and the developed

susceptibility map can serve as a valuable tool for decision-makers for prioritizing risk management efforts and enhancing disaster preparedness in the study area.

Author Contributions: P.B.T., Conceptualization, data, materials and funding acquisition; S.L., conceptualization, methodology, data curation and writing-original draft preparation, supervision, review and editing; K.P.J., conceptualization, methodology, data curation, writing-original draft preparation, review and editing; A.R.R., conceptualization, writing-original draft preparation, review and editing; D.B., conceptualization, writing-original draft preparation, review and editing; H.A., supervision, review and editing, funding acquisition. All authors have read and agreed to the published version of the manuscript.

Funding: This research received no external funding.

Data Availability Statement: The data presented in this study are available on request from the corresponding author.

Conflicts of Interest: The authors declare no conflict of interest.

References

1. Highland, L. *Estimating Landslide Losses–Preliminary Results of a Seven-State Pilot Project*; US Geological Survey Reston: Reston, VA, USA, 2006.
2. Kjekstad, O.; Highland, L. Economic and Social Impacts of Landslides. In *Landslides–Disaster Risk Reduction*; Sassa, K., Canuti, P., Eds.; Springer: Berlin/Heidelberg, Germany, 2009; pp. 573–587. ISBN 978-3-540-69970-5.
3. Petley, D.N.; Hearn, G.J.; Hart, A.; Rosser, N.J.; Dunning, S.A.; Oven, K.; Mitchell, W.A. Trends in Landslide Occurrence in Nepal. *Nat. Hazards* **2007**, *43*, 23–44. [CrossRef]
4. Upreti, B.N. The Physiography and Geology of Nepal and Their Bearing on the Landslide Problem. In *Landslide Hazard Mitigation in the Hindu Kush-Himalaya*; International Centre for Integrated Mountain Development: Kathmandu, Nepal, 2001; pp. 31–49.
5. Subedi, B.; Lamichhane, P.; Magar, L.K.; Subedi, T. Aboveground Carbon Stocks and Sequestration Rates of Forests under Different Management Regimes in Churia Region of Nepal. *Banko Janakari* **2022**, *32*, 15–24. [CrossRef]
6. Singh, B.K. Land Tenure and Conservation in Chure. *J. For. Livelihood* **2017**, *15*, 87–102. [CrossRef]
7. Department of Forest Research and Survey. *State of Nepal's Forests*; Department of Forest Research and Survey: Kathmandu, Nepal, 2014.
8. Chaudhary, R.; Subedi, C. Chure-Tarai Madhesh Landscape, Nepal from Biodiversity Research Perspective. *Plant Arch.* **2019**, *19*, 351–359.
9. PCTMCD. *President Chure-Tarai Madhesh Conservation and Management Master Plan*; President Chure-Tarai Madhesh Conservation Development Board: Lalitpur, Nepal, 2018.
10. Alharbi, T.; Sultan, M.; Sefry, S.; ElKadiri, R.; Ahmed, M.; Chase, R.; Milewski, A.; Abu Abdullah, M.; Emil, M.; Chounaird, K. An Assessment of Landslide Susceptibility in the Faifa Area, Saudi Arabia, Using Remote Sensing and GIS Techniques. *Nat. Hazards Earth Syst. Sci.* **2014**, *14*, 1553–1564. [CrossRef]
11. Nhu, V.-H.; Mohammadi, A.; Shahabi, H.; Ahmad, B.B.; Al-Ansari, N.; Shirzadi, A.; Clague, J.J.; Jaafari, A.; Chen, W.; Nguyen, H. Landslide Susceptibility Mapping Using Machine Learning Algorithms and Remote Sensing Data in a Tropical Environment. *Int. J. Environ. Res. Public Health* **2020**, *17*, 4933. [CrossRef]
12. Ullah, I.; Aslam, B.; Shah, S.H.I.A.; Tariq, A.; Qin, S.; Majeed, M.; Havenith, H.-B. An Integrated Approach of Machine Learning, Remote Sensing, and GIS Data for the Landslide Susceptibility Mapping. *Land* **2022**, *11*, 1265. [CrossRef]
13. Shi, X.; Liao, M.; Zhang, L.; Balz, T. Landslide Stability Evaluation Using High-Resolution Satellite SAR Data in the Three Gorges Area. *Q. J. Eng. Geol. Hydrogeol.* **2016**, *49*, 203–211. [CrossRef]
14. Van Westen, C.J.; Rengers, N.; Soeters, R. Use of Geomorphological Information in Indirect Landslide Susceptibility Assessment. *Nat. Hazards* **2003**, *30*, 399–419. [CrossRef]
15. Saleem, N.; Huq, M.E.; Twumasi, N.Y.D.; Javed, A.; Sajjad, A. Parameters Derived from and/or Used with Digital Elevation Models (DEMs) for Landslide Susceptibility Mapping and Landslide Risk Assessment: A Review. *ISPRS Int. J. Geo-Inf.* **2019**, *8*, 545. [CrossRef]
16. Zhao, C.; Lu, Z. Remote Sensing of Landslides—A Review. *Remote Sens.* **2018**, *10*, 279. [CrossRef]
17. Corominas, J.; van Westen, C.; Frattini, P.; Cascini, L.; Malet, J.-P.; Fotopoulou, S.; Catani, F.; Van Den Eeckhaut, M.; Mavrouli, O.; Agliardi, F.; et al. Recommendations for the Quantitative Analysis of Landslide Risk. *Bull Eng. Geol. Environ.* **2014**, *73*, 209–263. [CrossRef]
18. Ghimire, M.; Timalsina, N. Landslide Distribution and Processes in the Hills of Central Nepal: Geomorphic and Statistical Approach to Susceptibility Assessment. *J. Geosci. Environ. Prot.* **2020**, *8*, 276–302. [CrossRef]
19. Kanungo, D.P.; Arora, M.K.; Sarkar, S.; Gupta, R.P. A Comparative Study of Conventional, ANN Black Box, Fuzzy and Combined Neural and Fuzzy Weighting Procedures for Landslide Susceptibility Zonation in Darjeeling Himalayas. *Eng. Geol.* **2006**, *85*, 347–366. [CrossRef]

20. Raghuvanshi, T.K.; Ibrahim, J.; Ayalew, D. Slope Stability Susceptibility Evaluation Parameter (SSEP) Rating Scheme–an Approach for Landslide Hazard Zonation. *J. Afr. Earth Sci.* **2014**, *99*, 595–612. [CrossRef]
21. Carrara, A.; Cardinali, M.; Guzzetti, F.; Reichenbach, P. Gis Technology in Mapping Landslide Hazard. In *Geographical Information Systems in Assessing Natural Hazards*; Carrara, A., Guzzetti, F., Eds.; Advances in Natural and Technological Hazards Research; Springer: Dordrecht, The Netherlands, 1995; pp. 135–175. ISBN 978-94-015-8404-3.
22. Safaei, M.; Omar, H.; Huat, B.K.; Yousof, Z.B.; Ghiasi, V. Deterministic Rainfall Induced Landslide Approaches, Advantage and Limitation. *Electron. J. Geotech. Eng.* **2011**, *16*, 1619–1650.
23. Anis, Z.; Wissem, G.; Vali, V.; Smida, H.; Essghaier, G.M. GIS-Based Landslide Susceptibility Mapping Using Bivariate Statistical Methods in North-Western Tunisia. *Open Geosci.* **2019**, *11*, 708–726. [CrossRef]
24. Pradhan, B.; Lee, S. Landslide Susceptibility Assessment and Factor Effect Analysis: Backpropagation Artificial Neural Networks and Their Comparison with Frequency Ratio and Bivariate Logistic Regression Modelling. *Environ. Model. Softw.* **2010**, *25*, 747–759. [CrossRef]
25. Abdo, H.G. Assessment of Landslide Susceptibility Zonation Using Frequency Ratio and Statistical Index: A Case Study of Al-Fawar Basin, Tartous, Syria. *Int. J. Environ. Sci. Technol.* **2022**, *19*, 2599–2618. [CrossRef]
26. Mersha, T.; Meten, M. GIS-Based Landslide Susceptibility Mapping and Assessment Using Bivariate Statistical Methods in Simada Area, Northwestern Ethiopia. *Geoenviron Disasters* **2020**, *7*, 20. [CrossRef]
27. Guo, M.; Li, J.; Sheng, C.; Xu, J.; Wu, L. A Review of Wetland Remote Sensing. *Sensors* **2017**, *17*, 777. [CrossRef] [PubMed]
28. Abija, F.A.; Nwosu, J.I.; Ifedotun, A.I.; Osadebe, C.C. Landslide Susceptibility Assessment of Calabar, Nigeria Using Geotechnical, Remote Sensing and Multi-Criteria Decision Analysis: Implications for Urban Planning and Development. *SDRP-JESES* **2019**, *4*, 774–788. [CrossRef]
29. Brenning, A. Spatial Prediction Models for Landslide Hazards: Review, Comparison and Evaluation. *Nat. Hazards Earth Syst. Sci.* **2005**, *5*, 853–862. [CrossRef]
30. Atkinson, P.M.; Massari, R. Generalised Linear Modelling of Susceptibility to Landsliding in the Central Apennines, Italy. *Comput. Geosci.* **1998**, *24*, 373–385. [CrossRef]
31. Crovelli, R.A. *Probability Models for Estimation of Number and Costs of Landslides*; US Geological Survey: Reston, VA, USA, 2000.
32. Das, I.; Kumar, G.; Stein, A.; Bagchi, A.; Dadhwal, V.K. Stochastic Landslide Vulnerability Modeling in Space and Time in a Part of the Northern Himalayas, India. *Environ. Monit. Assess* **2011**, *178*, 25–37. [CrossRef] [PubMed]
33. Chung, C.-J.F.; Fabbri, A.G.; Van Westen, C.J. Multivariate Regression Analysis for Landslide Hazard Zonation. In *Geographical Information Systems in Assessing Natural Hazards*; Carrara, A., Guzzetti, F., Eds.; Advances in Natural and Technological Hazards Research; Springer: Dordrecht, The Netherlands, 1995; pp. 107–133. ISBN 978-94-015-8404-3.
34. Shrestha, K.; Khadka, U.R.; Singh Shrestha, M. Comparative GIS-Based Assessment of Landslide Susceptibility of Chepe River Corridor, Gandaki River Basin, Nepal. In *Integrated Research on Disaster Risks*; Djalante, R., Bisri, M.B.F., Shaw, R., Eds.; Disaster Risk Reduction; Springer International Publishing: Berlin/Heidelberg, Germany, 2021; pp. 111–136. ISBN 978-3-030-55562-7.
35. Thapa, D.; Bhandari, B.P. GIS-Based Frequency Ratio Method for Identification of Potential Landslide Susceptible Area in the Siwalik Zone of Chatara-Barahakshetra Section, Nepal. *Open J. Geol.* **2019**, *09*, 873. [CrossRef]
36. CBS. *National Population and and Housing Census 2021*; Central Bureau of Statistics: Kathmandu, Nepal; National Planning Commission: Kathmandu, Nepal, 2021.
37. Uprety, Y.; Tiwari, A.; Karki, S.; Chaudhary, A.; Yadav, R.K.P.; Giri, S.; Shrestha, S.; Paudyal, K.; Dhakal, M. Characterization of Forest Ecosystems in the Chure (Siwalik Hills) Landscape of Nepal Himalaya and Their Conservation Need. *Forests* **2023**, *14*, 100. [CrossRef]
38. Manandhar, E.; Kharel, B.P.; Basnet, L. Integrated River System Resource Management Planning: A Stepping Stone for Sustainable Conservation of Chure-TaraiMadhesh Landscape. In *Proceedings of the Seminar on Leaving no One Behind*; National Academy of Science and Technology: Khumaltar, Lalitpur, 12 October 2019.
39. Ghimire, M. Historical Land Covers Change in the Chure-Tarai Landscape in the Last Six Decades: Drivers and Environmental Consequences. In *Land Cover Change and Its Eco-Environmental Responses in Nepal*; Li, A., Deng, W., Zhao, W., Eds.; Springer Geography; Springer: Singapore, 2017; pp. 109–147. ISBN 978-981-10-2890-8.
40. Pourghasemi, H.R.; Kornejady, A.; Kerle, N.; Shabani, F. Investigating the Effects of Different Landslide Positioning Techniques, Landslide Partitioning Approaches, and Presence-Absence Balances on Landslide Susceptibility Mapping. *CATENA* **2020**, *187*, 104364. [CrossRef]
41. Devkota, K.C.; Regmi, A.D.; Pourghasemi, H.R.; Yoshida, K.; Pradhan, B.; Ryu, I.C.; Dhital, M.R.; Althuwaynee, O.F. Landslide Susceptibility Mapping Using Certainty Factor, Index of Entropy and Logistic Regression Models in GIS and Their Comparison at Mugling–Narayanghat Road Section in Nepal Himalaya. *Nat. Hazards* **2013**, *65*, 135–165. [CrossRef]
42. Regmi, A.D.; Poudel, K. Assessment of Landslide Susceptibility Using GIS-Based Evidential Belief Function in Patu Khola Watershed, Dang, Nepal. *Environ. Earth Sci.* **2016**, *75*, 743. [CrossRef]
43. Addis, A. GIS-Based Landslide Susceptibility Mapping Using Frequency Ratio and Shannon Entropy Models in Dejen District, Northwestern Ethiopia. *J. Eng.* **2023**, *2023*, e1062388. [CrossRef]
44. Lee, S.; Talib, J.A. Probabilistic Landslide Susceptibility and Factor Effect Analysis. *Environ. Geol.* **2005**, *47*, 982–990. [CrossRef]
45. He, S.; Pan, P.; Dai, L.; Wang, H.; Liu, J. Application of Kernel-Based Fisher Discriminant Analysis to Map Landslide Susceptibility in the Qinggan River Delta, Three Gorges, China. *Geomorphology* **2012**, *171–172*, 30–41. [CrossRef]

46. Shu, H.; Guo, Z.; Qi, S.; Song, D.; Pourghasemi, H.R.; Ma, J. Integrating Landslide Typology with Weighted Frequency Ratio Model for Landslide Susceptibility Mapping: A Case Study from Lanzhou City of Northwestern China. *Remote Sens.* **2021**, *13*, 3623. [CrossRef]
47. Ali, S.A.; Parvin, F.; Vojteková, J.; Costache, R.; Linh, N.T.T.; Pham, Q.B.; Vojtek, M.; Gigović, L.; Ahmad, A.; Ghorbani, M.A. GIS-Based Landslide Susceptibility Modeling: A Comparison between Fuzzy Multi-Criteria and Machine Learning Algorithms. *Geosci. Front.* **2021**, *12*, 857–876. [CrossRef]
48. Pham, B.T.; Bui, D.T.; Dholakia, M.B.; Prakash, I.; Pham, H.V.; Mehmood, K.; Le, H.Q. A Novel Ensemble Classifier of Rotation Forest and Naïve Bayer for Landslide Susceptibility Assessment at the Luc Yen District, Yen Bai Province (Viet Nam) Using GIS. *Geomat. Nat. Hazards Risk* **2017**, *8*, 649–671. [CrossRef]
49. Xu, C.; Dai, F.; Xu, X.; Lee, Y.H. GIS-Based Support Vector Machine Modeling of Earthquake-Triggered Landslide Susceptibility in the Jianjiang River Watershed, China. *Geomorphology* **2012**, *145–146*, 70–80. [CrossRef]
50. Clubb, F.J.; Mudd, S.M.; Attal, M.; Milodowski, D.T.; Grieve, S.W.D. The Relationship between Drainage Density, Erosion Rate, and Hilltop Curvature: Implications for Sediment Transport Processes. *J. Geophys. Res. Earth Surf.* **2016**, *121*, 1724–1745. [CrossRef]
51. Ding, Q.; Chen, W.; Hong, H. Application of Frequency Ratio, Weights of Evidence and Evidential Belief Function Models in Landslide Susceptibility Mapping. *Geocarto Int.* **2017**, *32*, 619–639. [CrossRef]
52. Moosavi, V.; Niazi, Y. Development of Hybrid Wavelet Packet-Statistical Models (WP-SM) for Landslide Susceptibility Mapping. *Landslides* **2016**, *13*, 97–114. [CrossRef]
53. Shirzadi, A.; Chapi, K.; Shahabi, H.; Solaimani, K.; Kavian, A.; Ahmad, B.B. Rock Fall Susceptibility Assessment along a Mountainous Road: An Evaluation of Bivariate Statistic, Analytical Hierarchy Process and Frequency Ratio. *Environ. Earth Sci.* **2017**, *76*, 152. [CrossRef]
54. Henriques, C.; Zêzere, J.L.; Marques, F. The Role of the Lithological Setting on the Landslide Pattern and Distribution. *Eng. Geol.* **2015**, *189*, 17–31. [CrossRef]
55. Kim, K.-S.; Song, Y.-S. Geometrical and Geotechnical Characteristics of Landslides in Korea under Various Geological Conditions. *J. Mt. Sci.* **2015**, *12*, 1267–1280. [CrossRef]
56. Guzzetti, F.; Peruccacci, S.; Rossi, M.; Stark, C.P. Rainfall Thresholds for the Initiation of Landslides in Central and Southern Europe. *Meteorol. Atmos. Phys.* **2007**, *98*, 239–267. [CrossRef]
57. Hadji, R.; Chouabi, A.; Gadri, L.; Raïs, K.; Hamed, Y.; Boumazbeur, A. Application of Linear Indexing Model and GIS Techniques for the Slope Movement Susceptibility Modeling in Bousselam Upstream Basin, Northeast Algeria. *Arab. J. Geosci.* **2016**, *9*, 192. [CrossRef]
58. Cellek, S. The Effect of Aspect on Landslide and Its Relationship with Other Parameters. In *Landslides*; IntechOpen: London, UK, 2021.
59. Singh, K.; Kumar, V. Hazard Assessment of Landslide Disaster Using Information Value Method and Analytical Hierarchy Process in Highly Tectonic Chamba Region in Bosom of Himalaya. *J. Mt. Sci.* **2018**, *15*, 808–824. [CrossRef]
60. Panchal, S.; Shrivastava, A.K. Landslide Hazard Assessment Using Analytic Hierarchy Process (AHP): A Case Study of National Highway 5 in India. *Ain. Shams Eng. J.* **2022**, *13*, 101626. [CrossRef]
61. R Core Team. *R: A Language and Environment for Statistical Computing*; R Foundation for Statistical Computing: Vienna, Austria, 2021.
62. LPDAAC. ASTER Global Digital Elevation Model V003 [Dataset]. NASA EOSDIS Land Processes Distributed Active Archive Center. 2019. Available online: https://lpdaac.usgs.gov/products/astgtmv003/ (accessed on 18 October 2022).
63. Fick, S.E.; Hijmans, R.J. WorldClim 2: New 1 km spatial resolution climate surfaces for global land areas. *Int. J. Climatol.* **2017**, *27*, 4302–4315. [CrossRef]
64. ICIMOD. Geology of Nepal [Dataset]. 2020. Available online: https://rds.icimod.org/home/datadetail?metadataid=2521 (accessed on 27 April 2022).
65. ESRI. Sentinel-2 10-Meter Land Use/Land Cover [Dataset]. 2020. Available online: https://livingatlas.arcgis.com/landcover (accessed on 22 May 2022).
66. OCHA Nepal. Nepal Road Network [Dataset]. Humanitarian Data Exchange. 2021. Available online: https://data.humdata.org/dataset/nepal-road-network (accessed on 18 October 2022).
67. Signorell, A.; Aho, K.; Alfons, A.; Anderegg, N.; Aragon, T.; Arppe, A.; Baddeley, A.; Barton, K.; Bolker, B.; Borchers, H.W. *DescTools: Tools for Descriptive Statistics*; R Package Version 0.99; R Project: Vienna, Austria, 2018; Volume 28, p. 17.
68. Racine, J.S. Rstudio: A Platform-Independent Ide for R and Sweave. *J. Appl. Econom.* **2012**, *27*, 167–172. [CrossRef]
69. Boomsma, A. Regression Diagnostics with R. In *Department of Statistics & Measurement Theory*; University of Groningen: Groningen, The Netherlands, 2014.
70. Chatterjee, S.; Hadi, A.S. Regression Diagnostics: Detection of Model Violations. In *Regression Analysis by Example*; John Wiley & Sons, Ltd.: Hoboken, NJ, USA, 2015; pp. 85–120. ISBN 978-0-470-05546-5.
71. Hosmer, D.W., Jr. Model-Building Strategies and Methods for Logistic Regression. *Appl. Logist. Regres.* **2013**, *22*, 89–151.
72. Bhandari, B.; Dhakal, S. Lithological Control on Landslide in the Babai Khola Watershed, Siwaliks Zone of Nepal. *Am. J. Earth Sci.* **2018**, *5*, 54–64.
73. Upreti, B.N. An Overview of the Stratigraphy and Tectonics of the Nepal Himalaya. *J. Asian Earth Sci.* **1999**, *17*, 577–606. [CrossRef]

74. Dhakal, S. Geological Divisions and Associated Hazards in Nepal. In *Contemporary Environmental Issues and Methods in Nepal*; Tribhuvan University: Kirtipur, Nepal, 2014; pp. 100–109.
75. McAdoo, B.G.; Quak, M.; Gnyawali, K.R.; Adhikari, B.R.; Devkota, S.; Rajbhandari, P.L.; Sudmeier-Rieux, K. Roads and Landslides in Nepal: How Development Affects Environmental Risk. *Nat. Hazards Earth Syst. Sci.* **2018**, *18*, 3203–3210. [CrossRef]
76. Lee, S. Geological Application of Geographic Information System. *Korea Inst. Geosci. Min. Resour.* **2014**, *9*, 109–118.
77. Ramli, M.F.; Yusof, N.; Yusoff, M.K.; Juahir, H.; Shafri, H.Z.M. Lineament Mapping and Its Application in Landslide Hazard Assessment: A Review. *Bull Eng. Geol. Environ.* **2010**, *69*, 215–233. [CrossRef]
78. Saha, A.; Saha, S. Comparing the Efficiency of Weight of Evidence, Support Vector Machine and Their Ensemble Approaches in Landslide Susceptibility Modelling: A Study on Kurseong Region of Darjeeling Himalaya, India. *Remote Sens. Appl. Soc. Environ.* **2020**, *19*, 100323. [CrossRef]
79. Gurung, A.; Bista, R.; Karki, R.; Shrestha, S.; Uprety, D.; Oh, S.E. Community-Based Forest Management and Its Role in Improving Forest Conditions in Nepal. *Small-Scale For.* **2013**, *12*, 377–388. [CrossRef]
80. Ghimire, M. Landslide Occurrence and Its Relation with Terrain Factors in the Siwalik Hills, Nepal: Case Study of Susceptibility Assessment in Three Basins. *Nat. Hazards* **2011**, *56*, 299–320. [CrossRef]
81. Cheng, Y.-S.; Yu, T.-T.; Son, N.-T. Random Forests for Landslide Prediction in Tsengwen River Watershed, Central Taiwan. *Remote Sens.* **2021**, *13*, 199. [CrossRef]
82. Du, J.; Glade, T.; Woldai, T.; Chai, B.; Zeng, B. Landslide Susceptibility Assessment Based on an Incomplete Landslide Inventory in the Jilong Valley, Tibet, Chinese Himalayas. *Eng. Geol.* **2020**, *270*, 105572. [CrossRef]
83. Gautam, A.P.; Shivakoti, G.P.; Webb, E.L. A Review of Forest Policies, Institutions, and Changes in the Resource Condition in Nepal. *Int. For. Rev.* **2004**, *6*, 136–148. [CrossRef]
84. Måren, I.E.; Karki, S.; Prajapati, C.; Yadav, R.K.; Shrestha, B.B. Facing North or South: Does Slope Aspect Impact Forest Stand Characteristics and Soil Properties in a Semiarid Trans-Himalayan Valley? *J. Arid. Environ.* **2015**, *121*, 112–123. [CrossRef]
85. Kayastha, P.; Dhital, M.R.; De Smedt, F. Application of the Analytical Hierarchy Process (AHP) for Landslide Susceptibility Mapping: A Case Study from the Tinau Watershed, West Nepal. *Comput. Geosci.* **2013**, *52*, 398–408. [CrossRef]
86. Zekkos, D.; Clark, M.; Whitworth, M.; Greenwood, W.; West, A.J.; Roback, K.; Li, G.; Chamlagain, D.; Manousakis, J.; Quackenbush, P.; et al. Observations of Landslides Caused by the April 2015 Gorkha, Nepal, Earthquake Based on Land, UAV, and Satellite Reconnaissance. *Earthq. Spectra* **2017**, *33*, 95–114. [CrossRef]
87. Alimohammadlou, Y.; Najafi, A.; Yalcin, A. Landslide Process and Impacts: A Proposed Classification Method. *Catena* **2013**, *104*, 219–232. [CrossRef]
88. Haigh, M.J.; Rawat, J.S.; Rawat, M.S.; Bartarya, S.K.; Rai, S.P. Interactions between Forest and Landslide Activity along New Highways in the Kumaun Himalaya. *For. Ecol. Manag.* **1995**, *78*, 173–189. [CrossRef]
89. Schmaltz, E.M.; Steger, S.; Glade, T. The Influence of Forest Cover on Landslide Occurrence Explored with Spatio-Temporal Information. *Geomorphology* **2017**, *290*, 250–264. [CrossRef]
90. Baral, S.; Vacik, H. What Governs Tree Harvesting in Community Forestry-Regulatory Instruments or Forest Bureaucrats' Discretion? *Forests* **2018**, *9*, 649. [CrossRef]
91. Dahal, R.K.; Hasegawa, S.; Bhandary, N.P.; Poudel, P.P.; Nonomura, A.; Yatabe, R. A Replication of Landslide Hazard Mapping at Catchment Scale. *Geomat. Nat. Hazards Risk* **2012**, *3*, 161–192. [CrossRef]
92. Gyawali, P.; Tamrakar, N.K. Landslide Susceptibility Assessment of the Chure Khola Catchment Area of the Siwalik Region, Central Nepal. *J. Nepal Geol. Soc.* **2018**, *56*, 19–30. [CrossRef]

land

MDPI

Review

Potential Interactions between Climate Change and Land Use for Forest Issues in the Eastern United States

Brice B. Hanberry [1,*], Marc D. Abrams [2] and Gregory J. Nowacki [3]

[1] USDA Forest Service, Rocky Mountain Research Station, Rapid City, SD 57702, USA
[2] Department of Ecosystem Science and Management, The Pennsylvania State University, 307 Forest Resources Bldg., University Park, PA 16802, USA; agl@psu.edu
[3] USDA Forest Service, Eastern Regional Office, Milwaukee, WI 53202, USA; gregory.nowacki@usda.gov
* Correspondence: brice.hanberry@usda.gov

Abstract: Applying an interaction framework, we examined whether climate change and combined land use and disturbance changes were synergistic, antagonistic, or neutral for forest issues of wildfires, tree growth, tree species distributions, species invasions and outbreaks, and deer herbivory, focused on the eastern United States generally since the 1800s and the development of instrumental records (1895). Climate largely has not warmed during 1981–2020 compared to 1895–1980, but precipitation has increased. Increased precipitation and land use (encompassing fire exclusion and forestation, with coarse fuel accumulation due to increased tree densities) have interacted synergistically to dampen wildfire frequency in the humid eastern U.S. For overall tree growth, increased precipitation, carbon fertilization, and land use (i.e., young, fast-growing dense stands) likely have been positive, generating a synergistic interaction. Human activities created conditions for expanding native tree species distributions, non-native species invasions, and damaging native species outbreaks. No strong evidence appears to exist for recent climate change or land use influences on deer populations and associated herbivory levels. In the future, a warmer and effectively drier climate may reverse synergistic and neutral interactions with land use, although effects of climate interactions with land use will vary by species. Management can help correct non-climate stressors due to land use and support resilient structures and species against climate change.

Keywords: deer; fire; growth; distribution; herbivory; production; non-native; outbreak; trees

1. Introduction to Climate Change and Land Use

Ecosystem dynamics are governed by a variety of interacting factors that operate over time and space, including climate change and the combination of land use and disturbance factors, which, whether natural or human-mediated, produce differential impacts on the overall composition, structure, and function of ecosystems [1]. During the past 50 years, habitat loss due to agricultural conversion and intensification, urbanization, and resource extraction had the greatest direct influence on loss of biodiversity, ecosystem functions, and ecosystem services from local to regional scales in all biomes [2]. Nonetheless, published work has documented that recent climate change forced by human use of fossil fuels has altered a suite of ecosystem processes worldwide [3].

Although climate has been variable during the Holocene (about 12,000 years BP), atmospheric CO_2 concentration has increased from 280 ppm prior to the Industrial Revolution (about year 1750) to 420 ppm present day, chiefly as the result of fossil fuel consumption [3]. The average temperature has increased about 1 °C in the northern hemisphere since 1900, with most of the warming concentrated during the last 40 years [3]. Even though anthropomorphically driven, recent temperature increases are within the range of historical variation during the Holocene, albeit on a trajectory to be exceeded in the foreseeable future [3].

Long-term global warming is accompanied by regional variability in both rate and magnitude of change. Specifically, the eastern U.S. displays an overall lack of warming

along with increased precipitation during the last forty years of climate relative to climate earlier during the 1900s, albeit with complex spatiotemporal dynamics (Figure 1; [4,5]). Exceptions to neutral temperature change include the Northeast and mid-Atlantic regions that have experienced mild warming of about 0.25–0.75 °C, whereas portions of the Central Plains and Southeast have cooled 0.25–0.75 °C (Figure 1A). Most of the eastern U.S. has experienced an increase in annual precipitation of 2–25 cm (Figure 1B), which combined with stable temperatures, results in reduced evapotranspiration (Figure 1C,D). Conversely, a large extent in the Southeast has received 2–10 cm less precipitation relative to 1895–1980. Lack of warming in the eastern U.S. extends into the Atlantic Ocean, with additional cooling in the North Atlantic Ocean, and remains under investigation [5,6]. While the future is unknown, general circulation models as a group predict continued precipitation gains in the eastern U.S. with temperatures warming by 3 to 6 °C [7].

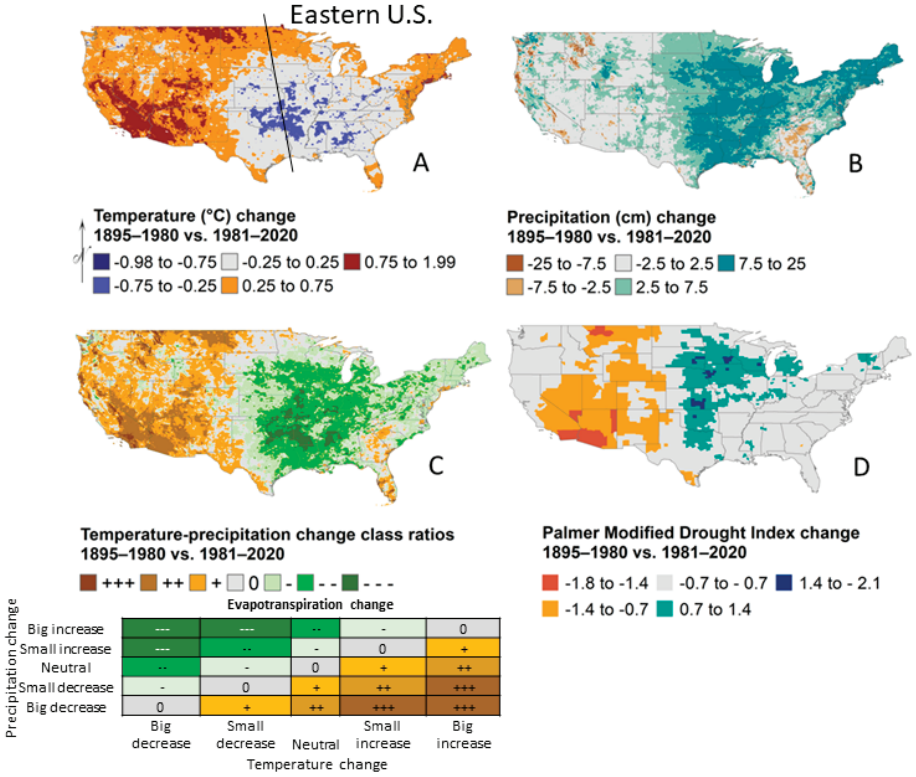

Figure 1. Changes in the mean annual temperature (**A**), precipitation (**B**), temperature-precipitation change class ratios (**C**), and Palmer Modified Drought Index (**D**) between 1895–1980 and 1981–2020 for the United States. The temperature-precipitation change class ratios were calculated by applying a simple classification to mean temperature and precipitation maps but presented similar changes of stable or decreased evapotranspiration in the eastern U.S. as the Palmer Modified Drought Index, which applied tree-ring reconstructions of available water and instrumental data. Data are modified [4,8].

Vegetation dynamics are intricately tied to human history, through the influences of hunting, agriculture, and land management in the form of fire [9–11]. Humans have been an agent of change since their permanent establishment across the North American continent about 15 thousand years ago; for example, numerous megaherbivores became extinct after human establishment [12]. Human populations and their role as disturbance agents on vegetation have changed appreciably during the Holocene, particularly since Euro-American settlement at the expense of Indigenous populations [10,13–15]. A suite of changes occurred at a rapid rate in the type, extent, and magnitude of land-use practices by timber harvest and agricultural conversion: abrupt shifts in fire regimes to eventual fire exclusion; overexploitation of native species; introduction and spread of non-native plants, animals, and diseases; and climate change due to fossil fuel extraction and use [11,16–19].

For example, prior to Euro-American settlement, vast areas of the U.S. were savannas and woodlands, which were dominated by warm-adapted, pyrogenic tree species, such as oak (*Quercus*) and pine (*Pinus*), that provided foodways in the form of plants and wildlife [11,20]. Under fire exclusion, these ecosystems have transitioned to closed forests, which are composed of diverse fire-sensitive tree species, that supply forest products [20–22].

Land use since Euro-American settlement is long-standing, whereas climate change is developing in the eastern U.S., with trends of increasing precipitation and overall stable temperatures during the past 40 years that are not yet outside of the range of historical variation. Nonetheless, climate change acts as another axis of disturbance on species and ecosystems that works within an interactive framework with land use and disturbance (hereafter, land use). Depending on the scenario, land use and climate change can (1) amplify or facilitate effects through synergistic interactions, (2) simply add effects with no (neutral) interactions, or (3) have antagonistic interactions, which can have a canceling effect (where factor strength is similar) or overriding effect (where factor strength is imbalanced and one factor diminishes the other). A range of outcomes are possible but the interactive framework between land use and climate change is not clearly specified by evidence from realized outcomes of the past, for guiding predictions to the future as warming increases beyond historical temperatures. Comprehensive studies typically are not available, research shows variation within regions due to different contexts and species, and publication bias for significant findings exists. Additionally for published research, while a driver may be associated with study results, typically both climate and land use are not examined simultaneously in studies, and climate and land use may be confounded, that is, the effects of one ascribed to the other [23]. Kane et al. [24] thoroughly examined fire interactions with drought, bark beetles, and pathogens in the western U.S. Seidl et al. [25] partitioned direct, indirect, and interaction effects of climate change on fire, drought, wind, snow and ice, insects, and pathogens in an analysis of reported pathways globally.

As a first step to incorporate land use effects into an interactive framework with climate change for a subset of forest issues, we explicitly (1) specified primary mechanisms and realized evidence by which climate and land use may have been influential since becoming operational (i.e., land use changes resulting from Euro-American settlement mainly since the late 1800s and climate change of the past 40 years relative to instrumental record networks since 1895), (2) synthesized interactions between climate and land use to determine their type and strength of interactions, and (3) suggested how climate, land use, and interactions may develop as warming progresses in the eastern U.S. (largely defined as Minnesota, Iowa, Missouri, Arkansas, and Louisiana and all states eastward; Figure 1A). Future work then could advance and test the conceptual framework through comprehensive literature reviews, meta-analyses, and framing of hypotheses for empirical studies with modeling and experimental approaches [25]. Defining land use, we mean direct changes to ecosystems through land conversion from wildlands to intensively and extensively human-controlled environments, associated with change from Indigenous to European management, which leads to compositional and structural changes in ecosystems and alterations in how disturbance regimes, such as fire and insects, operate. We also included pollution such as nitrogen deposition, non-native species introductions, and overexploitation of megaherbivores into the disturbance categories caused directly by humans. Our questions, including some contrast with the western U.S., encompassed the following forest topics:

1. What are the dynamics of wildfire in response to climate and land use?
2. What are the dynamics of tree growth and distributions in response to climate and land use?
3. What are the dynamics of non-native species, damaging native insects and disease, and white-tailed deer (*Odocoileus virginianus*, one of the last remaining widespread large herbivores) in response to climate and land use?
4. How can ecological and adaptive management mitigate negative impacts of climate change and land use to maintain forest resiliency?

For this examination, we focused principally on direct effects, rather than slower acting indirect effects that are less influential [25]. We did not include forest issues that have not been detected to change in severity over recent time or are predicted to decrease, such as wind events or snow and ice, or that are restricted in extent, such as sea level rise [26]. As for effects of land use on climate, although tree planting and new forestation have been advocated to increase carbon storage and reduce climate change, this is an unreliable and limited approach that may cause damage to intact ecosystems and Indigenous peoples, while avoiding the solution to climate change, which is to reduce the amount of carbon emissions [27].

2. Fire

2.1. Climate Change Effects

Drier and warmer climate increases the number of extreme wildfire weather days by reducing fuel moisture and increasing the likelihood of ignition [24,25]. Greater precipitation typically fosters vegetation production, generating fuel accumulation (see section on tree growth). Most of the eastern U.S. has experienced climate change of increased precipitation with stable temperatures, albeit with slight warming along the northern tier and mid-Atlantic coast, which likely has reduced extreme wildfire weather days and the chance of severe wildfires, while accumulating coarse woody fuels (i.e., trees; Figure 1).

2.2. Land Use Effects

Land use also influences fires, which in turn interact with weather, primarily by affecting fuel type of fine herbaceous fuels or coarse woody fuels from trees. Land use has trajectories to surface fires or severe forest fires, defined by mortality to overstory trees, depending on the height of dominant vegetation. Historically, frequent surface fires reduced tree density and promoted herbaceous vegetation. Herbaceous vegetation in turn promoted surface fires that were limited in flame length by small-statured vegetation but relatively frequent because fine herbaceous vegetation ignites more readily than coarse fuels. Without surface fires, tree densities increase and accumulate, reducing probability of ignition but creating fuels for severe fire behavior, with long flame lengths due to travel up tree boles into canopies (green ladders) and then spread within continuous canopies. Currently, due to widespread forestation in wildlands following Euro-American settlement, land use resulted in less frequent but more severe fires in ecosystems, due to greater tree densities [28]. Shifts in tree species composition from fire-tolerant to fire-sensitive species and wetter microclimates also altered the leaf litter and fuel bed properties and pyrogenicity tendencies of the understory, making most forest less conducive to burning (i.e., mesophication; [21]). Moreover, fire is limited by fragmentation through land use conversion. Agricultural areas of crops and grazing remove fuels, whereas suburban and urban areas have sparse vegetation and abundant firebreaks (i.e., concrete and impervious surfaces; [15]).

2.3. Interactions and Relative Factor Strength

A wetter climate due to climate change combined with continuous coarse fuels due to land use change to forests will reduce the frequency of fires. A drier climate allows coarse fuels to ignite more readily in closed forests, increasing the frequency of severe fires. Conversely, a wetter climate with seasonal drying increases herbaceous fuel production in open ecosystems and consequently encourages frequent surface fires. When surface fires were frequent in grasslands, savannas, and woodlands before Euro-American land use, drier climate likely suppressed fire frequency by limiting herbaceous growth, which is the primary surface fire fuel [29]. Fine herbaceous fuel development requires seasonal precipitation to grow vegetation followed by seasonal drying, which results in tinder for easy ignition, as opposed to coarse fuels, which generally resist ignition without extended drying.

In terms of relative factor strength, land use of fire exclusion and subsequent coarse fuel accumulation in high density forests has led to divergent wildfire pathways based on humid or dry climates, with wildfire frequency dampened in the humid eastern U.S. and wildfire frequency increasing in the dry western U.S. (Figure 2). While forestation and fuel accumulation have occurred throughout the U.S., trends of area burned by wildfire, excluding prescribed burns, over time are different when comparing the humid eastern U.S. to the dry western U.S. Predominantly coniferous tree species common in the western U.S may be more flammable relative to the greater proportion of mixed and broadleaf forests in the eastern U.S. Nonetheless, based on historical records, the eastern U.S. demonstrates that wildfires are rare after land use change resulting in forestation in a humid temperate region with moderate, and indeed increasing, precipitation.

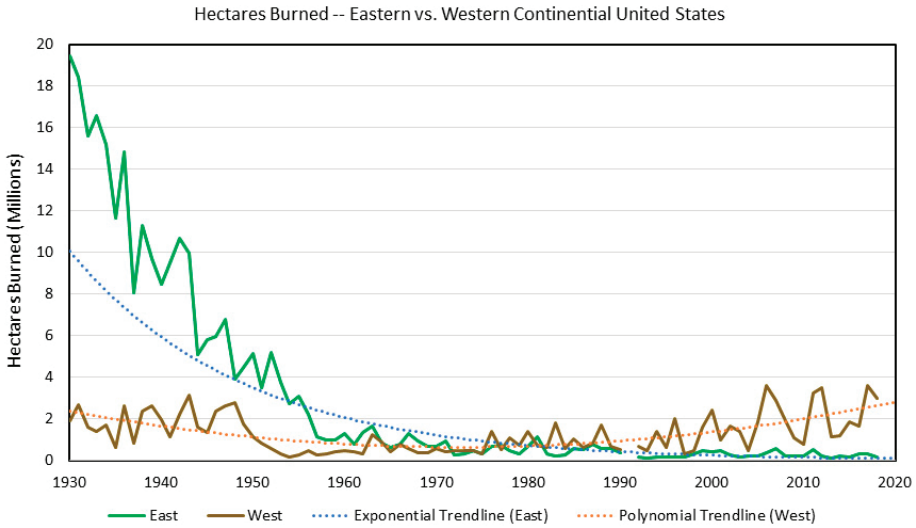

Figure 2. Area (hectares) burned and trendlines by region based on fire records provided by the USDA Forest Service, Washington Office, and Short [30]. The eastern region is composed of Minnesota, Iowa, Missouri, Arkansas, and Louisiana and all states eastward. The western region is composed of all states west of the eastern region states. In 1930, ten-fold more hectares burned in the east than the west based on long-term USDA Forest Service fire records (19 million vs. 1.9 million hectares, respectively; Figure 2). Some of this difference might be due to underreporting in the west associated with lower human population densities, hence fewer fire detections due to remoteness. At any rate, annual hectares burned held steady in the west until a noticeable drop occurred around 1950. In contrast, annual hectares burned by wildfire dropped sharply in the east until the mid-1950s, with slow decreases thereafter. The east and the west had similar total area burned by wildfire during the 1960s to the early 1980s, after which trendlines crossed, with the west surpassing the east in the extent of burning by wildfires. This upward trend separates two regions into the future, as the west is currently burning by wildfires at a similar rate as during the 1930s.

2.4. Summary and Future Prediction

Increased precipitation in the humid eastern U.S. probably has interacted synergistically with land use to reduce the frequency of severe fires. Overall, land use resulting in tree densification and forestation reduces frequency of fires but switches to severe forest fires compared to land use leading to frequent surface fires in ecosystems with herbaceous vegetation. When land use promotes forests, with a switch to severe forest fires, then a wet climate decreases (severe) fire frequency relative to dry climate. In contrast, a drier climate allows accumulated coarse fuels to ignite more readily, increasing the frequency of severe fires and overcoming land use conversion to infrequent severe fires in ecosystems with high tree density. Therefore, future warming in the eastern U.S., without concurrent offsetting increased precipitation, may flip the direction of the interaction, with the climate eventually canceling or reversing the dampening effects on (severe) fire frequency by

land use in an increasingly antagonistic interaction, such that warming increases severe wildfire frequency.

3. Tree Growth

3.1. Climate Change Effects

Climate change encompasses elevated temperature and carbon dioxide concentration and shifts in precipitation patterns, which can affect tree reproduction (through both fecundity and seedling establishment), growth, survival, and mortality, and overall forest productivity. Direct effects of climate change on tree growth and mortality may be more related to temperature in cold-limited forests and moisture in water-limited forests [31]. Boisvenue and Running [32] concluded that climate change has generally increased forest productivity where water was not limiting, describing the 'greening of the biosphere'. Way and Oren (2010) reviewed the generally positive temperature effects on tree physiology and growth, with greater growth by deciduous species than evergreen species and in cold-limited temperate and boreal regions rather than tropical regions, where warming may induce growth declines. The growing season has been extended by 10–20 days in temperate regions [3,33]. Despite the lengthening growing season, temperature increases become detrimental to tree regeneration, growth, and survival when compounded by worsening drought conditions, particularly for vulnerable seedlings before root establishment [34,35]. While temperature increases may appear beneficial for cold-limited forests, maximum temperatures and exceeding an optimal temperature range can be particularly impactful on tree regeneration, growth, and survival, especially for boreal species that are sensitive to high temperatures [35]. Additionally, increased temperatures allow entry of tree species from warmer regions, that is, expected poleward shifts in distributions that disrupt existing ecosystems.

The effects of enriched atmospheric CO_2 on tree growth have been investigated during the last 50 years [36,37]. Elevated CO_2 has positive effects, within limits, on tree growth because CO_2 uptake and fixation are the primary functions of photosynthesis [38,39]. Elevated CO_2 and photosynthetic enhancement improve water-use efficiency in trees, as stomata do not need to stay open as long to replenish CO_2 inside the leaf, thus reducing leaf transpiration [40,41]. Nevertheless, at some point photosynthesis will become CO_2-saturated, after which increased atmospheric CO_2 will not augment photosynthesis and growth [42,43].

Greater water availability, mild warming to date in cold-limited northern forests, and carbon fertilization on photosynthesis overall may have accelerated tree growth in the eastern U.S. [31,44–47]. Many portions of the eastern U.S. are now receiving more precipitation (see Figure 1), hence falling into the "greening biosphere" category. Voelker et al. [44] reported CO_2 growth enhancement in oak and pine in the central U.S., but growth declined with tree age. Data from 120 journal articles describing physiology and production in the 12 large-scale free air CO_2 enrichment experiments (FACE; 475–600 ppm) confirmed increased light-saturated carbon uptake and assimilation, growth, and aboveground production, whereas specific leaf area and stomatal conductance diminished under elevated CO_2 treatments [37]. In recent decades, net ecosystem productivity in hemlock-dominated forests increased 93%, which was attributed in part to an increase in mean annual temperature and growing season length [48].

Some studies show either neutral or negative effects of climate change on tree growth, with negative effects due to components of climate [49]. Canham and Murphy [50] reported little or no statistical relationship between growth and precipitation for 40 of the 50 most common tree species in the eastern U.S., but that tree species of colder environs experienced reduced survival in warmer climates. In the Adirondack Mountains of New York, most sugar maple (*Acer saccharum*) trees exhibited negative basal area growth trends in the last several decades [51], which was inconsistent with increased moisture availability and precipitation pH (less acidity) in the region [52]. Recent studies have shown that both timing and intensity of drought, especially during early season, can affect growth [53,54].

Increased forest mortality has occurred in some locations in the eastern U.S. related to drought and high temperatures, reducing any gains in productivity [55,56].

3.2. Land Use Effects

Regarding land use, young and fully stocked stands composed of fast-growing tree species overall have greatest annual growth and production, resulting in the basis of production forestry [47,49,57]. Widespread forest cutting has replaced old-growth forests with younger, faster-growing forests [57,58]. Tree growth rates slow with age [57]. Indeed, tree species that exhibit rapid early growth particularly may slow in growth after a few decades, as they divert resources to reproduction, allowing some slow-growing long-lived species to eventually surpass the overall growth of tree species with fast life strategies; that is, the greatest annual rate of production may not yield the greatest long-term production, or carbon storage, for a stand [57,59,60]. Overstory tree removal remains frequent at 25 to 80 years in the eastern U.S. [61]. Fire exclusion had increased tree densities (see fire section above). Additionally, composition generally has shifted from a few relatively slow-growing, long-lived tree species that are stress-tolerant to numerous early-seral species that grow quickly in response to severe disturbance, reproduce young, and die within 100 years in the eastern U.S. [62]. Perhaps in consequence, mortality is seven-fold greater in diverse stands than monospecific stands [63]. Moreover, nitrogen deposition may enhance the growth of some tree species [35,64].

3.3. Interactions and Relative Factor Strength

Both climate change and land use have mechanisms and evidence for increasing annual growth in the eastern U.S. Land use trades maximizing total production in old-growth stands for maximizing annual growth rates in young stands. Climate change of increased precipitation, with warming in northern forests and carbon fertilization, has encouraged overall growth. In terms of the relative factor strengths of climate change and land use change, a study of forest responses to climate change for 38 eastern tree species over a recent 6-to-18-year period concluded that the effect of competition on growth and mortality risk exceeded the effects of climate variation in space or time for almost all species [65]. Moreover, forest recovery from past human disturbance is predicted to supersede climate change effects well into the future [66]. For trees located in Kentucky, New York, Ohio, and Pennsylvania, tree mortality between 1959 and 1985 was more affected by competition than climate factors [67]. Lines et al. [68] reported that tree diameter had the greatest relationship with mortality rate across the eastern U.S., due to lower mortality rates for trees of intermediate size than smaller or larger trees. Furthermore, Dietze and Moorcroft [35] reported that atmospheric pollutants, specifically acid deposition and ozone, and stand-level biotic dynamics, of moderate diameters, were the main drivers of tree mortality in the eastern U.S.

3.4. Summary and Future Prediction

We have presented mechanisms and evidence by which climate change and land use change may affect tree growth. In the eastern U.S., the overall direct effects of climate change on tree growth have likely been at least slightly positive due to elevated CO_2 and the predominance of available water, with warming in cold-limited northern forests, while land use has likely increased growth rates through a change to productive young forests composed of fast-growing tree species at high densities. Although climate and land use interactions related to tree growth probably cover the full spectrum of synergistic to antagonistic, both of these drivers are likely to have overall positive effects on tree growth rates in the eastern U.S, with synergy in that climate conditions support the growth rate of fast-growing trees in fully stocked stands. In terms of carbon, fast carbon sequestration in young, small diameter trees that have short lifespans is not to be confused with long-term carbon storage potential of old, large diameter trees [69]. In the future, it is possible that the lack of stress tolerance in the fast-growing tree species of dense forests will result in

increased die-offs due to flash droughts, heat waves, and insect outbreaks, as diverse stands already exhibit greater mortality rates than less diverse stands in temperate regions [63]. These mortality events may eliminate any gains in productivity due to warm and wet conditions and result in uncontrolled boom and bust cycles of growth and mortality. Eventually, warming temperatures may exceed tolerances for tree species adapted to current temperatures, producing disordered growth, survival, and reproduction, but with replacement by southern tree species that may be more productive, due to allocation of resources for growth rather than frost tolerance.

4. Tree Species Distributions

4.1. Climate Change Effects

Climate provides an outline of potential distributions. However, most species have not achieved their full potential distributions based on climate, even across contiguous space within the potential distribution [70]. Species are restricted in distributions due to different barriers to migration, from physical (e.g., mountains, deserts) to biological (e.g., interactions and metapopulation dynamics) to disturbance regimes (e.g., frequent fire). Indeed, due to land use through fire exclusion that changed competition for growing space in the eastern U.S., some historically dominant fire-tolerant tree species have contracted in range (e.g., longleaf pine, *Pinus palustris*; shortleaf pine, *Pinus echinata*) while fire-sensitive species have expanded, demonstrating examples of both reduced and increased filling of climate space [15]. Moreover, species have naturalized outside of their native ranges, leading to increases in the known suitable climate space [70].

Expectations are that most species will move poleward to higher, cooler latitudes to maintain their ideal climate envelope in response to warming climate [71]. Many tree species have expanded distributions in the U.S. (e.g., 15 studies located by Taheri et al. [72]). Nonetheless, causation and whether species may be moving in multiple directions is not determined in most studies [72]. Instead, expected patterns are interpreted as evidence for species migration in response to climate change, despite an overall lack of warming in the eastern U.S. The most definitive examples to date of climate change effects on tree distributions are observed outside the eastern U.S., specifically at high latitudes and altitudes [73] with tree line advancement [74], although land (pasture) abandonment may also influence the latter [75]. Recent upward shifts in forest ecotones in mountainous regions have been attributed to climate change in eastern forests [76]. Equally, phenological changes have been equivocal in this region, given relatively stable temperatures, with anomalous delayed start of season dates [77,78], but phenological changes may display the first climate signal before tree species distribution shifts.

4.2. Land Use Effects

Attribution of climate change to movement of tree species is challenging, given that tree distribution and density changes followed Euro-American settlement, regardless of climate variation [20]. Historical accounts since the 1600s from across the U.S. have consistently documented rapid tree growth and expansion following the wave of Euro-American land use change [15,79,80]. Trees invaded the westernmost grasslands in the eastern U.S. by 1800 and migrated since 1850 from eastern forests into the central Great Plains grasslands. Fire-sensitive tree species expanded from fire-protected wetlands, rocky outcrops and barren land cover, or high elevations. Inconsistent changes in moisture availability, which are within the range of natural variation, have not provided correlations with comprehensive tree expansion, but land use change has corresponded with tree changes based on timing, magnitude and direction of change, and mechanism [15,22]. Native tree species have increased within U.S. forests and grasslands, arguably with much greater effects, by replacing historical ecosystems, than non-native invasive species [62]. Shifts in tree species composition occurred due to land use change, from a regime of frequent surface fires combined with infrequent overstory disturbance to a regime of fire exclusion combined with chronic overstory disturbance.

4.3. Interactions and Relative Factor Strength

Currently, limited evidence supports shifts to higher latitudes or elevations in tree species distributions under increased precipitation with only slight warming in northern forests, but strong evidence supports that tree species have expanded due to land use. Expansion has been multi-directional, with prominent westward expansion into central Great Plains grasslands. Therefore, no interaction currently occurs.

4.4. Summary and Future Prediction

In summary, no strong evidence appears to exist for recent climate driving changes in species distributions because species began to shift following the front of Euro-American settlement, generally with the timing of agricultural development. However, climate does delineate overall potential distributions, with land use allowing trees to fill any treeless growing space in wildlands within suitable climate space. In the future, warmer temperature will facilitate poleward shifts in species distributions, producing compositional changes from boreal to temperate species, temperate to subtropical species, and subtropical to tropical species. Due to the strong yet varied influence by land use disturbance, this may result in a range of interactions and divergent outcomes, including rapid movement, lags, and direction reversals, varying by species. Land use pathways may guide species into warmer or drier locations, such as North American grasslands, regardless of the expectation that species will follow climate change.

5. Invasions and Outbreaks: Non-Native Plants and Non-Native and Native Insects and Diseases

5.1. Non-Native Species

Species typically are most successful at survival, growth, and reproduction within an ecological context or niche, including broad climate envelopes of temperature and precipitation. Nevertheless, species are not distributed throughout their global climate envelopes, due to dispersion barriers, competition, consumers (i.e., predators, herbivores, humans), disease, disturbance regimes, and other abiotic and biotic factors. Equally, because of constraining factors, species may have a broader climate tolerance than realized by current occurrences, because the physiological range is unknown.

Non-native plant species richness is greatest in the northeastern U.S. and along western coastal states, whereas the southeastern and interior U.S. have fewer non-native plant species [81]. Therefore, effects of non-native plants on forests may vary regionally and proportionally to the number of invasive species. Norway maple (*Acer platanoides*), tree of heaven (*Ailanthus altissima*), and Chinese tallow tree (*Triadica sebifera*) are examples of invasive non-native tree species. Garlic mustard (*Alliaria petiolata*), Japanese barberry (*Berberis thunbergia*), honeysuckles (*Lonicera maackii* and *L. japonica*), Japanese stilt grass (*Microstegium vimineum*), multiflora rose (*Rosa multiflora*), cogongrass (*Imperata cylindrica*), Chinese privet (*Ligustrum sinense*), and kudzu *(Pueraria montana var. lobata*) are some invasive non-native upland plant species. Direct changes in temperature and water availability do not appear overall to benefit invasive plant species [82].

Invasive forest insects in the eastern U.S. include the spongy moth (*Lymantria dispar dispar*), hemlock woolly adelgid (*Adelges tsugae*), Asian longhorned beetle (*Anoplophora glabripennis*), and emerald ash borer (*Agrilus planipennis*). Increased temperatures may be most beneficial for non-native insects as a group because warming increases mobility, growth, reproduction, and overwinter survival, albeit mortal thermal thresholds may occur [83–85]. Species such as the hemlock woolly adelgid and emerald ash borer are currently limited by cold winter temperatures but predicted future warming likely will allow expansion throughout the range of the host species in North America [86,87]. Frost-sensitive and non-diapausing species experience increased survival during warm winters [83,85]. However, warming reduces the amount and duration of insulating snow cover, perhaps resulting in greater over-winter mortality [85]. The decoupling of temperature and photoperiod cues may be disruptive for both insects and host plants [85] and increased temperatures could

disconnect synchrony with native host plants [83], which are tracking climate change less closely than invasive plants [88,89]. Changes in plant defense chemistry due to climate may produce variable effects in plant susceptibility to infection, depending on interacting species and chemicals, while plant palatability and predators of insects also may be affected by climate change [86,90].

Invasive diseases of trees include chestnut blight (*Cryphonectria parasitica*), beech bark disease (*Neonectria*) that enters through wounds created by *Cryptococcus fagisuga*, Dutch elm disease (*Ascomycota*), white pine blister rust (*Cronartium ribicola*), and oak wilt (*Bretziella fagacearum*). Pathogens may be most sensitive to timing and quantity of precipitation, relative humidity, and factors that influence moisture [86,91]. Fungi in particular are very sensitive to factors that influence leaf-surface or soil moisture, and benefit from increased precipitation [91]. Pathogens may become more or less virulent under changed precipitation patterns, and disease epizootics generally will be unexpected, in part due to hybridization and other genetic changes [86,92].

Non-native species introductions into new distributions arose through human agency, not climate, by and large during the past centuries. Since Euro-American settlement, humans have moved thousands of species beyond their native ranges and dispersion barriers, including 2600 plants, 600 insects, and 100 diseases commonly observed in the U.S. [93]. Most non-native plants have been introduced deliberately for ornamental or agricultural purposes but imported nursery stock is a common pathway for non-native disease and insect introductions [94].

Regarding interactions between non-native species introductions, climate, and the future, plants introduced for ornamental or agricultural purposes are generally easy to propagate, show rapid growth, and tolerate wide climatic conditions [82]. Colonizing traits of rapid growth, less pressure from biotic constraints (e.g., release from parasites and consumers), and pre-selection to wide climate conditions position non-native species at a competitive advantage to increase and expand compared to native species, under many climates. Non-native species overall may be limited to climate envelopes of their native ranges, but as many as 15% of all non-native species are adapting to climate conditions outside of native climate envelopes [95]. For changing climate, non-native species overall appear to be tracking climate change phenologically more closely than native species [88,89]. Nevertheless, few non-native species are considered invasive, as measured by effects on native species, communities, and ecosystems. Unlike introduced species, native populations contain the full array of genetic variation and phenotypic plasticity that will aid in adaptation to changing climate conditions. Furthermore, given that climate change and associated extreme weather events are stressors to survival and growth, it may be that stress-tolerant traits, such as slower aboveground growth, may be more beneficial than rapid growth, a trait of invasive species, under climate change [96].

5.2. Outbreaks of Native Insects and Fungi

Outbreaks of several species of native insects (e.g., southern pine beetle, *Dendroctonus frontalis*; red oak borer, *Enaphalodes rufulus*) and fungi (e.g., fusiform rust, *Cronartium quercumm f.sp. fusiforme*; oak wilt; *Ceratocystis fagacearum*) that attack trees consistently occur in current forests with high densities and basal area [97], which typically are greater than in historical forests that had low tree densities due to frequent fire. While increased tree densities occur regardless of climate variation, greater water availability ameliorates stress on trees, particularly in high density stands. Many predisposing long-term factors influence insect and disease outbreaks and tree susceptibility, which are related to land use and disturbance, such as previous disturbance, fire exclusion, stand structure, tree age, and site location. Inciting factors are short-term conditions such as drought, related to climate, that weakens trees, especially in high density stands. Outbreaks outside of historical variation have occurred in the western U.S., due to a combination of land use change, resulting in trees with reduced vigor in dense forests, and climate change of warm

summers that accelerate insect growth and development and warm winters that allow insect larvae to survive, along with, in some locations, drought-stressed trees [98].

5.3. Summary and Future Prediction

In summary, invasions by non-native species were facilitated mainly by human vectors and native insect outbreaks likely are due to land use resulting in forests of greater basal area. However, future climate change may interact with land use change to amplify outbreaks outside the range of historical variation through drought-stressed trees, warm summers that accelerate insect growth and development, warm winters that allow insect larvae to survive, coupled with land use change that creates dense forest stands with reduced tree vigor. Non-native species responses to future climate change may be quite variable, counter to expectations, and complicated by land use disturbance, producing no general trends by taxa [99]. Land use may cancel expected climate change effects given that some species are able to be successful outside of climate envelopes. Therefore, climate interactions with land use span the range from synergistic effects on invasions and outbreaks to canceling climate change effects on invasions and outbreaks.

6. Deer, a Remaining Large Herbivore

6.1. Deer Herbivory as a Forest Health Issue

A diverse array of megaherbivores once roamed the North American continent, surviving through all Pleistocene ice age cycles until the last one. Quite tellingly, their demise occurred about 13,000 to 11,000 years ago, after human establishment [12]. Most of the approximately 30 megaherbivores in the eastern U.S. truly were mega-sized, with 10 species exceeding 1000 kg. In contrast, the only remaining widespread large herbivore in the eastern U.S. is the white-tailed deer at 45 kg, not qualifying as mega-sized by some thresholds. The population of white-tailed deer is unknown during megaherbivore extinction, but likely deer numbers increased after loss of competitors. Consequently, megaherbivore extinction probably reduced overall herbivory on vegetation while benefiting extant herbivore species. The disturbance regime switch from megaherbivores to surface fire was continuous in North America, with the importance of fire (as measured in charcoal) increasing proportionally with megafauna decrease (measured in dung fungal spores; [100,101]). Indeed, the changeover to fire as a disturbance likely lessened ecological changes expected from loss of megaherbivores as a disturbance.

Although deer are considered an overabundant, invasive forest health problem, best available evidence suggests that deer currently are within historical population limits after recovering from overexploitation during Euro-American settlement [102,103]. The influence of deer on trees is relatively minor compared to when megaherbivores were a major disturbance agent; for example, deer herbivory at current populations have not been able to shift ecosystem states from closed, dense forests back to open forests of savannas and woodlands [104]. Deer remain a natural disturbance on young trees, albeit minor except in localized areas, as demonstrated by problem areas of high densities even when deer populations were recovering after overharvesting during Euro-American settlement [105]. Tree species (e.g., *Thuja occidentalis*) browsed heavily by deer at local scales have increased at regional scales since Euro-American settlement, whereas historically dominant tree species have decreased due to land use changes of frequent overstory disturbance and limited understory disturbance [106].

6.2. Climate Change Effects

No distinct effect from climate is apparent on deer distributions, and deer populations generally remain with historical levels, with fluctuations. Deer have a wide range and an even larger climate envelope that remains unfilled for now. Climate change effects on deer distributions appear minimal, both in the recent past and for the future, based on modeling (Figure 3).

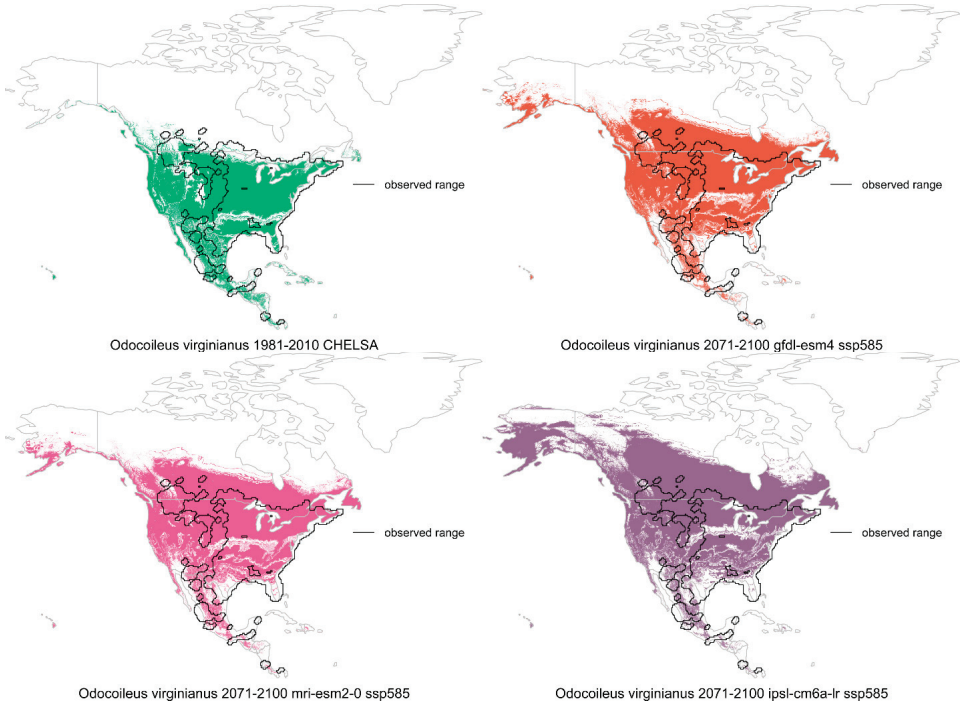

Figure 3. Modeled species distributions of white-tailed deer that show observed range (outlined) from occurrence records, the climate envelope (temperature and precipitation of occurrences) during 1981–2010 (green), and the likely future climate envelopes during 2071–2100, under three general circulation models and high emissions (non-green colors; modeling followed [107]).

6.3. Land Use Effects

No distinct effect from land use is apparent on deer populations. After population reduction due to historical overexploitation, subsequent deer populations have recovered to within historical levels, with some fluctuation. Deer prefer forests to various land uses and while forests have increased in tree density over time, in spite of deer herbivory, deer are coping with current land use by browsing trees and using clearcuts and other forest openings [108].

6.4. Interactions, Relative Factor Strength, and Summary

Despite dynamics, we found no permanent effects on deer populations, and herbivory by extension, due to recent land use and climate change and, consequently, no interactions, but future effects and interactions may develop.

7. Ecological Forestry to Mitigate Climate Change

General recommendations for ecological forestry to lessen impacts of climate change include retaining genetic diversity and phenotypic plasticity and promoting warm-adapted species with wide amplitudes of climate tolerance and good dispersal ability. Nonetheless, differentiating the ability of species to survive, grow, disperse, and reproduce under climate change compared to whether a species is competitive under climate change is critical. That is, northern tree species may be able to complete their life cycles under warmer temperatures but may not be able to compete against faster-growing southern species, as no species can have the most competitive traits under all conditions [109]. Even so, spruce, aspen, pine, and other boreal tree species may be desirable and possible to maintain with active silviculture. Reducing additional stressors, such as risk of insect outbreaks, and competition for limited resources will help trees survive and thrive under climate change. This may be accomplished in part by restricting tree densities [96,97].

Assisted migration through management is an option to help tree species migrate, given that species will not be able to migrate at the same rate as projected warming and

also that land use and other factors may drive tree species to warmer or drier locations, a conflicting or confounding outcome. Assisted migration and plantings may be desirable for species of conservation concern with limited ranges and dispersal abilities. Assisted migration is controversial, but species may be selected for tolerance of stresses, such as fire, drought, and insects, and be compatible with restoration objectives. For example, historically dominant oak species and longleaf and shortleaf pines are fire-tolerant, drought-tolerant, and windfirm, complementing the structural characteristics of open forests [110]. Fire-tolerant species such as oaks and pines that commit to early root development are likely to survive extreme weather events in early growth stages better than species committed to rapid early growth (e.g., longleaf pine height eventually may exceed loblolly pine [*Pinus taeda*] height, but after 25 to 30 years; [59]). Likewise, tolerant large diameter oaks and pines within open forests are more probable to survive droughts, fires, hurricanes, and insect outbreaks compared to fast-growing species in dense forests. Although oaks and pines are wide-ranging, they are not good dispersers compared to fast-growing species that produce abundant lightweight seeds. Therefore, oak and pine species are suitable candidates for assisted migration and plantings.

Conversely, assisted migration and plantings may be undesirable for native invasive species, such as red maple (*Acer rubrum*), that have been released by land use disturbance. Currently, many native tree species are expanding, sometimes with assistance through plantings such as for reforestation and tree initiatives. Indiscriminate planting of fast-growing and stress-intolerant species, with traits of fast growth and little reserves for fire and drought tolerance, at high densities, may foster forest vulnerability to climate change in terms of greater tree die-offs during extreme weather events. Also, caution may be needed in replanting after die-offs to not simply replace the same species with characteristics and structures that are not resistant to fire, drought, insects, and wind damage.

The historical open forest structure of understocked savannas and woodlands is ideally suited for tolerating climate change while restoring effects of Euro-American land use. The lower density structure means that trees require fewer resources, including less water requirement, resulting in greater ecosystem-level drought tolerance. Lower densities and understocking below maximum potential forest growth reduce competition for moisture and other resources, creating a "resource availability buffer" as a strategy for extreme climatic conditions and outbreaks of insects and disease [96]. Larger diameter trees are more fire-resistant and the lack of midstory and understory trees helps prevent fires from ascending to severe flame lengths, while discontinuous canopies also prevent canopy spread. The open structure is a firebreak and fuel treatment, which may prevent and reduce high severity fire, unlike the successional forest structure, with ladder fuels and dense canopies. The open structure is more windfirm to hurricanes and other severe wind events than high contrast edges of successional forests [111]. Open forests also support native species diversity, while providing a range of conditions that may supply refugia [112]. Additionally, for some damaging native species and a fire-sensitive subset of non-native species, open forests to reduce basal area and fire treatments may prevent outbreaks [113].

Open forest management is an alternative to conventional silvicultural systems, which concentrate on managing growth to optimize periodic yield and new overstory recruitment [112]. Instead, open forest management focuses on prevention of regeneration with rare recruitment of desired canopy dominants, maintenance of an understocked overstory, and treatments to encourage a more extensive groundlayer dominated by herbs. Open forest management involves multiple tools such as prescribed fire, herbicide use, and periodic harvests or deadenings to control stocking, permit recruitment of new canopy dominants, and financially support understory maintenance treatments [112]. Even with silvicultural targets that emulate the historic disturbance regime, achieving historical forest conditions is a challenge. Increased herbivory may be a necessary and missing component for restoration, particularly as propagule pressure from fire-sensitive tree species has increased. Thinning and burning treatments may be needed to reduce stand densities and fuel loads to help avert large-scale catastrophic canopy fires. In the eastern

U.S., warming temperatures that effectively result in a drying climate may facilitate the success of prescribed burning to restore fire-tolerant communities by countering the influx of fire-sensitive, fire-dampening competitors.

8. Summary of Interactions

Climate change interacts with land use and disturbance, influencing ecosystem dynamics across time. Climate change and human practices have directly or indirectly impacted nearly every ecosystem in the eastern United States since continental deglaciation began approximately 15,000 years before present. When climate was cooler, boreal tree species extended into the southeastern U.S., and tree species have shifted northward over time as temperatures have warmed. The first humans to live on the continent affected ecosystems, including maintenance of fire-adapted tree genera such as oak, pine, and hickory in open forests that supply food resources. Due to European colonial expansion starting in the 16th century, land use practices changed, and open forests transitioned to closed forests, which are now used primarily for forest products. Despite these influences, some species such as deer have recovered from past overexploitation in the eastern U.S.

This synthesis of climate interactions with human activities, encompassing land use and anthropogenic disturbances, reveals a greater factor strength of land use than climate change on ecosystems during the past century or two in the eastern U.S. (Table 1). These findings concur with other studies that have determined land use disturbance plays a major role in ecosystems over time, at times overriding climate, especially during the latter portion of the Holocene, when human activities intensified [2,114–116]. Indeed, besides influencing terrestrial ecosystems, humans directly affect climate because current climate change is also an outcome of human activities. Specifying an interactive framework results in a more thorough understanding of forest ecosystem responses to a changing environment and ecosystem management for the future as warming increases beyond past temperatures. Incorporating the framework into explicit testable hypotheses could guide future research directions and inform management strategies aimed at mitigating the adverse effects of climate change and land use on forest ecosystems.

Land use that causes an immediate reaction in terms of tree mortality or species migration has been a stronger and more immediate force than climate change to date. Climate change is a relatively slow, subtle process, with lag effects in combination with phenotypic plasticity in tree species and genetic traits due to past adaptation to similar temperature regimes [71]. The unusual aspect of climate change, due to human activities, has been overall lack of warming in the eastern U.S. combined with increased precipitation, albeit warming likely will occur in the future due to forcing by increased greenhouse gas levels [3]. Climate change since 1980 has been subtle, including warming in the Northeast and along the mid-Atlantic coast and a large dome of stable temperature over most of the remaining region with an overall increase in precipitation, except for decreased precipitation in the Southeast. Therefore, studies that attribute changes to warming temperatures in the eastern U.S. may be located in an area of exception or may have a suspect attribution to climate change.

Fire exclusion, resulting from changed land use and leading to continuous coarse fuel accumulation due to high density forests, has divergent ecological pathways, with wildfire dampened in the humid eastern U.S., along with increased precipitation. Fire has occurred in the eastern U.S. throughout a range of precipitation, but wildfire has been rare since land conversion to ecosystems with greater tree density, as fire regimes shifted in type from frequent surface fires in ecosystems with a dominant herbaceous layer to infrequent severe fires in closed forests. Conversely, climate change exerts a strong influence to enhance the frequency of severe fires in the dry western U.S., where tree densities also have increased; the western U.S. is currently burning with wildfire areas equivalent to those during the 1930s. If future warming generates effectively drier conditions in the eastern U.S., outside of historical ranges, then it is likely that severe fire frequency will increase in an antagonistic interaction between climate change and land use.

Table 1. Mechanisms by which climate and land use may affect different forest issues, with the realized outcome and current interaction in the eastern United States, and prediction of the future interaction under warming climate.

Forest Issue	Climate	Land Use	Realized Outcome in the Eastern U.S.	Current Interaction under Increased Precipitation	Future Interaction under Warming without Offsetting Precipitation
Fire	Fuel moisture, ignition probability, fuel quantity	Switches fire severity and frequency through fuel type (fine herbaceous or coarse fuels with mesophication of conditions)	Increased precipitation decreases fire frequency because land use (surface fire exclusion) produces forests	Synergistic to reduce fires	Antagonistic
Tree growth	Growth, reproduction, and mortality, and overall forest productivity	Species, age, densities	Increased precipitation and carbon fertilization promote tree growth; land use produces young, dense stands of fast-growing tree species	Synergistic to maximize annual tree growth	Antagonistic
Tree distribution	Shifts to stay within climate envelope	Expansion to fire-free areas	Expansion to fire-free areas	None	Varies by species
Non-native plants, insects, fungi	Survival, growth, reproduction, mortality, distribution shifts; water availability for trees; fire	Introduction, spread; tree densities, basal area, age; fire	Non-native species introduction and spread due to human activities	None overall	Varies by species
Native insects and fungi	Survival, growth, reproduction, mortality, distribution shifts; water availability for trees; fire	Tree densities, basal area, age; fire	Outbreaks in dense forests from land use	None overall	Varies by species
Deer	Survival, growth, reproduction, mortality, distribution shifts	Overexploitation, forest cover	Recovery after overexploitation	None	None to slight

Climate and land use currently have a synergistic interaction for increasing tree growth rates in eastern forests. Climate change through increased available water, carbon fertilization, and slight warming in cold-limited northern forests generally is stimulatory to growth in forests. Land use probably has increased growth rates through a change to productive, fully stocked young forests composed of fast-growing tree species. In the future, it is possible that the lack of stress tolerance in the fast-growing tree species of fully stocked forests will result in increased die-offs due to flash droughts, heat waves, insect outbreaks, or simply even-aged stands of short-lived tree species reaching the typical mortality age.

Attribution of climate change effects on tree species distributions is difficult in the U.S. Rapid tree growth and expansion in multiple directions, but principally westwards to the grasslands of central North America, followed the wave of Euro-American land use change, regardless of climate variation. Inconsistent changes in moisture availability, which are within the range of natural variation, have not provided correlations with comprehensive tree increases, based on timing, magnitude and direction of change, and mechanism. Nonetheless, warming likely will direct species northwards, which for some species will be in the same direction as land use, but climate change and land use may be antagonistic interactions for other species.

Conditions that produced non-native species invasions and damaging native species outbreaks were created by human activities. No strong evidence appears to exist for climate change causing changes in non-native species distributions, because species were introduced through human vectors, with relative recency of information about non-native species distributions. After climate warms, combined with the strong but varied influence of land use disturbance, rapid movement and also lags and direction reversals by species may ensue. Species responses to climate change may be quite variable; therefore, climate

interactions with land use disturbance span the range from synergistic to antagonistic effects on invasions and outbreaks.

Climate change is expected to become more influential in the future with warming and perhaps effectively a drier climate due to evapotranspiration. Depending on the characteristics of climate change and land use disturbance, synergistic interactions between climate change and land use disturbance may accelerate appropriate, expected responses by tree species to climate change, but these changes may not be desired, such as replacement of boreal tree species by temperate tree species. Antagonistic interactions between land use disturbance and climate change will generate surprising outcomes, which in some cases may be damaging, by overriding the appropriate, optimal response, in terms of survival, growth, reproduction, or productivity, to climate change. However, management may reduce land use and climate stressors on ecosystems. A resilient range of forest structures, with an abundant and diverse herbaceous component, and stress-tolerant tree species may be more stable under climate change than fast-growing tree species with short lifespans in high density forests. Future research and adaptive management can test the stipulated conceptual framework as climate warming unfolds in the eastern United States.

Author Contributions: Conceptualization, M.D.A. and B.B.H.; data curation, B.B.H. and G.J.N.; formal analysis, B.B.H. and G.J.N.; investigation, B.B.H., M.D.A. and G.J.N.; writing—original draft preparation, B.B.H., M.D.A. and G.J.N.; writing—B.B.H., M.D.A. and G.J.N.; visualization, B.B.H. and G.J.N. All authors have read and agreed to the published version of the manuscript.

Funding: This research received no external funding.

Data Availability Statement: The original contributions presented in the study are included in the article, further inquiries can be directed to the corresponding author.

Acknowledgments: This research was supported by the USDA Forest Service, Rocky Mountain Research Station. The findings and conclusions in this publication are those of the authors and should not be construed to represent any official USDA or U.S. Government determination or policy.

Conflicts of Interest: The authors declare no conflicts of interest.

References

1. Oliver, C.D.; Larson, B.C. *Forest Stand Dynamics: Updated Edition*; John Wiley and Sons: Hoboken, NJ, USA, 1996.
2. Intergovernmental Science-Policy Platform on Biodiversity and Ecosystem Services [IPBES]. *Global Assessment Report on Biodiversity and Ecosystem Services of the Intergovernmental Science-Policy Platform on Biodiversity and Ecosystem Services*; IPBES Secretariat: Bonn, Germany, 2019; Available online: https://www.ipbes.net/global-assessment (accessed on 10 January 2022).
3. Intergovernmental Panel on Climate Change [IPCC]. Summary for Policymakers. In *Climate Change 2021, The Physical Science Basis. Contribution of Working Group I to the Sixth Assessment Report of the Intergovernmental Panel on Climate Change*; Masson-Delmotte, V., Zhai, P., Pirani, S., Connors, C., Péan, S., Berger, N., Caud, Y., Chen, L., Goldfarb, M.I., Monteiro, S., et al., Eds.; Cambridge University Press: Cambridge, UK, 2021; pp. 3–32.
4. PRISM Climate Group. Oregon State University. 2021. Available online: https://prism.oregonstate.edu (accessed on 29 October 2021).
5. Eischeid, J.K.; Hoerling, M.P.; Quan, X.W.; Kumar, A.; Barsugli, J.; Labe, Z.M.; Kunkel, K.E.; Schreck, I.I.I.C.J.; Easterling, D.R.; Zhang, T.; et al. Why has the summertime central US warming hole not disappeared? *J. Clim.* **2023**, *36*, 7319–7336. [CrossRef]
6. Keil, P.; Mauritsen, T.; Jungclaus, J.; Hedemann, C.; Olonscheck, D.; Ghosh, R. Multiple drivers of the North Atlantic warming hole. *Nat. Clim. Chang.* **2020**, *10*, 667–671. [CrossRef]
7. Abatzoglou, J.T. Development of gridded surface meteorological data for ecological applications and modelling. *Int. J. Climatol.* **2013**, *33*, 121–131. [CrossRef]
8. Cook, E.R.; Seager, R.; Heim, R.R., Jr.; Vose, R.S.; Herweijer, C.; Woodhouse, C. Megadroughts in North America: Placing IPCC projections of hydroclimatic change in a long-term paleoclimate context. *J. Quat. Sci.* **2010**, *25*, 48–61. [CrossRef]
9. Abrams, M.D. Fire and the development of oak forests. *BioScience* **1992**, *42*, 346–353. [CrossRef]
10. Nevle, R.J.; Bird, D.K.; Ruddiman, W.F.; Dull, R.A. Neotropical human–landscape interactions, fire, and atmospheric CO_2 during European conquest. *Holocene* **2011**, *21*, 853–864. [CrossRef]
11. Abrams, M.D.; Nowacki, G.J.; Hanberry, B.B. Oak forests and woodlands as Indigenous landscapes in the Eastern United States. *J. Torrey Bot. Soc.* **2022**, *149*, 101–121. [CrossRef]
12. Malhi, Y.; Doughty, C.E.; Galetti, M.; Smith, F.A.; Svenning, J.C.; Terborgh, J.W. Megafauna and ecosystem function from the Pleistocene to the Anthropocene. *Proc. Natl. Acad. Sci. USA* **2016**, *113*, 838–846. [CrossRef] [PubMed]

13. Ellison, A.M.; Bank, M.S.; Clinton, B.D.; Colburn, E.A.; Elliott, K.; Ford, C.R.; Foster, D.R.; Kloeppel, B.D.; Knoepp, J.D.; Lovett, G.M.; et al. Loss of foundation species: Consequences for the structure and dynamics of forested ecosystems. *Front. Ecol. Environ.* **2005**, *3*, 479–486. [CrossRef]
14. Nowacki, G.J.; MacCleery, D.W.; Lake, F.K. Native Americans, ecosystem development, and historical range of variation. In *Historical Environmental Variation in Conservation and Natural Resource Management*; Weins, J.A., Hayward, G.D., Safford, H.D., Giffen, C.M., Eds.; Wiley-Blackwell: West Sussex, UK, 2012; pp. 76–91.
15. Hanberry, B.B. Timing of tree density increases, influence of climate change, and a land use proxy for tree density increases in the eastern United States. *Land* **2021**, *10*, 1121. [CrossRef]
16. Denevan, W.M. The pristine myth: The landscape of the Americas in 1492. *Ann. Assoc. Am. Geogr.* **1992**, *82*, 369–385. [CrossRef]
17. Foster, D.R. Land use history (1730–1990) and vegetation dynamics in central New England, USA. *J. Ecol.* **1992**, *80*, 753–771. [CrossRef]
18. Whitney, G.G. *From Coastal Wilderness to Fruited Plain: A History of Environmental Change in Temperate North America from 1500 to the Present*; Cambridge University Press: New York, NY, USA, 1994.
19. Munoz, S.E.; Gajewski, K.; Peros, M.C. Synchronous environmental and cultural change in the prehistory of the northeastern United States. *Proc. Natl. Acad. Sci. USA* **2010**, *107*, 22008–22013. [CrossRef] [PubMed]
20. Nowacki, G.J.; Abrams, M.D. Is climate an important driver of post European vegetation change in the eastern U.S.? *Glob. Chang. Biol.* **2015**, *21*, 314–334. [CrossRef] [PubMed]
21. Nowacki, G.J.; Abrams, M.D. Demise of fire and mesophication of eastern U.S. forests. *BioScience* **2008**, *58*, 123–138. [CrossRef]
22. Hanberry, B.B.; Abrams, M.D.; Arthur, M.A.; Varner, J.M. Reviewing fire, climate, deer, and foundation species as drivers of historically open oak and pine forests and transition to closed forests. *Front. For. Glob. Chang.* **2020**, *3*, 56. [CrossRef]
23. Davison, C.W.; Rahbek, C.; Morueta-Holme, N. Land-use change and biodiversity: Challenges for assembling evidence on the greatest threat to nature. *Glob. Chang. Biol.* **2021**, *27*, 5414–5429. [CrossRef] [PubMed]
24. Kane, J.M.; Varner, J.M.; Metz, M.R.; van Mantgem, P.J. Characterizing interactions between fire and other disturbances and their impacts on tree mortality in western US Forests. *For. Ecol. Manag.* **2017**, *405*, 188–199. [CrossRef]
25. Seidl, R.; Thom, D.; Kautz, M.; Martin-Benito, D.; Peltoniemi, M.; Vacchiano, G.; Wild, J.; Ascoli, D.; Petr, M.; Honkaniemi, J.; et al. Forest disturbances under climate change. *Nat. Clim. Chang.* **2017**, *7*, 395–402. [CrossRef]
26. Gensini, V.A.; Brooks, H.E. Spatial trends in United States tornado frequency. *NPJ Clim. Atmos. Sci.* **2018**, *1*, 38. [CrossRef]
27. Holl, K.D.; Brancalion, P.H. Tree planting is not a simple solution. *Science* **2020**, *368*, 580–5811. [CrossRef]
28. Reilly, M.J.; Norman, S.P.; O'Brien, J.J.; Loudermilk, E.L. Drivers and ecological impacts of a wildfire outbreak in the southern Appalachian Mountains after decades of fire exclusion. *For. Ecol. Manag.* **2022**, *524*, 120500. [CrossRef]
29. Shuman, B.; Henderson, A.K.; Plank, C.; Stefanova, I.; Ziegler, S.S. Woodland-to-forest transition during prolonged drought in Minnesota after ca. AD 1300. *Ecology* **2009**, *90*, 2792–2807. [CrossRef]
30. Short, K.C. *Spatial Wildfire Occurrence Data for the United States, 1992–2020*; Forest Service Research Data Archive: Fort Collins, CO, USA, 2022. [CrossRef]
31. Way, D.A.; Oren, R. Differential responses to changes in growth temperature between trees from different functional groups and biomes: A review and synthesis of data. *Tree Physiol.* **2010**, *30*, 669–688. [CrossRef]
32. Boisvenue, C.; Running, S.W. Impacts of climate change on natural forest productivity—Evidence since the middle of the 20th century. *Glob. Chang. Biol.* **2006**, *12*, 862–882. [CrossRef]
33. Menzel, A.; Fabian, P. Growing season extended in Europe. *Nature* **1999**, *397*, 659. [CrossRef]
34. Adams, H.D.; Guardiola-Claramonte, M.; Barron-Gafford, G.A.; Villegas, J.C.; Breshears, D.D.; Zou, C.B.; Troch, P.A.; Huxman, T.E. Temperature sensitivity of drought-induced tree mortality portends increased regional die-off under global-change-type drought. *Proc. Natl. Acad. Sci. USA* **2009**, *106*, 7063–7066. [CrossRef] [PubMed]
35. Dietze, M.C.; Moorcroft, P.R. Tree mortality in the eastern and central United States: Patterns and drivers. *Glob. Chang. Biol.* **2011**, *17*, 3312–3326. [CrossRef]
36. Bazzaz, F.A. The response of natural ecosystems to the rising global CO_2 levels. *Annu. Rev. Ecol. Syst.* **1990**, *21*, 167–196. [CrossRef]
37. Ainsworth, E.A.; Long, S.P. What have we learned from 15 years of free-air CO_2 enrichment (FACE)? A meta-analytic review of the responses of photosynthesis, canopy properties and plant production to rising CO_2. *New Phytol.* **2015**, *165*, 351–372. [CrossRef] [PubMed]
38. Karnosky, D.F. Impacts of elevated atmospheric CO_2 on forest trees and forest ecosystems: Knowledge gaps. *Environ. Int.* **2003**, *29*, 161–169. [CrossRef]
39. Norby, R.J.; Warren, J.M.; Iversen, C.M.; Medlyn, B.E.; McMurtrie, R.E. CO_2 enhancement of forest productivity constrained by limited nitrogen availability. *Proc. Natl. Acad. Sci.* **2010**, *107*, 19368–19373. [CrossRef]
40. Keenan, T.F.; Hollinger, D.Y.; Bohrer, G.; Dragoni, D.; Munger, J.W.; Schmid, H.P.; Richardson, A.D. Increase in forest water-use efficiency as atmospheric carbon dioxide concentrations rise. *Nature* **2013**, *499*, 324–327. [CrossRef]
41. Mathias, J.M.; Thomas, R.B. Global tree intrinsic water use efficiency is enhanced by increased atmospheric CO_2 and modulated by climate and plant functional types. *Proc. Natl. Acad. Sci. USA* **2021**, *118*, e2014286118. [CrossRef] [PubMed]
42. Korner, C. Carbon limitation in trees. *J. Ecol.* **2003**, *91*, 4–17. [CrossRef]

43. Sperry, J.S.; Venturas, M.D.; Todd, H.N.; Trugman, A.T.; Anderegg, W.R.; Wang, Y.; Tai, X. The impact of rising CO_2 and acclimation on the response of US forests to global warming. *Proc. Natl. Acad. Sci. USA* **2019**, *116*, 25734–25744. [CrossRef]
44. Voelker, S.L.; Muzika, R.; Guyette, R.P.; Stambaugh, M.C. Historical CO_2 growth enhancement declines with age in *Quercus* and *Pinus*. *Ecol. Monogr.* **2006**, *76*, 549–564. [CrossRef]
45. McMahon, S.M.; Parker, G.G.; Miller, D.R. Evidence for a recent increase in forest growth. *Proc. Natl. Acad. Sci. USA* **2010**, *107*, 3611–3615. [CrossRef]
46. Davis, E.C.; Sohngen, B.; Lewis, D.J. The effect of carbon fertilization on naturally regenerated and planted US forests. *Nat. Commun.* **2022**, *13*, 5490. [CrossRef]
47. Hogan, J.A.; Domke, G.M.; Zhu, K.; Johnson, D.J.; Lichstein, J.W. Climate change determines the sign of productivity trends in US forests. *Proc. Natl. Acad. Sci. USA* **2024**, *121*, e2311132121. [CrossRef] [PubMed]
48. Finzi, A.C.; Giasson, M.A.; Barker Plotkin, A.A.; Aber, J.D.; Boose, E.R.; Davidson, E.A.; Dietze, M.C.; Ellison, A.M.; Frey, S.D.; Goldman, E.; et al. Carbon budget of the Harvard Forest Long-Term Ecological Research site: Pattern, process, and response to global change. *Ecol. Monogr.* **2020**, *90*, e01423. [CrossRef]
49. Caspersen, J.P.; Pacala, S.W.; Jenkins, J.C.; Hurtt, G.C.; Moorcroft, P.R.; Birdsey, R.A. Contributions of land-use history to carbon accumulation in US forests. *Science* **2000**, *290*, 1148–1151. [CrossRef] [PubMed]
50. Canham, C.D.; Murphy, L. The demography of tree species response to climate: Sapling and canopy tree survival. *Ecosphere* **2017**, *8*, e01701. [CrossRef]
51. Bishop, D.A.; Beier, C.M.; Pederson, N.; Lawrence, G.B.; Stella, J.C.; Sullivan, T.J. Regional growth decline of sugar maple (*Acer saccharum*) and its potential causes. *Ecosphere* **2015**, *6*, 179. [CrossRef]
52. Oswald, E.M.; Pontius, J.; Rayback, S.A.; Schaberg, P.G.; Wilmot, S.H.; Dupigny-Giroux, L.A. The complex relationship between climate and sugar maple health: Climate change implications in Vermont for a key northern hardwood species. *For. Ecol. Manag.* **2018**, *422*, 303–312. [CrossRef]
53. Peters, R.L.; Groenendijk, P.; Vlam, M.; Zuidema, P.A. Detecting long-term growth trends using tree rings: A critical evaluation of methods. *Glob. Chang. Biol.* **2015**, *21*, 2040–2054. [CrossRef]
54. D'Orangeville, L.; Houle, D.; Duchesne, L.; Phillips, R.P.; Bergeron, Y.; Kneeshaw, D. Beneficial effects of climate warming on boreal tree growth may be transitory. *Nat. Commun.* **2018**, *9*, 3213. [PubMed]
55. Allen, C.D.; Macalady, A.K.; Chenchouni, H.; Bachelet, D.; McDowell, N.; Vennetier, M.; Kitzberger, T.; Rigling, A.; Breshears, D.D.; Hogg, E.T.; et al. A global overview of drought and heat-induced tree mortality reveals emerging climate change risks for forests. *For. Ecol. Manag.* **2010**, *259*, 660–684. [CrossRef]
56. Crosby, M.K.; Fan, Z.; Fan, X.; Leininger, T.D.; Spetich, M.A. Assessing forest mortality patterns using climate and FIA data at multiple scales. In *Moving from Status to Trends: Forest Inventory and Analysis (FIA) Symposium 2012*; Morin, R.S., Liknes, G.C., Eds.; U.S. Department of Agriculture, Forest Service, Northern Research Station: Newtown Square, PA, USA, 2012; pp. 319–324.
57. Johnson, S.; Abrams, M.D. Age class, longevity and growth rate relationships: Protracted growth increases in old trees in the eastern United States. *Tree Physiol.* **2009**, *29*, 1317–1328. [CrossRef]
58. Abrams, M.D. Where has all the white oak gone? *BioScience* **2003**, *53*, 927–939. [CrossRef]
59. Cram, M.M.; Outcalt, K.W.; Zarnoch, S.J. Growth of longleaf and loblolly pine planted on South Carolina sandhill sites. *South. J. Appl. For.* **2010**, *34*, 79–83. [CrossRef]
60. Bragg, D.C. A reevaluation of superior tree performance after 48 years for a loblolly pine progeny test in southern Arkansas. *Front. For. Glob. Chang.* **2021**, *4*, 716443. [CrossRef]
61. Pan, Y.; Chen, J.M.; Birdsey, R.; McCullough, K.; He, L.; Deng, F. Age structure and disturbance legacy of North American forests. *Biogeosciences* **2011**, *8*, 715–732. [CrossRef]
62. Hanberry, B.B. Confronting the issue of invasive native tree species due to land use change in the eastern United States. *Land* **2022**, *11*, 161. [CrossRef]
63. Searle, E.B.; Chen, H.Y.; Paquette, A. Higher tree diversity is linked to higher tree mortality. *Proc. Natl. Acad. Sci. USA* **2022**, *119*, e2013171119. [CrossRef] [PubMed]
64. Quinn Thomas, R.; Canham, C.D.; Weathers, K.C.; Goodale, C.L. Increased tree carbon storage in response to nitrogen deposition in the US. *Nat. Geosci.* **2010**, *3*, 13–17. [CrossRef]
65. Clark, J.S.; Bell, D.M.; Hersh, M.H.; Nichols, L. Climate change vulnerability of forest biodiversity: Climate and competition tracking of demographic rates. *Glob. Chang. Biol.* **2011**, *17*, 1834–1849. [CrossRef]
66. Duveneck, M.J.; Thompson, J.R.; Gustafson, E.J.; Liang, Y.; de Bruijn, A.M. Recovery dynamics and climate change effects to future New England forests. *Landsc. Ecol.* **2017**, *32*, 1385–1397. [CrossRef]
67. Yaussy, D.A.; Iverson, L.R.; Matthews, S.N. Competition and climate affects US hardwood-forest tree mortality. *For. Sci.* **2013**, *59*, 416–430. [CrossRef]
68. Lines, E.R.; Coomes, D.A.; Purves, D.W. Influences of forest structure, climate and species composition on tree mortality across the eastern US. *PLoS ONE* **2010**, *5*, e13212. [CrossRef]
69. Brienen, R.J.; Caldwell, L.; Duchesne, L.; Voelker, S.; Barichivich, J.; Baliva, M.; Ceccantini, G.; Di Filippo, A.; Helama, S.; Locosselli, G.M.; et al. Forest carbon sink neutralized by pervasive growth-lifespan trade-offs. *Nat. Commun.* **2020**, *11*, 4241. [CrossRef]

70. Perret, D.L.; Leslie, A.B.; Sax, D.F. Naturalized distributions show that climatic disequilibrium is structured by niche size in pines (*Pinus* L.). *Glob. Ecol. Biogeogr.* **2019**, *28*, 429–441. [CrossRef]
71. Davis, M.B.; Shaw, R.G. Range shifts and adaptive responses to Quaternary climate change. *Science* **2001**, *292*, 673–679. [CrossRef] [PubMed]
72. Taheri, S.; Naimi, B.; Rahbek, C.; Araújo, M.B. Improvements in reports of species redistribution under climate change are required. *Sci. Adv.* **2021**, *7*, eabe1110. [CrossRef] [PubMed]
73. Roe, G.H.; Baker, M.B.; Herla, F. Centennial glacier retreat as categorical evidence of regional climate change. *Nat. Geosci.* **2017**, *10*, 95–99. [CrossRef]
74. Smith, W.K.; Germino, M.J.; Johnson, D.M.; Reinhardt, K. The altitude of alpine treeline: A bellwether of climate change effects. *Bot. Rev.* **2009**, *75*, 163–190. [CrossRef]
75. Gehrig-Fasel, J.; Guisan, A.; Zimmermann, N.E. Tree line shifts in the Swiss Alps: Climate change or land abandonment? *J. Veg. Sci.* **2007**, *18*, 571–582. [CrossRef]
76. Beckage, B.; Osborne, B.; Gavin, D.G.; Pucko, C.; Siccama, T.; Perkins, T. A rapid upward shift of a forest ecotone during 40 years of warming in the Green Mountains of Vermont. *Proc. Natl. Acad. Sci. USA* **2008**, *105*, 4197–4202. [CrossRef]
77. Liu, L.; Zhang, X. Effects of temperature variability and extremes on spring phenology across the contiguous United States from 1982 to 2016. *Sci. Rep.* **2020**, *10*, 17952. [CrossRef]
78. Bórnez, K.; Verger, A.; Descals, A.; Peñuelas, J. Monitoring the responses of deciduous forest phenology to 2000–2018 climatic anomalies in the Northern Hemisphere. *Remote Sens.* **2021**, *13*, 2806. [CrossRef]
79. Day, G.M. The Indian as an ecological factor in the northeastern forest. *Ecology* **1953**, *34*, 329–346. [CrossRef]
80. Hanberry, B.B.; Noss, R.F. Locating potential historical fire-maintained grasslands of the eastern United States based on topography and wind speed. *Ecosphere* **2022**, *13*, e4098. [CrossRef]
81. Hanberry, B.B. Non-native plant species richness and influence of greenhouses and human populations in the conterminous United States. *Ecol. Process.* **2023**, *12*, 27. [CrossRef]
82. Bradley, B.A.; Blumenthal, D.M.; Wilcove, D.S.; Ziska, L.H. Predicting plant invasions in an era of global change. *Trends Ecol. Evol.* **2010**, *25*, 310–318. [CrossRef]
83. Bale, J.S.; Masters, G.J.; Hodkinson, I.D.; Awmack, C.; Bezemer, T.M.; Brown, V.K.; Butterfield, J.; Buse, A.; Coulson, J.C.; Farrar, J.; et al. Herbivory in global climate change research: Direct effects of rising temperature on insect herbivores. *Glob. Chang. Biol.* **2002**, *8*, 1–16. [CrossRef]
84. Deutsch, C.A.; Tewksbury, J.J.; Huey, R.B.; Sheldon, K.S.; Ghalambor, C.K.; Haak, D.C.; Martin, P.R. Impacts of climate warming on terrestrial ectotherms across latitude. *Proc. Natl. Acad. Sci. USA* **2008**, *105*, 6668–6672. [CrossRef]
85. Bale, J.S.; Hayward, S.A.L. Insect overwintering in a changing climate. *J. Exp. Biol.* **2010**, *213*, 980–994. [CrossRef]
86. Dukes, J.S.; Pontius, J.; Orwig, D.; Garnas, J.R.; Rodgers, V.L.; Brazee, N.; Cooke, B.; Theoharides, K.A.; Stange, E.E.; Harrington, R.; et al. Responses of insect pests, pathogens, and invasive plant species to climate change in the forests of northeastern North America: What can we predict? *Can. J. For. Res.* **2009**, *39*, 231–248. [CrossRef]
87. Sobek-Swant, S.; Crosthwaite, J.C.; Lyons, D.B.; Sinclair, B.J. Could phenotypic plasticity limit an invasive species? Incomplete reversibility of mid-winter deacclimation in emerald ash borer. *Biol. Invasions* **2012**, *14*, 115–125. [CrossRef]
88. Wolkovich, E.M.; Cleland, E.E. Phenological niches and the future of invaded ecosystems with climate change. *AoB Plants* **2014**, *6*, plu013. [CrossRef]
89. Wolkovich, E.M.; Davis, T.J.; Schaefer, H.; Cleland, E.E.; Cook, B.I.; Travers, S.E.; Willis, C.G.; Davis, C.C. Temperature-dependent shifts in phenology contribute to the success of exotic species with climate change. *Am. J. Bot.* **2013**, *100*, 1407–1421. [CrossRef]
90. Robinson, E.A.; Ryan, G.D.; Newman, J.A. A meta-analytical review of the effects of elevated CO_2 on plant-arthropod interactions highlights the importance of interacting environmental and biological variables. *New Phytol.* **2012**, *194*, 321–336. [CrossRef] [PubMed]
91. Meentemeyer, R.K.; Cunniffe, N.J.; Cook, A.R.; Filipe, J.A.; Hunter, R.D.; Rizzo, D.M.; Gilligan, C.A. Epidemiological modeling of invasion in heterogeneous landscapes: Spread of sudden oak death in California (1990–2030). *Ecosphere* **2011**, *2*, 1–24. [CrossRef]
92. Brasier, C.M. Rapid evolution of introduced plant pathogens via interspecific hybridization. *BioScience* **2001**, *51*, 123–133. [CrossRef]
93. EDDMapS. 2021. Available online: https://www.eddmaps.org/species/ (accessed on 19 November 2021).
94. Liebhold, A.M.; Brockerhoff, E.G.; Garrett, L.J.; Parke, J.L.; Britton, K.O. Live plant imports: The major pathway for forest insect and pathogen invasions of the United States. *Front. Ecol. Environ.* **2012**, *10*, 135–143. [CrossRef]
95. Petitpierre, B.; Kueffer, C.; Broennimann, O.; Randin, C.; Daehler, C.; Guisan, A. Climatic niche shifts are rare among terrestrial plant invaders. *Science* **2012**, *335*, 1344–1347. [CrossRef]
96. McNulty, S.G.; Boggs, J.L.; Sun, G. The rise of the mediocre forest: Why chronically stressed trees may better survive extreme episodic climate variability. *New For.* **2014**, *45*, 403–415. [CrossRef]
97. Asaro, C.; Koch, F.H.; Potter, K.M. Denser forests across the USA experience more damage from insects and pathogens. *Sci. Rep.* **2023**, *13*, 3666. [CrossRef] [PubMed]
98. Romme, W.H.; Clement, J.; Hicke, J.; Kulakowski, D.; MacDonald, L.H.; Schoennagel, T.L.; Veblen, T.T. *Recent Forest Insect Outbreaks and Fire Risk in Colorado Forests: A Brief Synthesis of Relevant Research*; Colorado Forest Restoration Institute: Fort Collins, CO, USA, 2006.

99. De Chazal, J.; Rounsevell, M.D. Land-use and climate change within assessments of biodiversity change: A review. *Glob. Environ. Chang.* **2009**, *19*, 306–315. [CrossRef]
100. Robinson, G.S.; Burney, L.P.; Burney, D.A. Landscape paleoecology and megafaunal extinction in southeastern New York State. *Ecol. Monogr.* **2005**, *75*, 295–315. [CrossRef]
101. Gill, J.L.; Williams, J.W.; Jackson, S.T.; Lininger, K.B.; Robinson, G.S. Pleistocene megafaunal collapse, novel plant communities, and enhanced fire regimes in North America. *Science* **2009**, *326*, 1100–1103. [CrossRef]
102. Seton, E.Y. *Lives of Game Animals*; Branford: Boston, MA, USA, 1927; Volume III, Part I; Available online: https://archive.org/details/livesofgameanima0003seto/page/n15/mode/2up (accessed on 19 June 2022).
103. Hanberry, B.; Hanberry, P. Rapid digitization to reclaim thematic maps of white-tailed deer density from 1982 and 2003 in the conterminous US. *PeerJ* **2020**, *8*, e8262. [CrossRef]
104. Hanberry, B.B.; Abrams, M.D. Does white-tailed deer density affect tree stocking in forests of the eastern United States? *Ecol. Process.* **2019**, *8*, 30. [CrossRef]
105. Leopold, A.; Sowls, L.K.; Spencer, D.L. A survey of over-populated deer ranges in the United States. *J. Wildl. Manag.* **1947**, *11*, 162–177. [CrossRef]
106. Hanberry, B.B.; Faison, E.K. Re-framing deer herbivory as a natural disturbance regime with ecological and socioeconomic outcomes in the eastern United States. *Sci. Total Environ.* **2023**, *868*, 161669. [CrossRef]
107. Hanberry, B.B. Practical guide for retaining correlated climate variables and unthinned samples in species distribution modeling, using random forests. *Ecol. Inform.* **2024**, *79*, 102406. [CrossRef]
108. Hanberry, B.B. Addressing regional relationships between white-tailed deer densities and land classes. *Ecol. Evol.* **2021**, *11*, 13570–13578. [CrossRef] [PubMed]
109. Loehle, C. Height growth rate tradeoffs determine northern and southern range limits for trees. *J. Biogeogr.* **1998**, *25*, 735–742. [CrossRef]
110. Abrams, M.D. Adaptations and responses to drought in *Quercus* species of North America. *Tree Physiol.* **1990**, *7*, 227–238. [CrossRef] [PubMed]
111. Stanturf, J.A.; Goodrick, S.L.; Outcalt, K.W. Disturbance and coastal forests: A strategic approach to forest management in hurricane impact zones. *For. Ecol. Manag.* **2007**, *250*, 119–135. [CrossRef]
112. Bragg, D.C.; Hanberry, B.B.; Hutchinson, T.F.; Jack, S.B.; Kabrick, J.M. Silvicultural options for open forest management in eastern North America. *For. Ecol. Manag.* **2020**, *474*, 118383. [CrossRef]
113. Holzmueller, E.J.; Jose, S.; Jenkins, M.A. The relationship between fire history and an exotic fungal disease in a deciduous forest. *Oecologia* **2008**, *155*, 347–356. [CrossRef]
114. Danneyrolles, V.; Dupuis, S.; Fortin, G.; Leroyer, M.; de Römer, A.; Terrail, R.; Vellend, M.; Boucher, Y.; Laflamme, J.; Bergeron, Y.; et al. Stronger influence of anthropogenic disturbance than climate change on century-scale compositional changes in northern forests. *Nat. Commun.* **2019**, *10*, 1265. [CrossRef] [PubMed]
115. Knight, C.A.; Anderson, L.; Bunting, M.J.; Champagne, M.; Clayburn, R.M.; Crawford, J.N.; Klimaszewski-Patterson, A.; Knapp, E.E.; Lake, F.K.; Mensing, S.A.; et al. Land management explains major trends in forest structure and composition over the last millennium in California's Klamath Mountains. *Proc. Natl. Acad. Sci. USA* **2022**, *119*, e2116264119. [CrossRef] [PubMed]
116. Napier, J.D.; Chipman, M.L. Emerging palaeoecological frameworks for elucidating plant dynamics in response to fire and other disturbance. *Glob. Ecol. Biogeogr.* **2022**, *31*, 138–154. [CrossRef]

land

MDPI

Review

Urban Flood Hazard Assessment and Management Practices in South Asia: A Review

Bikram Manandhar [1,2,3,4], Shenghui Cui [1,3,*], Lihong Wang [1,2,3] and Sabita Shrestha [5]

[1] Key Laboratory of Urban Environment and Health, Institute of Urban Environment, Chinese Academy of Sciences, Xiamen 361021, China
[2] University of Chinese Academy of Sciences, Beijing 100049, China
[3] Xiamen Key Lab of Urban Metabolism, Institute of Urban Environment, Chinese Academy of Sciences, Xiamen 361021, China
[4] Institute of Forestry, Tribhuvan University, Hetauda 44107, Nepal
[5] Youth Innovation Lab, Banshidhar Marg, Kathmandu 44600, Nepal
* Correspondence: shcui@iue.ac.cn; Tel.: +86-592-6190777

Abstract: Urban flooding is a frequent disaster in cities. With the increasing imperviousness caused by rapid urbanization and the rising frequency and severity of extreme events caused by climate change, the hydrological status of the urban area has changed, resulting in urban floods. This study aims to identify trends and gaps and highlight potential research prospects in the field of urban flooding in South Asia. Based on an extensive literature review, this paper reviewed urban flood hazard assessment methods using hydraulic/hydrological models and urban flood management practices in South Asia. With the advancement of technology and high-resolution topographic data, hydrologic/hydraulic models such as HEC-RAS/HMS, MIKE, SWMM, etc., are increasingly used for urban flood hazard assessment. Urban flood management practices vary among countries based on existing technologies and infrastructures. In order to control urban flooding, both conventional physical structures, including drainage and embankments, as well as new innovative techniques, such as low-impact development, are implemented. Non-structural flood mitigation measures, such as improved flood warning systems, have been developed and implemented in a few cities. The major challenge in using process-based hydraulic models was the lack of high-resolution DEM and short-duration rainfall data in the region, significantly affecting the model's simulation results and the implementation of flood management measures. Risk-informed management must be implemented immediately to reduce the adverse effects of climate change and unplanned urbanization on urban flooding. Therefore, it is crucial to encourage emergency managers and local planning authorities to consider a nature-based solution in an integrated urban planning approach to enhances urban flood resilience.

Keywords: climate change; early warning system; flood; hydrological model; land use land cover change; urbanization

1. Introduction

Among all environmental hazards, flooding is one of the most common and destructive, independent of the impacted nation's geography, climate, or level of development. Floods accounted for 44% of all disasters, affecting 1.6 billion people worldwide from 2000 to 2019 [1]. In the past, flooding was primarily limited to the river basin and only occurred during rainy seasons. Nowadays, urban flooding has become one of the most common and widely-distributed disasters in urban areas around the world because of the rise in impermeable areas due to haphazard urbanization and the increasing frequency and intensity of extreme events due to a changing climate [2,3]. Urban flooding may result from riverine floods, coastal flooding, pluvial flooding, groundwater, and the failure of artificial drainage systems.

Flooding in cities began to receive more attention due to increasing flood events and devastation, resulting in massive loss of life and damage to property worldwide. A study in more than 616 cities reported that floods endanger more urban areas than any other natural hazard, posing a threat to over 379 million residents [4]. As imperviousness has increased on the surface, drainage construction and renovation have lagged behind the rate of urbanization, adding stress on cities attempting to deal with extreme events. At the same time, urbanization increases rainfall intensity due to the perturbation of urban heat islands [5]. Due to the abundance of economic prospects, there is a significant migration to urban areas; this increases the risk receptors' exposure through the occupation of floodplains.

Over the past few decades, urbanization rates have risen sharply in various parts of the world. More people now reside in cities than in rural areas worldwide. By 2050, it is predicted that 68% of the world's population will live in urban agglomerations, up from the current 55% in 2018 [6,7]. Most of the world's largest cities and over 75 percent of its urban population live in low- and middle-income nations. New towns and urban areas are growing, and existing ones are expanding without carefully considering urban planning. Uncontrolled and rapid urbanization in developing countries, particularly since 2000, has increased the vulnerability of the urban environment [8,9]. Floods in urban areas are often devastating because high densities of people and assets are concentrated in certain areas, resulting in economic loss and human casualties [10,11]. Urban infrastructure, industry, trade, commerce, and utility services are crucial urban sectors severely impacted by floods. As such, regular productivity is hindered during and after significant floods, which increases the vulnerability of city residents [12].

1.1. Urban Flood in South Asia

As shown in Figure 1, Afghanistan, Bangladesh, Bhutan, India, Maldives, Nepal, Pakistan, and Sri Lanka are the eight nations that comprise South Asia. With about 5032 million sq. km., South Asia is a very densely populated area, home to around 24 percent of the world's population [13]. This vast area has a wide range of climates, from temperate in the north to tropical monsoons in the south. The vast expanses of South Asia are particularly susceptible to frequent disasters due to the increasing rate of urbanization and heavily populated areas.

Flooding significantly impacts Asia, accounting for 41% of global flooding incidents, affecting 1.5 billion people (93% of all flood victims globally). Extreme riverine flooding is becoming more common in countries such as India, Bangladesh, Pakistan, Sri Lanka, and Nepal; this has caught the attention of the international media. The June 2013 floods in India (6054 fatalities) and the July 2010 floods in Pakistan (1985 deaths) were the two deadliest flooding incidents between 2000 and 2019 [1], followed by the mid-June to Aug 2022 Pakistan flood (nearly 1500 deaths) [14]. The global urban exposure to flooding (UEF) increased more than four-fold from 1985 to 2018 with accelerated temporal trends. Asia experienced the most significant increase in UEF (74.1%) [15]. Urban flooding has become an alarming issue in urban areas since the Mumbai flood in 2005, a mega-disaster. Over the past two decades, several megacities–Dhaka in Bangladesh; Mumbai, Kolkata, Chennai, and New Delhi in India; Karachi, Rawalpindi, and Lahore in Pakistan–have suffered numerous flooding incidents. Most of these megacities are situated along the banks of major rivers and coastal areas, which exposes an increasing number of people and assets to floods.

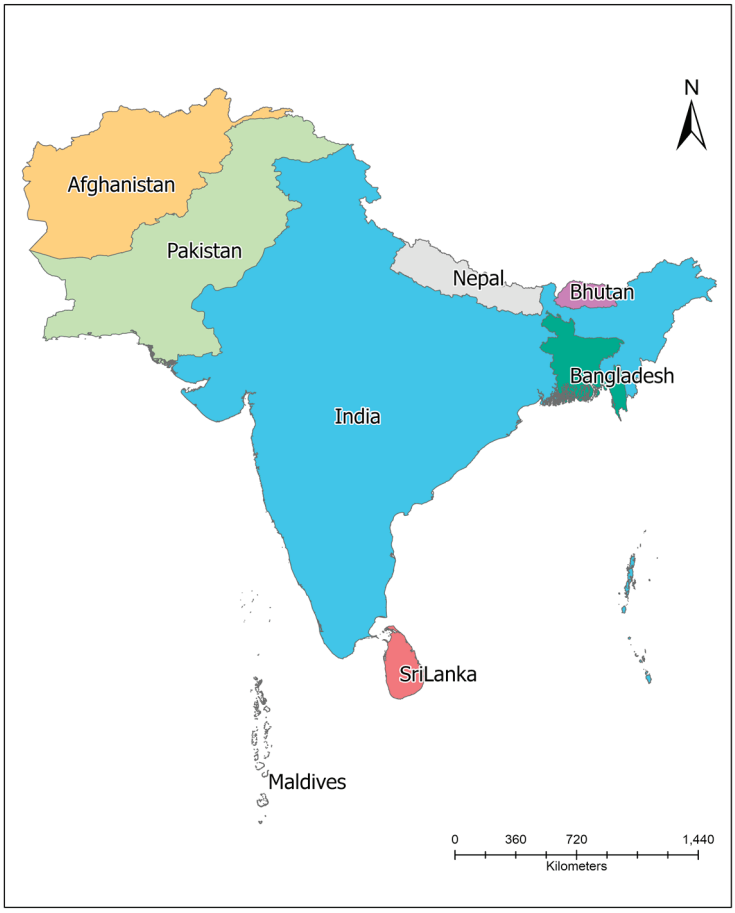

Figure 1. Map of South Asia (data source: https://www.diva-gis.org/gdata (accessed on 12 July 2021) and Survey Department, Nepal).

1.2. Causes of Urban Flooding

Evidence indicates that urban floods are increasing due to climate change [16,17]. According to the IPCC report, there is a high likelihood that the risk of pluvial flooding will increase in urban areas where excessive precipitation is expected to persist due to high levels of global warming [18]. In South Asia, climate change severely affects monsoons and tropical cyclones, two significant causes of flooding in the region [19]. There is strong evidence of an increasing trend in extreme rainfall in South Asia [14,20,21]. From 1951 to 2022, extreme rainfall events that produced more than 150 mm of rain in a single day nearly doubled in frequency [22], as shown in Figure 2. Due to climate change, extreme events are becoming more unpredictable, and weather forecasting models cannot predict this increase in chaos. Meanwhile, over central India, the frequency of extreme rainfall events (day rainfall 150 mm) has increased by nearly 75% throughout the period (significant at a 95% confidence level). This indicates that the frequency of extreme incidents is rising by roughly 13 per decade (more than one per year). However, the extremes are becoming more intense over time, as shown by a rise in the 99.5th percentile values [23]. The increase in summer precipitation and river water due to glacier melt in summer may cause extreme summer flash floods over this region in the future [24]. In most of the country's river basins, extreme precipitation and flood events have increased over the past 20 years. It has been estimated that, under a high-emission scenario, the frequency of multi-day flooding will surge significantly towards the end of the century [25]. Additionally, it is anticipated that, when temperatures rise, snow and glacier ice will melt more quickly, increasing the flows of the Himalayan rivers. Erratic monsoon patterns have seen a geographical shift and a change in the timing of onset and withdrawal, resulting in flooding [26,27].

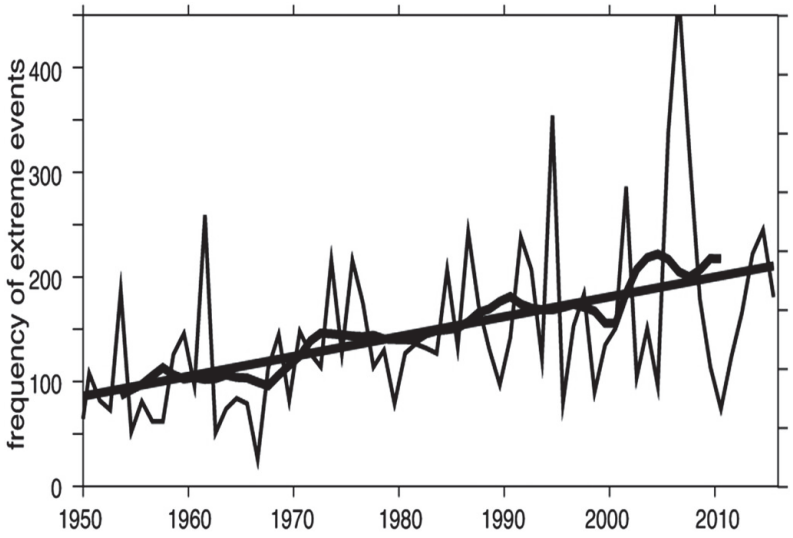

Figure 2. Frequency of extreme rain events exceeding 150 mm day^{-1} yr^{-1} over central India for the summer monsoon (June–September) during 1950–2015. The trend lines are significant at a 95% confidence level [28].

Parallel to this, flooding has emerged as a significant issue in different South Asian cities due to haphazard urbanization over the last two decades [29,30]. It is a fundamental environmental challenge affecting the lives and livelihoods of millions of urban dwellers whenever urban areas receive intense rainfall [31]. Urbanization-related land-use changes increase the paved area, influencing the local hydrometeorological processes that change the urban microclimate. Urban watersheds dominated by built-up areas inhibit rainwater infiltration, cause extreme runoff [32], and sometimes affect precipitation because of the UHI effect [33]. Urban areas, on average, lose 90% of storm rainfall to runoff [34] because of increased impervious surface area; this is more than a five-fold increase in runoff when compared to agricultural areas or the same size with the same intensity of rainfall [35,36]. Unprecedented rural-to-urban migration has led to reckless urban expansion. This has increased human settlements, industrial growth, and infrastructure expansion over some floodways, where floods may eventually occur, reducing the space into which floods can naturally overflow. An IPCC report also emphasizes that urbanization would worsen climate consequences, including floods, and cause significant economic losses throughout the region [18]. The prospects are worse in fast-growing cities, especially in densely populated urban areas [37]. However, due to global climate change, inadequate drainage systems, and rising urbanization [38], flooding is occurring more frequently, more intensely, and to a greater extent [39]. Increasing urban populations have raised the likelihood and severity of climate-related calamities [40], dramatically increasing the vulnerabilities and risks of urban inhabitants in already exposed areas [41]. With high population densities and concentrations of diverse socioeconomic activities, cities in South Asian countries face the tremendous impact of, and challenges in dealing with, flood-related problems [42], as shown in Table 1.

Table 1. Major Urban Flood events in South Asian Cities.

Date	Location	Meteorological Driver	Reported Impacts	Ref.
23 July 2001	Islamabad and Rawalpindi, Pakistan	620 mm rainfall in just 10 hrs.	74 people lost their lives, and affected 400,000 people	[43]
September 2004	Dhaka, Bangladesh	341 mm rainfall in a day and >600 mm in 5 days	730 people lost their lives, and 30 million people were made homeless	[44]

Table 1. *Cont.*

Date	Location	Meteorological Driver	Reported Impacts	Ref.
26 July 2005	Mumbai, India	944 mm of rainfall in 24 hrs.	At least 400 people and 20,000 cattle lost their lives.	[45]
September 2014	Srinagar, Jammu and Kashmir, India	Discharge of ~1, 15,218 upstream at Sangam and ~72,585 cusecs downstream	282 people lost their lives, and 253,000 houses were damaged	[46]
November–December 2015	Chennai, India	>400 mm of rainfall	400 people lost their lives and caused enormous economic damages	[47]
December 2015	Chennai, Tamil Nadu	494 mm of rain over a 24-h	Deaths of around 250 people	[48]
28 August 2016	Lahore, Pakistan	12 h and 30 min of intense rainfall of 59 mm	Lahore district was inundated by urban flooding	[49]
23 September 2016	Hyderabad, Telangana, India	165 mm rainfall	Economic losses of 137,839 USD	[50]
15 May 2016	Colombo, Sri Lanka	256 mm rainfall	Death of 3 lives and 185,000 people were directly affected	[51]
29 August 2017	Mumbai, India	468 mm of rainfall in 12 h	Confirmed death of 14 people	[52]
11–12 July 2018	Kathmandu, Nepal	129.6 mm of rain in 10 h	Damaged 522 houses, 15 sheds, 28 industries, and factories, including petrol pumps	[53]
14–15 August 2018	Kerala, India	Rainfall range of 270–300 mm.	483 people lost their lives, and 5000 thousand people were affected, with a 200 billion USD loss	[54]
27 June 2019	Mumbai, India	Five days received 137.8 mm of rainfall	32 people lost their lives, and the transportation was disrupted	[55]
4–8 August 2019	Malappuram and Wayanad districts of Kerala, India	400% over the normal average rainfall	81 people lost their lives, >39 houses and a walkover bridge washed away	[56]
1 March 2019	Kandahar city, Afghanistan	Rainfall of 97 mm in 30 h	20 people lost their lives, and many houses collapsed	[57]
11–12 July 2019	Kathmandu, Nepal	Around 150 mm of rainfall in 12 h	100 families were affected, and Balkhu and Kuleshwor witnessed levels of flooding never seen before	[58]
25–27 August 2020	2020 Karachi, Pakistan	345 mm rainfall for a single day	More than 40 people lost their lives	[59]
19 July 2020	Delhi, India	Recorded nearly 100 mm of rainfall	Four people lost their lives	[60]

Urban flooding is an increasingly significant issue in India due to the growth of urban areas [61,62]. From 1985 to 2018, India's UEF expanded from 171 km^2 to 3745 km^2, contributing 4.7% to worldwide growth [15]. Cities like Chennai (2015), Bengaluru (2016), Gujarat (2017), Kerala (2018), Maharashtra (2019), Assam (2020), Bihar (2020), Hyderabad (2020), and Delhi (2020) have been affected by urban floods of a greater magnitude [63], causing significant loss of life and devastation to infrastructure and agriculture [64]. Urban flooding from intense rainfall is a recurring phenomenon in Dhaka, Chittagong, Khulna, and Sylhet. Dhaka experienced significant floods in 1988, 1998, 2004, 2007, 2015, 2016, and 2017, caused by the overflowing of the surrounding rivers, affecting communications, livelihoods, and service facilities for many days. Waterlogging occurs in densely populated places where excessive rainfall-induced water is trapped due to poor drainage [65,66]. Pakistan also experienced frequent flooding in 2010, 2011, 2012, 2014, 2015, and 2017 [67]. During the monsoon season, urban flooding is anticipated in Pakistan's major cities, including Islamabad, Rawalpindi, Peshawar, Lahore, Karachi, Faisalabad, Hyderabad, etc. [68]. Over the past few decades, flooding in Colombo, Sri Lanka, and the nearby suburbs has increased exponentially [69]. In Kathmandu, local climate change and growing surface imperviousness increases the likelihood of regular pluvial floods [70]. Due to high rainfall

and poor drainage, urban flooding during the monsoon season has become a major concern on the northern side of Kabul city [71]. It is becoming a challenging daily issue for urban dwellers, authorities, and governments in the region [72]. As most studies focus on riverine floods in the region, there are few urban flood studies examining Afghanistan, Bangladesh, Bhutan, India, Nepal, Pakistan, and Sri Lanka. This study aims to identify trends and gaps and highlight potential research prospects in the field of urban flooding in South Asia. Thus, this paper reviewed the state-of-the-art methodology used for urban flood hazard assessment using the hydraulic/hydrological models and urban flood management practices in south Asian countries based on an extensive literature review of studies conducted in the last two decades (2001–2021).

2. Materials and Methods

This review paper adopted a keyword-based search approach through the Web of Science, Google Scholar, Science Direct, and ResearchGate databases. The keywords 'urban flood', 'urban flood hazard assessment', and 'urban flood management' in major cities of South Asian countries were used. Initially, irrelevant and duplicate publications were excluded based on their titles. Further, the abstracts of the remaining articles were reviewed and prioritized based on the study's objective. Considering these screening criteria, 105 publications were selected for analysis. Figure 3 shows the framework adopted for this paper, that primarily includes four parts: the first part discusses the current situation and causes of urban floods in South Asian cities. The second part discusses the application of hydrologic/hydraulic models for flood hazard assessment in urban areas of India, Bangladesh, Pakistan, Sri Lanka, Nepal, Bhutan, and Afghanistan. The third part analyzes the structural and non-structural measures applied for flood management in urban areas of South Asian cities. The fourth section examines the gap in urban flood hazard assessment and management practices between South Asian and developed countries.

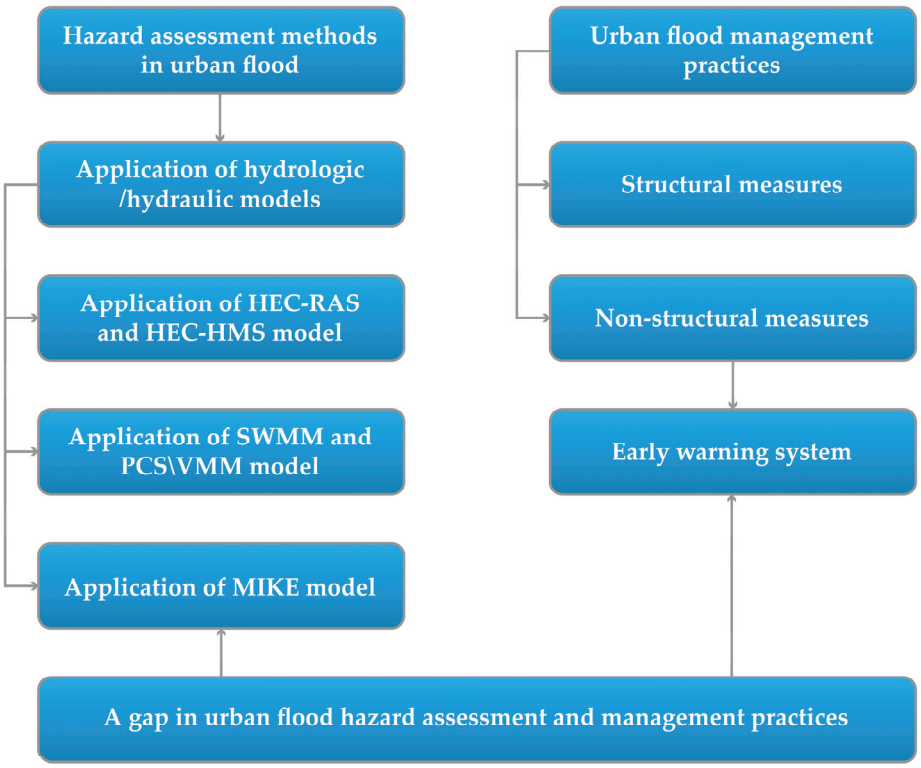

Figure 3. A research framework for assessing and analyzing urban flood hazard assessment and management practices in South Asian cities.

3. Methodology Used for Urban Flood Hazard Assessment in South Asian Cities

Urban flood hazard assessment is the initial step of urban flood management, during which the occurrence probability and the magnitude metrics of the potential flooding over a specific time in a given location are identified [73]. The parameters that commonly indicate the flood hazard are the extent of the flood, the flow rate, the depth, the duration, and the rise in the water level [74]. The assessment of urban flood hazards requires many data. In-depth terrain features are needed, including relief, land use, land cover, soil, channel flow pattern, meteorological parameters, etc. [75–77]. Several numerically-based models, physically-based models, and techniques, such as RS and GIS, multi-criteria analysis, and a social survey, have been used to create flood hazard maps in urban areas [78]. In recent years, urban flood susceptibility mapping has successfully utilized a variety of statistical techniques, including advanced soft computing technologies such as machine learning (ML) and artificial intelligence (AI) [79]. This section of the study reviewed the application of hydraulic/hydrological models for flood hazard assessment in the urban areas of South Asia.

3.1. Application of Hydraulic/Hydrological Models

Among the various methods available to undertake urban flood hazard assessment, the most used method is the application of the hydraulic/hydrological modeling approach. These models often work together, as the runoff results from the hydrologic model are used as input for the hydraulic model [80]. With the progress in computational resources and high-resolution topographical data, DEM, the hydrologic and hydraulic modeling approach, is increasingly used for flood hazard assessment in urban catchments [81]. Numerous one-dimensional (1D), two-dimensional (2D), 1D/2D linked, and three-dimensional (3D) numerical models have been developed to simulate the flow dynamics and scope of probable flooding events. These models are available in both open-access and paid ones with different capacities [82,83]. An important concern about hydrodynamic modeling is selecting an appropriate modeling approach. This primarily depends on the purpose of the study, flow conditions, and available data. Geospatial data and techniques have outperformed conventional comprehensive monitoring and assessment approaches, particularly in dynamic and complex urban environments [84]. Despite their benefits, the chaotic and complex nature of floods makes it challenging to develop a credible flood inundation model [85]. Some of the widely applied models in South Asian cities are HEC-RAS and HEC-HMS (US Army), SWMM and PCSWMM (CHI), and MIKE (DHI), among others.

3.1.1. HEC-RAS and HEC-HMS Model

The Hydrologic Engineering Center (HEC) offers a collection of hydrologic and hydraulic modeling software. HEC-RAS (hydraulic) and HEC-HMS (hydrologic) are the most used software packages. HEC-HMS is used to determine rainfall-runoff relationships, and HEC-RAS is used for the hydraulic modeling of rivers and pipes based on watershed characteristics. This open-source software is widely used for flood hazard assessment in South Asian cities, as described below and Table S1.

Many studies have been conducted in the Oshiwara, Mithi, and Poisar river catchments in Mumbai to investigate the impact of LULC and urbanization on floods using the integrated approach of hydrologic (HEC-HMS) and hydraulic models (HEC-RAS) with GIS and RS [86–89]. In Mumbai, India, the settlement of the world's largest urban population has caused rapid Land Use Land Cover (LULC) changes on both temporal and spatial scales. Daily time series data of precipitation and temperature, land use, soil, and DEM were used to run the model. Soil Conservation Service—Curve Number (SCS-CN) was used to derive flood hydrographs for different land-use conditions. In turn, flood extent and depth generated by models were used for developing flood hazard maps for the city [87]. Similarly, the 1D HEC-RAS model was employed to determine the water surface profile in the Thirusoolam sub-watershed of Chennai, India. The weighted curve number (CN) was derived based on the land use and hydrologic soil groups. A study shows the flooded area

increased from 31.70 sq. km. in 1976 to 36.61 sq. km. in 2005, and the flood depth increased from 3.71 m in 1976 to 4.55 m in 2005; this signifies that the extent and depth of flooding have increased due to urbanization [90]. In 2015, Chennai suffered a devastating flood; simulating such a destructive flood event in a metropolis with expanding urban sprawl and a changing environment is crucial for improving flood preparedness. Therefore, Devi et al. used HEC-HMS and 2D HEC-RAS to model the runoff response of the event for flood inundation extent and depths corresponding to the baseline flood scenario (in 2015) and the future flood scenario (in 2030). A study shows that, considering the worst possible urban sprawl and extreme rainfall, 1.7 times more buildings will be exposed to flood hazards, on average. The average increase in inundation extent will be between 20% and 33% [91].

Similarly, Hyderabad also regularly suffers urban flooding; in 2001, 2003, 2008, 2016, and 2017, many low-lying areas were inundated. In 2019, Rangari et al. developed a regional framework for flood modeling by fusing GIS with HEC-RAS and HEC-HMS for the city. As a starting point, base maps were created using the Shuttle Radar Topography Mission (SRTM) DEM 30 m and LULC map; hourly rainfall and evaporation data, the current drainage network, and future planned new drainage line were also used. Three significant flood events—July 1989, August 2000, and August 2008—were chosen as case studies to analyze the modeling framework, and flood inundation maps were prepared to show the area at risk. According to the model's findings, 17% of the land is vulnerable to flooding [92]. Also, Rangari et al. developed a 1D–2D urban flood model by integrating GIS with HEC-RAS and HEC-HMS. The model is run under various climate change scenarios (RCP 2.6, RCP 4.5, RCP 6.0, and RCP 8.5) to determine the most vulnerable locations and investigate potential increases in flood risk and hazards due to climate change. According to the model, the likelihood of flooding increases as the RCP scenario's severity and return interval increase. The study prepared a hazard map of the city based on inundation depth and floodwater velocity [93]. An urban flood event was modeled using HEC-RAS 1D–2D, comparing the 13 October 2020, flood event with the 24 August 2000. According to the study, urban hydrology has been significantly impacted by rapid, unchecked urbanization (16.5% rise) over the past two decades, leading to increased flood volumes after relatively moderate rainfall events [94]. Similarly, Surwase and Manjusree assessed urban flooding using HEC-RAS 2D, PCSWMM, and HAND to identify the vulnerable low-lying areas in the city. The study used 10-m CARTO DEM, hourly rainfall, and stream discharge data. The study shows that, if 144 mm of rainfall occurs uniformly over the catchment within 10–12 h, the catchment will experience flooding [95]. Navasari, a city in Gujarat, India, experienced a devastating flood on 4 August 2004. For urban flood modeling in the city, [96] used the 2D HEC-RAS model for unsteady flow simulation, and [97] used 1D HEC-RAS for steady flow analysis and validated this analysis using the 2004 flood event. The flood depth maps indicate that the city's low-lying areas are susceptible to flooding when the river discharge exceeds 8836 m^3/s and that it will take 11 to 13 h to inundate the town.

Similarly, in Pakistan, the extent of floods in the Malir Basin of Karachi City was investigated using HEC-HMS to simulate runoff and HEC–RAS for flood modeling. For this purpose, historical rainfall data from 1985 to 2014 were used, and drainage networks and streambeds were extracted from SRTM DEM and topographic maps. For the rainfall events in 2013 and 2009, the maximum simulated flows recorded at the river outlet were around 1800 m^3/s and 2832 m^3/s, with rainfall periods of an hour and four hours, respectively; these events generated massive runoffs that flowed into the stream and hit Karachi's urban area [98]. In Bangladesh, Masood and Takeuchi used a 1D hydrodynamic simulation based on SRTM DEM and hydrologic field-observed data for 32 years (1972–2004) to assess flood hazards for mid-eastern Dhaka (37.16 km^2). The HEC-RAS inundation simulation for a flood with a 100-year return period indicates that the maximum flood depth is 7.55 m in the southeast, and more than 50% of the region is affected. A flood hazard map was created and validated by comparing the degree of flooding with the destructive cyclone Sidr, that hit Bangladesh on 16 November 2007 [99].

HEC-RAS and HEC-HMS have been widely used in flood hazard assessment in urban areas of Nepal. Pandey and Dugar studied urban flood hazards and inundations at Hanumante Basin, near Bhaktapur, using GIS and HEC-RAS 5.0.7 hydraulic modeling. DEM was generated using the survey data and applied for the extraction of the geometry of the river. As the river was not gauged, the extreme river flows were predicted using the Catchment Area Ratio method. The HEC-RAS model prepared floodplain maps that showed that the built-up areas were more vulnerable to flooding from 2005 to 2018 [100]. Talchabhadel et al. conducted citizen science-based urban flood monitoring of the Hanumante River, Bhaktapur, during the 2019 monsoon season. A network of six hydrologic and sixteen precipitation stations were established in the Hanumante River basin, where citizen scientists continuously recorded daily water level and precipitation measurements. A two-dimensional shallow water equation unsteady flow model was then used to simulate the inundation process. The hydrologic model was validated against the observed citizen-based water level measurements [101]. Similar flood mapping was conductede in Tulsipur, Nepal, along the Patu River using HEC-RAS modeling for 25, 50, and 100-year return periods. The Catchment Area Ratio method was used to calculate the peak flood, with estimates of 109.9 m^3/s and 158.1 m^3/s for the 25- and 100-year return periods. The study shows that only 0.009 km^2 of the settlement area was inundated in 2004; this increased to 0.043 km^2 and 0.096 km^2 in 2010 and 2019, respectively. Rising urbanization near the river has exacerbated the town's flood risk [102]. A study by Dongol and Bormudoi in the Bishnumati catchment, Kathmandu, analyzed flood hazards and vulnerability using 1D HEC-RAS with the HEC-GeoRAS interface and ArcGIS, which demonstrated that the flood area grew more prominent with increasing flood severity. The outcome reflects the flooding of significant urban areas, indicating that future flood disasters will pose a greater risk to human life [103]. In Bhutan, a study by Tenzin and Bhaskar modeled the flash flood due to heavy rainfall at Sarpang to determine the suitability of integrating HEC-RAS and ArcGIS methods in mountainous terrain. The average discharge of the river outflow was calculated using meteorological data, and SRTM DEM and Landsat 8 OLI satellite images were used as base maps. According to flood simulations, floodwater can reach depths of up to 3 m downstream and stretch up to 200 m to 300 m on either side of the stream's centerline. The flood extended, and the inundation depth was approximate with the July 2016 flash flood area, validating the model [104]. In Kabul, Afghanistan, a 1D HEC-HMS hydrological model was applied to simulate the effects of pre-and post-development land-use changes on flooding. Climate Hazard Group InfraRed Precipitation with Station (CHIRPS) rainfall data from 2008 to 2018 generated discharge for each urban flooding event. According to the study, between 1960 and 2009, imperviousness increased dramatically, from 7.1% to 59%, while pervious surface decreased from 21% to 6%. A hydrological model simulation revealed that runoff volumes caused by floods might be related to significant LULC changes in the city [71].

3.1.2. Application of SWMM and PCSWMM

The Storm Water Management Model (SWMM) is a dynamic rainfall-runoff model used to simulate the quality and quantity issues related to watershed runoff in urban settings. SWMM primarily calculates the two-dimensional overland surface and one-dimensional flow through drainage pipes. It has been regularly updated to accommodate the dynamic urban setting [84]. PCSWMM is the GIS-based model capable of modeling urban drainage networks using SWMM. Some research that applied SWMM and PCSWMM in the region are described below and Table S2.

In Hyderabad city, India, Rangari et al. developed flood inundation and flood risk maps using a coupled 1D-2D flood modeling approach when extreme rainfall occurred. An SWMM was coupled with a 2D PCSWMM model to simulate extreme flood events to determine the low-lying areas and overflowing drainage nodes that require emergency attention [105]. Similarly, Vemula et al. evaluated the effects of extreme rainfall on the drainage capacity, flood risk, and inundation extent. The runoff simulations were carried

out for historical and future extreme rainfall events. The findings indicate that the current network could handle RCP 6.0 with an 82% runoff. However, it was insufficient to transport runoff from RCPs 2.6, 4.5, and 8.5, which shows that Hyderabad could see future intense rains that will increase runoff volumes and result in flooding [50]. At the National Institute of Technology in Telangana, India, Rangari and Prashanth used the SWMM model to analyze the campus's drainage systems. The model used the LULC maps, the Cartosat 30 m DEM, and other drainage information from the municipal corporation. The model simulated recent storm events with a design storm intensity with a 2-year return period; the study result showed that some parts of the campus are frequently affected by floods [106]. A study by Andimuthu et al. in Chennai evaluated the existing state of stormwater drains under current and future climate scenarios. IPCC CMIP5 models of RCP 4.5 were used to develop possible future climate change scenarios and generated IDF curves for 2, 5, 10, 50, and 100-year return periods. The Differential Geographic Positioning System (DGPS) surveyed the storm drainage network. The HEC-HMS model for watershed runoff and SWMM for storm drainage network was used to estimate the discharge and flooded areas and to suggest mitigation measures [77].

In Bangalore, India, Avinash et al. applied an SWMM hydrological model using a high-resolution LULC map, a 2 m resolution DEM, real-time hydrometeorological data, and stormwater drainage data to construct the flood extent map. A study ran numerous simulations for various rainfall intensities to obtain the runoff details. Then, using the Inp.PINS tool, predicted rainfall and flood extent maps were produced from the SWMM model [107]. In Vijayawada, India, SWMM was used to evaluate the overflow volume. The model's set-up used the city map, daily rainfall data, and stormwater network drainage. The model simulations assisted in visualizing the runoff from extreme precipitation events, analyzing the correctness of the stormwater network system, and understanding the flood area [108,109]. Similarly, SWMM was employed in Bhubaneswar, India, to understand the urban flood risk based on the degree of urbanization. To set up the model, information on land use and micro-watersheds were gathered using LiDAR data (1 m) and thirty years of hourly rainfall data. The Gumbel Distribution determined the frequencies and probabilities of maximum rainfall for various return periods. This distribution demonstrated the region's high prevalence of rainfall events, which contribute to the severity of urban flooding in the city [84]. At IIT Kharagpur, India, Bisht et al. tried to solve the stormwater management problem. SWMM and MIKE URBAN models were used to develop a reliable drainage system to simulate flood extent and inundation. Model simulation showed that extreme rainfall events that happen quickly would cause flooding from any drainage system, regardless of the drainage system's design [79]. Similarly, in Pune, India, used the SWMM 5.1 model to create and simulate urban floods utilizing rainfall events in the past. The model set-up included hourly rainfall data, SRTM 30 m DEM, drainage information, and catchment data. The model simulation considered the two most significant past rainfall events, in August 2007 and July 2016. It proved that the drainage system is insufficient to withstand intense rainfall and is overwhelmed by rainfall [110].

In Bangladesh, urban flooding and waterlogging during the monsoon season become unavoidable due to changes in land use and irregular rainfall. In cities, the current drainage systems frequently need to remove stagnant water. In the Begunbari canal catchment, Eastern Dhaka, Ahammad et al. modeled stormwater management using GeoSWMM, where 10 m DEM, land use, canal cross-sections, water level, discharge, and rainfall data were used as input data. The model simulation results showed that maximum flood depths and inundated areas can be reduced by pumping. To maintain the desired water level, 55 cumecs capacity pumps with a 1.5 sq. km. retention area are needed [111]. Similarly, Akter et al. used 2D PCSWMM to determine the flood depth in Chittagong. Analyses of rainfall trends and frequency were performed, and a model was run for various return periods. The flood hazard map was created using ArcGIS and PCSWMM with simulated flood depths [112]. In Chittagong, urban flooding typically happens during the rainy season. Akter et al. coupled the HEC-RAS inundation model with SWMM to observe the

detailed and spatial extent of the flood. The HEC-RAS and remote sensing data-based flood simulations exhibited a good match compared to SWMM-simulated floods, with correlation coefficients of 0.98 and 0.70, respectively [113].

Urban centers in Nepal, such as Kathmandu Valley, Birjung, Banepa, and other emerging cities, pose a severe threat of urban flood risk due to the combined effects of unplanned urbanization and climate change. The study by Salike and Pokharel investigated the connection between increasing urban flooding due to extreme rainfall events brought by climate change and increased imperviousness in Kathmandu. The study used RClimdex, a statistical downscaling model, PCSWMM, and a survey approach for urban flood modeling. A study shows that future climate change will increase pluvial floods in the city at the present state of urbanization [114]. Similarly, KC et al. used the PCSWMM model to assess how urbanization and climate change affect flooding in Kathmandu Metropolitan City. For a 2-year and a 20-year return period, the RCP 4.5 scenario indicates the most significant rise in flood volume (60–90%) for present (75%) and extreme (90%) imperviousness, with the extent of the flood area growing more than the depth. The findings demonstrate that climate change is expected to have a more significant overall impact on pluvial floods than urbanization [70].

3.1.3. Application of MIKE

MIKE Powered by DHI is a range of software products that accurately analyze, model, and simulate any challenge in water environments. Some research conducted with the MIKE application in the region are described below and Table S3. In a study in two south Asian cities, Bharatpur in Nepal and Sylhet in Bangladesh, urban drainage models were created using MIKE11 hydraulic models. The study collected water discharge, drainage networks, cross sections, historical water level, and rainfall data to simulate and calibrate the models. Study results show that under the current scenario, 12.7% of the land in Bharatpur and 22.3% of the land in Sylhet are at risk of flooding. Enhancing the drainage system can decrease the risk area to 5.5% in Bharatpur and 3.6% in Sylhet. However, if solid waste is not managed correctly, the site at risk of urban flooding could rise to 7.6% in Bharatpur and 18.5% in Sylhet in five years [115].

In Dhaka, water logging is a severe problem. This metropolis has two drainage systems: a protected western side with predominantly piped drainage and an unprotected eastern side with primarily open canals. A study by Khan et al. used MIKE Flood to model the one-dimensional drainage and 2D surface flow. An urban rainfall-run-off model was used to estimate the runoff from the rainfall based on the time-area method. The study's findings indicated that the damage will increase dramatically if the 2004 flood event is repeated in 2050 [116]. In Central Dhaka, Mark et al. developed a flood model using MIKE URBAN, where a time area model simulates the rainfall-runoff process. The urban drainage network was computed using MIKE FLOOD, while the surface flow was calculated using a 2D model with a 10 m grid size. The model was calibrated for water levels in the urban rivers for the flood extent of the 2004 flood and compared with the prepared flood map, showing a good agreement between the detected and simulated flood zones [117]. Dasgupta et al. predicted urban flooding in Western and Central Dhaka using the MIKE Urban coupled 1D-2D model using the 25 m^2 grid DEM topography data, historical daily and three-hourly rainfall, drainage network, sedimentation depth, and pump discharge to produce time-series inundation data. Using simulated data, inundation depth, a duration table, and location-specific flood maps were generated [66]. Chen et al. used the MIKE Urban model to simulate urban flooding in Eastern and Central Dhaka. The MOUSE and MIKE FLOOD models simulated storm sewer and river channel flows. The rainfall and water levels in the rivers for flood modeling were calculated based on a statistical analysis of 50 years of historical data from Dhaka's catchments [118].

Similarly, in the Kolonnawa basin of Colombo, Sri Lanka, the MIKE FLOOD model was used to represent flow and storage on land. The study used the Unit Hydrograph approach to schematize the rainfall-runoff processes and the SCS-CN method to calculate

the surface runoff. The 2D overland flow was simulated by MIKE 21 using a standard grid with a resolution of 25 m. The collective model performance was validated, and showed reasonable results for the May 2016 flood event. Due to the disparity between observation and simulation at the Wellawatta outfall location, it underestimated the peak flood level in the canal system by about 0.2 m [119]. Additionally, the complete canal system in the Metro Colombo region of Sri Lanka was modeled using the MIKE11, MIKE21, and MIKE FLOOD models to determine the capacity of the canals to control floods. Lidar created a DEM with 1.0 m horizontal and 0.15 m to 0.20 m vertical accuracy. MIKE FLOOD modeled the canal system with rainfall return periods of 10, 25, and 50 years to produce the corresponding floods. MIKE21 and MIKE11 models were coupled with MIKE FLOOD by specifying the connections between canals and floodplains. The study result showed that, under the current conditions, the canal system can only withstand a 10-year rainfall flood event, and the safe flood level in the basin is 2.0 m [120].

3.2. Application of Remote Sensing and GIS in Urban Flood Studies

Geospatial technology, coupled with remote sensing (RS) and Geographic Information Systems (GIS), has become a powerful tool for urban flood management and thus gained significant attention [86,88,90,93,121–126]. The ability of the satellite to map floods has been known for more than 40 years. However, over the last decade, with a proliferation of open-access Earth Observation (EO) data, there has been significant progress in developing EO products and services tailored to various end-user needs, as well as its integration with flood modeling and prediction efforts [127]. Optical to microwave remote sensing has provided the data for flood mapping analysis in all weather conditions. GIS help map flood hazard, potential areas, and vulnerable regions. As such, the use of both technologies has become imperative. Urban flood simulation software frequently inputs DEM and LULC data [128]. New remote sensing technology, such as multisensory systems, radar, and LIDAR, offers vast area coverage and time revisits to measure episodic severe precipitation and the resulting urban floods [129]. Synthetic aperture radar (SAR) is a form of satellite imagery unaffected by weather conditions, such as cloud coverage during flooded periods, making it suitable for detecting floods [130]. Aerial drones have expanded the remote sensing toolkit for disaster management activities [131]. Real-time information acquisition has its benefits, but it also has disadvantages, including the need for verification. The application of open-source data as geospatial tools in urban flood studies, such as OpenStreetMap (OSM), Java OpenStreetMap (JOSM), QGIS, GPS Essentials, and Open Map Kit (OMK), is also increasing [132].

Roy et al. modelled and identified the waterlogging hazard in Siliguri, India, with the help of an integrated analytical hierarchy process (AHP) and GIS techniques. A primary field investigation was conducted to prepare a waterlogging inventory map along with ten parameters related to urban waterlogging conditioning. GIS and remote sensing-based data Landsat 8 OLI/TIRS, ASTER GDEM, and Vector layers were used for spatial analysis, including change detection. NDVI, NDMI, and NDWI were used interactively during analysis. The results suggest that about 46% of the city is located in high to very high waterlogging hazard zones [122]. Wijeratne and Li studied the effects of unplanned urban growth on the rise in hydrological extremes in Sri Lanka's lower Kelani River basin. The study analyzed various remote sensing data, including night-time light images (NOAA/AVHRR) and Landsat (TM/ETM+/OLI) data of different wavelengths. The study's findings indicate that there has been a rapid urban spread over the last 23 years and that the overall urban land area has expanded by 130%. Due to urban growth, the flood frequency has also increased significantly over the past 20 years [123]. Singh and Sharma applied geospatial technologies, including IRS-1D LISS IV with PAN satellite data at 5.8 m resolution, Survey of India topo-sheets at 1:50,000 scales, and high-resolution Google-earth data at the sub-meter scale, to prepare urban flood hazard maps in Tapi catchment, India. Time series data on stage and discharge, stored as *.ASCII format files, have been linked with GIS software-based analysis tools, thereby interlinking spatial and

temporal data using GIS software and customized DBMS tools [125]. A study by Sadiq et al. used Sentinel-1 imagery to detect flood water in Bhubaneswar and Cuttack, India. The study experimented with two deep learning methods that were trained and tested on an open-source labeled satellite imagery dataset called Sen1Floods11. They then compared the performance of these two deep learning models with a conventional thresholding-based flood segmentation model, Otsu. The flood extent from the model that performed the best was then displayed on a map [130]. A study by Sowmya et al. assessed the flood zoning of Cochin City by applying a multi-criteria evaluation approach in a geographical information system environment with inputs from remotely sensed images acquired by the LISS-III sensor of IRS-P6 satellite with a spatial resolution of 23.5 m and SRTM DEM. The standard software package ArcGIS 9.3 was used for all GIS operations, including database generation and spatial analysis; ERDAS Imagine was used for all image processing [133]. A study by Tomar et al. proposes an integrated remote sensing, geographic information system (GIS), and field survey-based approach for identifying and predicting urban flood-prone areas [126]. A study by Dammalage and Jayasinghe in Colombo analyzes the impact of land-use change on the 2016 flood compared to the land use during the 1989 flood. NDVI, NDBI, and NDWI indices were used to determine land use from Landsat. SVM classification was selected, and change detection was performed with remote sensing and a GIS environment. The comparison of land-use changes between 1989 and 2016 shows that the area of the Kelani river watershed changed into an urban area, significantly impacting flood inundation [134]. Zope et al. assessed the impact of land use–land cover (LULC) change and urbanization on floods for an expanding urban catchment of the Oshiwara River in Mumbai, India. The land use change was mapped for 1966, 2001, and 2009 using the topographic map and satellite images. Advanced spaceborne Thermal and Reflection Radiometer (ASTER), the Global Digital Elevation Model (GDEM) of Terra satellite, and the Shuttle Radar Topography Mission (SRTM) DEM were used for the delineation of the watershed boundary of the study area. The actual surveyed data were used to generate a better geometric profile along the river cross sections. Catchment and drainage networks were generated using the Arc GIS extension of HEC-GeoHMS software [88]. Remote sensing and GIS technologies support disaster management, especially for rapid and sudden urban flood hazards. Combining a remotely sensed hydrography dataset with a hydraulic model enables the accurate modeling of flooding, even in areas with little available data [135]. Rijal et al. monitored underlying land-cover dynamics and flood hazards in Birendranagar, a rapidly urbanizing city in Nepal. A study assessed spatiotemporal urban dynamics and associated LULC changes in the city using Landsat imagery classifications; the results show several settlements and cultivated lands along river banks are at high risk of flood hazards [121].

4. Urban Flood Management Practices in South Asian Cities

Urban floods have become a severe problem in South Asian cities. The management of these floods is vital to ensure people's safety and maintain socioeconomic conditions [136]. Management practices vary among nations and depend on current infrastructure, technologies, and the level of urban planning [137]. The flood risk is increasing due to poor management and inadequate mitigation measures worldwide, especially in developing countries [138]. Therefore, protecting the wellbeing of people and communities depends on sensible management programs and risk mitigation techniques. Currently, there is increasing attention towards a new paradigm of flood management based on effective risk mitigation (structural flood measures, such as embankments, dikes, and drainage, or low impact development, LID) and adaptation strategies (non-structural soft measures, such as early warning systems, flood awareness, and policy initiatives) [139].

4.1. Structural Measures

Urban flooding is often regarded as an infrastructure issue that can be resolved with engineering technologies since they considerably lower the risk and harm from flooding.

In South Asian nations, most government initiatives aim to enhance structural elements such as embankments, retaining walls, levees, culverts, detention ponds, drainage channel upgrades, and removing floodplain barriers. In Surat city, India embankment and the retaining wall on the River Tapi are the city's most critical flood protection measures. Novel stormwater management strategies and Low Impact Development (LID) have been employed in some cities, including rain gardens (RGs), green roofs, infiltration trenches, rainwater harvesting, and porous pavements to address urban flooding [50], as shown in Table 2. In Hyderabad, India, RGs built with depths ranging from 400 to 500 mm have performed well during the monsoon season. For two years and five years of design with precipitation of 1 h, urban green and open spaces retained 44–50% of the rain [140]. In contrast, bioretention basins were unsuitable for high-intensity rainfall [62]. In Guwahati, India, the flooding in nearby canals has been lessened, but not entirely eradicated, by widening some channels and building detention ponds. A study shows that a detention pond lowered the city's inundation by 43% and the maximum flood depth by 46% [141]. Similarly, Sarmah and Das designed seven distinct trapezoidal drainage sections to create an integrated drainage network that can, to some extent, "self-heal" urban flood mitigation [142]. The Poisar River basin in Mumbai shows a decrease in peak discharge from 10.7% for the 2-year return period to 34.5% for the 200-year return period when looking at the impact of detention ponds on surface runoff and floodplain extent. Additionally, for LULC in the year 2009, there was a decrease in flood extent from 4.5% for the 25-year return period to 7.7% for the 100-year return period and a decrease in the total flood hazard area of 14.9% [89] due to the use of a detention pond.

In Bangladesh, dikes, embankments, polders, levees, bunds, or floodwalls along the main rivers and estuaries, and retention ponds, pumping stations, and the diversion of flood flows through distributaries are some of the structural flood control techniques commonly employed in urban areas. After the flood hazard in 1988, the western side of Dhaka was surrounded by embankments, floodwalls, and raised roads to protect against riverine floods. A further 2460 km of surface drains that transport stormwater to the significant sewer lines have been built and maintained by the Dhaka City Corporation. Pumps are used at the outputs to remove the stormwater. Due to substantial investments in drainage networks, urban flooding conditions have improved in several areas of Central Dhaka since 2004. The Dhaka Water and Sewerage Authority (DWASA) has enhanced conveyance in pipes and open drains through desilting, installing new drainage pipes, and reclaiming encroached open drains [66]. Similarly, Sirajganj is protected by large detention ponds than can hold water during storm events and flood embankments along the right bank of the Jamuna River [143]. As rainwater harvesting is crucial in reducing water logging in metropolitan areas caused by storm runoff, the government has made it mandatory to install the RWH system in all proposed new buildings [144]. In an urbanized area of Chittagong where urban flooding is frequent, Akter et al. investigated the viability of a distributed rain barrel RWH system as a flood mitigation strategy. As an application of LID, RWH shows that a reduction of 28.66% could be achieved in reducing flood extent. Moreover, the study showed that 10–60% imperviousness of the sub-catchment area could yield a monthly RWH potential of 0.04–0.45 m^3 from a square meter of rooftop area [113].

In Pakistan, flood protection involves structural solutions, including flood protective embankments, flood dikes, guided head spurs, flood diversion channels, channel enlargements, and channel straightening [40]. However, such structural mitigation measures are expensive and beyond the financial capability of developing nations like Pakistan [145]. In Sri Lanka, urban flood management uses diversion canals, tunnels to discharge water, a new pumping station, and widening locks as structural adaptation measures; however, stopping wetland encroachment has a much more significant impact [119]. Additionally, rainwater harvesting has been used for many years to prevent urban flooding. RWH has become a mandatory requirement of modern buildings due to the growing trend in urban green buildings and changes in current laws, which will soon increase the total number

of RWH systems in use [146]. In Nepal, embankment and drainage construction are the primary structural measures implemented for urban flood management.

A functional drainage system is essential to reduce water logging issues and guarantee adequate sanitation facilities for the urban population. However, due to their limited space, it is challenging to construct structural flood control measures in urban areas [147]. In many urban areas, installed drains are either undersized or nonexistent, primarily because stormwater drainage funding needs to be prioritized [62]. Additionally, these are expensive, particularly for developing nations [148]. In the past, storm sewers were constructed to handle 12 to 20 mm of rain per hour [149]. This makes sewers in many cities small, resulting in significant urban flooding during increasingly extreme events. Similarly, where structures are not routinely examined, they could degrade, collapse during a flood event, and negatively affect people's lives, livelihoods, and the biophysical environment, creating more problems than they solve. There is a necessity for regular cleaning and maintenance of the drainage system by removing garbage, increasing water infiltration capacity, and decreasing surface runoff. Urban areas urgently need sustainable drainage management schemes [136].

Table 2. Application of structural measures in urban flood management in South Asian cities.

Location	BGI Considered	Results	Ref.
Hyderabad, India	Rain gardens	RGs with a depth varying from 400 to 500 mm have shown excellent performance during the monsoon season	[62]
Mumbai, India	Bioretention basins	Found unsuitable for heavy rainfall intensity	[62]
Hyderabad, India	Green spaces	44–50% of the precipitation is retained by the urban green and open spaces	[140]
Hyderabad, India	Porous pavements and vegetated roofs	Reduced surface runoff	[50]
Guwahati city, India	Detention pond, widening of the channels	Maximum flood depth and inundated area reduced flooding adjacent to the channels.	[141]
Guwahati city, India	De-siltation and cleaning of drains; rainwater harvesting; establishing new pumping stations	Integrated drainage network act as 'self-healing' to flood certain extent	[142]
Mumbai, India	Detention ponds	Decrease in peak discharge and total flood hazard area	[89]
Sirajganj town, Bangladesh	Detention ponds	Store water during storm events	[143]
Bangladesh	RWH system in all the proposed new buildings	Controlling water logging in urban areas	[144].
Metro Colombo basin, Sri Lanka	Diversion	The flood water level at different locations was reduced	[120]
Sri Lanka	Mandatory requirement of RWH in modern buildings	Reduce water logging in urban areas	[146]

4.2. Non-Structural Measures

Structural mitigation measures may be challenging to implement in highly urbanized locations due to resource and space limitations and the fact that high-density structures have already taken up much of the land surface. Non-structural flood mitigation measures, such as urban floodproofing management, cleaning drainage networks, flood defense systems, evacuation plans, and flood forecasting and early warning systems, are more practical in reducing flood damage. Some examples of non-structural measures being implemented in the region are: a disaster risk awareness-raising program through radio drama in Afghanistan; emergency planning and management, including local flood warning systems, in the Lai Nullah Basin; designing the evacuation plan for Rawalpindi, Pakistan; flood hazard maps called "Flood Atlas" produced by the Central Water Commission (CWC) in India; inundation maps of the entire country up to district level, and of Dhaka city in

Bangladesh [150]; and automatic weather stations to disseminate real-time rainfall and flood alerts in Mumbai [151], among others.

Early Warning System

The early warning system (EWS) is considered an essential component of disaster risk reduction by the Hyogo Framework for Disaster Reduction (2005–2015) and the Sendai Framework for Disaster Risk Reduction (2015–2030). Some EWS initiatives have been implemented at the regional and national levels in the region (Table 3). In Chennai, India, an "integrated expert urban flood forecasting system for Chennai" was created and used; it consists of six key, interconnected components. All links are automated to convey information about floods through real-time prediction monitoring and data sharing [152]. Similarly, in Mumbai, automatic weather stations have been installed to track rainfall and send real-time rain and flood notifications via websites and mobile devices [153]. In Guwahati, a fully automated web-based flood warning system was launched in August 2020 to alert local authorities about flash floods, heavy rainfall, and waterlogging with 72 h lead time; this is helpful for taking precautions to avoid unfavorable situations and prepare for flood conditions [154]. In Bangalore, high-intensity rainfall alerts, flood forecast alerts, and early warnings are sent via email, social media, and SMS to zonal heads, ward-level officers, and all concerned line departments in the city. A website and mobile app are developed to notify the public about urban flooding in the town. "VARUNA MITRA," a 24/7 interactive help desk, offers the general public weather-related data, forecasts, and guidance [107]. For planning and implementing effective control measures in cities, rainfall data with a 5-min resolution is optimum [62]. Accurate forecasting requires real-time data acquisition from telemetry stations. The delays in establishing new telemetry stations and the failure of already established stations explain India's poor condition for flood forecasting [155]. In the 2015 Chennai floods, social media networks such as Facebook and WhatsApp became early warning systems and disaster management tools for social activism. These networks gathered people worldwide to contribute toward rescue and relief for flood victims [156]. In Kerela, India, schoolchildren log daily rainfall and river-flow measurements in their rain book and send the data by WhatsApp to a group that oversees the operation. Two hundred twenty river gauges and 13 rain gauges are spread across the 1272-square-kilometre watershed. With deep knowledge of the surrounding topography, and aided by the data, students can predict when areas downhill will flood [22].

In Bangladesh, flood forecasting technology protects people's lives and property [150]. The Flood Forecasting and Warning Center (FFWC) is responsible for forecasting and is based on simulation results of MIKE 11 models. Deterministic forecasts are disseminated from central to district levels through email, website, and cell phone services [157]. However, early warnings only sometimes reach local stakeholders; information needs to be more frequently understood, and insufficient follow-up on activities hinders operations [158]. With financial support worth USD 113 million in 2017, the government enhanced weather forecasting, EWS, and dissemination of information [159]. The current hydrometeorological information services are being upgraded.

Since 1975, Pakistan's flood preparedness and response system have benefited from the flood forecasting and warning system. The national-level Flood Forecasting Division (FFD), located in Lahore, is responsible for flood forecasting and disseminating information to the warning centers. The 2010 Pakistan flood led the government to establish a flood forecasting and early warning system for the Lai basin, that flows through Islamabad and Rawalpindi. However, the FEW only covers some of the river basins [160]. Some cities have developed flood mitigation strategies, but municipal authorities still need to take more action [40,161].

The 2004 tsunami highlighted Sri Lanka's urgent need for an efficient National Early Warning System. As the focal point of coordination for the early warning system and its transmission, the Disaster Management Center (DMC) was established. Premasiri and Chandranath worked to create a warning system to lessen the risks of urban flooding in

the Panadura urban council region. To monitor and warn of real-time flood events and display a flooding area in the online system, they used GPS, RS, GIS, PIC control circuit, Google API, Arc Server, PHP, JavaScript, and Google My Maps [162].

Since 2010, Nepal's Early Warning Systems for water-related disasters have used automatic sensing and mobile communication technology to collect and disseminate real-time climate and hydrological data. National early warnings are issued by the Department of Hydrology and Meteorology's (DHM) Flood Forecasting Section. It is publicly available at http://www.hydrology.gov.np. It provides flood forecasts and real-time river and rainfall gauge data, displaying which rivers are rising or declining and their current warning level. Additionally, it sends mobile SMS to residents in the risk zone. Human casualties have been reduced significantly due to the development of EWS technology. The installation of real-time stations by DHM to monitor the river's hourly water level and rainfall stations inside the Kathmandu basin has assisted in determining the river's danger level [163]. However, the flood that occurred due to extreme rainfall in August 2017 in Terai and Kathmandu attests to the urgent need for more preparation and people-centered EWSs that reach all communities [164].

In Bhutan, EWSs were initially introduced by the Department of Hydro-Met Services (DHMS) in 1988 [165]. In 2009, the impact of Cyclone Aila boosted the urgency of and commitment to the development of Bhutan's early warning system. The hydro-met monitoring network has been upgraded with technology to relay real-time data. Currently, 15 stations transmit real-time data every 15 min to the DHMS servers at the National Weather and Flood Forecasting and Warning Centre (NWFFWC) [166]. In Afghanistan, there needs to be an organized network of EWS. The Afghanistan Meteorological Department issues province-scale flood warnings, which are ineffective for risk reduction. Even though alerts are shared via their websites and social media, there needs to be more comprehensive information at the local or watershed level [167]. In addition, even when the public is informed of early warnings, they may still choose not to leave owing to suspicion of EWS, travel time to shelters, or fear that they cannot return after the flood [168].

Table 3. Some of the early warning systems in operation.

Location	Early Warning System	Designed by	Ref.
Chennai	Integrated expert urban flood forecasting system with a real-time forecast, monitoring, and data sharing	Chennai Flood Warning System (C-FLOWS) designed by NCCR	[152]
Mumbai	Automatic weather stations were installed for rainfall monitoring and dissemination of real-time rainfall, flood alerts on the webpage as well as on smartphones	Municipal Corporation of Greater Mumbai (MCGM) area	[153]
Guwahati	Fully automated web-based flood warning system	Energy and Resources Institute (TERI) in New Delhi and National Disaster Management Authority (NDMA)	[154]
Bangalore city India	High-intensity rainfall alerts and rainfall Forecasts Alerts, Flood forecasts, Early warnings	Karnataka State Natural Disaster Monitoring Center (KSNDMC)	[107]
Bangladesh	Produce up to 48- to 72-h—forecasts, disseminating forecasts from national to district levels through email, website, and cell phone services.	Flood Forecasting and Warning Center of the Bangladesh Water Development Board	[169]
Bangladesh	Flood EWS at the community level, using existing 48-hrs. forecasts	The Center for Environmental and Geographical Information Service	[157]
Panadura urban council area Sri Lanka	GPS, RS, GIS techniques, PIC Control circuit, Google API, Arc Server, PHP, JavaScript, and Google My maps to monitor and warn real-time flood event displays flooding area in the web system		[162]

Table 3. *Cont.*

Location	Early Warning System	Designed by	Ref.
Nepal	Early Warning Systems for water-related hazards utilize automatic sensing and mobile communication technology for real-time climate and hydrological data acquisition and warning dissemination and send mobile SMS to residents of the risk zone.	Flood Forecasting Section of the DHM, Nepal	[163]
Bhutan	The hydrometeorological observation network transmits real-time data at a pre-set interval of 15 min.	Department of Hydro-Met Services (DHMS)	[166]
Afghanistan	Flood warnings are disseminated to the public through websites and social media accounts at the scale of a province	AMD and NWARA	[167]

5. Existing Gap in Urban Flood Hazard Assessment and Management Practices between SA Countries and the Developed World

A vast gap exists between South Asian and developed countries in urban flood hazard assessment and management practices. In South Asian cities, high-resolution DEM data and short-duration rainfall are still lacking. In contrast, urban flood hazard assessment in developed countries is moving towards refinement and efficiency (as shown below in Table 4). The application of high-resolution DEMs is rising for realistic terrain representation, which is essential for simulating surface runoff [170]. The cellular automata (CA) approach, that requires very fine-resolution data, processing time, and computing resources, is increasing. In Manhattan, New York City, 140 sub-basins were created from a 0.30 m Lidar DEM and multiple flood maps for each sub-basin were created [171]. The risk of a pluvial flood in Olfen, Germany, was assessed using a 2D hydrodynamic model, and ANUGA Software, using 1 m DEM acquired from the laser scan, and plausibility was checked based on the flow paths and sink analysis [172]. In Bacau, Romania, a 2D HEC-RAS model predicted urban flooding with 0.5 m resolution DEMs obtained from airborne LiDAR technology and built-up data digitalized from 0.5 m resolution orthophotos digital image [173]. An investigation in Fengxi New Town, China, used a novel high-accuracy and long lead time urban flood forecasting model by coupling atmospheric and hydrodynamic models. As an atmospheric model, the GRAPE MESO model is used to forecast rainstorms. The reconstructed predicted rainstorm is then used as input data for the hydrodynamic flood model. Moreover, the urban flood inundation was predicted using 2 m DEM and Digital Orthophoto Map (DOM) [174]. In Nanjing, China, a new technique that included data from social media, land use, and other sources was used to analyze the spatiotemporal patterns of public responses to urban flooding during 1–21 July 2016 [175]. In Alcester, UK, numerical experiments have been carried out integrating a 2D shallow-water model using a 10 cm DEM. Studies show that localized, decimetric-scale modifications in the elevation of roads can lead to significant differences in flood inundation [176]. Based on big data, machine learning techniques are utilized in the USA to examine the effects of various flood types [177]. In a study conducted in Fredericton, Canada, the HAND model created a preliminary flood map. After that, pseudo-training samples for a Random Forest model were created utilizing the conditions of height, slope, aspect, distance from the river, and LULC maps. The findings demonstrate that the suggested approach can enhance flood extent prediction without using real-world training data [178]. Using the GIS-based SCS-CN approach, Sabita et al. examined the effects of urbanization-related land use change on surface runoff in Xiamen, China, between 1980 and 2015, a period of intense urban growth. The impact of urbanization shows that the amount of runoff contributed by built-up land use increased from 14.2% to 27.9% with the rise of urban expansion from 1980 to 2015 [179].

Skilodimou et al. applied the analytical hierarchy process (AHP) method and a geographical information system (GIS) to create the flood hazard assessment map in Nea Makri, Greece [180]. A study by Joo et al. in 2019 assessed flood risk for the Midwest region

of the Republic of Korea using factor analysis and principal component analysis (PCA). This assessment involved choosing the leading indicators that have the greatest impact on flood damage and weighting them using the analytic hierarchy process (AHP), constant sum scale (CSS), and entropy [181]. A flood risk assessment of urban areas in Kaohsiung along the Dianbao River was carried out by Liu et al. in 2021, based on flood hazards and societal vulnerability. A rainfall-runoff model (HEC-HMS) was selected to simulate discharge for hazard assessment, and the simulated discharges were used as inputs for the inundation model (FLO-2D). Using the flooding depths and extents that would occur in the areas under various rainfall return periods, the validated HEC-HMS and FLO-2D models were used to create hazard maps [182]. Vojtek and Vojtekova defined the flood susceptibility zones for the territory of Slovakia using a multi-criteria approach, particularly the analytical hierarchy process (AHP) technique and geographic information systems (GIS). Seven flood conditioning factors were chosen: hydrography (distance from rivers), river network density; hydrology (flow accumulation); morphometry (elevation, slope); and permeability (curve numbers, lithology). The relative importance of the selected factors prioritized slope degree as the most important factor, followed by river network density, distance from rivers, flow accumulation, elevation, curve number, and lithology. The flood susceptibility map was validated using earlier floods, showing that 70.9% were coincident, thus confirming the effectiveness of the methodology [183]. Khoirunisa assessed precipitation, near-surface air temperature, and maximum wind speed to examine the future climate of and identify potential hazards in Prague using the Regional Model RCA4's Recipient Concentration Paths (RCP) 4.5 and 8.5 scenarios. Based on the model scenario RCP 8.5, it was determined that Prague will experience increased urban flooding over several years up until 2060. The results could serve as the foundation for an urban early-warning system [184].

Regarding urban flood management in South Asia, cities still focus on enhancing gray infrastructure over building sustainable solutions to strengthen the urban drainage system. Cities in developed countries focus on using green infrastructure (or gray + green) to alleviate urban flooding because gray infrastructure alone cannot control stormwater. It is insufficient to handle current and anticipated future extreme weather occurrences by relying on expensive, inflexible gray infrastructure. The use of climate-proofing strategies in urban planning today could significantly lower expenses in the future. For example, Low Impact Developments (LID) in the USA, Sustainable Urban Drainage Systems (SuDs) in the UK, Water Sensitive Urban Design (WSUD) in Australia, Low Impact Developments Urban Design (LIDUD) in New Zealand, and Sponge City in China were introduced to address challenges linked to urban water management and surface-water flooding that occur yearly [185]. However, green infrastructure and nature-based solutions are more efficient in urban development when used in the planning stages. Their implementation in built-up areas is challenging due to various considerations, such as few green spaces, the uncertainty of land ownership, etc.

According to a study conducted in Beijing, the baseline volume capture ratio could be raised from 59.9% to 82.2% by installing green roofs on 30% of roof surfaces, rain gardens in 10% of the green areas, and permeable pavement in 35% of the paved areas. This signifies that Sponge City's goals can be achieved at realistic levels through LID implementation [186]. In Zhuhai, China, LID effectively reduces runoff from small and moderate rainfall amounts by capturing 52.9% of yearly rainfall volume for long-term operation and 28% of annual runoff [187]. In the Nakagyo area of Kyoto, as part of LID practices, rain gardens effectively manage rainfall over a five-year return period and increase resistance to short-term rainstorms [188]. In Eindhoven, the Netherlands, several nature-based solutions, including green roofs, vegetated grid pavement to ordinary parking lots, and inserting swales or bio-swales for stormwater storage in traffic islands, were evaluated for urban flood control depending on the location and available space. The Infoworks I.C.M. numerical model was used to simulate the effects of NBS scenarios for floods with different return periods. Overall, the simulated NBS reduced flood risk by reducing the flood area and depth. Studies show that green infrastructure alternatives to

gray infrastructure for managing urban flooding are more affordable and provide more co-benefits [189]. In the developed world, water-wise urban development is becoming more popular. Cities use a hybrid approach of integrated green and gray infrastructure solutions at the municipal, neighborhood, and city levels to increase flood resilience [190]. Technical solutions are essential for reducing the risk of flooding. A study by Goniewicz and Burkle in 2019 in Poland showed how to consolidate information regarding hazardous events and gather them in a professional Information Technology (IT) system, using an integrated database and a modern module for disseminating information to end users. An IT system for the Country's Protection against Extreme Hazards is being developed, that emphasizes reducing the risks of natural disasters and minimizing crisis management problems. One such initiative is creating an early warning system for inhabitants to help guard against the extraordinary threat associated with natural disasters, especially floods. The creation of such a system is aimed at increasing public safety and limiting losses caused by the occurrence of natural, technological, and synergistic hazards [191] The eastern region of Belgium observed a devastating flood in July 2021, where rainfall equivalent to three months fell in two days. Castro et al. assessed hazards and vulnerability in those municipalities mostly affected along the Vesdre River. It shows that, even though the country and the region have flood early warning systems, 99% of the population received no formal warning, and less than 50% implemented mitigation measures [192].

Table 4. Models, data used, and adaptation methods used in developed countries.

Country	City	Model	Topographic and Rainfall Data	Adaptation Method	Ref.
Denmark	Aarhus	1D–2D coupled urban inundation model	DEM derived from LIDAR data of grid resolution 2 m, Chicago Design Storms (CDSs)	Pipe enlargement, LID, Open Urban Drainage Systems (OUDs)/recreational basins	[193]
Denmark	Roskilde and Aalborg	Mike Urban	Topography data were obtained using laser scanning from aircraft, CDSs	Sewer enlargement, open basin strategy, dikes.	[194]
Denmark	Odense	Mike Urban and Mike Flood	DEM of 1.6 m * 1.6 m resolution, rainfall scenarios A2 based on RCM HIRHAM4, CDSs	Sewer enlargement and infiltration	[195]
USA	South Weymouth Naval Air Station	SG WATER	Daily precipitation data, six precipitation scenarios	Conventional practices and LID practices	[196]
USA	Bronx river watershed, New York	SWMM	Daily precipitation is disaggregated to hourly precipitation using the CFA	Rainwater harvesting, bioretention, and permeable pavements	[197]
Korea	Incheon	XP-SWMM	Daily rainfall data produced from the HadGEM3-RA climate model	Sewer enlargement	[198]
Canada	Greater Montreal region, Quebec	Improved Rational Hydrograph method and SWMM	Sewer network, rainfall data	Detention ponds; infiltration trenches; green roofs; and rain gardens	[199]
Sweden	Arvika	MOUSE and TSR	Land-use map, high-resolution DEM, a network map of the main sewer pipes, time series of 30-min precipitation intensities from a matrix of 3×3 RCA3 grid boxes	Sewer enlargement and detention ponds	[200]
Austria	Tyrol municipality	SWMM	Sewer system network, land use map, precipitation data temporal resolution of 1 min	Sewer rehabilitation	[201]
UK	London	Infoworks ICM (1D-2D)	The current drainage system, precipitation data	Green roofs, porous pavements, lake deepening, sewer enlargement, and combinations	[202]

6. Conclusions

Floods that devastate urban areas are becoming more common and affecting more people in South Asian cities. The primary causes of increased flood risk in the region are climate change and uncontrolled urbanization. Flood impact can be reduced by using hazard mapping to predict potential flood areas accurately. However, selecting the appropriate model for a particular purpose is crucial. Hydraulic/hydrological models, HEC-RAS/HMS, SWMM/PCSWMM, and MIKE are primarily used to assess urban flood hazards in South Asian cities. The region's primary challenge in hazard assessment is the need for high-resolution DEM and short-duration rainfall data, that significantly affect the model's simulation results and negatively affect the implementation of flood management measures. South Asian cities still rely on structural flood protection measures, i.e., mainly optimizing urban drainage systems and embankments. At the same time, only a few places have introduced LID, rain gardens, and detention basins. Depending on the capacity of the countries, improved flood EWSs have been developed and implemented in some cities. However, EWS frequently fails to reach local stakeholders. In developed countries, urban flood hazard assessment is moving towards refinement and efficiency by applying a high-resolution DEM representing realistic terrain and rainfall of short duration, which plays a fundamental role in modeling surface processes. Cities use a water-prudent hybrid strategy of integrated nature-based solutions, green and gray infrastructure solutions, at the street, neighborhood, and city levels to increase flood resilience.

Despite advancements in scientific technologies and numerous international and national initiatives to reduce disaster risk, the social and economic effects of disasters on developing nations are growing. In South Asian cities, it is urgent to begin risk-based management to lessen the detrimental effects of urban flooding. Establishing a robust disaster information system should be a top priority of the local government to enable risk-based, comprehensive, and contextualized urban development and hazard mapping. Urban development in the region needs to be reevaluated, and local planning authorities must be encouraged to consider the role of nature-based solutions, which can lead to a stronger relationship between the built and natural environments, improving the quality of life of urban residents.

Limitations of Study

In South Asian countries, urban flood study is still at the early stage, as more focus is given to riverine floods. A major limitation of this study is that the study considers the application of only three hydrodynamic models, HEC-RAS/HMS, PC/SWMM, and MIKE, for urban flood hazard assessment in the region. The literature review on urban risk management practices might not have been fully captured as documentation of good practices at the local level in the South Asian region is still in its infancy.

Supplementary Materials: The following supporting information can be downloaded at: https://www.mdpi.com/article/10.3390/land12030627/s1, Table S1: Application of HEC-RAS/HMS in flood hazard assessment in the urban area of South Asian cities; Table S2: Application of SWMM/PCSWMM in flood hazard assessment in the urban area of South Asian cities; Table S3: Application of MIKE in flood hazard assessment in the urban area of South Asian cities.

Author Contributions: B.M.: (First author) Conceptualization, Methodology, Investigation/Collect Data, Data Curation, Analysis, Writing—Original Draft, Writing Review and Editing, Visualization. S.C.: Conceptualization, Supervision, Project administration, Funding acquisition, Writing—review and editing. L.W.: Data Curation, Writing—review and editing. S.S.: Conceptualization, review and editing. All authors have read and agreed to the published version of the manuscript.

Funding: This research was funded by the National Natural Science Foundation of China (Grant Nos.: 41661144032), the international partnership program of the Chinese Academy of Sciences "Multifunctional urban green space planning based on transdisciplinary learning" (Grant Nos.: 132C35KYSB20200007), and the International (Regional) Cooperation and Exchange Program, the National Natural Science Foundation of China (Grant Nos.:32261143730).

Data Availability Statement: Not applicable.

Acknowledgments: Acknowledgement to Diva-GIS and Survey Department of Nepal for providing GIS shapefile. We would like to acknowledge Greater K. Oyejobi, Kadir Uludag for English editing.

Conflicts of Interest: The authors declare no conflict of interest.

References

1. CRED; UNDRR. *Human Cost of Disasters an Overview of the Last 20 Years 2000–2019*; UNDRR: Geneva, Switzerland, 2020.
2. Shariat, R.; Roozbahani, A.; Ebrahimian, A. Risk Analysis of Urban Stormwater Infrastructure Systems Using Fuzzy Spatial Multi-Criteria Decision Making. *Sci. Total Environ.* **2019**, *647*, 1468–1477. [CrossRef] [PubMed]
3. Zhou, Q.; Leng, G.; Su, J.; Ren, Y. Comparison of Urbanization and Climate Change Impacts on Urban Flood Volumes: Importance of Urban Planning and Drainage Adaptation. *Sci. Total Environ.* **2019**, *658*, 24–33. [CrossRef] [PubMed]
4. Sundermann, L.; Schelske, O.; Hausmann, P. *Mind the Risk a Global Ranking of Cities under Threat from Natural Disasters*; Swiss Re: Zürich, Switzerland, 2014; pp. 1–30.
5. Rosenfeld, D. Suppression of Rain and Snow by Urban and Industrial Air Pollution. *Science* **2000**, *287*, 1793–1796. [CrossRef] [PubMed]
6. O'Donnell, E.C.; Thorne, C.R. Drivers of Future Urban Flood Risk. *Philos. Trans. R. Soc. A Math. Phys. Eng. Sci.* **2020**, *378*, 20190216. [CrossRef]
7. United Nations. *World Urbanization Prospects: The 2018 Revision (ST/ESA/SER.A/420)*; Department of Economic and Social Affairs, Population Division, United Nations: New York, NY, USA, 2019; ISBN 9789211483192.
8. Hernantes, J.; Maraña, P.; Gimenez, R.; Sarriegi, J.M.; Labaka, L. Towards Resilient Cities: A Maturity Model for Operationalizing Resilience. *Cities* **2019**, *84*, 96–103. [CrossRef]
9. Seto, K.C.; Güneralp, B.; Hutyra, L.R. Global Forecasts of Urban Expansion to 2030 and Direct Impacts on Biodiversity and Carbon Pools. *Proc. Natl. Acad. Sci. USA* **2012**, *109*, 16083–16088. [CrossRef] [PubMed]
10. Kong, F.; Ban, Y.; Yin, H.; James, P.; Dronova, I. Environmental Modelling & Software Modeling Stormwater Management at the City District Level in Response to Changes in Land Use and Low Impact Development. *Environ. Model. Softw.* **2017**, *95*, 132–142. [CrossRef]
11. Xie, J.; Wu, C.; Li, H.; Chen, G. Study on Storm-Water Management of Grassed Swales and Permeable Pavement Based on SWMM. *Water* **2017**, *9*, 840. [CrossRef]
12. Denissen, A.-K. Climate Change & Its Impacts on Bangladesh. 2012, pp. 86–95. Available online: http://www.ncdo.nl/artikel/climate-change-its-impacts-bangladesh (accessed on 5 April 2021).
13. Li, A.; Deng, W.; Zhao, W.; Liu, B.; Zhang, J.; Kong, B.; Nan, X.; Bian, J.; Koirala, H.L.; Gilani, H.; et al. A Geo-Spatial Database about the Eco-Environment and Its Key Issues in South Asia. *Big Earth Data* **2018**, *2*, 298–319. [CrossRef]
14. Otto, F.E.L.; Zachariah, M.; Saeed, F.; Siddiqi, A.; Shahzad, K.; Mushtaq, H.; AchutaRao, K.; T, C.S.; Barnes, C.; Philip, S.; et al. Climate Change Likely Increased Extreme Monsoon Rainfall, Flooding Highly Vulnerable Communities in Pakistan. *World Weather Attrib.* **2022**, *10*, 12.
15. Cao, W.; Zhou, Y.; Güneralp, B.; Li, X.; Zhao, K.; Zhang, H. Increasing Global Urban Exposure to Flooding: An Analysis of Long-Term Annual Dynamics. *Sci. Total Environ.* **2022**, *817*, 153012. [CrossRef]
16. Emilsson, T.; Sang, Å.O. Impacts of Climate Change on Urban Areas and Nature-Based Solutions for Adaptation. In *Nature-based Solutions to Climate Change Adaptation in Urban Areas, Theory and Practice of Urban Sustainability Transitions*; Kabisch, N., Korn, H., Stadler, J., Aletta, B., Eds.; Springer: Berlin/Heidelberg, Germany, 2017; pp. 15–27, ISBN 9783319560915.
17. Zhou, Q. A Review of Sustainable Urban Drainage Systems Considering the Climate Change and Urbanization Impacts. *Water* **2014**, *6*, 976–992. [CrossRef]
18. IPCC. *Regional Fact Sheet—Urban Areas*; IPCC: Geneva, Switzerland, 2021.
19. Douglas, I. Climate Change, Flooding and Food Security in South Asia. *Food Secur.* **2009**, *1*, 127–136. [CrossRef]
20. Mukherjee, S.; Aadhar, S.; Stone, D.; Mishra, V. Increase in Extreme Precipitation Events under Anthropogenic Warming in India. *Weather Clim. Extrem.* **2018**, *20*, 45–53. [CrossRef]
21. Ali, H.; Mishra, V. Contrasting Response of Rainfall Extremes to Increase in Surface Air and Dewpoint Temperatures at Urban Locations in India. *Sci. Rep.* **2017**, *7*, 1228. [CrossRef]
22. Vaidyanathan, G. How India Is Battling Deadly Rain Storms. *Nature* **2023**, *614*, 210–213. [CrossRef]
23. Roxy, M.K.; Ghosh, S.; Pathak, A.; Athulya, R.; Mujumdar, M.; Murtugudde, R.; Terray, P.; Rajeevan, M. A Threefold Rise in Widespread Extreme Rain Events Over Central India. *Nat. Commun.* **2017**, *8*, 708. [CrossRef]
24. Krishnan, R.; Sabin, T.P.; Ayantika, D.C.; Kitoh, A.; Sugi, M.; Murakami, H.; Turner, A.G.; Slingo, J.M.; Rajendran, K. Will the South Asian Monsoon Overturning Circulation Stabilize Any Further? *Clim. Dyn.* **2013**, *40*, 187–211. [CrossRef]
25. Ali, H.; Modi, P.; Mishra, V. Increased Flood Risk in Indian Sub-Continent under the Warming Climate. *Weather Clim. Extrem.* **2019**, *25*, 100212. [CrossRef]
26. Milesi, C.; Churkina, G. Measuring and Monitoring Urban Impacts on Climate Change from Space. *Remote Sens.* **2020**, *12*, 3494. [CrossRef]

27. Mujumdar, M.; Bhaskar, P.; Ramarao, M.V.S.; Uppara, U.; Goswami, M.; Borgaonkar, H.; Chakraborty, S.; Ram, S.; Mishra, V.; Rajeevan, M.; et al. *Assessment of Climate Change over the Indian Region*; Springer: Singapore, 2020; ISBN 9789811543272.
28. Wang, B.; Biasutti, M.; Byrne, M.P.; Castro, C.; Chang, C.P.; Cook, K.; Fu, R.; Grimm, A.M.; Ha, K.J.; Hendon, H.; et al. Monsoons Climate Change Assessment. *Bull. Am. Meteorol. Soc.* **2021**, *102*, E1–E19. [CrossRef]
29. Schreider, S.Y.; Smith, D.I.; Jakeman, A.J. Climate Change Impacts on Urban Flooding. *Clim. Chang.* **2000**, *47*, 91–115. [CrossRef]
30. Dutta, D.; Herath, S.; Musiake, K. A Mathematical Model for Flood Loss Estimation. *J. Hydrol.* **2003**, *277*, 24–49. [CrossRef]
31. McMichael, A.J.; Woodruff, R.E.; Hales, S. Climate Change and Human Health: Present and Future Risks. *Lancet* **2006**, *367*, 859–869. [CrossRef] [PubMed]
32. Shanableh, A.; Al-Ruzouq, R.; Yilmaz, A.G.; Siddique, M.; Merabtene, T.; Imteaz, M.A. Effects of Land Cover Change on Urban Floods and Rainwater Harvesting: A Case Study in Sharjah, UAE. *Water* **2018**, *10*, 631. [CrossRef]
33. Richards, D.R.; Edwards, P.J. Using Water Management Infrastructure to Address Both Flood Risk and the Urban Heat Island. *Int. J. Water Resour. Dev.* **2018**, *34*, 490–498. [CrossRef]
34. Sheng, J.; Wilson, J.P. Watershed Urbanization and Changing Flood Behavior across the Los Angeles Metropolitan Region. *Nat. Hazards* **2009**, *48*, 41–57. [CrossRef]
35. Li, Y.; Wang, C. Impacts of Urbanization on Surface Runoff of the Dardenne Creek Watershed, St. Charles County, Missouri. *Phys. Geogr.* **2009**, *30*, 556–573. [CrossRef]
36. Kumar, M.; Sharif, M.; Ahmed, S. Impact of Urbanization on the River Yamuna Basin. *Int. J. River Basin Manag.* **2019**, *18*, 461–475. [CrossRef]
37. Du, S.; Cheng, X.; Huang, Q.; Chen, R.; Ward, P.J.; Aerts, J.C.J.H. Brief Communication: Rethinking the 1998 China Floods to Prepare for a Nonstationary Future. *Nat. Hazards Earth Syst. Sci.* **2019**, *19*, 715–719. [CrossRef]
38. Vorobevskii, I.; Al Janabi, F.; Schneebeck, F.; Bellera, J.; Krebs, P. Urban Floods: Linking the Overloading of a Storm Water Sewer System to Precipitation Parameters. *Hydrology* **2020**, *7*, 35. [CrossRef]
39. Morita, M. Flood Risk Impact Factor for Comparatively Evaluating the Main Causes That Contribute to Flood Risk in Urban Drainage Areas. *Water* **2014**, *6*, 253–270. [CrossRef]
40. Rahman, A.U.; Shaw, R. Flood Risk and Reduction Approaches in Pakistan. In *Disaster Risk Reduction Approaches in Pakistan*; Rahman, A.U., Khan, A.N., Shaw, R., Eds.; Springer: Berlin/Heidelberg, Germany, 2015; pp. 145–160, ISBN 9784431553694.
41. Lyu, H.; Dong, Z.; Roobavannan, M.; Kandasamy, J.; Pande, S. Rural Unemployment Pushes Migrants to Urban Areas in Jiangsu Province, China. *Palgrave Commun.* **2019**, *5*, 92. [CrossRef]
42. Montoya, L. Geo-Data Acquisition through Mobile GIS and Digital Video: An Urban Disaster Management Perspective. *Environ. Model. Softw.* **2003**, *18*, 869–876. [CrossRef]
43. WMO. *Integrated Flood Management Case Study Pakistan: Lai Nullah Basin Flood Problem Islamabad-Rawalpindi Cities*; WMO: Geneva, Switzerland, 2004.
44. Okubo, K.; Khan, M.S.A.; Hassan, M.Q. Hydrological Processes of Adsorption, Sedimentation, and Infiltration into the Lake Bed during the 2004 Urban Flood in Dhaka City, Bangladesh. *Environ. Earth Sci.* **2010**, *60*, 95–106. [CrossRef]
45. Lei, M.; Niyogi, D.; Kishtawal, C.; Pielke, R.A.; Beltr, A. Effect of Explicit Urban Land Surface Representation on the Simulation of the 26 July 2005 Heavy Rain Event over Mumbai, India. *Atmos. Chem. Phys* **2008**, *8*, 5975–5995. [CrossRef]
46. Alam, A.; Bhat, M.S.; Farooq, H.; Ahmad, B.; Ahmad, S.; Sheikh, A.H. Flood Risk Assessment of Srinagar City in Jammu and Kashmir, India. *Int. J. Disaster Resil. Built Environ.* **2018**, *9*, 114–129. [CrossRef]
47. Narasimhan, B.; Bhallamudi, S.M.; Mondal, A.; Ghosh, S.; Mujumdar, P. *Chennai Floods 2015 A Rapid Assessment*; Interdisciplinary Centre for Water Research (ICWaR): Bengaluru, India, 2016.
48. Devi, N.N.; Sridharan, B.; Bindhu, V.M.; Narasimhan, B.; Bhallamudi, S.M.; Bhatt, C.M.; Usha, T.; Vasan, D.T.; Kuiry, S.N. Investigation of Role of Retention Storage in Tanks (Small Water Bodies) on Future Urban Flooding: A Case Study of Chennai City, India. *Water* **2020**, *12*, 2875. [CrossRef]
49. Zia, S.; Shirazi, S.A. Spatio-Temporal Analysis of Areas Vulnerable to Urban Flooding: A Case Study of Lahore, Pakistan. *Int. J. Econ. Env.* **2019**, *10*, 85–89.
50. Vemula, S.; Raju, K.S.; Veena, S.S.; Kumar, A.S. Urban Floods in Hyderabad, India, under Present and Future Rainfall Scenarios: A Case Study. *Nat. Hazards* **2018**, *95*, 637–655. [CrossRef]
51. Gehrels, H. Protecting Colombo against Future Floods. Available online: https://www.deltares.nl/en/projects/protecting-colombo-against-future-floods/ (accessed on 15 December 2021).
52. Jadhav, R.; Bhat, S. Death Toll from Mumbai Floods Jumps to 14, Rain Eases Up. Available online: https://www.reuters.com/article/us-india-monsoon-idUSKCN1BA0GH (accessed on 30 August 2021).
53. Bhatta, B.P.; Pandey, R.K. Bhaktapur Urban Flood Related Disaster Risk and Strategy after 2018. *J. APF Command. Staff. Coll.* **2020**, *3*, 72–89. [CrossRef]
54. Mishra, A.K.; Nagaraju, V. Space-Based Monitoring of Severe Flooding of a Southern State in India during South-West Monsoon Season of 2018. *Nat. Hazards* **2019**, *97*, 949–953. [CrossRef]
55. Sangomla, A. Mumbai Rains Once Again Prove Climate Change Is No Hoax. Available online: https://www.downtoearth.org.in/news/climate-change/mumbai-rains-once-again-prove-climate-change-is-no-hoax-65387 (accessed on 2 July 2021).
56. Wadhawan, S.K.; Singh, B.; Ramesh, M.V. Causative Factors of Landslides 2019: Case Study in Malappuram and Wayanad Districts of Kerala, India. *Landslides* **2020**, *17*, 2689–2697. [CrossRef]

57. Read, C. Flash Floods DEVASTATE Afghanistan Killing 20 and Destroying 2000 Homes. Available online: https://www.express.co.uk/news/world/1094803/afghanistan-floods-death-toll-Kandahar-city-united-nations (accessed on 20 October 2021).
58. Uprety, M. A Dramatic Start to Nepal's 2019 Monsoon Season. Available online: https://floodresilience.net/blogs/a-dramatic-start-to-nepals-2019-monsoon-season/ (accessed on 4 November 2021).
59. Shams, S. *Urban Flooding—Who Is Responsible for Karachi's Woes? DW Made Minds*; Deutsche Welle (DW): Bonn, Germany, 2020.
60. Priyam, S. Four Die, Houses Crumble as Heavy Monsoon Rains Swamp Delhi-NCR. *More Rains Forecast*. Available online: https://weather.com/en-IN/india/monsoon/news/2020-07-20-two-die-houses-crumble-roads-flood-heavy-monsoon-rains-delhi-ncr-more (accessed on 30 June 2021).
61. Atta-ur-Rahman; Shaw, R.; Surjan, A.; Parvin, G.A. Urban Disasters and Approaches to Resilience. *Urban Disasters Resil. Asia* **2016**, 1–19. [CrossRef]
62. Gupta, K. Challenges in Developing Urban Flood Resilience in India. *Philos. Trans. R. Soc. A Math. Phys. Eng. Sci.* **2020**, *378*, 20190211. [CrossRef]
63. Surampudi, S.; Yarrakula, K. Mapping and Assessing Spatial Extent of Floods from Multitemporal Synthetic Aperture Radar Images: A Case Study on Brahmaputra River in Assam State, India. *Environ. Sci. Pollut. Res.* **2020**, *27*, 1521–1532. [CrossRef]
64. Ray, K.; Pandey, P.; Pandey, C.; Dimri, A.P.; Kishore, K. On the Recent Floods in India. *Curr. Sci.* **2019**, *117*, 204–218. [CrossRef]
65. Kabir, M.H.; Ahmed, I.; Von Meding, J.; Forino, G.; Ghosh, A.K. Impacts of Prolonged Waterlogging on Educational Continuity at Schools in Peri-Urban Areas of Dhaka, Bangladesh. *Dhaka Univ. J. Earth Environ. Sci.* **2021**, *9*, 13–23. [CrossRef]
66. Dasgupta, S.; Zaman, A.; Roy, S.; Huq, M.; Jahan, S.; Nishat, A. *Urban Flooding of Greater Dhaka in a Changing Climate*; World Bank Publications: Washington, DC, USA, 2015; ISBN 9781464807107.
67. UNDRR. *Disaster Risk Reduction in Pakistan: Status Report 2019*; UNDRR: Bangkok, Thailand, 2019.
68. Shah, S.M.H.; Mustaffa, Z.; Teo, F.Y.; Imam, M.A.H.; Yusof, K.W.; Al-Qadami, E.H.H. A Review of the Flood Hazard and Risk Management in the South Asian Region, Particularly Pakistan. *Sci. African* **2020**, *10*, e00651. [CrossRef]
69. Manawadu, L.; Wijeratne, V.P.I.S. Anthropogenic Drivers and Impacts of Urban Flooding—A Case Study in Lower Kelani River Basin, Colombo Sri Lanka. *Int. J. Disaster Risk Reduct.* **2021**, *57*, 102076. [CrossRef]
70. Kc, S.; Shrestha, S.; Ninsawat, S.; Chonwattana, S. Predicting Flood Events in Kathmandu Metropolitan City under Climate Change and Urbanisation. *J. Environ. Manag.* **2021**, *281*, 111894. [CrossRef]
71. Manawi, S.M.A.; Nasir, K.A.M.; Shiru, M.S.; Hotaki, S.F.; Sediqi, M.N. Urban Flooding in the Northern Part of Kabul City: Causes and Mitigation. *Earth Syst. Environ.* **2020**, *4*, 599–610. [CrossRef]
72. Villordon, M.B.B.L.; Gourbesville, P. Community-Based Flood Vulnerability Index for Urban Flooding: Understanding Social Vulnerabilities and Risks. *Springer Water* **2016**, *2014*, 75–96. [CrossRef]
73. Yin, J.; Ye, M.; Yin, Z.; Xu, S. A Review of Advances in Urban Flood Risk Analysis over China. *Stoch. Environ. Res. Risk Assess.* **2014**, *29*, 1063–1070. [CrossRef]
74. De Moel, H.; Van Alphen, J.; Aerts, J.C.J.H. Flood Maps in Europe—Methods, Availability and Use. *Nat. Hazards Earth Syst. Sci.* **2009**, *9*, 289–301. [CrossRef]
75. Jain, G.V.; Agrawal, R.; Bhanderi, R.J.; Jayaprasad, P.; Patel, J.N.; Agnihotri, P.G.; Samtani, B.M. Estimation of Sub-Catchment Area Parameters for Storm Water Management Model (SWMM) Using Geo-Informatics. *Geocarto Int.* **2016**, *31*, 462–476. [CrossRef]
76. Jacobson, C.R. Identification and Quantification of the Hydrological Impacts of Imperviousness in Urban Catchments: A Review. *J. Environ. Manag.* **2011**, *92*, 1438–1448. [CrossRef]
77. Andimuthu, R.; Kandasamy, P.; Mudgal, B.V.; Jeganathan, A.; Balu, A.; Sankar, G. Performance of Urban Storm Drainage Network under Changing Climate Scenarios: Flood Mitigation in Indian Coastal City. *Sci. Rep.* **2019**, *9*, 7783. [CrossRef] [PubMed]
78. Rahmati, O.; Darabi, H.; Panahi, M.; Kalantari, Z.; Naghibi, S.A.; Ferreira, C.S.S.; Kornejady, A.; Karimidastenaei, Z.; Mohammadi, F.; Stefanidis, S.; et al. Development of Novel Hybridized Models for Urban Flood Susceptibility Mapping. *Sci. Rep.* **2020**, *10*, 12937. [CrossRef]
79. Bisht, D.S.; Chatterjee, C.; Kalakoti, S.; Upadhyay, P.; Sahoo, M.; Panda, A. Modeling Urban Floods and Drainage Using SWMM and MIKE URBAN: A Case Study. *Nat. Hazards* **2016**, *84*, 749–776. [CrossRef]
80. Feng, B.; Wang, J.; Zhang, Y.; Hall, B.; Zeng, C. Urban Flood Hazard Mapping Using a Hydraulic–GIS Combined Model. *Nat. Hazards* **2020**, *100*, 1089–1104. [CrossRef]
81. Rajib, A.; Golden, H.E.; Lane, C.R.; Wu, Q. Surface Depression and Wetland Water Storage Improves Major River Basin Hydrologic Predictions. *Water Resour. Res.* **2020**, *56*, e2019WR026561. [CrossRef] [PubMed]
82. Henonin, J.; Russo, B.; Mark, O.; Gourbesville, P. Real-Time Urban Flood Forecasting and Modeiling—A State of the Art. *J. Hydroinformatics* **2013**, *15*, 717–736. [CrossRef]
83. Jiang, L.; Chen, Y.; Wang, H. Urban Flood Simulation Based on the SWMM Model. In Proceedings of the RSHS14 and ICGRHWE14, Guangzhou, China, 24–27 August 2014; Volume 368.
84. Bhattacharjee, S.; Kumar, P.; Thakur, P.K.; Gupta, K. Hydrodynamic Modelling and Vulnerability Analysis to Assess Flood Risk in a Dense Indian City Using Geospatial Techniques. *Nat. Hazards* **2021**, *105*, 2117–2145. [CrossRef]
85. Bellos, V.; Kourtis, I.M.; Tsihrintzis, V.A. A Simplified Methodology for Flood Simulation in Urban Catchments. *Eur. Water* **2017**, *57*, 307–313.
86. Pathak, S.; Liu, M.; Jato-Espino, D.; Zevenbergen, C. Social, Economic and Environmental Assessment of Urban Sub-Catchment Flood Risks Using a Multi-Criteria Approach: A Case Study in Mumbai City, India. *J. Hydrol.* **2020**, *591*, 125216. [CrossRef]

87. Zope, P.E.; Eldho, T.I.; Jothiprakash, V. Impacts of Urbanization on Flooding of a Coastal Urban Catchment: A Case Study of Mumbai City, India. *Nat. Hazards* **2015**, *75*, 887–908. [CrossRef]
88. Zope, P.E.; Eldho, T.I.; Jothiprakash, V. Impacts of Land Use-Land Cover Change and Urbanization on Flooding: A Case Study of Oshiwara River Basin in Mumbai, India. *Catena* **2016**, *145*, 142–154. [CrossRef]
89. Zope, P.E.; Eldho, T.I.; Jothiprakash, V. Hydrological Impacts of Land Use–Land Cover Change and Detention Basins on Urban Flood Hazard: A Case Study of Poisar River Basin, Mumbai, India. *Nat. Hazards* **2017**, *87*, 1267–1283. [CrossRef]
90. Suriya, S.; Mudgal, B.V. Impact of Urbanization on Flooding: The Thirusoolam Sub Watershed—A Case Study. *J. Hydrol.* **2012**, *412–413*, 210–219. [CrossRef]
91. Devi, N.N.; Sridharan, B.; Kuiry, S.N. Impact of Urban Sprawl on Future Flooding in Chennai City, India. *J. Hydrol.* **2019**, *574*, 486–496. [CrossRef]
92. Rangari, V.A.; Sridhar, V.; Umamahesh, N.V.; Patel, A.K. Floodplain Mapping and Management of Urban Catchment Using HEC-RAS: A Case Study of Hyderabad City. *J. Inst. Eng. Ser. A* **2019**, *100*, 49–63. [CrossRef]
93. Rangari, V.A.; Umamahesh, N.V.; Patel, A.K. Flood-Hazard Risk Classification and Mapping for Urban Catchment under Different Climate Change Scenarios: A Case Study of Hyderabad City. *Urban Clim.* **2021**, *36*, 100793. [CrossRef]
94. Rangari, V.A.; Bhatt, C.M.; Umamahesh, N.V. Rapid Assessment of the October 2020 Hyderabad Urban Flood and Risk Analysis Using Geospatial Data. *Curr. Sci.* **2021**, *120*, 1840–1847. [CrossRef]
95. Surwase, T.; Manjusree, P. Urban Flood Simulation—A Case Study of Hyderabad City. In Proceedings of the National Conference on Flood Early Warning for Disaster Risk Reduction, Hyderabad, India, 30–31 May 2019; pp. 133–143.
96. Pathan, A.I.; Agnihotri, P.G.; Patel, D.; Prieto, C. Improving Assessment of Flood Inundation of Navsari (India) via Open-Source Data and HEC-RAS Model. In Proceedings of the vEGU21: Gather Online, Online, 19–30 April 2021. [CrossRef]
97. Pathan, A.I.; Agnihotri, P.G. Application of New HEC-RAS Version 5 for 1D Hydrodynamic Food. *Pdf. Model. Earth Syst. Environ.* **2020**, *7*, 1133–1144. [CrossRef]
98. Zafar, S.; Zaidi, A. Impact of Urbanization on Basin Hydrology: A Case Study of the Malir Basin, Karachi, Pakistan. *Reg. Environ. Chang.* **2019**, *19*, 1815–1827. [CrossRef]
99. Masood, M.; Takeuchi, K. Assessment of Flood Hazard, Vulnerability and Risk of Mid-Eastern Dhaka Using DEM and 1D Hydrodynamic Model. *Nat. Hazards* **2012**, *61*, 757–770. [CrossRef]
100. Pandey, P.; Dugar, S. Flood Hazard Mapping in an Urban Context: A Case Study of Hanumante Stream, Bhaktapur (Nepal). *Proc. IOE Grad. Conf.* **2019**, *6*, 435–444.
101. Talchabhadel, R.; Prajapati, R. Numerical Simulation of Urban Inundation Using Citizen-Based Data: A Case Study of Monsoon 2019 in Hanumante River Basin, Kathmandu Valley. In Proceedings of the 8th International Conference on Flood Management, Iowa City, IA, USA, 17–19 August 2021.
102. Basnet, K. Flood Modelling of Patu River in Tulsipur City of Nepal and Analysis of Flooding Impact on Encroached Settlement along the River. *Int. J. Adv. Res. Ideas Innov. Technol. ISSN* **2020**, *6*, 375–384.
103. Dangol, S.; Bormudoi, A. Flood Hazard Mapping and Vulnerability Analysis of Bishnumati River, Nepal. *Nepal. J. Geoinformatics Surv. Dep. Nepal* **2015**, *14*, 20–24. [CrossRef]
104. Tenzin, J.; Bhaskar, A.S. Modeling of the Precipitation Induced Flash Flood in Sarpang, Bhutan Using HEC-RAS. *Rasayan J. Chem.* **2017**, *10*, 399–406.
105. Rangari, V.A.; Gonugunta, R.; Umamahesh, N.V.; Patel, A.K.; Bhatt, C.M. 1D-2D Modeling of Urban Floods and Risk Map Generation for the Part of Hyderabad City. *Int. Arch. Photogramm. Remote Sens. Spat. Inf. Sci.* **2018**, *XLII–5*, 445–450. [CrossRef]
106. Rangari, V.A.; Sai Prashanth, S. Simulation of Urban Drainage System Using a Storm Water Management Model (SWMM). *Asian J. Eng. Appl. Technol.* **2018**, *7*, 7–10. [CrossRef]
107. Avinash, S.; Prasad, K.L.; Reddy, G.S.S.; Mukund, D. Urban Flood Forecast System—A Case Study of Bangalore, India Urban Flood Forecast System—A Case Study of Bangalore, India. *Univers. Rev.* **2018**, *7*, 170–179.
108. Harsha, S.S.; Agarwal, S.; Kiran, C.H. Regional Flood Forecasting Using SWMM for Urban Catchment. *Int. J. Eng. Adv. Technol.* **2020**, *9*, 1027–1031. [CrossRef]
109. Harsha, S.S.; Agarwal, S.; Kiran, C.H. Urban Flood Modelling and Management Using Storm Water Management Model. *Test Eng. Manag.* **2020**, *83*, 6160–6167.
110. Sonavane, N.; Rangari, V.A.; Waikar, M.L.; Patil, M. Urban Storm-Water Modeling Using EPA SWMM-a Case Study of Pune City. In Proceedings of the 2020 IEEE Bangalore Humanitarian Technology Conference (B-HTC), Vijiyapur, India, 8–10 October 2020; pp. 9–13. [CrossRef]
111. Ahammad, M.; Tarek, M.H.; Khan, M.S.M. Stormwater Management in Begunbari Canal Catchment of Dhaka, Bangladesh. In Proceedings of the World Environmental and Water Resources Congress 2018, Minneapolis, MN, USA, 3–7 June 2018; Volume 1, p. 489.
112. Akter, A.; Asce, M.; Alam, M.T. Urban Flood Hazard Modeling and Mapping Using PCSWMM. In Proceedings of the International Conference on Sustainable Infrastructure 2019, Online, 6–10 December 2018.
113. Akter, A.; Tanim, A.H.; Islam, M.K. Possibilities of Urban Flood Reduction through Distributed-Scale Rainwater Harvesting. *Water Sci. Eng.* **2020**, *13*, 95–105. [CrossRef]
114. Pradhan-Salike, I.; Raj Pokharel, J. Impact of Urbanization and Climate Change on Urban Flooding: A Case of the Kathmandu Valley. *J. Nat. Resour. Dev.* **2017**, *7*, 56–66. [CrossRef]

115. Pervin, I.A.; Rahman, S.M.M.; Nepal, M.; Haque, A.K.E.; Karim, H.; Dhakal, G. Adapting to Urban Flooding: A Case of Two Cities in South Asia. *Water Policy* **2020**, *22*, 162–188. [CrossRef]
116. Khan, D.M.; Veerbeek, W.; Chen, A.S.; Hammond, M.J.; Islam, F.; Pervin, I.; Djordjević, S.; Butler, D. Back to the Future: Assessing the Damage of 2004 Dhaka Flood in the 2050 Urban Environment. *J. Flood Risk Manag.* **2018**, *11*, S43–S54. [CrossRef]
117. Mark, O.; Jørgensen, C.; Hammond, M.; Khan, D.; Tjener, R.; Erichsen, A.; Helwigh, B. A New Methodology for Modelling of Health Risk from Urban Flooding Exemplified by Cholera—Case Dhaka, Bangladesh. *J. Flood Risk Manag.* **2018**, *11*, S28–S42. [CrossRef]
118. Chen, A.S.; Hammond, M.J.; Djordjević, S.; Butler, D.; Khan, D.M.; Veerbeek, W. *From Hazard to Impact: Flood Damage Assessment Tools for Mega Cities*; Springer Nature: Berlin/Heidelberg, Germany, 2016; Volume 82, ISBN 1106901622.
119. Wagenaar, D.J.; Dahm, R.J.; Diermanse, F.L.M.; Dias, W.P.S.; Dissanayake, D.M.S.S.; Vajja, H.P.; Gehrels, J.C.; Bouwer, L.M. International Journal of Disaster Risk Reduction Evaluating Adaptation Measures for Reducing Fl Ood Risk: A Case Study in the City of Colombo, Sri Lanka. *Int. J. Disaster Risk Reduct.* **2019**, *37*, 101162. [CrossRef]
120. Moufar, M.M.M.; Perera, E.D.P. Floods and Countermeasures Impact Assessment for the Metro Colombo Canal System, Sri Lanka. *Hydrology* **2018**, *5*, 11. [CrossRef]
121. Rijal, S.; Rimal, B.; Sloan, S. Flood Hazard Mapping of a Rapidly Urbanizing City in the Foothills (Birendranagar, Surkhet) of Nepal. *Land* **2018**, *7*, 60. [CrossRef]
122. Roy, S.; Bose, A.; Singha, N.; Basak, D.; Chowdhury, I.R. Urban Waterlogging Risk as an Undervalued Environmental Challenge: An Integrated MCDA-GIS Based Modeling Approach. *Environ. Chall.* **2021**, *4*, 100194. [CrossRef]
123. Wijeratne, V.P.I.S.; Li, G. Urban Sprawl and Its Stress on the Risk of Extreme Hydrological Events (EHEs) in the Kelani River Basin, Sri Lanka. *Int. J. Disaster Risk Reduct.* **2022**, *68*, 102715. [CrossRef]
124. Bui, D.T.; Khosravi, K.; Li, S.; Shahabi, H.; Panahi, M.; Singh, V.P.; Chapi, K.; Shirzadi, A.; Panahi, S.; Chen, W.; et al. New Hybrids of ANFIS with Several Optimization Algorithms for Flood Susceptibility Modeling. *Water* **2018**, *10*, 1210. [CrossRef]
125. Singh, A.K.; Sharma, A.K. GIS and a Remote Sensing Based Approach for Urban Flood-Plain Mapping for the Tapi Catchment, India. *Iahs-Aish Publ.* **2009**, *331*, 389–394.
126. Tomar, P.; Singh, S.K.; Kanga, S.; Meraj, G.; Kranjčić, N.; Đurin, B.; Pattanaik, A. Gis-Based Urban Flood Risk Assessment and Management—A Case Study of Delhi National Capital Territory (NCT), India. *Sustainability* **2021**, *13*, 12850. [CrossRef]
127. Schumann, G.; Giustarini, L.; Tarpanelli, A.; Jarihani, B.; Martinis, S. Flood Modeling and Prediction Using Earth Observation Data. *Surv. Geophys.* **2022**, 1–26. [CrossRef]
128. Mondal, B.K.; Sahoo, S. Application of Geospatial Techniques for Urban Flood Management: A Review. In *Spatial Modelling of Flood Risk and Flood Hazards. GIScience and Geo-Environmental Modelling*; Pradhan, B., Shit, P.K., Bhunia, G.S., Adhikary, P.P., Pourghasemi, H.R., Eds.; Springer Nature: Berlin/Heidelberg, Germany, 2022; pp. 225–236. [CrossRef]
129. Lammers, R.; Li, A.; Nag, S.; Ravindra, V. Prediction Models for Urban Flood Evolution for Satellite Remote Sensing. *J. Hydrol.* **2021**, *603*, 127175. [CrossRef]
130. Sadiq, R.; Akhtar, Z.; Imran, M.; Ofli, F. Integrating Remote Sensing and Social Sensing for Flood Mapping. *Remote Sens. Appl. Soc. Environ.* **2022**, *25*, 100697. [CrossRef]
131. Kucharczyk, M.; Hugenholtz, C.H. Remote Sensing of Environment Remote Sensing of Natural Hazard-Related Disasters with Small Drones: Global Trends, Biases, and Research Opportunities. *Remote Sens. Environ.* **2021**, *264*, 112577. [CrossRef]
132. Suthakaran, S.; Jayakody, S.; Subasinghe, S.; Seneviratne, N.; Alahakoon, R. Mapping the Flood Risk Exposure Using Open-Source Geospatial Tools and Techniques: A Case of Gampaha Divisional Secretariat Division, Sri Lanka. *J. Geosci. Environ. Prot.* **2022**, *10*, 18–31. [CrossRef]
133. Sowmya, K.; John, C.M.; Shrivasthava, N.K. Urban Flood Vulnerability Zoning of Cochin City, Southwest Coast of India, Using Remote Sensing and GIS. *Nat. Hazards* **2015**, *75*, 1271–1286. [CrossRef]
134. Dammalage, T.L.; Jayasinghe, N.T. Land-Use Change and Its Impact on Urban Flooding: A Case Study on Colombo District Flood on May 2016. *Eng. Technol. Appl. Sci. Res.* **2019**, *9*, 3887–3891. [CrossRef]
135. Smith, A.; Bates, P.D.; Wing, O.; Sampson, C.; Quinn, N.; Neal, J. New Estimates of Flood Exposure in Developing Countries Using High-Resolution Population Data. *Nat. Commun.* **2019**, *10*, 1814. [CrossRef]
136. Notaro, V.; Fontanazza, C.M.; Freni, G.; La Loggia, G. Assessment of Modelling Structure and Data Availability Influence on Urban Flood Damage Modelling Uncertainty. *Procedia Eng.* **2014**, *89*, 788–795. [CrossRef]
137. Hula, M.A.; Udoh, J.C. An Assessment of the Impact of Flood Events in Makurdi, Nigeria. *Civ. Environ. Res.* **2015**, *7*, 53–60.
138. Texier, P. Floods in Jakarta: When the Extreme Reveals Daily Structural Constraints and Mismanagement. *Disaster Prev. Manag. An Int. J.* **2008**, *17*, 358–372. [CrossRef]
139. Kubal, C.; Haase, D.; Meyer, V.; Scheuer, S. Integrated Urban Flood Risk Assessment—Adapting a Multicriteria Approach to a City. *Nat. Hazards Earth Syst. Sci.* **2009**, *9*, 1881–1895. [CrossRef]
140. Kadaverugu, A.; Nageshwar, C.; Viswanadh, R.G.K. Quantification of Flood Mitigation Services by Urban Green Spaces Using InVEST Model: A Case Study of Hyderabad City, India. *Model. Earth Syst. Environ.* **2020**, *7*, 589–602. [CrossRef]
141. Sahoo, S.N.; Pekkat, S. Detention Ponds for Managing Flood Risk Due to Increased Imperviousness: Case Study in an Urbanizing Catchment of India. *Nat. Hazards Rev.* **2018**, *19*, 05017008. [CrossRef]
142. Sarmah, T.; Das, S. Urban Flood Mitigation Planning for Guwahati: A Case of Bharalu Basin. *J. Environ. Manag.* **2018**, *206*, 1155–1165. [CrossRef]

143. Ali, M.H.; Bhattacharya, B.; Islam, A.K.M.S.; Islam, G.M.T.; Hossain, M.S.; Khan, A.S. Challenges for Flood Risk Management in Flood-Prone Sirajganj Region of Bangladesh. *J. Flood Risk Manag.* **2019**, *12*, e12450. [CrossRef]
144. Bashar, M.Z.I.; Karim, M.R.; Imteaz, M.A. Reliability and Economic Analysis of Urban Rainwater Harvesting: A Comparative Study within Six Major Cities of Bangladesh. *Resour. Conserv. Recycl.* **2018**, *133*, 146–154. [CrossRef]
145. Khan, A.N.; Ali, A. *Disaster Risk Reduction Methods, Approaches and Practices*; Springer: Berlin/Heidelberg, Germany, 2015; pp. 281–294. [CrossRef]
146. Lo, K.F.A.; Koralegedara, S.B. Effects of Climate Change on Urban Rainwater Harvesting in Colombo City, Sri Lanka. *Environments* **2015**, *2*, 105–124. [CrossRef]
147. Jonkman, S.N.; Dawson, R.J. Issues and Challenges in Flood Risk Management—Editorial for the Special Issue on Flood Risk Management. *Water* **2012**, *4*, 785–792. [CrossRef]
148. Sahu, A.; Bose, T.; Samal, D.R. Urban Flood Risk Assessment and Development of Urban Flood Resilient Spatial Plan for Bhubaneswar. *Environ. Urban. ASIA* **2021**, *12*, 269–291. [CrossRef]
149. CPHEEO. *Manual on Sewerage and Sewage Treatment*; Ministry of Urban Development: New Delhi, Indai, 2013.
150. Jha, A.K.; Bloch, R.; Lamond, J. *Cities and Flooding: A Guide to Integrated Urban Flood Risk Management for the 21st Century*; World Bank: Washington, DC, USA, 2012.
151. Gupta, K. Urban Flood Resilience Planning and Management and Lessons for the Future: A Case Study of Mumbai, India. *Urban Water J.* **2007**, *4*, 183–194. [CrossRef]
152. Ghosh, S.; Karmakar, S.; Saha, A.; Mohanty, M.P.; Ali, S.; Raju, S.K.; Krishnakumar, V.; Sebastian, M.; Behera, M.R.; Ashrit, R.; et al. Development of India's First Integrated Expert Urban Flood Forecasting System for Chennai. *Curr. Sci.* **2019**, *117*, 741–745. [CrossRef]
153. Gupta, K.; Nikam, V. Technological and Innovative Measures to Improve Flood Disaster Recovery Following Mumbai 2005 Mega-Flood. In *Disaster Recovery: Used or Misused Development Opportunity*; Shaw, R., Ed.; Springer: Tokyo, Japan, 2014; pp. 287–297, ISBN 978-4-431-54255-1.
154. Das, K. Guwahati Gets an Experimental Flood Warning System. *Sci. Wire*. 2020. Available online: https://science.thewire.in/environment/guwahati-assam-flood-warning-system/ (accessed on 10 October 2021).
155. Mohanty, M.P.; Mudgil, S.; Karmakar, S. Flood Management in India: A Focussed Review on the Current Status and Future Challenges. *Int. J. Disaster Risk Reduct.* **2020**, *49*, 101660. [CrossRef]
156. Bhuvana, N.; Arul Aram, I. Facebook and Whatsapp as Disaster Management Tools during the Chennai (India) Floods of 2015. *Int. J. Disaster Risk Reduct.* **2019**, *39*, 101135. [CrossRef]
157. Riaz, K.; Hassan, A.; Fakhruddin, S.H. Community Participation in Flood Management. In *Options for Flood Risk and Damage Reduction in Bangladesh*; Siddiqui, K., Hossain, A.N., Eds.; The University Press Ltd.: Dhaka, Bangladesh, 2010.
158. Deltares. *Mobile Services for Flood Early Warning in Bangladesh: Final Report*; Deltares: Silver Spring, MD, USA, 2015.
159. World Bank Bangladesh and World Bank Sign $113 Million to Improve Weather Forecasting and Early Warning Systems. Available online: https://www.worldbank.org/en/news/press-release/2017/04/05/bangladesh-and-world-bank-sign-113-million-to-improve-weather-forecasting-and-early-warning-systems (accessed on 20 August 2021).
160. Rahman, A.U.; Shaw, R. Disaster Resilience: Generic Overview and Pakistan Context. In *Disaster Risk Reduction Approaches in Pakistan*; Rahman, A.U., Khan, A.N., Shaw, R., Eds.; Springer: Berlin/Heidelberg, Germany, 2015.
161. Mustafa, D.; Gioli, G.; Qazi, S.; Waraich, R.; Zahoor, R. Gendering Flood Early Warning Systems: The Case of Pakistan. *Environ. Hazards* **2015**, *7891*, 312–328. [CrossRef]
162. Premasiri, R.; Chandranath, R. Development of Warning System for Mitigation of Urban Flood Hazard. In Proceedings of the 37th Asian Conference Remote Sensing, ACRS 2016, Colombo, Sri Lanka, 17–21 October 2016; Volume 3, pp. 1771–1777.
163. Budimir, M.; Donovan, A.; Brown, S.; Shakya, P.; Gautam, D.; Uprety, M.; Cranston, M.; Sneddon, A.; Smith, P.; Dugar, S. Communicating Complex Forecasts: An Analysis of the Approach in Nepal's Flood Early Warning System. *Geosci. Commun.* **2020**, *3*, 49–70. [CrossRef]
164. UNDRR. *Disaster Risk Reduction in Nepal: Status Report 2019*; UNDRR: Bangkok, Thailand, 2019.
165. DHMS. Flood Early Warning. Available online: http://www.hydromet.gov.bt/?q=21 (accessed on 5 June 2021).
166. ICIMOD. *Flood Early Warning Systems in Bhutan*; ICIMOD: Kathmandu, Nepal, 2016.
167. Noori, M.M.; Sherzad, M.H. *Current State of Early Warning System in Afghanistan: An Outlook of the Flood Early Warning System*; UN: New York, NY, USA, 2020.
168. Roy, C.; Sarkar, S. The Current Cyclone Early Warning System in Bangladesh: Providers' and Receivers' Reviews. *Int. J. Disaster Risk Reduct.* **2015**, *12*, 285–299. [CrossRef]
169. Brouwer, R.O.Y.; Akter, S.; Brander, L.; Haque, E. Economic Valuation of Flood Risk Exposure and Reduction in a Severely Flood Prone Developing Country. *Environ. Dev. Econ.* **2009**, *14*, 397–417. [CrossRef]
170. Leitão, J.P.; Boonya-aroonnet, S.; Prodanović, D.; Maksimović, Č. The Influence of Digital Elevation Model Resolution on Overland Flow Networks for Modelling Urban Pluvial Flooding. *Water Sci. Technol.* **2009**, *60*, 3137–3149. [CrossRef]
171. Al-Suhili, R.; Cullen, C.; Khanbilvardi, R. An Urban Flash Flood Alert Tool for Megacities-Application for Manhattan, New York City, USA. *Hydrology* **2019**, *6*, 56. [CrossRef]
172. Othmer, F.J.; Becker, D.; Schulte, L.M.; Greiving, S. A Methodological Approach to Municipal Pluvial Flood Risk Assessment Based on a Small City Case Study. *Sustainability* **2020**, *12*, 10487. [CrossRef]

173. Mihu-pintilie, A.; Alexandru, U.; Cuza, I.; Cimpianu, C.I.; Alexandru, U.; Cuza, I.; Stoleriu, C.; Alexandru, U.; Cuza, I. Using High-Density LiDAR Data and 2D Streamflow Hydraulic Modeling to Improve Urban Flood Hazard. *Water* **2019**, *11*, 1832. [CrossRef]
174. Chen, G.; Hou, J.; Zhou, N.; Yang, S.; Tong, Y.; Su, F.; Huang, L.; Bi, X. High-Resolution Urban Flood Forecasting by Using a Coupled Atmospheric and Hydrodynamic Flood Models. *Front. Earth Sci.* **2020**, *8*, 545612. [CrossRef]
175. Wang, B.; Loo, B.P.Y.; Zhen, F.; Xi, G. Urban Resilience from the Lens of Social Media Data: Responses to Urban Flooding in Nanjing, China. *Cities* **2020**, *106*, 102884. [CrossRef]
176. de Almeida, G.A.M.; Bates, P.; Ozdemir, H. Modelling Urban Floods at Submetre Resolution: Challenges or Opportunities for Flood Risk Management? *J. Flood Risk Manag.* **2018**, *11*, S855–S865. [CrossRef]
177. Saravi, S.; Kalawsky, R.; Joannou, D.; Casado, M.R.; Fu, G.; Meng, F. Use of Artificial Intelligence to Improve Resilience and Preparedness against Adverse Flood Events. *Water (Switzerland)* **2019**, *11*, 973. [CrossRef]
178. Esfandiari, M.; Abdi, G.; Jabari, S.; McGrath, H.; Coleman, D. Flood Hazard Risk Mapping Using a Pseudo Supervised Random Forest. *Remote Sens.* **2020**, *12*, 3206. [CrossRef]
179. Shrestha, S.; Cui, S.; Xu, L.; Wang, L.; Manandhar, B.; Ding, S. Impact of Land Use Change Due to Urbanisation on Surface Runoff Using GIS-Based SCS–CN Method: A Case Study of Xiamen City, China. *Land* **2021**, *10*, 839. [CrossRef]
180. Skilodimou, H.D.; Bathrellos, G.D.; Alexakis, D.E. Flood Hazard Assessment Mapping in Burned and Urban Areas. *Sustain.* **2021**, *13*, 4455. [CrossRef]
181. Joo, H.; Choi, C.; Kim, J.; Kim, D.; Kim, S.; Kim, H.S. A Bayesian Network-Based Integrated for Flood Risk Assessment (InFRA). *Sustainability* **2019**, *11*, 3733. [CrossRef]
182. Liu, W.C.; Hsieh, T.H.; Liu, H.M. Flood Risk Assessment in Urban Areas of Southern Taiwan. *Sustainability* **2021**, *13*, 3180. [CrossRef]
183. Vojtek, M.; Vojteková, J. Flood Susceptibility Mapping on a National Scale in Slovakia Using the Analytical Hierarchy Process. *Water* **2019**, *11*, 364. [CrossRef]
184. Khoirunisa, R. Forecasted Climate Analysis from 2000 to 2100 Using RCP 4.5 and RCP 8.5 Model Scenario as A Hazard Early-Warning System in Prague City, Czech Republic. *Smart City* **2022**, *2*, 4. [CrossRef]
185. Chan, F.K.S.; Griffiths, J.A.; Higgitt, D.; Xu, S.; Zhu, F.; Tang, Y.T.; Xu, Y.; Thorne, C.R. "Sponge City" in China—A Breakthrough of Planning and Flood Risk Management in the Urban Context. *Land Use Policy* **2018**, *76*, 772–778. [CrossRef]
186. Randall, M.; Sun, F.; Zhang, Y.; Jensen, M.B. Evaluating Sponge City Volume Capture Ratio at the Catchment Scale Using SWMM. *J. Environ. Manag.* **2019**, *246*, 745–757. [CrossRef]
187. Yin, D.; Evans, B.; Wang, Q.; Chen, Z.; Jia, H.; Chen, A.S.; Fu, G.; Ahmad, S.; Leng, L. Integrated 1D and 2D Model for Better Assessing Runoff Quantity Control of Low Impact Development Facilities on Community Scale. *Sci. Total Environ.* **2020**, *720*, 137630. [CrossRef]
188. Zhang, L.; Ye, Z.; Shibata, S. Assessment of Rain Garden Effects for the Management of Urban Storm Runoff in Japan. *Sustainability* **2020**, *12*, 9982. [CrossRef]
189. Costa, S.; Peters, R.; Martins, R.; Postmes, L.; Keizer, J.J.; Roebeling, P. Effectiveness of Nature-Based Solutions on Pluvial Flood Hazard Mitigation: The Case Study of the City of Eindhoven (The Netherlands). *Resources* **2021**, *10*, 24. [CrossRef]
190. Goswami, S.; Basak, S. Is Urban India Going Underwater Again? Available online: https://wri-india.org/blog/urban-india-going-underwater-again (accessed on 12 July 2021).
191. Goniewicz, K.; Burkle, F.M. Analysis of the Potential of IT System Support in Early Warning Systems: Mitigating Flood Risk in Poland. *Prehosp. Disaster Med.* **2019**, *34*, 563–565. [CrossRef]
192. Rodriguez Castro, D.; Roucour, S.; Archambeau, P.; Cools, M.; Erpicum, S.; Habchi, I.; Hardy, J.; Pirotton, M.; Weber, L.; Teller, J.; et al. Modelling Direct Flood Losses: What Can We Learn from the July 2021 Flood in the Meuse Basin (Belgium)? *KAHR Sci. Conf.* **2022**, 2021–2022.
193. Zhou, Q.; Panduro, T.E.; Thorsen, B.J.; Arnbjerg-Nielsen, K. Adaption to Extreme Rainfall with Open Urban Drainage System: An Integrated Hydrological Cost-Benefit Analysis. *Environ. Manag.* **2013**, *51*, 586–601. [CrossRef] [PubMed]
194. Arnbjerg-Nielsen, K.; Fleischer, H.S. Feasible Adaptation Strategies for Increased Risk of Flooding in Cities Due to Climate Change. *Water Sci. Technol.* **2009**, *60*, 273–281. [CrossRef] [PubMed]
195. Zhou, Q.; Mikkelsen, P.S.; Halsnæs, K.; Arnbjerg-Nielsen, K. Framework for Economic Pluvial Flood Risk Assessment Considering Climate Change Effects and Adaptation Benefits. *J. Hydrol.* **2012**, *414–415*, 539–549. [CrossRef]
196. Pyke, C.; Warren, M.P.; Johnson, T.; Lagro, J.; Scharfenberg, J.; Groth, P.; Freed, R.; Schroeer, W.; Main, E. Landscape and Urban Planning Assessment of Low Impact Development for Managing Stormwater with Changing Precipitation Due to Climate Change. *Landsc. Urban Plan.* **2011**, *103*, 166–173. [CrossRef]
197. Zahmatkesh, Z.; Burian, S.J.; Karamouz, M.; Tavakol-davani, H.; Goharian, E. Low-Impact Development Practices to Mitigate Climate Change Effects on Urban Stormwater Runoff: Case Study of New York City. *J. Irrig. Drain. Eng.* **2015**, *141*, 04014043. [CrossRef]
198. Kang, N.; Kim, S.; Kim, Y.; Noh, H.; Hong, J.S. Urban Drainage System Improvement for Climate Change Adaptation. *Water* **2016**, *8*, 268. [CrossRef]
199. Sebti, A.; Fuamba, M.; Bennis, S. Optimization Model for BMP Selection and Placement in a Combined Sewer. *J. Water Resour. Plan. Manag.* **2016**, *142*, 04015068. [CrossRef]

200. Olsson, J.; Amaguchi, H.; Alsterhag, E. Adaptation to Climate Change Impacts on Urban Storm Water: A Case Study in Arvika, Sweden. *Clim. Chang.* **2013**, *116*, 231–247. [CrossRef]
201. Tscheikner-gratl, F.; Zeisl, P.; Kinzel, C.; Leimgruber, J.; Ertl, T.; Rauch, W.; Kleidorfer, M. Lost in Calibration: Why People Still Do Not Calibrate Their Models, and Why They Still Should—A Case Study from Urban Drainage Modelling. *Water Sci. Technol.* **2016**, *74*, 2337–2348. [CrossRef]
202. Babovic, F.; Mijic, A. Economic Evaluation of Adaptation Pathways for an Urban Drainage System Experiencing Deep Uncertainty. *Water* **2019**, *11*, 531. [CrossRef]

MDPI AG
Grosspeteranlage 5
4052 Basel
Switzerland
Tel.: +41 61 683 77 34

Land Editorial Office
E-mail: land@mdpi.com
www.mdpi.com/journal/land

Academic Open
Access Publishing

mdpi.com

ISBN 978-3-7258-6379-2